

**Proceedings of the Workshop  
on Photocathodes for Polarized Electron Sources  
for Accelerators**

**Stanford Linear Accelerator Center  
Stanford, California**

**September 8 - 10, 1993**

Prepared for the Department of Energy  
under contract number DE-AC03-76SF00515

**STANFORD LINEAR ACCELERATOR CENTER**  
Stanford University • Stanford, California

SLAC-432 Rev.  
CONF-9309288  
US-414  
(M)

**PROCEEDINGS OF THE WORKSHOP ON  
PHOTOCATHODES FOR POLARIZED ELECTRON  
SOURCES FOR ACCELERATORS**

September 8-10, 1993

Stanford Linear Accelerator Center  
Stanford University, Stanford, California 94309

*Editors*

M. Chatwell  
J. Clendenin  
T. Maruyama  
D. Schultz

*Prepared for the Department of Energy under contract number DE-AC03-76SF00515. Printed in the United States of America. Available from the National Technical Information Service, U.S. Department of Commerce, 5285 Port royal Road, Springfield, Virginia 22161.*

April 8, 1994

**Workshop on  
Photocathodes for Polarized Electron Sources for  
Accelerators**

September 8 - 10, 1993

The revised edition of **SLAC 432**, the *Proceedings of the Workshop on Photocathodes for Polarized Electron Sources for Accelerators*, adds pages 228-1 through 228-36 and makes a few minor changes in the non-scientific portions of the Proceedings. All of the original material including the original page numbers are retained.

In light of the above, our recommendation is that you replace the original SLAC 432 with the revised version, discarding the original.

The Editors

# Proceedings of the Workshop on Photocathodes for Polarized Electron Sources for Accelerators

## Table of Contents

Operating Experience with the MAMI Polarized Electron Source.....	1
<i>Kurt Aulenbacher, U. Mainz</i>	
Experiences with Strained GaAs Photocathodes.....	13
<i>Guenter Baun, Universität Bielefeld</i>	
Polarized e <sup>-</sup> Source Requirements for Linear Colliders.....	25
<i>Stan Ecklund, SLAC</i>	
MIT-Bates Polarized Injector System.....	33
<i>Manouchar Farklondeh, MIT-Bates Linear Accelerator Center</i>	
A New Polarized Electron Source and Electron Polarimeter.....	67
<i>Timothy Gay, University of Missouri-Rolla</i>	
Experimental Study on the Time Resolution of Negative Electron Affinity GaAs.....	85
<i>Vincenzo Guidi, Ferrara</i>	
Polarized Electron Source for the Stanford Linear Collider.....	101
<i>Lowell Klaisner, SLAC</i>	
Energy and Spin Analysis of Photoelectrons from Layered Semiconductor Structures.....	122
<i>Georges Lampel, PMC Ecole Polytechnique</i>	
The Characterization of Strained-Layer GaAs Photocathodes Using Photoluminescence.....	139
<i>Robin Mair, SLAC</i>	
Spin-Polarized Photoemission from InGaAs, AlGaInAs, GaAs, and GaAsP Strained Layers.....	157
<i>Yuri Mamaev, Division of Experimental Physics, St. Petersburg Technical University</i>	
High Polarization Photocathode R&D at SLAC.....	174
<i>Takashi Maruyama, SLAC</i>	
Low Energy Polarized Electron Source Test Facilities at SLAC.....	211
<i>Gregory Mulhollan, SLAC</i>	
High Polarization Cathode Research in Japan.....	221
<i>T. Nakanishi, Nagoya U.</i>	



Application of the GaAs Polarized Electron Source to Studies of Surface Magnetism .....	229
<i>Daniel Pierce, Electron Physics Group, NIST</i>	
Thermal Stability of Cs on NEA III-V-Photocathodes and its Effect on Quantum Efficiency.....	248
<i>Erwin Reichert, U. Mainz</i>	
AFEL Accelerator.....	261
<i>Richard Sheffield, Los Alamos National Laboratory</i>	
Production and Detection of SPIN Polarized Electrons .....	281
<i>H. Siegmann, ETH Hönggerberg (Zürich)</i>	
Emittance Measurements on a 100-keV Beam from a GaAs Photocathode Electron Gun .....	298
<i>Charles Sinclair, CEBAF</i>	
Modern Theory of Photoemission and its Applications to Practical Photocathodes ....	314
<i>William Spicer, Stanford University</i>	
Experimental Studies of the Charge Limit Phenomenon in GaAs Photocathodes.....	344
<i>Huan Tang, SLAC</i>	
New Material for Photoemission Electron Source: Semiconductor Alloy InGaAsP Grown on GaAs Substrate.....	369
<i>A.S. Terekhov, Institute of Semiconductor Physics</i>	
NEA Photocathode Surface Preparation: Technology and Physics.....	382
<i>A.S. Terekhov, Institute of Semiconductor Physics</i>	
Metalorganic Chemical Vapor Deposition of GaAs-GaAsP Spin-Polarized Photocathodes.....	397
<i>S.M. Vernon, Spire Corporation</i>	
Development of Photocathode Injectors for JLC-ATF .....	407
<i>M. Yoshioka, KEK</i>	
Effect of Radiation Trapping on Polarization of Photoelectrons from Semiconductors .....	435
<i>Max Zolotarev, SLAC</i>	
Energy Analysis of Electrons Emitted by a Semiconductor Photocathode .....	445
<i>S. Zwickler, U. Heidelberg</i>	
List of Workshop Participants .....	457



**Workshop on**  
**Photocathodes for Polarized Electron Sources for Accelerators**  
September 8 - 10, 1993

Photograph identification front to back, left to right.

Prone:	R. Miller
Kneeling:	D. Pierce A. Herrera-Gómez H. Aoyagi J. Frisch P. Sáez J. Clendenin H. Poppa M. Yoshioka H. Tang
Sitting:	G. Baum W. Spicer R. Kirby M. Farkhondeh C. Prescott E. Garwin G. Lampel H. Siegmann S. Ecklund
Standing:	T. Nakanishi T. Gay F. Ciccacci D. Schultz Y. Mamaev J. Sheppard L. Klaisner N. Papadakis C. Sinclair K. Aulenbacher A. Terekhov E. Reichert D. Yeremian F-J. Decker V. Guidi R. Sheffield (unfortunately partially obscured) V. Aebi (also partially obscured) T. Maruyama G. Mulhollan K. Costello E. Tsentalovich A. Odian R. Alley J. Turner

**Kurt Aulenbacher  
U. Mainz**

**Operating Experience with the MAMI Polarized  
Electron Source**

# Operating experience with the MAMI polarized electron source

The B2-collaboration

H.G.Andresen, K.Aulenbacher, T.Dombo, P.Drescher, H.Euteneuer, H.Fischer,  
D.v.Harrach, P.Hartmann, P.Jennewein, K.H.Kaiser, S.Koebis, H.J.Kreidel,  
C.Nachtigall, S.Pluetzer, E.Reichert, K.H.Steffens, T.Weis

presented by Kurt Aulenbacher

## Abstract

A polarized electron source is used for nuclear physics experiments at the Mainz 855 MeV electron accelerator since summer 1992. The polarized beam is produced by photoemission from a  $GaAs_{1-x}P_x$ -semiconductor crystal. The normalized emittance of the 100 keV d.c.-beam is about  $0.32 \pi \cdot mm \cdot mrad \cdot m_0c$ , fulfilling the demands given by the acceptance of the accelerator. The beam polarization was determined to be 34% by a Mott polarimeter installed in the 100keV injection beamline. The operation time of the source is about 100 hours at  $50 \mu A$  primary current. Up to now the total estimated runtime for several nuclear physics experiments is more than 500 hours, primary currents were ranging from 5 to  $60 \mu A$ . Lifetime effects correlated with high d.c.-currentdensities are discussed.

## 1 Introduction

The Mainz-Microtron (MAMI) produces a high quality c.w.-electron beam at 855MeV [HER76]. It is an instrument dedicated to intermediate energy (nuclear-)physics experiments. Many experiments use a polarized electron beam, e.g. those trying to do a precision measurement of the electric form factor of the neutron [HEI90]. The requirements for the polarized beam are given in table 1.

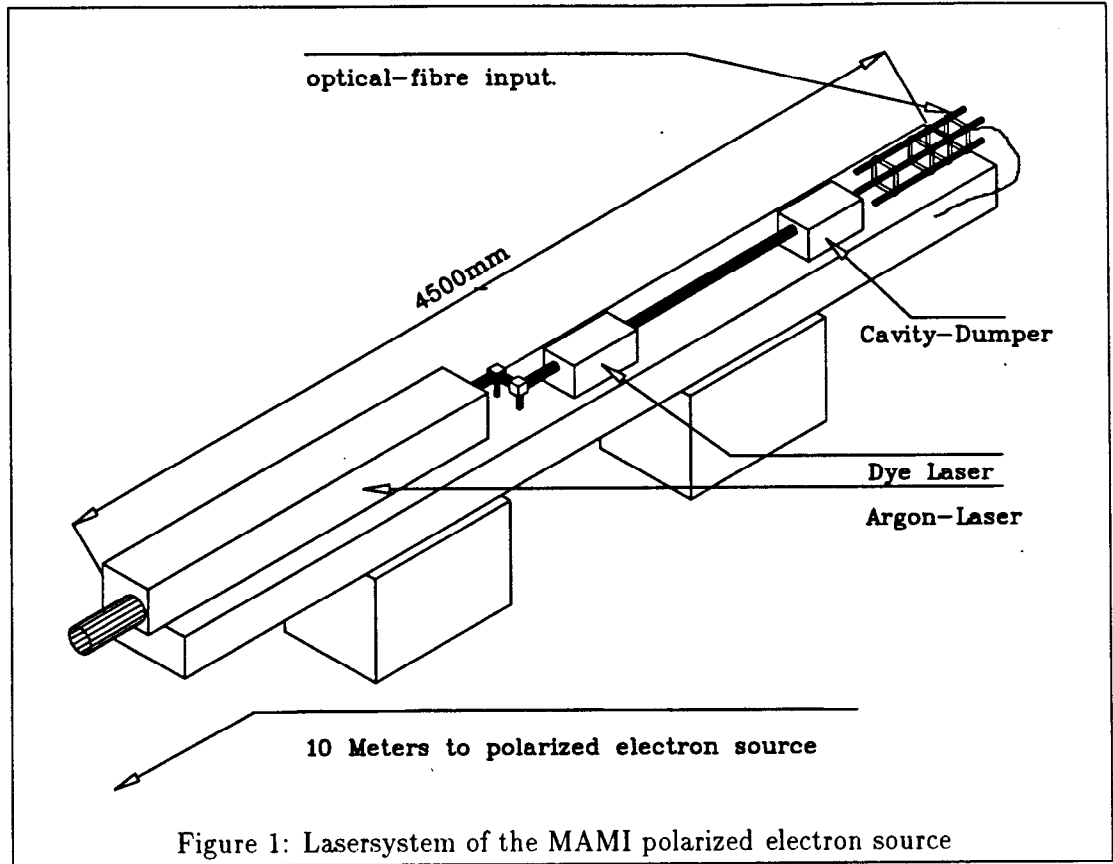
Two of the values given in table 1 influence the operation of the source severely: In the first place the longitudinal acceptance of the accelerator only permits a transmission of 20% to the target. Under this conditions the average current at the source has to be 5 times larger than that at the target position. The other stringent boundary condition is also resulting from the operating principle of MAMI: The normalized emittance at the injection point must not exceed  $0.5\pi \cdot mm \cdot mrad \cdot m_0c$  if one wants to avoid operation with excessive background. Both boundary conditions together lead to the demand that an electron beam of high average brightness has to be produced.

## 2 Experimental setup

### 2.1 Lasersystem

Figure 1 shows the laser system of the MAMI polarized electron source. Because our cathode material is bulk- $GaAs_{0.6}P_{0.4}$  with a bandgap of 1.88 eV a laser operating at approximately

## 2 EXPERIMENTAL SETUP



640 nm is required. This can be achieved by a d.c.-dye-laser system that is pumped by an argon-ion-laser. The dye-laser-cavity contains an acousto-optic-modulator ('cavity-dumper') in order to obtain flexibility in the time structure of the produced laser beam [MAY70]. This is necessary because one has to provide an appropriate time structure of the electron-beam. Though operation for experiments requires a d.c.-beam, the beam diagnostics in the microtron sections of MAMI is based on r.f.-induction by 8ns long electron pulses of about 1mA pulse height. These pulses should have a repetition rate of 10kHz. It is necessary to

PARAMETER	VALUE	REMARKS
Polarization	40%	based on beam time estimation for $G_E^N$ - Experiment
av. current	5 - 10 $\mu A$	
cont. operation time	100 - 200h	
accelerator transmission	0.2	values given by the design of accelerator
injection energy	100keV	
norm. emittance	$0.5\pi \cdot mm \cdot mrad \cdot m_0 c$	
time structure	d.c. + 8ns, 10kHz	

Table 1: Parameters for the operation of the polarized source.

### 3 RESULTS CONCERNING POLARIZATION AND EMITTANCE

switch between both modes of operation without changing the parameters of the electron beam.

These demands can be met by optical modulation of the electron beam via the cavity dumping mechanism.

The laser beam is transported towards the source by a 20 meter long single-mode fibre which preserves linear polarization. The pointing stability of the laser spot on the cathode surface is good because the output coupler of the optical fibre is attached directly to the support of the polarized source. This is important because even small deviations ( $<0.1\text{mm}$ ) of the position will lead to intolerable fluctuations of the electron beam.

#### 2.2 polarized electron source

Figure 2 shows the 100keV-source and the first part of the injection beamline. The laser beam emerges from the output coupler of the fibre, passes through the polarization optics and is then focussed onto the cathode. The GaAsP-crystal is held at a negative potential of 100kV. Figure 3 displays a magnified view of the central vacuum chamber of the source. The electron beam is accelerated on a ten centimeter long distance towards the bottom of the vacuum chamber which forms the anode for the electron beam. The electrode geometry has been calculated using the Herrmannsfeldt-EGUN code [HER79]. The front ends of the electrodes have not only been designed to produce an optimized electron beam but have also a special shape that minimizes the electric field gradient on the surface. This is necessary to avoid field emission effects caused by the cesiation of the electrode surface during the cathode activation process.

In the polarized source all devices needed for beam optics and crystal preparation are combined in one vacuum chamber. This offers the advantage that recesiation may be done during operation without interference with the experiment. Pumping speed inside the source is provided by a 110l/s Ion Pump and a 500l/s NEG-pump. These are attached directly to the accelerating stage/prep. chamber by ports of 150mm diameter (see fig: 2 and 3).

During transportation through the injection-beamline the beam is focussed by quadrupoles and bending is done by alpha-magnets. A differential pumping stage is used for decoupling the UHV-vacuum-system of the source from the  $10^{-8}\text{mbar}$ -vacuum of MAMI.

### 3 Results concerning polarization and emittance

#### 3.1 polarization measurements

Only bulk-GaAsP-crystals have been used so far as a cathode material. For this reason the degree of beam-polarization was 34%. This value was measured with a Mott-polarimeter that is integrated in the 100keV beamline. At 855 MeV a Moeller polarimeter offers the possibility to determine the orientation and the degree of the polarization. So far the polarizations measured by the Mott and the Moeller polarimeter are in agreement with each other in the range of their error bars.

Due to the ( $g-2$ )-precession during the 159 beam-recirculations in MAMI a deviation from longitudinal spin orientation at 855MeV had to be expected. This is demonstrated in figure 4: If the beam is injected into the accelerator with longitudinal polarization the Moeller scattering asymmetry does not reach its maximum value. A solution of this problem is to

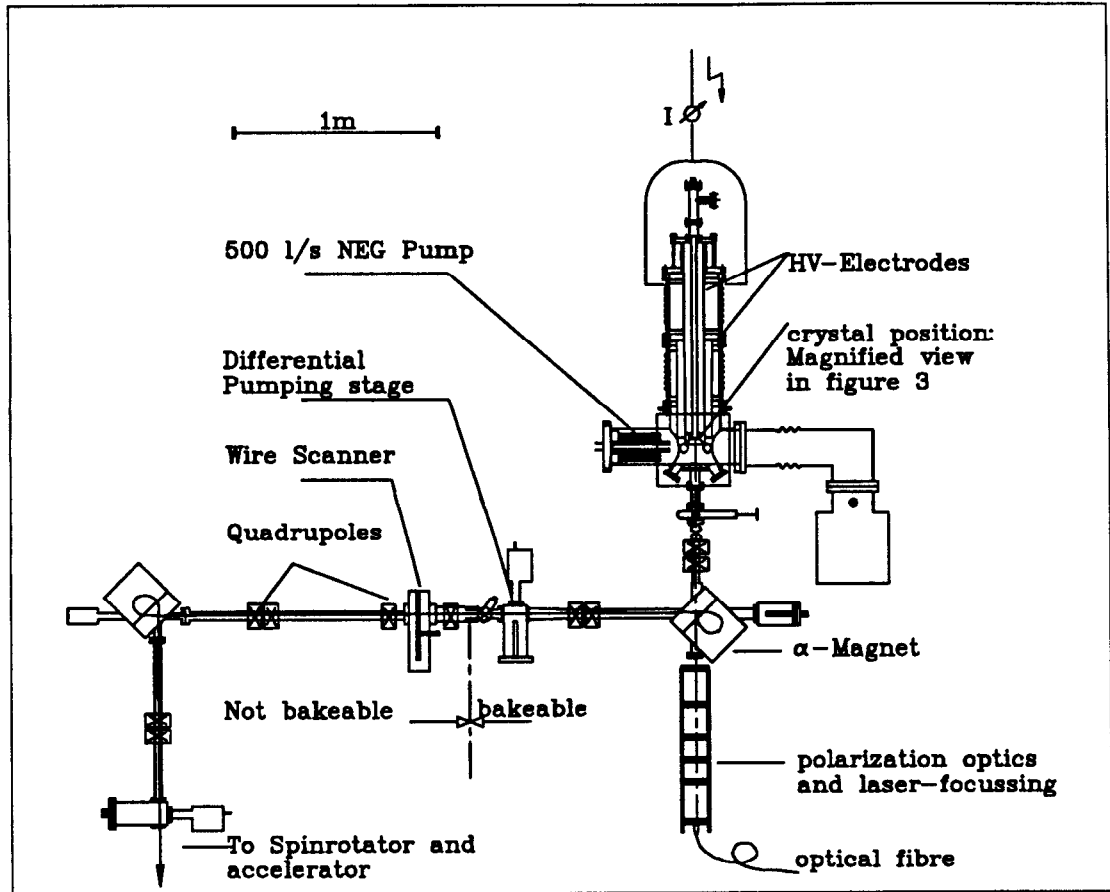


Figure 2: 100keV Polarized electron source and first part of injection beamline

rotate the polarization in the accelerator plane by the spin-rotator that is integrated in the 100keV injection beamline. This device is described in [STE93]. At a rotation angle of -50 degrees the maximum longitudinal polarization component is achieved. The spin rotator setting once found had not to be changed for more than half a year, which is due to the excellent energy stability ( $\frac{\Delta E}{E} \leq 1 \cdot 10^{-4}$ ) of the microtron.

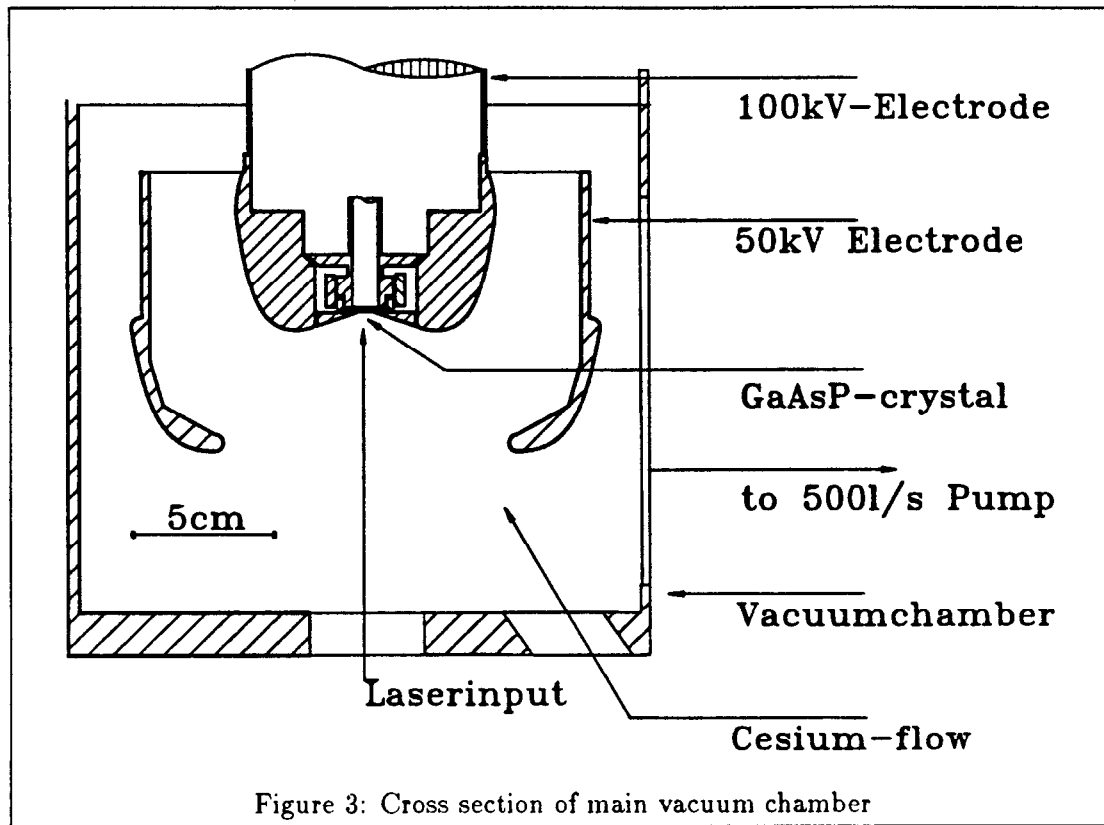
### 3.2 Emittance

As mentioned above the emittance should not exceed a value of  $0.5\pi \cdot mm \cdot mrad \cdot m_0c$  at the injection point.

The value of emittance should be a linear function of the laser spot diameter. This was confirmed by experimental data.

Some increase of emittance was observed in the injection system. For this reason the emittance at the source was even further reduced in order to compensate for that. The final value of the emittance at the source was  $0.32\pi mm \cdot mrad \cdot m_0c$ . This was achieved at a laser spot diameter ( $1/e^2$  points) of 0.29mm. It is clear that as a consequence of the small emitting area the average current density on the area is high. The average current density used in experiments was as high as  $70mA/cm^2$ .





A summary of the most important operating parameters is given in table 2.

## 4 Operational stability

### 4.1 Stability under high voltage

It is remarkable that a satisfying stability during high voltage operation could only be achieved after the field emission current had been reduced below the detection limit ( $\approx 10nA$ ). This was done by minimizing the field gradients at the electrode surfaces. Under this conditions there is no need for high voltage processing of the electrode which would certainly damage the crystal.

### 4.2 Effect of recession

The left hand side of figure 5 shows the decay of the photocathode yield during operation at a current of  $20\mu A$ . The data are fitted by an exponential curve with a decay constant of  $\tau = 20h^{-1}$ .

The solid line at the bottom of the graph indicates the minimum quantum efficiency (q.e.) required for the production of  $20\mu A$  beam current (These data were taken during a  $D(\vec{\epsilon}, e'\vec{n})$ -Experiment.). After the first 20 hours of operation we decided to recessiate the cathode. This is possible in our configuration without affecting the experiment.

## 4 OPERATIONAL STABILITY

PARAMETER	VALUE	REMARKS
quantum efficiency	0.5-0.9%	
polarization	0.34	longitudinal at 855 MeV
vacuum stability	$\approx 1000\text{h}$	$>4000\text{h}$ recessiated
field emission	$<10\text{nA}$	after in situ prep. at 100kV
emittance	$0.32\pi \cdot \text{mm} \cdot \text{mrad} \cdot m_0c$	0.29mm diameter of laserspot
av. current density	$70\text{mA}/\text{cm}^2$	at $50\mu\text{A}$ av. current
cont. operation time	150-200h	at $20\mu\text{A}$
operation time @ $50\mu\text{A}$	$>100\text{h}$	with movement of laser-spot

Table 2: Operating parameters of the MAMI-PES. All values correspond to 642nm Laser-wavelength.

In the right hand part of figure 5 the results are shown on a larger time scale. Cesium was switched on after 20 hours and a continuous Cs-flow was maintained until q.e. reached its maximum again. After this the decay constant was again about 20 hours, so that recession became necessary in periodic intervals. In this mode of operation there is obviously still a decrease in q.e.: The maxima of the curve after recession may still be fitted by an exponential decay. The decay constant of this new exponential curve is  $\tau = 95\text{h}^{-1}$ . Because the initial q.e. was a factor of 7 higher than the minimum value required, it was possible to compensate for the decrease of q.e. by increasing the laser power. The maximum possible continuous operation time would have been 150-200 hours. We did not reach this limit because the experiment was successfully completed before.

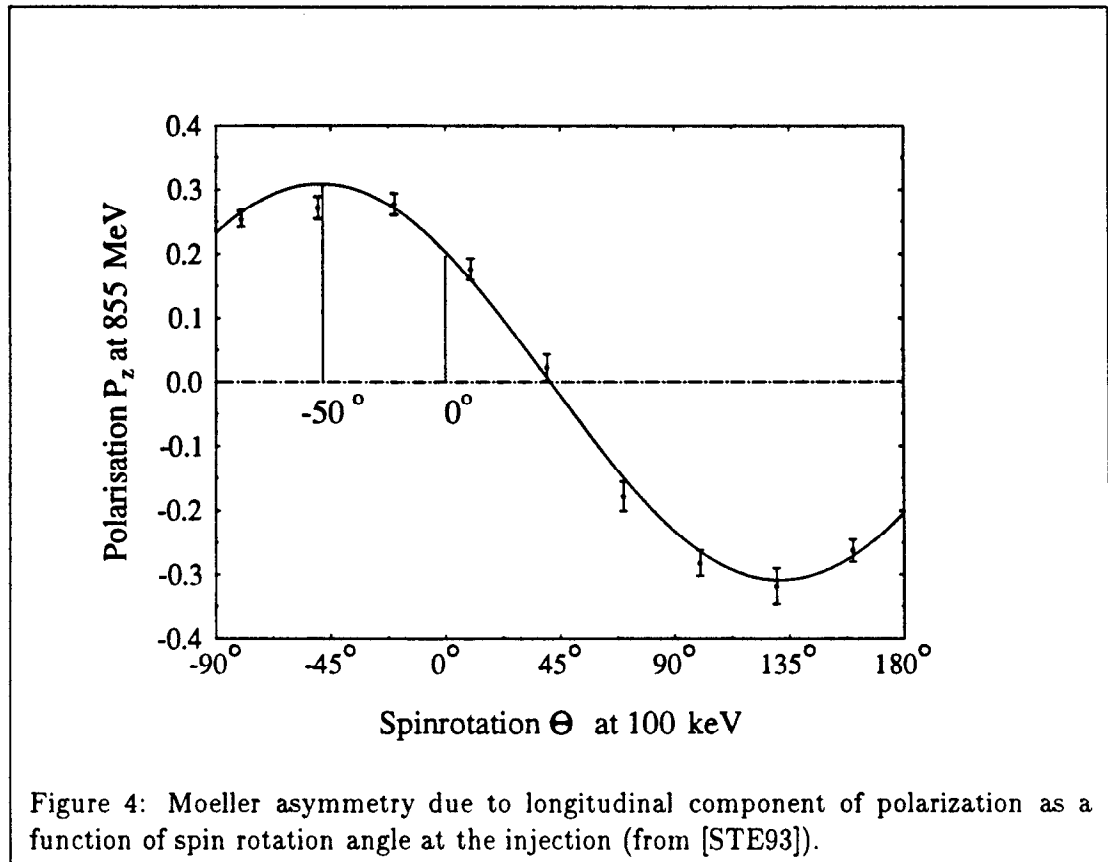
### 4.3 Local changes in quantum efficiency during operation

In order to find the effect that is responsible for the limited lifetime even with recession an investigation concerning the q.e.-distribution on the crystal was carried out. Our guess was, that the reduction of q.e. may be restricted to the emitting spot itself. For this reason q.e. was measured on a square area of the cathode of  $2\text{mm} \times 2\text{mm}$  size<sup>1</sup> at a mesh of points  $0.2\text{mm}$  apart from each other. The emitting spot during source operation was located in the center of the square.

The specific geometry used in the experiment needs some further explanation: In the left hand side of figure 6 the investigated area (square) does not include the center of the crystal, i.e. the starting point of the electron beam is not on the symmetry-axis of the gun. This is due to practical reasons, because we found out that emitting spots in the periphery of the crystal have higher q.e. and longer lifetimes than those near the symmetry-axis. The focussing properties of the polarized gun offer the possibility to start the beam on any point

<sup>1</sup>So far no automatic data acquisition was available for this type of experiment. It would of course be better to investigate the whole crystal surface.

#### 4 OPERATIONAL STABILITY



of the crystal surface without affecting beam characteristics too much.

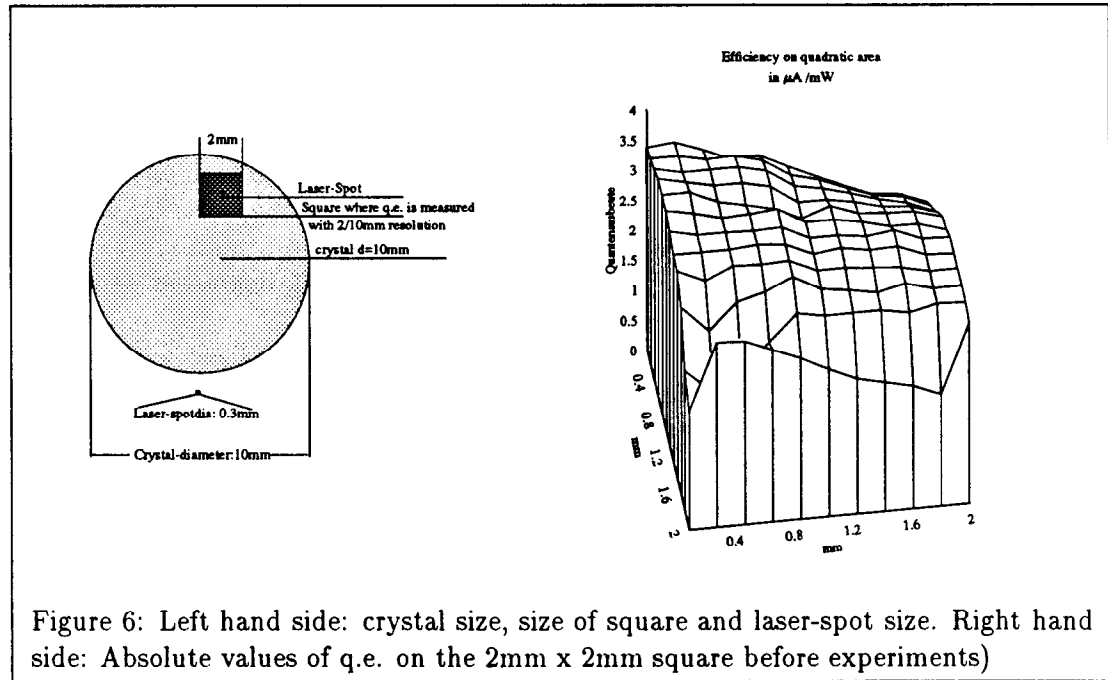
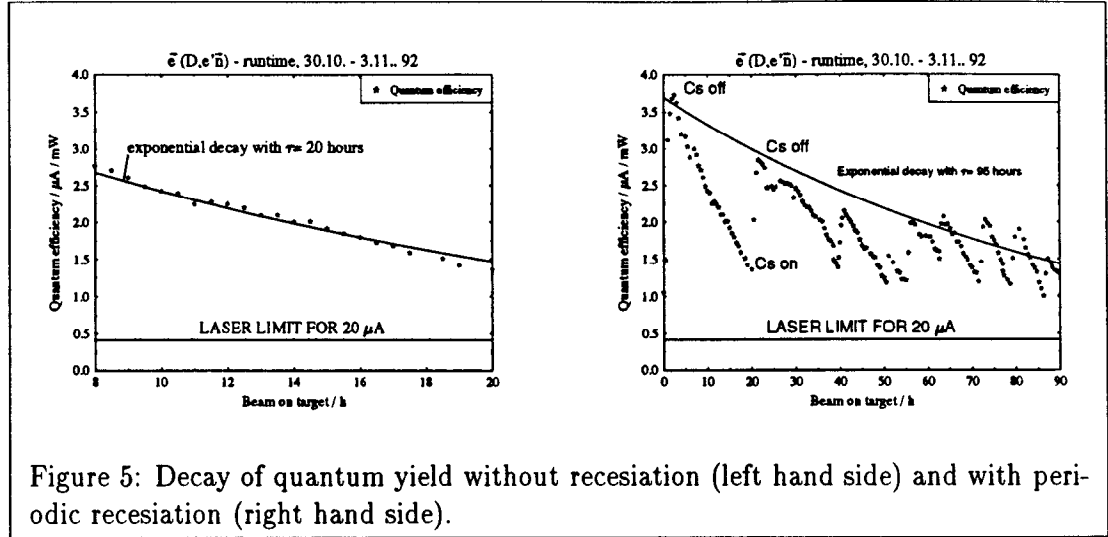
The right hand side of figure 6 shows the absolute values of q.e. on the square. During the experiments we were interested in the relative changes of q.e. on each meshpoint. In the following plots (figure 7, and 8) the quotient q.e. after the experiments divided by the initial value is plotted over the square mesh. A value of 1 means that there has been no change of q.e. during the experiment.

The first experiment was done in order to find out if the laser beam intensity itself damages the crystal. To do so we irradiated the crystal with 50mW without producing an electron beam, i.e. the crystal was held at ground potential during the experiment. The graph on the left hand side of 7 shows the result: No significant change of q.e. was observed under this condition.

In the next experiment we used the same intensity for producing an electron beam. The result of this three hour run is plotted on the other side of figure 7. We observed a relative loss of 20-30% on the whole area. Because the experiment was done without recession and at high current (100-200  $\mu\text{A}$ ) this had to be expected. Later experiments confirmed that this 'global' loss may be cured by recession.

The effect on the area of the laserspot itself is more pronounced. Surprisingly a groove-like structure is emerging from the position of the emitting spot. It has about the same loss (relatively 60%) than the emitting spot. The 'groove' is roughly directed towards the center of the crystal.

#### 4 OPERATIONAL STABILITY



The conclusion from this results is the following: The observed decay constant in the mode of operation with recesiation (see figure 5) is caused by a 'local-effect' that degrades q.e. on the emitting spot and on the groove-area.

We took advantage of this information during a  ${}^3\vec{H}e(\vec{e}, e'n)$  -experiment when the current had to be increased to  $50 \mu A$ . At this current the minimum required q.e. is increased and the decay of the q.e. is faster than at  $20 \mu A$ .

Under this conditions the requested current could only be produced for 20-30 hours from one single emitting spot. After this period the laserspot was moved by a distance of about 0.3-0.4 mm. At the new position the q.e. was nearly unchanged, so that another production interval became possible. After changing the emission site an optimization of the beam

## 5 OUTLOOK

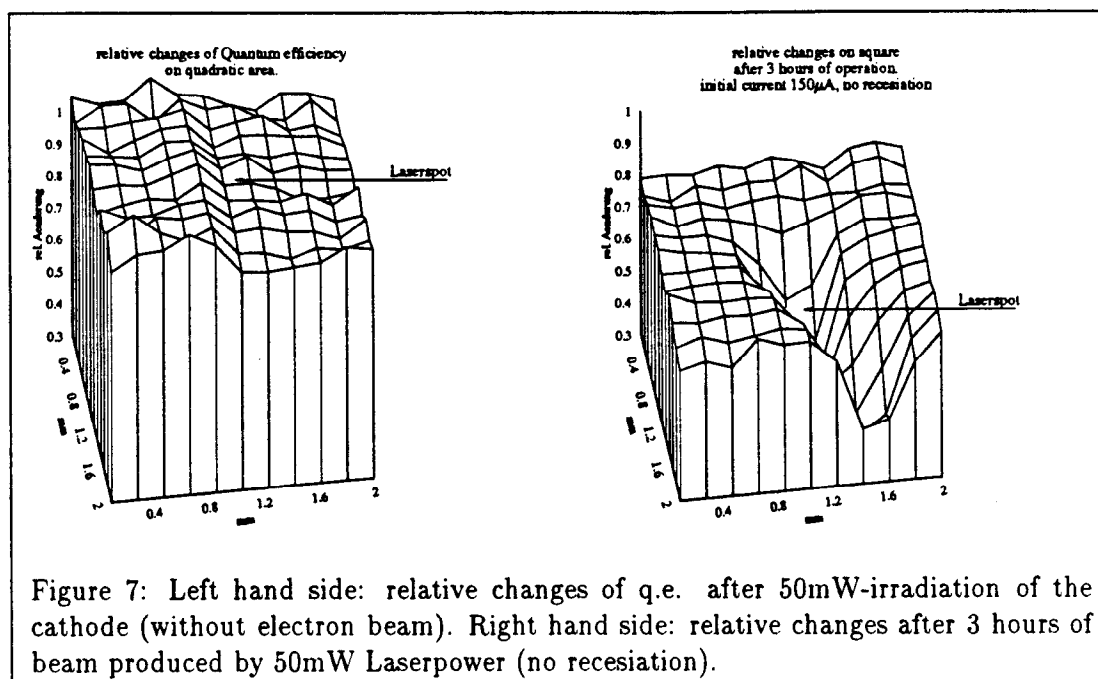


Figure 7: Left hand side: relative changes of q.e. after 50mW-irradiation of the cathode (without electron beam). Right hand side: relative changes after 3 hours of beam produced by 50mW Laserpower (no recession).

injection is necessary. This procedure usually takes between one and three hours. For that reason the availability of the source dropped to 90-95% during the experiment. The left hand side of figure 8 shows the relative changes of q.e. after more than 100 hours at 50µA. Seven different beamspots had been used. The big depression in q.e. is the result of the many overlapping 'grooves'.

The right hand side of figure 8 shows, that the local effect may be cured by the standard heat cleaning procedure. Large parts of the square are regenerated to 90% of the initial value whereas the regions in the center have not yet recovered. The situation was further improved by another heat cleaning procedure with elevated temperature.

## 5 Outlook

Though nuclear physics experiments with longitudinal Polarization  $P_l = .34$  and 10 mikroamperes of average beam current (equivalent to 50 µA at the source) have become possible, there is need for improvements.

On the one hand photocathodes with the possibility of  $P_e > 50\%$  have to be employed. On the other hand many experiments demand even higher currents ranging up to 200 µA at the source.

For this reason we are installing a twin gun system at the accelerator. This will offer some advantages. One possible option could be 'tandem operation' for very high currents. In this mode one source may be producing current for an experiment while the crystal of the other is regenerated by the heat cleaning procedure. Another possibility may be used, if strained cathodes do not give enough q.e. or do not have enough stability under extreme conditions. It will then be possible to use one bulk-cathode for high currents and one strained cathode for experiments with lower beam current. The installation of the twin-gun system will be

## 5 OUTLOOK

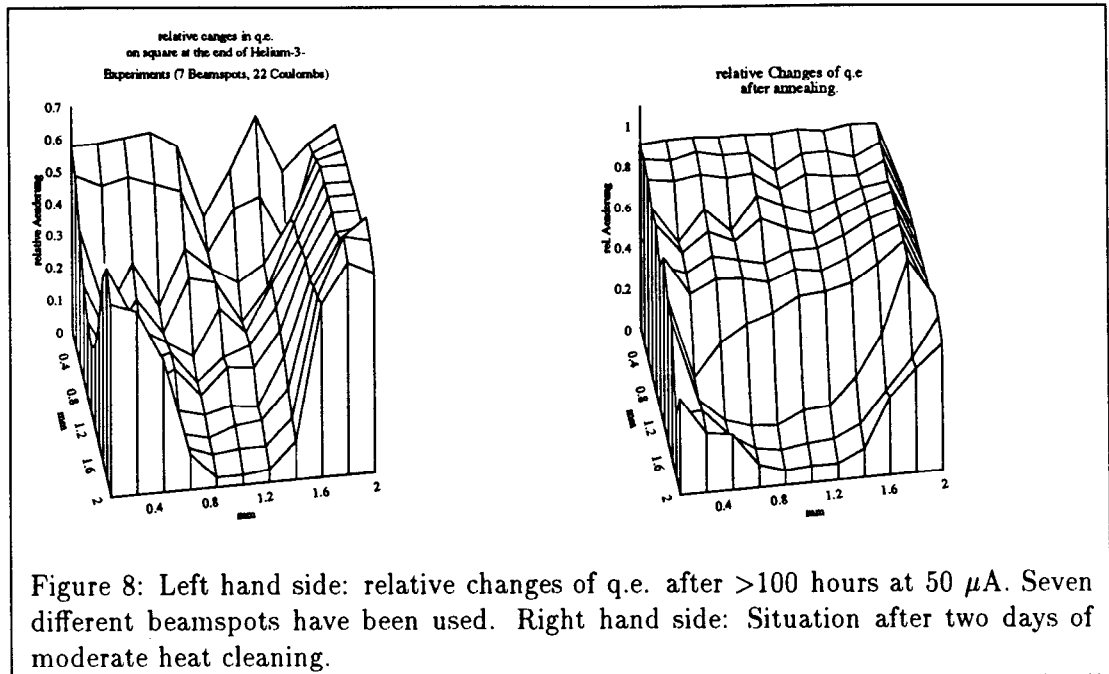


Figure 8: Left hand side: relative changes of q.e. after  $>100$  hours at  $50 \mu\text{A}$ . Seven different beams have been used. Right hand side: Situation after two days of moderate heat cleaning.

finished by the fall of this year. After that one of the two guns will be equipped with a load-lock system which we plan to install by the end of 94.

## REFERENCES

### References

- [HEI90] *W. Heil*: Spin Physics at MAMI. Proceedings of the 6th international Symposium on high energy Spin Physics Bd.1; Springer, Berlin (1991) p. 250-259
- [HER76] *H. Herminghaus*: The design of a cascaded 800 MeV, normal conducting c.w. race-track microtron. Nucl. Instr. Meth. **138** (1976) p. 1-12
- [HER79] *W.B. Herrmannsfeldt*: SLAC Report 166, Stanford (1979)
- [MAY70] *D. Maydan*: Fast Modulator for Extraction of Internal Laser Power. Journ. appl. Phys. **41, 4** (1970) p. 1552
- [STE93] *K.H. Steffens et. al.* : A Spin rotator for producing a longitudinally polarized electron beam with MAMI. Nucl. Instr. Meth. **A325** (1993) p. 378-383

**Guenter Baun  
Universitat Bielefeld**

**Experiences with strained layer GaAs-photocathodes**

We have used strained GaAs layers as photoemitters of polarized electrons to study atomic physics processes. The wafers were obtained commercially (SPIRE Corp.). As light source a laser diode operating dc at 837 nm with 30 mW max. output was taken. Electron polarizations up to 70% and emission currents up to 10  $\mu$ A were obtained. The preparation and operation procedures will be described and our measurements in respect to the polarized electron characteristics will be presented.



# Experiences with strained GaAs - photocathodes

Günter Baum

Univ. Bielefeld

for

Bernd Lener

Stefan Hesse,

Mathias Tondera -

Karsten Rott

Liane Grau

Wilhelm Raith

Wolfgang Blask

## OUTLINE:

- Context of work
- Polarimeter
- Cathode handling
- Results

SUPPORTED BY DFG - SFB 216

## Two atomic physics experiments:

- (e $\uparrow$ , 2e) : Spin asymmetries in triple differential cross section on hydrogen, lithium
- (e $\uparrow$ , e) : Spin orbit and spin exchange effects in cesium

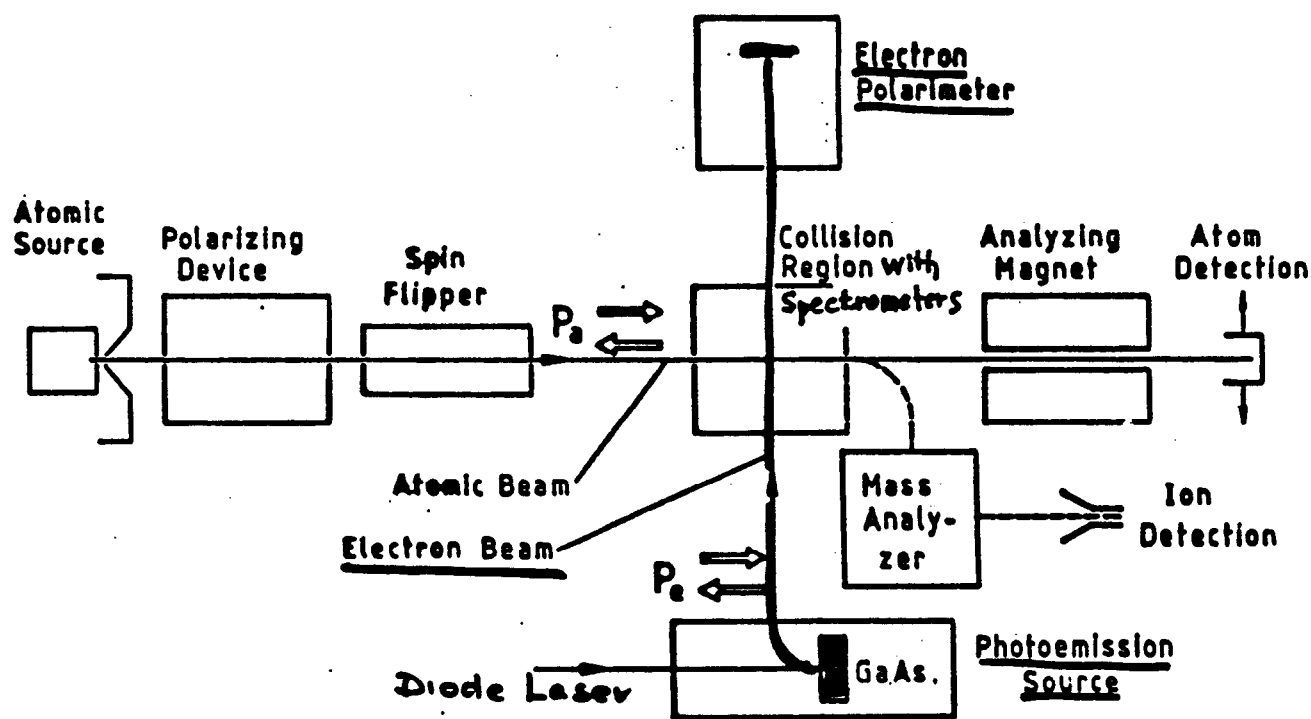
Recently installed strained layer photocathodes in the two e $\uparrow$ -sources; wafers were obtained from SPIRE corporation:

### TARGET STRUCTURE: ELECTRON POLARIZER

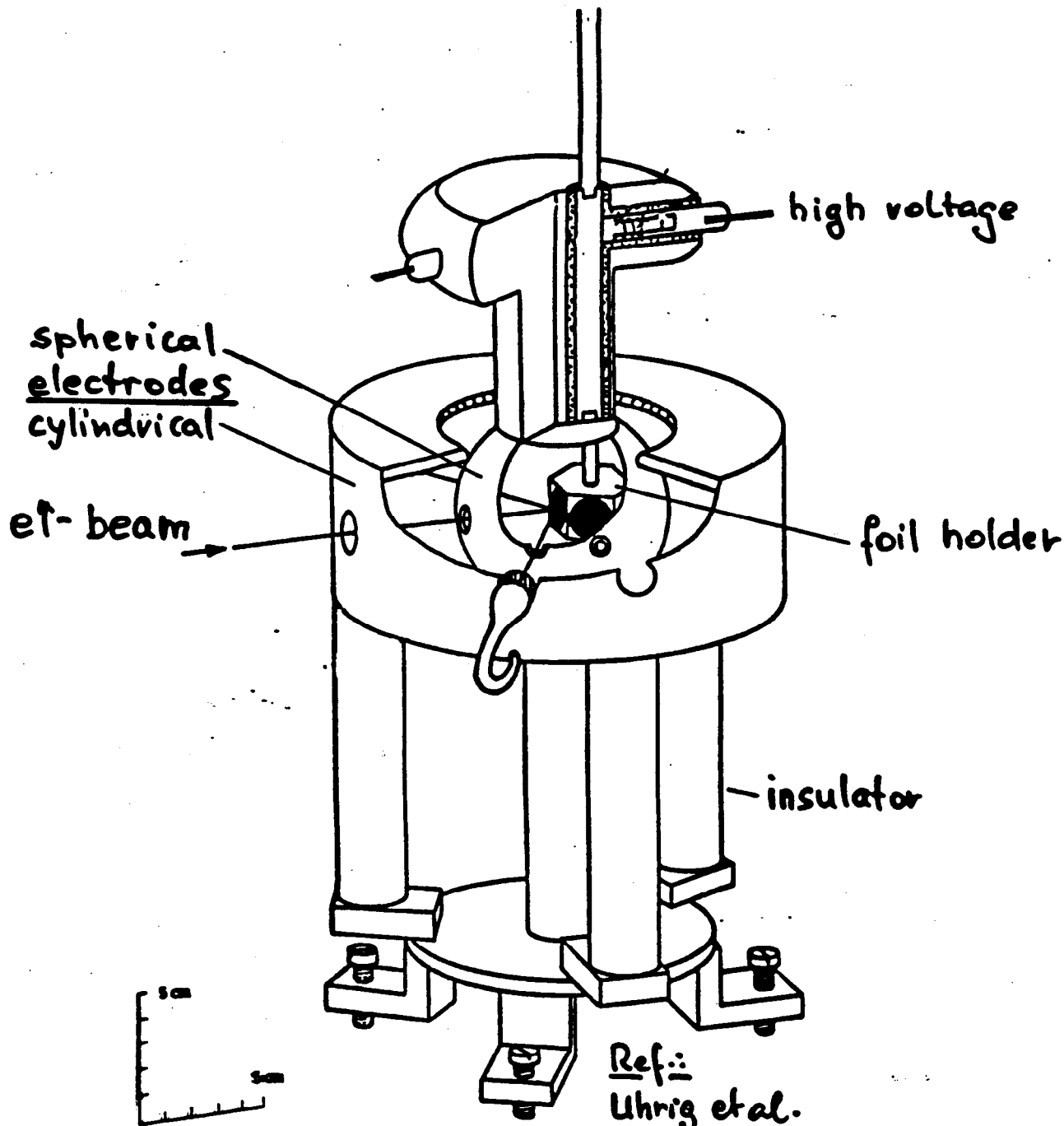
LAYER	COMPOSITION (x)	CARRIER CONC/TYPE (cm <sup>-3</sup> , P or N)	LAYER THICKNESS ( $\mu$ m)
1	GaAs	P = 4-6E18	0.25
2	GaAs <sub>1-x</sub> P <sub>x</sub> Graded X = 0-30.0%	P = 4E18	2.50
3	GaAs <sub>0.7</sub> P <sub>0.3</sub>	P = 4E18	2.50
4	GaAs	P = 5E18	0.10

1. Thickness and doping obtained from previous calibration runs.
2. GaAsP composition determined from XRDC measurements. For this wafer x was
  - a) 27.3%
  - b) 25.2%

# Schematic diagram of experiments

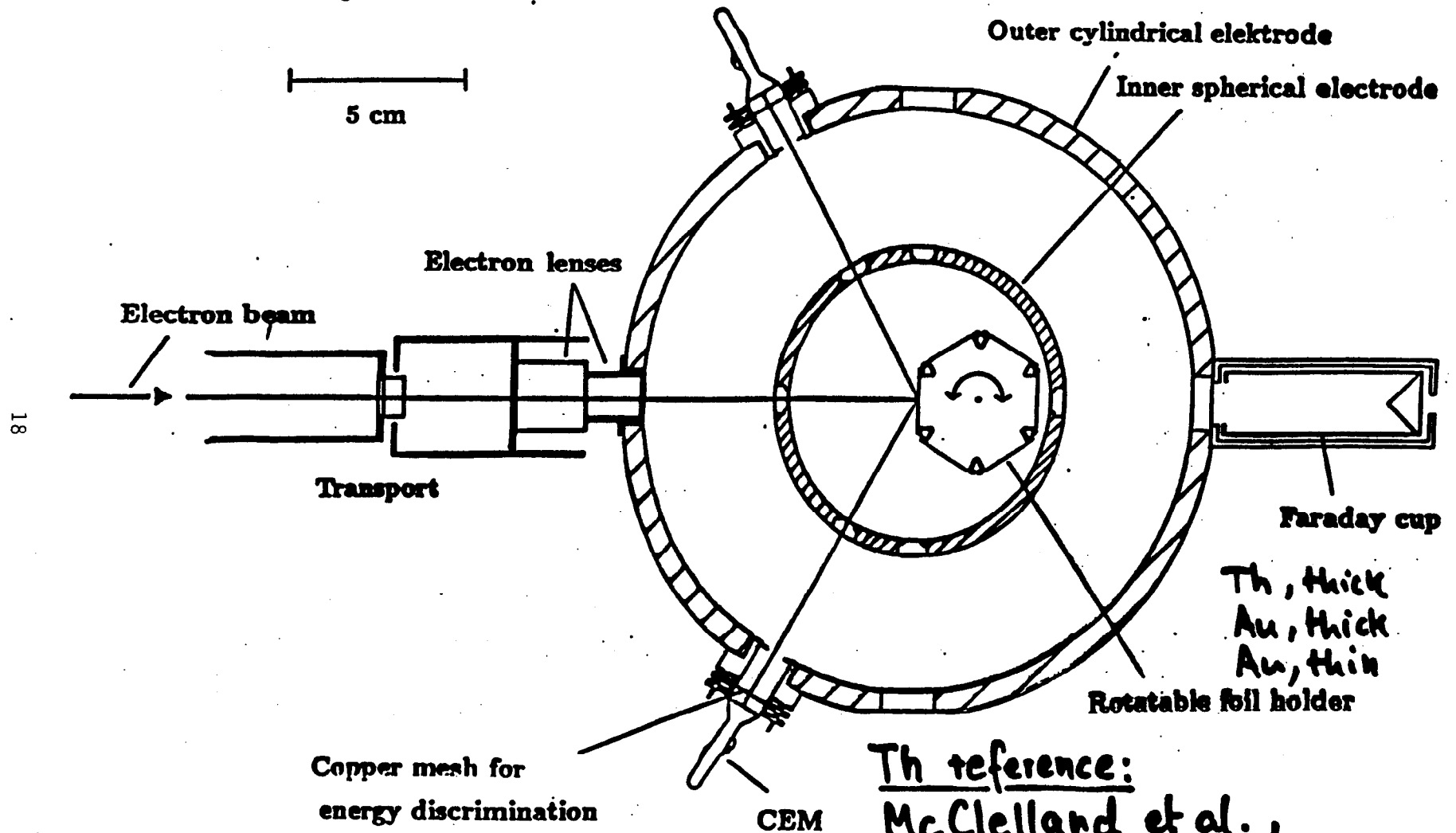


# Retarding field Mott polarimeter



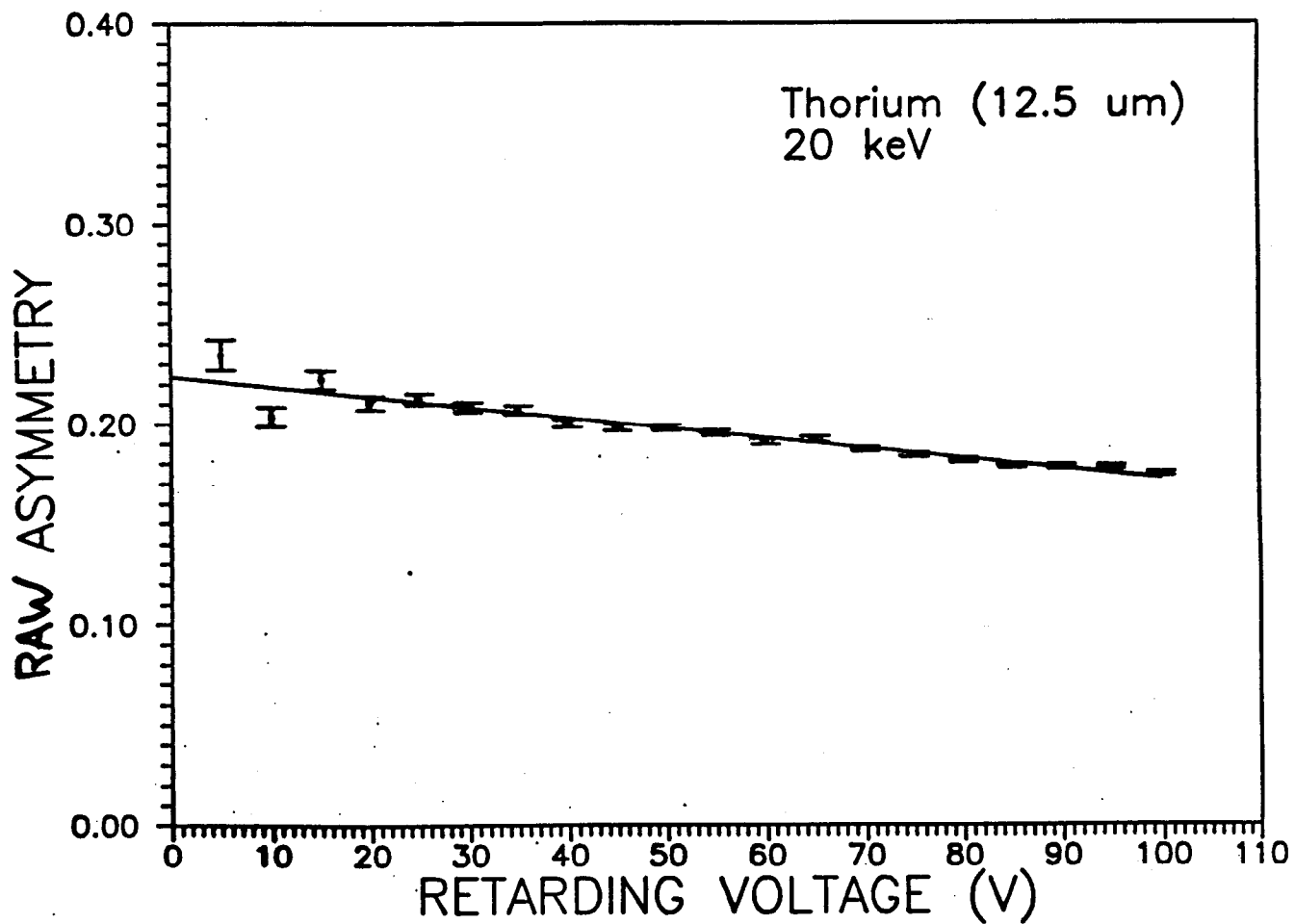
Ref.:  
Uhrig et al.  
Rev. Sci. Instrum 60 (1989) 872

# Details of retarding field Mott polarimeter

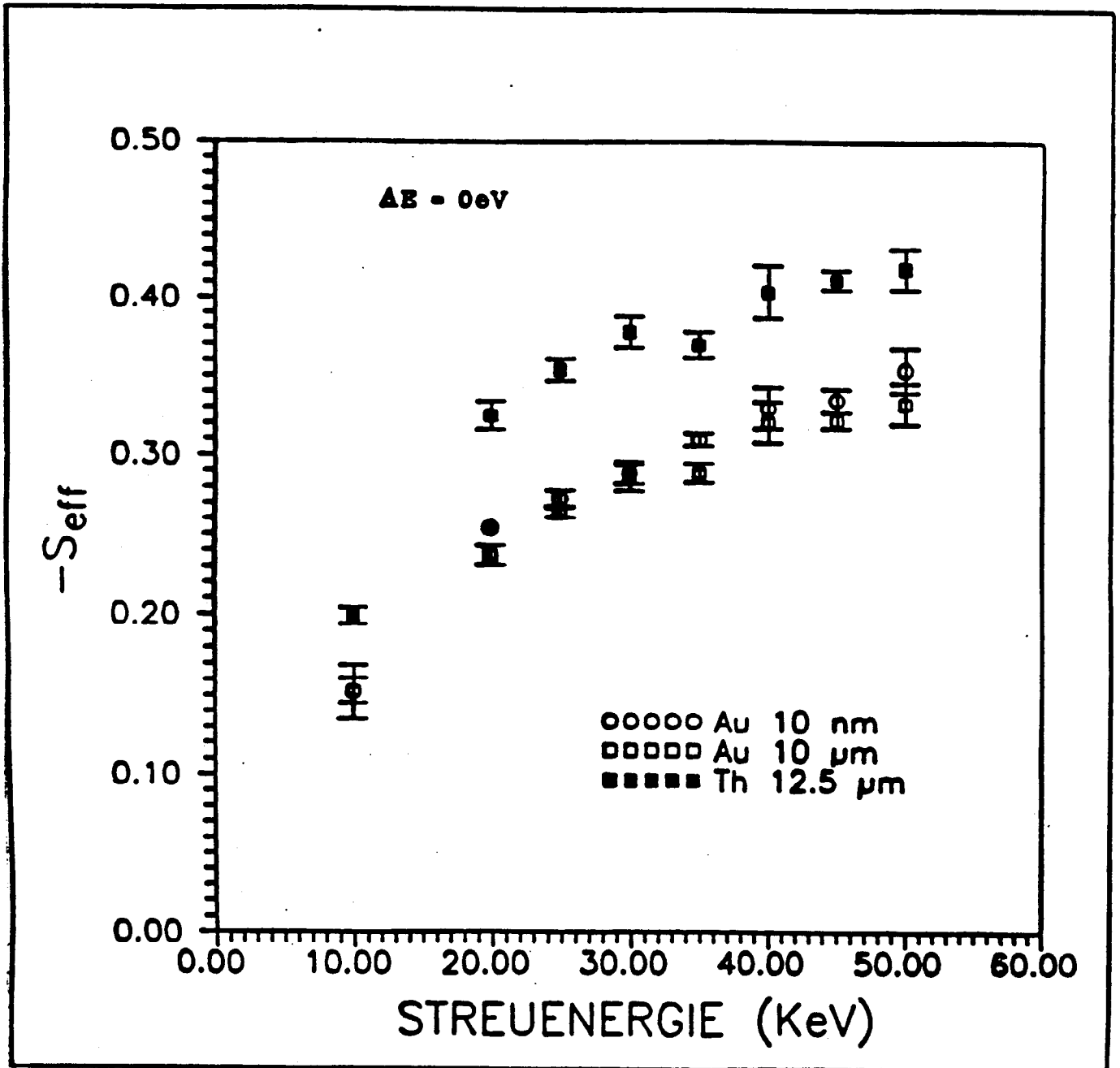


Th reference:  
McClelland et al.,  
Rev. Sci. Instrum 60 (1989) 683

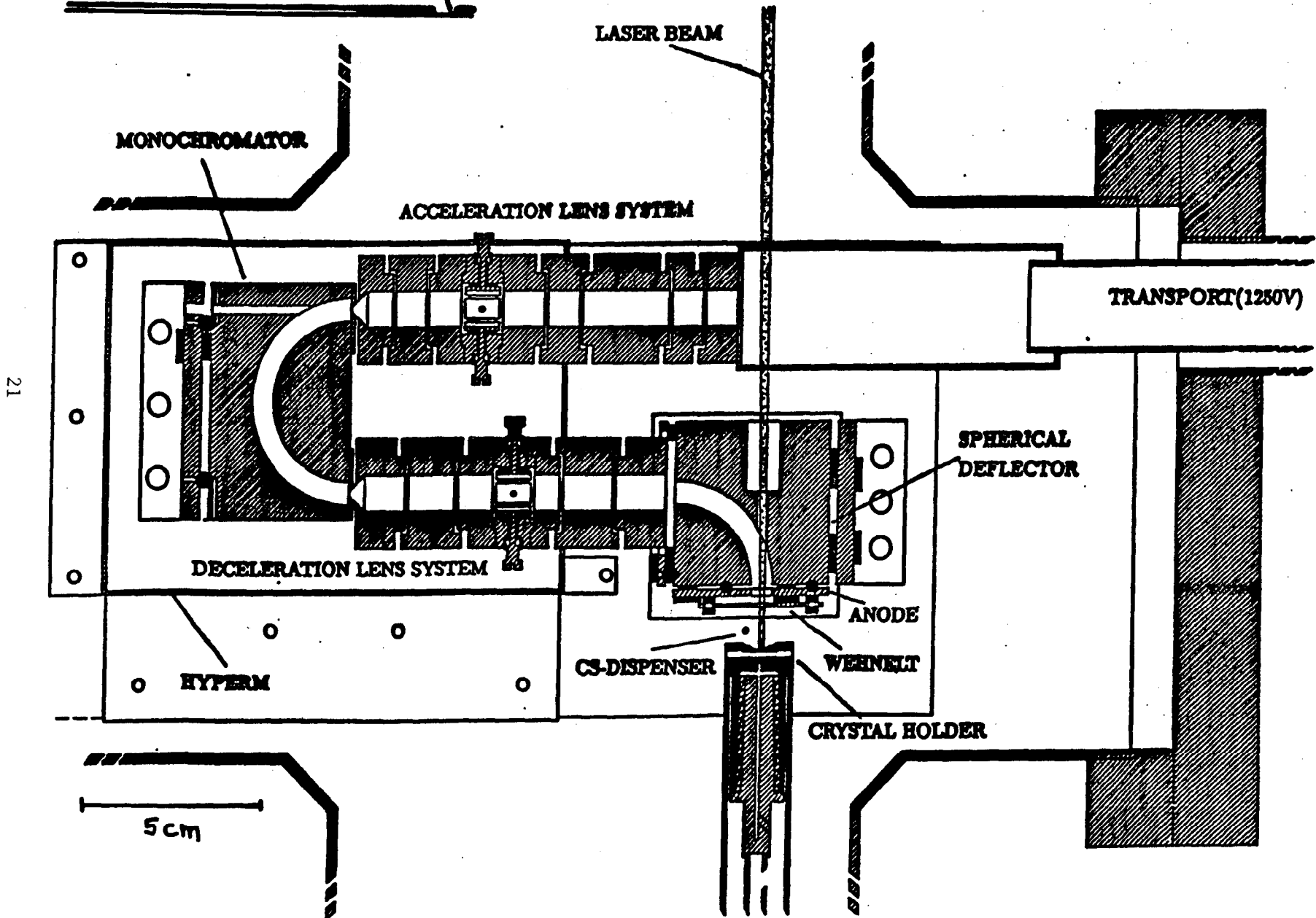
Extrapolation to  
zero-energy loss



# Analyzing power of retarding field Mott polarimeter



# e<sup>-</sup> source set-up





## Preparation of cathodes

- small pieces ( $4 \times 4 \text{ mm}^2$ ) split from wafer
- immersed in 25% ammonium hydroxide, 10-15'
- excess liquid "drained" with tissue from edge
- mounted on crystal holder immediately
- pumped down to  $10^{-8}$  torr with turbo pump
- baked out at  $250^\circ\text{C}$  for 60 h ; cathode at  $450^\circ\text{C}$  (Max) and dispenser at 2A
- cool-down ;  $p \approx 3 \times 10^{-10}$  torr
- sublimation pump on for 30' ;  $p \approx 7 \times 10^{-11}$  torr
- cathode cooled to room temperature

## Activation

- Prior to any activation, heat treatment of cathode at  $450^\circ\text{C}$  (max.) for 1/2 h (min)
- Cs and  $\text{O}_2$  application ; emission monitored at operating wavelength of 837 nm

- sequence : Cs dispenser at 4.5A till emission optimum with overshoot
- $O_2$  at  $p \approx 3 \times 10^{-9}$  torr (max) till emission optimum with overshoot
- Cs,  $O_2$ -cycle repeated up to 10 times

### Operation

- cathode at room temperature ;  $p \approx 4 \times 10^{-11}$  torr
- Cs applied continuously ; dispenser: 2 to 3 A (low level)
- 30 mW of 837 nm, single mode laser light (Hitachi HL 8314E), stabilized intensity to  $\approx 1\%$

### Regeneration

- by activation cycle after  $\approx$  1 week

### Results

- emission currents : 10  $\mu$ A
- Q.E. : 0.05 %
- Polarisation, wafer a) :  $(70 \pm 2)\%$   
wafer b) :  $(62 \pm 2)\%$

## Comparison:

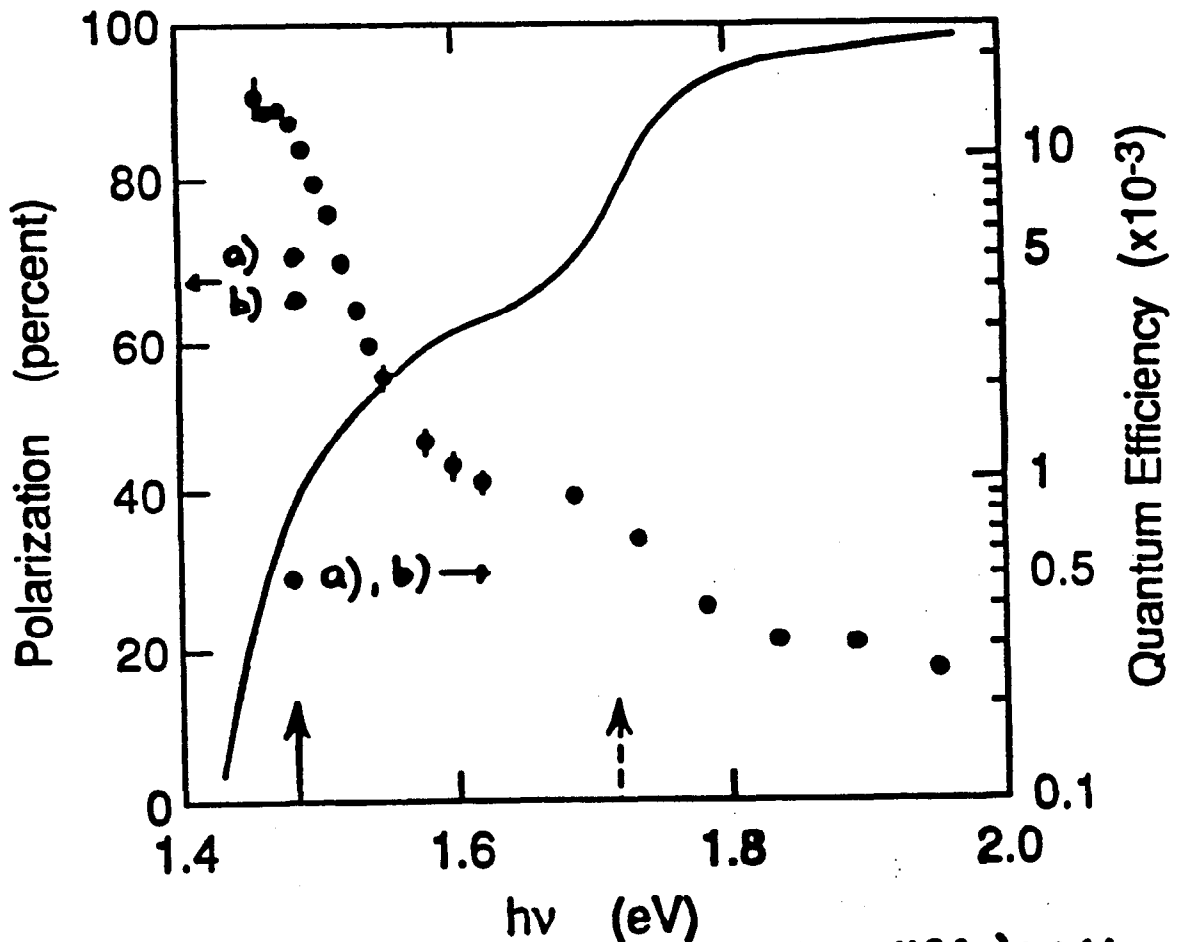


Fig.1 from Maruyama et al, Phys. Rev. B 46 (1992) 4261  
(sample 3)

a)  $x = 27.3\%$

b)  $x = 25.2\%$

**Stan Ecklund**  
**SLAC**

**Polarized e- Source Requirements for Linear Colliders**

## Linear Colliders

SLC	Provides practical experience on an operating machine. Improvements have been made over a period of years. Good reliability achieved.
NLC	SLAC design based on SLC experience and R&D on X-band RF, FFTB, NLCTA, ASSET.
JLC	KEK design. R&D ATF, FFTB, RF.
CLIC	CERN. Uses high frequency and rep rate. Requires intense drive beam.
DESY-THD	Conventional S-Band accelerator.
TESLA	DESY design. Super conducting LINAC.
VLEPP	High intensity single bunch, requires tight alignment tolerances.

## Other Machines

### LINAC - Fixed Target Machines

CEBAF  
LAL-Orsay  
MIT-Bates  
SLAC

FEL

# Linear Collider Components

## e<sup>-</sup> Source

Laser

Photo Cathode

Gun (DC HV, Pulsed HV, or RF)

Bunching System

Sub-harmonic

Main RF

photo cathode

Booster LINAC

Damping Ring (1-2 GeV)

Bunch Length Compressor

Accelerator

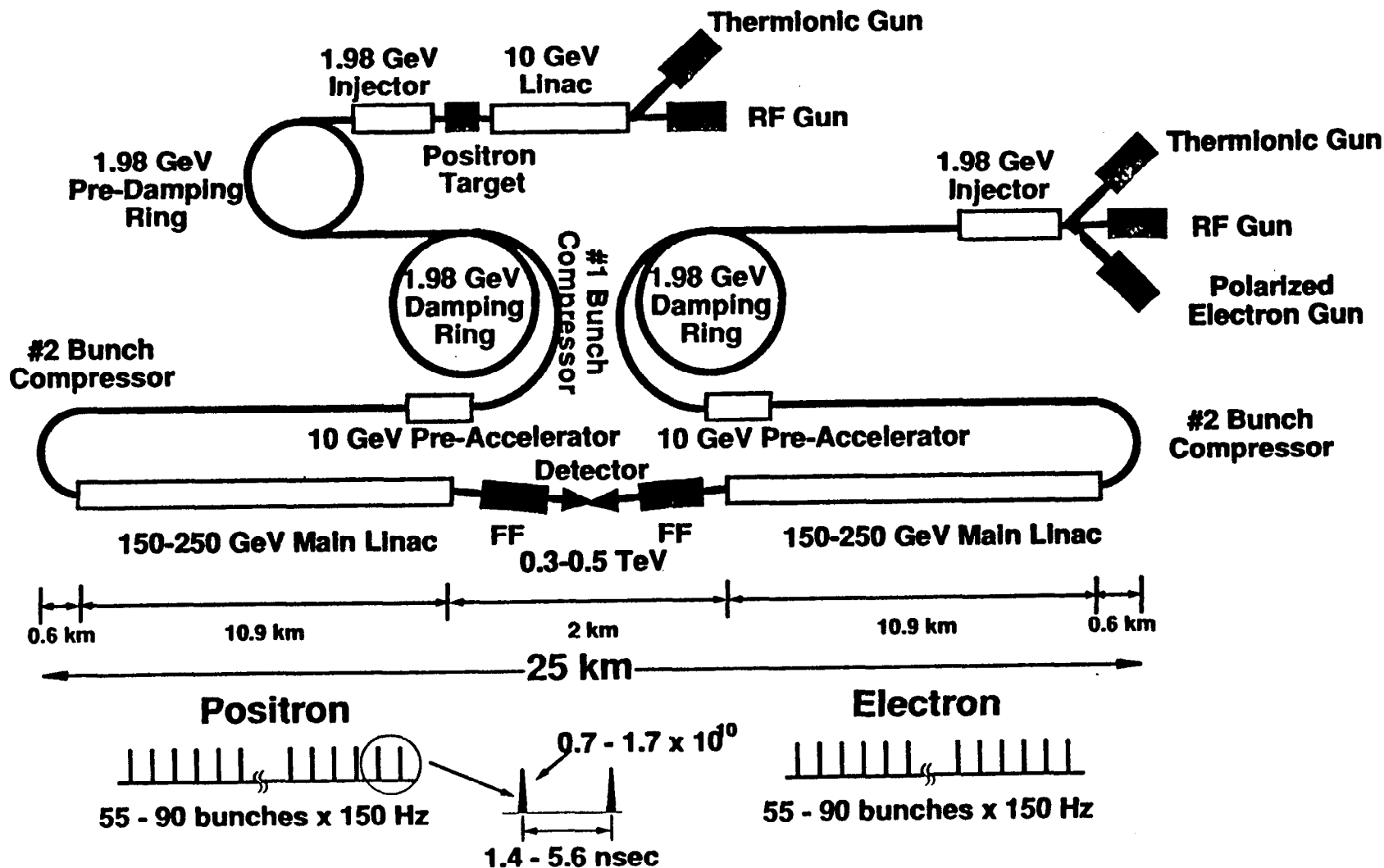
Additional Bunch Length Compressor

Main Accelerator

Collimation

Final Focus

# Schematic Diagram of JLC-1



## Linear Collider e- Source Parameters

		SLC	NLC	JLC	CLIC	CLIC Drive	DESY-THD	TESLA	VLEPP
C.M. Energy at IP	(GeV)	100	500	500	500 to 2000		500	500	500
Luminosity	/(cm <sup>2</sup> -sec)	3.00E+29	9.00E+33	6.30E+33	2.70E+33		2.40E+33	2.60E+33	1.20E+34
Main RF frequency	(GHz)	2.876	1.14E+01	11.4	30	0.35	3.00E+00	1.3	14
Bunch Intensity @ IP	Ne-	3.00E+10	6.50E+09	7.00E+09	6.00E+09		2.10E+10	5.10E+10	2.00E+11
Bunch Intensity @ Source	Ne-	5.00E+10	1.00E+10	1.10E+10	8.30E+09	2.50E+11			
	(ncoul)	8	1.6	1.76	1.328	40	3.36	8.16	32
Bunches per pulse		2	90	90	4	43	172	800	1
Pulse Intensity @ Source	(ncoul)	16	144	158	5.31	1720	578	6528	32
Pulses per second	(Hz)	120	180	150	1700	1700	50	10	300
Bunch Spacing	(ns)	59	1.4	1.4	0.333	2.9	10.7	1000	
Bunch Train Length	(ns)	118	126	126	1.332	123	1840	800000	
Average Current in Train	(Amp)	0.14	1.14	1.26	4	14	0.31	0.0082	
Bunch Length @ IP	(mm)	1	0.1	0.08	0.17		0.5	1	0.75
Bunch Length @ Cathode	(ns)	2.5	0.7						
Peak Current @ Cathode	(Amp)	3.2	2.3						
Bunch Length @ 200 MeV	(mm)		2		1	1			
Energy Spread	(%)	1	1				0.3	0.1	
Bunch Intensity Variation	(%)	3	0.1 to 1.0	0.5					
Horz. Invar. Emittance @ IP	(rad-m)	4.00E-05	2.00E-06	3.00E-06	1.50E-06		5.00E-06	2.00E-05	3.00E-05
Vert. Invar. Emittance @ IP	(rad-m)	7.00E-06	2.00E-08	3.00E-08	5.00E-08		5.00E-07		3.00E-09
Invar. Emittance @ Source	(rad-m)	2.00E-04	1.00E-04	5.00E-05	1.60E-06			1.00E-05	

4 trains/pulse  
multiple injectors  
3 GeV  
not pol.

wiggler



ELECTRON PRODUCTION/PARAMETERS/Ver-1/7-28-93

NLC Electron Source Parameters

Parameter	500 GeV CM Energy	1 TeV CM Energy
Gun voltage	120 kV	120 kV
Injector	200 MeV	200 MeV
Invariant emittance (RMS)	$1 \times 10^{-4}$ rad-m	$\sim 1 \times 10^{-4}$ rad-m
Bunch length (Full width)	$\sim 4$ mm	4 mm
Energy spread without compression	1%	1%
Bunch length after compression ??		
Energy spread after compression??		
Bunch frequency	714 MHz	714 MHz
Bunches per pulse	90	67
Electrons per bunch (at 200 MeV)	$1 \times 10^{10}$	$2 \times 10^{10}$
Electrons per pulse(at 200 MeV)	$9 \times 10^{11}$	$1.34 \times 10^{12}$
Pulse repetition rate	180 Hz	120 Hz

**e<sup>-</sup> PRODUCTION/POLARIZED ELECTRONS/DC OR  
PULSED GUN/Ver-1/7-28-93**

**Electron Gun Specifications**

Type	Pierce Triode
Voltage	~120 kV
Pulse structure	714 MHz Train of Ninety ~700 ps Pulses
Pulse train risetime	1.4 ns
Charge per $\mu$ pulse	$1.4 \times 10^{10}$
Cathode type	Strained GaAs
Cathode area	3 to 6 cm <sup>2</sup>
Polarization	$\geq 80\%$
Operating regime	Space charge limited cathode (Controlled by Grid or Modulating anode) or space charge limited transport
Macro-pulse to pulse Intensity Stability	0.1%
Max $\Delta N$ deviation in any portion of pulse train	$< 1.4 \times 10^9 e^-$
Micro-pulse to pulse Intensity Stability	$\leq 1.0\%$
Micro pulse timing jitter	$\leq 30$ ps

## **Issues**

### **Charge Limit.**

Can the required charge with the desired time structure be obtained from the cathode.

### **Generation of Pulse Train.**

Because of LINAC beam loading, bunch to bunch intensity uniformity tolerance is small. Performance of collider may be strongly dependent on final energy spread which depends on single bunch and bunch train loading.

### **High Polarization**

Because statistical error improves as  $(N P^2)$ , high polarization is desired. Polarization vs. quantum efficiency needs to be considered. There may be a trade-off between quantum efficiency and laser power.

### **Emittance**

Can the emittance from the gun be smaller and preserved in order to simplify down stream components, e.g. Damping Rings. What is optimum cathode size.

### **Reliability**

Achievable with sufficient resources and care.

## **Manouchar Farklondeh MIT-Bates Linear Accelerator Center**

### **MIT-Bates Polarized Injector System**

The MIT-Bates polarized injector has produced over 2500 hours of high quality polarized beam for nuclear physics research and parity violating experiments. With bulk GaAs crystals, this PEGGY style gun producing 15 microseconds pulses at 600 HZ with average currents of 30  $\mu$ A, incorporates an Argon-laser pumped Titanium-Sapphire CW laser, chopper and helicity pockels cells and an optical transport system. A substantial differential pumping is employed to maintain the gun at ultra high vacuums of 11-13 scales with the accelerator of 8-9 scale. A newly added Wein filter manipulates the spin vector to any desired direction. The polarized injector, its unique features and requirements, and the laser system will be presented. Also to be discussed are the new injectors under construction with multiple crystals and load-lock capabilities. A new technique for maximizing the output of a CW Ti-Sapphire laser will be presented.

# **MIT-Bates Polarized Injector**

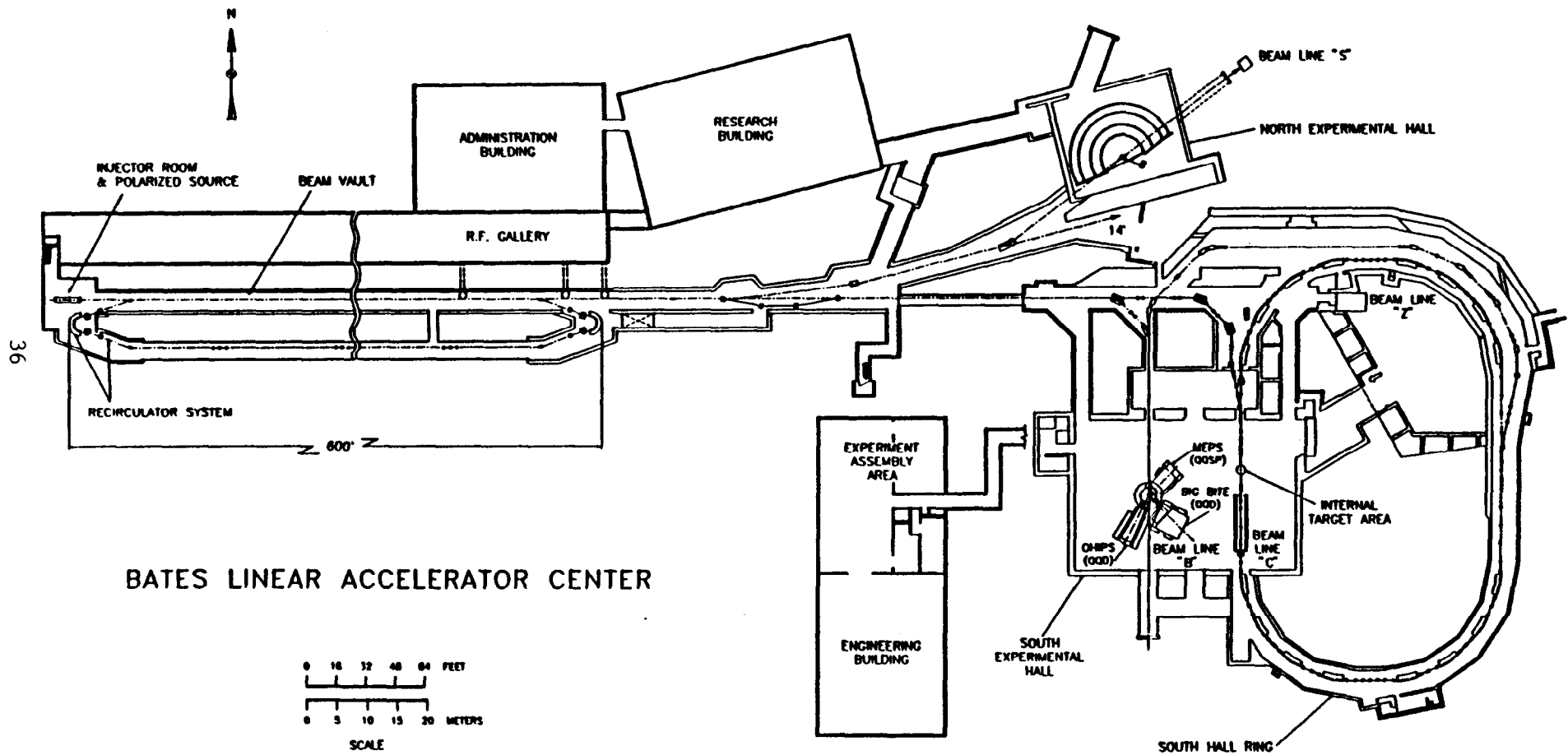
**G. Dodson, M. Farkhondeh, E. Ihloff and  
E. Tsentalovich**

**Massachusetts Institute of Technology  
Bates Linear Accelerator Center  
Middleton, MA 01949**

**(September 8, 1993)**

# Outline

- 1) -- Overview
- 2) -- Polarized Injector
- 3) -- Spin Manipulation and Measurement
- 4) -- Recent Progress in Quantum Efficiencies
- 5) -- Strained GaAs Crystals
- 6) -- Ti-Sapphire Laser Development
- 7) -- Design of a New Injector
- 8) -- Summary



BATES LINEAR ACCELERATOR CENTER



# 1) Overview

● The MIT-Bates polarized electron injector has produced over 2500 hours of beam for medium energy nuclear physics experiments for the last few years.

● The experiments included:  $^{12}\text{C}$  parity violation, measurement of nucleon Form Factors,  $G_E^n$  and  $G_M^n$  using electron scattering on  $^2\text{H}$  and polarized  $^3\text{He}$  targets. First out of plane measurement of fifth structure function of  $^2\text{H}$  and  $^{12}\text{C}$  .

● For the near future, over 80 percent of the physics program requires polarized beam of high quality and high intensity .

● Immediate major experimental programs :

- Measurement of  $^2\text{H}$  and  $^{12}\text{C}$  polarization observables using polarized beam, a new Focal Plane Polarimeter (FPP) and Out-Of-Plane spectrometers (OOPS).

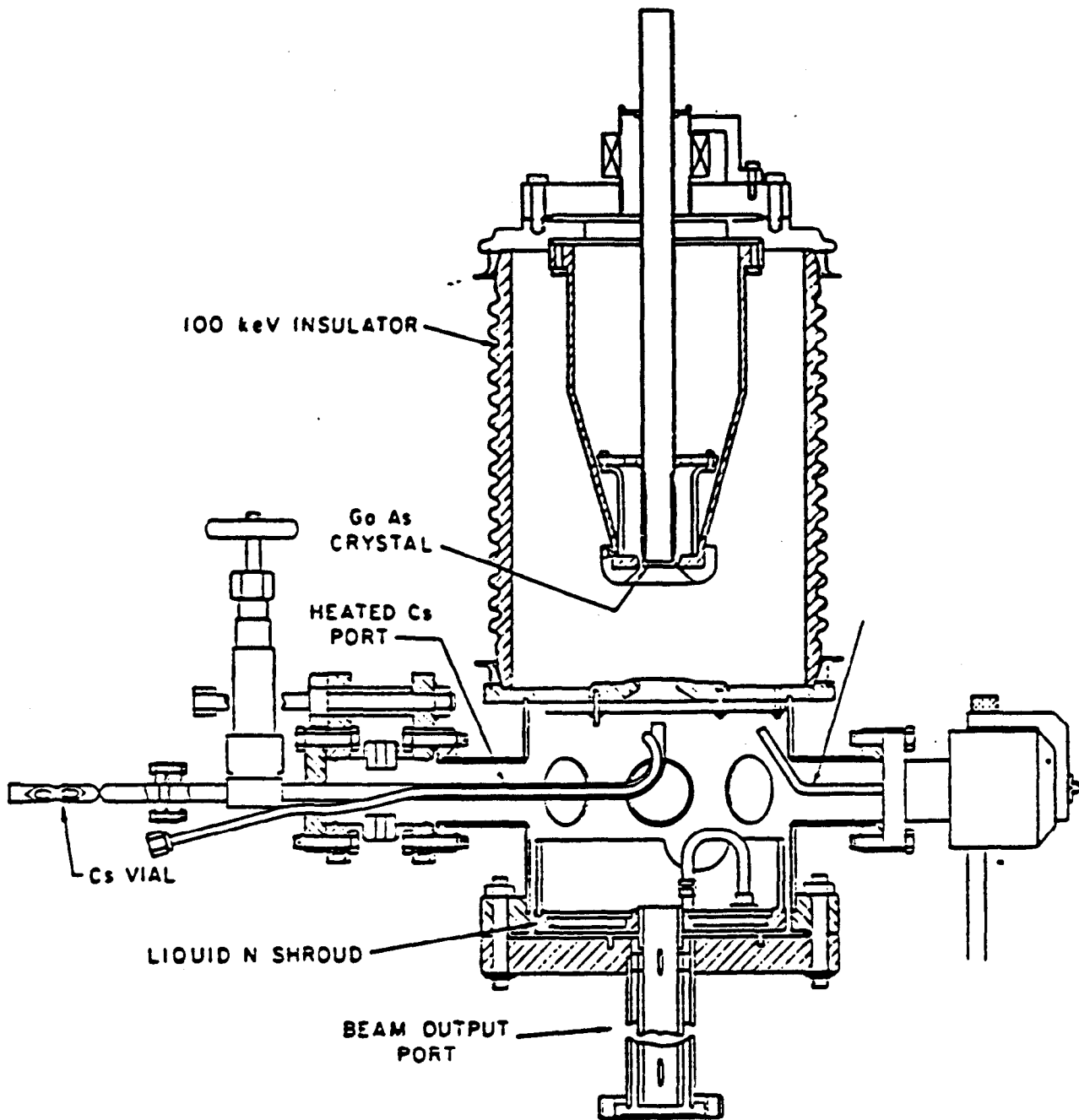


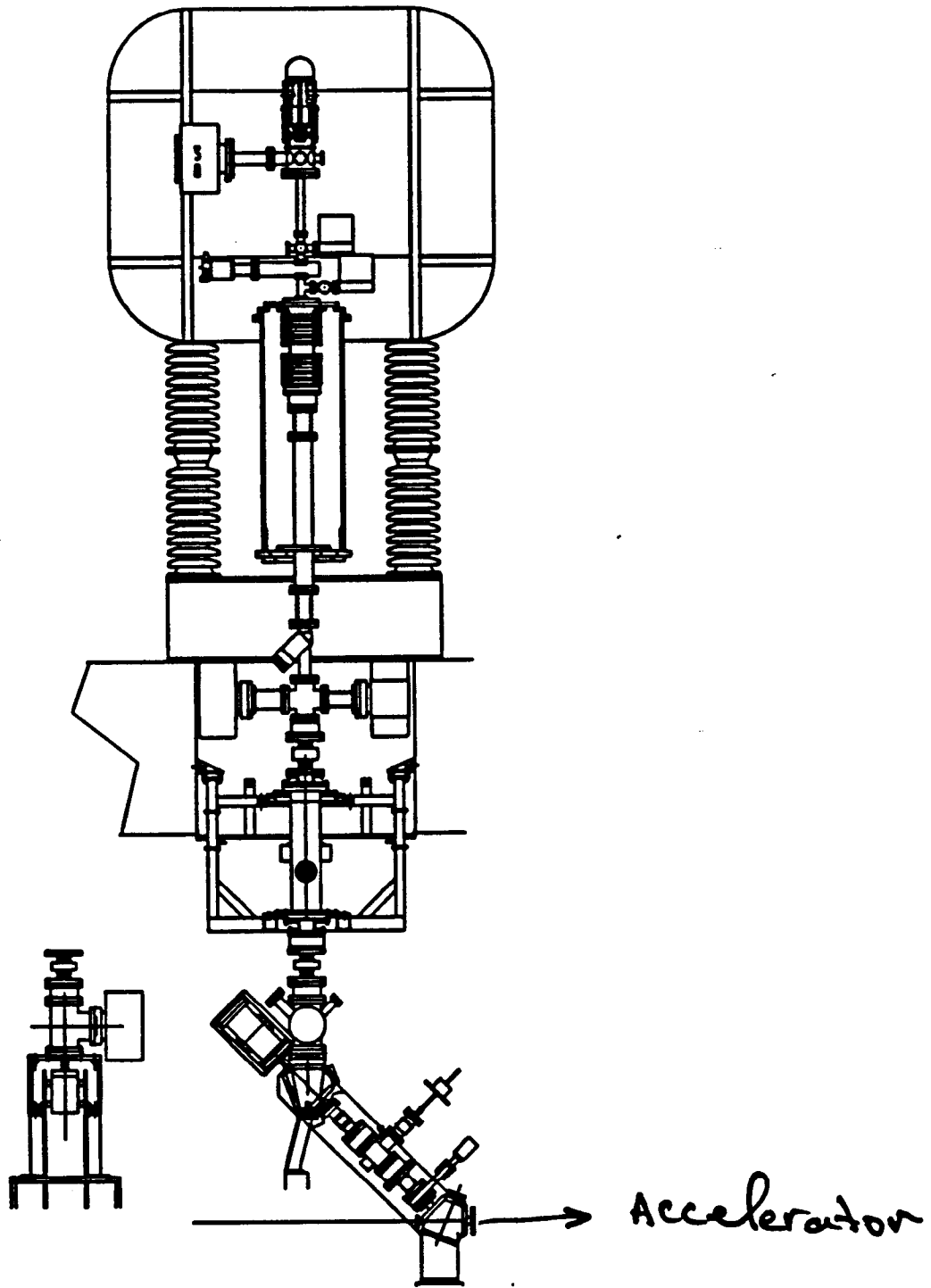
- Measurement of the Singlet Anomalous Magnetic Moment of the proton using Parity Violating Electron Scattering (SAMPLE) which will provide new information on the strange quark content of the nucleon.

● The physics program with polarized beam for the South Hall Ring (SHR) requires injection of  $1.3 \mu\text{s}$  long pulses of 40 mA into the ring at 1 kHz which is very demanding for the polarized injector. This will require some upgrades of the injector and the beam transfer line for handling higher peak currents.

## 2)- Polarized Injector

- Source parameters are given in Table 1
- Gun chamber, a PEGGY II style photocathode at -60kV
- Substantial differential pumping for achieving  $\sim 10^{-11}$  -  $10^{-12}$  torr vacuum.
- Laser System : CW Ar laser driving a Ti-Sapphire laser.
- Accelerating High Voltage: 320 kV
- Beam Transfer line: lenses, steerers, an achromat with two  $45^\circ$  bends, targets and toroids.
- Accommodates only one crystal, bake out needed every time a new crystal is installed. Crystal activation (NEA) in the gun chamber with Cs and  $\text{NF}_3$ .





## Table 1

### ■ Injector Parameters

Injection Energy	380kV
Maximum Intensity	20mA peak 200 $\mu$ A average
Duty Factor	1%
Pulse width	15 $\mu$ s (1.3 $\mu$ s for SHR)
Repetition Rate	600HZ (1kHz for SHR)
Polarization	0.4 for bulk GaAs 0.8 for strained GaAs
Phase Space	$< 10^{-3} \pi$ mr.mm
Intensity Stability	$< 1\%$ jitter pulse-to-pulse
Spin Reversal	—pockels cell: rapid random — $\lambda/2$ : slow
Spin manipulation	Wien filter — slow — arbitrary $\theta, \phi$ angles
Linac Capture Fraction	1/3

# ● Photocathodes

- Bulk GaAs crystals:
  - Q.E. as high as 6.5%
  - Dark current life times: > 200 hours
  - Polarizations: ~ 40%
  
- Strained thin GaAs on  $\text{GaAs}_{(1-x)}\text{P}_x$ 
  - Q.E.  $\leq .1\%$  at  $\lambda=840$  nm and recently as high as 0.5% .
  - Dark current life time: ~ 200 hours
  - Polarization: 42-75% at 830-870 nm but Møller polarimeter may have had problems.

# 3) Spin Manipulation and Measurement

## ● Spin Manipulation:

■ Pockels cell : Fast Spin Flip (pulse-to-pulse) by reversal of the handedness of the laser light.

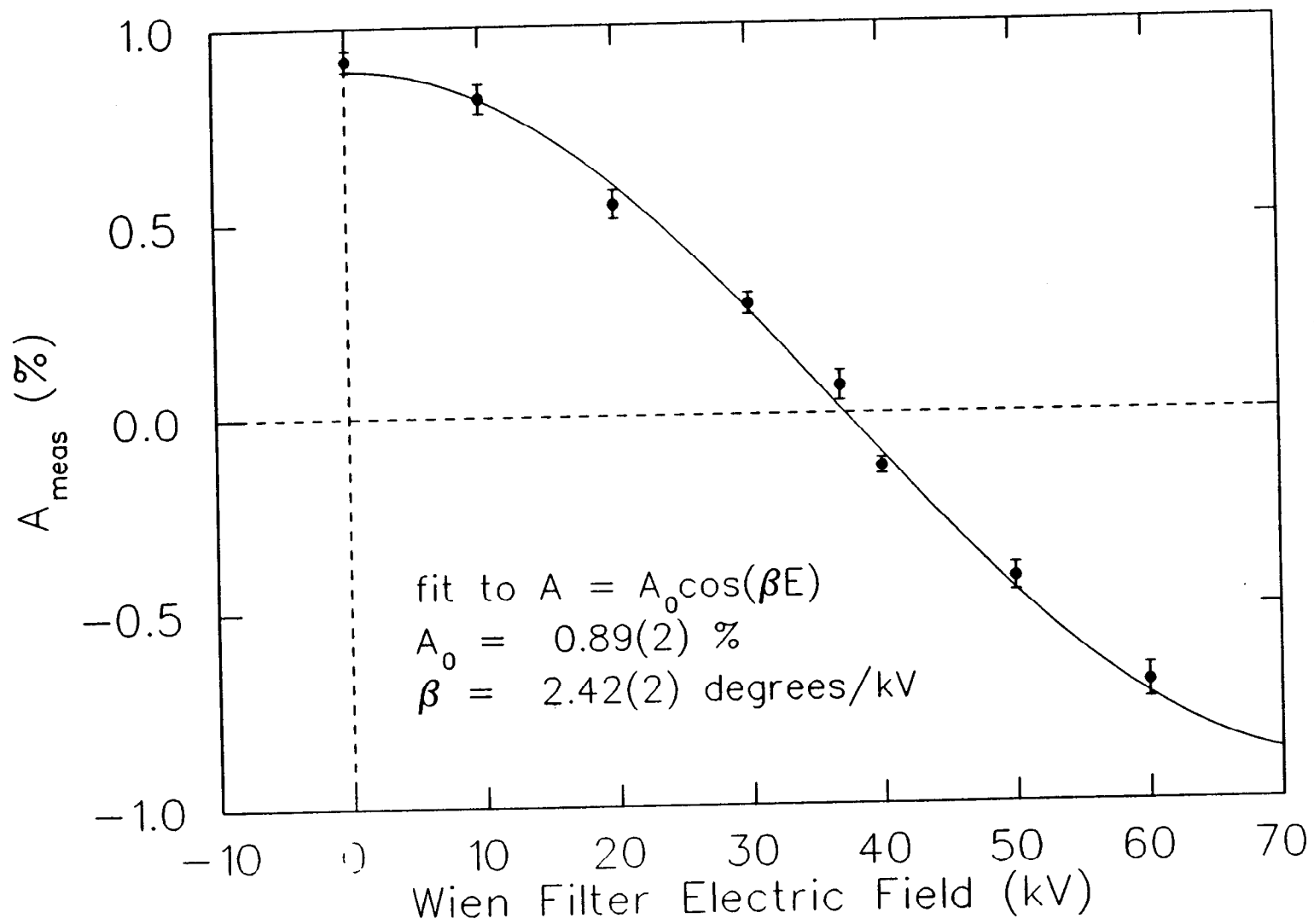
■ Wien filter : Slow arbitrary spin rotation by a crossed E and B field. The fields are set to precisely compensate for the precession of the spin passing through bends in the recirculator and /or the experimental beam lines by

$$\Omega = (g-2)\gamma\theta_B .$$

Required field strength is proportional to  $\gamma^2 \beta$

E Field max :	80kV over 1.2 cm
B Field max :	160 Gauss
Effective Length	50 cm
Aperture:	1.2 cm
Status	operational since 2/93

Wien filter calibration curve





Smallest aperture in the transport line, making beam tuning and steering very critical. Installing a Wien filter after the 60 kV anode and before the 320kV would provide a combined factor of 4 in reduced effective length and increased gap given by  $\gamma^2\beta$ . This will require installing the gun horizontally followed by a  $90^\circ$  achromat and the Wien filter.

■ Magic Energies : For certain discrete beam energies a longitudinal spin ends up longitudinal at the target after precessing by

$$\Omega = \sum_i (g-2)\gamma_i \theta_{Bi} = n\pi$$

in the bending sections. 570 and 860 MeV are two recirculated magic energies for the B line with the Wien filter turned off.

## ● Polarization Measurements

### ■ Møller Polarimeters:

- B- Line : variable energy, measures only longitudinal comp.
- S- Line : 200 MeV, measures both comp. (SAMPLE)

### ■ Compton Polarimeter:

Obtained from Chalk River, requires substantial vacuum rework and installation before the first  $45^\circ$  bend in the injector beam transport line.

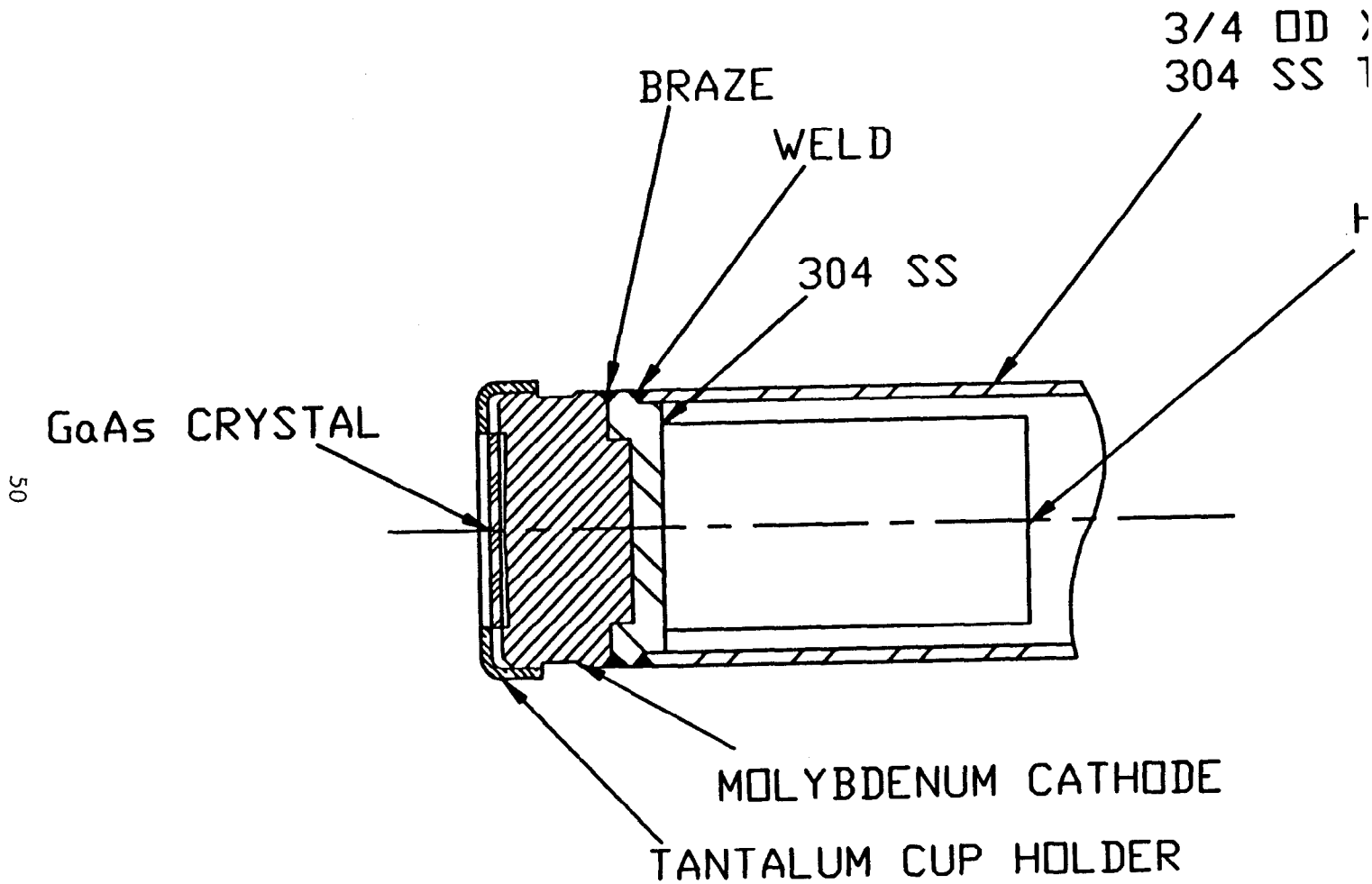
## 4) Recent Progress in Q.E.

● Until recently, Quantum Efficiency of our bulk GaAs crystals was decreasing with each activation, an indication of inadequate heat cleaning.

- Heat cleaning Temperature :  $650^{\circ}\text{C}$  at the tip of the heater stalk assembly .
- Crystal Temperature: Unknown, no direct line of sight for a pyrometer.
- Past May and June, polarized  $^3\text{He}$  experiment: started with Q.E. of 6% and quickly fell below 1% needing activation every two-three days.
- Duration of heat cleaning had only a small effect on maximum Q.E.

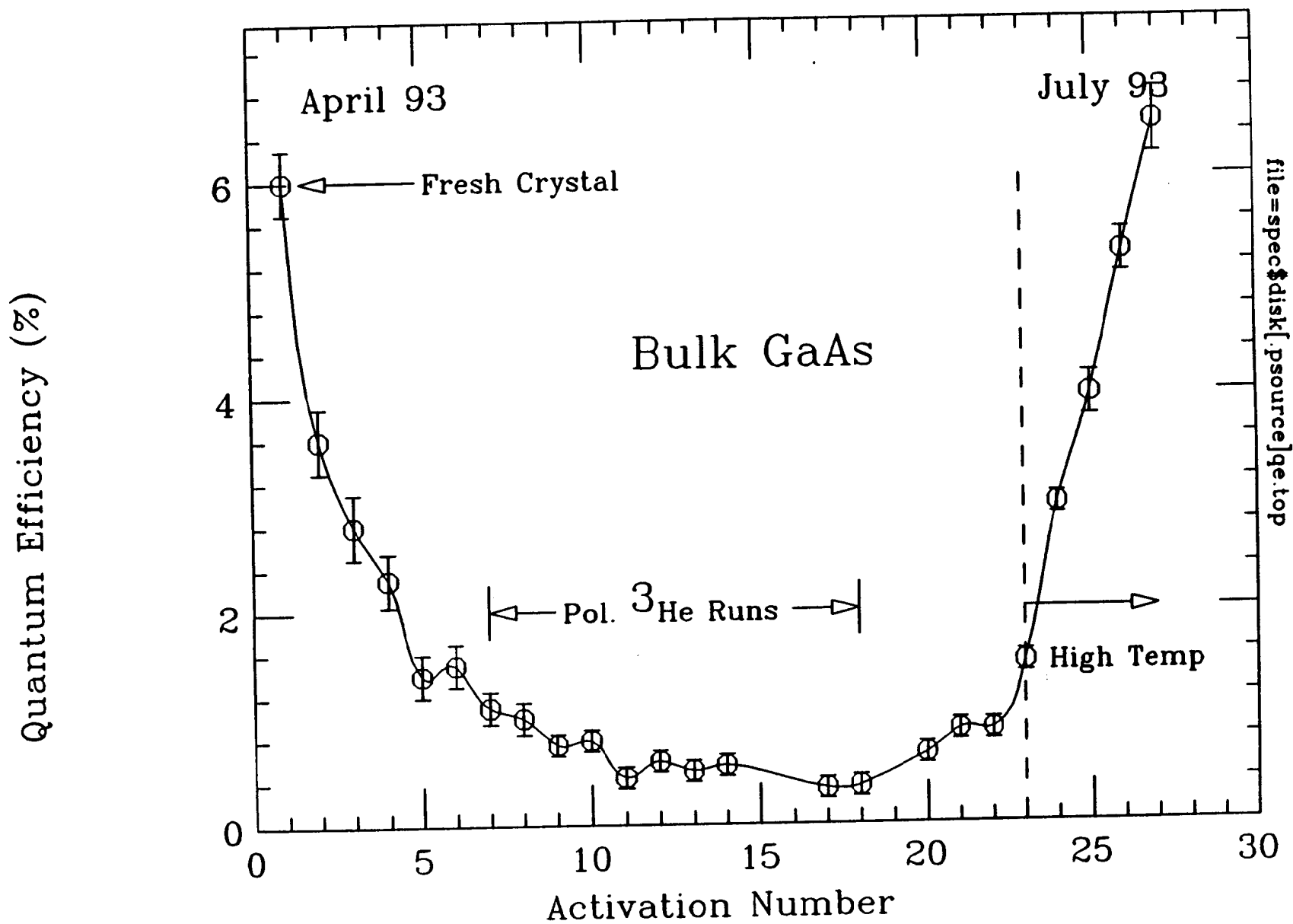
● After the  $^3\text{He}$  experiment:

- Raised the heat cleaning temperature in steps of  $25^\circ\text{C}$ , noticed Q.E. recovery at  $725^\circ\text{C}$  and a complete recovery at  $825^\circ\text{C}$ . This indicates a  $\Delta T > 100^\circ\text{C}$  between the tip of the stalk and the crystal.
- No visual sign of overheating of the crystal.
- Plot of Q.E. vs. time shown.

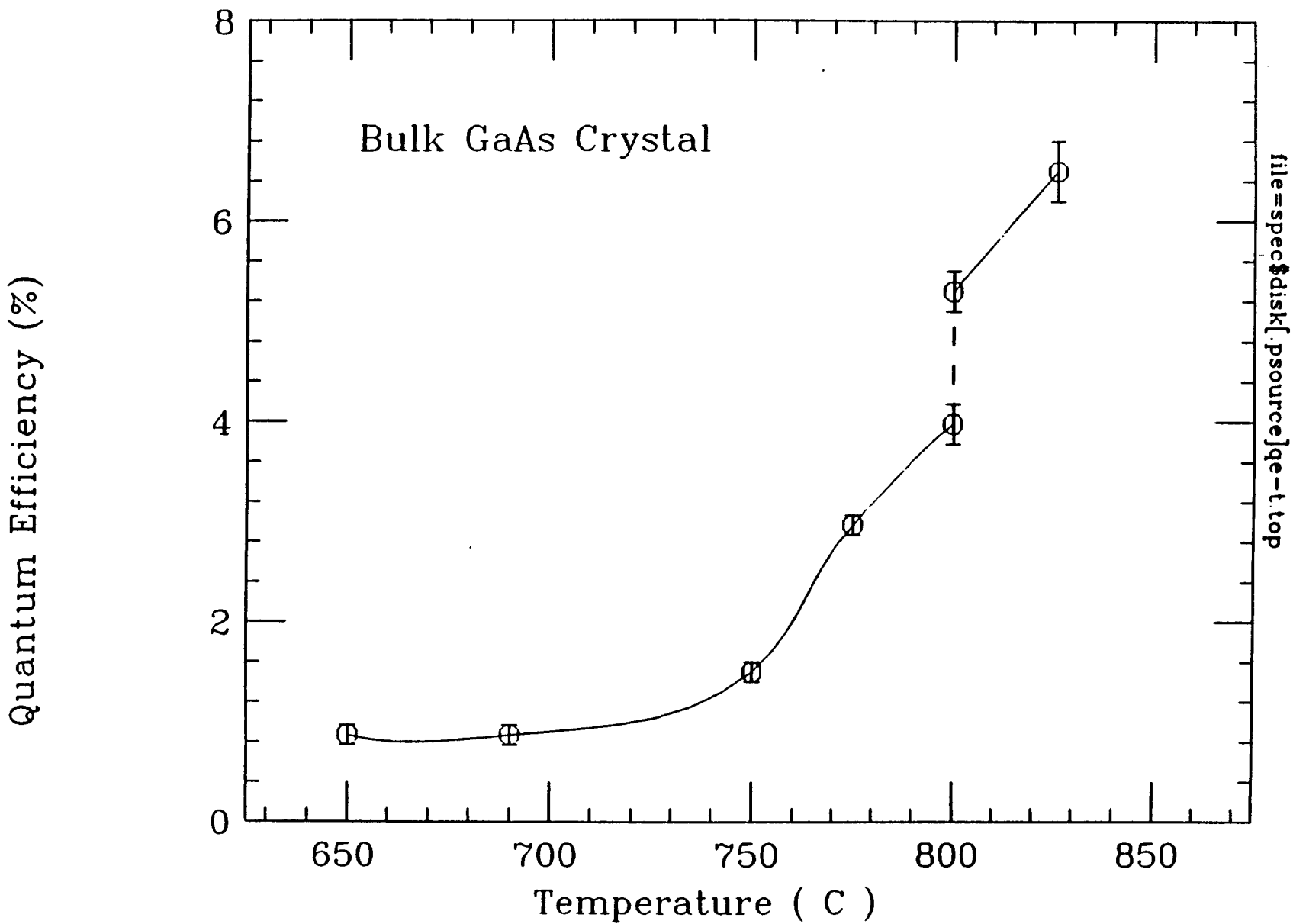


MIT BATES POLARIZED SOURCE  
CATHODE SUB-ASSEMBLY

# QE history as a function of Activations



# QE Vs. Heat Cleaning Temperature



## 5) Strained Crystals

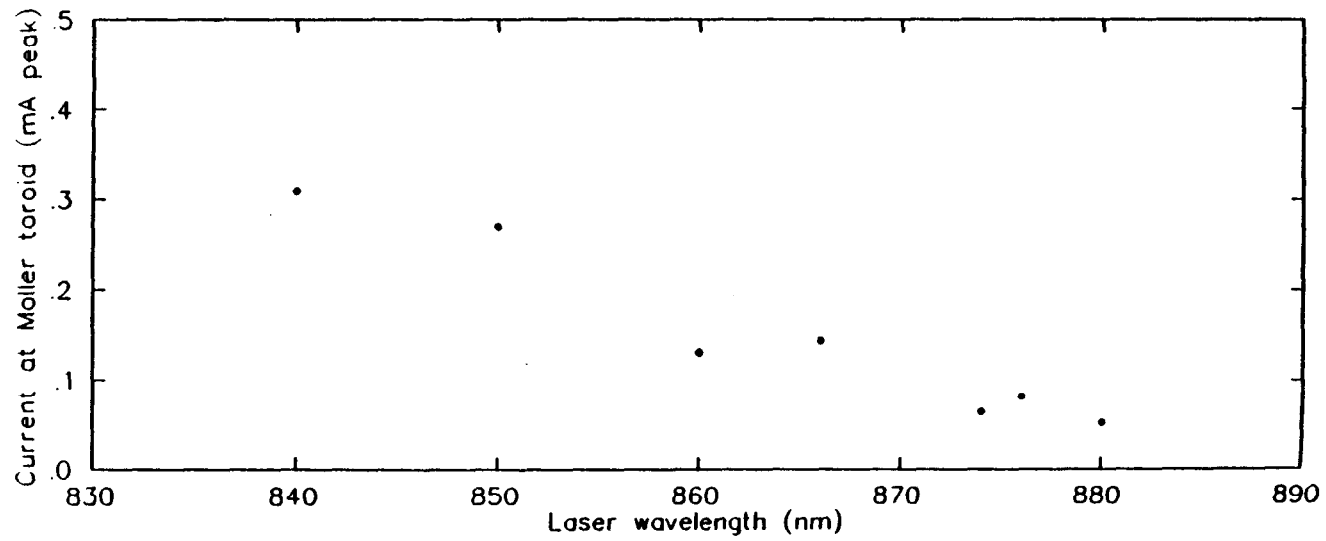
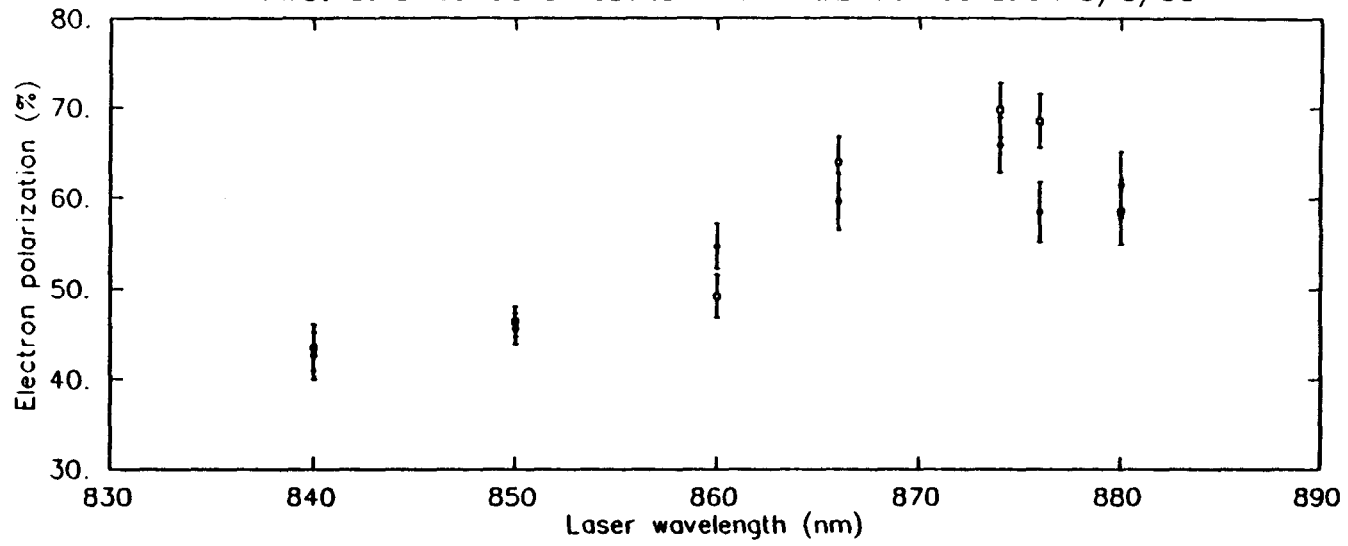
● In January 1993, installed a strained  $0.3\mu\text{m}$  thin GaAs crystal epitaxially grown on a  $\text{GaAs}_{(1-x)}\text{P}_x$  buffer manufactured by Spire corporation.

Layer	Composition (x)	Thickness ( $\mu\text{m}$ )
1	GaAs	0.25
2	$\text{GaAs}_{1-x}\text{P}_{x=0\rightarrow 0.29}$	2.5
3	$\text{GaAs}_{1-x}\text{P}_{x=0.29}$	2.5
4	GaAs	0.3

- Polarization: 42-75% for  $\lambda \approx 830\text{-}875\text{nm}$ ,  
polarimeter problems?
- Q.E. :  $\sim 0.1\text{-}0.15\%$
- Heat cleaning :  $650^\circ\text{C}$



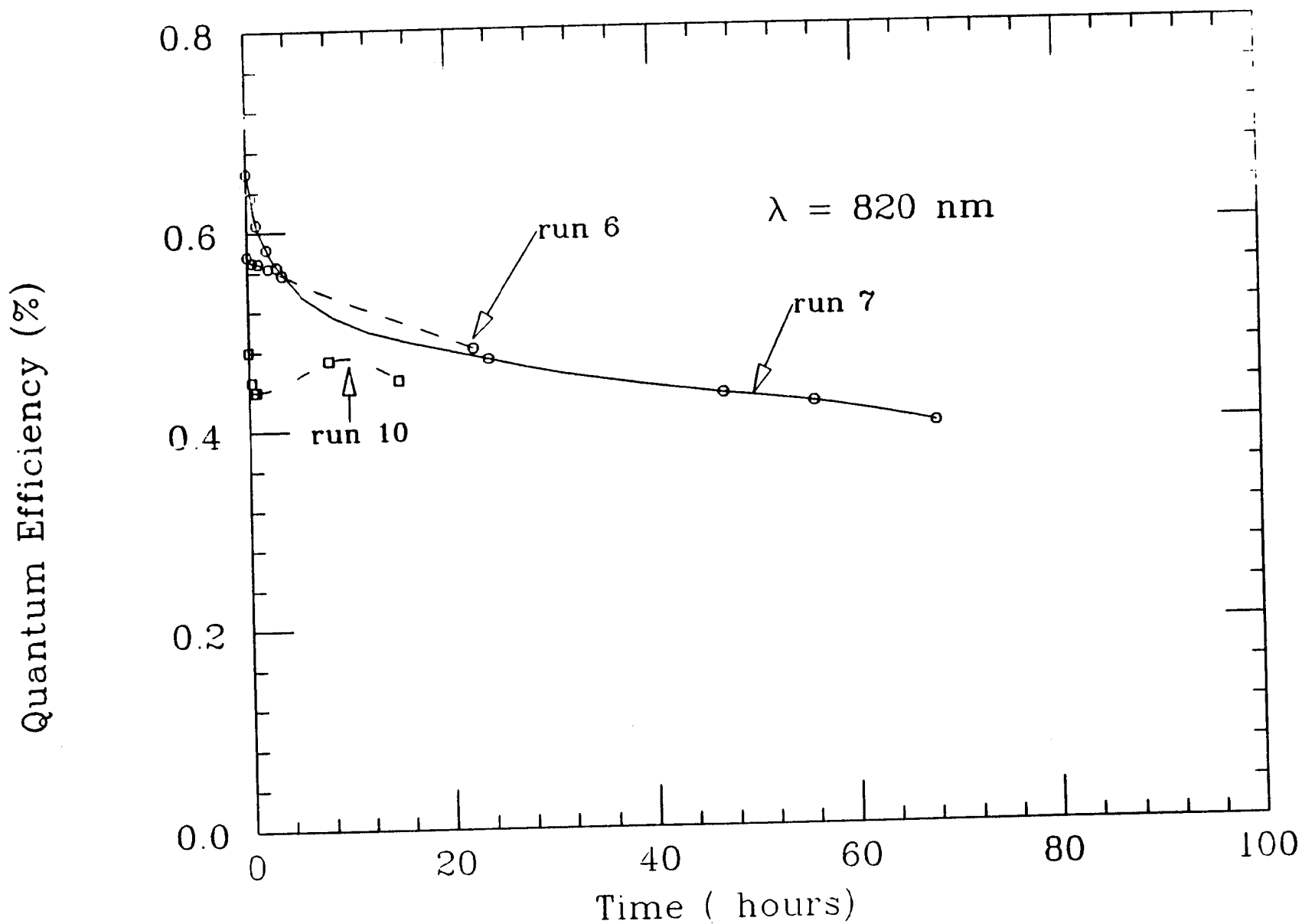
First strained GaAs results - SAMPLE Collaboration 3/8/93



- In August 1993, after successful recovery of Q.E. for bulk GaAs, decided to install a  $0.3\mu\text{m}$  strained GaAs described above. The upcoming FPP experiment will greatly benefit from the high polarization and needs only  $10\mu\text{A}$  average current which can be delivered.

- Figure of merit:  $P^2I$  P=polarization  
I=current
- Heat cleaning Temp.  $775^\circ\text{C}$
- Measured Q.E.:  $0.5\%$  at  $\lambda=840\text{ nm}$
- Dark life time :  $\sim 200$  hours
- Reduced immediate drop of Q.E. by stopping the flow of  $\text{NF}_3$  before reaching the final peak.
  
- Will measure beam polarization with S line møller. Soon after confirmation of high polarization will begin the FPP experiment.

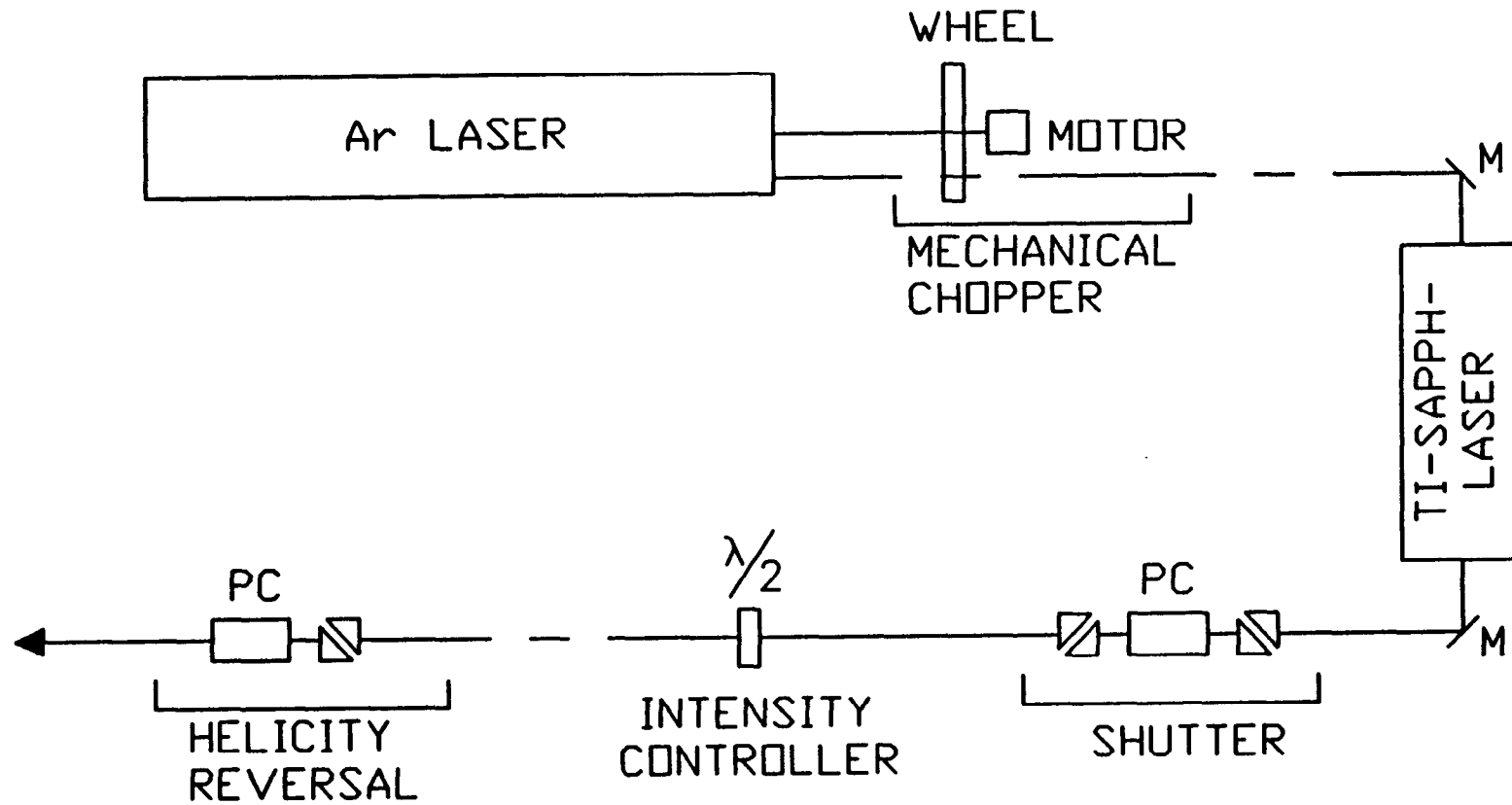
# QE for Thin Strained GaAs Crystal



## 6) Ti-Sapphire Laser development

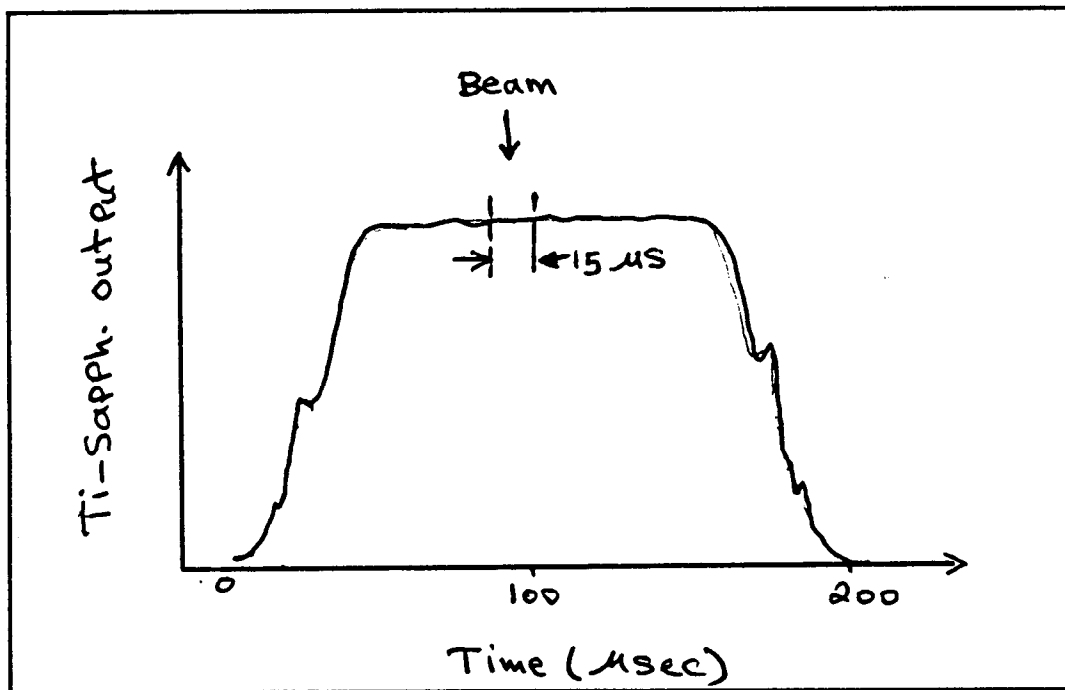
● The Coherent Ti-Sapphire laser model 890 can produce a maximum DC IR power of 4.2W (TEM00 mode) at 16W DC drive laser. By chopping the output of the drive laser, we are able to obtain IR peak powers as high as 9W from the Ti-Sapph with the drive laser at 30W peak. The loss-free chopper consists of a slotted wheel and a synchronous AC electromotor.

- chopped laser duty cycle      14%
- Drive laser pulse length    180 $\mu$ s
- Chopper repetition rate      600HZ
- Phase stability                5-15 $\mu$ s
- Maximum IR peak output    9W
- thermal load on Ti-Sapph.   minimal
- Gain in peak power            2.2



# LASER OPTICS FOR THE BATES POLARIZED INJECTOR

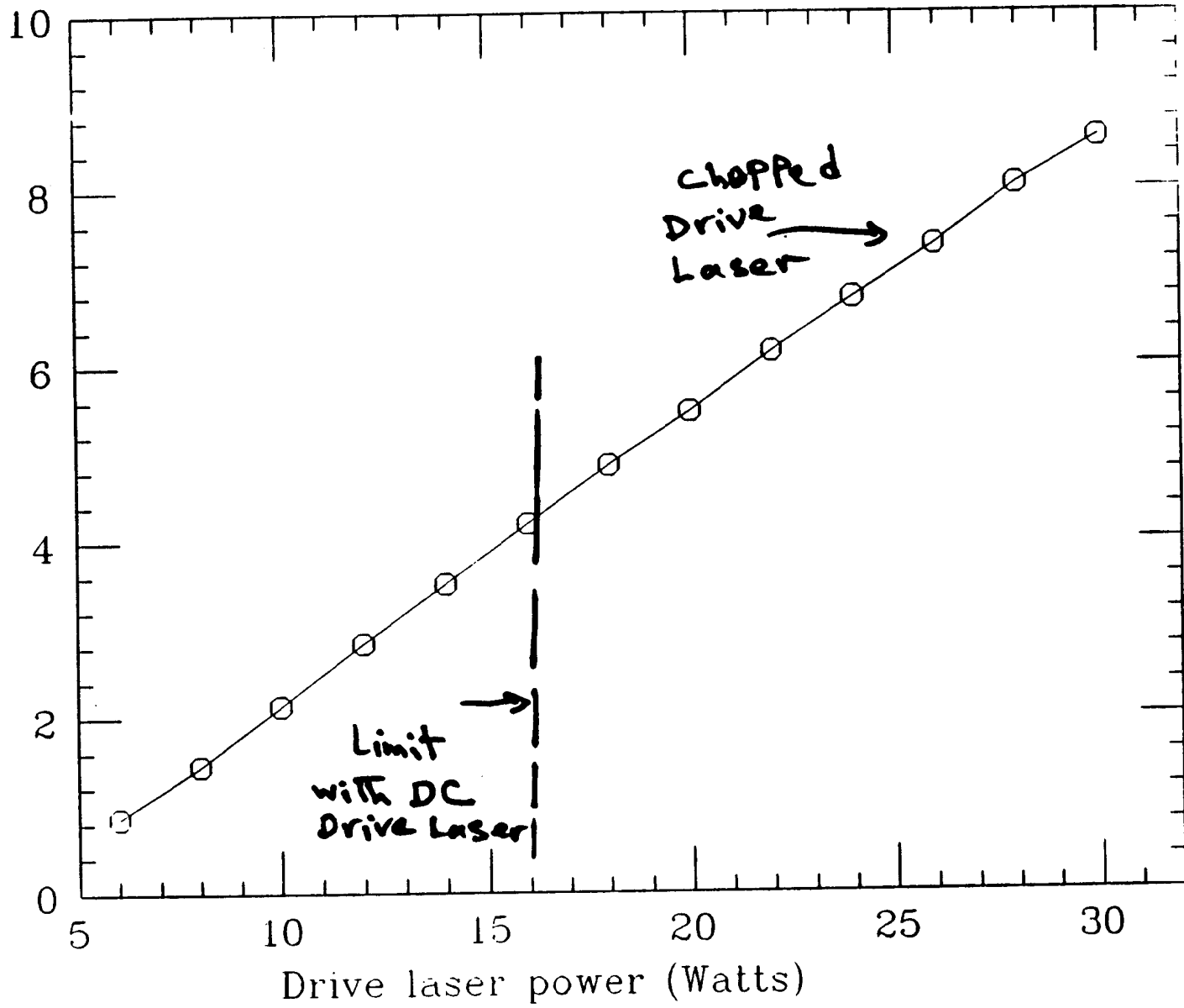
■ Have not yet measured the mode structure, but appears to be only the TEM00 mode. Used the chopper reliably during the recent polarized  $^3\text{He}$  runs.



# Ti-Sapphire power with Chopper

09

Ti-Sapphire output peak Power (Watts)



file=spec\$disk[.psource]laspower.top

## **7) Design of a New Injector**

● We are designing and fabricating a new polarized injector which will incorporate a load lock system for achieving higher Q.E. It is a diode gun similar to PEGGY II and the current Illinois/CEBAF gun, with a custom preparation chamber for handling multiple crystals.

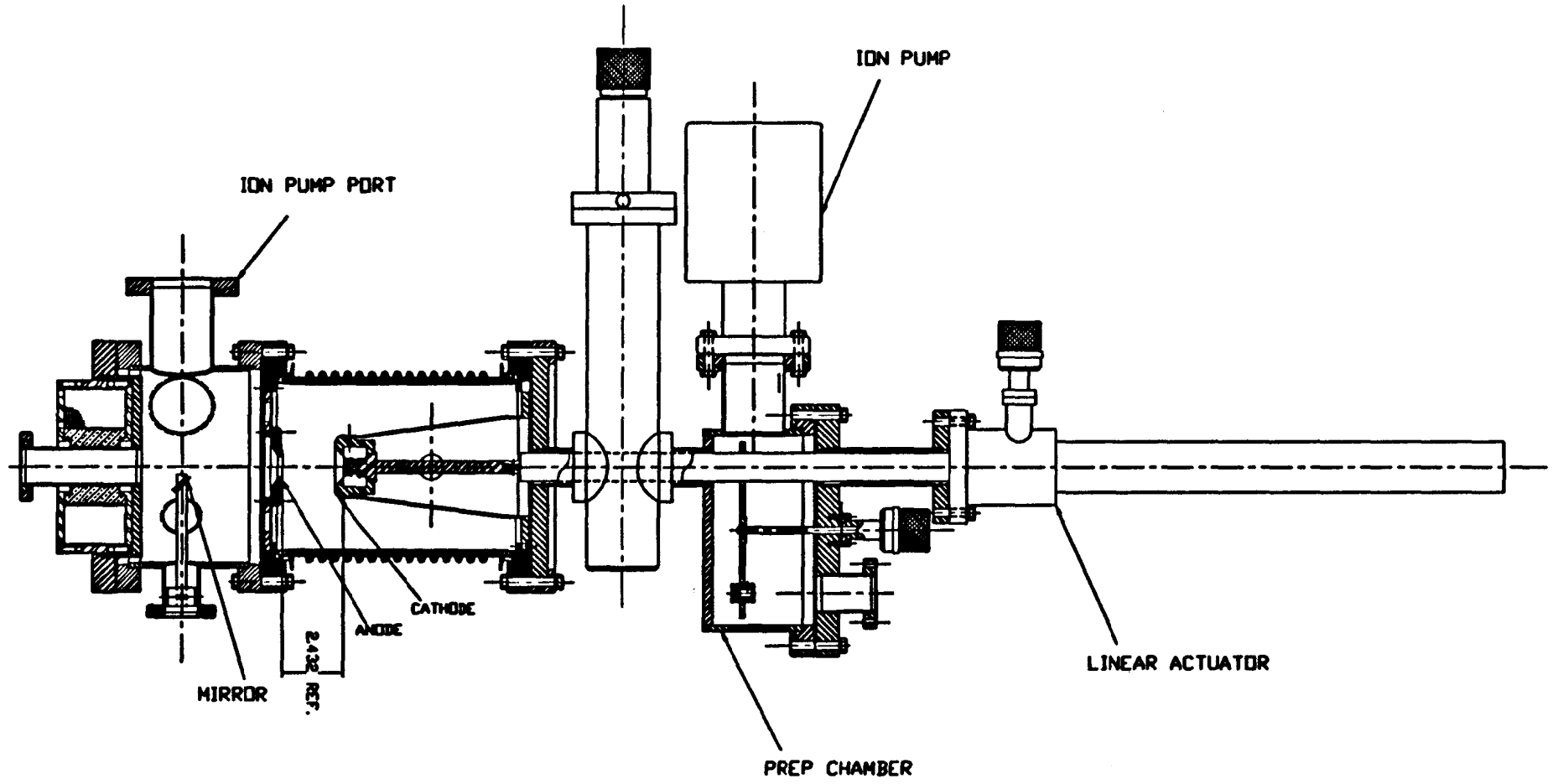
### **FEATURES:**

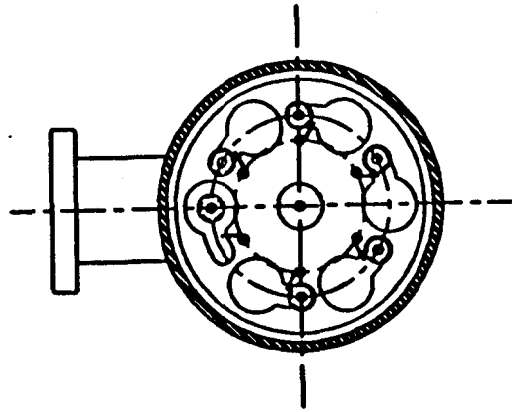
- Ultra high vacuum
  - Multiple crystals
  - Load lock, higher Q.E.
  - Reliability, ease of operation
  - Bakable chambers
  - Direct crystal temperature measurement
- Status: two chambers being built, some details still have to be resolved. Will be installed in 4-6 months.



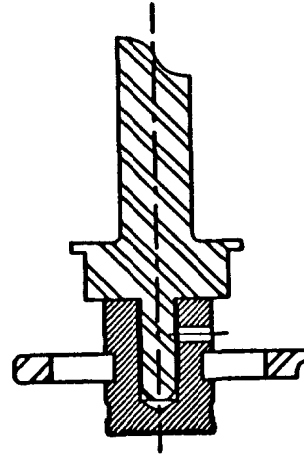
- Gun chamber:
  - bakable, PEGGY II
  - Cs,  $\text{NF}_3$  and heater
- Preparation Chamber:
  - bakable
  - Cs,  $\text{NF}_3$  lines and heater
  - holds up to 6 crystals
  - direct line of sight for a pyrometer
- Detachable loading chamber
  - unbaked
  - high vacuum
  - holds one crystal at a time

63

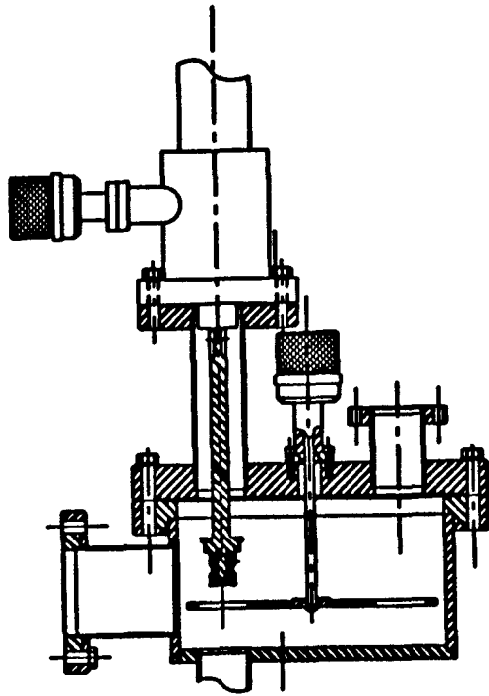




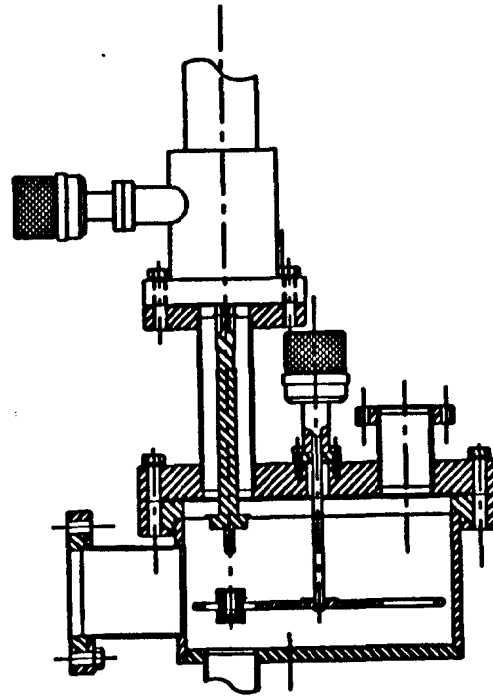
TOP VIEW



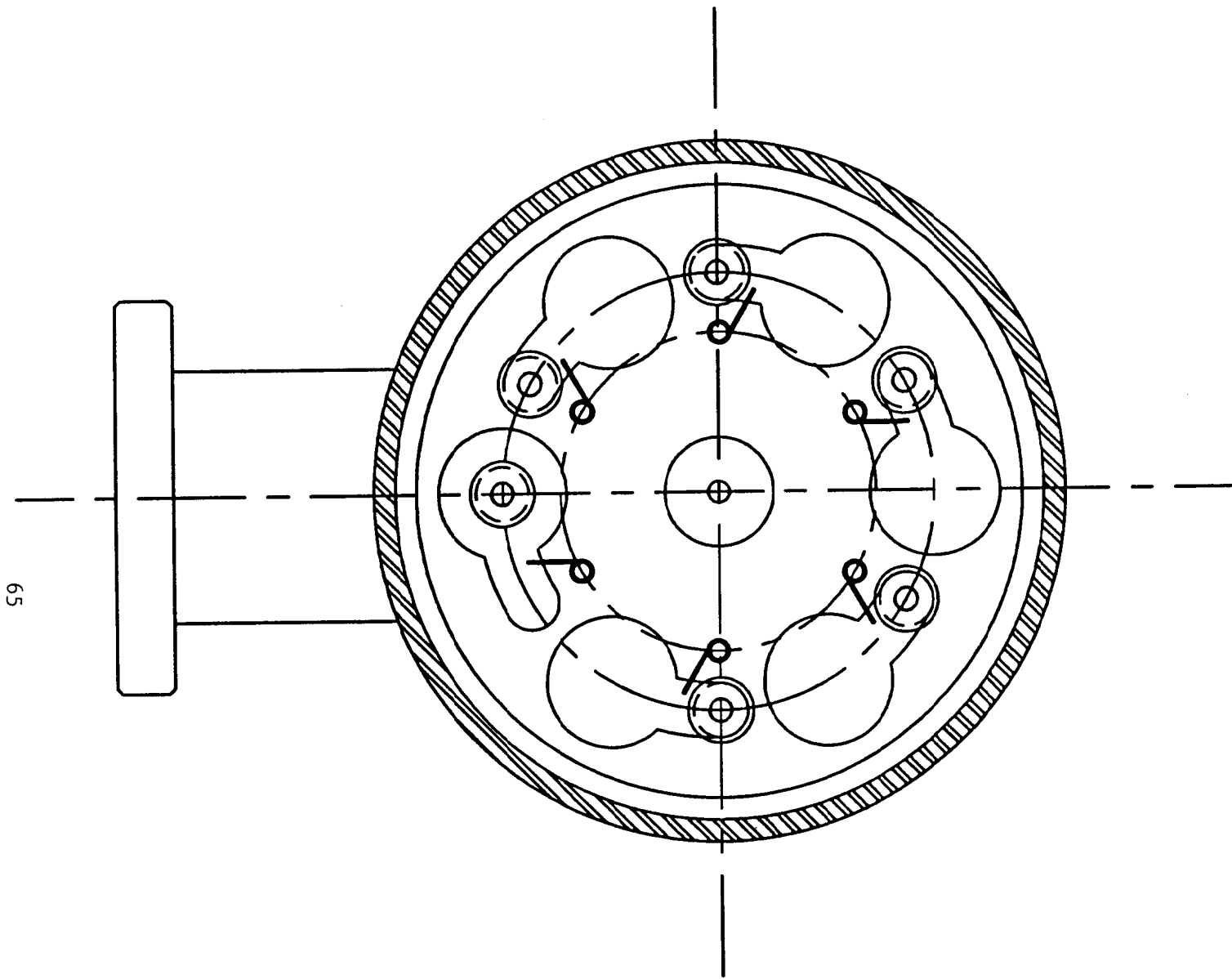
BAYONET SHOWN IN  
LOCK POSITION



VIEW SHOWN IN CLOSED POSITION



VIEW SHOWN IN OPEN POSITION



65

CARROUSEL CHAMBER

## 8) Summary

● The MIT-Bates polarized injector has delivered over 2500 hours for the past few years for medium energy nuclear physics experiments.

● Routinely ran with bulk GaAs with 40% polarization. Higher heat cleaning temperatures are necessary for maintaining high Q.E.'s.

● Recently installed a thin strained GaAs crystal for higher polarizations and obtained Q.E's as high as 0.5% in a system without a load lock. This will be the first time that a high polarization crystal is used for nuclear physics experiments.

● New injector with load lock capabilities being constructed and will be installed soon.

*note,  
this paper  
needs a lot  
of work and  
a pp to finish  
it up.*

**Timothy Gay**  
**University of Missouri-Rolla**

## **A New Polarized Electron Source & Electron Polarimeter**

I will discuss recent attempts in our laboratory to extract electrons with high degrees of longitudinal polarization from the negative glow and anode fall regions of a He DC discharge. The discharge is optically pumped by a recently developed Nd:LMA crystal laser which can produce metastable He polarizations in the discharge of better than 95%. The best polarization we have observed to date is about 6%, with several milliamps of beam current. The use of a new heavy-noble-gas inline optical electron polarimeter will also be discussed.

# A NEW POLARIZED ELECTRON SOURCE & ELECTRON POLARIMETER

Ken Trantham<sup>+§</sup>  
Ray Vandiver<sup>+</sup>  
Laird Scheerer<sup>+•</sup>  
Tim Gay<sup>+§</sup>

- Died 7 March 1993
- + University of Missouri - Rolla
- § University of Nebraska

Support : NSF Physics  
U. of Missouri  
U. of Nebraska

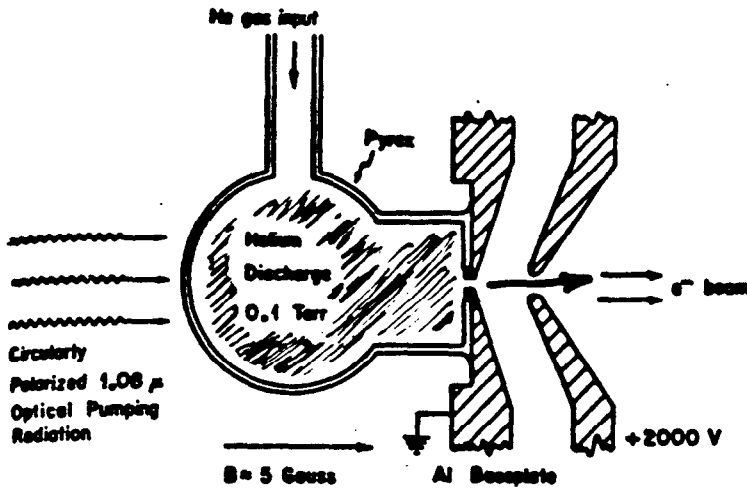


FIG. 4. Schematic diagram of the optical-pumping cell attached to the metal base plate. Also shown is the electrode used to extract the electrons from the discharge.

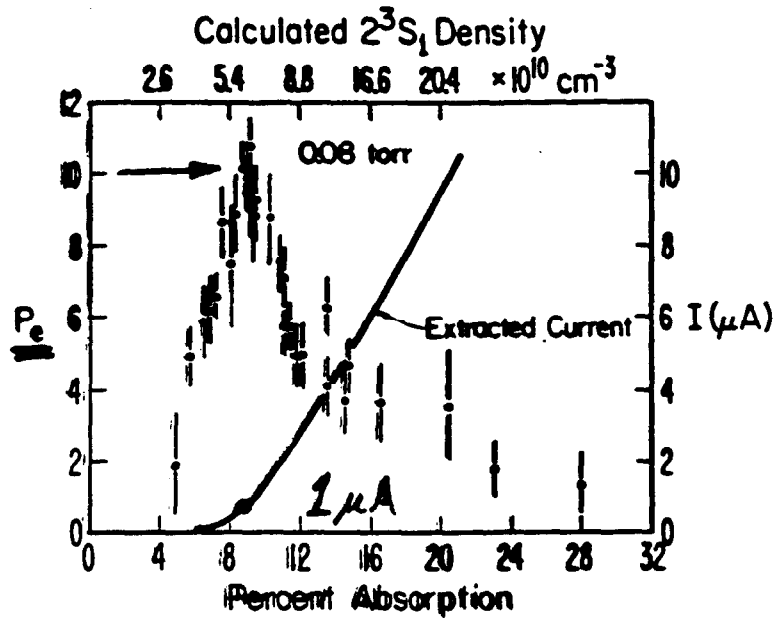


FIG. 6. Observed polarization and beam intensity of electrons extracted from an active discharge vs discharge intensity. The gas pressure is 0.08 torr. As in Figs. 1, 2, and 3 the relative absorption of the 1.08- $\mu$  pumping light characterizes the discharge intensity.

McCusker *et al.* PRA 5,  
177 (1972)



## Discharge Processes

### Ionization:



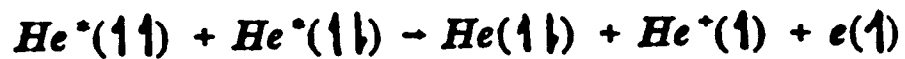
$$\sigma = \underline{3 \times 10^{-16}} \text{ cm}^2$$

### Spin Exchange:



$$\sigma = \underline{2 \times 10^{-14}} \text{ cm}^2$$

### Metastable - Metastable Collisions:

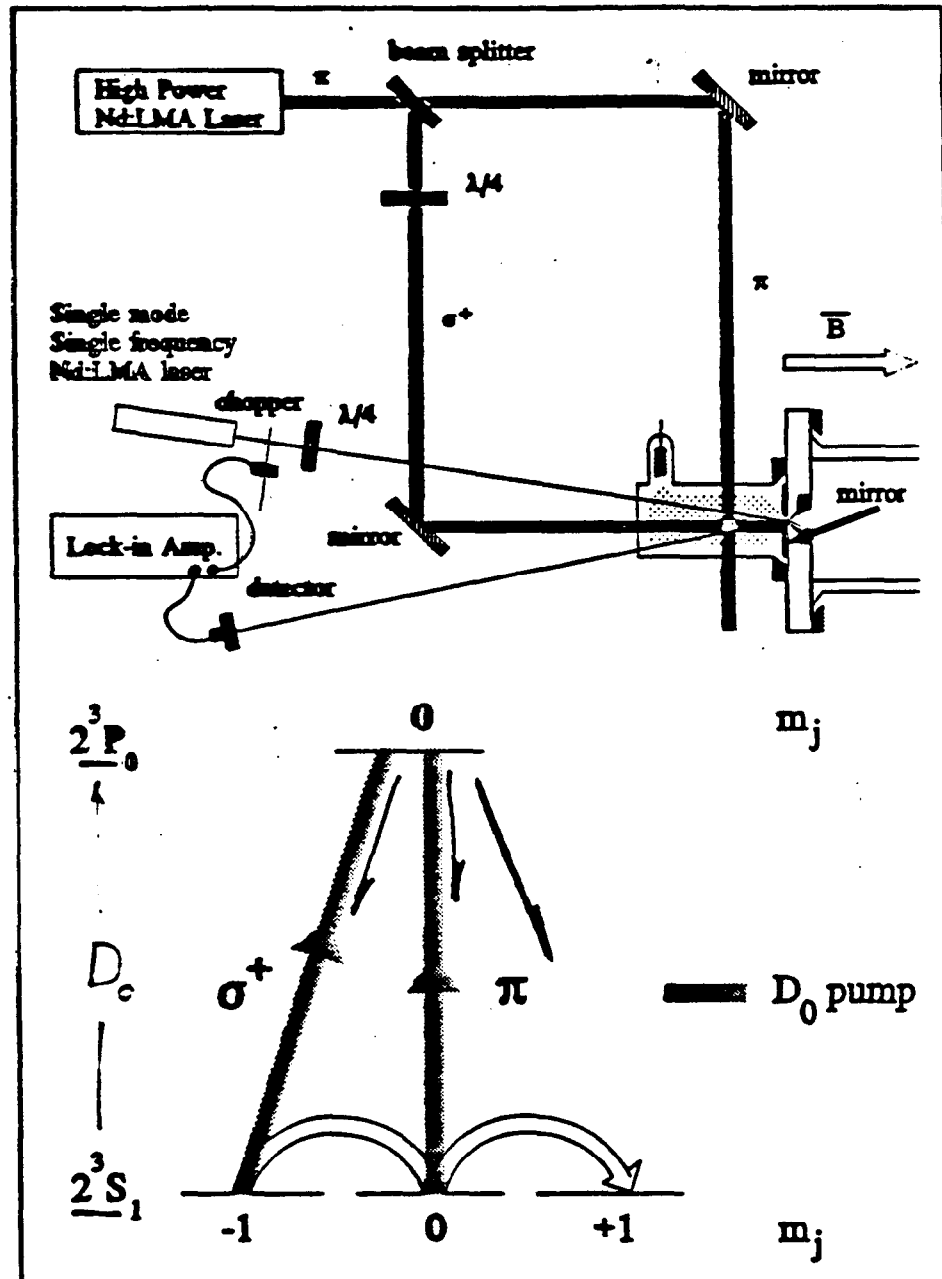


$$\sigma = \underline{1 \times 10^{-14}} \text{ cm}^2$$

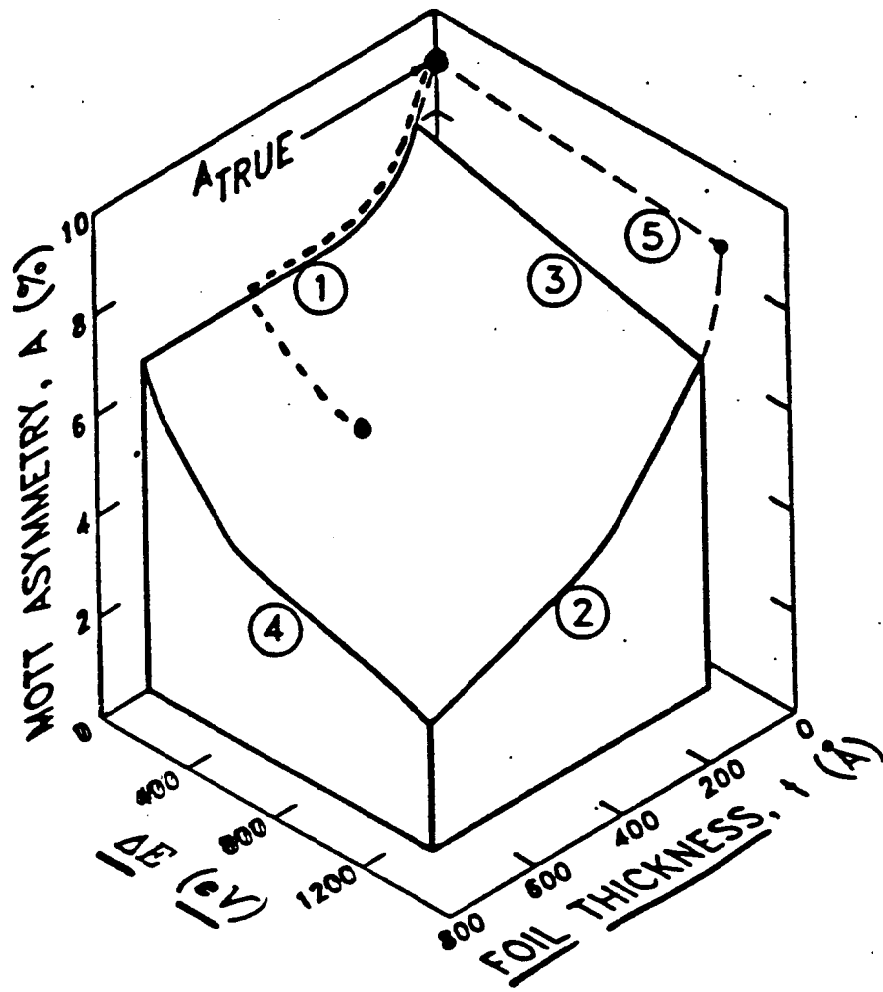
### Penning Ionization:



# Optical Pumping Setup



$$P_{He^*} > 0.97$$



Gay et al. RSI 63 114, 1635  
(1992)

# GENERIC OPTICAL ELECTRON

## POLARIMETER EQUATION :

$$\eta_2 = P_e (a + b\eta_3)$$



$$\eta_2 \Rightarrow P_e$$

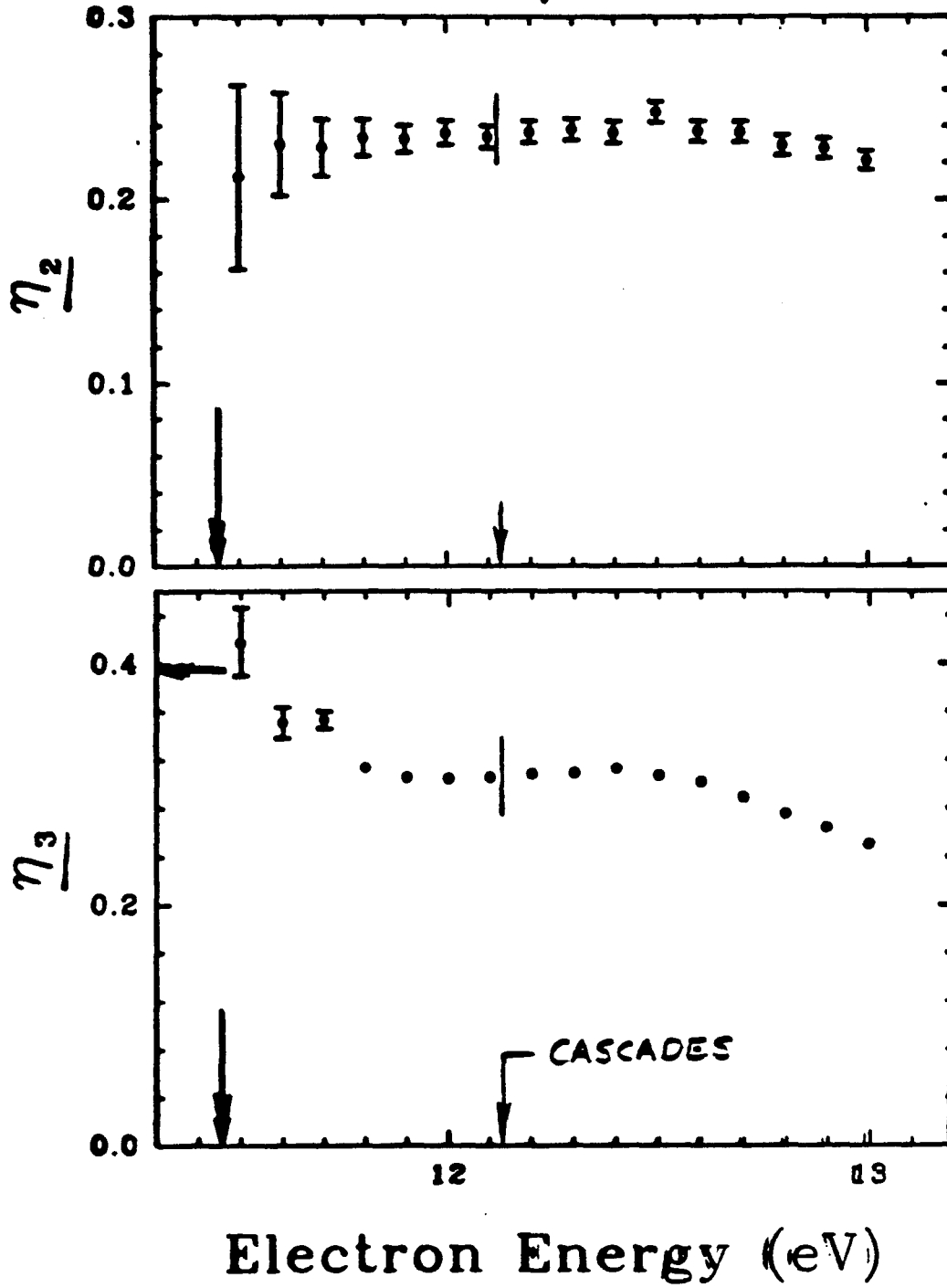


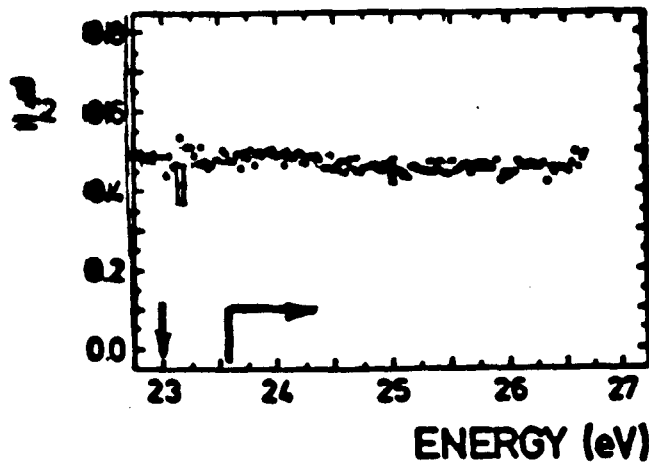
$$\eta_3 \Rightarrow \text{ANALYZING POWER}$$



$$\eta_1 \Rightarrow \text{VALIDITY OF KINEMATIC ASSUMPTIONS}$$

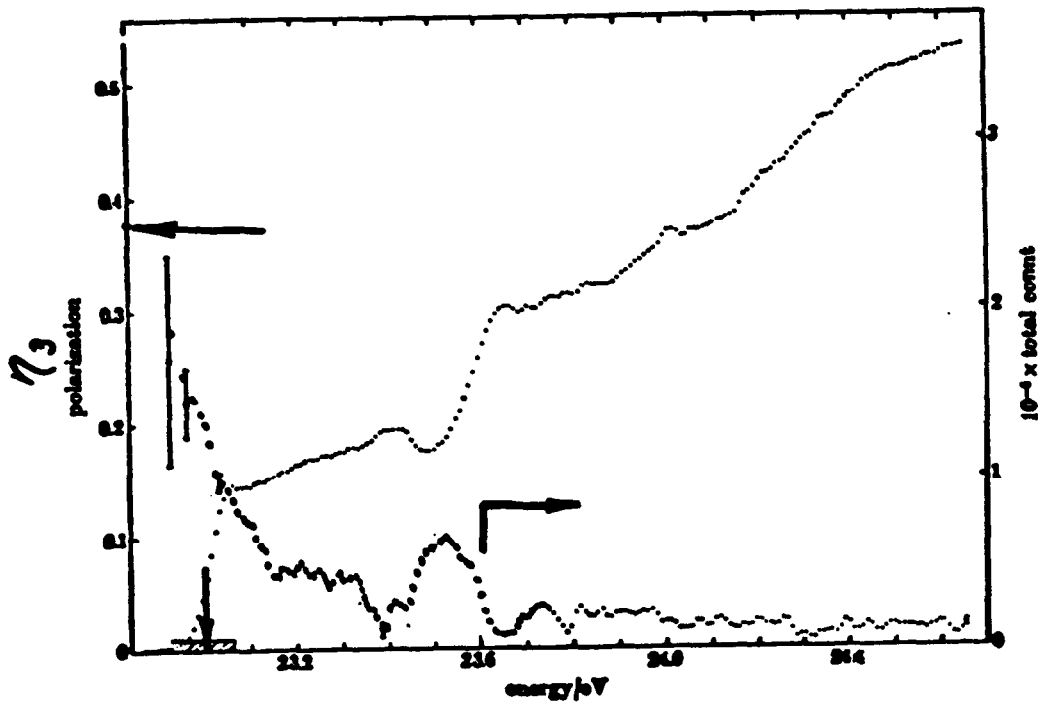
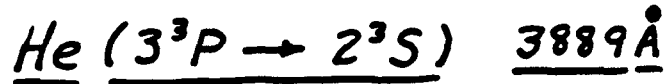
Kr ( $4p^5 5p^3 D_3$ )





Goehc, Kessler  
u. Harnc  
F.R.L. 59, 1413  
(1987)

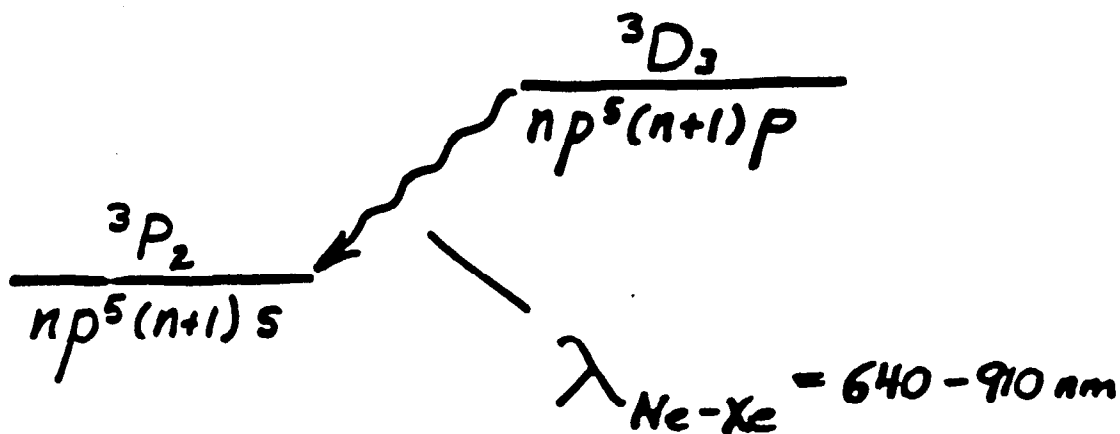
FIG. 2. Circular light polarization  $\eta_2$  normalized to the electron polarization by which it is caused. Transition He  $3^3P-2^3S$  (388.9 nm).



Hedde, Kessing & Parkin, F.R.S.L. 157, 415  
(1977)

# Choose target:

- heavy noble gases
  - easy to handle
  - $Z$ -dependence
- Russell-Saunders state
- optical decay
- isolation from cascading levels



# POLARIMETER EFFICIENCY

Element	Threshold Energy (eV)	Emission Wavelength (Å)	Closest Cascade Energy (eV)	Threshold $\eta/P_0$	$\eta/P_0$
Xenon J=3	9.72	8819	9.94 (5p <sup>5</sup> 5d <sup>2</sup> F <sub>2</sub> )	0.7080	0.6322 (1 + 0.3098 $\eta_0$ )
Krypton J=3	11.44	8112	12.11 (4p <sup>4</sup> 4d)	0.6959	0.6245 (1 + 0.2863 $\eta_0$ )
Argon J=3	13.07	8115	14.07 (3p <sup>3</sup> 3s <sup>2</sup> P <sub>2</sub> )	0.7317	0.6667 (1 + 0.2222 $\eta_0$ )
Neon J=3	18.55	6402	19.66 (2p <sup>4</sup> 4s <sup>2</sup> P <sub>2</sub> )	0.7315	0.6663 (1 + 0.2230 $\eta_0$ )
Krypton J=2	11.44	8777	12.03 (4p <sup>4</sup> 4d)	0.0000	0.2319 (1 - 3.264 $\eta_0$ )

He  
(3<sup>3</sup>P-  
2<sup>3</sup>S)

23.0      3889      23.6(4<sup>3</sup>S) 0.4382

• "figure of merit" =  $\sqrt{IA^2}$

- A = analyzing power

- I = detected intensity

TARGET

(IA<sup>2</sup>)<sup>0.5</sup>

He	1.0
Ne	12
Ar	10
Kr	34
Xe	3.1



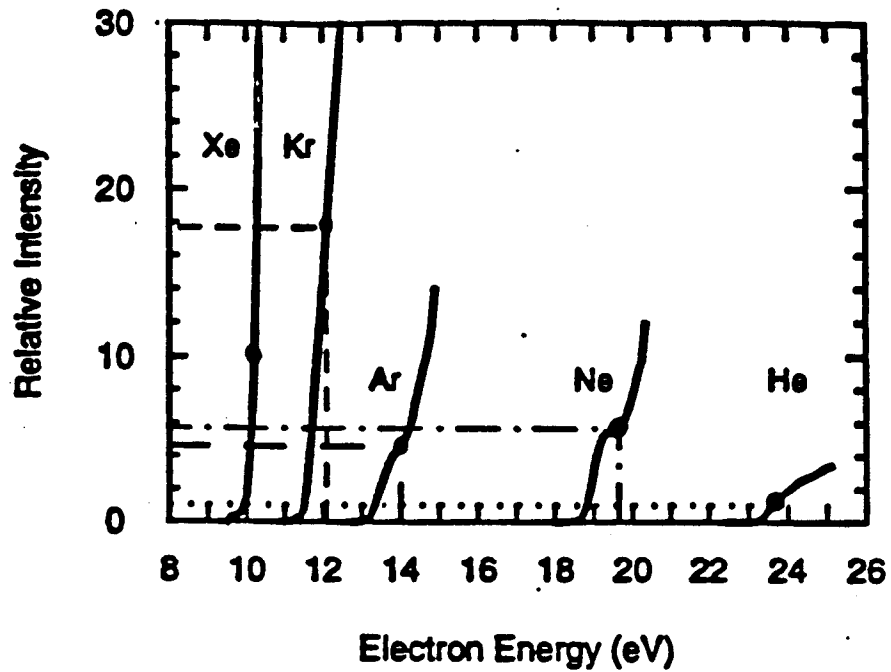
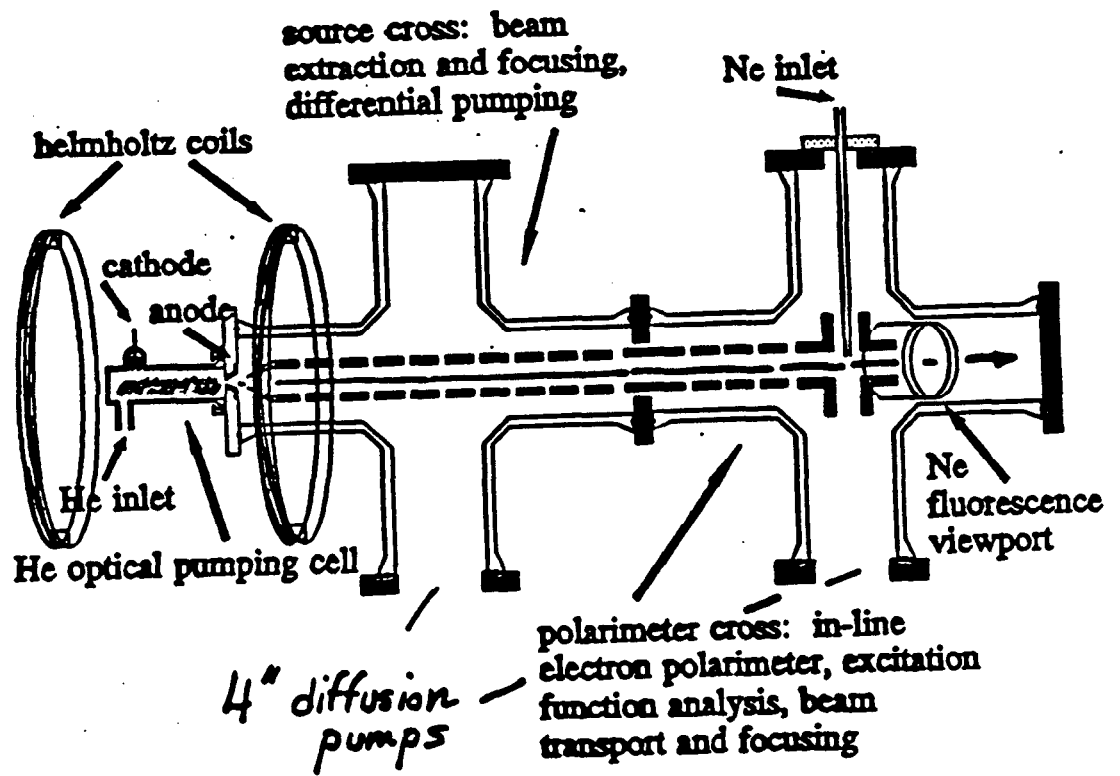
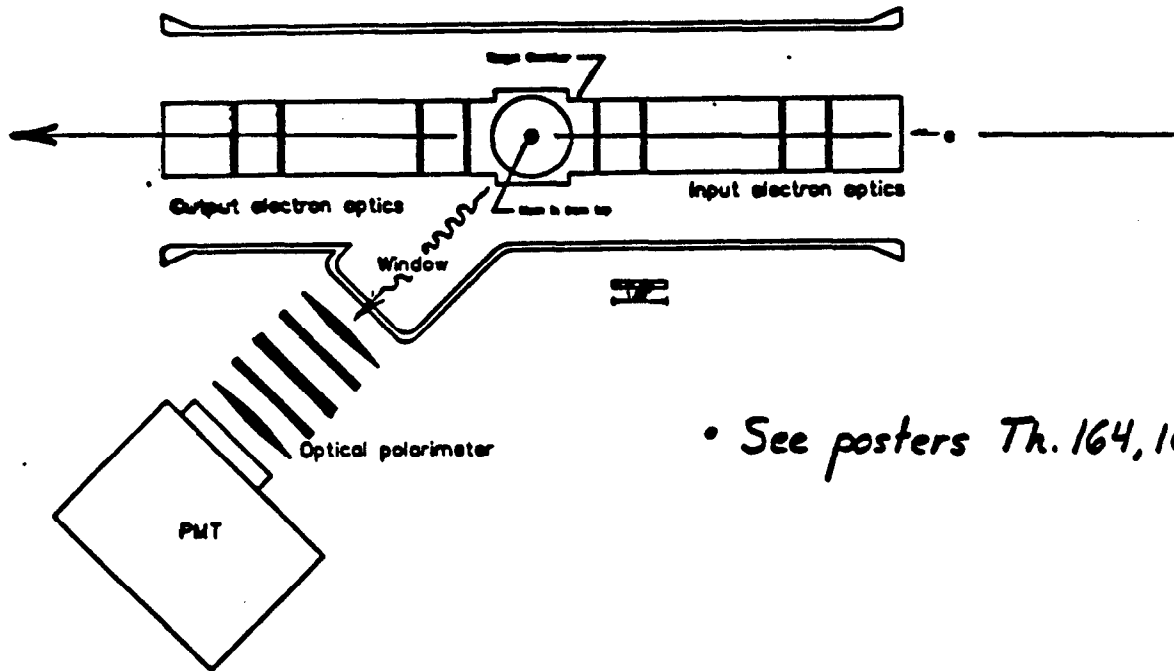


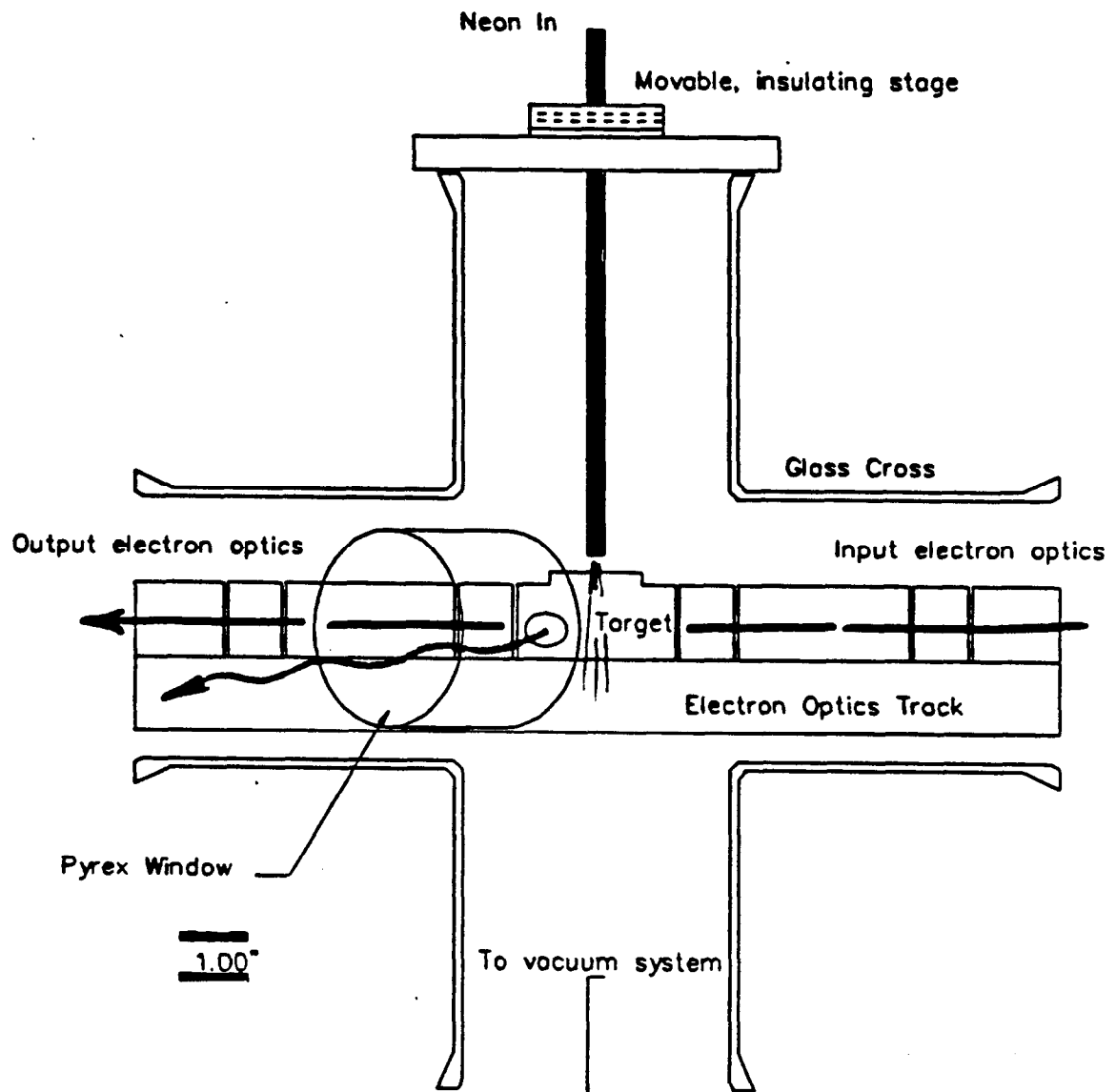
Figure 45. Relative photon intensity plotted versus the electron energy for the  $J = 3$  states in the noble gases Xe, Kr, Ar, Ne, and He.

Table XXXVI. ANALYZING POWERS AND RELATIVE EFFICIENCIES OF THE NOBLE GAS ELECTRON POLARIMETERS.

Element	Analyzing Power	Usable Energy Width (eV)	Relative Efficiency
He	0.49	<u>0.6</u>	1
Ne	0.72	<u>1.1</u>	12
Ar	0.71	<u>1.0</u>	10
Kr	0.67	<u>0.7</u>	33
Xe	0.70	<u>0.2</u>	2

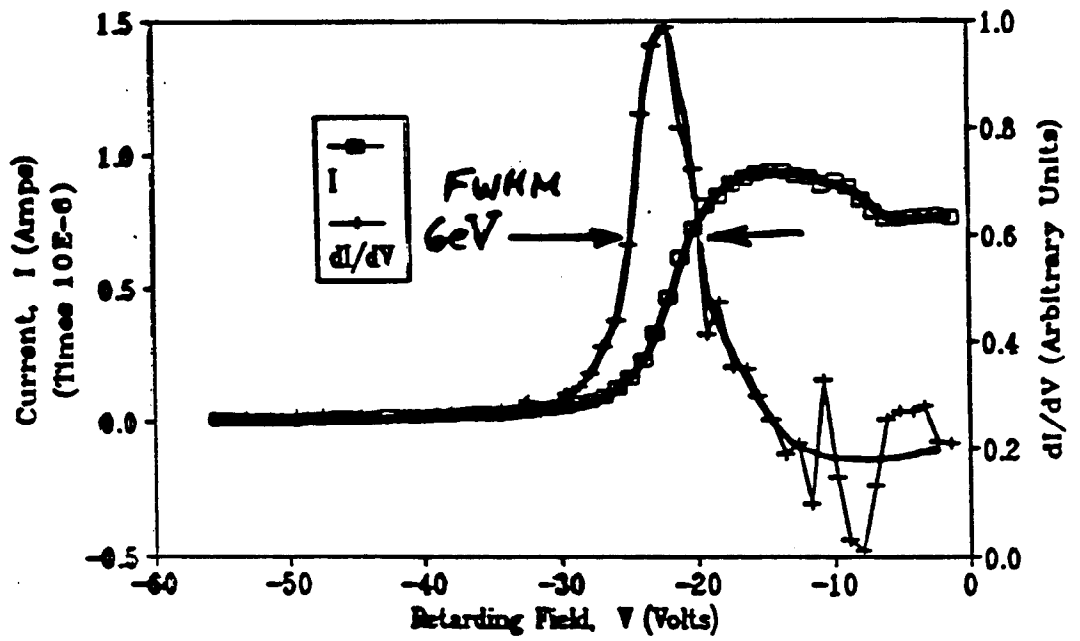






# Retarding Field Analysis

## Electron Beam Energy Profile



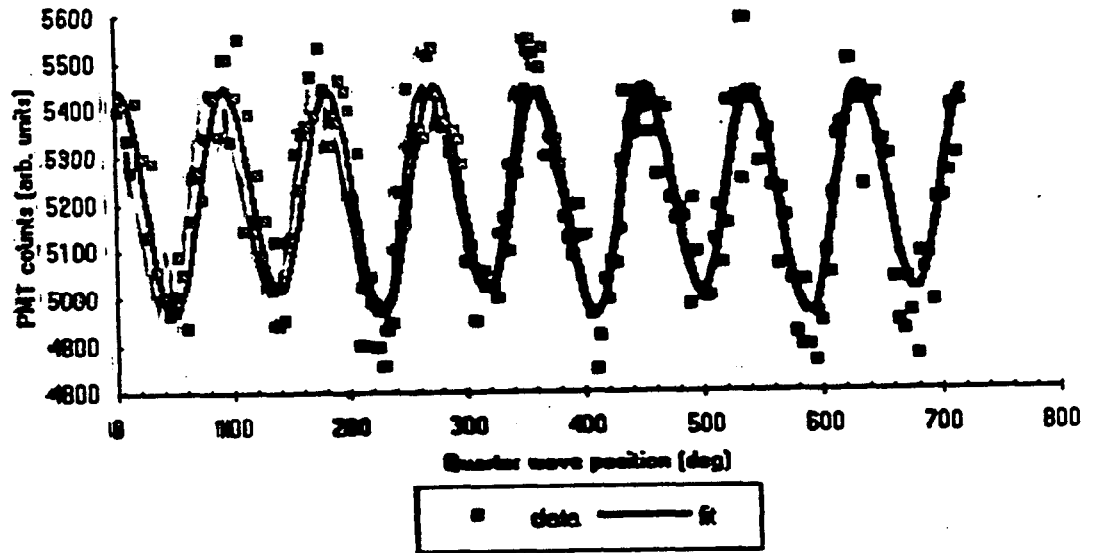


Figure 8. Sample data taken with optical polarimeter using an unpolarized electron beam.

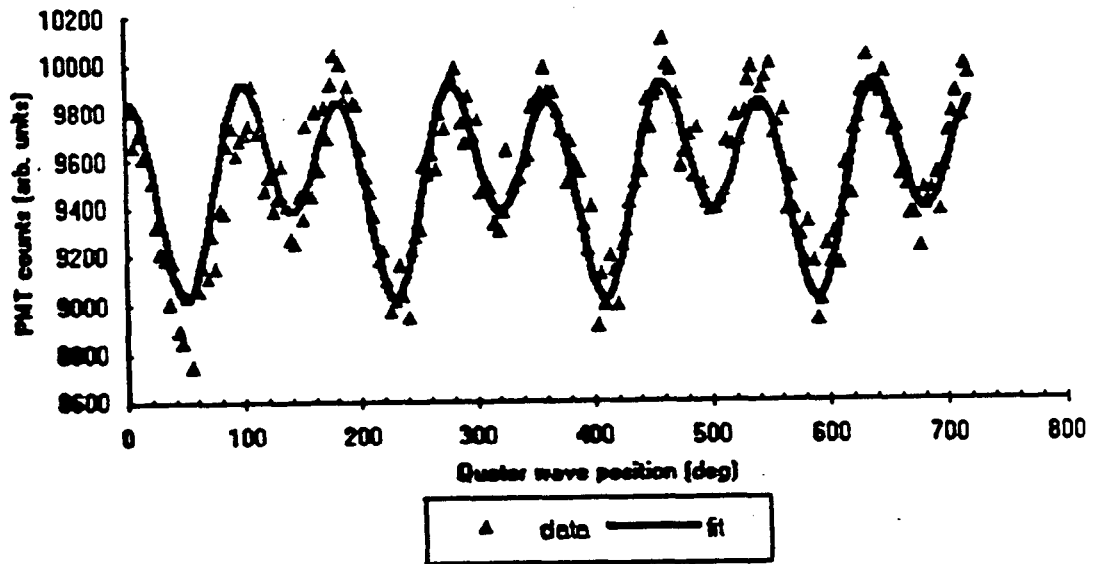


Figure 9. Sample data taken with optical polarimeter using a polarized electron beam,  $P_e = 5\%$ .

## Characteristics of Selected Polarized Electron Sources

Source	Polarization	I ( $\mu$ A)	$\Delta E$ (eV)	$P^2 I$ (A)
UMR Source (present work)	0.06	$> 200$	$\leq 10$	$7 \times 10^{-7}$
Rice He Afterglow Source <sup>1</sup>	0.8	<del>50</del> $0.05$	$\leq 0.15$	$8 \times 10^{-6}$
AlGaAs-GaAs Superlattice <sup>2</sup>	0.71	0.05		$3 \times 10^{-8}$
NEA GaAs <sup>3</sup>	0.43	$20^a$	0.13	$4 \times 10^{-6}$

<sup>a</sup>For 1 mW incident radiation.

1. L.G. Gray, K.W. Giberson, Chu Cheng, R.S. Keiffer, F.B. Dunning, and G.K. Walters, Rev. Sci. Instrum. **54** 271 (1982).

2. T. Omori, Y. Kurihara, T. Nakanishi, H. Aoyagi, T. Baba, T. Furuya, K. Itoga, M. Mizuta, S. Nakamura, Y. Takeuchi, M. Tsubata, and M. Yoshioka, Phys. Rev. Lett. **67** 3294 (1991).

3. D.T. Pierce, R.J. Celotta, G.C. Wang, W.N. Unertl, A. Galejs, C.E. Kuyatt, and S.R. Mielczarek, Rev. Sci. Instrum. **51** 478 (1980).

**Vincenzo Guidi  
Ferrara**

**Experimental Study on the Time Resolution of Negative  
Electron Affinity GaAs**



# EXPERIMENTAL STUDY ON THE TIME RESOLUTION OF NEGATIVE ELECTRON AFFINITY GaAs

A.V.Aleksandrov<sup>1)</sup>, R.Calabrese<sup>2)</sup>, G.Ciullo<sup>3)</sup>, N.S.Dikansky<sup>1)</sup>  
V.Guidi<sup>2)</sup>, G.Lamanna<sup>4)</sup>, P.Lenisa<sup>3)</sup>, P.V.Logachov<sup>1)</sup>,  
A.V.Novokhatsky<sup>1)</sup>, L.Tecchio<sup>5)</sup>, and B.Yang<sup>3)</sup>

- 1) Institute for Nuclear Physics, Novosibirsk, Russia
- 2) Dipartimento di Fisica dell'Università and INFN, I-44100 Ferrara, Italy.
- 3) Laboratori Nazionali di Legnaro, I-35020 Legnaro, Italy
- 4) Dipartimento di Fisica dell'Università di Bari and INFN, I-70125 Bari, Italy
- 5) Dipartimento di Fisica Sperimentale dell'Università and INFN, I-10125 Torino, Italy.

## **Abstract**

We describe our results relative to a study on the time resolution of GaAs. We measured an upper limit of 200 ps for this parameter. We demonstrated the possibility to produce high-density electron bunches in the picoseconds region using GaAs as photoemitter.

## Introduction

GaAs is a good candidate as photoemitter in a RF-gun for production of high-intensity spin-polarized electron bunches. The design of such RF-gun requires the knowledge of the frequency of the accelerating cavity; this should be much longer than the duration of photoemitted electron bunches. Thus, the knowledge of the intrinsic time resolution of GaAs turns out to be of great relevance. An investigation over this parameter is the aim of the present work.

## Experimental set-up

The GaAs cathode (p-doped by Zn,  $10^{19} \text{ cm}^{-3}$ ) is prepared in NEA condition by depositing Cs and O<sub>2</sub> at its surface with standard procedure [1]. Once activation has been accomplished, the cathode is fastened to the DC-gun through manipulator. This allows to carry out activation in a separate chamber and bypass all the problems connected with sparking due to high-voltage. The cathode is negatively biased with a voltage ranging within 0-50 kV. At 50 kV, the DC-gun is limited by space-charge at 3 A cw current. Fig. 1 illustrates a layout of the experimental apparatus.

Photoemission is excited by three lasers: a cw 75 mW Ar<sup>+</sup> for activation, a frequency doubled Nd:YAG (532 nm), producing pulses 15 ns long, and a 1.5 mJ/pulse Nd:YLF (535 nm) with 10 Hz repetition rate. The first pulsed laser is useful

for calibration of the diagnostic system as it will result clear later on. The Nd:YLF is the laser used for investigating the time resolution ( $\tau_{\text{GaAs}}$ ) of GaAs. Fig. 2 shows the temporal profile of a typical laser shot: it is 98 ns wide at FWHM. This nominal parameter is not useful for characterizing the time-of-extraction of electrons from GaAs. This owes to the saturation imposed by space-charge which makes the tails of the laser profile to be important. Thus, the interval  $\tau_L$ , corresponding to 10% of the top-height was referred to as temporal length of the laser pulse; we measured  $\tau_L=(188\pm 10)$  ps

### Diagnostics

The first diagnostic tool is a wall-current monitor, the resolution of which is estimated to be approximately 500 ps. This kind of diagnostics provides only preliminary results, not being much accurate. Fig. 3 shows a current pulse recorded by this device and displayed through a 8 GHz bandwidth oscilloscope. The width at half maximum of this pattern turns out to be 430 ps, indicating that  $\tau_{\text{GaAs}}$  might be lower than the results of some theoretical predictions [2].

Our most accurate diagnostics device is a combination of a RF-cavity and a "2 $\pi$ -detector". The RF-cavity operates in TM<sub>210</sub> mode with two power inputs, geometrically shifted by  $\pi/2$  rad in angle (Fig. 4a) and supplied by a magnetron. Figs. 4b,c display the patterns of electric and magnetic fields in the cavity relative to the two power inputs. When the electron beam and the cavity

are coaxial, no action of the electric field is exerted on electrons. The two magnetic fields are shifted by  $\pi/2$  in time and equally strong in amplitude; their vector composition results in a magnetic field, constant in modulus, rotating at the frequency of the cavity ( $\nu=2.465$  GHz). This magnetic field imparts the incoming electrons a transverse kick whose direction depends on the time at which a single electron enters the cavity. As a result, the trace of electrons over a cross section orthogonal to the beam axis would be an arc of a circle, provided the bunch length be lower than one cycle of the RF-cavity (400 ps). The " $2\pi$ -detector" is a series of 30 molybdenum sectors perpendicular to the axis with a hole inside; each sector acts as a Faraday cage to collect the electrons of the bunch. Looking at the number of sectors excited one can assess the duration of the bunch. The maximum resolution of this instrument is  $400/30=13.5$  ps. Electronic noise limits the maximum measurable charge to  $10^6$  electrons, collected by all sectors.

Alternatively to the " $2\pi$ -detector", there is a phosphorescent screen which gives a lively image of what would have been the distribution of electrons on the sectors. This device is only a qualitative check but helps much in the initial setting-up of the device.

## Results

Fig.5 shows the response of the detector when the beam, accelerated to 32 kV with the cavity switched off, passes

through the central hole of the detector and therefore no sector is excited. The Nd:YAG laser is used for this measurement. External coils allow to drive the beam in the X-Y plane, perpendicular to the beam axis. In this way, the beam can be centered in the detector. We now switch on the RF-cavity then observing a pattern with an homogeneous number of counting for each sector (Fig. 6). This is not the case when the beam is not centered. Fig. 7 illustrates the response of the detector when a kick is imparted rightward by external coils.

With the cavity off, we move the beam leftward (Fig. 8): we see that, at 45 kV, three channels are excited (equivalent to approximately 40 ps); this is the resolution of the device.

Fig. 9 shows that, at 45 kV, 16 channels are excited; after deconvolution with the resolution of the apparatus, the duration of the electron bunch is  $\tau_B=(200\pm 20)$  ps. The 15-th channel got broken during the carrying out of experiment and therefore its response is always zero. We repeated the measurement at 40 kV observing 17 channels excited, equivalent to  $\tau_B=(210\pm 20)$  ps. Fig. 10 is the result of a measurement at 30 kV: a large broadening is recorded due to space-charge. We calculated that, at 45 kV, the lengthening provided by space-charge to an arbitrarily short pulse is about 150 ps. As a consequence, an improvement of the system's performance can be achieved both by raising up the voltage to 100 kV and shortening the laser pulse.

Tab. 1 summarizes the experimental values of bunch duration versus voltage. Although we were limited by space-

charge we produced  $4 \cdot 10^9$  electrons/pulse at 45 kV with a lifetime of 3 days.

## Discussion

On the strength of the experimental evidences recorded through this work, GaAs seems to be very rapid. We provide an upper limit for the response time of GaAs, measured to be lower than 200 ps. This result is very promising for future developments of GaAs photocathodes in the picosecond range.

*Table 1*

Voltage (kV)	$\tau_B$ (ps)
45	$200 \pm 20$
40	$210 \pm 20$
30	$\geq 400$

## References

- [1] D.T.Pierce, R.J.Celotta, G.-C.Wang, W.N.Unertl, A.Galejs, C.E.Kuyatt and S.R.Mielczarek; *Rev. Sci. Instrum.* **51** (1980) 478.
- [2] R.L. Bell, *Negative Electron Devices*, (Clarendon Press, Oxford 1973).

## Figure captions

*Fig.1* Layout of the experimental apparatus.

*Fig.2* Temporal profile of a laser bunch.

*Fig.3* Current pulse recorded by a wall-current monitor.

*Fig.4* a) sketch of the cavity with two power inputs;  
b) electric and magnetic fields in the cavity due to the first power input;  
c) the same as *b* relative to the second input.

*Fig.5* Pattern recorded by the " $2\pi$ -detector" with the cavity off; the voltage is set at 32 kV and the Nd:YAG laser is used.

*Fig.6* Same parameters as figure 4 but the cavity is switched on. The circular scanning is the result of the magnetic field in the cavity.

*Fig.7* Response of the detector when a kick is imparted rightward by external coils. The cavity is switched on.

*Fig.8* With the cavity on, the beam is kicked leftward. The number of sectors excited determines the resolution of the device (about 40 ps). Here the voltage is 45 kV.



*Fig.9* Response, at 45 kV, of excitation by Nd:YLF laser. When the resolution of the device is accounted for, the duration of the electron bunch is  $\tau_B=(200\pm 20)$  ps.

*Fig.10* The same as figure 9 but with 30 kV voltage; it appears clear from the figure the broadening due to space-charge.

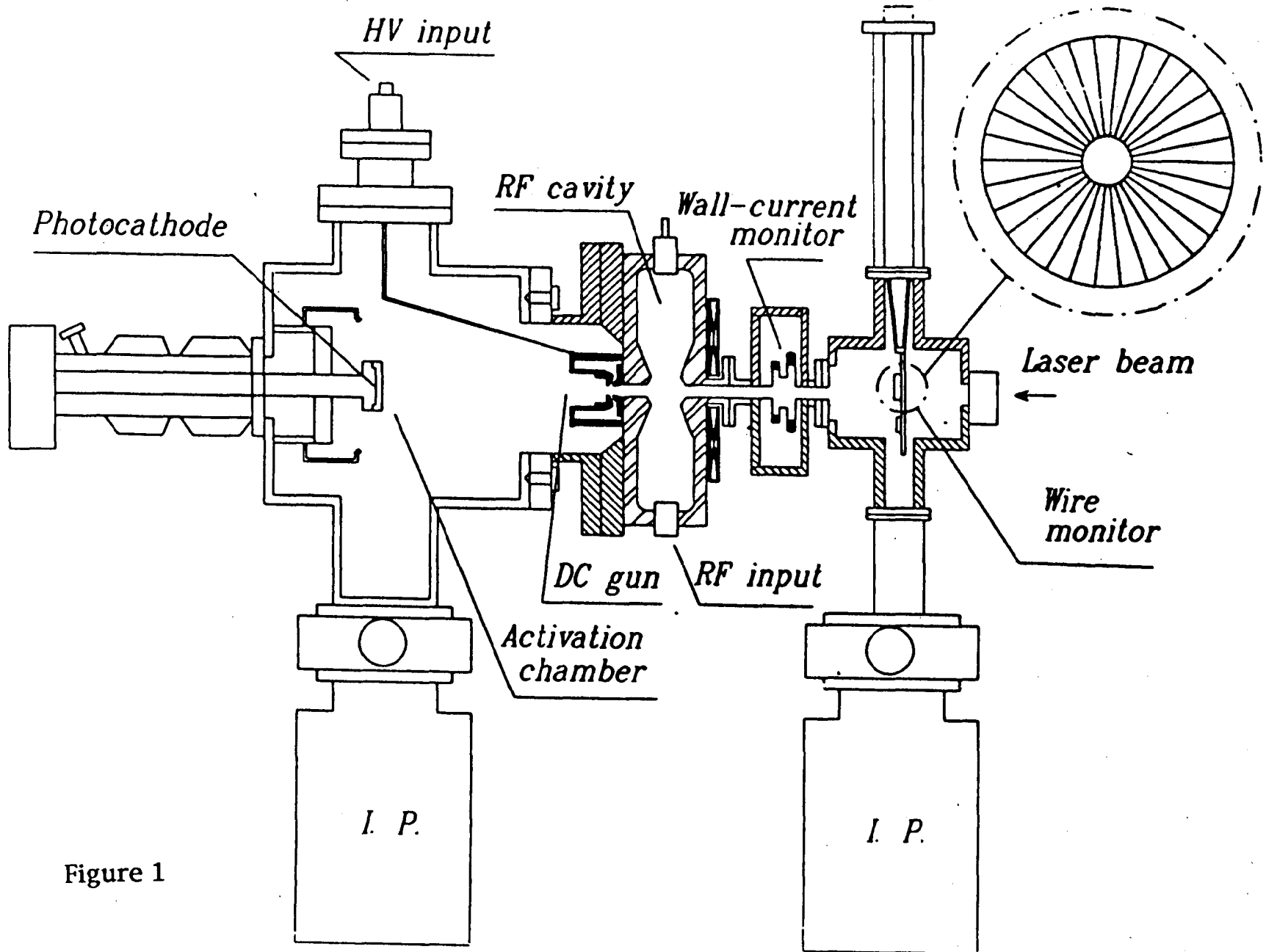


Figure 1

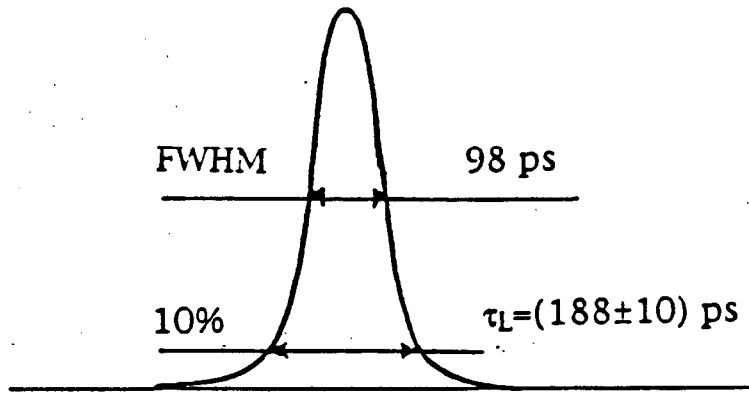


Figure 2

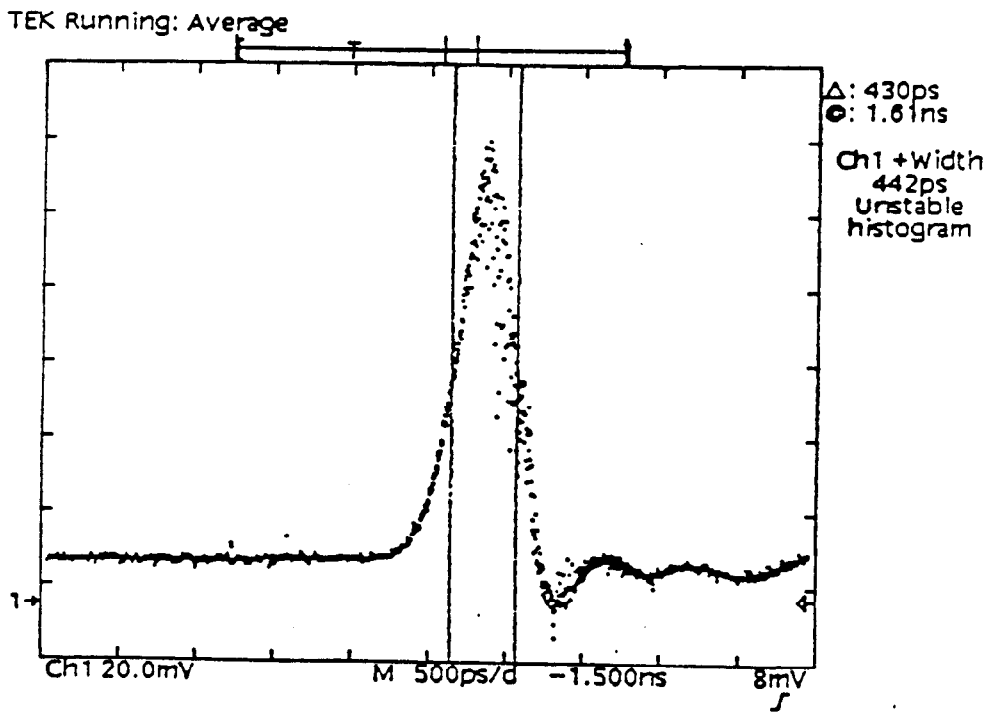


Figure 3

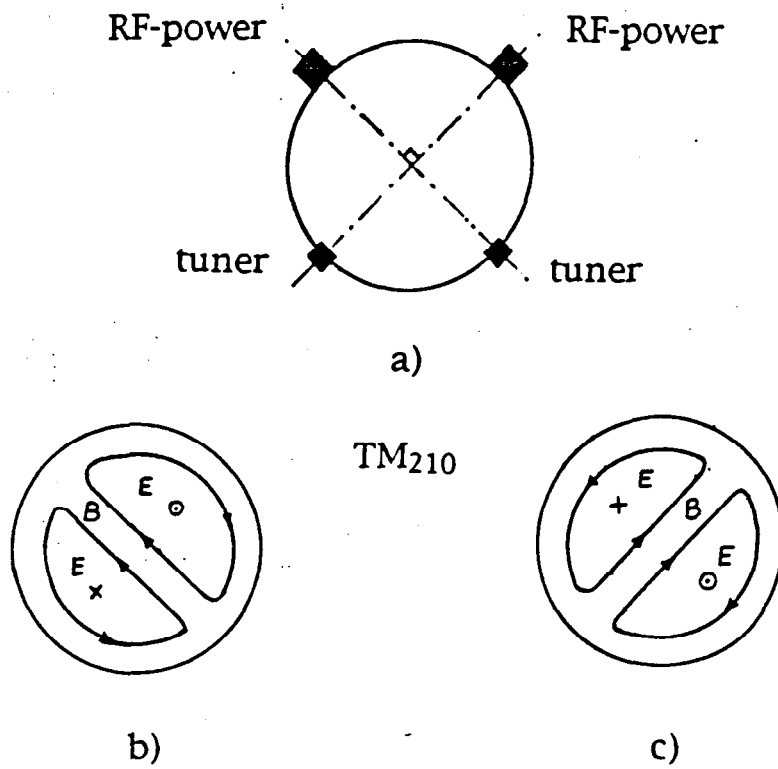


Figure 4

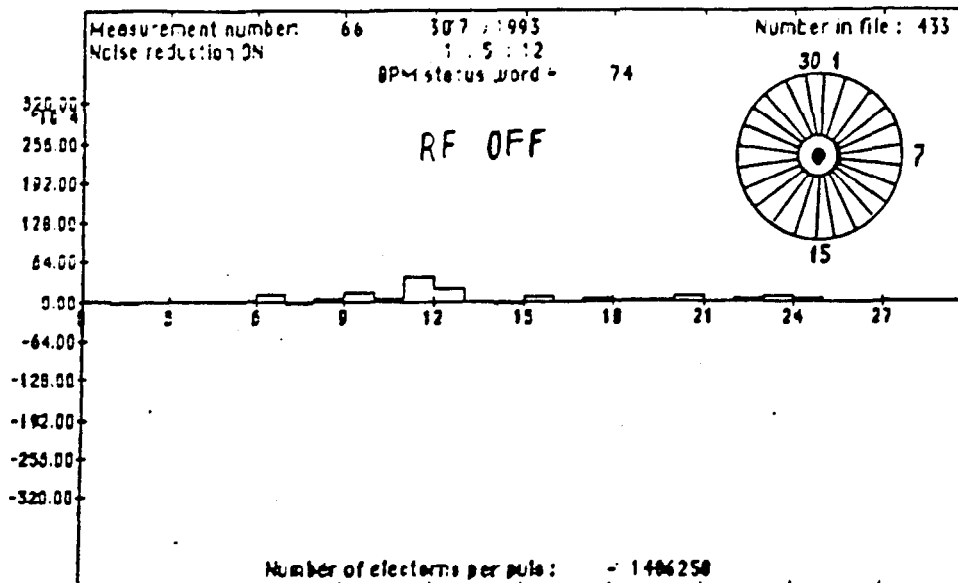


Figure 5

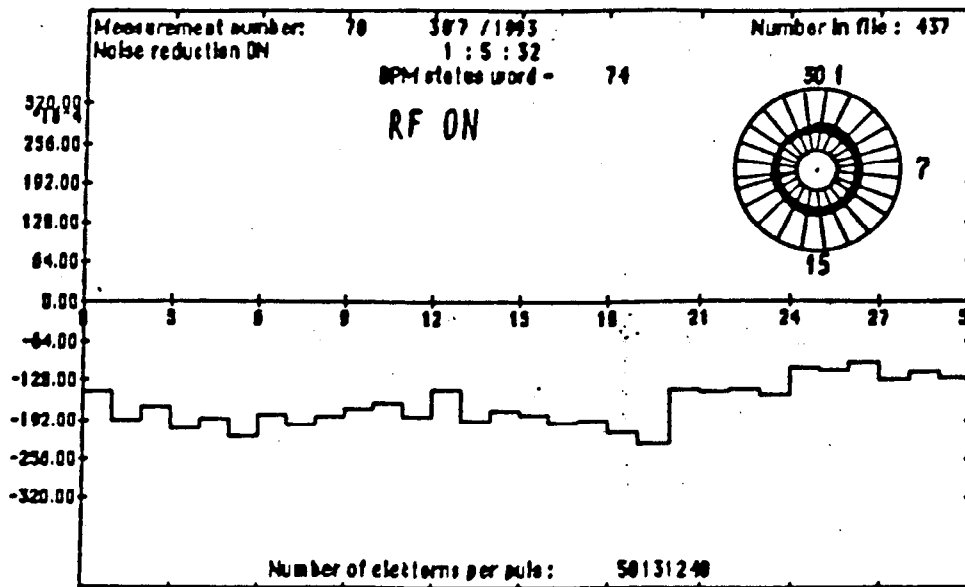


Figure 6

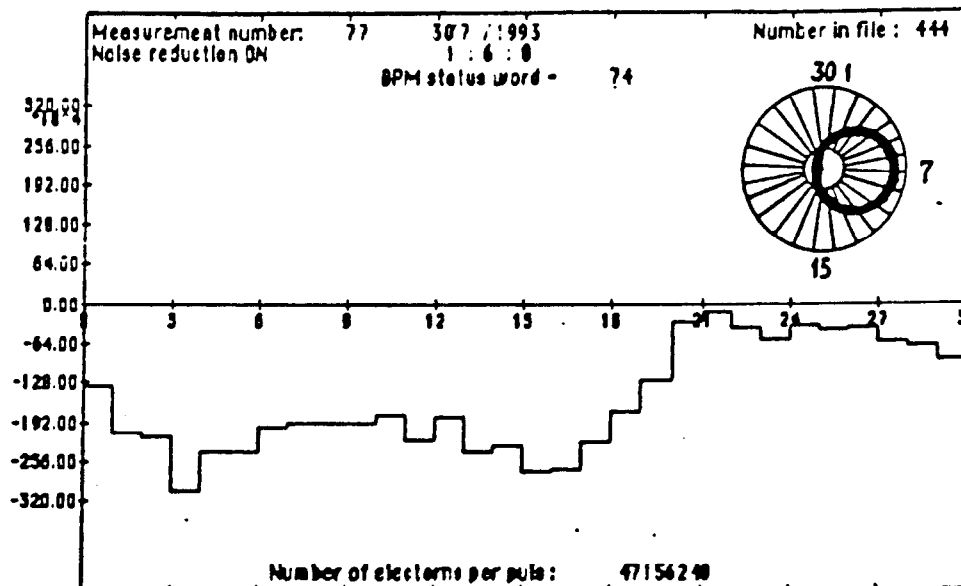


Figure 7

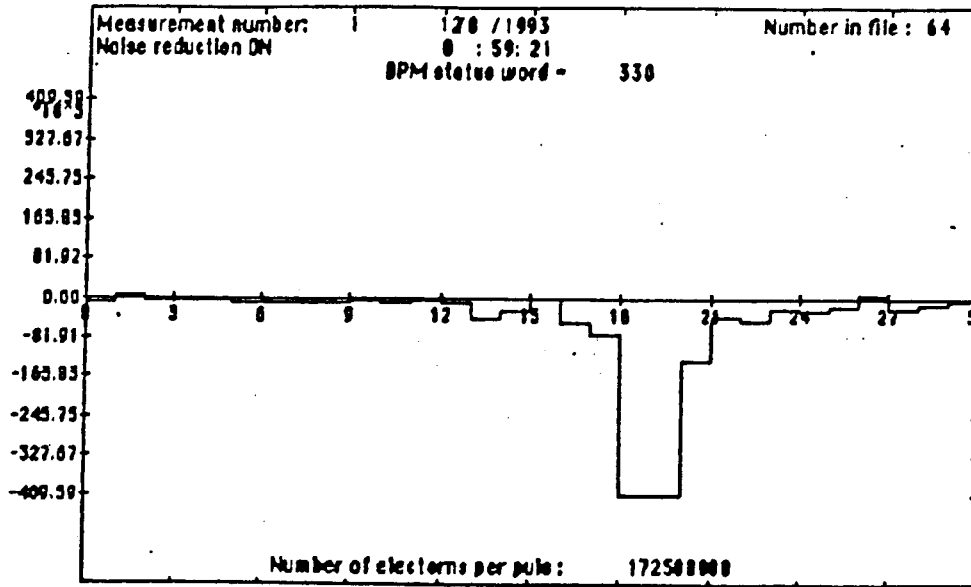


Figure 8

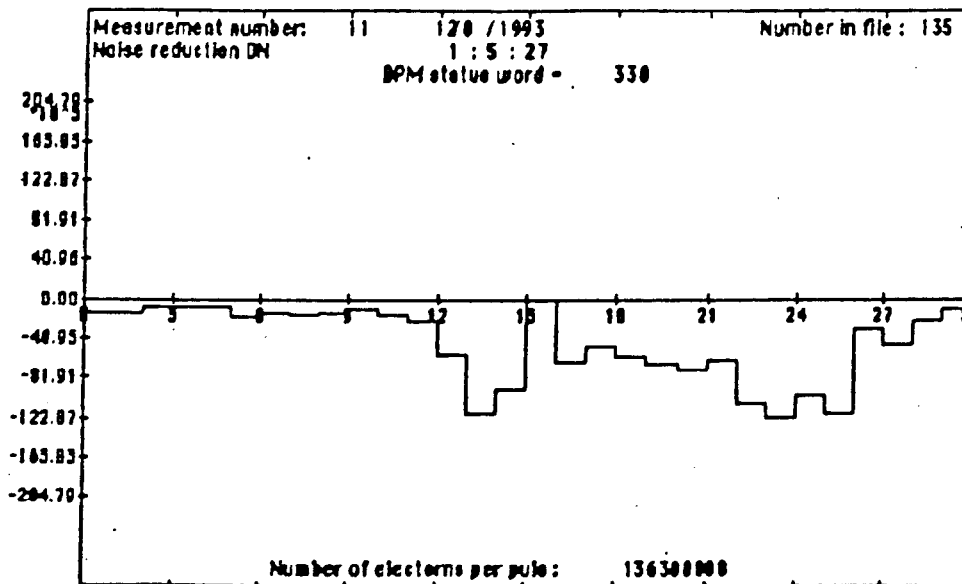


Figure 9

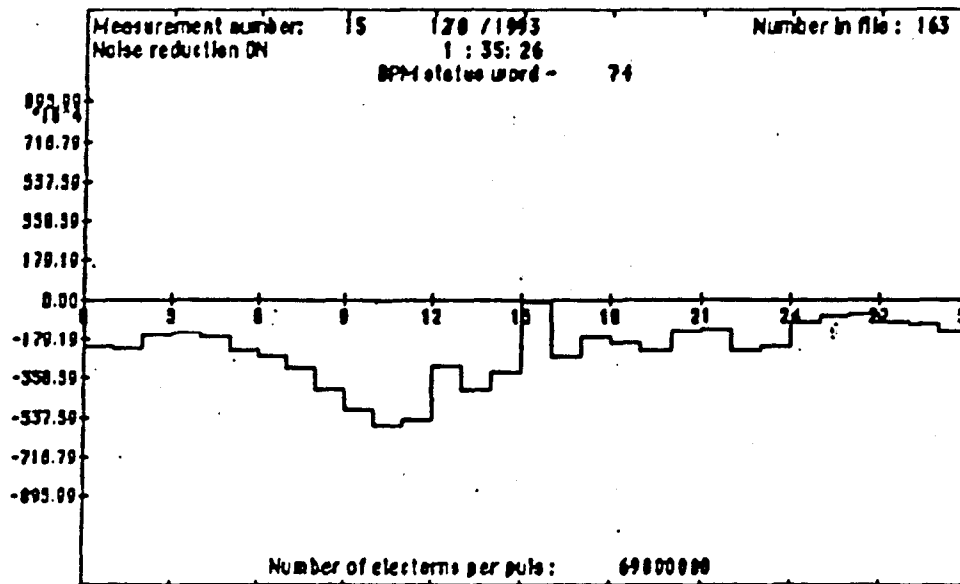


Figure 10

## Lowell Klaisner SLAC

### Polarized Electron Source for the Stanford Linear Collider

The Stanford Linear Collider (SLC) requires two short (2 nSec), high current (6 A) pulses at a 120 Hz repetition rate. During the 1993 run, the experiment on the machine measured ALR in Z<sup>0</sup> production. The statistics for this experiment are proportional to  $L \cdot p^2$  where L is the luminosity and p the polarization. This places a high premium on high polarization.

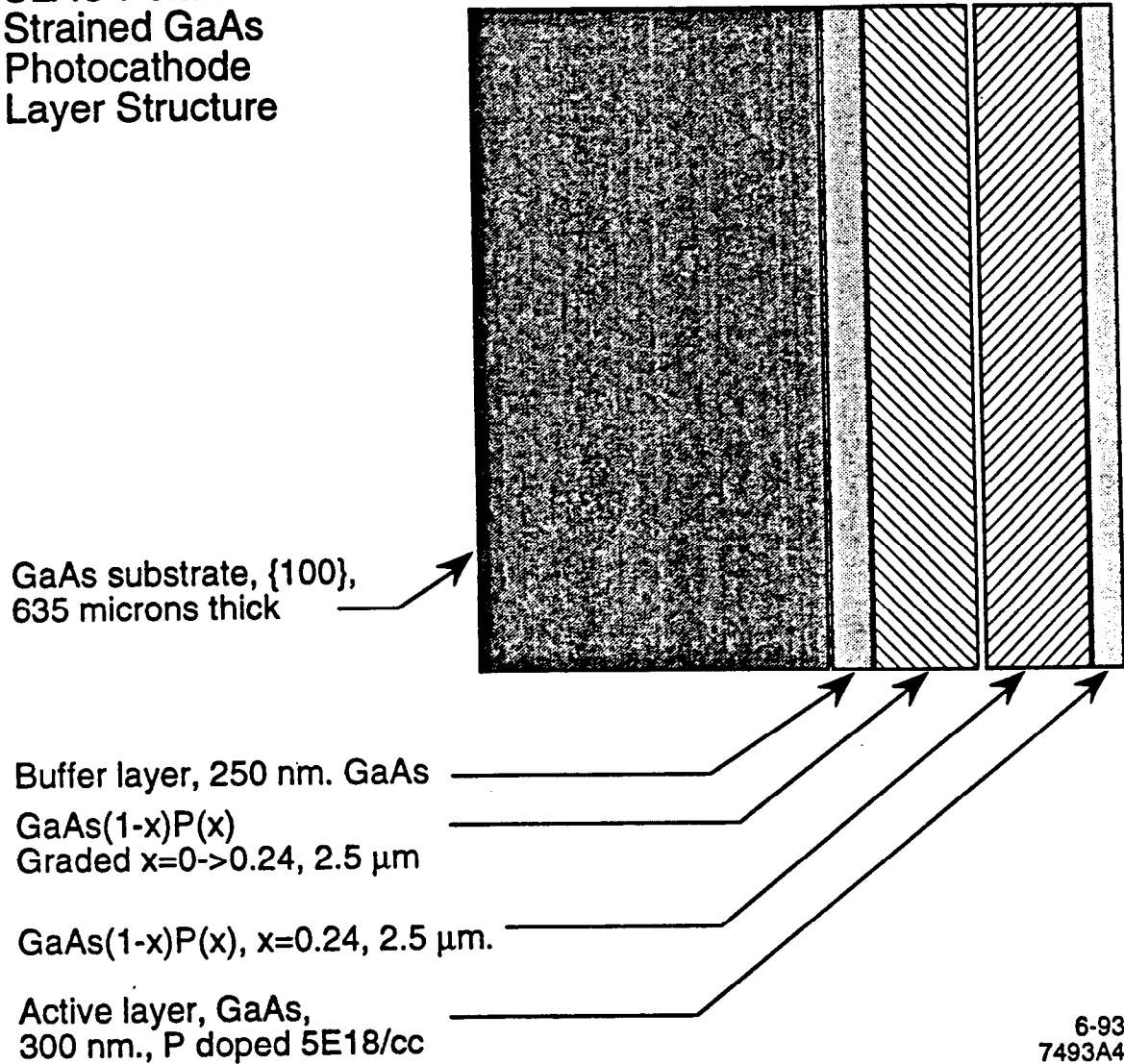
The operation of the polarized electron source in 1993 was a complete success. All of the expectations were met. The electron polarization at the cathode was 80%, the charge was achieved reliably; the time between cesiations was many days; and the system operated, unattended, with high availability. This high performance was achieved with integration into the SLC control system, careful attention to high vacuum, and the addition of a load-lock system which isolated the photocathode from the bakeout and high voltage processing of the gun.



## SLC Requirements

Energy	120 KeV
Charge	$6 \times 10^{10}$ e <sup>-</sup> /pulse
Current jitter	~1% RMS
Pulses	2
Spacing	61 nsec
Pulse Length	2 nsec FWHM
Repetition Rate	120 Hz
Timing jitter	<50 psec RMS
Polarization at experiment	>40%
Position stability	<100 $\mu$

SLAC Polarized Source  
Strained GaAs  
Photocathode  
Layer Structure



# Polarization

## Cathode

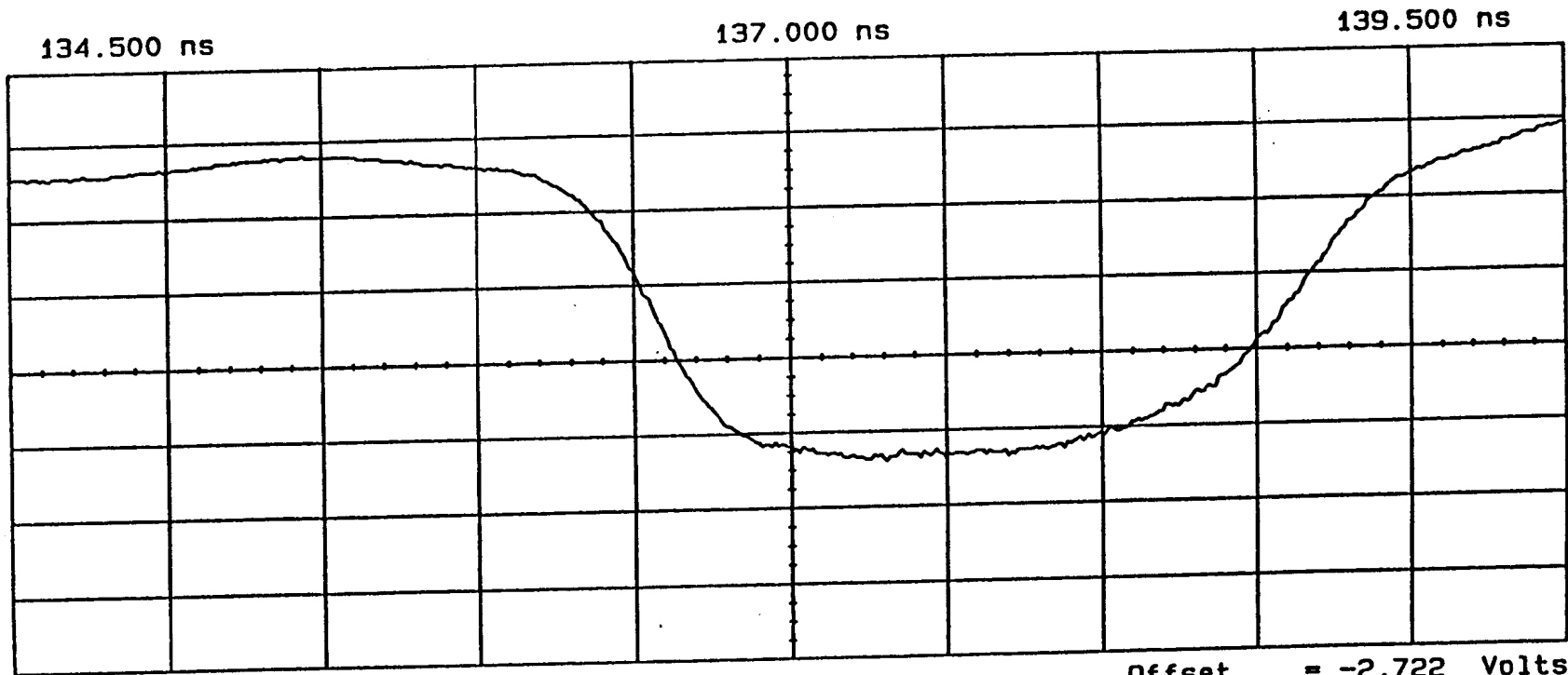
Strained GaAs on GaAsP  
300 nm strained layer  
865 nm laser wavelength

## Polarization

In Laboratory - Mott Polarimeter	~80%
At end of linac - Møller Polarimeter	~75%
At interaction point - Compton Polarimeter	~62%



106

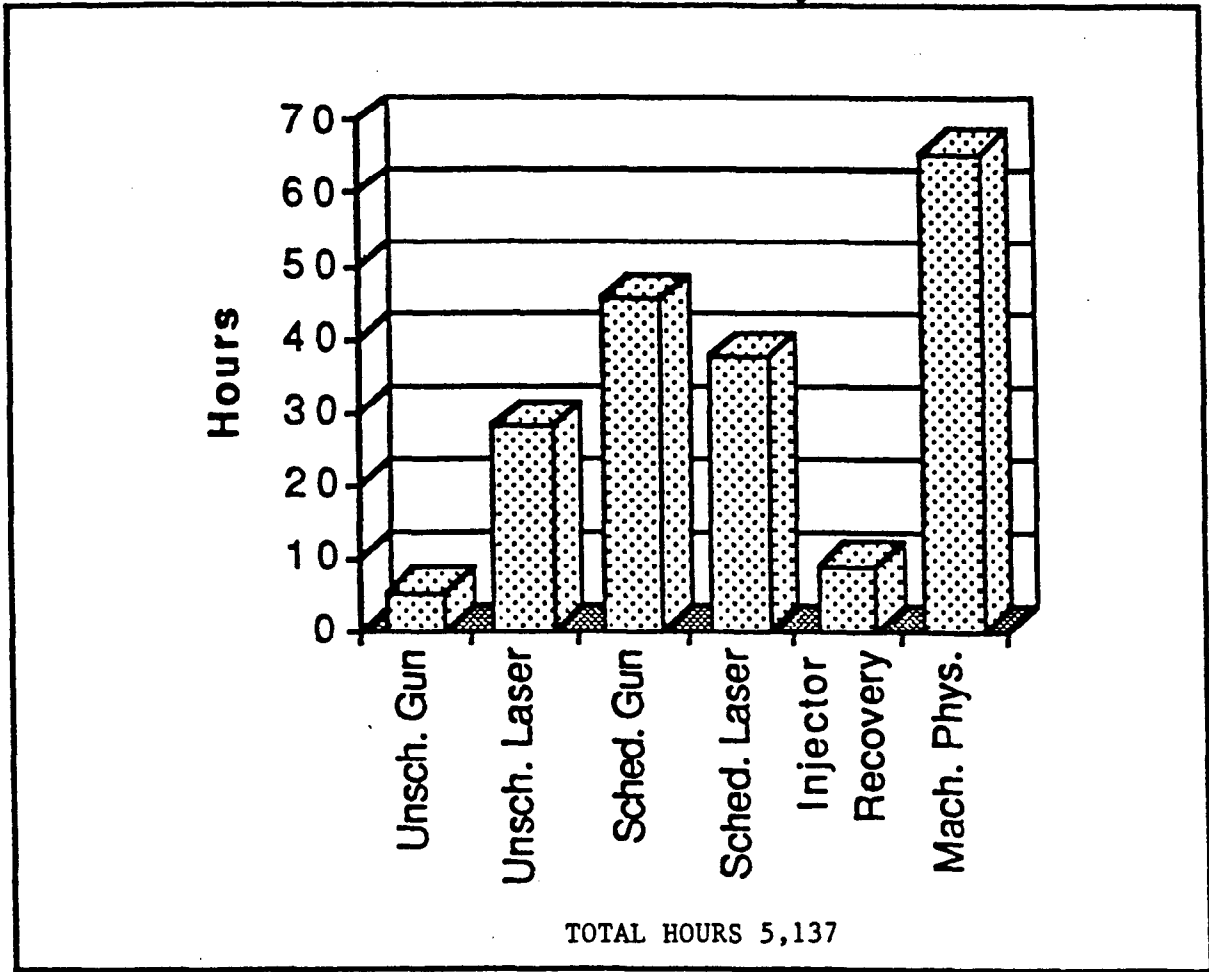


Ch. 1 = 995.2 mVolts/div  
Timebase = 500 ps/div

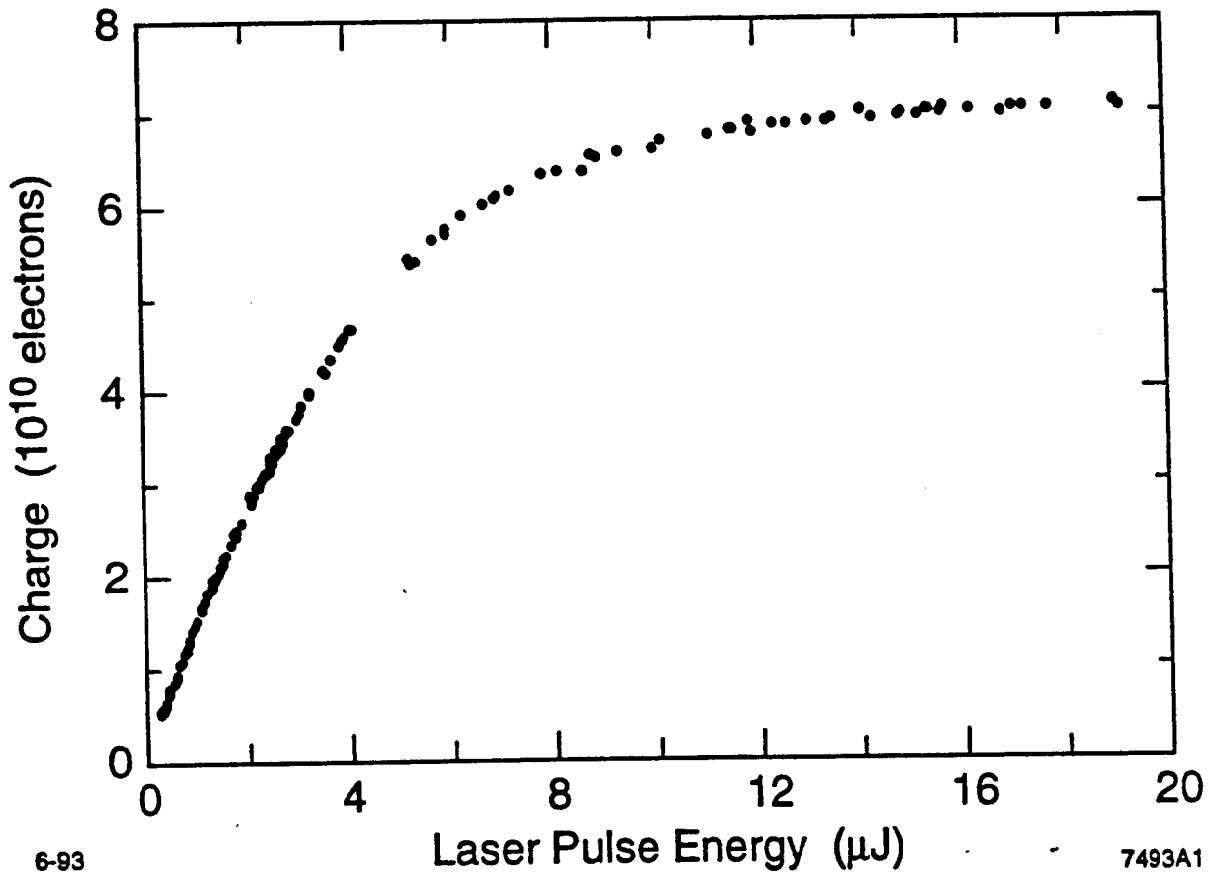
Offset = -2.722 Volts  
Delay = 137.000 ns

GUN

**1993 SLC Run  
Polarized Electron Source  
Unavailable for HE Physics**



August 27, 1993



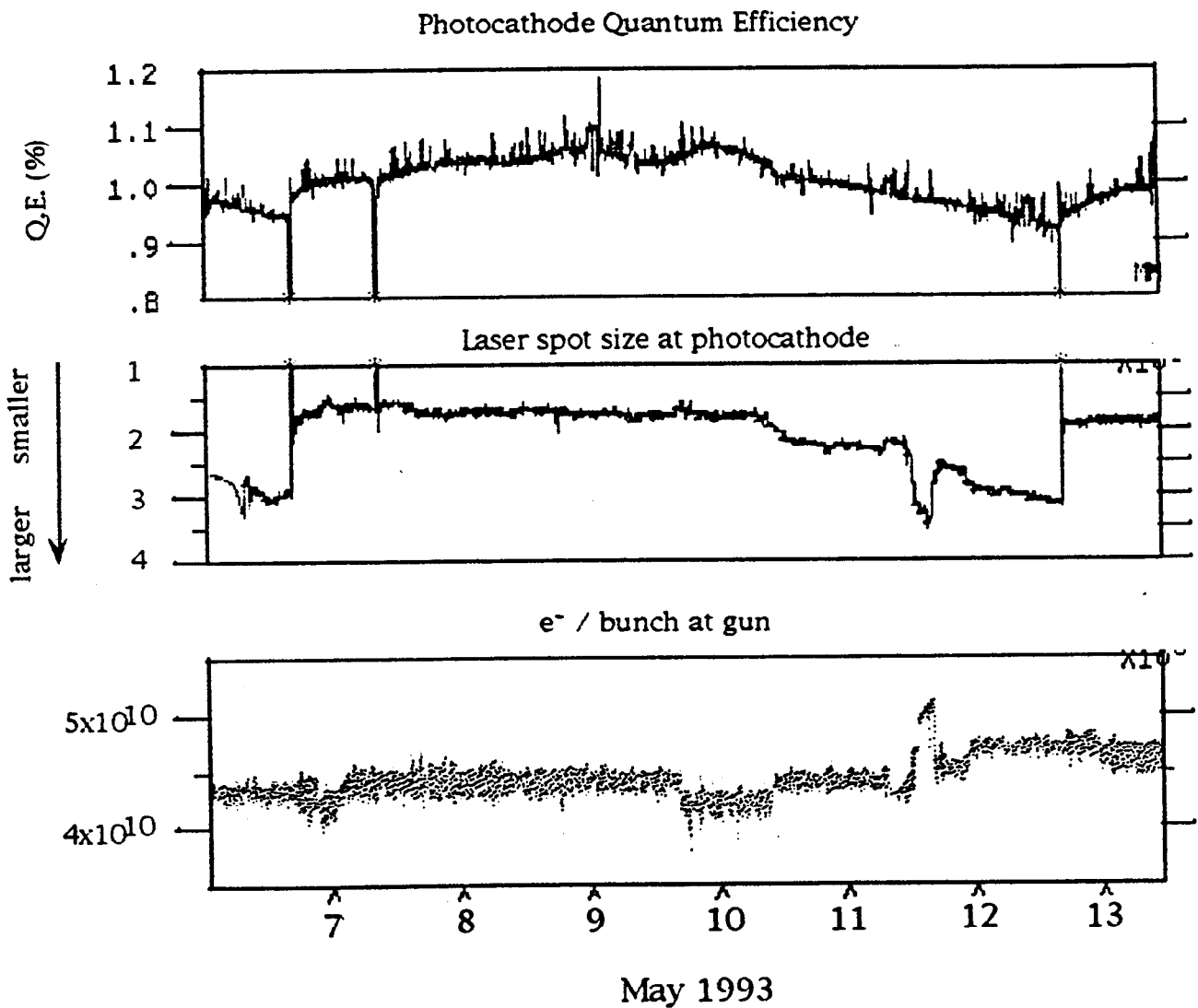
6-93

7493A1

## Lifetime / Cycletime and Operations

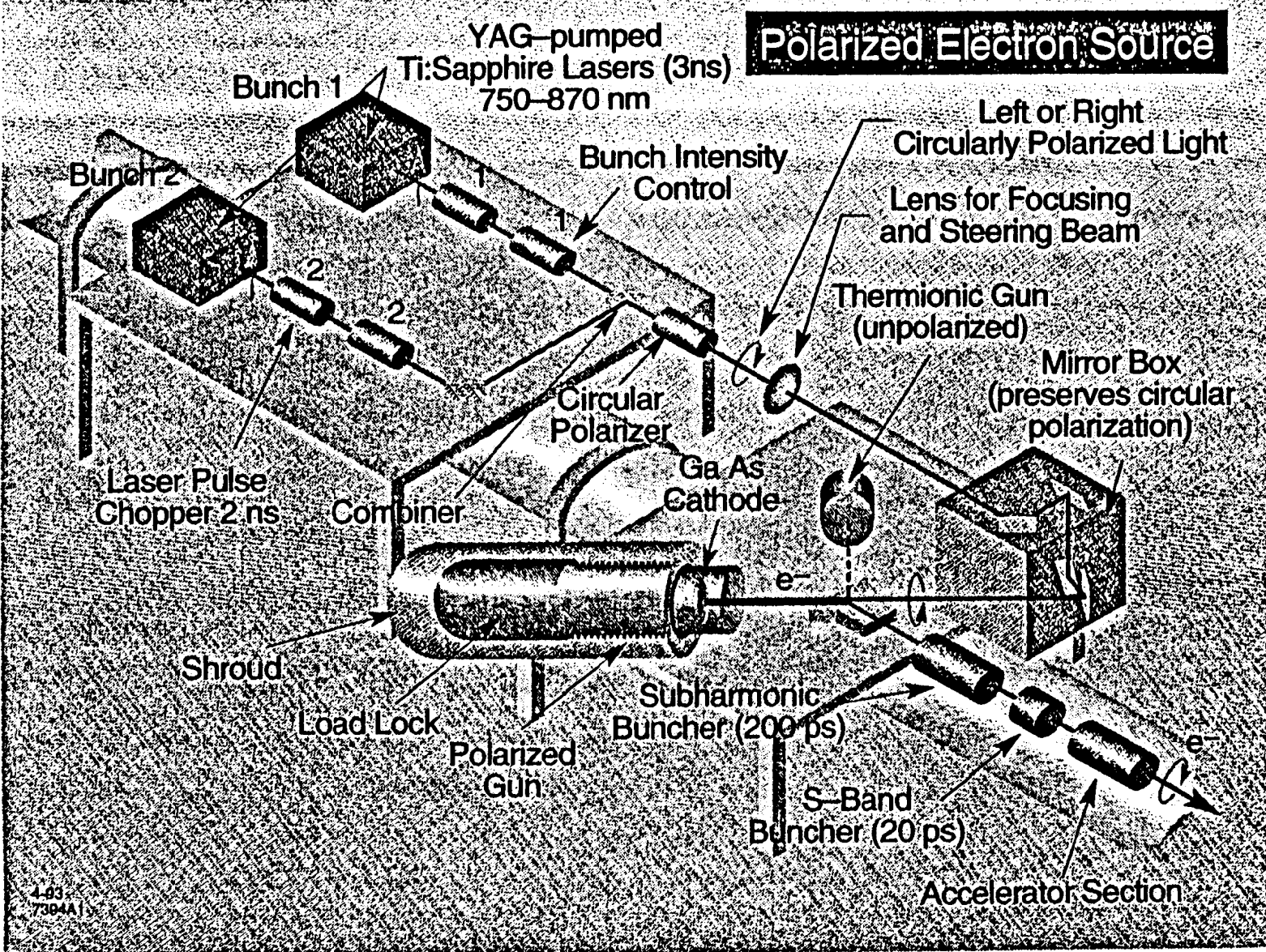
As quantum efficiency decreases, a feedback system increases the laser spot size to maintain beam current. After a few day's spot size growth, the photocathode is recesiated (~20 min. process) and the cycle begins again.

The YAG laser flashlamps age and need to be replaced every few weeks.



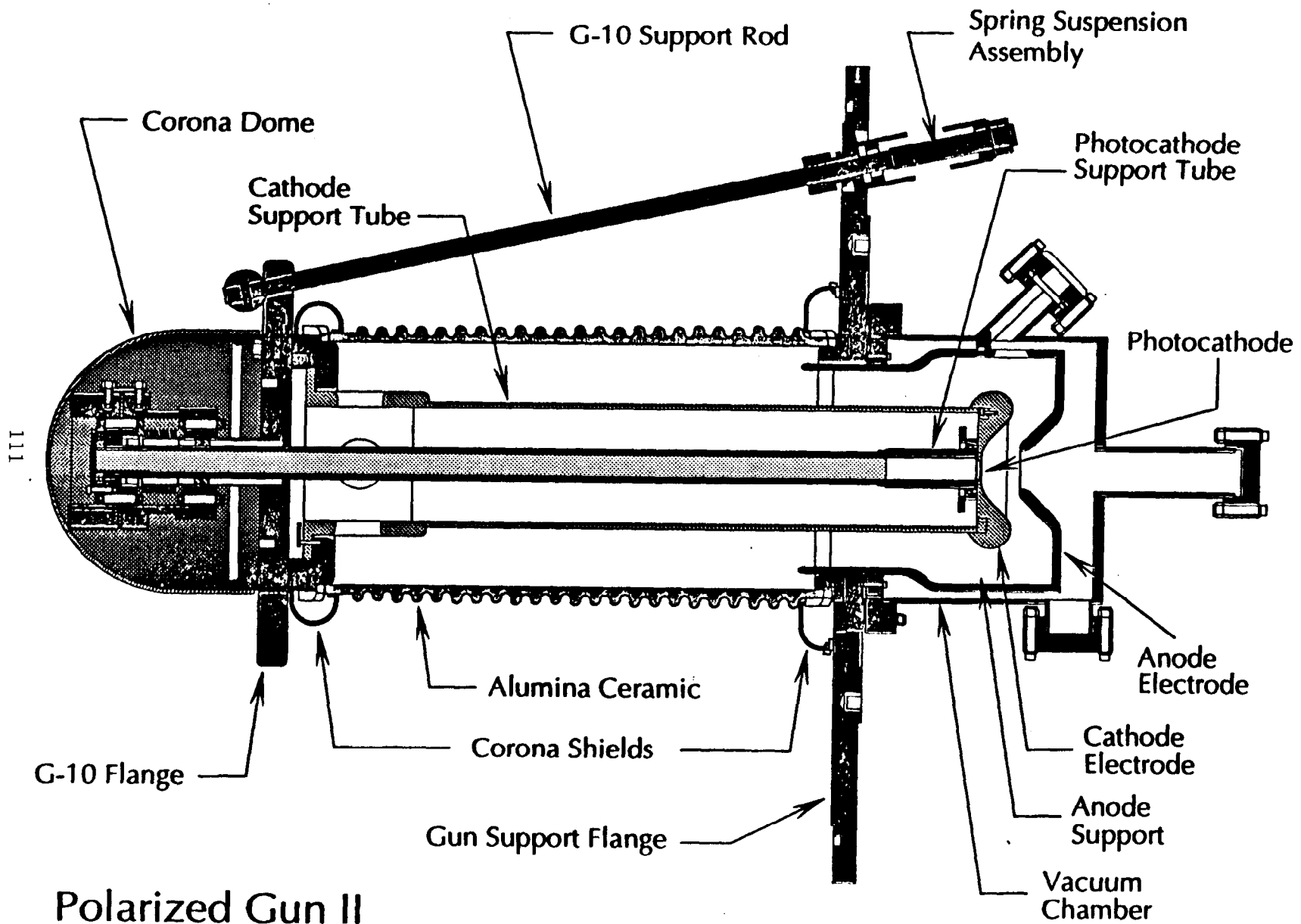


# Polarized Electron Source



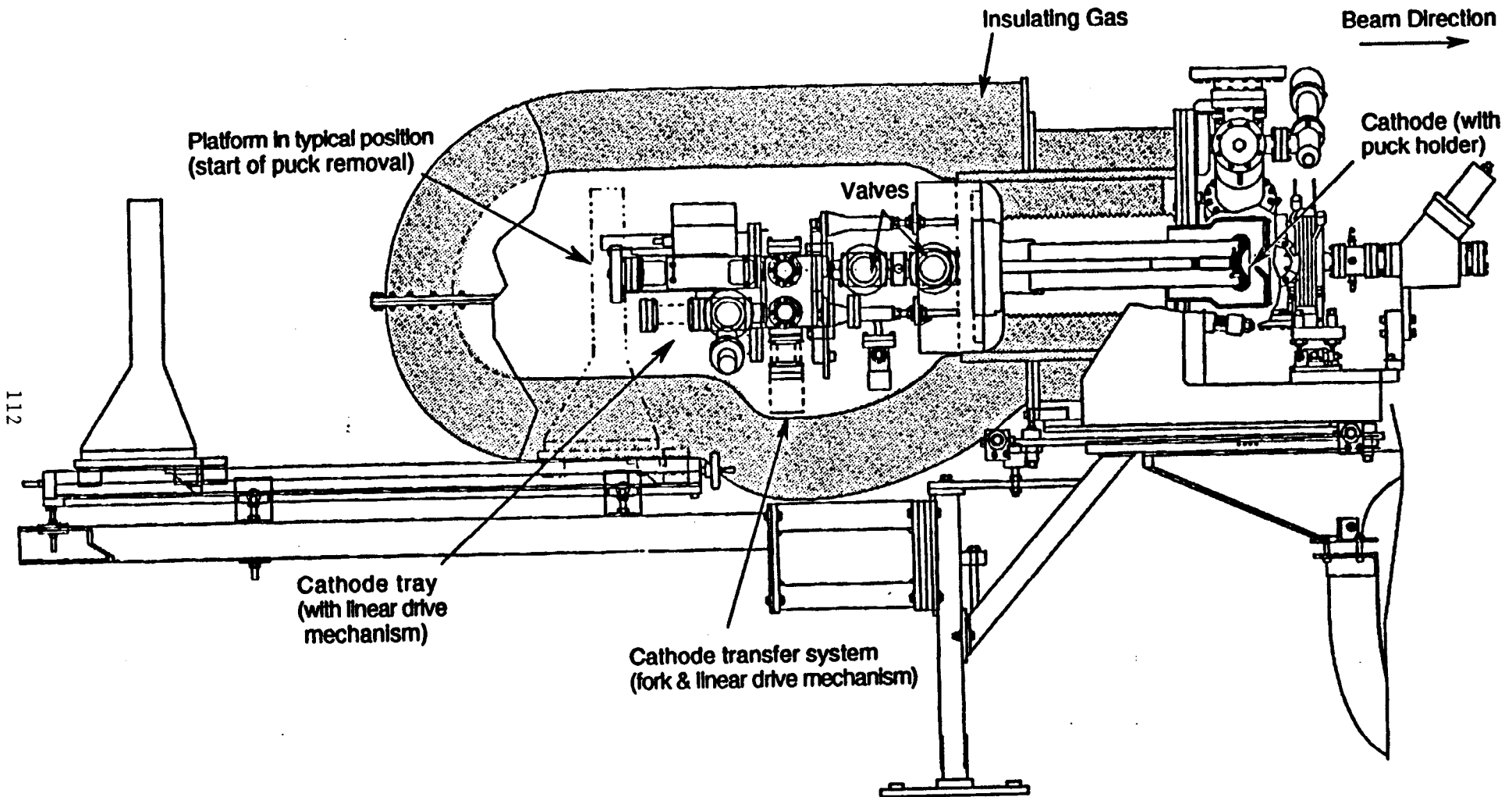
110

4-93  
7304A1



Polarized Gun II

# SLAC Polarized Electron Gun



# Vacuum System

## Gun

120 l/s Ion Pump

200 l/s Non-Evaporative Getter (NEG) Pump  
SAES Model 200

## Load-Lock

20 l/s Ion Pump (Fiber Optically isolated  
power supply)

50 l/s NEG Pump, SAES Model 50

## Vacuum Isolation Volume

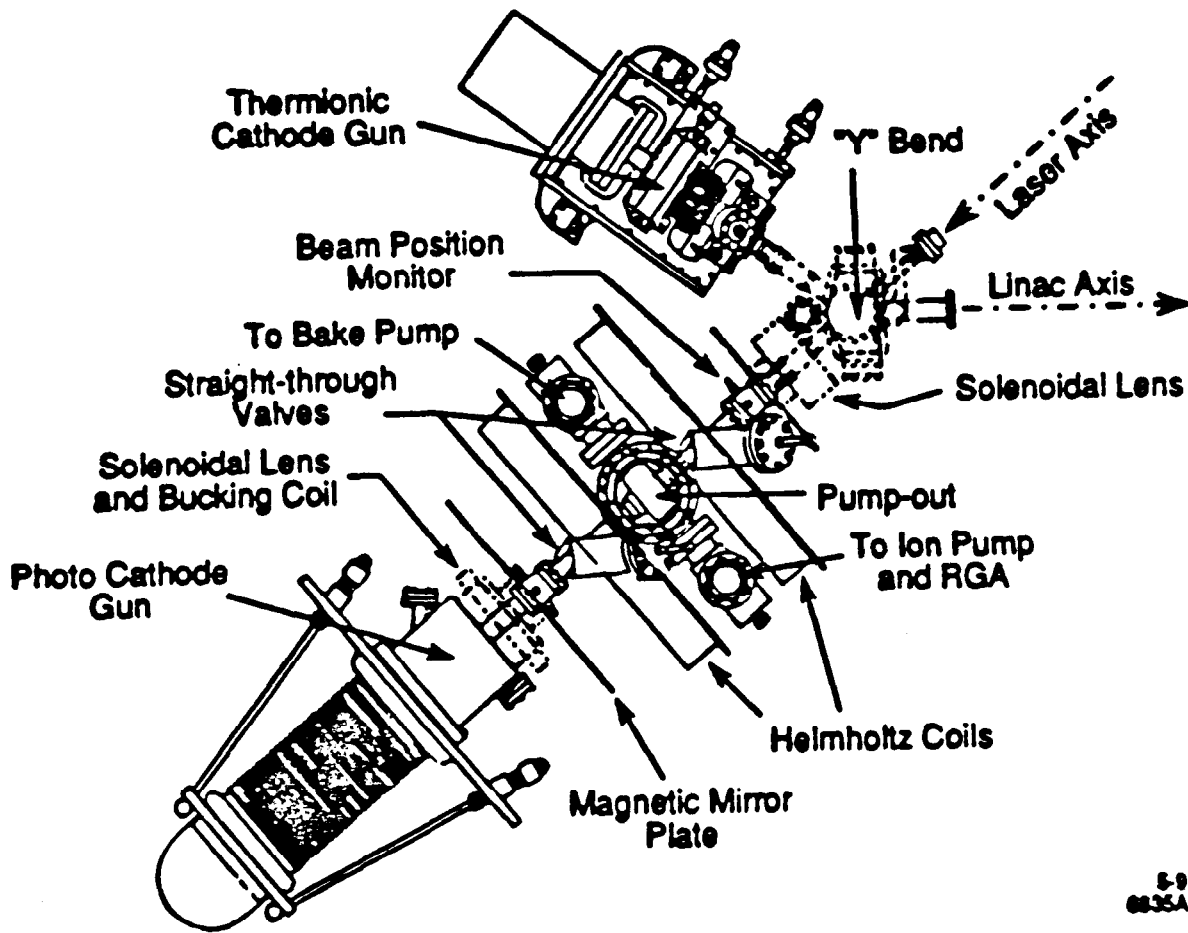
220 l/s Ion Pump

500 l/s NEG Pump, SAES Model 500

## Residual Gas Analyser on Gun

$8 \times 10^{-12}$  torr total pressure

$2 \times 10^{-12}$  torr CO pressure



S-91  
 0035A1

## Ultra High Vacuum Processes

- 1) Chemically Clean
- 2) Bake in Vacuum 300°C to 600°C
- 3) Assemble in class 100 clean room
- 4) Bake complete assembly 100 hrs. @ 250°C  
(Process NEG pump)
- 5) Heat Clean and process cathodes in  
Load-Lock system

## Electrical Parameters

Voltage	120 kV
Charge per pulse	10 nC typical
Peak current	5 A typical
Energy per pulse	1.2 mJ
Energy stored within 30 cm	144 mJ
Voltage droop	~2%
Natural frequency	~50 MHz
Leakage current	50 nA maximum 25 nA typical
Gradient on photocathode	2.25 MV/m
Maximum gradient on cathode electrode	9 MV/m

- a) Hand polish electrodes
- b) High voltage process to 180 kV

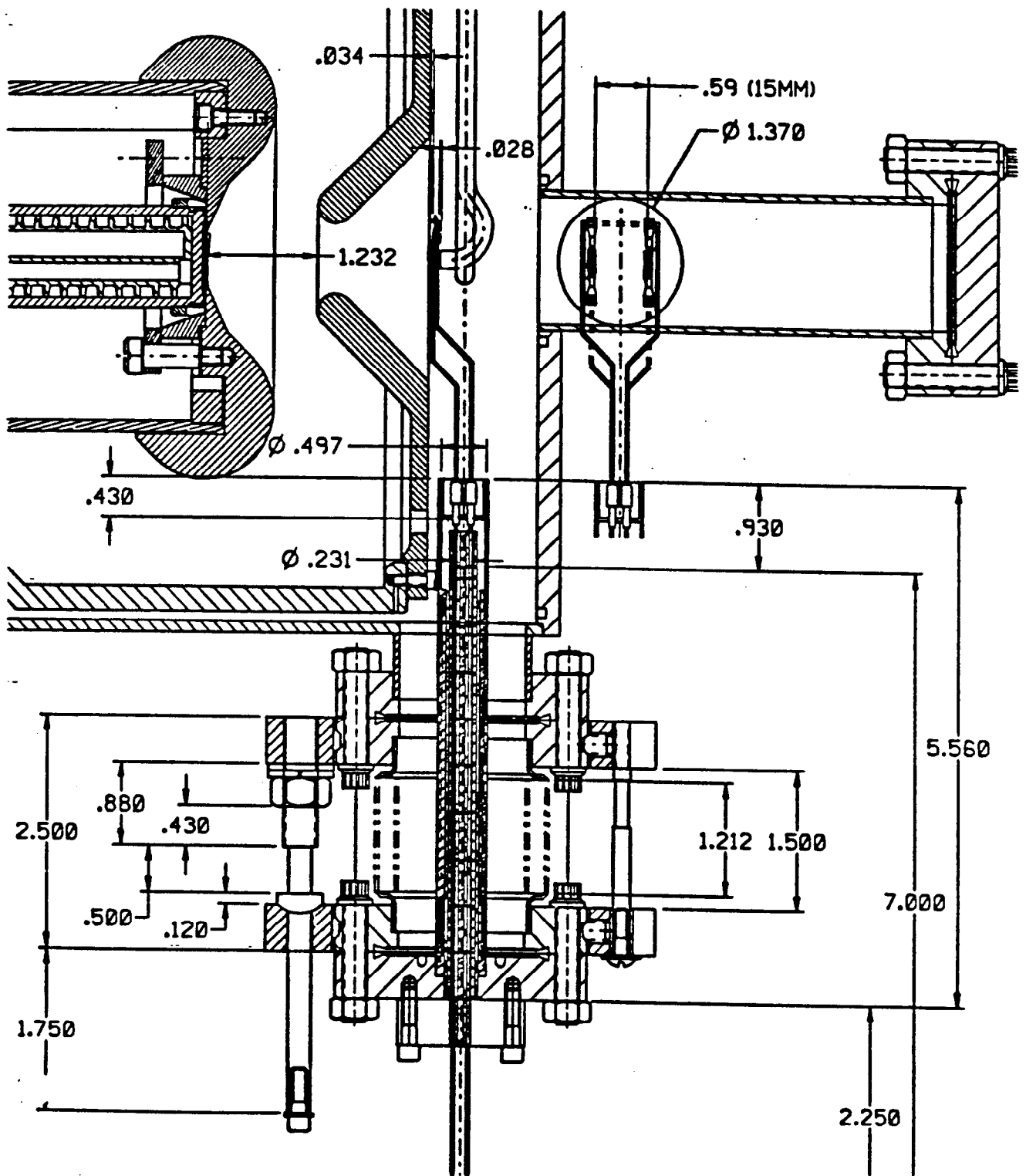
## Cesiation

- |                               |                 |
|-------------------------------|-----------------|
| 1) Measure QE @ 830 nm        | 120 sec.        |
| 2) Ramp HV down to 1 kV       | 120 sec.        |
| 3) Cesiator at 3 A to outgass | 50 sec.         |
| 4) Cesiator at 4 A to cesiate | 200 sec.        |
| 5) Ramp HV back to 120 kV     | 120 sec.        |
| 6) Measure QE @ 830 nm        | <u>120 sec.</u> |
|                               | 730 sec.        |

Typically takes 20 minutes.

Typically over cesiate by 5%.

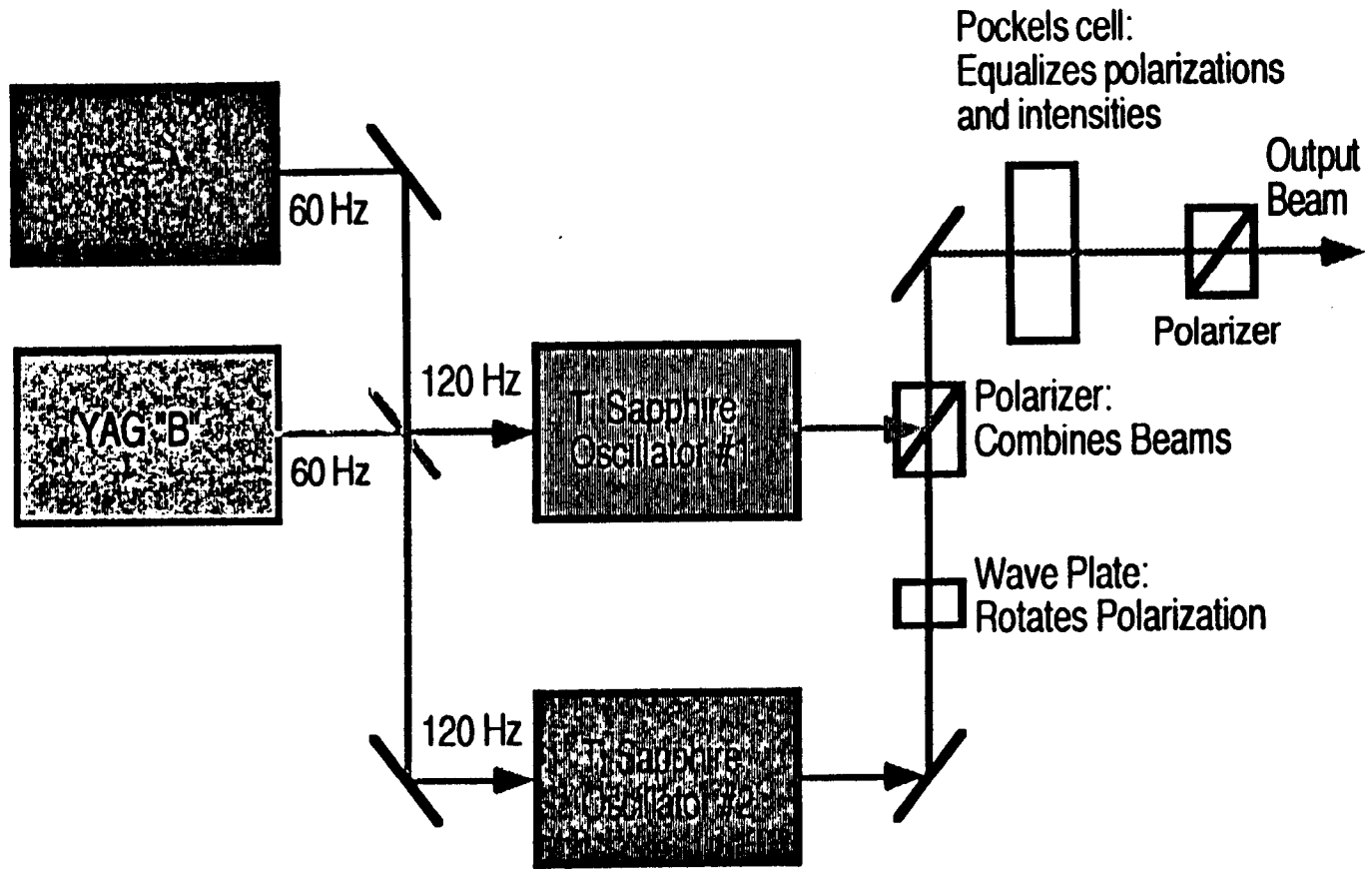




# LASER SPECIFICATIONS

Operating wavelength	760-870 nm
Pulse energy at cathode	>50 $\mu$ J
Pulse length	2.0 ns
Timing jitter	<50 ps RMS
Pulse Structure	2 pulses, 61 ns apart
Repetition rate	120 Hz
Energy stability	<3% RMS
Pointing stability	<5 $\mu$ R RMS
Reliability	>95% uptime
System lifetime	>10,000 hours

# Ti:Sapphire laser system for the SLAC polarized source



## Future Plans

Increase aperture

14 mm to 20 mm

Decrease active layer thickness

300 nm to 100 nm

Add long pulse laser

Flash lamp pumped Ti:Sapphire

Add cells to cesiator

2 cells to 4 cells

Add Mott polarimeter to test beam line

**Georges Lampel**  
**PMC Ecole Polytechnique**

**Energy and Spin Analysis of Photo-electrons from  
Layered Semiconductor Structures**

# **ENERGY AND SPIN ANALYSIS OF PHOTO-ELECTRONS FROM LAYERED SEMICONDUCTOR STRUCTURES**

**Laboratoire P.M.C. – Ecole Polytechnique – Palaiseau, France**

**H.-J. DROUHIN**

**T.H. GENTNER**

**C. HERMANN**

**G. LAMPEL**

**Y. LASSAILLY**

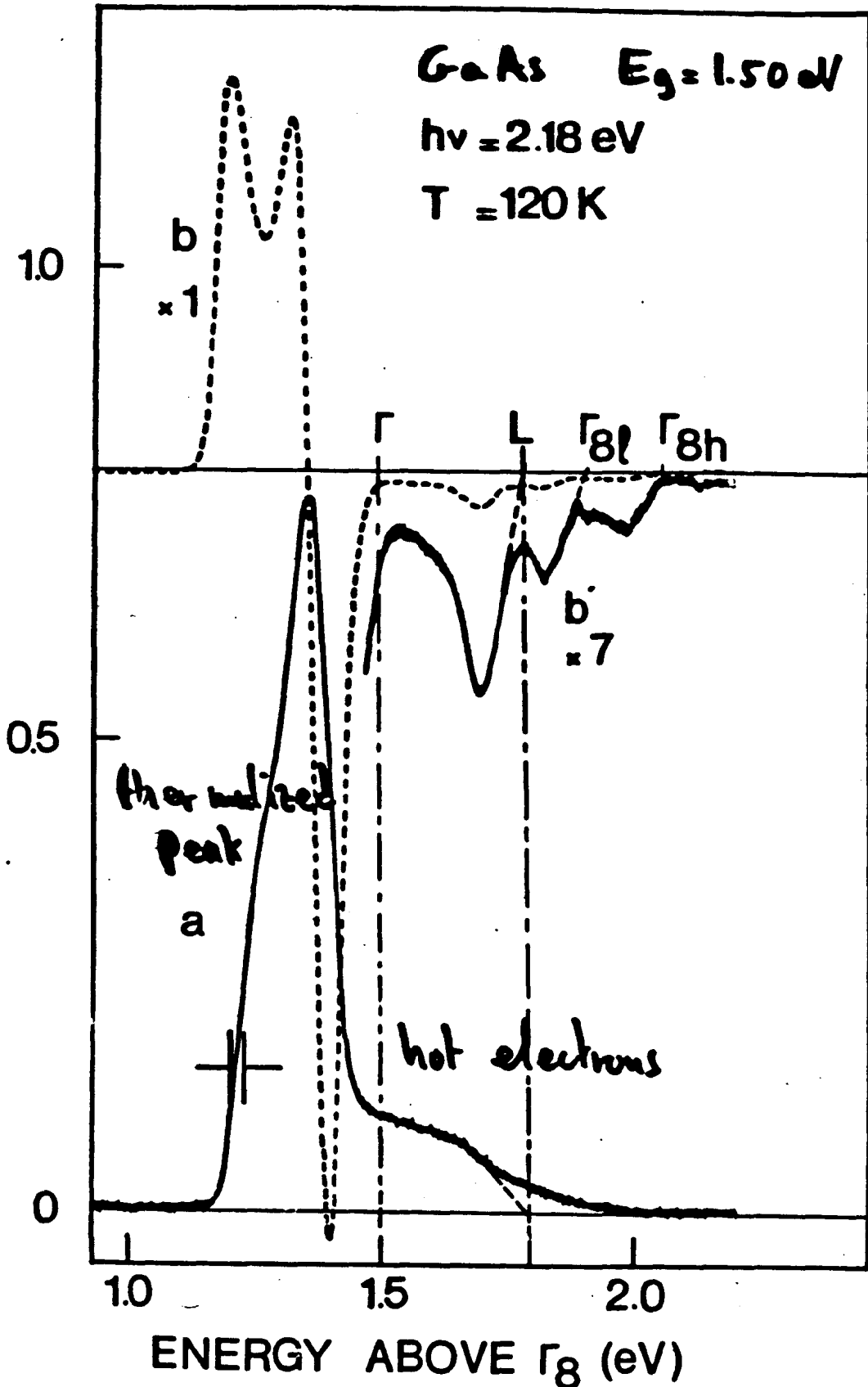
**D. PAGET**

**J. PERETTI**

- **Introduction**
  
- **AlGaAs / GaAs superlattices**  
— **mainly: energy analysis**
  
- **GaAs layer on Si substrate**  
— **mainly: spin analysis**



INTENSITY (nA) AND EDC DERIVATIVE (A.U.)



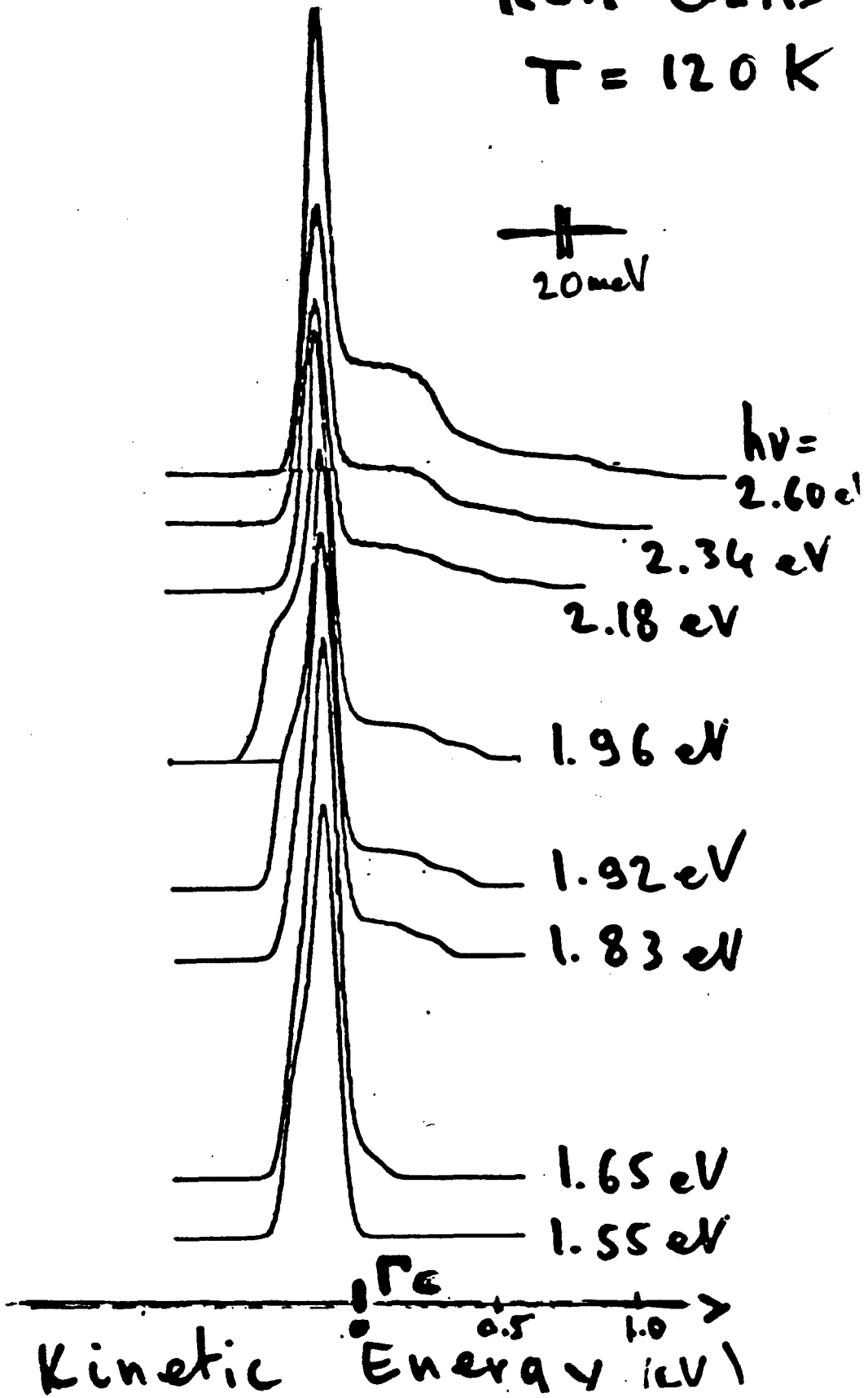
$\Gamma_8 =$  top of the valence band



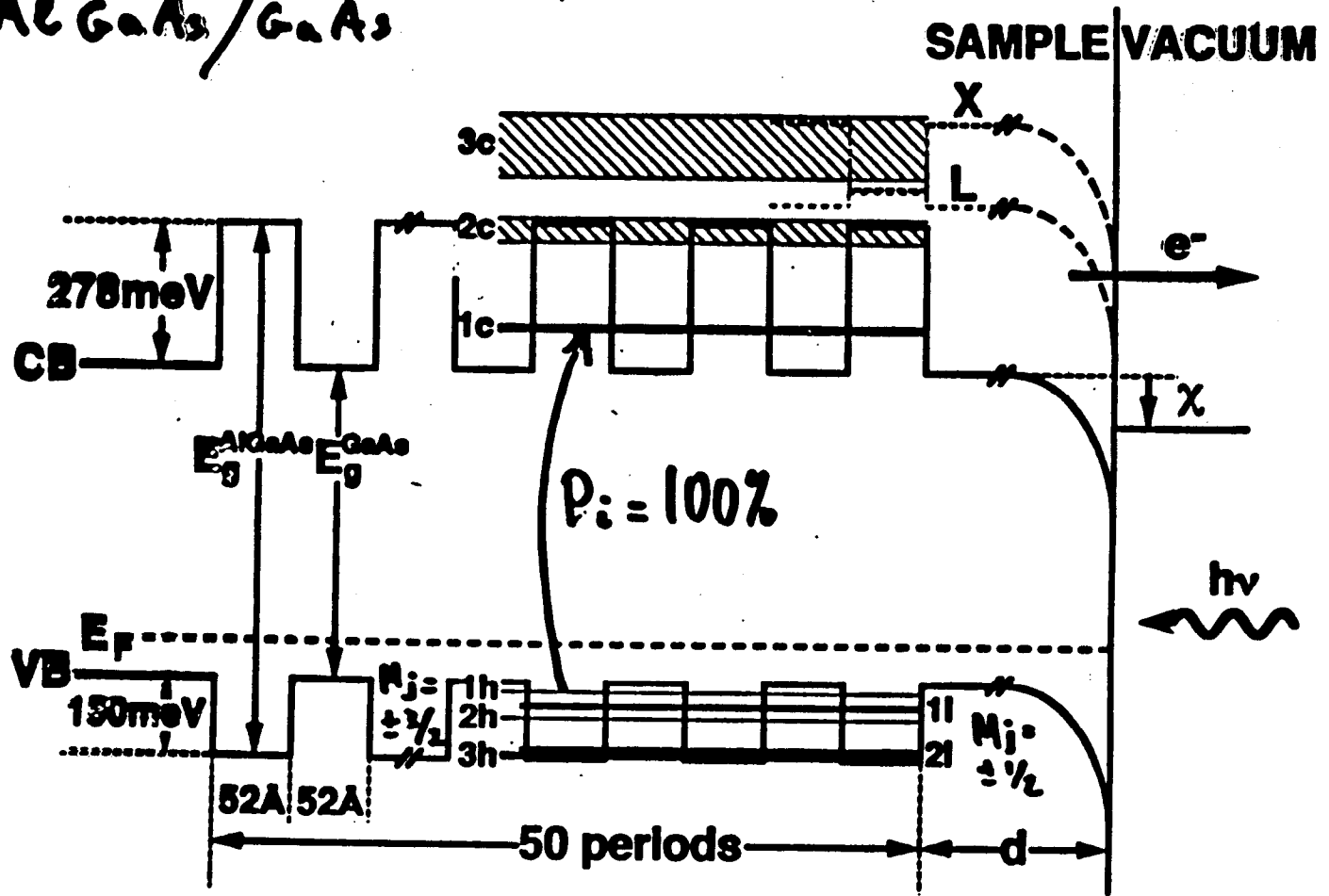
NEA GaAs

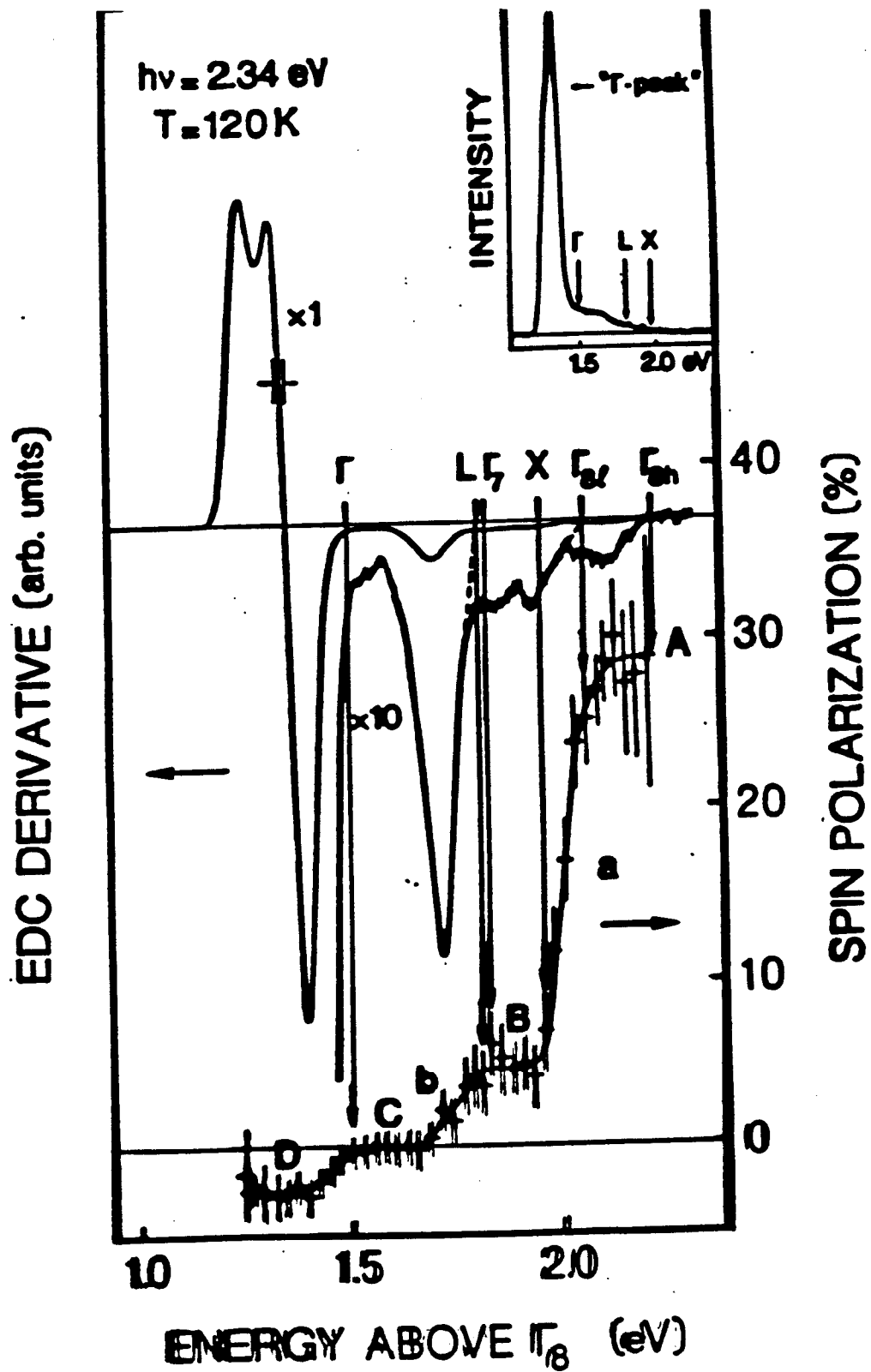
T = 120 K

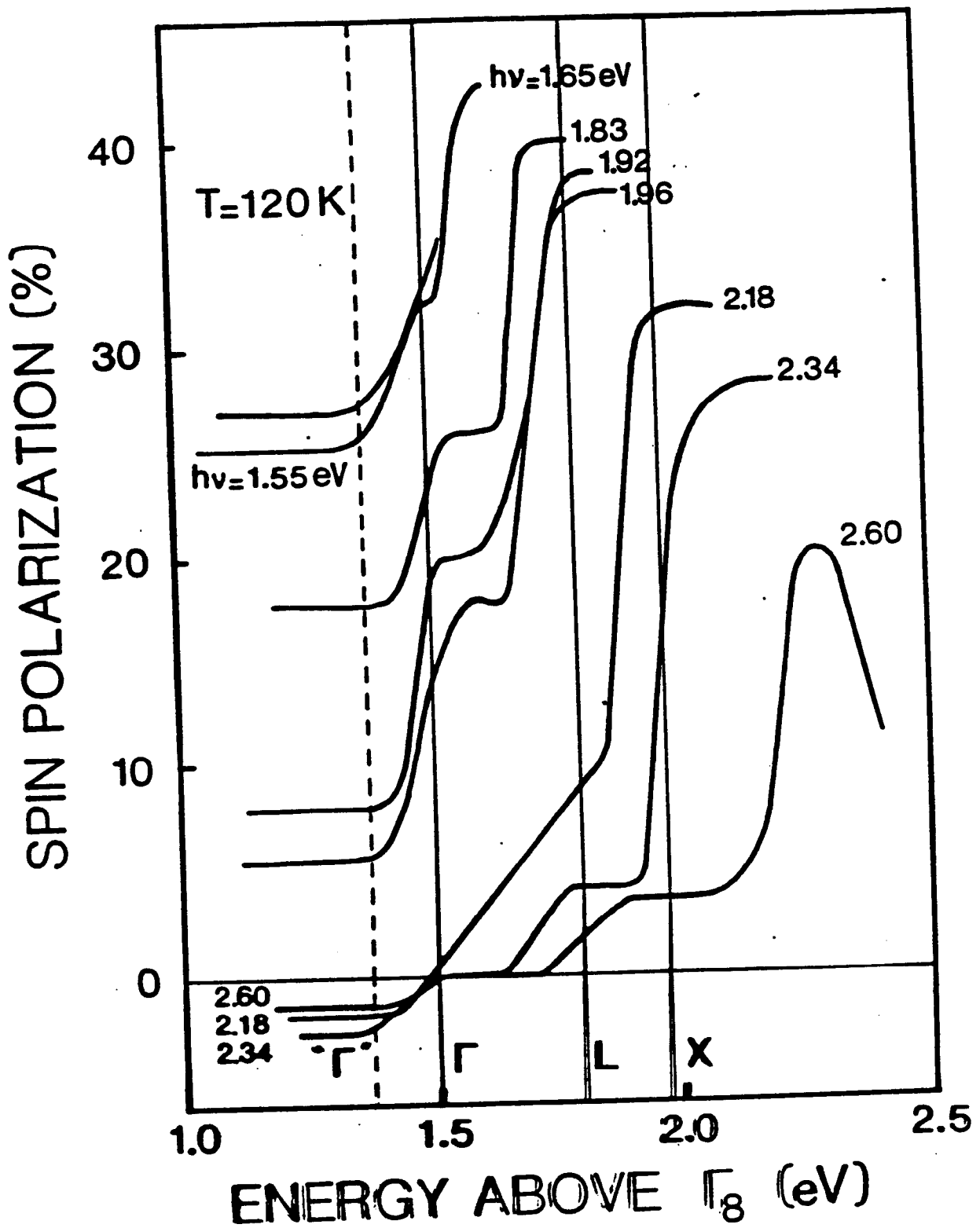
20 meV



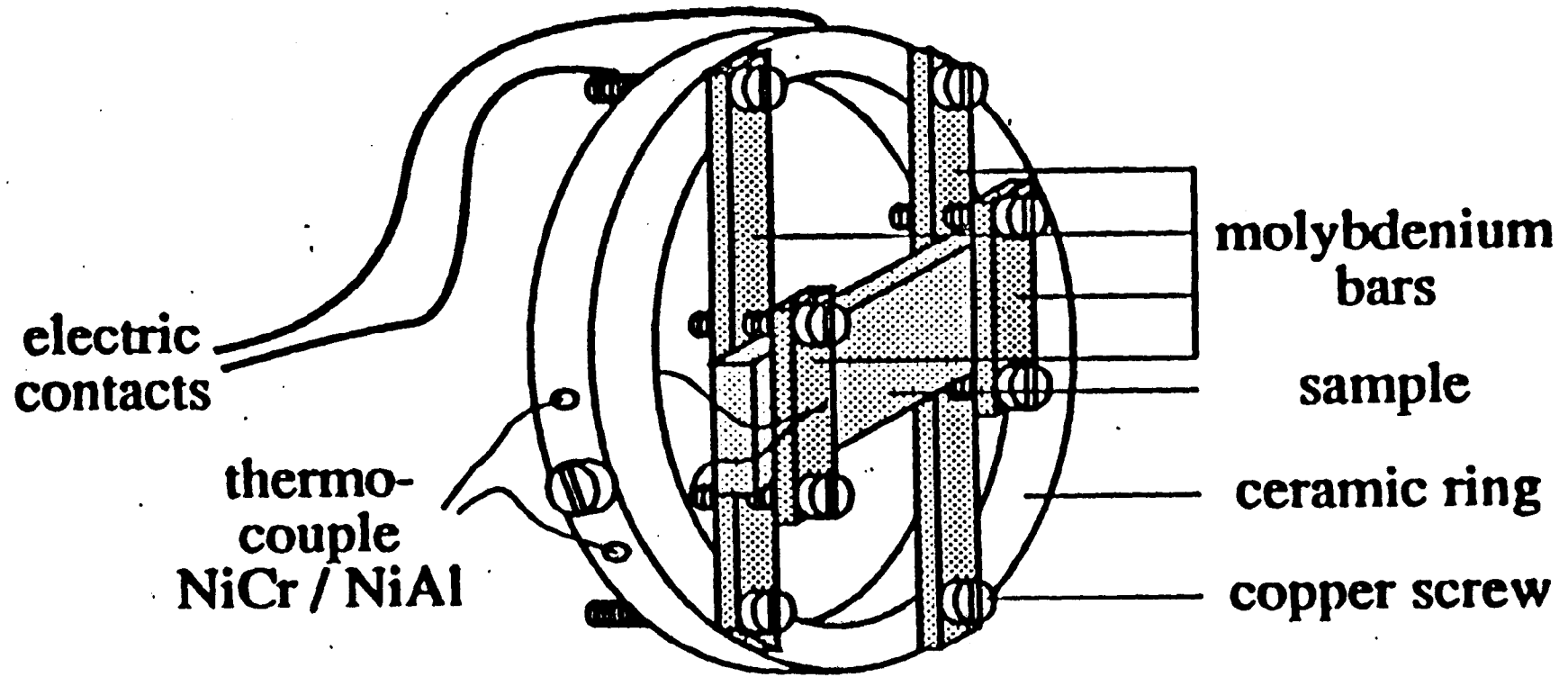
# AlGaAs/GaAs





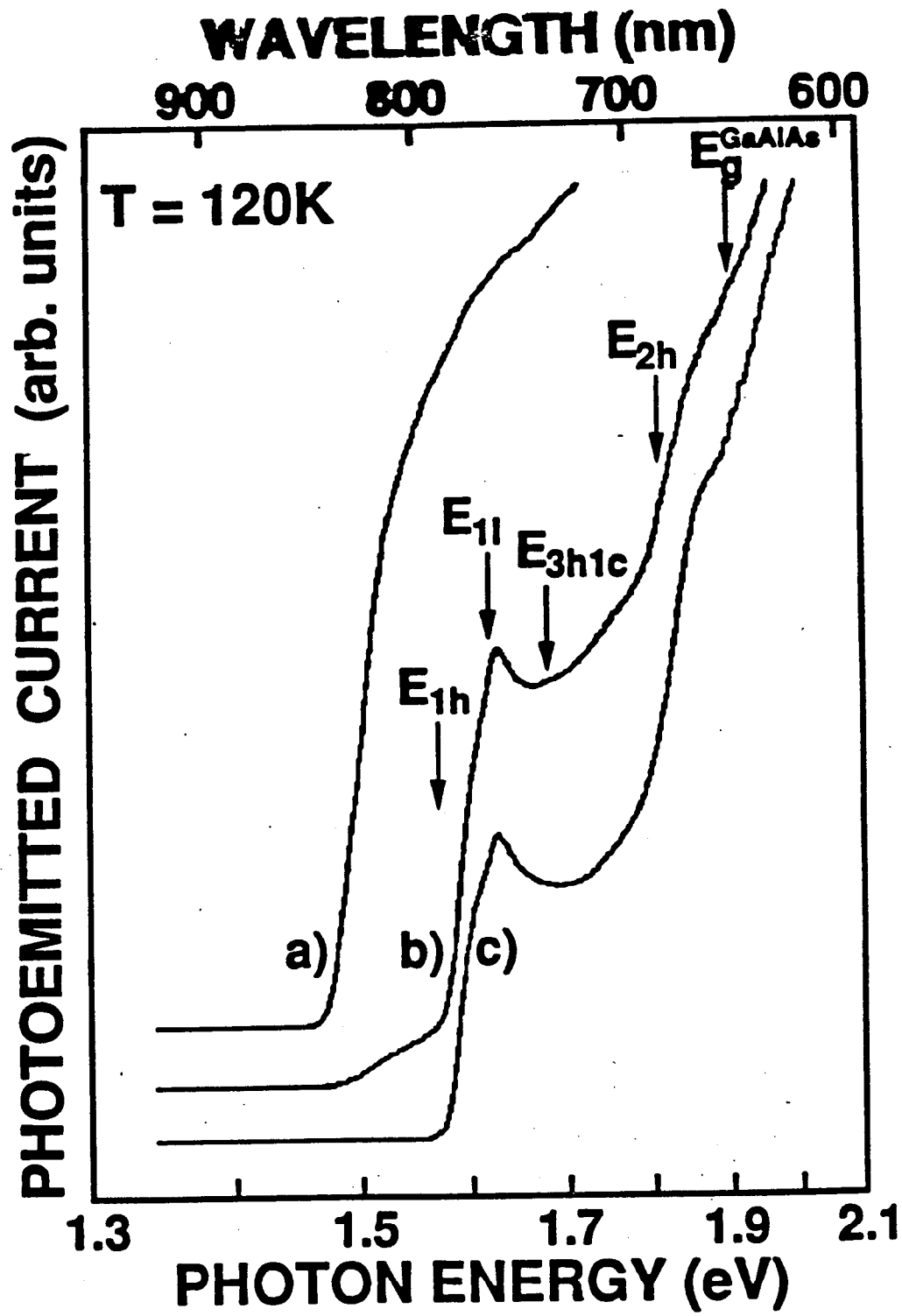


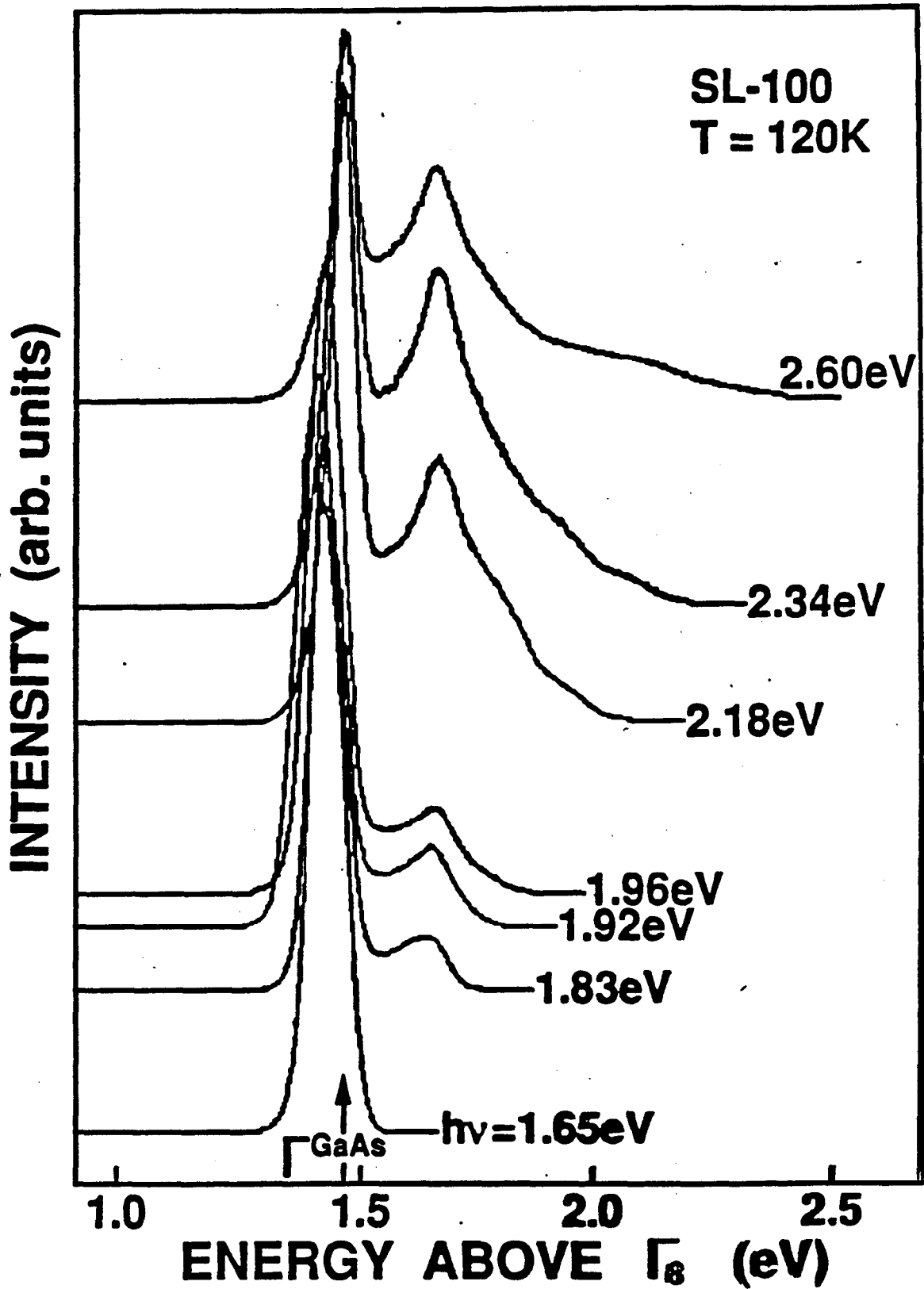
H. J. Drouhin, C. Hermann and G. Lampel, Phys. Rev. B31  
 3859 (1985); B31, 3872 (1985)

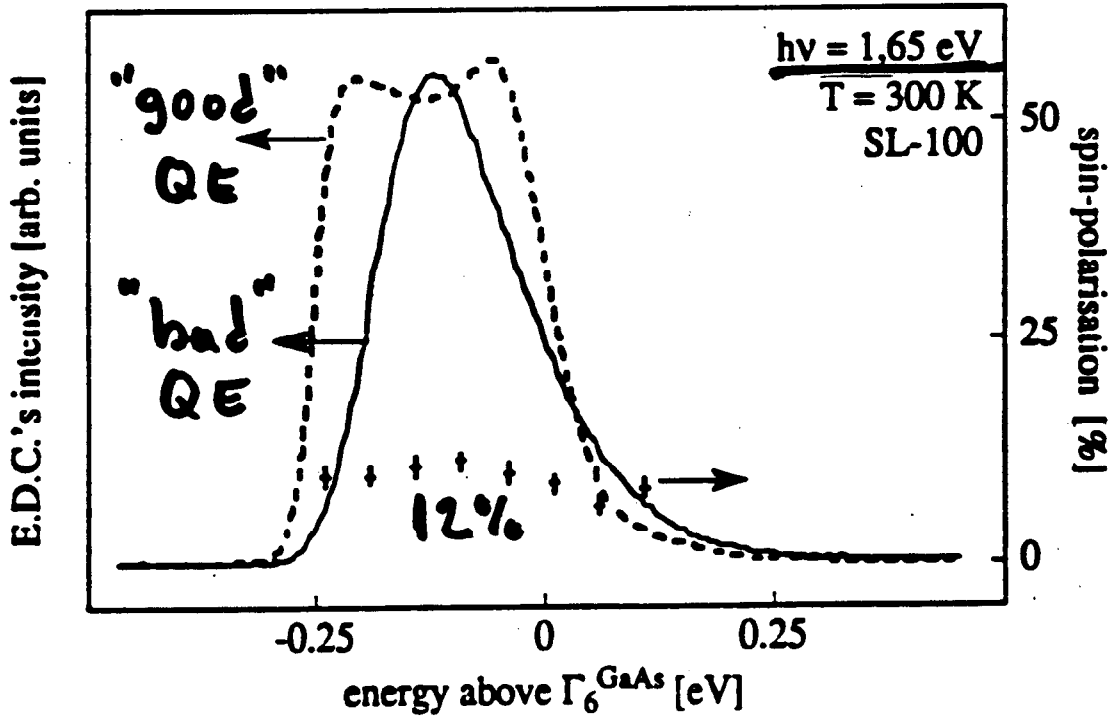
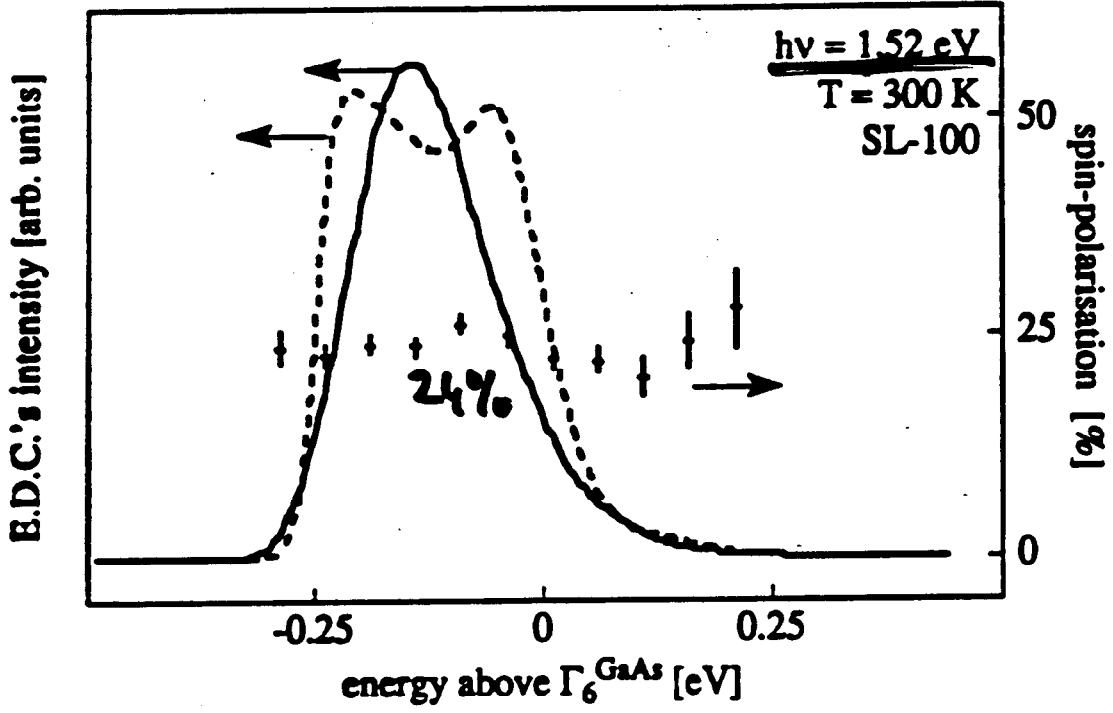


T.H. Gantner et al.  
T.H. Gantner et al.

Applied Surf. Science 56-58 (1992) p. 632  
21<sup>st</sup> ICPS Beijing (1992) p. 697

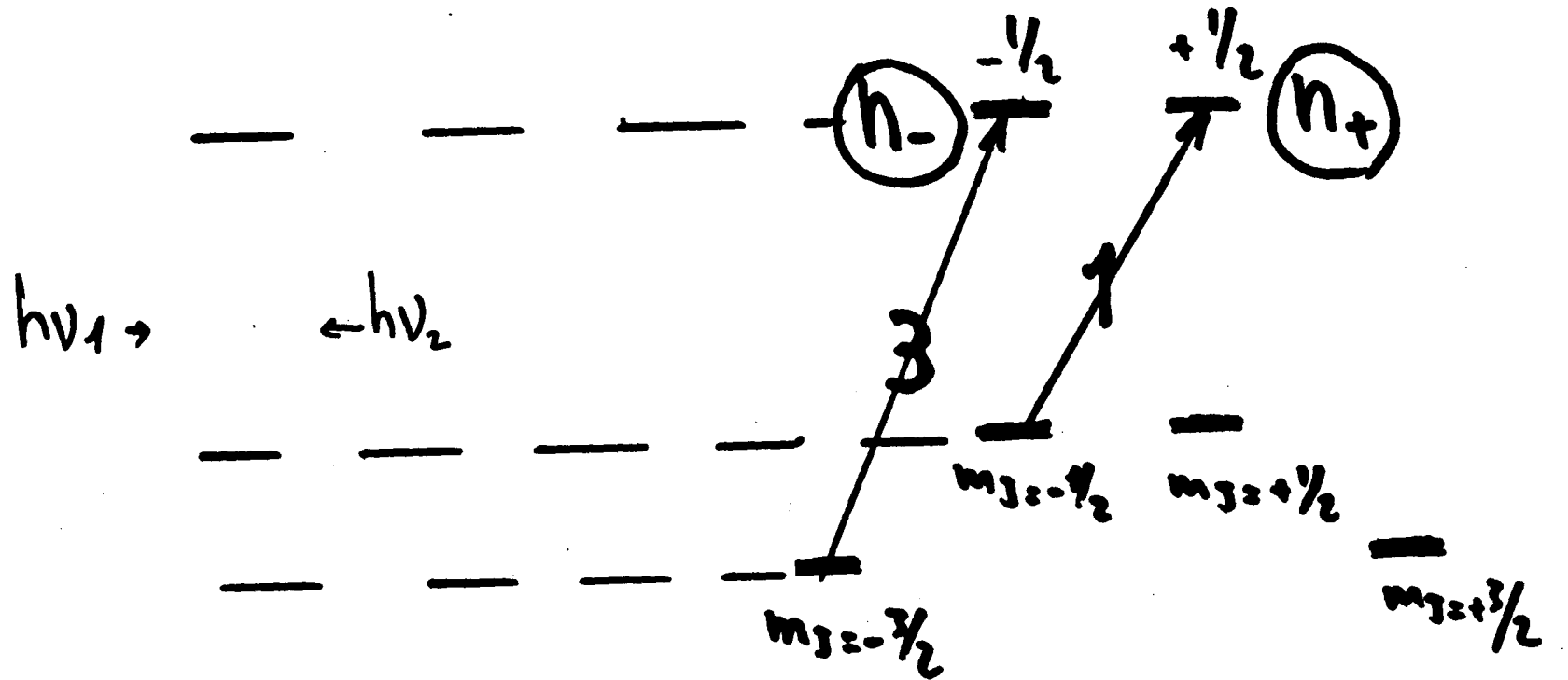






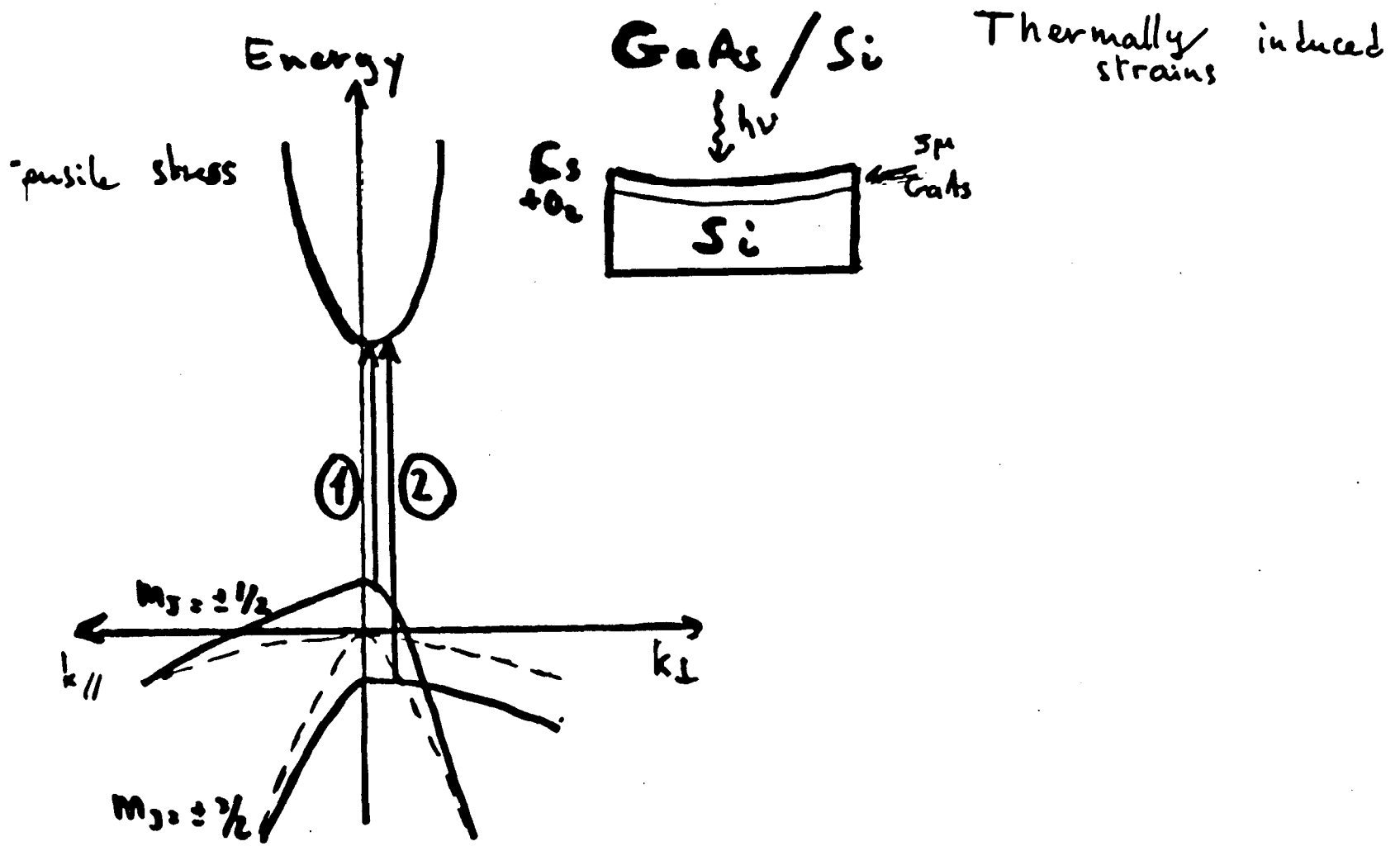


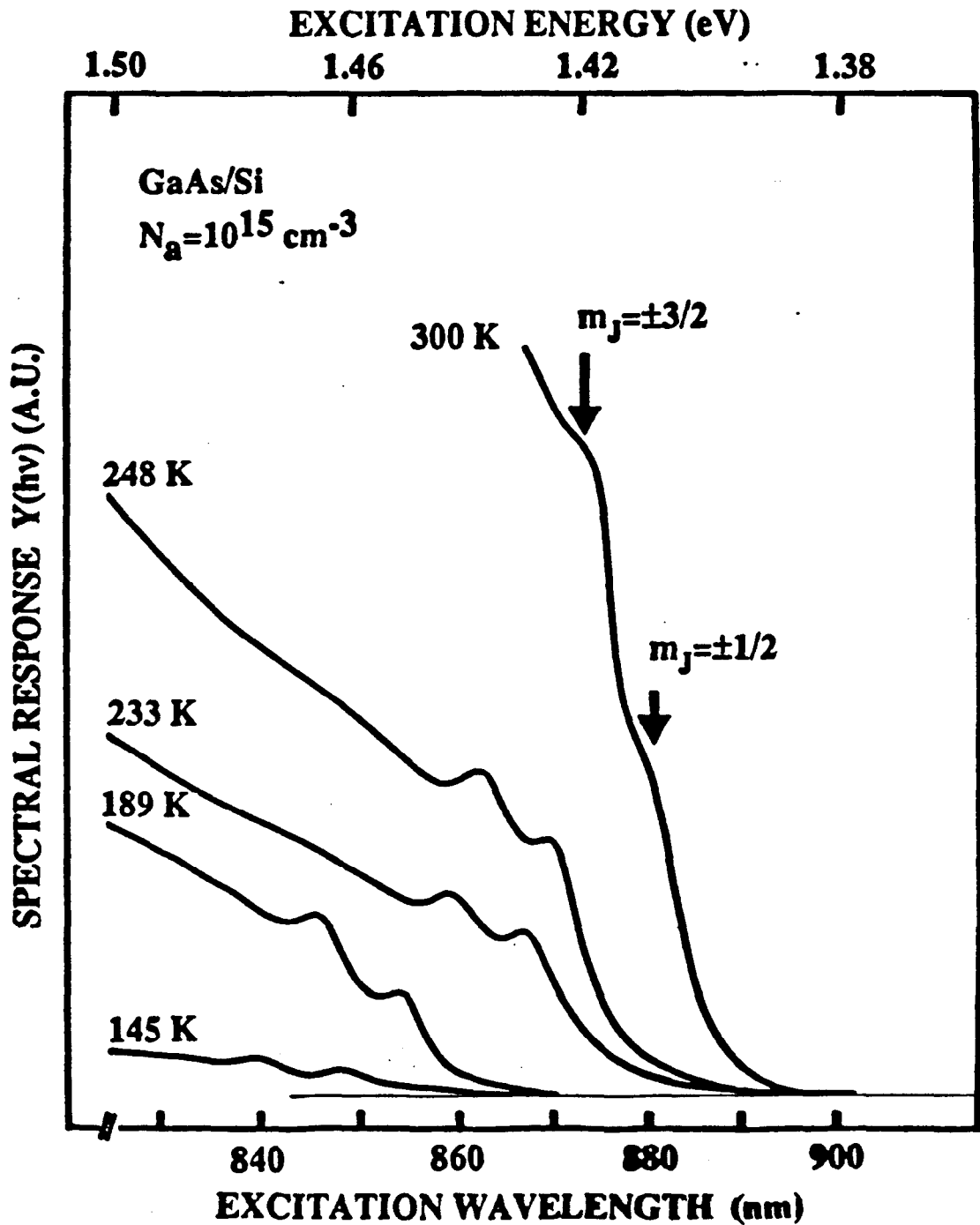
$$\Delta M = +1$$

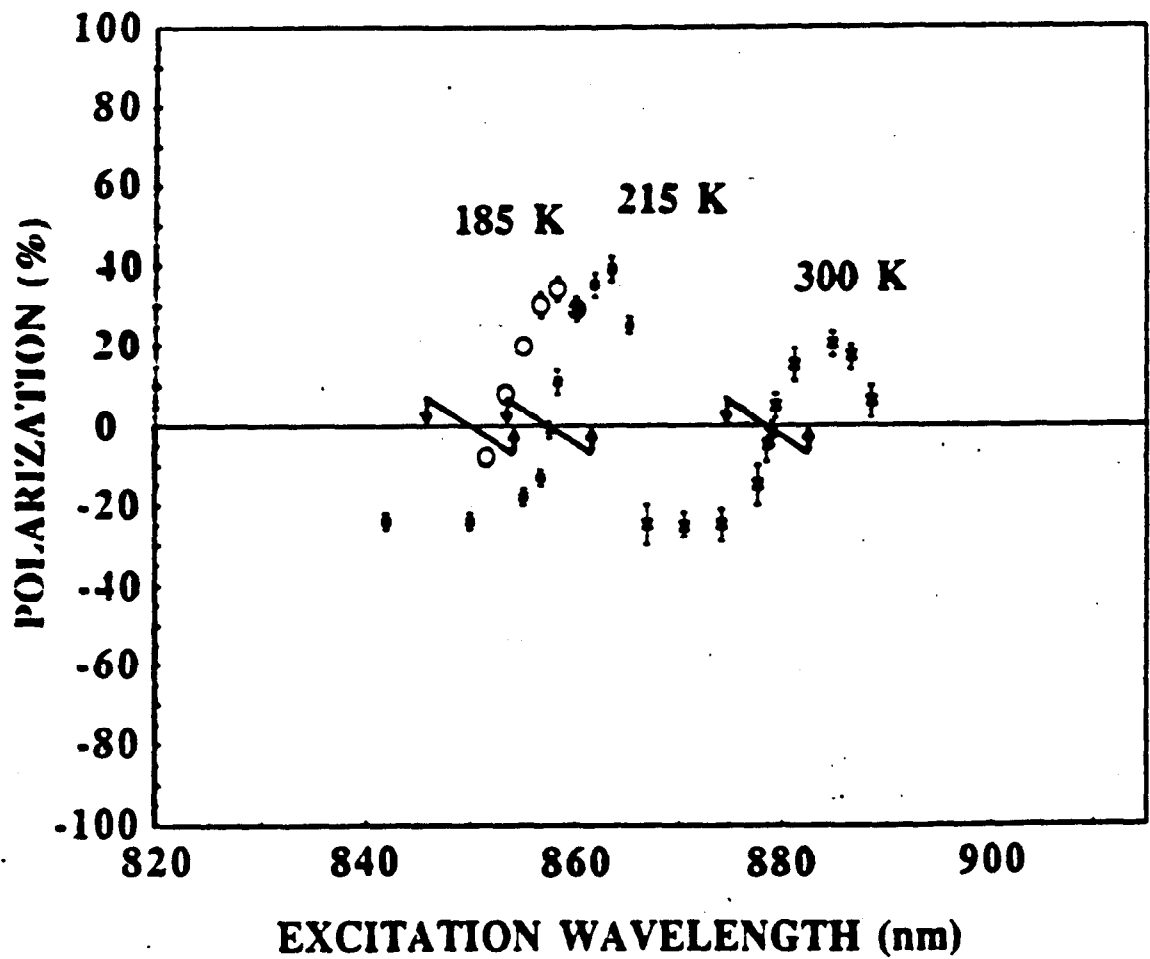
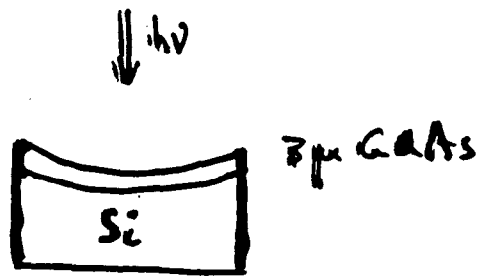


$$P_i = \frac{n_+ - n_-}{n_+ + n_-} = \frac{1 - 0}{1 + 0} \quad \text{for } h\nu_1 < h\nu_2 < h\nu_2$$

$$= \frac{1 - 3}{1 + 3} \quad \text{for } h\nu_1 \gg h\nu_2$$







It may be useful to change the sign of the electron polarization by changing an external parameter such as the excitation energy

# Conclusion

A decrease in Q.E. may occur:

- 1) by raising the vacuum level.

In that case the proportion of hot electrons is larger and so is the polarization.

- 2) by diminishing the escape probability with no change in the vacuum level.

In that case the beam is "polluted" by unpolarized "parasitic" electrons and the total polarization decreases.

**Robin Mair**  
**SLAC**

## **The Characterization of Strained-Layer GaAs Photocathodes Using Photoluminescence**

Photoluminescence has been used to characterize the quality of strained epitaxial GaAs photocathodes. The observed location of the photoluminescence peak from the strained GaAs epitaxial layer relative to unstrained GaAs directly determines the epitaxial layer strain. The splitting of the heavy-hole and light-hole valence bands may then be determined from the measured strain. The quality of the strain may be assessed from the observed location of the photoluminescence peak from the GaAsP buffer layer since this measurement may be used to determine the P fraction and thus the lattice mismatch grown into the structure.

**The Characterization of Strained-Layer  
GaAs Photocathodes Using Photoluminescence**

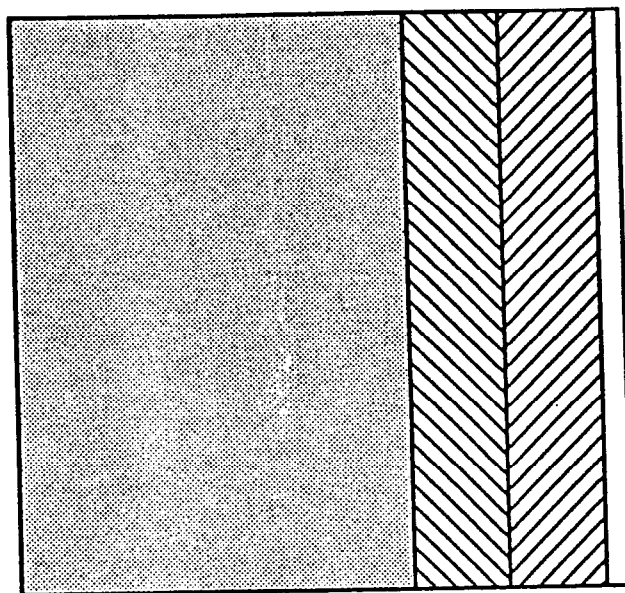
Robin Mair U. Wisconsin-Madison / SLAC

E.L. Garwin SLAC


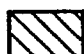
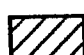

T. Maruyama SLAC

R. Prepost U. Wisconsin

## SLAC Strained Layer Photocathode Structure



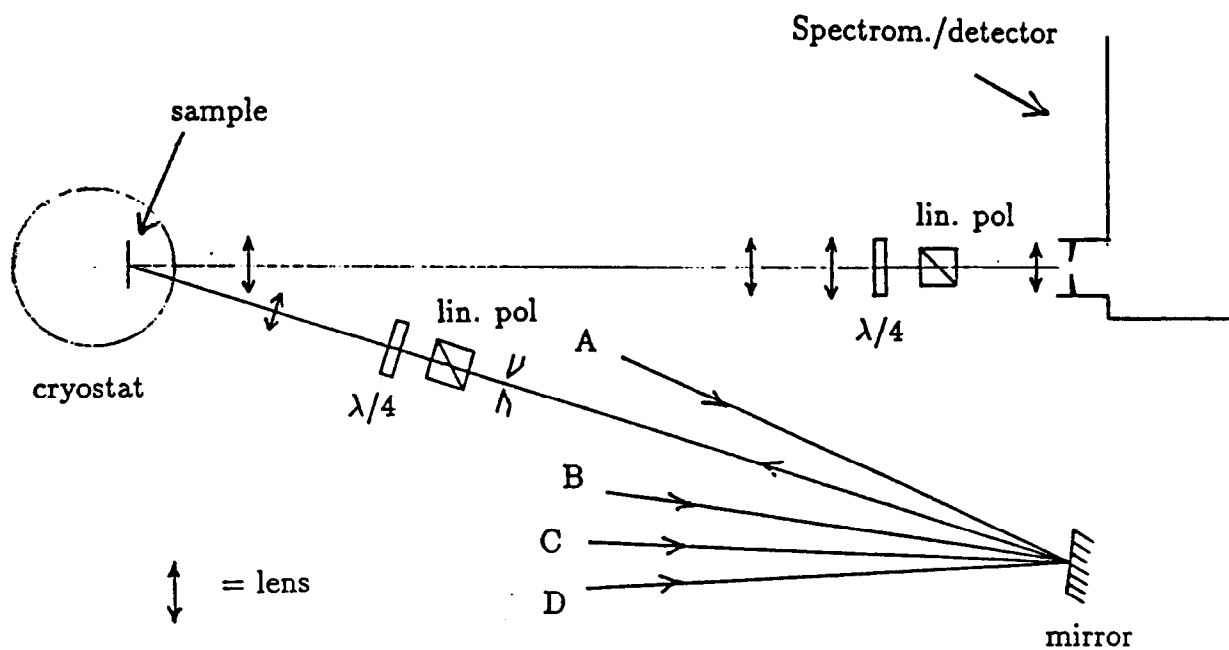
All layers Zn doped at approximately  $5 \times 10^{18} \text{ cm}^{-3}$

-  Substrate: GaAs
-  Graded Layer:  $\text{GaAs}_{(1-x)}\text{P}_x$   $x$  from 0 to  $x_0$  ( $2.5 \mu\text{m}$ )
-  Buffer Layer:  $\text{GaAs}_{(1-x_0)}\text{P}_{x_0}$   $x_0 = .20 - .30$  ( $2.5 \mu\text{m}$ )
-  Active Layer: Strained GaAs ( $.1 - .3 \mu\text{m}$ )

All samples grown by the SPIRE Corporation, using MOCVD



## Photoluminescence Setup



A-D = various pump lasers

Spectrometer: 320mm focal length, single grating (600groove/mm)

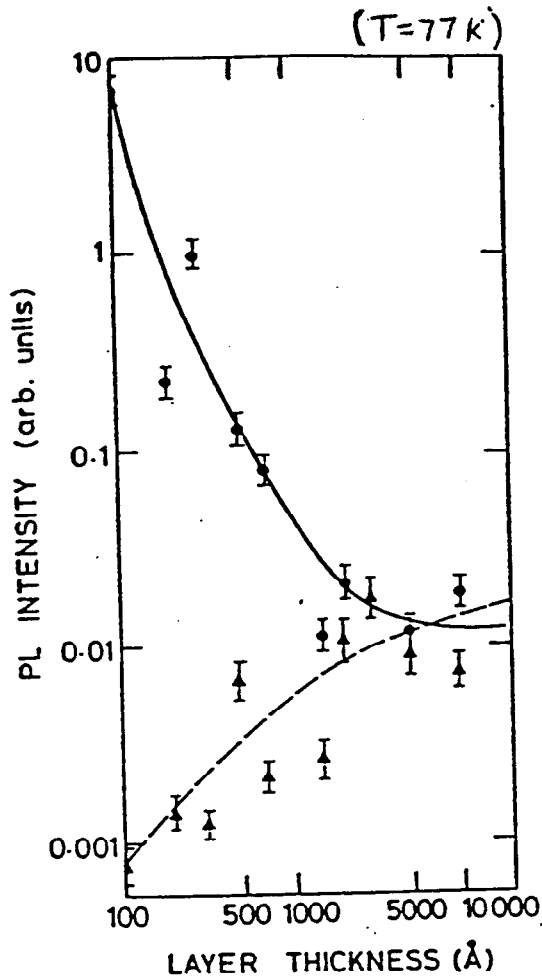
Detector: microchannel plate - intensified diode array

- wavelength calibrated with Ne lamp line spectrum
- spectral response calibrated with a Tungston ribbon lamp

Samples can be mounted in cryostat or on an external mount

## Observing PL from Strained Epilayers

Photoluminescence efficiency from strained epilayers is very low.



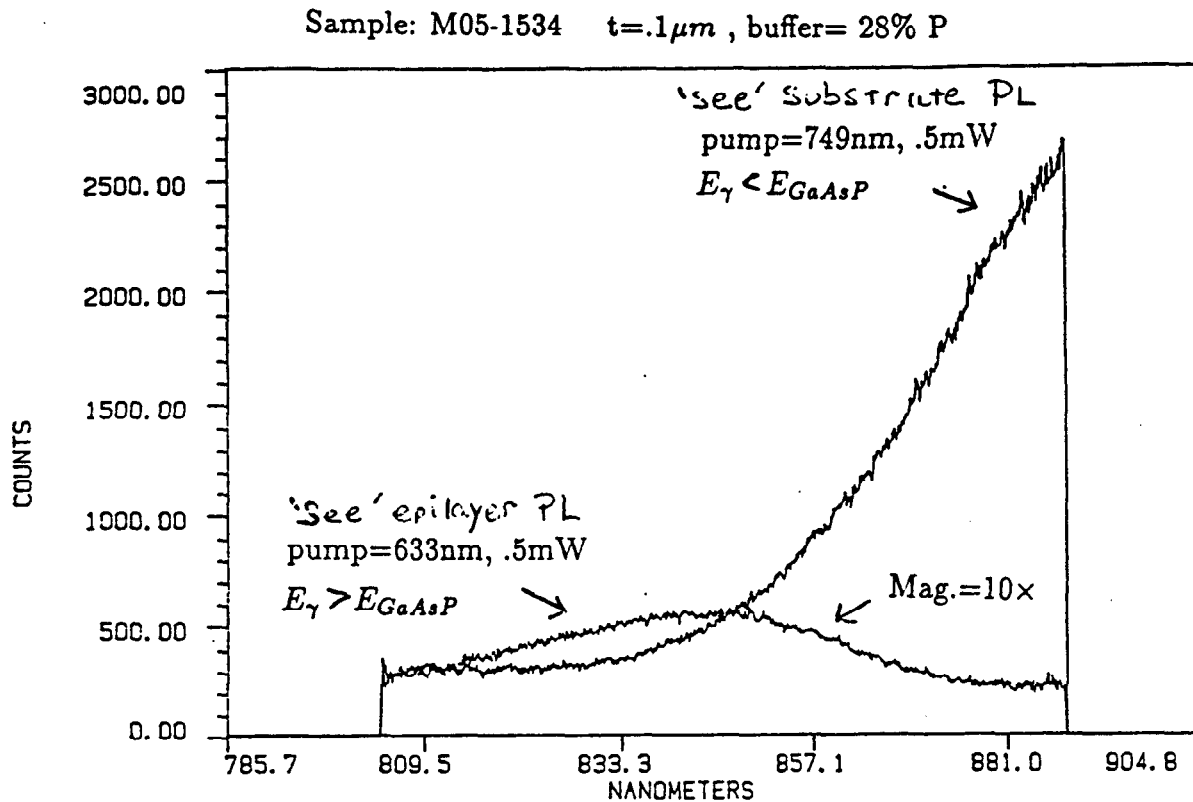
Plot from Joyce *et al*,  
JAP 65 p.1377 (1989)

Samples of  $\text{In}_{.17}\text{Ga}_{.83}\text{As}$  grown on GaAs, capped with GaAs. Shows decreasing PL intensity from a strained layer with increasing layer thickness.

Solid line = exciton PL

dashed line = broad band PL feature  
(dislocation related??)

Must pump sample with a source such that  $E_\gamma$  is larger than the buffer layer bandgap. This prevents excitation of GaAs Substrate.



It is sometimes possible to enhance the PL efficiency of the epilayer by passivating the surface.

e.g. 1 Molar  $Na_2S \cdot 9H_2O$  application (Skromme *et al*, APL 51 p.2022 (1987))

- We have seen enhancements of  $\sim 3\times$  on a  $.3\mu m$  strained layer. This, however, is not sufficient to overcome unwanted substrate contribution to the PL.

## Plotting epilayer PL peak energies vs measured strain

Biaxial strain in GaAs breaks the degeneracy of uppermost valence bands. This is critical to the degree of electron polarization obtainable from the photocathode. The net shift of each valence band relative to the conduction band can be expressed as a function of strain ( $\epsilon_{\parallel}$ ), elastic compliance coefficients ( $c_{11}, c_{12}$ ), and deformation potentials ( $a, b$ ) of GaAs. Photoluminescence can measure this shift in bandgap. For a biaxial compressive strain, the bandgap shift is determined by

$$\delta E_{hh} = \left[ -2a \frac{(c_{11} - c_{12})}{c_{11}} + b \frac{(c_{11} + 2c_{12})}{c_{11}} \right] \epsilon_{\parallel} = (-7.43 \text{ eV}) \epsilon_{\parallel}$$

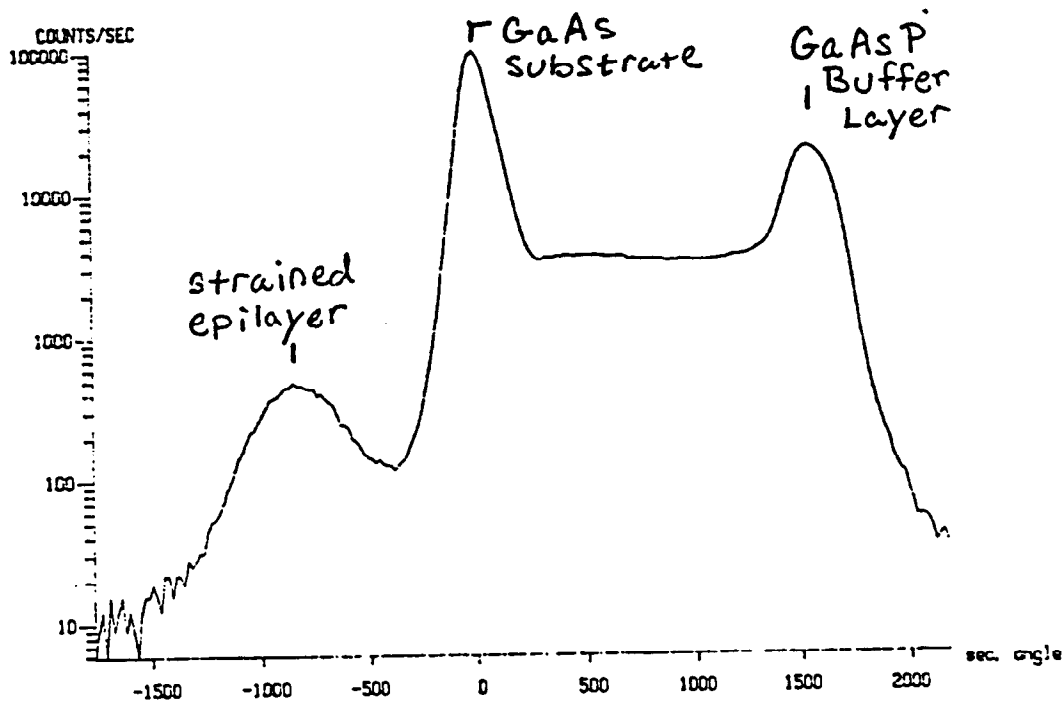
Strain measurements - made by X-ray diffraction

- 004 Bragg reflection using Cu- $k_{\alpha}$  line
- $\theta / 2\theta$  scans
- this geometry gives  $a_{\perp}$  only.  $a_{\parallel} = \left( \frac{-c_{11}}{2c_{12}} \right) a_{\perp}$
- strain =  $(a_{\parallel} - a_{relax}) / (a_{relax})$

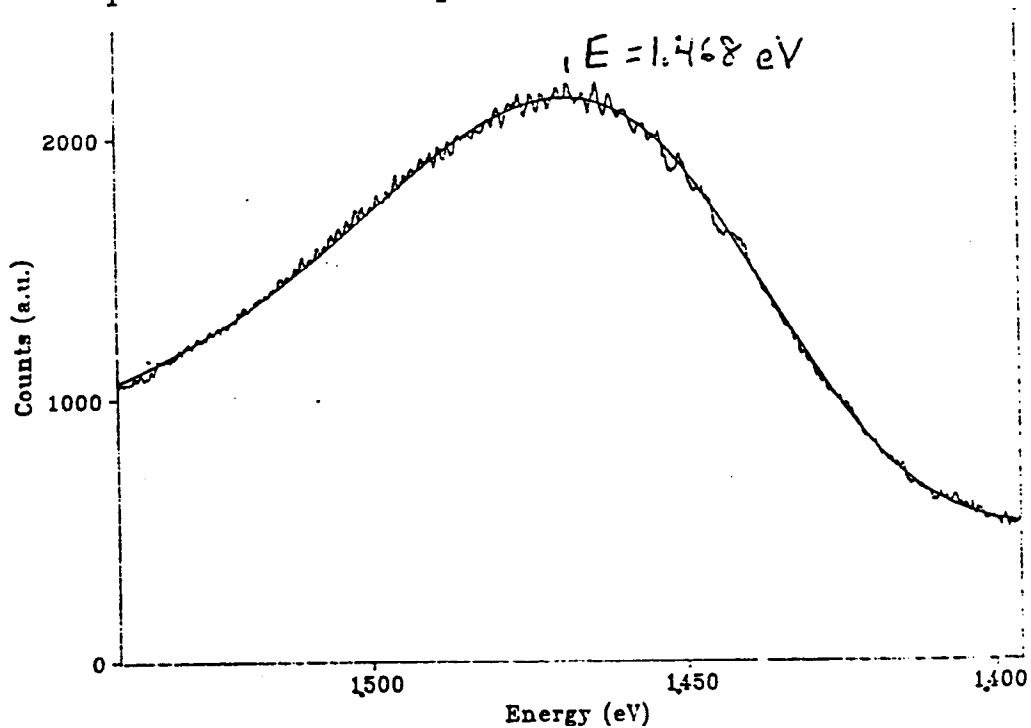
PL measurements

- made at room temperature with HeNe (633nm) pump
- peaks were empirically fit with Log-Normal curves
- average of three spectra used for each sample

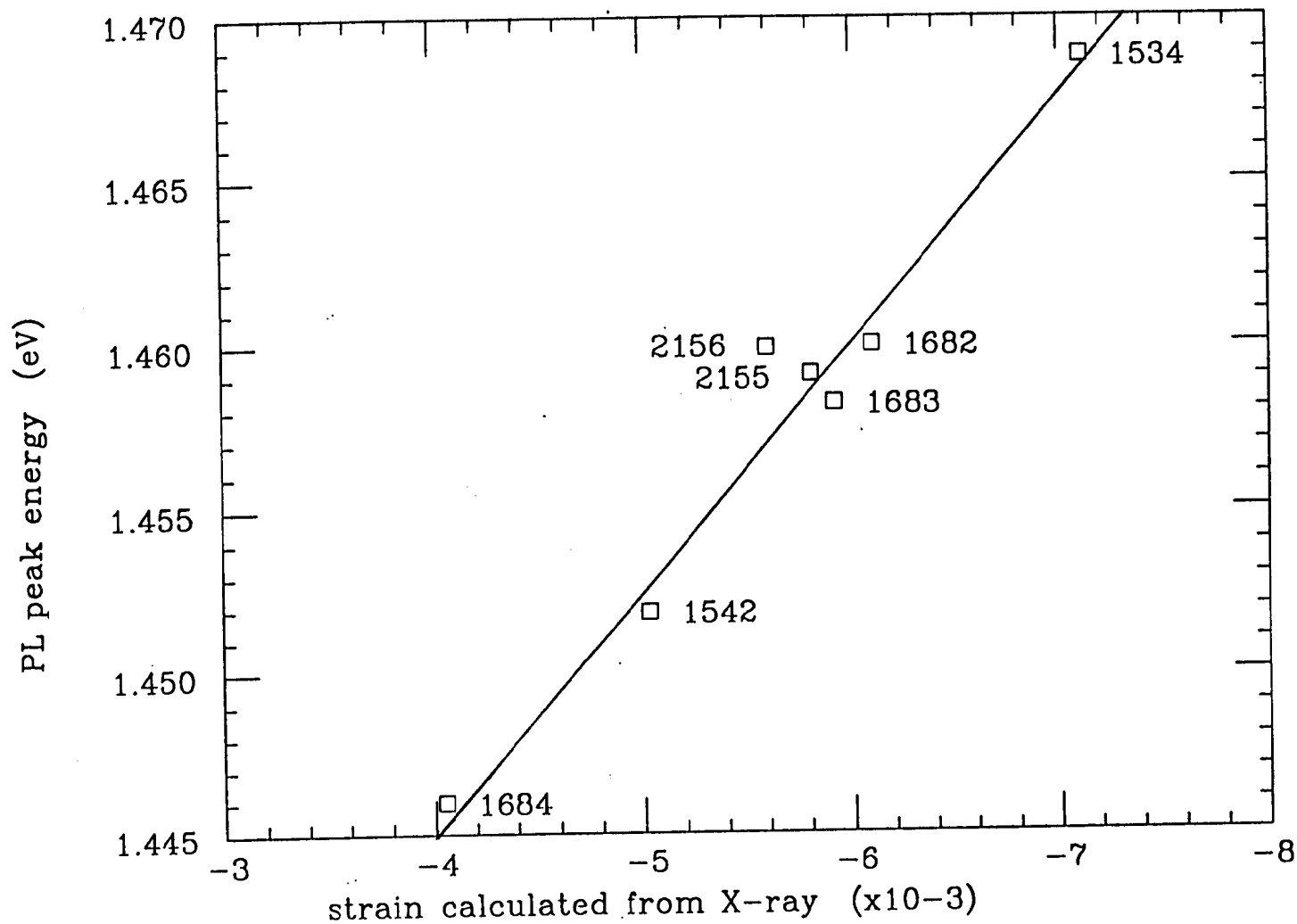
X-ray diffraction curve sample M05-1534  $t=0.1\mu\text{m}$ , buffer= 28% P



PL peak with fit sample M05-1534

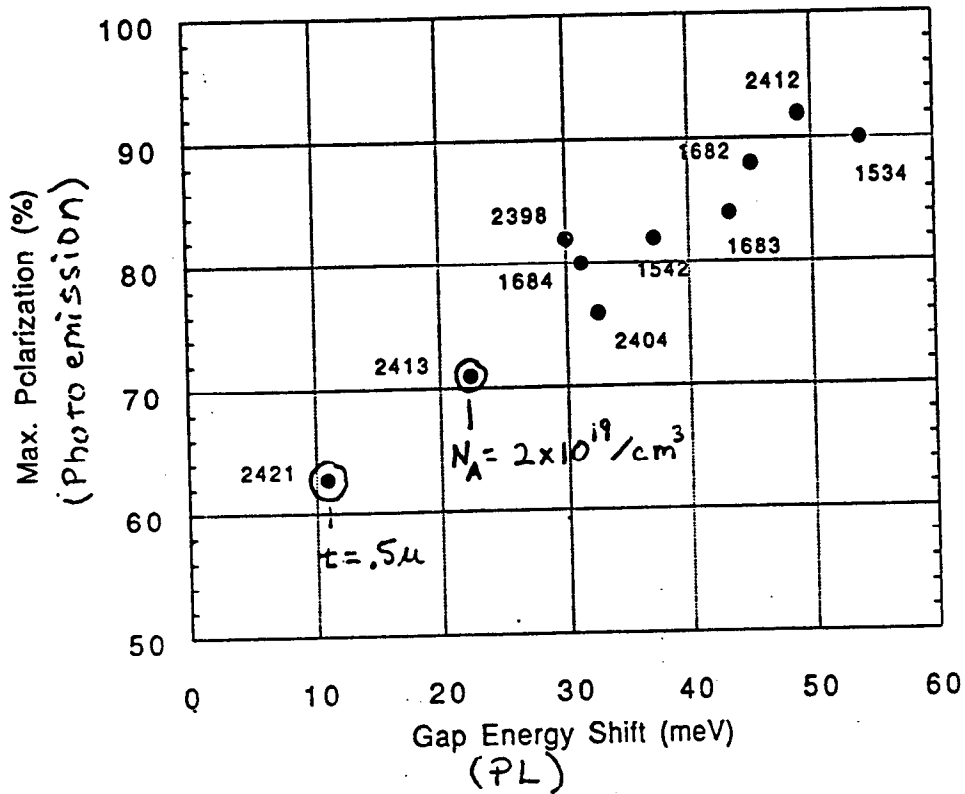


# PL Peak Energy vs Measured Strain (X-ray)

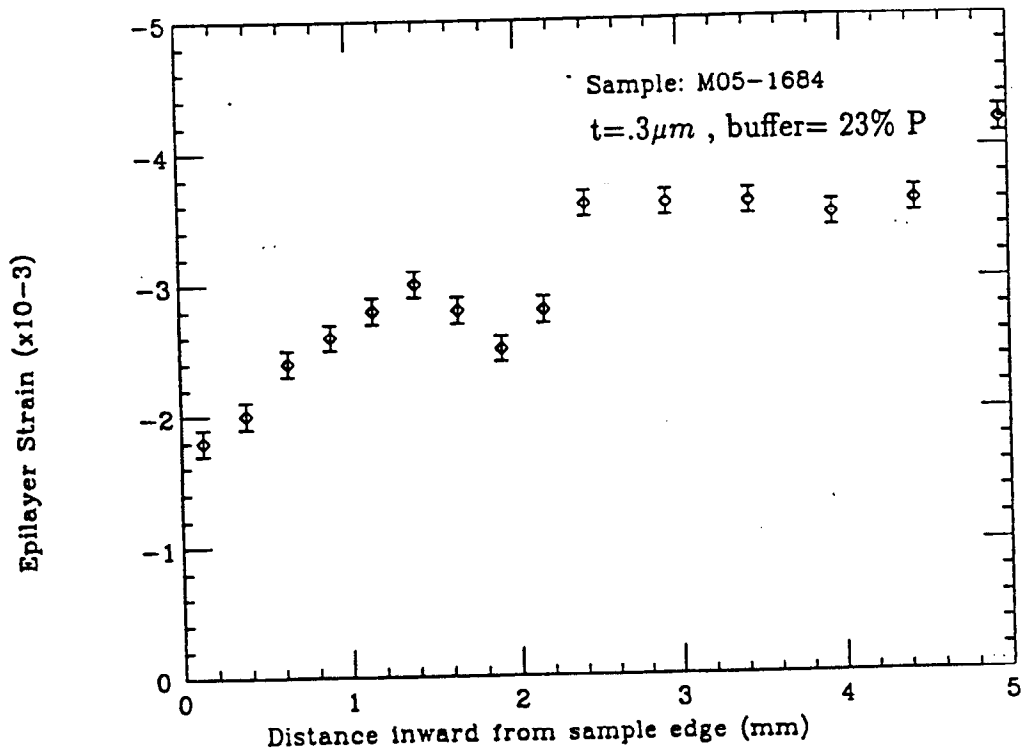


Linear Least Square :  $E_{PL} = 1.4148 \text{ eV} - 7.53 \text{ eV } \epsilon_{||}$

Max. Polarization vs. Gap Energy Shift  
 (Photoemission) (Photoluminescence)



Epilayer Strain vs. Proximity to Wafer edge



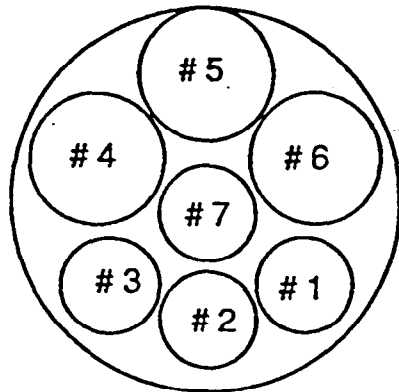
## Buffer layer Photoluminescence

Buffer layer ( $\text{GaAs}_{(1-x)}\text{P}_x$ ) PL peak position is related to the phosphorus content. The lattice mismatch, necessary for incorporating strain into the epilayer, is also related to phosphorus content.

Bandgap of  $\text{GaAs}_{(1-x)}\text{P}_x$  as a function of  $x$ :

$$E(x) = 1.404^*eV + 1.150eV(x) + .176eV(x^2)$$

\*use measured PL energy of GaAs substrate rather than the intrinsic (1.424eV)



	PL measured
	Phosphorus content
# 1	23.1%
# 2	23.0%
# 3	23.6%
# 4	23.0%
# 7	23.2%

The data shows good uniformity in the phosphorus fraction of the buffer layer across the wafer.



## Recent PL work - Etching Samples

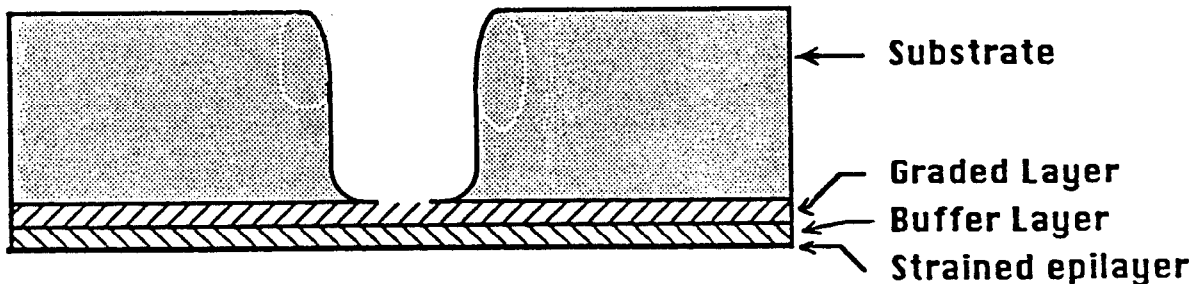
Would like to be able to pump samples near band edge

- to allow asymmetry measurements as function of  $\lambda_{pump}$
- to perform spin relaxation experiments (Hanle effect)

Must eliminate substrate PL contribution

Etch Substrate away from a portion of the sample

- used 8:1:1  $H_2O_2(30\%):H_2SO_4:H_2O$
- sample waxed face down to microscope slide
- etch resistant lacquer covers all but  $\sim 1mm$  hole
- periodically stop etch, check hole depth
- slower etch - 1(20 $NH_4OH:7H_2O_2$ ):500 $H_2O$  - when nearing buffer layer
- periodic check of substrate PL intensity
- when PL vanishes, etch complete



## Epilayer PL from etched samples

### Room Temp

Sample	PL peak (nm)		Relative intens. (thin)/(nonthin)
	Nonthin	Thin	
M05-1684 ( $t=.3\mu m$ )	863.5	864.5	~1.3
M05-1683 ( $t=.2\mu m$ )	851.0	857.5	~2.6
M05-2412 ( $t=.1\mu m$ )	846.0	852.0	~3.6

### Liq N<sub>2</sub> Temp ( 78K)

Sample	PL peak (nm)		Relative intens. (thin)/(nonthin)
	Nonthin	Thin	
M05-1684 ( $t=.3\mu m$ )	827.0	825.5	~2.5
M05-1683 ( $t=.2\mu m$ )	813.5	814.5	~8.0
M05-2412 ( $t=.1\mu m$ )	—	808	≥10

At room temperature, PL peak positions imply some strain lost in the thinned region of samples (less than 25% relaxation)

At 78K, PL peak positions do not show relaxation in the thinned region of samples

See an Enhancement in the PL intensity from the thinned region of the samples as compared with non-thinned. The effect is much more pronounced at low temperature.

## Asymmetry measurements with etched samples

Asymmetry:  $A = \frac{(I_{\sigma^-} - I_{\sigma^+})}{(I_{\sigma^-} + I_{\sigma^+})}$  (pumping  $\sigma_+$ )

The asymmetry in circularly polarized photoluminescence is directly related to the electron polarization in the conduction band.

$$A = P_{e^-} \times H \times R$$

H = hole coupling factor

$$R = \text{spin relaxation term } \frac{\tau_S}{(\tau_L + \tau_S)}$$

Asymm. measurements on etched samples

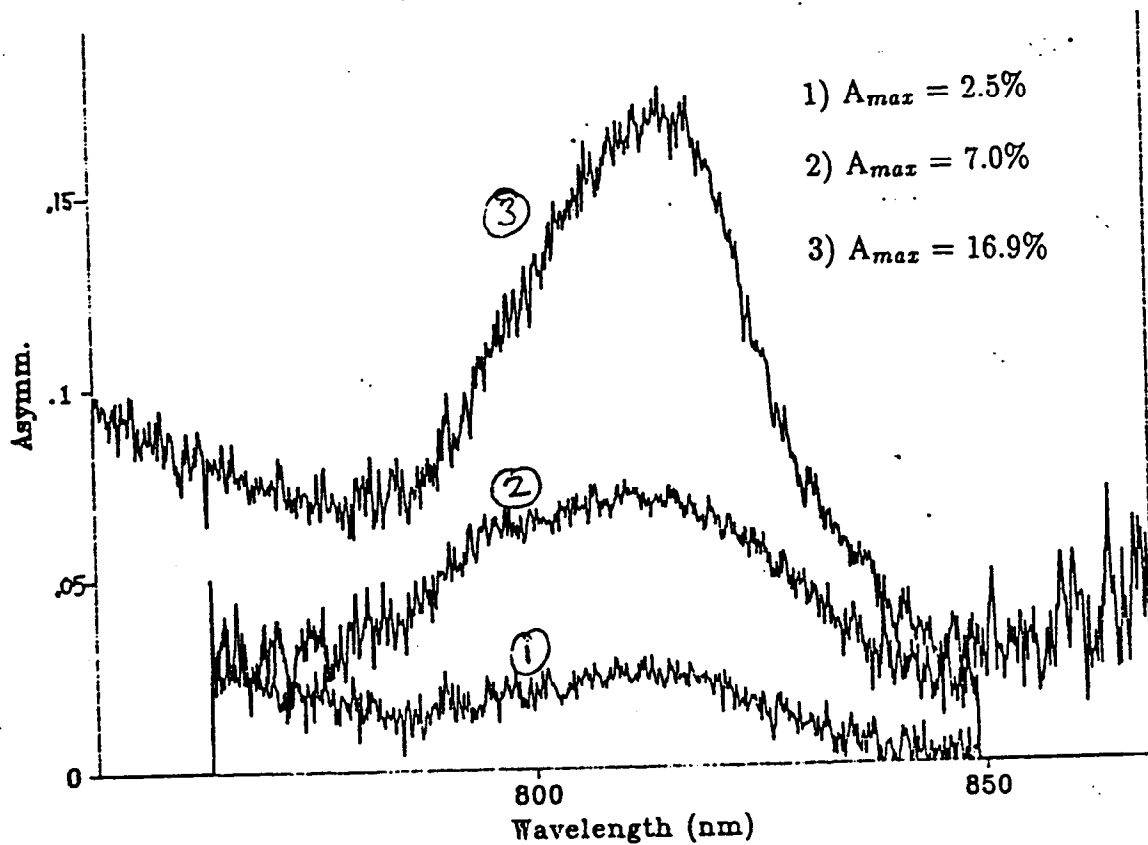
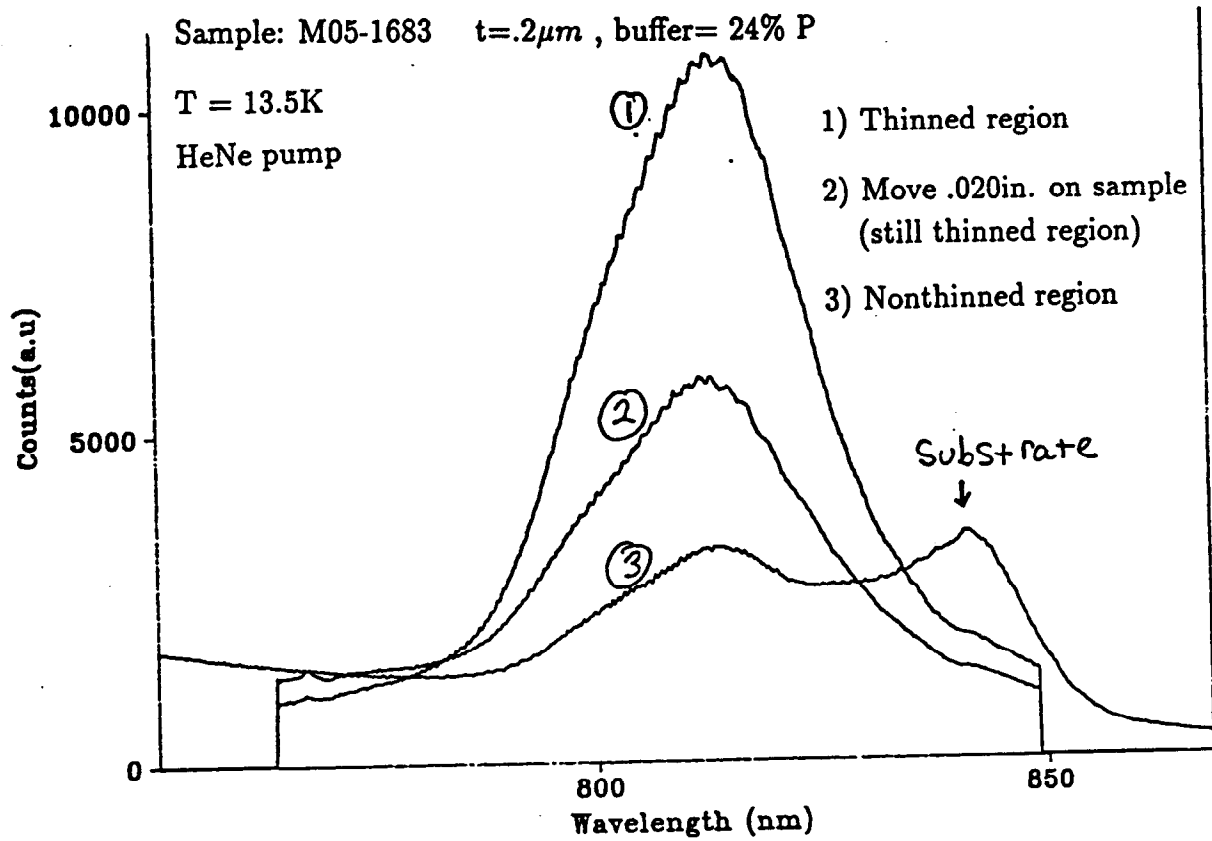
- 633nm pump  $\approx 5\text{mW}$  ( $\sigma_+$  excitation),  $T = 78\text{K}$
- raw asymm. good to  $\leq 1\%$  absolute. (systematic)
- not corrected for  $< 100\%$  pump pol. ( $\sim 5\%$  correction)

Sample	Asymmetry (thinned)	Asymmetry (nonthinned)
M05-1684	5.4%	11.5%
M05-1683	2.6%	14.6%
M05-2412	1.9%	6.2%

Can lower asymmetry in thinned sample regions be due to longer minority carrier lifetimes?

$$\text{Efficiency} \propto \frac{\tau_L}{\tau_R}, \quad \text{Spin relax. } R = \frac{\tau_S}{\tau_S + \tau_L}$$

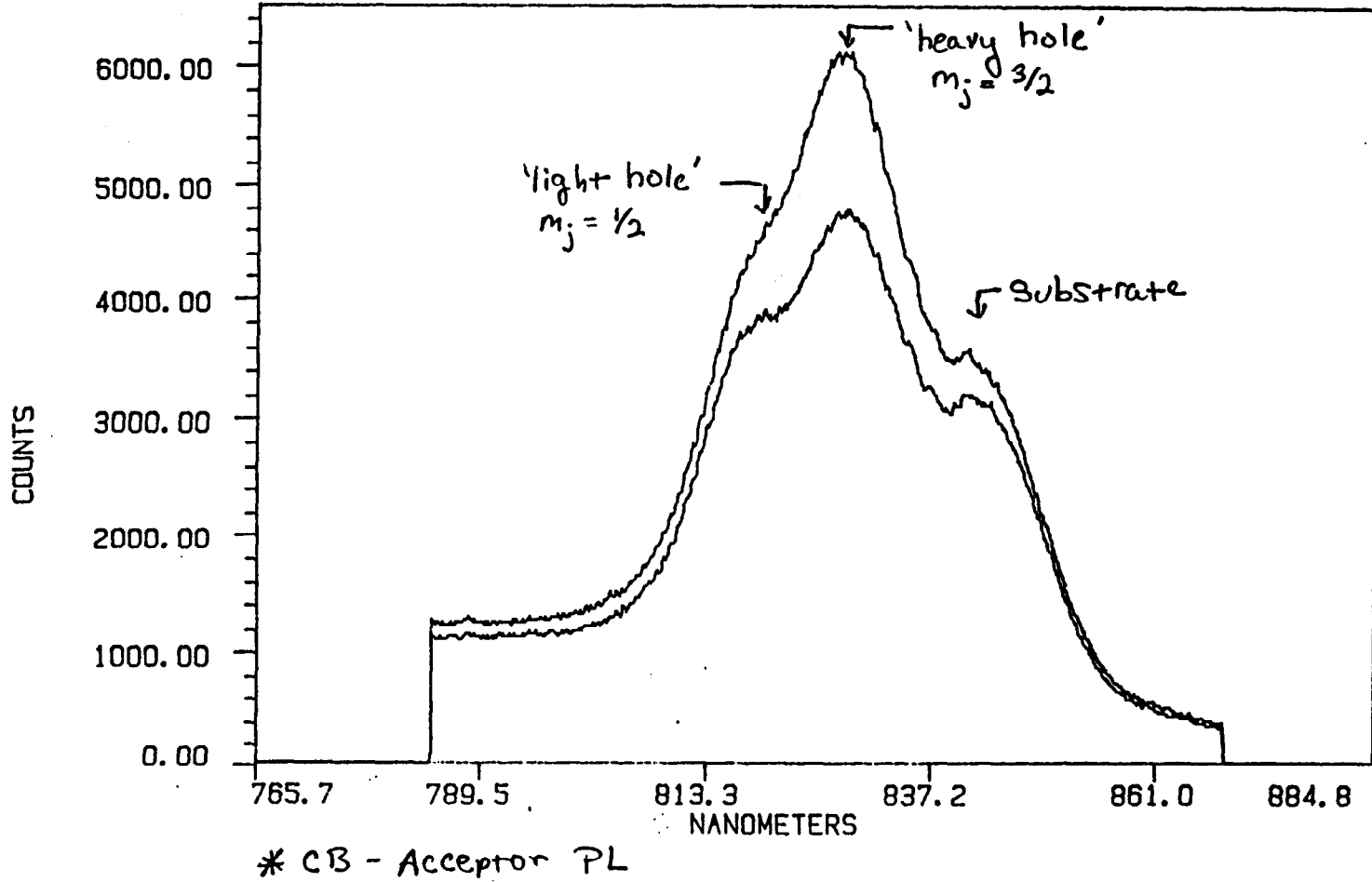
if  $\tau_L \uparrow$ , then effc.  $\uparrow$  and  $R \downarrow$  (lower asymm)



This plot clearly shows recombination to split levels with opposite  $\gamma$  helicities.

Sample: M05-1684  $t=0.3\mu\text{m}$ , buffer= 23% P (Non-thinned Region)

T = 10.6K Hene Pump ( $\sigma_+$ )



## Conclusions

Strained layer photocathode quality can be characterized with fairly simple PL measurements.

- measurement of epilayer strain
- measurement of buffer layer phosphorus concentration
  - both measurements are very quickly made (minutes).
  - suitable for mapping of samples or entire wafers.

Photocathodes have been etched (substrate) to allow pumping with wavelengths appropriate for large conduction band electron spin polarization.

- appears that epilayer strain is preserved to a high degree
- a very interesting increase in the PL efficiency appears
  - this phenomena is not fully understood
- a decrease in measured asymmetry also appears
  - simply related to increased efficiency through a change in electron lifetime ??

## **Addendum**

Since the time of the workshop, we have identified the source of PL enhancement and asymmetry degradation in our thinned samples.

Normally, in a nonthinned sample, only  $\sim 2\%$  of the internally generated PL escapes through the sample surface. The remaining 98% is travelling backwards or reflected backwards and is absorbed in the GaAs substrate. In the thinned samples, the substrate is replaced by an air interface. PL photons are not absorbed, but experience total internal reflection (TIR) until they escape out either surface or are absorbed in the buffer/epilayer. It is important to note that TIR photons have opportunities to escape due to surface roughness and nonparallel surfaces. It is also important to note that the reflected photons experience phase shifts which destroy their average polarization.

The enhancement effect (and corresponding asymm. degradation) was successfully suppressed by applying a graphite based coating (DAG) to the backside of a sample's thinned region. This coating effectively prevented TIR and also absorbed PL photons. Unlike the substrate, however, this coating does not produce a large unwanted PL contribution in the vicinity of the strained layer PL.

**Yuri Mamaev**  
**Division of Experimental Physics, St. Petersburg**  
**Technical University**

**Spin-polarized Photoemission from InGaAs, AlGaInAs,  
GaAs and GaAsP Strained Layers**



Spin-polarized photoemission from InGaAs, AlGaInAs, GaAs and GaAsP  
strained layers \*

Yu A. Mamaev<sup>2</sup>, J.C. Gröbli<sup>1</sup>, B.S. Yavich<sup>3</sup>, Yu. P. Yashin<sup>3</sup>, F. Meier<sup>1</sup>,  
A.V. Subashiev<sup>2</sup>,

N.N. Faleev<sup>3</sup>, M.S. Galaktionov<sup>2</sup>, D. Guarisco<sup>1</sup>

I.V. Kochnev<sup>3</sup>, S.A. Starovoitov<sup>2</sup>, A. Vaterlaus<sup>1</sup>

E. Reichert<sup>4</sup>, S. Plützer<sup>4</sup>

1- Laboratorium für Festkörperphysik, ETH Hönggerberg,  
CH-8093 Zürich, Switzerland

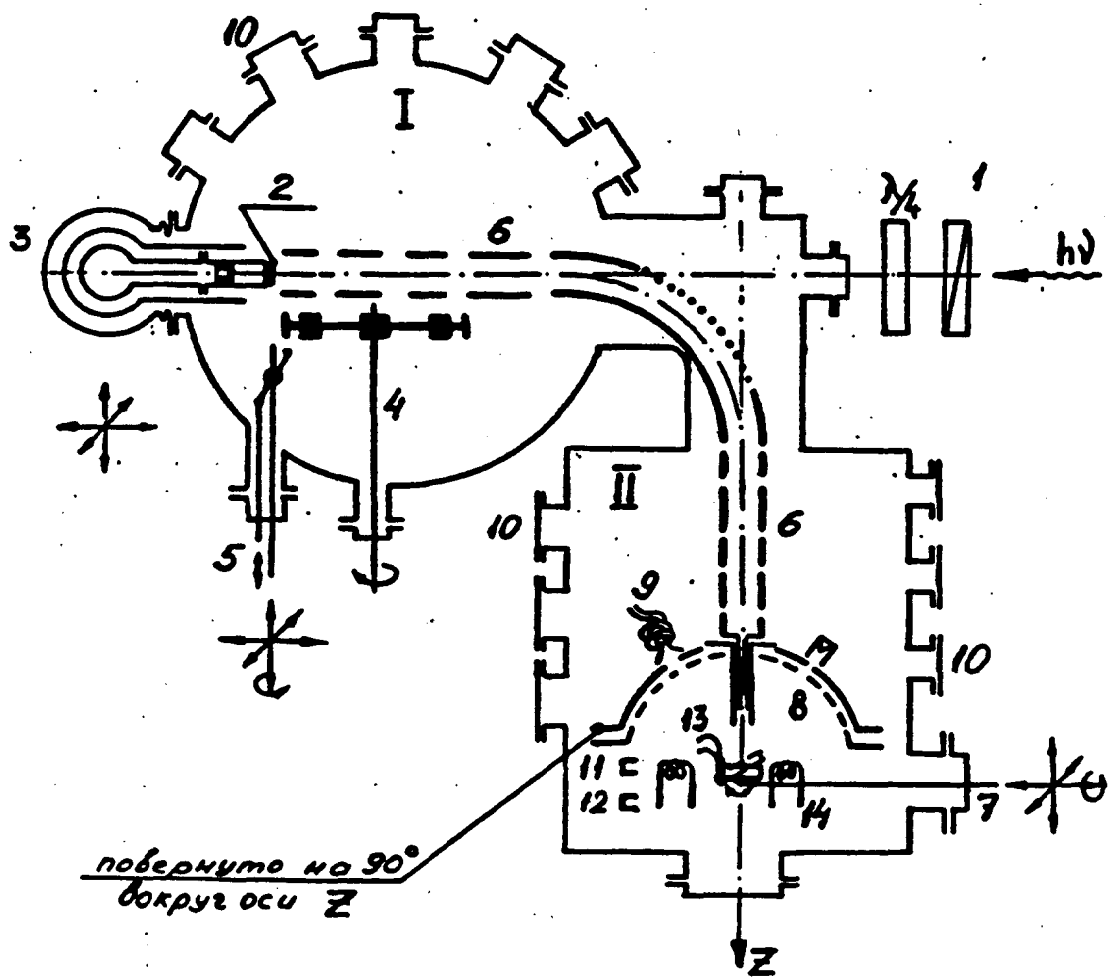
2- Division of Experimental Physics, St. Petersburg Technical University,  
195251 St. Petersburg, Russia

3- Ioffe Physicotechnical Institute, Russian Academy of Sciences,  
194021 St. Petersburg, Russia

4- Institut für Physik, Universität, Mainz, Postfach 3988, D-6500  
Mainz1, Germany

An experimental study of the polarization and quantum yield as a function of layer thickness and temperature was performed for different MOCVD-grown heterostructures. With the systems investigated so far we measured a polarization  $P$  up to 80% with  $\text{In}_{0.15}\text{Ga}_{0.85}\text{As}/\text{GaAs}$  and 70% with  $\text{GaAs}/\text{GaAs}_{0.8}\text{P}_{0.2}$ . We further report first results with  $(\text{Al}_{0.3}\text{Ga}_{0.7})_{0.85}\text{In}_{0.15}\text{As}/\text{Al}_{0.7}\text{Ga}_{0.3}\text{As}$  ( $P=74\%$ ,  $Y=2.10^{-4}$  at  $h\nu=1.52$  eV) and  $\text{GaAs}_{0.9}\text{P}_{0.1}/\text{GaAs}_{0.65}\text{P}_{0.35}$  ( $P=72\%$ ,  $Y=6.10^{-3}$  at  $h\nu = 1.58$  eV, layer thickness  $700\text{\AA}$ ) at room temperature. Because  $\text{Al}_{0.7}\text{Ga}_{0.3}\text{As}$  has an indirect energy gap its contribution to the photocurrent is negligible even for photon energies far from photothreshold. By varying the amount of Al and/or In in the overlayer it is possible to influence both the energy gap and the internal strain and to investigate the photoelectric yield and the spin polarization of the electrons emitted exclusively from the overlayer. The compounds with phosphorus seem to be good candidates for practical photoemitters of polarized electrons. Theoretical studies and experimental results on p- or n-doped substrates showed that the yield from the overlayer strongly depends on the recombination rate at the interface and on the values of the band offsets  $\Delta E_c$  and  $\Delta E_v$  in the heterojunction.

\* This work is supported in part by the Russian National Foundation Research, Grant N 93-02-15264



Yu. Mamaev et al. *Izv. Acad. Nauk USSR*  
 Ser. Fiz., 1986, v. 50, p. 301

LEED-detector

ETH - apparatus with Mott (100 kV)  
 Mainz apparatus with mini-Mott

Photoluminescence ; X-ray diffraction  
 Raman scattering ; Hall  
 Volt-capacity ; RBS

	As - cap	$d = 0.05 \mu\text{m}$
$E_g = 1.29 \text{ eV}$	In <sub>0.12</sub> Ga <sub>0.88</sub> As Be $p = 4 \times 10^{18} \text{ cm}^{-3}$	$d_1 = 0.1 \mu\text{m}$ $d_2 = 1.14 \mu\text{m}$
$E_g = 1.42 \text{ eV}$	GaAs Be $p = 6 \times 10^{18} \text{ cm}^{-3}$	$d = 0.2 \mu\text{m}$
$E_g = 1.42 \text{ eV}$	GaAs $n = \text{doped}$	$d = 0.6 \mu\text{m}$
	substrate GaAs(100) $n = \text{doped}$	

*T. Maruyama et al. Ph. Rev. Lett., 1991, v66, p2376*

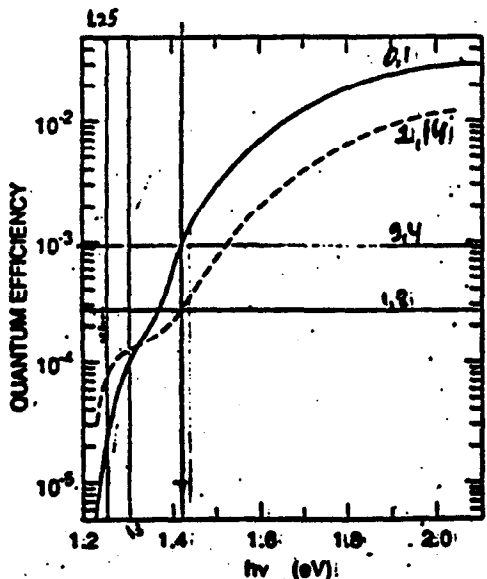


FIG. 2. Cathode quantum efficiency as a function of excitation photon energy. The solid curve is for the 0.1- $\mu\text{m}$ -thick sample, and the dashed curve for the 1.14- $\mu\text{m}$ -thick sample. The band-gap energies of GaAs (solid arrow) and relaxed InGaAs (dashed arrow) are indicated.

measurements the sample was scanned with x-ray diffraction. The InGaAs peak showed a 40-arcsec shift from the original location and had a peak broadening, indicating some strain relaxation due to the thermal treatments.

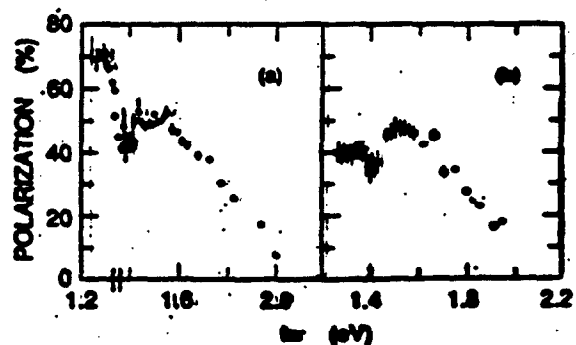
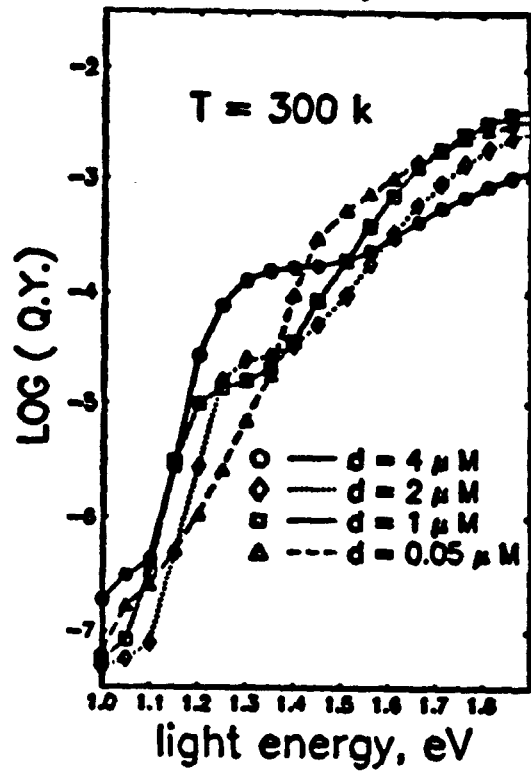


FIG. 3. Electron spin polarization as a function of excitation photon energy: (a) for the 0.1- $\mu\text{m}$ -thick sample and (b) for the 1.14- $\mu\text{m}$ -thick sample. The shaded region in (a) shows the expected light-hole to conduction-band energy difference compatible with the indium concentration uncertainty and the thin-sample x-ray analysis.

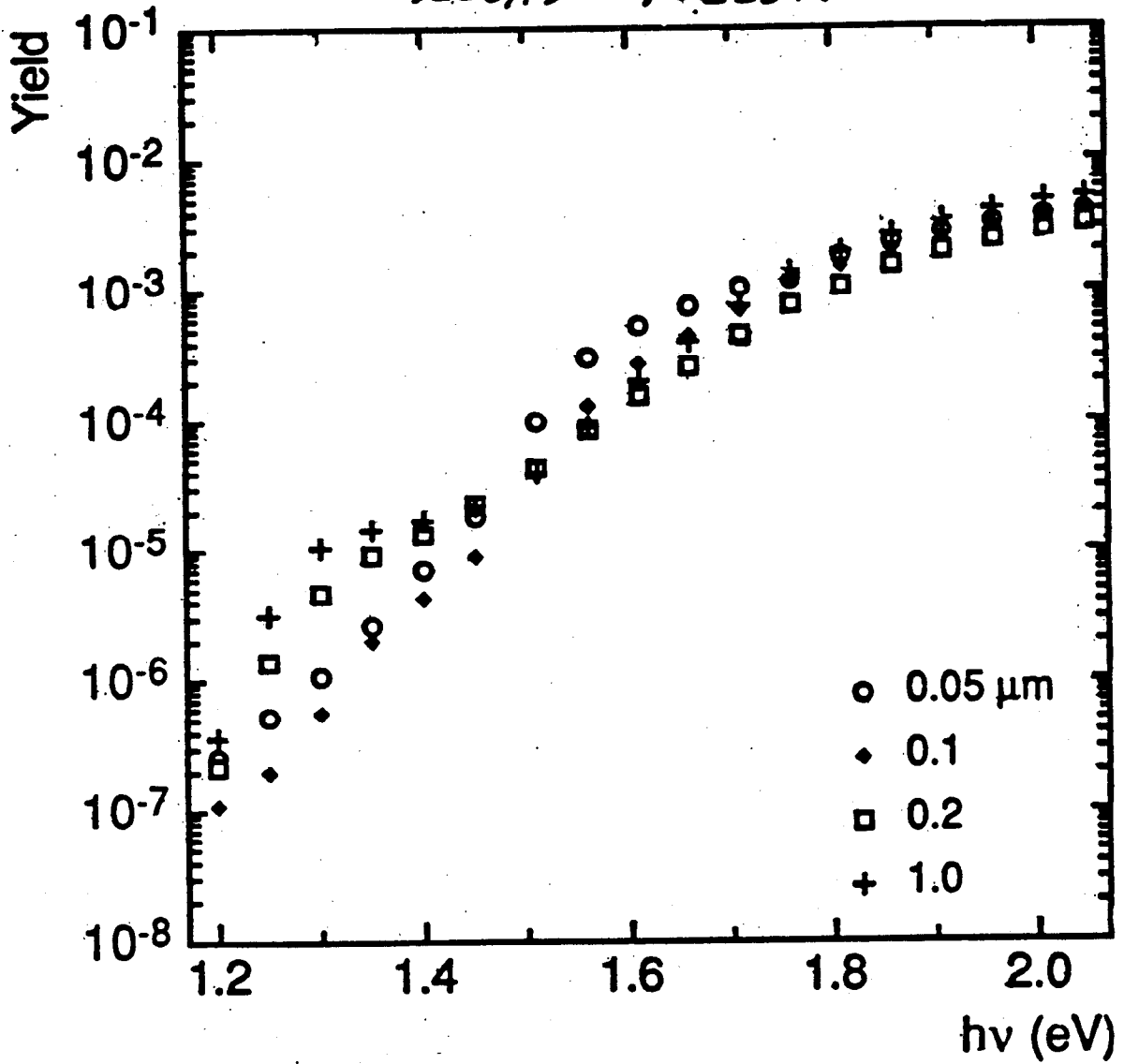
# InGaAs/GaAs

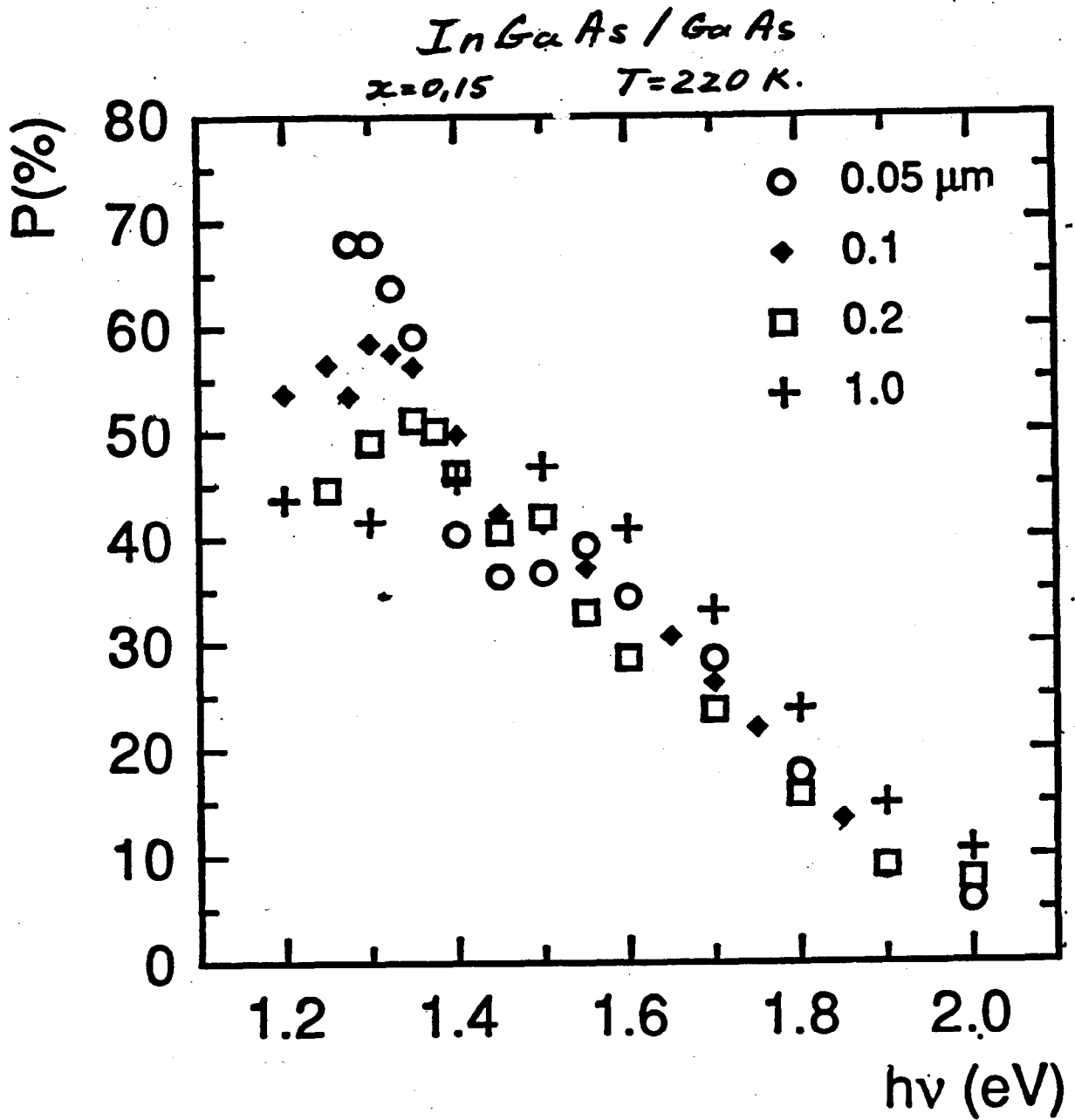
$E_g = 1.24 \text{ eV}$   $E_g = 1.42 \text{ eV}$

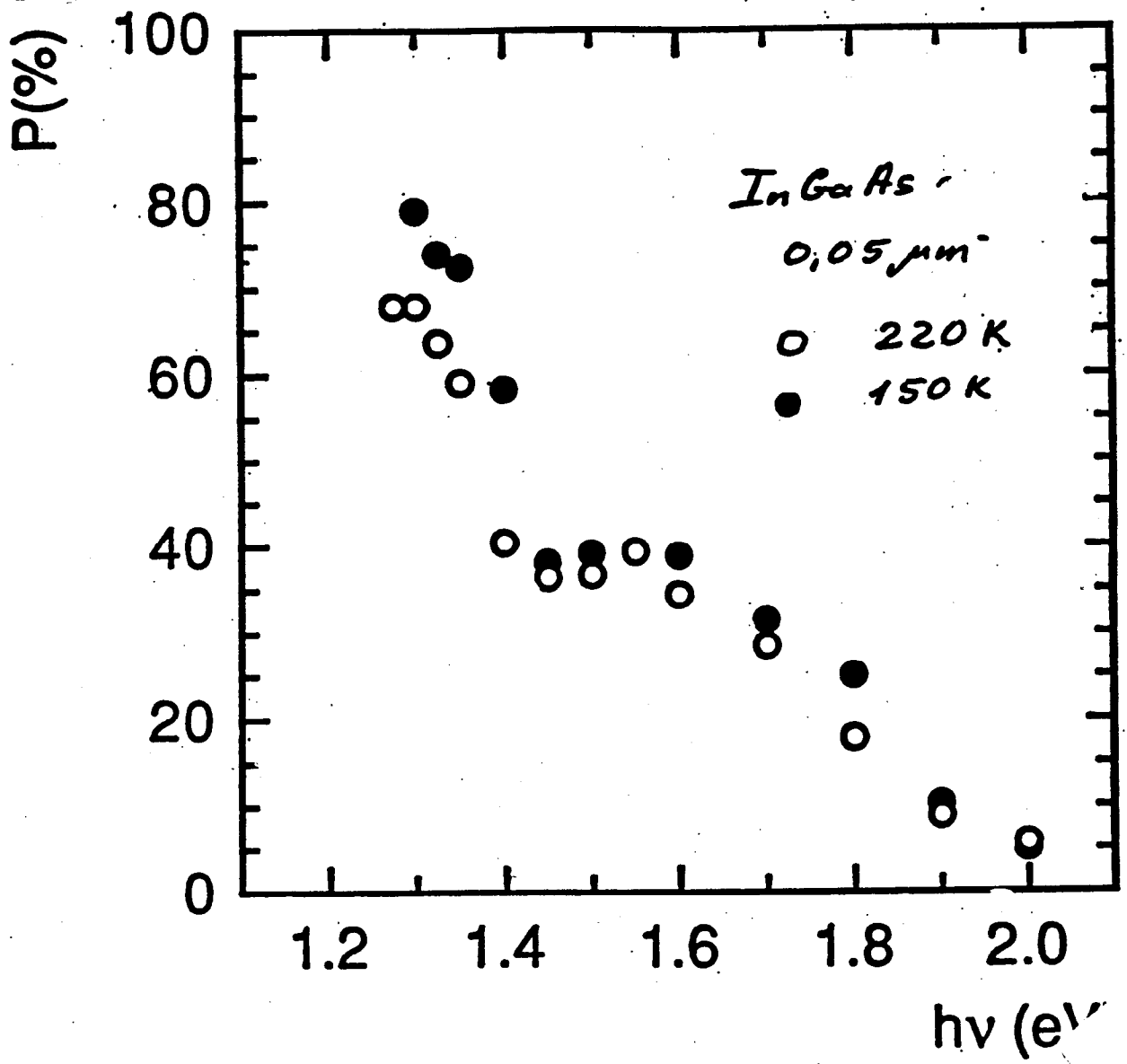


	As - cap	$d = 0.02 \mu\text{M}$
$E_g = 1.24 \text{ eV}$	In <sub>0.15</sub> Ga <sub>0.85</sub> As p-doped Mg, $p = 3 \cdot 10^{18} \text{ cm}^{-3}$	$d = \text{var}$
$E_g = 1.42 \text{ eV}$	fresh GaAs p-doped Mg, $p = 1 \cdot 10^{18} \text{ cm}^{-3}$	$d = 0.5 \mu\text{M}$
	substrate	
	GaAs(100) Zn = $1 \cdot 10^{18} \text{ cm}^{-3}$	

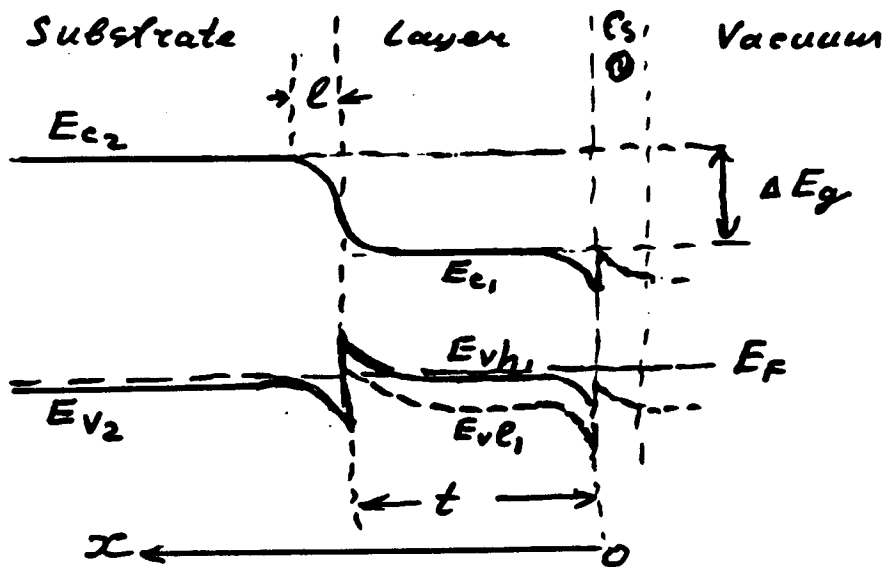
InGaAs/GaAs  
 $x=0,15$   $T=220K$







## $\gamma(h\nu)$ - "knee"



For doping:  $n_p \geq 10^{18} \text{ cm}^{-3}$  the width of the space charge regions  $l \approx \frac{\epsilon \Delta V}{2\pi e^2 n_p} \ll t$ .

In the neutrality condition we have the diffusion equation ( $n$ -el. concentr.):

$$D \frac{\partial^2 n}{\partial x^2} - \frac{n}{\tau} + I(1-R) \exp(-\alpha x) = 0 \quad (1)$$

Surface  $\longleftrightarrow$  Boundary conditions  
Interface

$$D \frac{\partial n}{\partial x} \Big|_{x=0} = (S_1 + S_{ph}) \cdot n \Big|_{x=0} \quad (2)$$

$S_1$  - the surface recombination rate

$S_{ph} \cdot n(0)$  - photoemitted current.

$$-D \frac{\partial n}{\partial x} \Big|_{x=t-e} + D \frac{\partial n}{\partial x} \Big|_{x=t+e} = S_2 \cdot n(t) \quad (3)$$

(\*) Yu. Yashin, Yu. Mamaev et al., *Sov. Phys. Techn. Phys.*, 1989, vol. 59, N 6



$S_2$  - recomb. rate at the interface

$$n(\infty) = 0$$

For  $E_{g1} < h\nu < E_{g2}$

$$n(x \rightarrow t) = 0$$

(4)

Yield:

$$Y = \frac{B(1-R)\alpha L}{1 - \alpha^2 L^2} \cdot f(\alpha L; \sigma_1; \sigma_2; t; \sigma_{ph}) \quad (5)$$

here  $\sigma_1 = \frac{S_1 \cdot L}{D}$ ;  $\sigma_2 = \frac{S_2 L}{D}$

$L$  - diffusion length;  $B$  - probability of electrons to be escaped into vacuum.

If  $\sigma_1 \gg 1$  (5)  $\Rightarrow$  eq. (6) in (\*)

If  $t \rightarrow \infty$  (5)  $\Rightarrow$  well known formula

$$Y = \frac{B(1-R)\alpha L}{1 + \alpha L} \quad (6)$$

$\Delta$  But if  $\sigma_1 \ll 1$  and  $t/L \ll 1$  then the result is strongly dependent on  $\sigma_2$  and electron injection from the substrate.

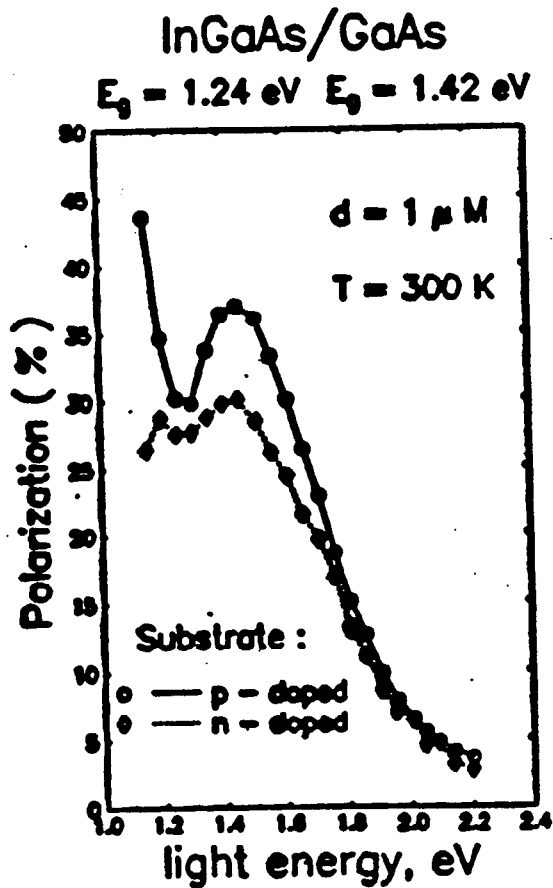
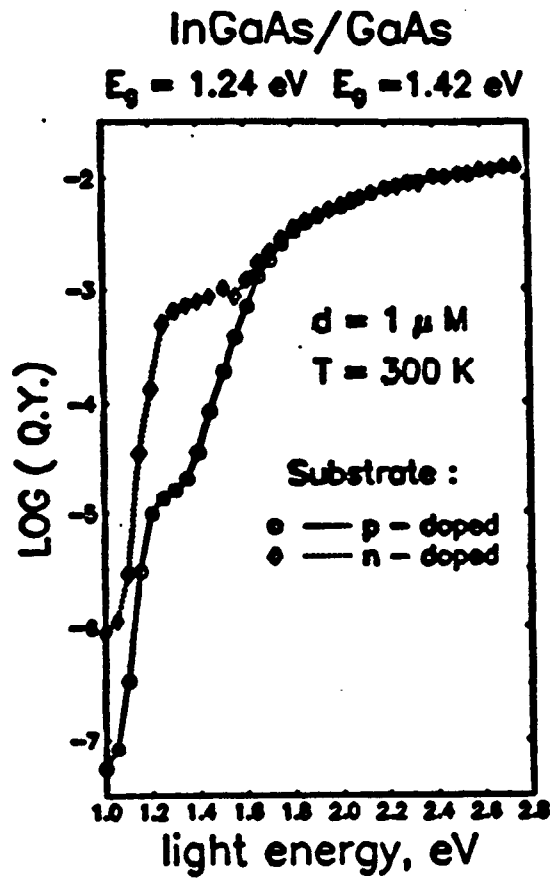
Usually for Cs-O activated surface  $S_1 \approx 10^5$  so that  $\sigma_1 \approx 0,1$  ( $D \approx 100$ ;  $L \gg 1 \mu m$ ) and for better activated surface  $S_1 \approx 10^4$  so that  $\sigma_1 \approx 10^{-2}$

(see M.G. Clark J. Phys. D, 1976, v 9, N 14, p. 2139)

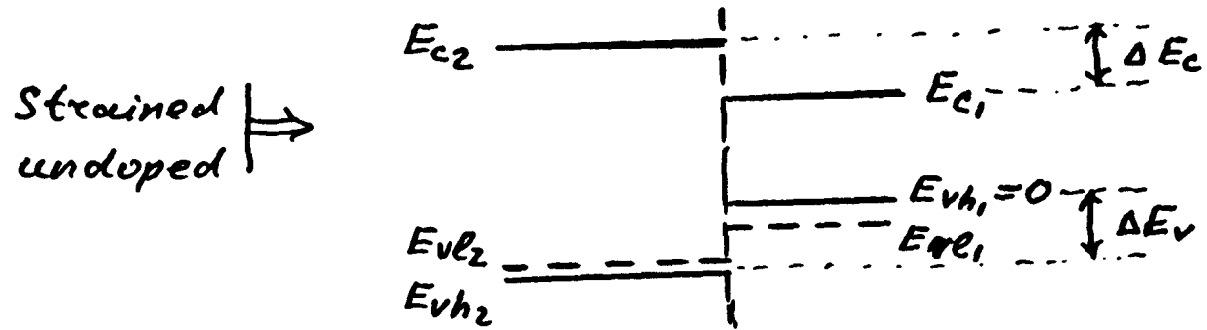
so that even for  $t/L \approx 0,5$   $\beta_2$  does influence on  $\gamma$  rather strongly.

The direct measurement of  $\beta_2$  showed  $\beta_2 \approx 0,01$  ( R.I. Dzhiboev, K. V. Kavokin : Sov. Phys. Sol. St. , 1991, v. 33, N 10 ), but it can vary on the excitation conditions.

Structure	Substate	„Knee“ $\gamma(h\nu)$
InGaAs/GaAs	p-doped n-doped	Yes - big Yes - less
GaAs/GaAsP	p-doped	Yes
AlGaInAs/AlGaAs	p-doped !indirect!	no
GaAsP <sub>0,1</sub> /GaAsP <sub>0,5</sub>	p-doped	no



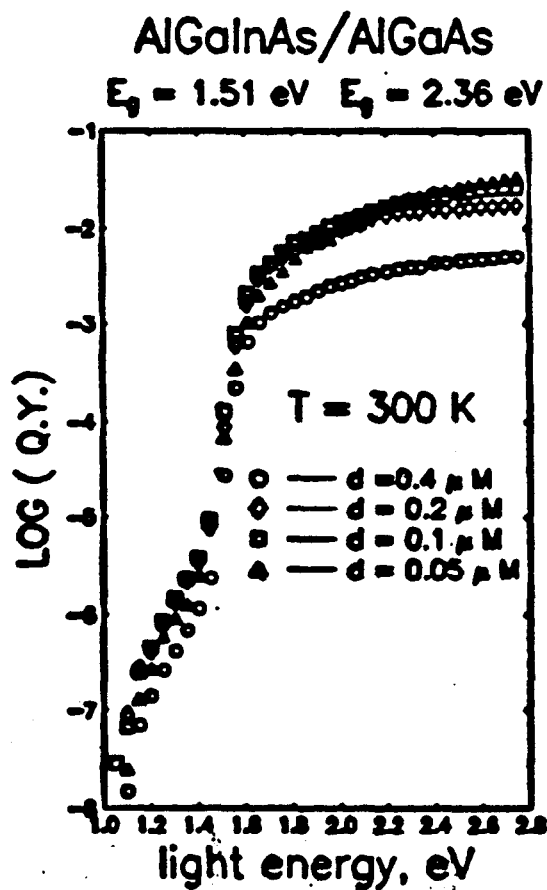
"Bandspec" program - calculation



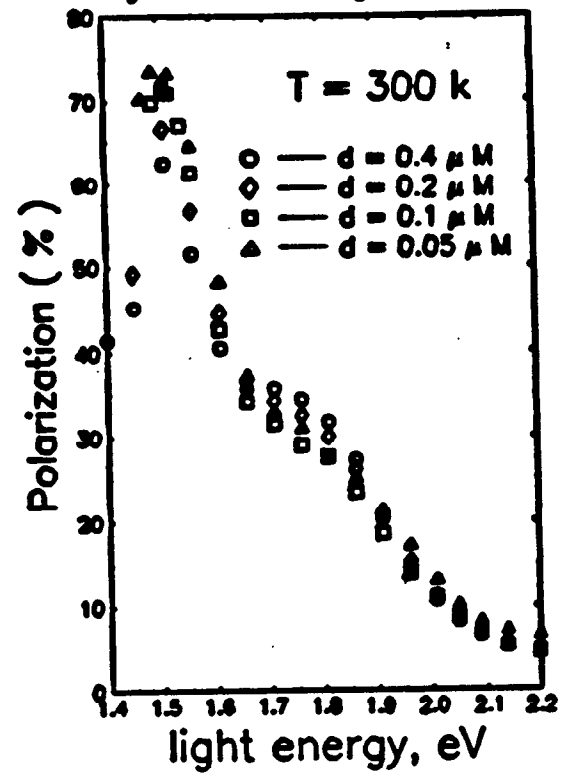
eV

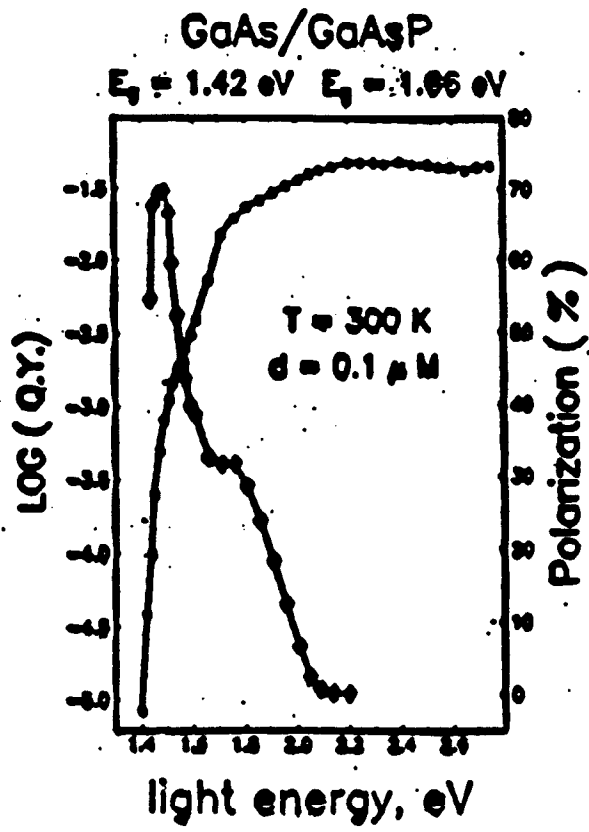
	$E_{ve1}$	$E_{vh2}$	$E_{ve2}$	$E_{c1}$	$E_{c2}$
InGaAs	-0,069	-0,056	-0,053	1,265	1,366
GaAs	-0,045	-0,128	-0,126	1,464	1,538
InGaAlAs	-0,063	-0,312	-0,31	1,605	2,153
GaAsP	-0,049	-0,144	-0,142	1,59	1,688

	As - cap	$d = 0.02\mu\text{M}$
$E_g = 1.51\text{ eV}$	$(\text{Al}_{0.5}\text{Ga}_{0.7})_{0.25}\text{In}_{0.15}\text{As}$ Mg, $p = 3 \times 10^{18}\text{ cm}^{-3}$	$d = \text{var}$
$E_g = 2.36\text{ eV}$	$\text{Al}_{0.7}\text{Ga}_{0.3}\text{As}$ Mg $p = 3 \times 10^{18}\text{ cm}^{-3}$	$d = 0.5\mu\text{M}$
	fresh $\text{Al}_{0.7}\text{Ga}_{0.3}\text{As}$ i - doped	$d = 1.5\mu\text{M}$
	substrate GaAs(100) i - doped	



AlGaInAs/GaAsAL  
 $E_g = 1.51 \text{ eV}$   $E_g = 2.36 \text{ eV}$





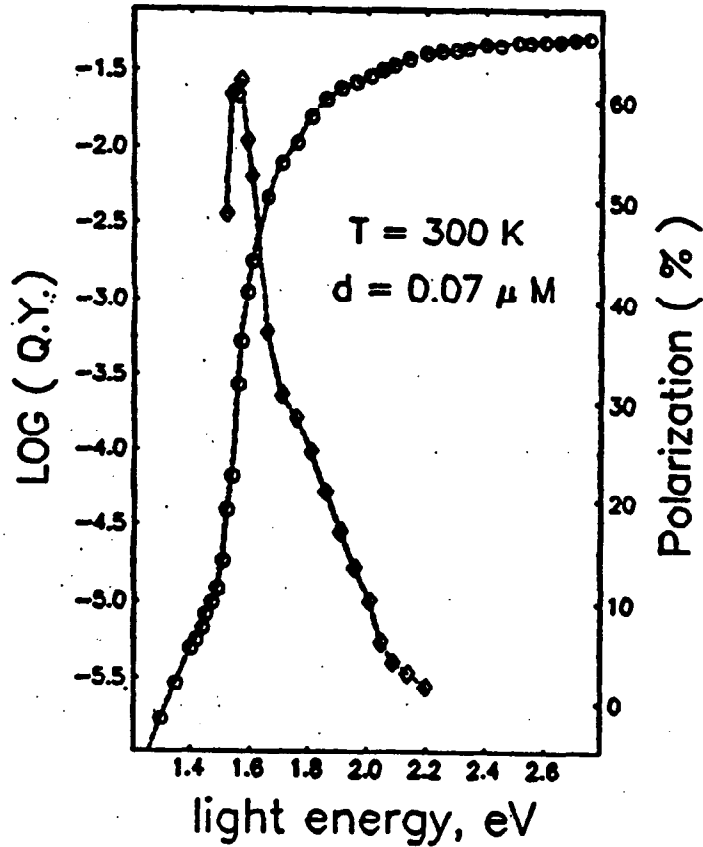
	As - cap	$d = 0.05 \mu\text{M}$
$E_g = 1.42 \text{ eV}$	GaAs Mg, $p = 3 \times 10^{18} \text{ cm}^{-3}$	$d = 0.1 \mu\text{M}$
$E_g = 1.86 \text{ eV}$	GaAs <sub>0.5</sub> P <sub>0.5</sub> Mg, $p = 3 \times 10^{18} \text{ cm}^{-3}$	$d = 1 \mu\text{M}$
$E_g = \text{var}$	GaAs <sub>1-x</sub> P <sub>x</sub> $x = \text{var}$ $p = \text{doped}$	$d = 0.3 \mu\text{M}$
	substrate GaAs(100) $p - \text{doped}$	

	As - cap	$d = 0.05 \mu\text{M}$
$E_g = 1.58 \text{ eV}$	$\text{GaAs}_{0.9}\text{P}_{0.1}$ Mg, $p = 3 \times 10^{18} \text{ cm}^{-3}$	$d = 0.07 \mu\text{M}$
$E_g = 1.85 \text{ eV}$	$\text{GaAs}_{0.55}\text{P}_{0.45}$ Mg, $p = 3 \times 10^{18} \text{ cm}^{-3}$	$d = 0.3 \mu\text{M}$
$E_g = \text{var}$	$\text{GaAs}_{1-x}\text{P}_x$ $x = \text{var}$ $p = \text{doped}$	$d = 30 \mu\text{M}$
	substrate $\text{GaAs}(100)$ $n = \text{doped}$	

another run:  $P = 72\%$ ;  $Y = 0.6\%$  at  $1.58 \text{ eV}$

### GaAsP/GaAsP

$E_{g1} = 1.58 \text{ eV}$   $E_{g2} = 1.85 \text{ eV}$





**Takashi Maruyama**  
**SLAC**

**High Polarization Photocathode R&D at SLAC**

# **High Polarization Photocathode R&D at SLAC**

**Takashi Maruyama (SLAC)**

## **Collaborators:**

**E. Garwin (SLAC)**

**T. Maruyama (SLAC)**

**R. Prepost (Wisconsin)**

**G. Zapalac (Wisconsin)**

**R. Mair (Wisconsin)**

## **OUTLINE**

- **Cathode materials for high polarization**
- **Brief summary of chalcopyrite and superlattice work**
- **Strained materials**
  - 1) **Strained InGaAs**
  - 2) **Strained GaAs**

**Summary**

# Photocathode Materials for High Polarization.

- Chalcopyrites

	$E_G$ (ev)	$\Delta$ (mev)
Cd Si As <sub>2</sub>	1.6	240
→ Zn Ge As <sub>2</sub>	1.2	60
Cd Ge P <sub>2</sub>	1.9	200
Cd Sn P <sub>2</sub>	1.3	100

- Super lattices

	$\Delta$ (mev)
GaAs - AlGaAs	~40
→ (GaAs) <sub>1</sub> - (AlAs) <sub>1</sub>	~30

- Strained materials

Mechanical strain  $\leq 25$ meV

Thermal expansion

GaAs on Si  $\leq 20$

→ Lattice mismatch

InGaAs on GaAs ~ 60

GaAs on GaAsP

# United States Patent (119)

Pierce et al.

(11) 3,968,376

(45) July 6, 1976

## [54] SOURCE OF SPIN POLARIZED ELECTRONS

[76] Inventors: Daniel Thornton Pierce, 10120 Little Pond Place, Gaithersburg, Md.; Felix Andrea Meier, 6 Kastanienweg, Kilchberg, Zurich; Hans-Christoph Siegmann, 21 Burstwiesenstrasse, Greifensee, Zurich, both of Switzerland

[22] Filed: June 3, 1975

[21] Appl. No.: 581,837

## [30] Foreign Application Priority Data

Jan. 13, 1975 Switzerland..... 597/75

[52] U.S. Cl. .... 250/493; 313/94

[51] Int. Cl.<sup>2</sup> ..... G21G 4/00; H01J 39/00

[58] Field of Search ..... 250/396, 493, 225, 310, 250/526; 313/94

## [56] References Cited UNITED STATES PATENTS

3,672,992 6/1972 Schofer ..... 313/94

Primary Examiner—Alfred E. Smith  
Assistant Examiner—T. N. Grigsby

## [57] ABSTRACT

The invention concerns a method of producing intense beams of polarized free electrons in which a semiconductor with a spin orbit split valence band and negative electron affinity is used as a photocathode and irradiated with circularly polarized light.

9 Claims, 4 Drawing Figures

Only a 50% electron polarization is attained by using GaAs because the heavy and light hole bands are degenerate at the  $\Gamma$  point. This degeneracy is lifted as soon as the cubic crystal structure is distorted by stress which can be caused mechanically or by the addition of foreign atoms. Also, the chalcopyrite compounds, as for example ZnSiAs<sub>2</sub> or CdSiAs<sub>2</sub>, show no degeneracy at the  $\Gamma$  point. Even higher electron polarization can be attained under these circumstances.

8. A source of spin polarized electrons as in claim 1, wherein the degeneracy between the heavy and light hole bands at the  $\Gamma$  point in a cubic crystal structure is removed by stress.

9. A source of spin polarized electrons as in claim 1 comprising a semiconductor of the chalcopyrite type as photocathode, said semiconductor having no degeneracy of the heavy and light hole bands at the  $\Gamma$  point.

• • • • •

• **Chalcopyrites**

**Collaborated with C. Sinclair (CEBAF)**

**Samples grown by MOCVD at Research Triangle Institute**

**Samples:**

**ZnGeAs<sub>2</sub>**  
**ZnGe(As<sub>1-y</sub>Py)<sub>2</sub>**  
**Zn(Ge<sub>1-x</sub>Si<sub>x</sub>)As<sub>2</sub>**

**Results:**

- 1) QE  $\leq 10^{-5}$  in the wavelength region where high polarization is expected.**
- 2) QE vs.  $\lambda \Rightarrow$  NEA surface is questionable**
- 3) No polarization measurements**

• **Superlattice**

**Collaborated with S. Smith/J. Walker (UC-Berkeley)**

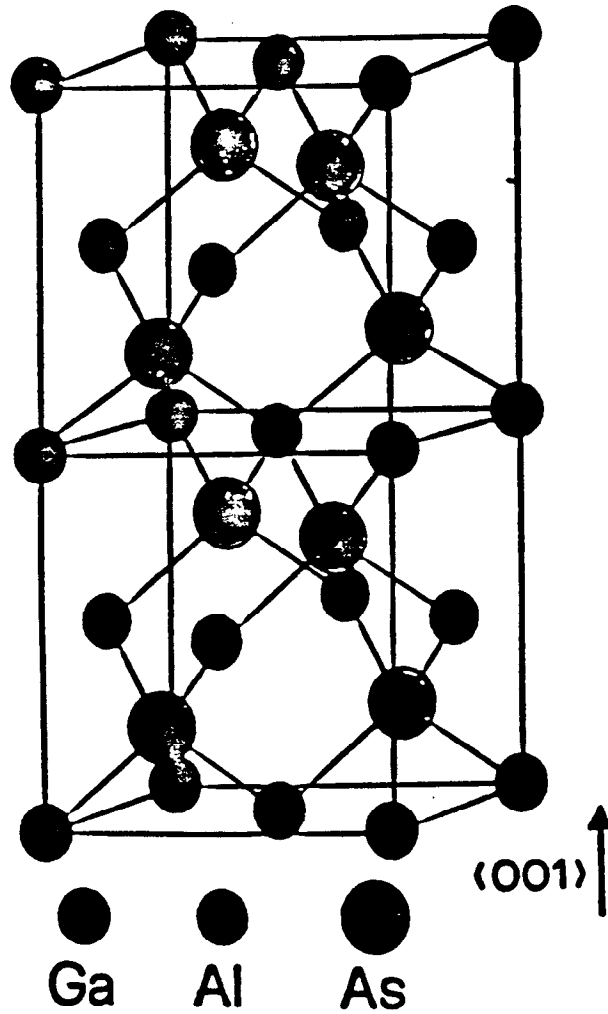
**Samples grown by MBE at UC-Berkeley**

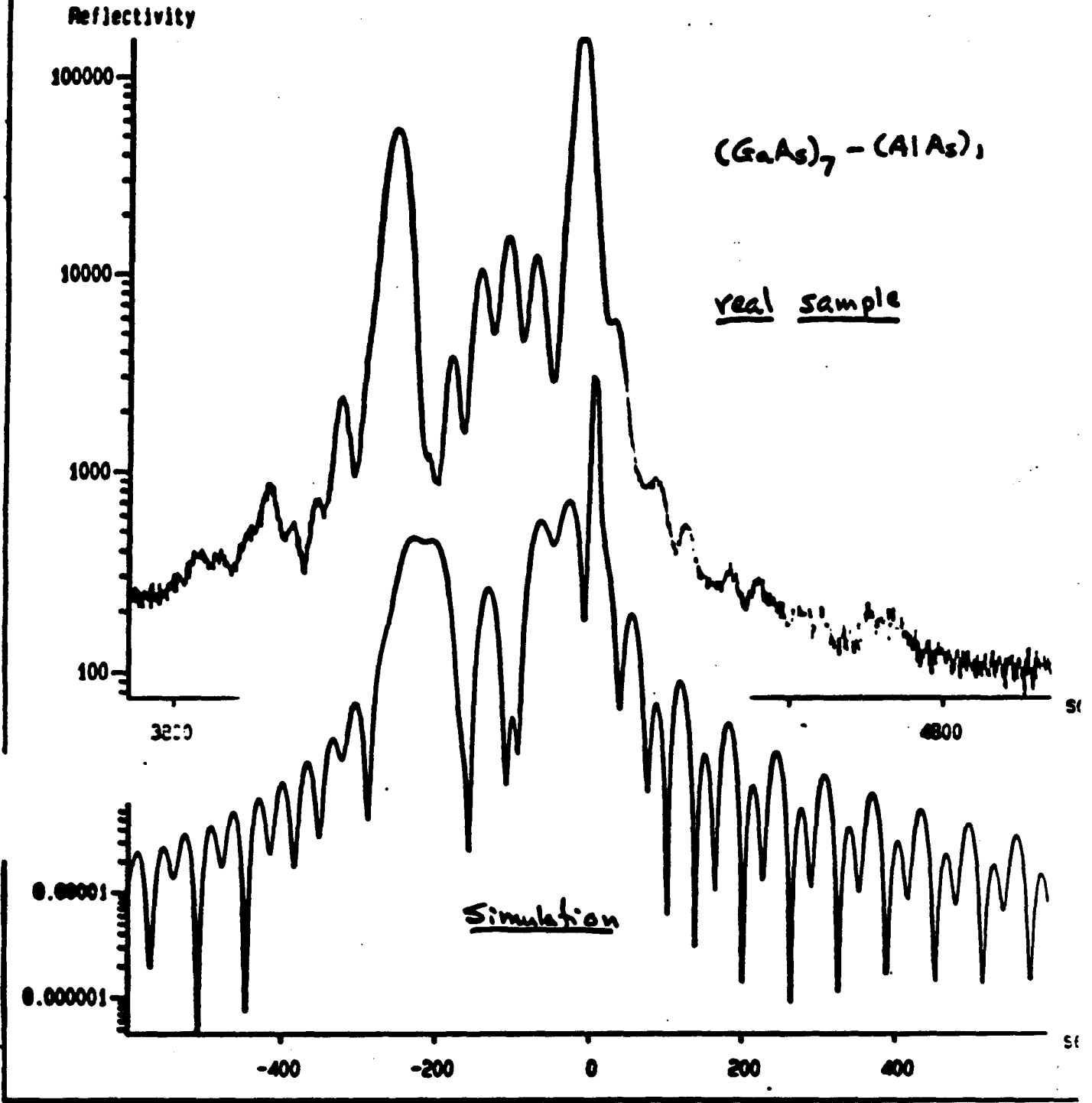
**Samples:**

**(GaAs)<sub>7</sub>-(AlAs)<sub>1</sub>**  
**(GaAs)<sub>2</sub>-(AlAs)<sub>1</sub>**  
**(GaAs)<sub>1</sub>-(AlAs)<sub>1</sub>**



Ciccacci et al. *Solid State Com.*  
62, 1 (1987)



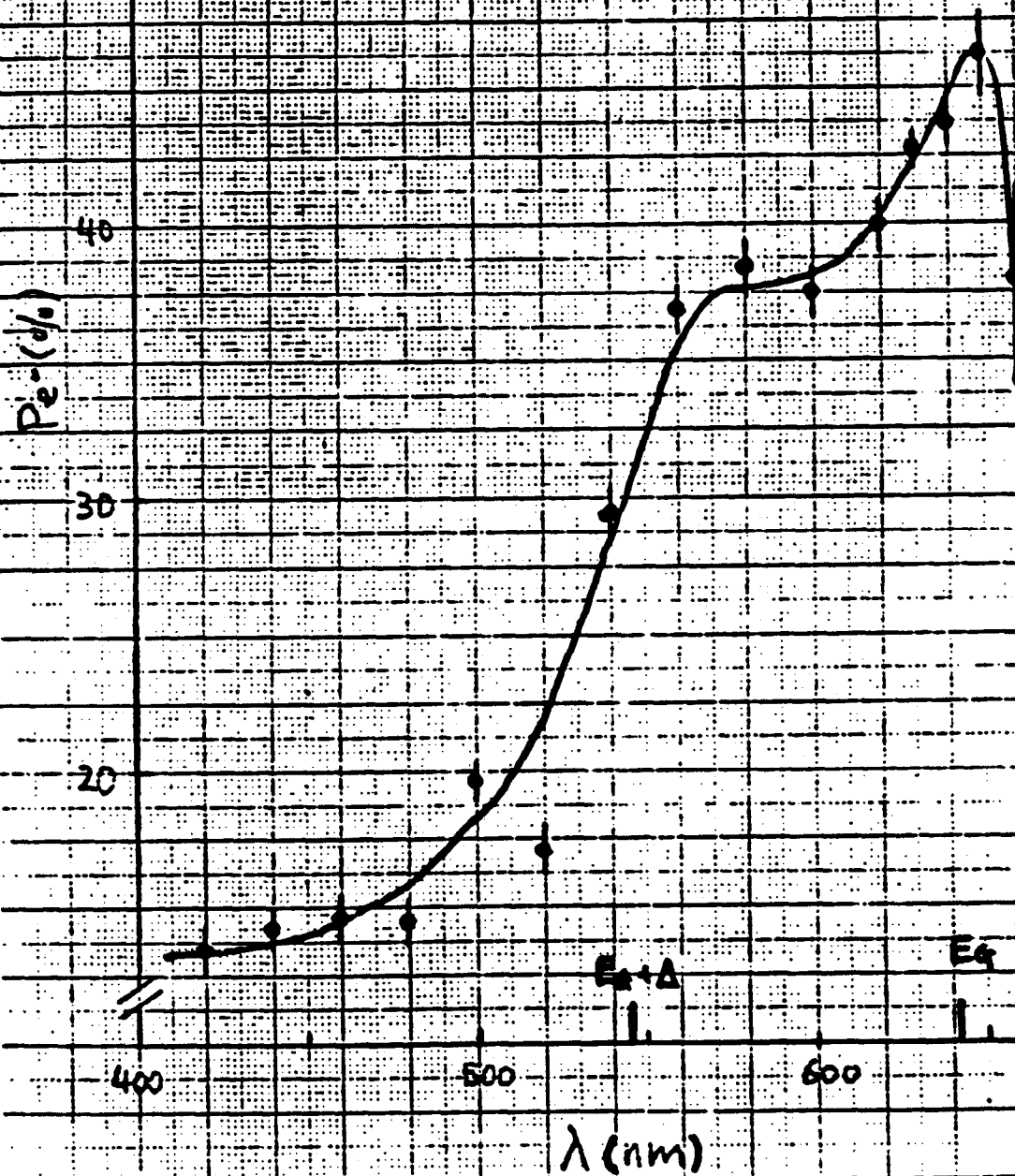




# Electron Polarization vs. $\lambda$

(GaAs), (AlAs)<sub>1</sub>

1 hour after activation



## Strained Cathodes

- Strain effects on band structure

$$E^{C,HH} = E_0 + \delta E_H - \delta E_S$$

$$E^{C,LH} = E_0 + \delta E_H + \delta E_S + O(\delta E_S^2/\Delta_0)$$

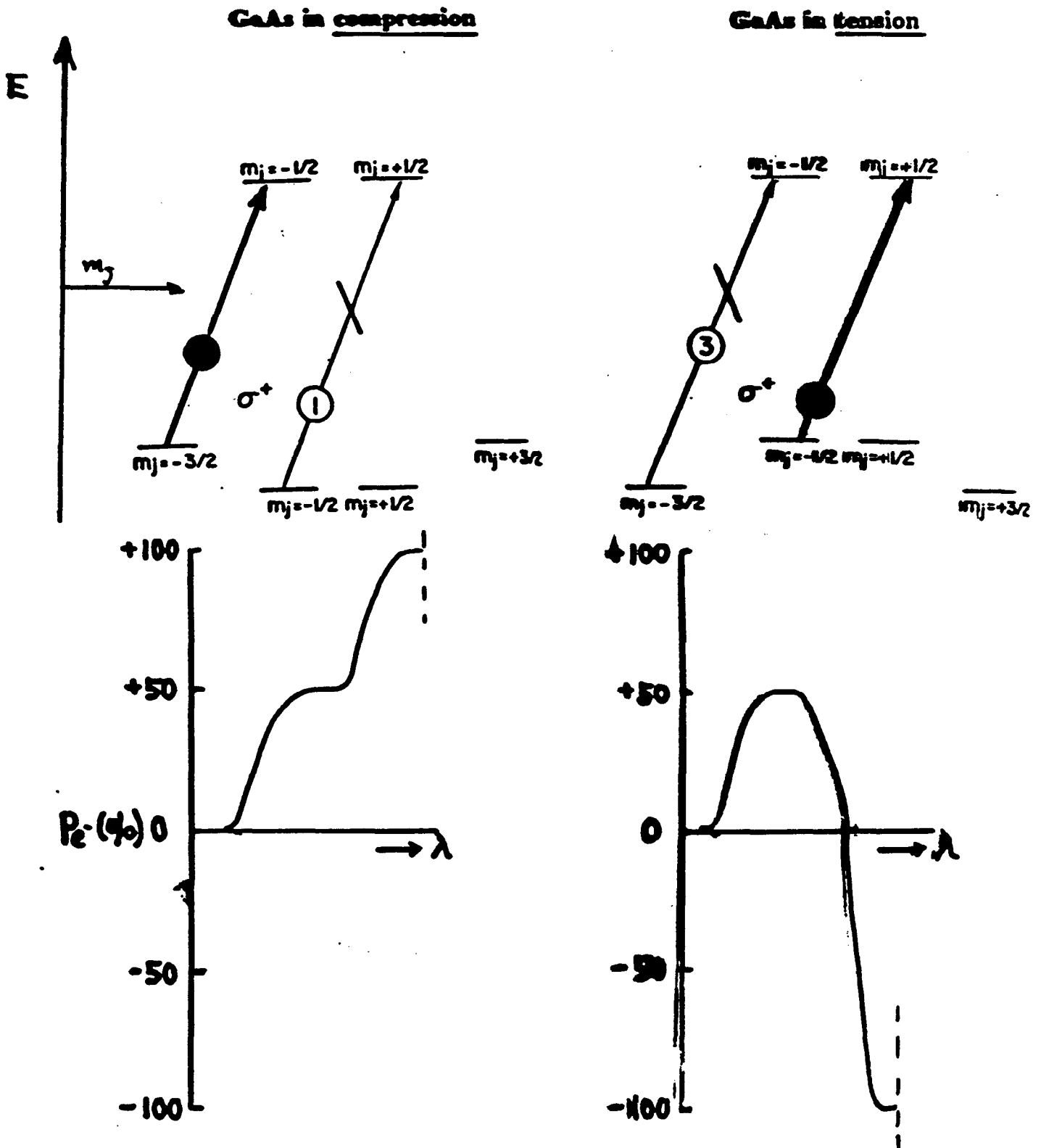
$$\delta E_H = 2a \left[ \frac{C_{11} - C_{12}}{C_{11}} \right] \cdot \epsilon$$

$$\delta E_S = b \left[ \frac{C_{11} + 2C_{12}}{C_{11}} \right] \cdot \epsilon$$

$\epsilon$ : biaxial strain  
( $< 0$  for compressive strain)

- ⇒
- i) Heavy-hole and light-hole band-splitting
  - ii) Band gap increases for compressive strain.

# Valence Band Splitting of Strained GaAs



9/1/87 Talk with Roger Rortz

As low

P high resistivity

Cd Ge As<sub>2</sub>

Cd Ge P<sub>2</sub>

Cd Sn As<sub>2</sub>

Ag Ga Se<sub>2</sub>

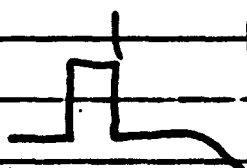
Ag Ga S<sub>2</sub> defect chalcopyrite

• Jim Harris

0.2, 0.4 μm

MBE

In, Al, Ga



As comes off @ 350°C

400°C ~ 1 hour

$$1-2 \times 10^5 \text{ A/cm}^2$$

$$5 \times 10^{18} / \text{cm}^3 \text{ doping}$$

In Ga As stressed crystal.

degeneracy removed.

smooth

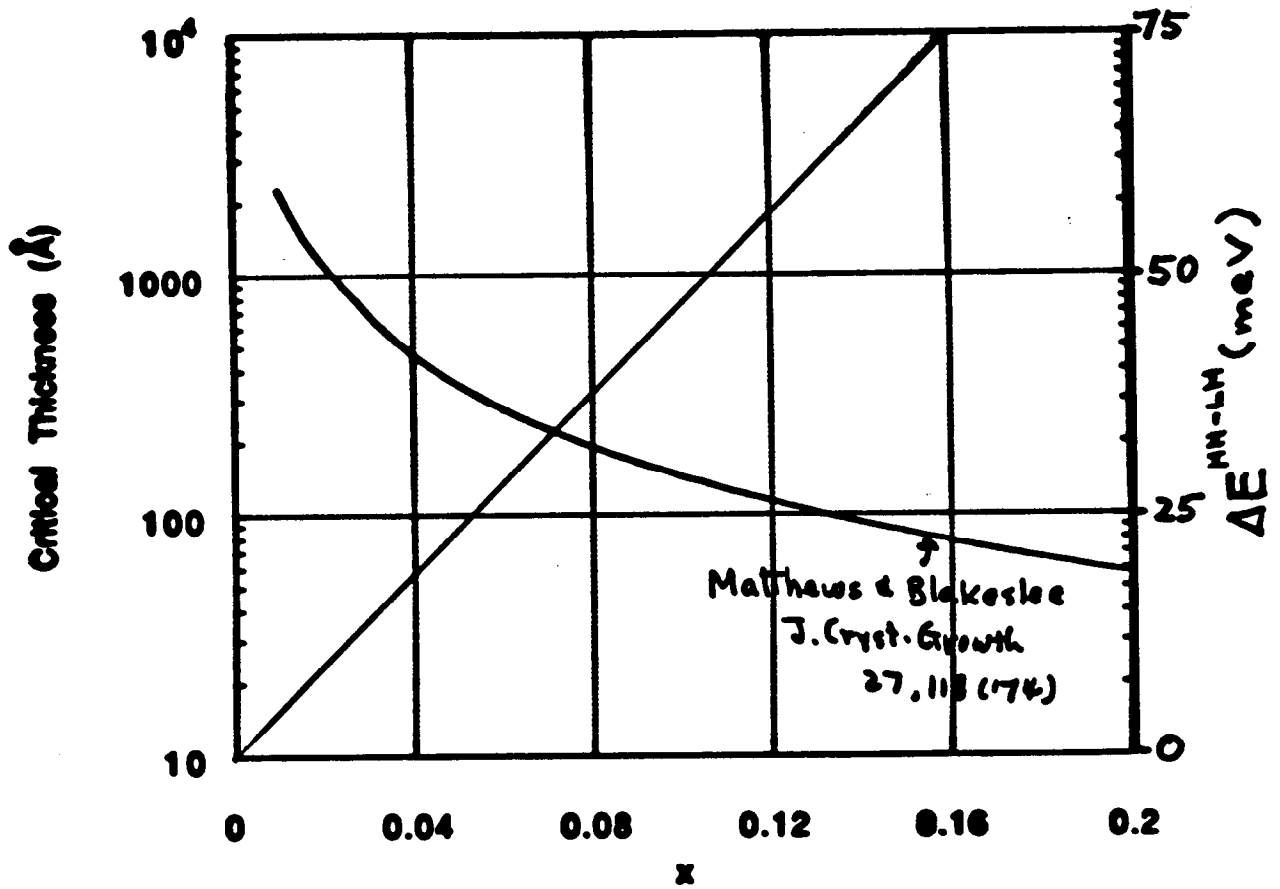
lattice ~ 1000 Å 10% In-mixture

HARRIS@SIERRA

**Pierce and Celotta in "Optical Orientation," P. 270:  
(1984)**

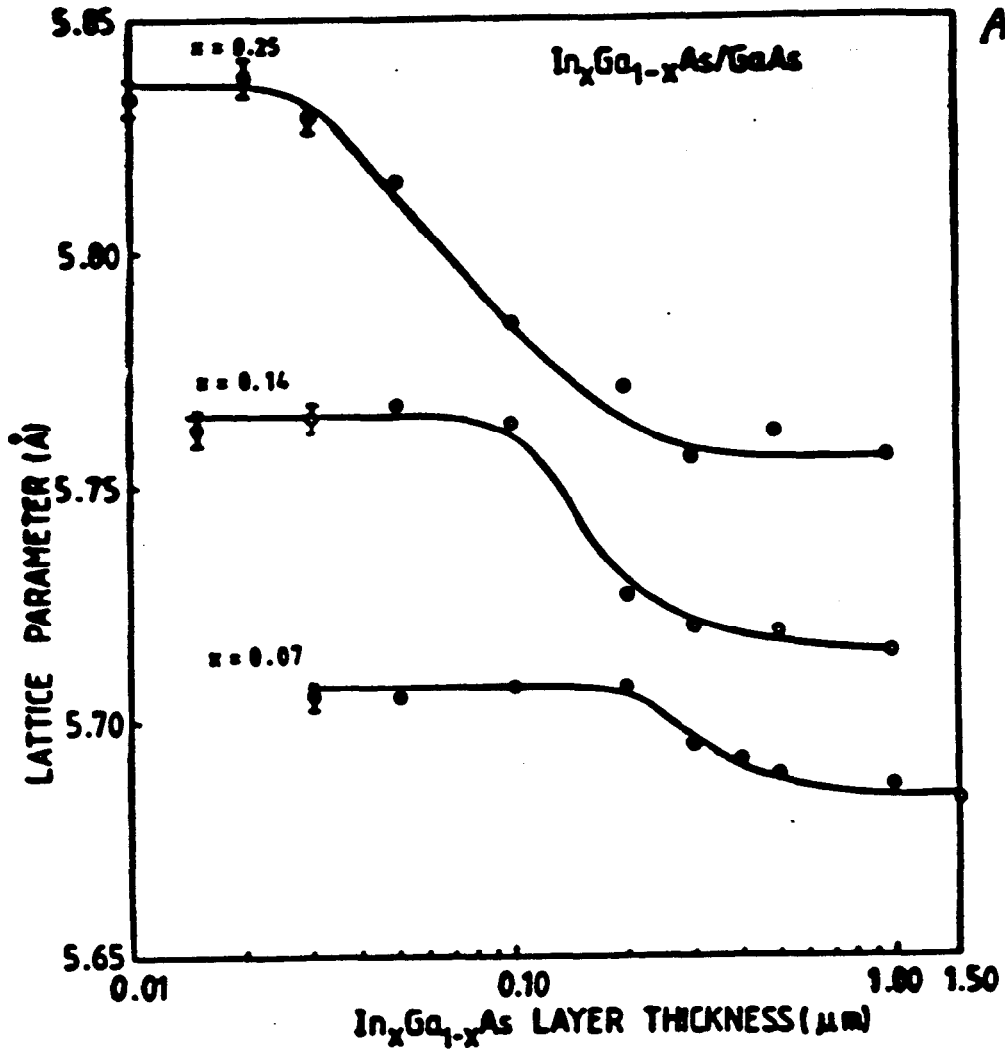
**A possible exception to this is when the stress results naturally in the epitaxial growth of a GaAs layer on a substrate for which there is a lattice mismatch. There is a resulting compression or expansion of the GaAs lattice constants parallel to the interface and a corresponding expansion or compression of the lattice perpendicular to the interface, leading to a tensile or compressive uniaxial strain respectively. Strained layers with a mismatch of 1.5 to 2.5% can be grown with thicknesses up to a few hundred Angstroms.**

### Critical Thickness vs. $x$ $\text{In}_x\text{Ga}_{1-x}\text{As}$



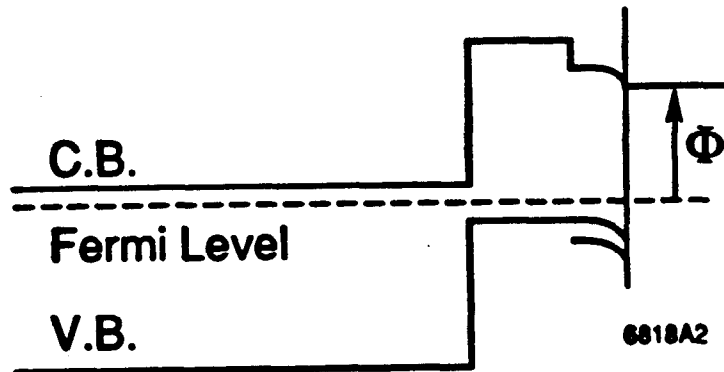
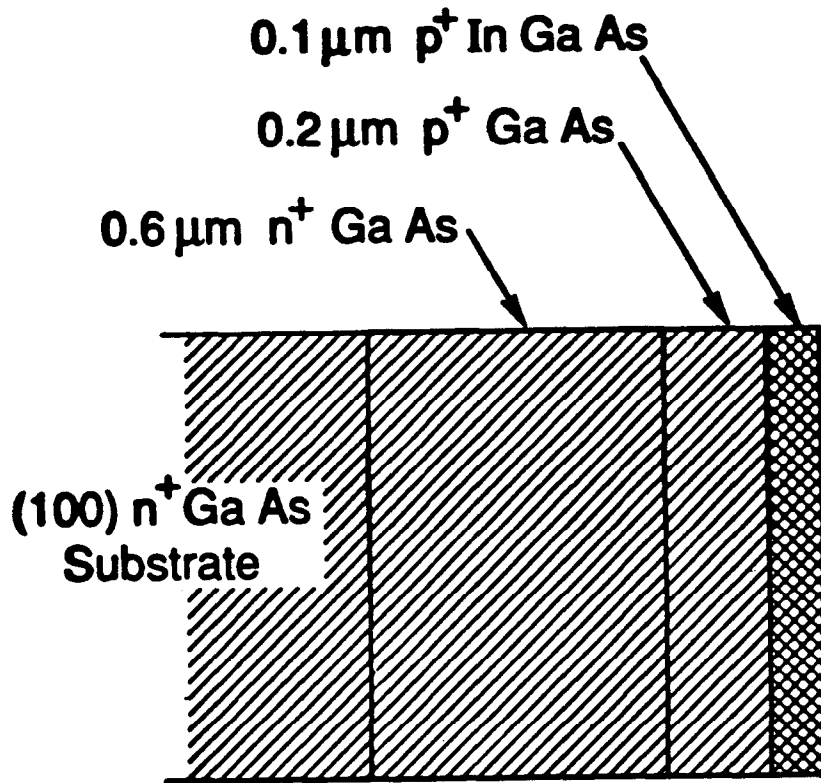
Orders & Usher

APL 50,980('87)



# Strained InGaAs Grown on GaAs Lattice-mismatched Heterostructure

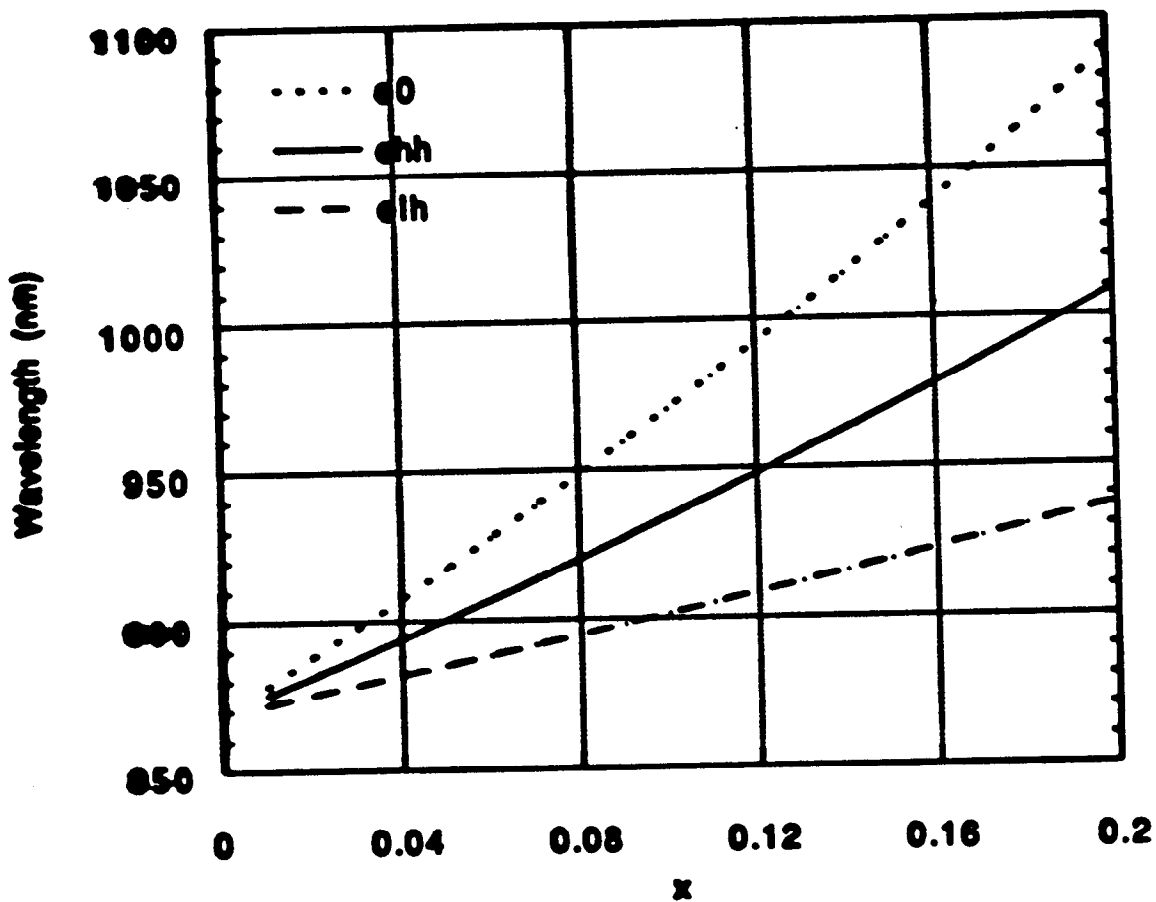
PRL 66 2376 ('91)



Samples grown by smith/walker (UCB)

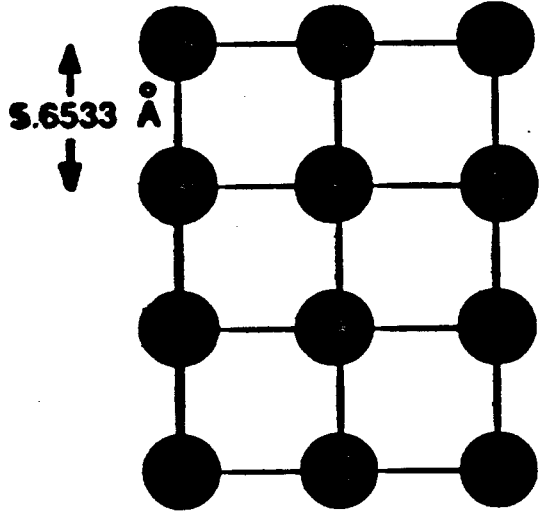


### InGaAs on GaAs

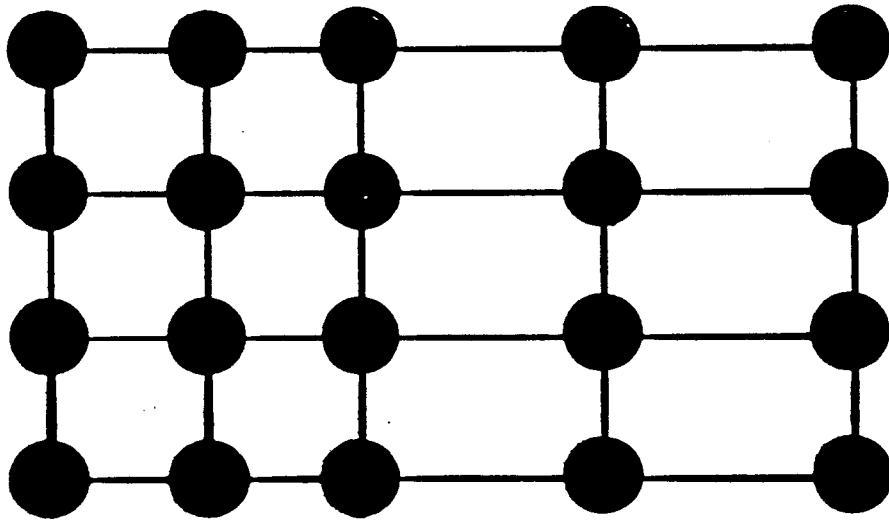
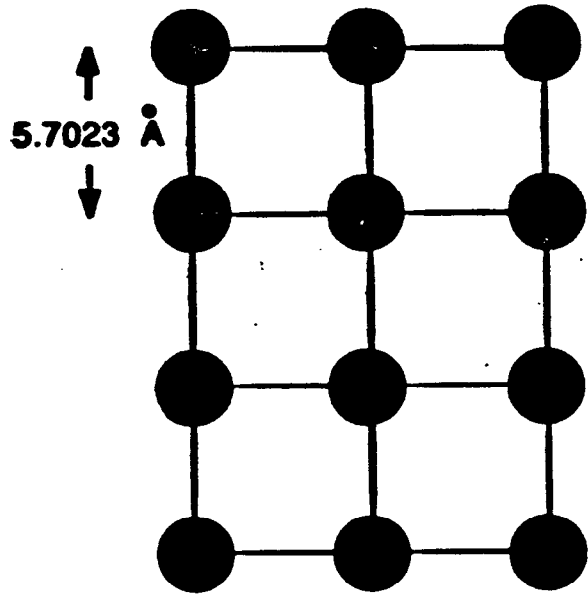


$$\left( \begin{array}{l} E_{C,HH} = E_0 + \delta H_H - \delta E_S \\ E_{C,LH} = E_0 + \delta H_H + \delta E_S \end{array} \right.$$

GaAs



InGaAs



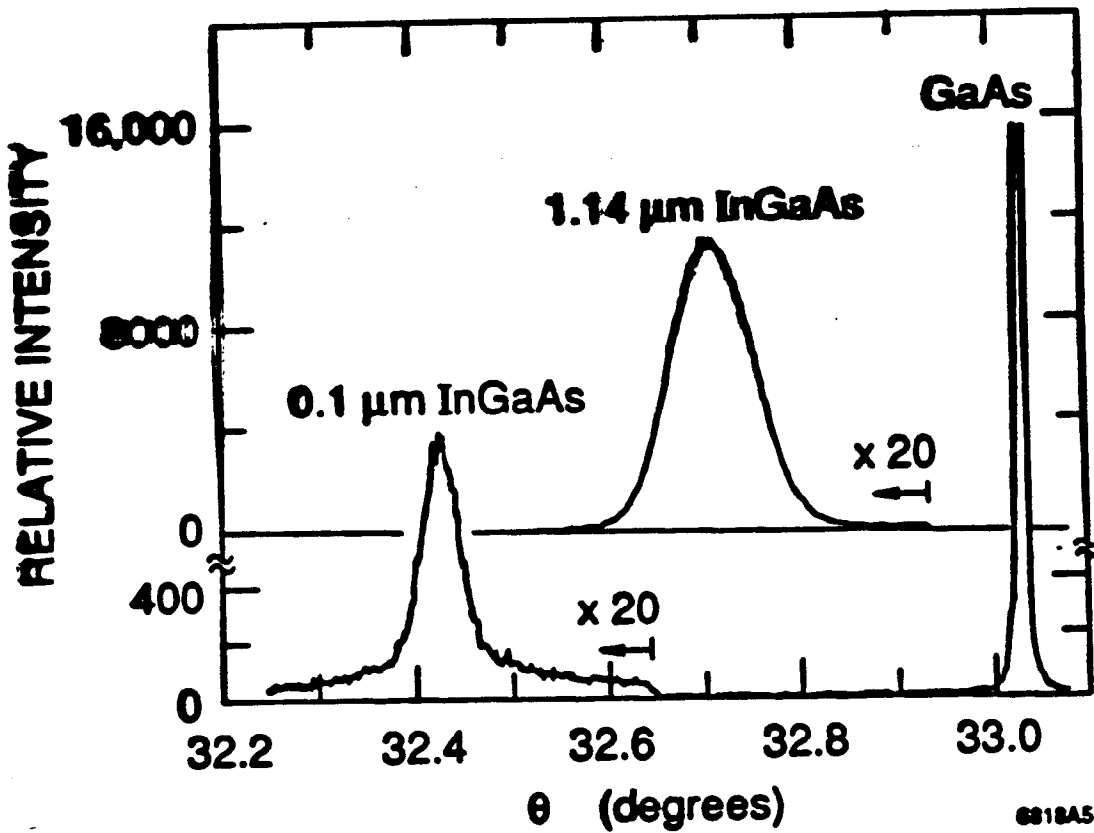
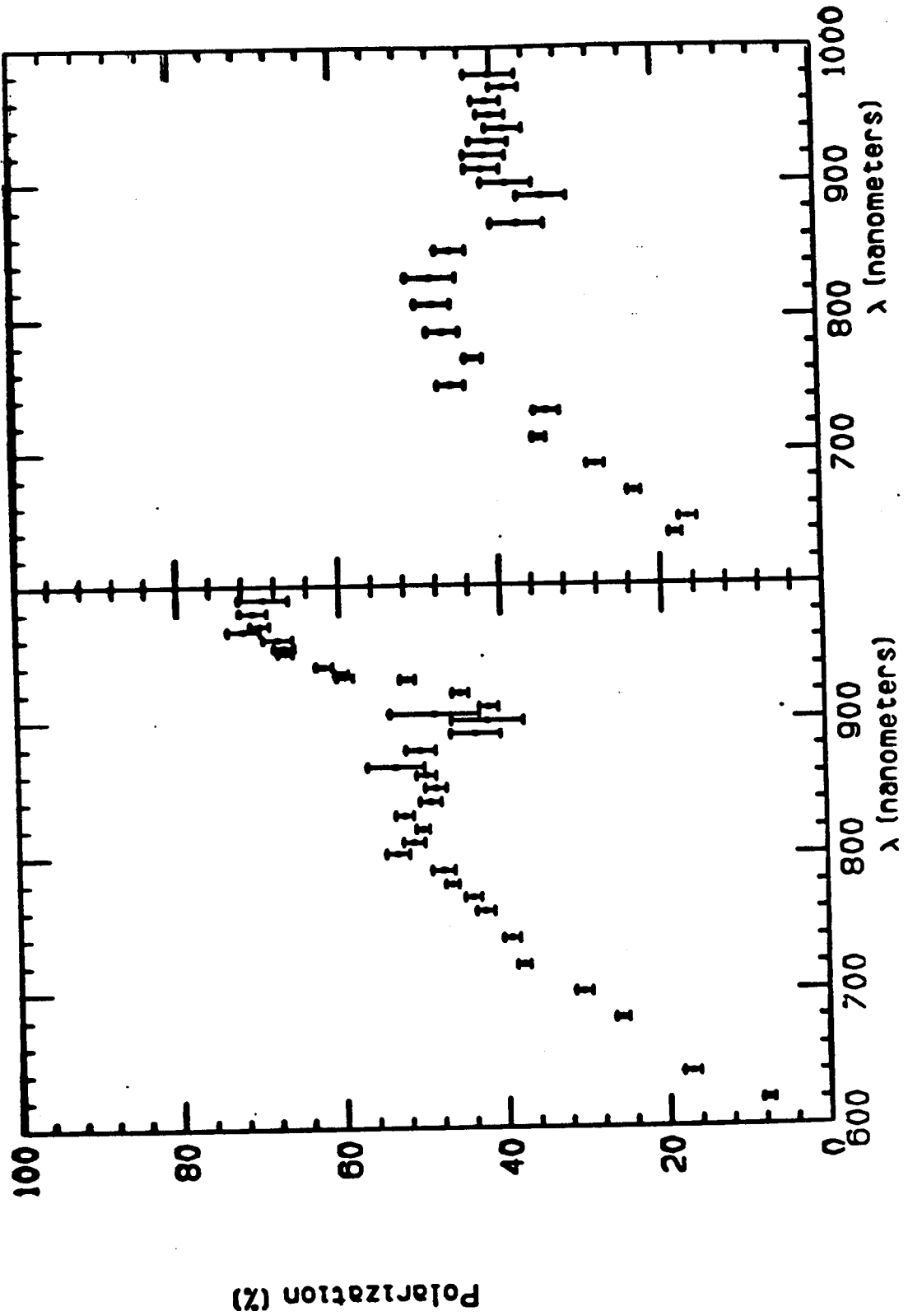


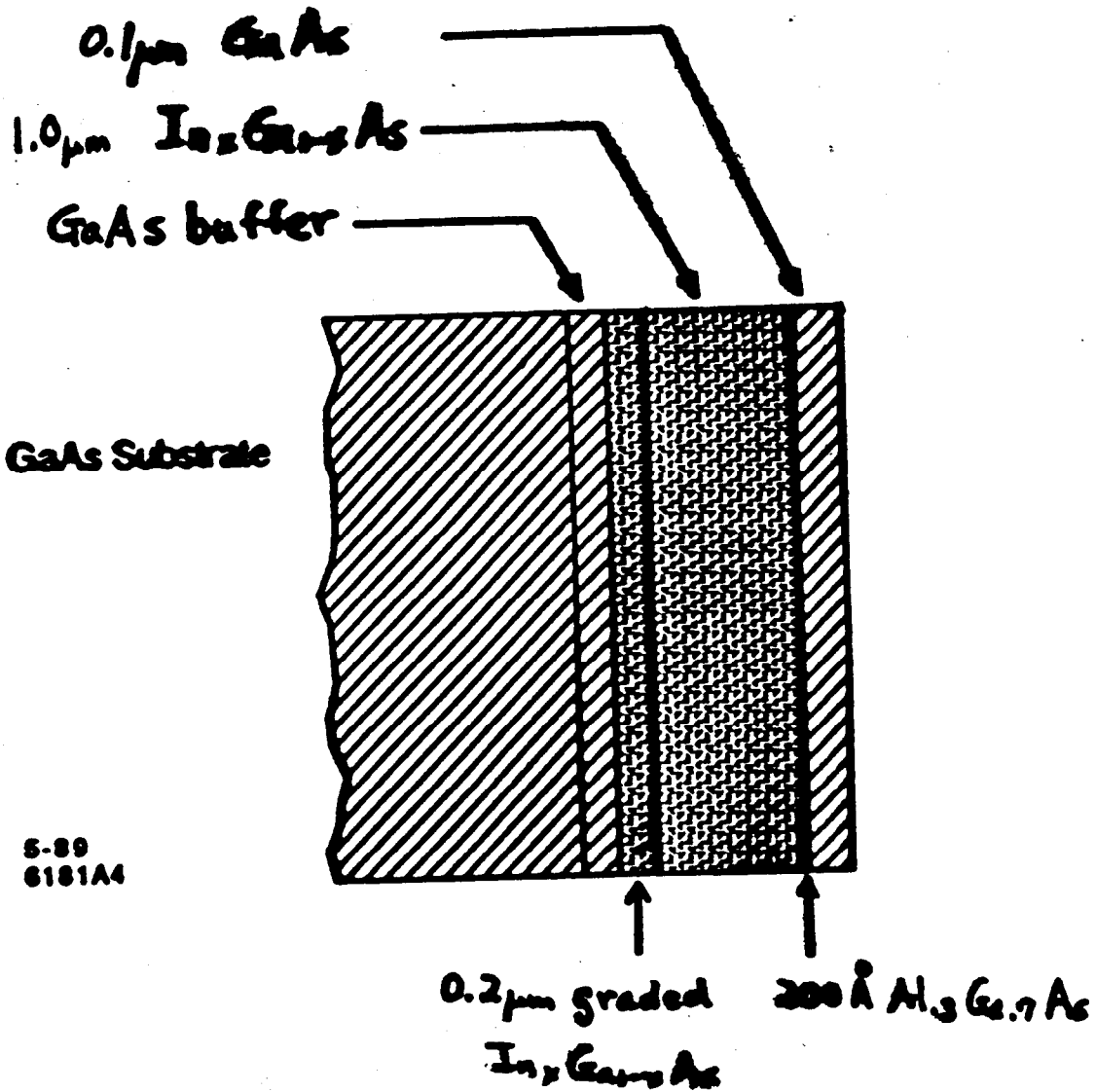
Fig. 1

$$\sin \theta = \frac{n\lambda}{2d}$$

0.10 Micron Sample      1.14 Micron Sample



# GaAs on $\text{In}_x\text{Ga}_{1-x}\text{As}$



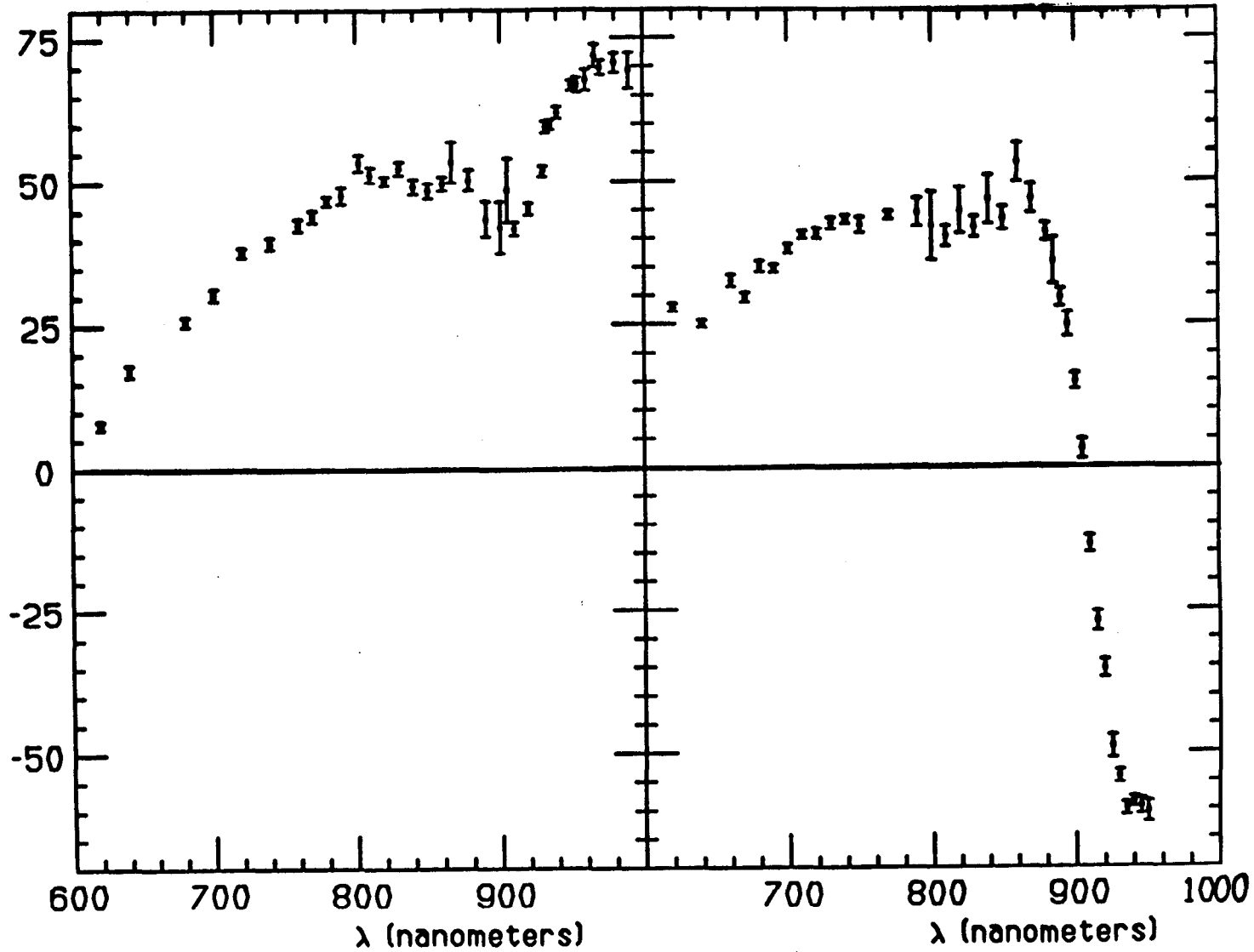
1991

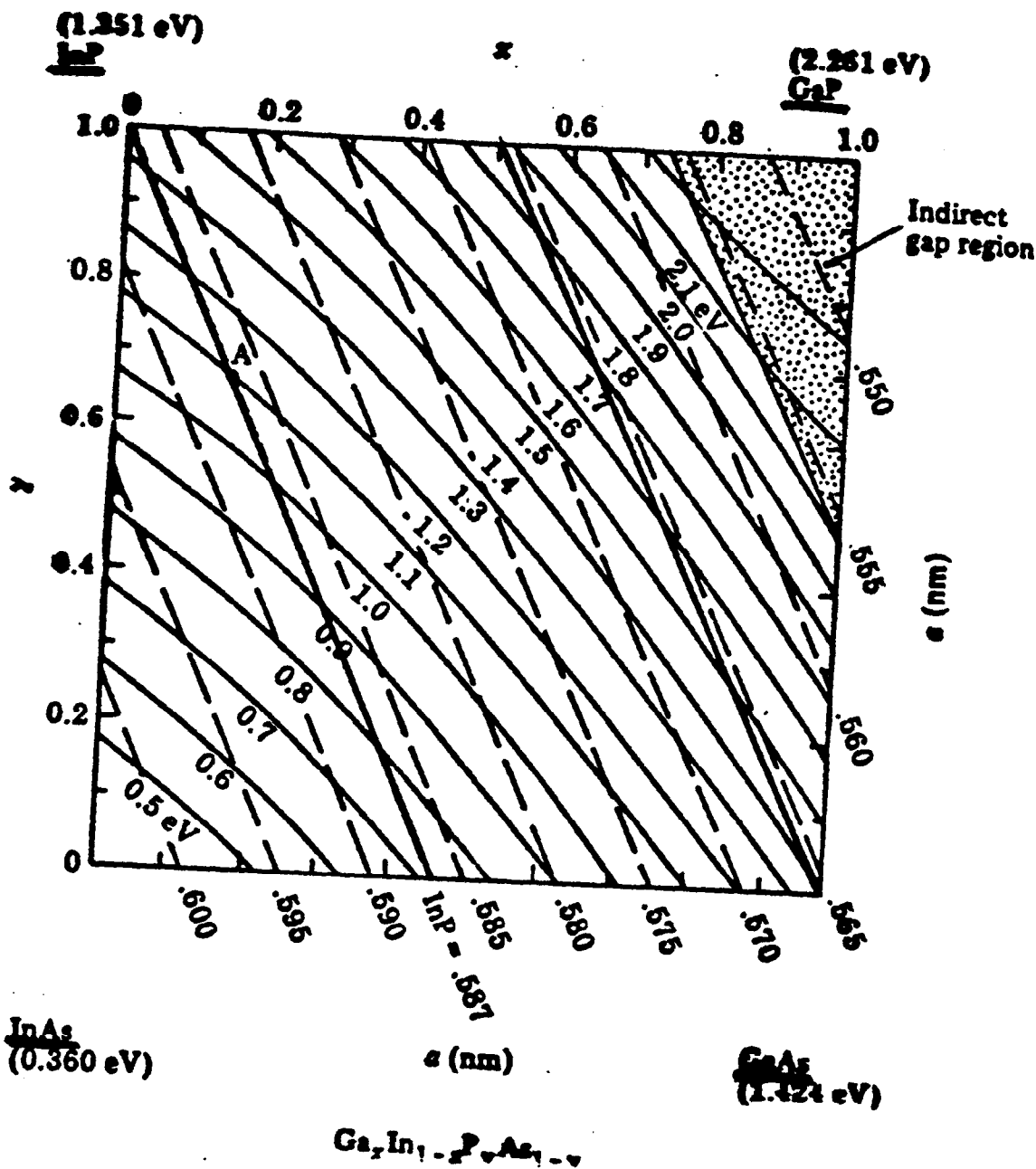
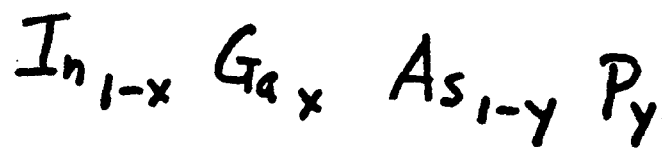
SAC/WISCONSIN  
UC Berkeley

InGaAs (Compression)

GaAs (Tension)

Polarization (%)





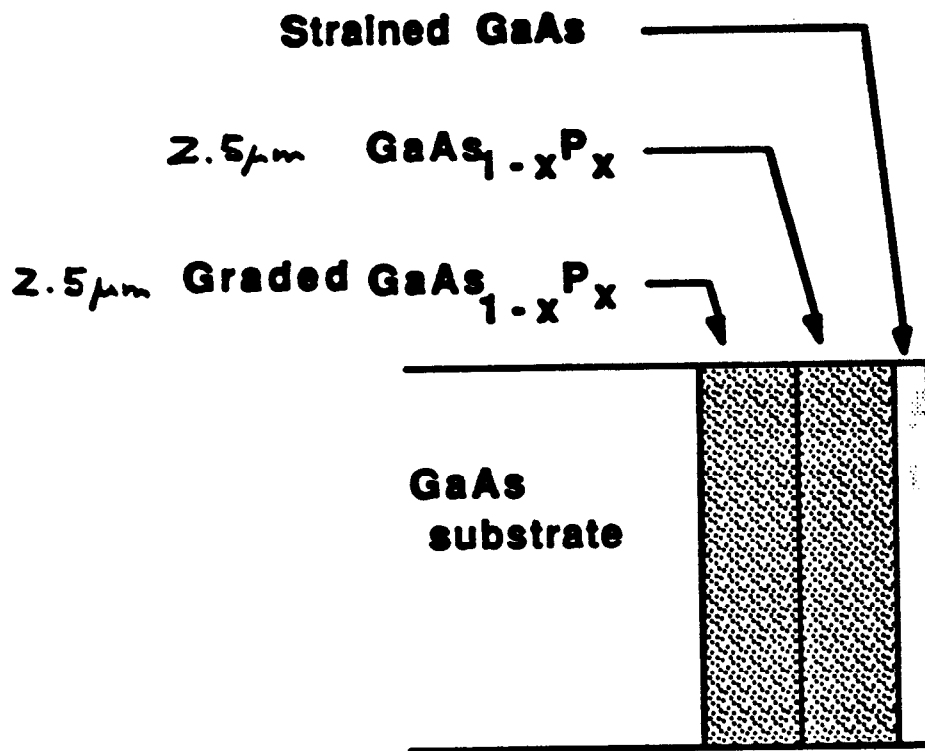
### Strained photocathodes:

	$E_g$ (eV)	MBE
$\text{In}_{1-z}\text{Ga}_z\text{As}$ on GaAs	1.2	y
$\text{In}_{1-z}\text{Ga}_z\text{P}$ on GaAs	1.7	y
GaAs on $\text{In}_{1-z}\text{Ga}_z\text{P}$	1.42	y
GaAs on $\text{GaAs}_{1-y}\text{P}_y$	1.42	
InP on $\text{In}_{1-x}\text{Ga}_x\text{P}$	1.35	y
InP on $\text{In}_{1-x}\text{Ga}_x\text{As}$	1.35	y



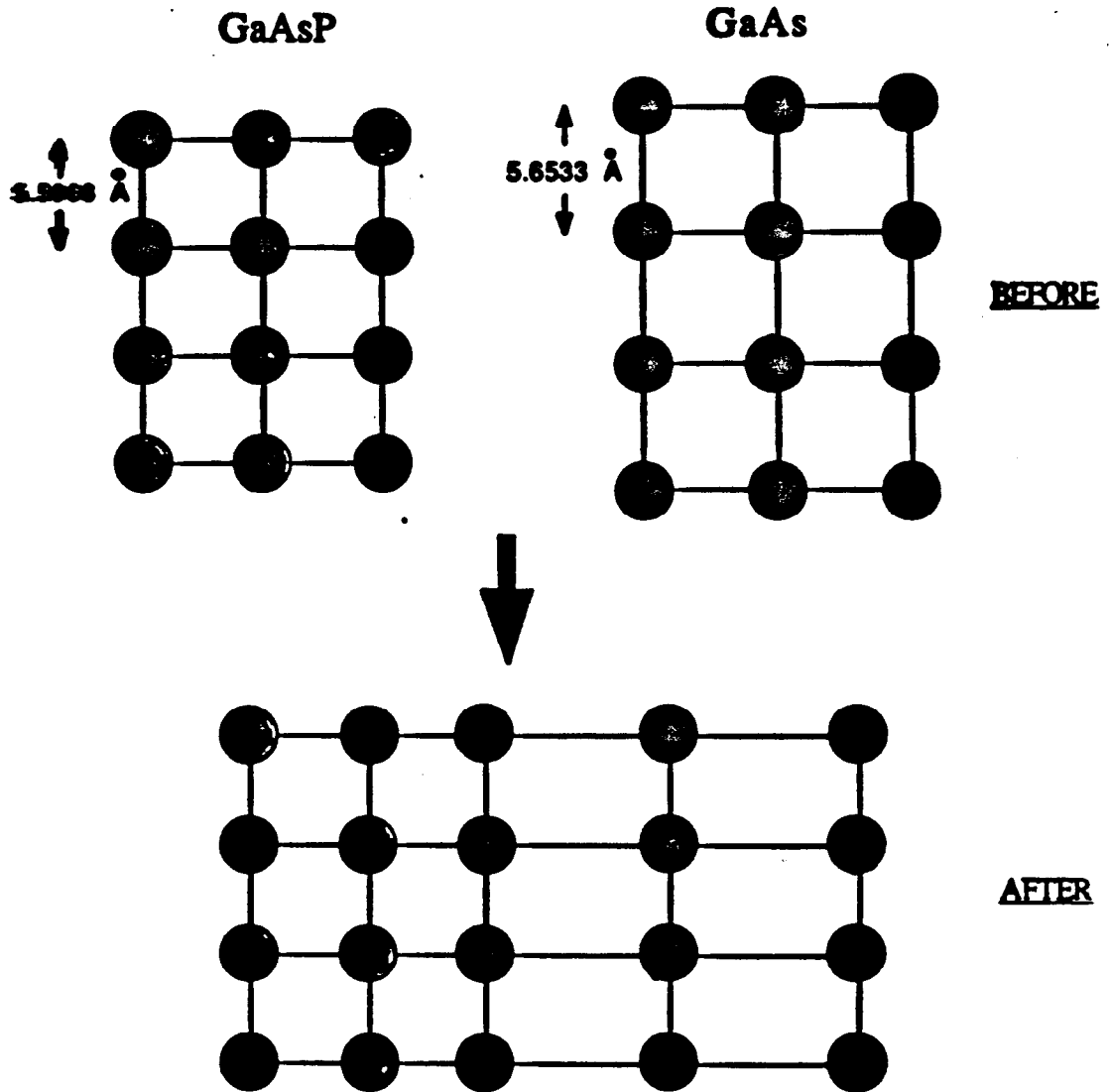
Strained GaAs grown on  $\text{GaAs}_{1-x}\text{P}_x$ \*

Phys. Rev. B46, 4261 ('92)



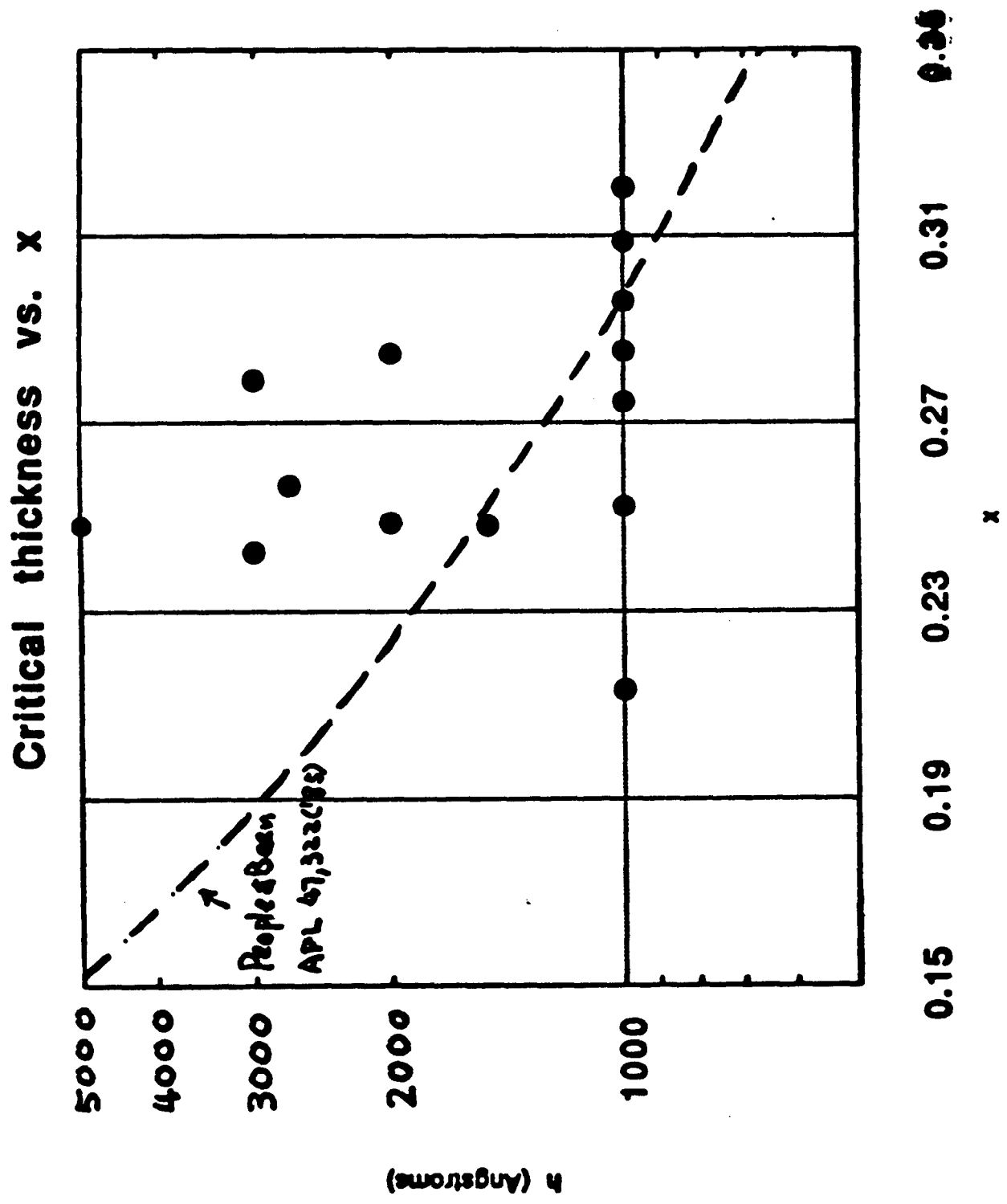
Wafers grown by Spire Co.

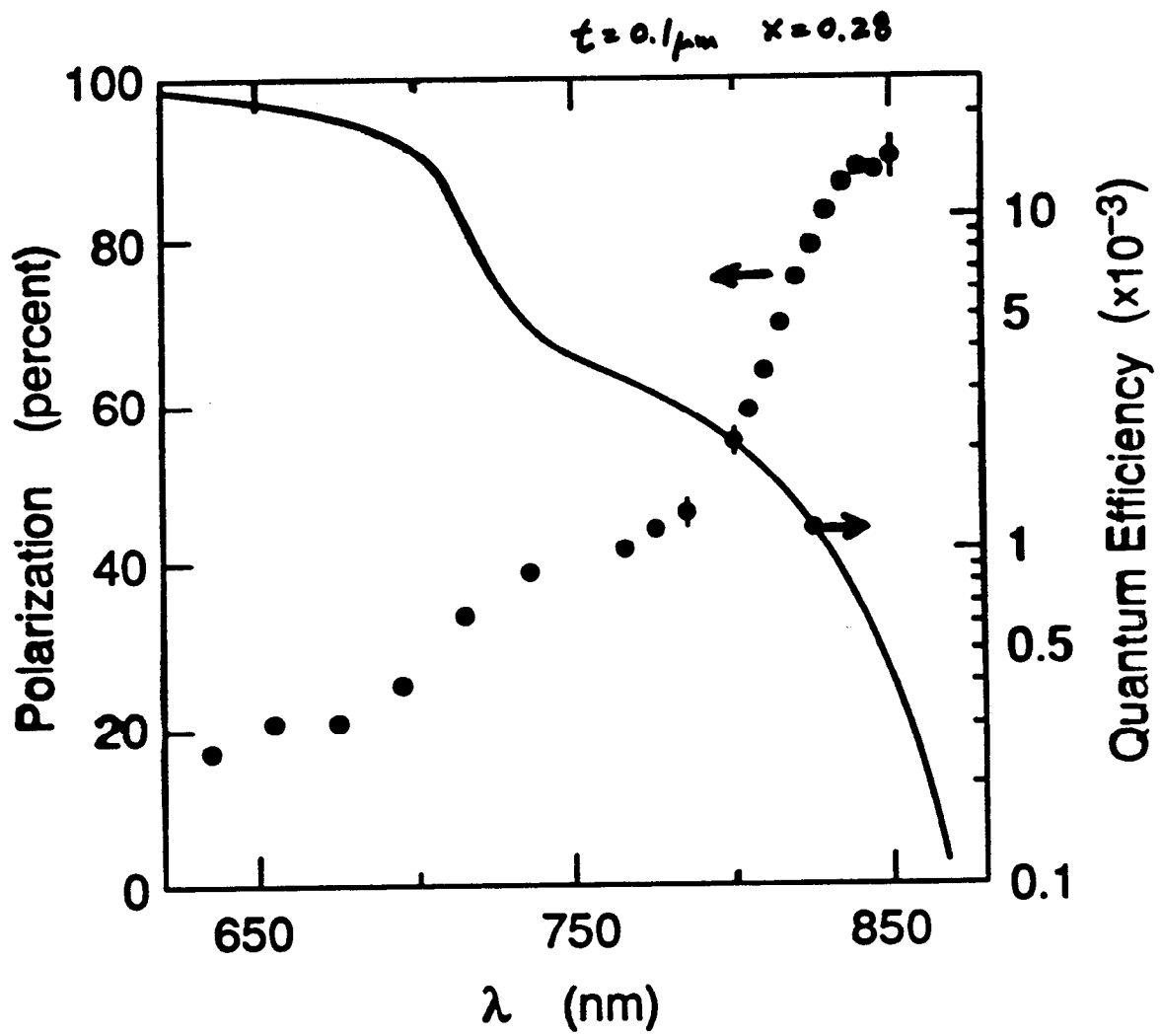
\* First high polarization observation made by Nakanishi et al., Phys. Lett A158, 345 ('91).



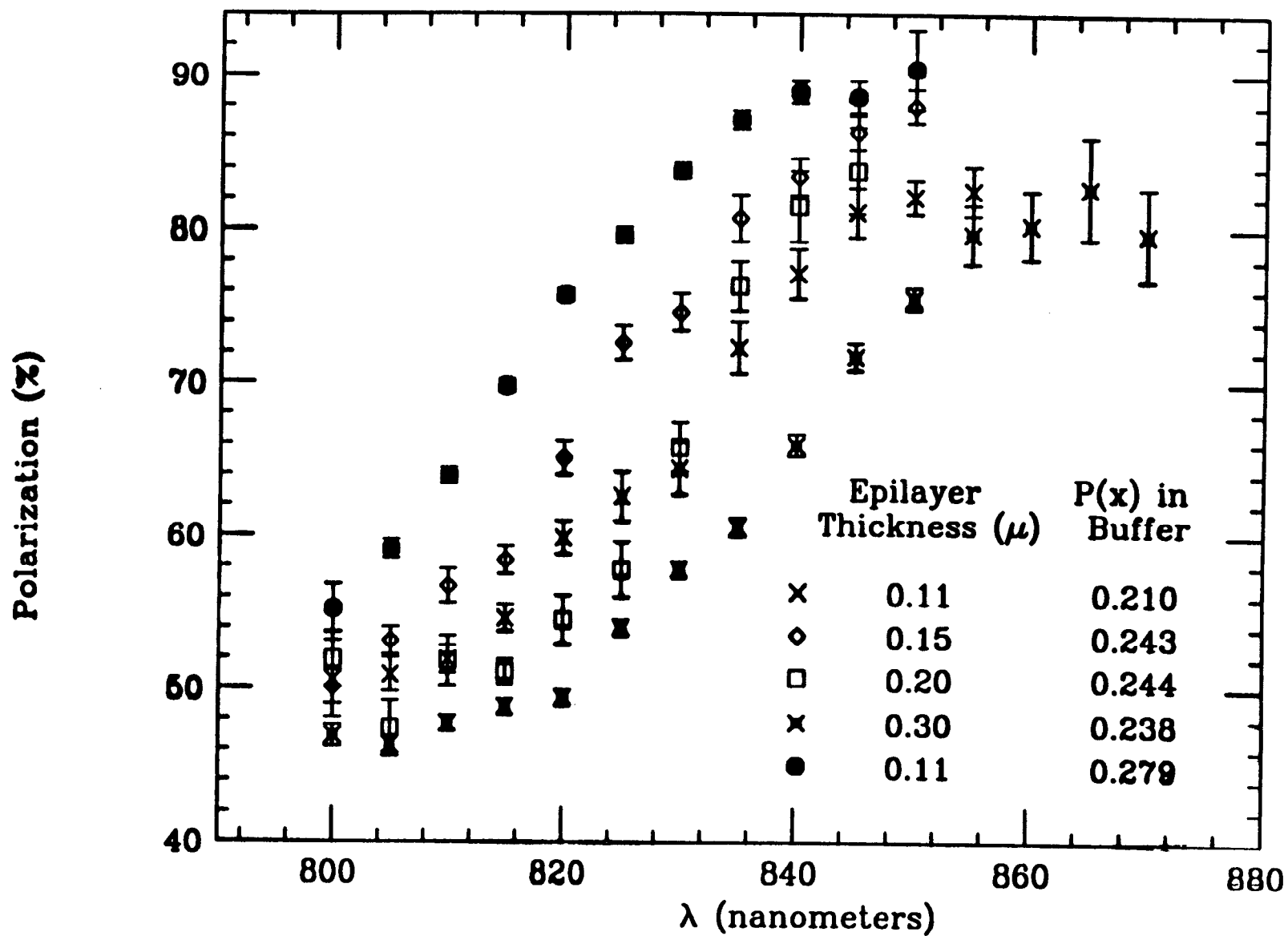
Parameters :

- Phosphorus fraction  $x$  in  $GaAs_{1-x}P_x$   
 $0.24 \leq x \leq 0.30$  (larger  $x \rightarrow$  larger strain)
- GaAs thickness  
 $0.1 \mu m \leq t \leq 0.5 \mu m$  (thicker  $\rightarrow$  higher Q.E.  
critical thickness)

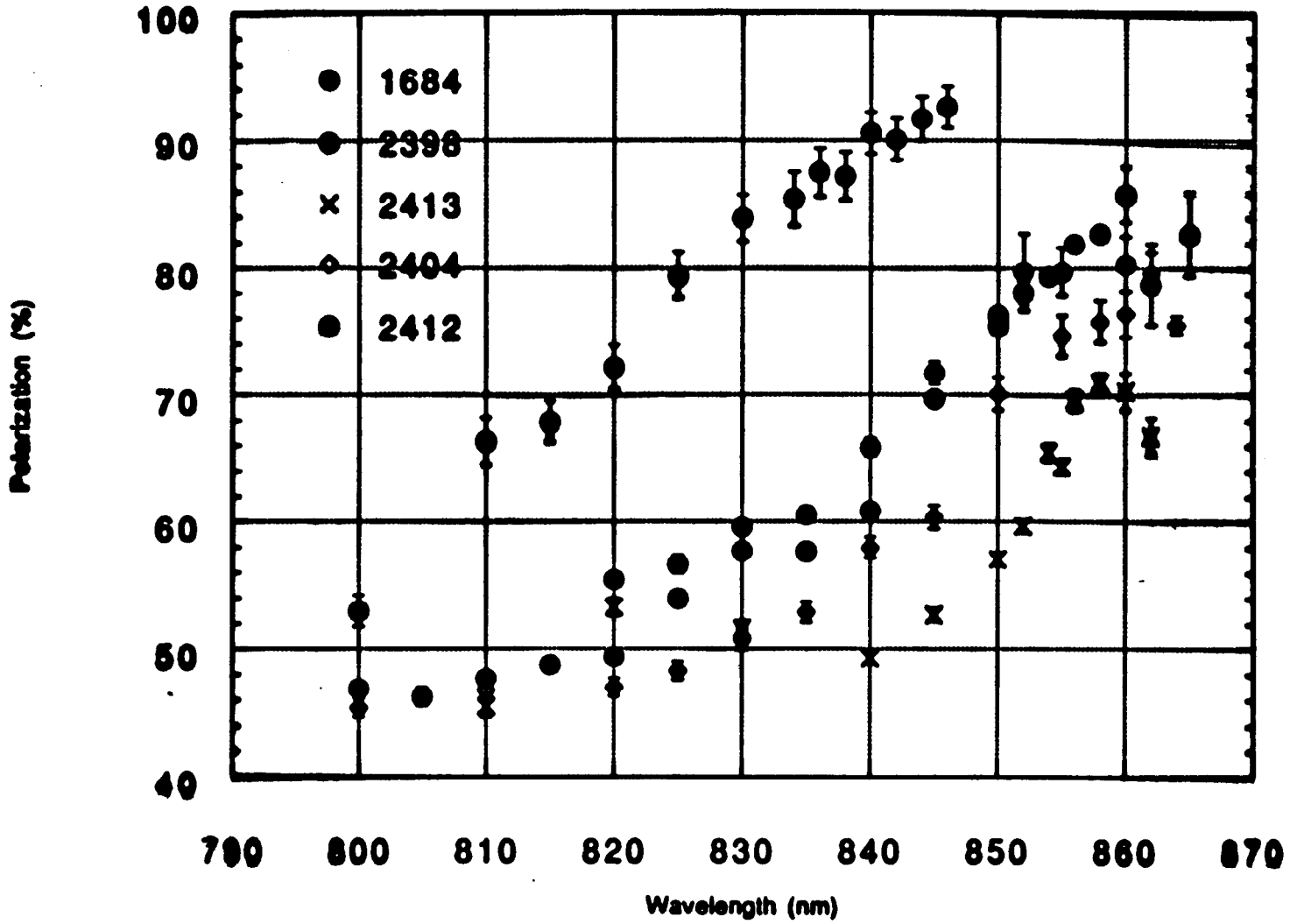




# GaAs Epilayer on GaAs<sub>1-x</sub>P<sub>x</sub> Buffer



# Polarization vs. Wavelength



63%

80%

70%

84%

84%

76%

88%

83%

88%

90%

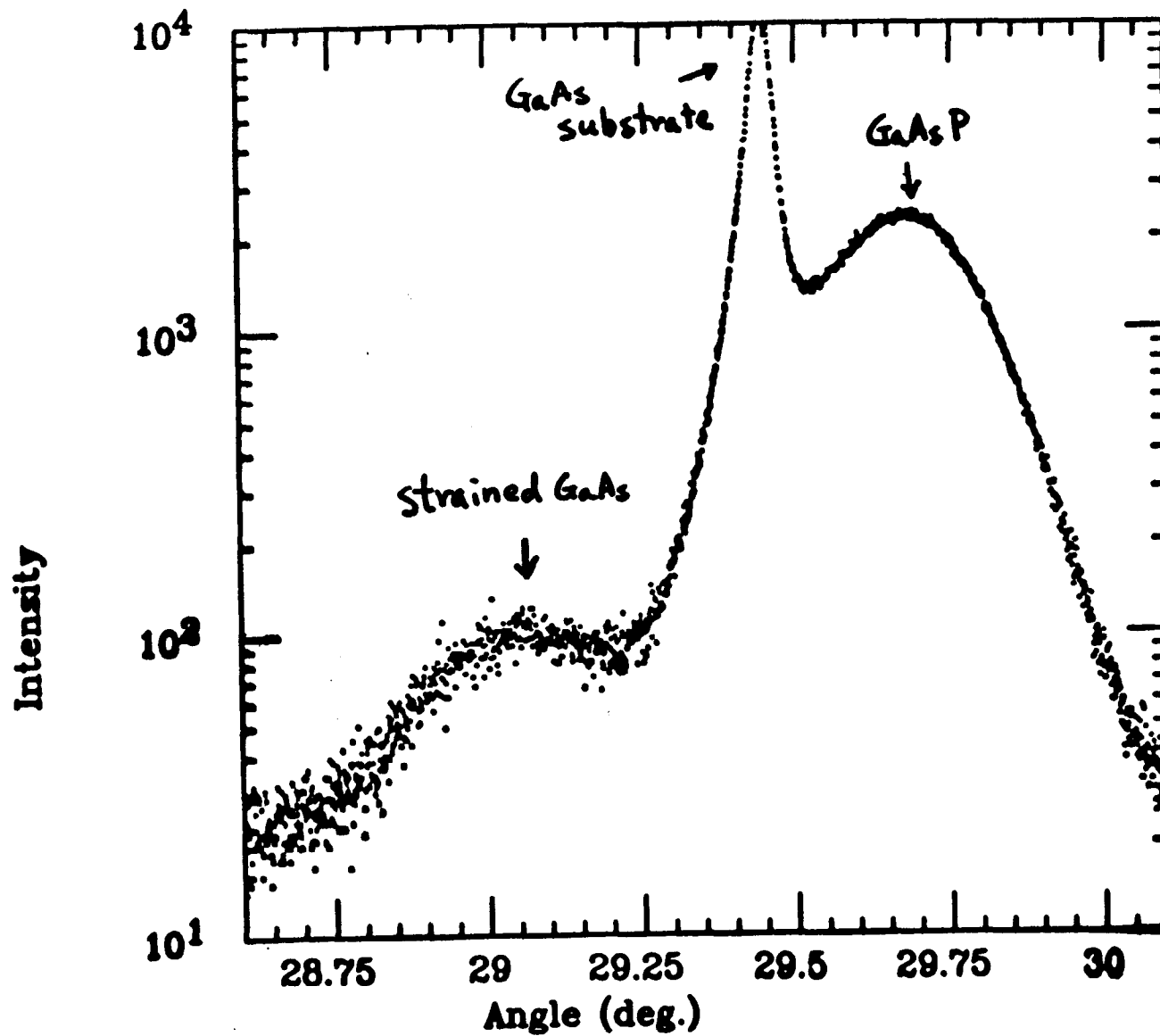
92%

72%

85%

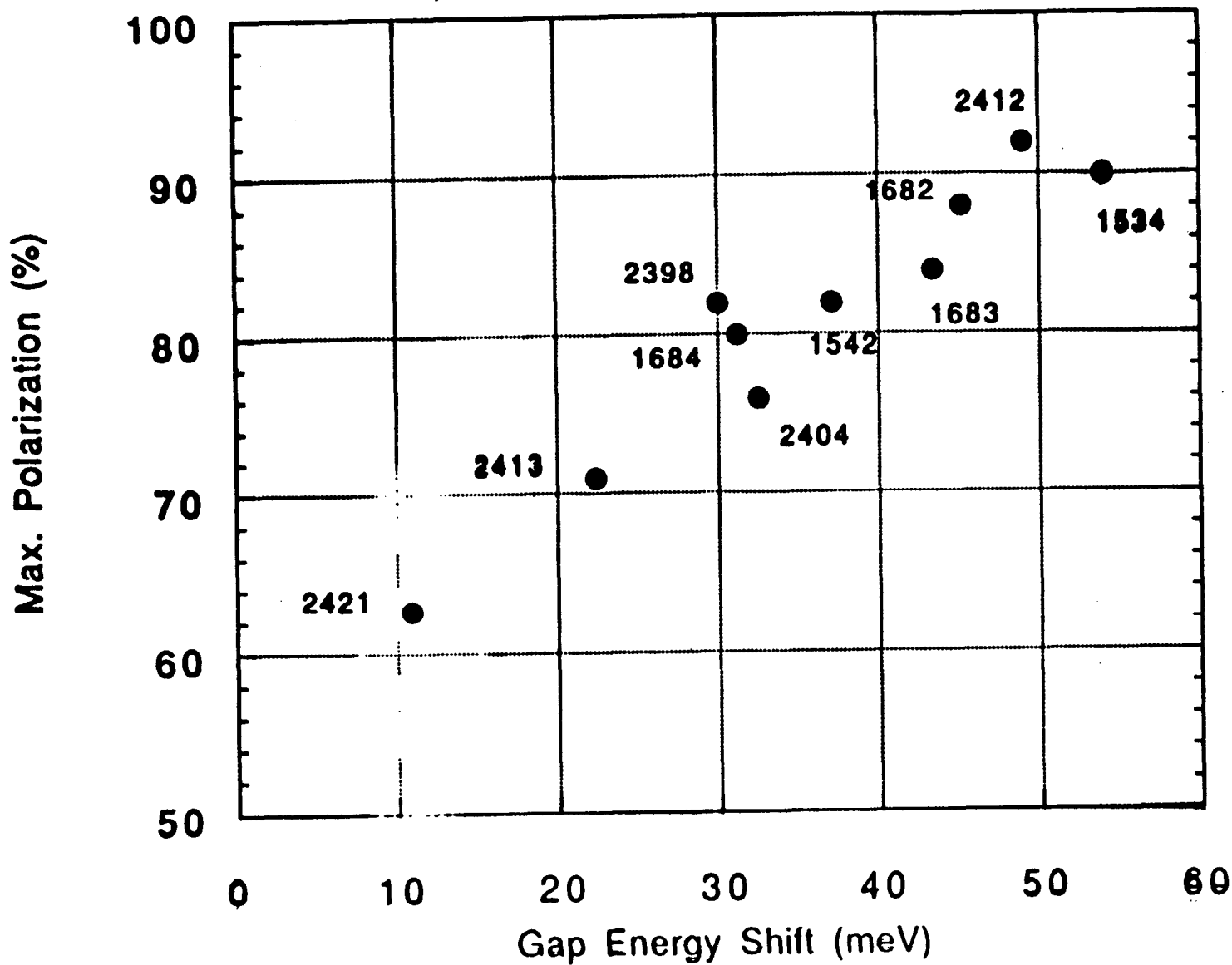
80%

4) X-ray diffraction SPIRE M05-2276 ( 180deg.)





# Max. Polarization vs. Gap Energy Shift (Photoluminescence)



## Spire M05-1684

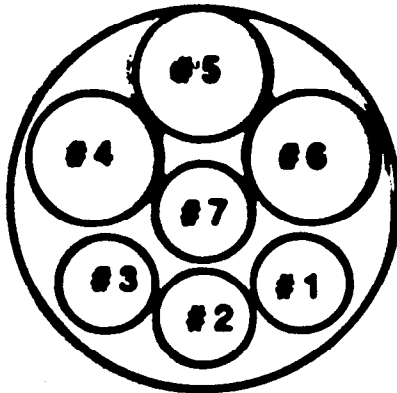
**Substrate:** 2" (001) GaAs (500  $\mu$  m)

### **Parameters:**

**Strained GaAs thickness:** 0.3  $\mu$ m  
**with GaAs<sub>1-x</sub>P<sub>x</sub>:** 0.24

### **Cathodes:**

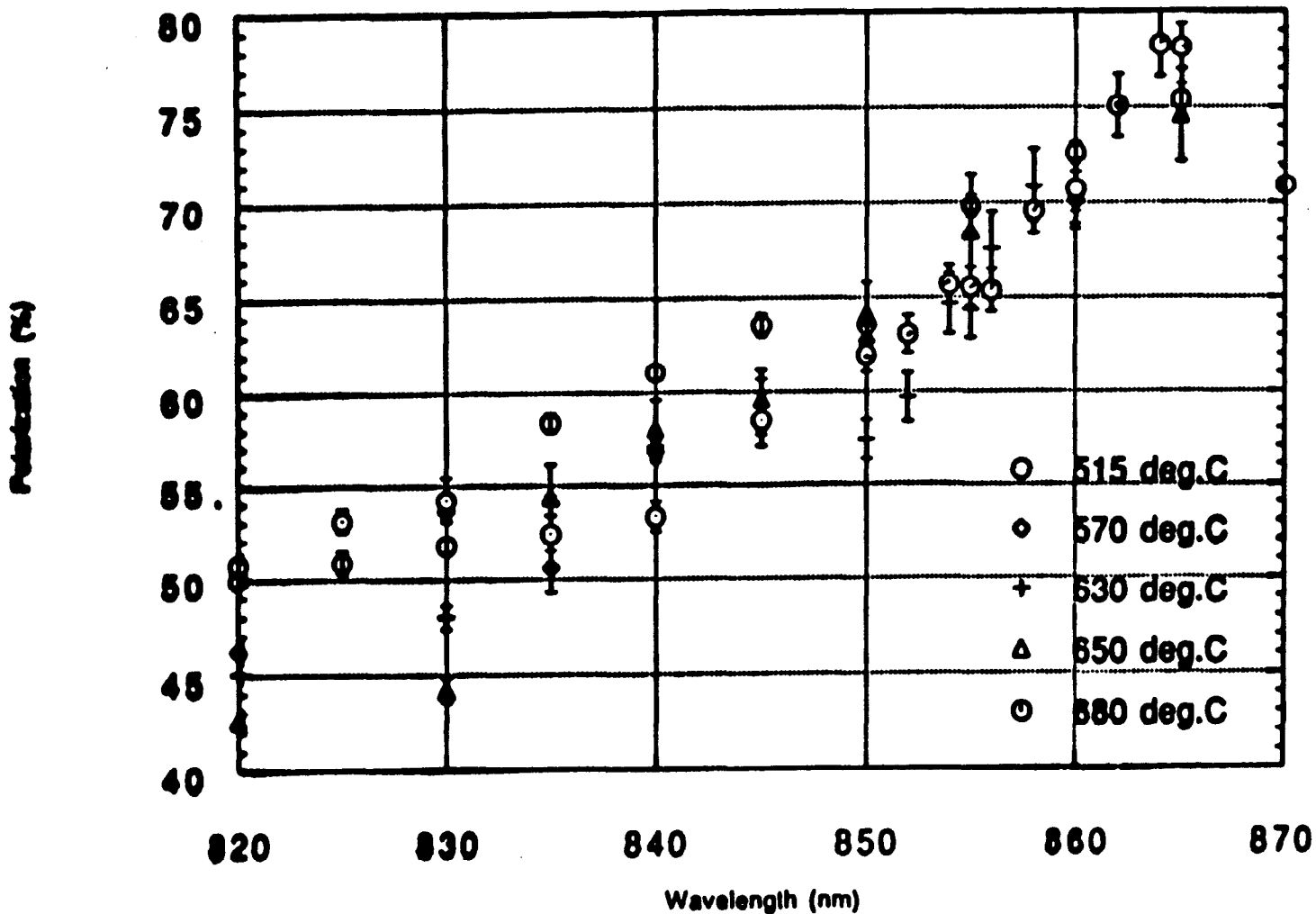
The following picture shows how the wafer was cut.



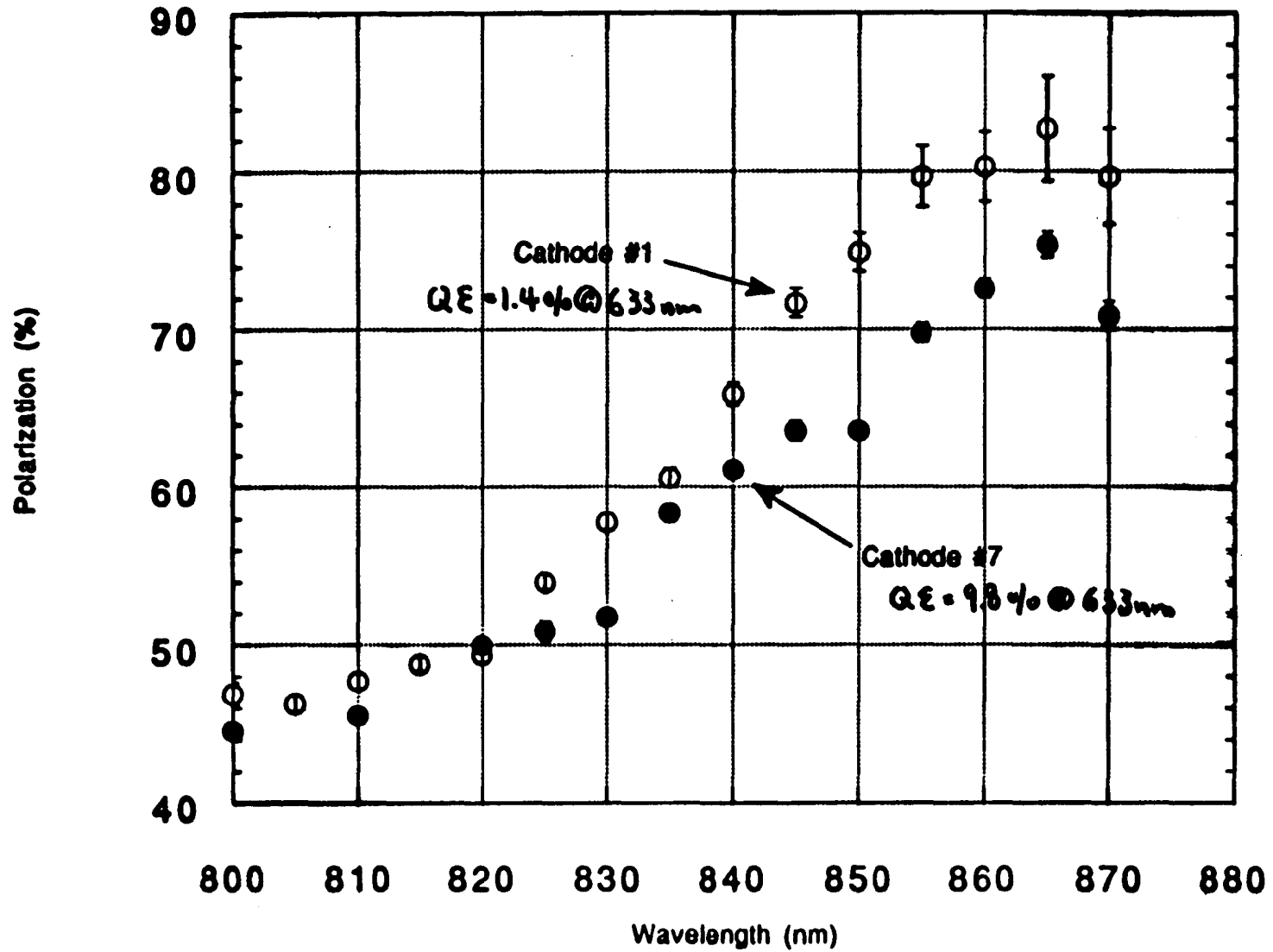
Wafer is anodized to form  
 $\sim 100 \text{ \AA}$  of oxide layer for  
surface protection

<b>Cathode</b>	<b>#1</b>	<b>measured with PEGGY</b>
	<b>#2</b>	<b>used for x-ray analysis</b>
	<b>#3</b>	<b>used for photoluminescence study</b>
	<b>#4</b>	<b>one half of surface shiny and rejected for SLC</b>
	<b>#5</b>	<b>in Diode gun #2</b>
	<b>#6</b>	<b>in Diode Gun #2</b>
	<b>#7</b>	<b>measured with PEGGY</b>

# Polarization vs. Heat-cleaning Temp.



# Polarization vs. wavelength (M05-1684)



## Summary

- First observation of strain enhanced electron polarization from InGaAs on GaAs (Jan. 1991)
- Strained GaAs successfully used for high-energy experiment (SLC/SLD) for the first time (1993).
- 80% polarization routinely reproduced with strained GaAs

**Gregory Mulhollan,  
SLAC**

**Low Energy Polarized Electron Source Test Facilities at  
SLAC**

# Low Energy Polarized Electron Source Test Facilities at SLAC

Gregory A. Mulhollan  
*Accelerator Department*  
*Stanford Linear Accelerator Center*

## ***Abstract***

A key part of accelerator operations at the Stanford Linear Accelerator Center (SLAC) is the polarized electron source, the heart of which is the photoemitting cathode. A recently constructed cathode test facility intended for characterizing candidate photocathode materials is described. Essential features include the capability to monitor the electron spin-polarization and rapid sample turnaround. Preliminary results include the effects of low temperature activations and the measurement of the electron spin-polarization from thin, strained GaAs.

## ***Introduction***

The low energy polarized electron source test facilities at SLAC are intended to provide information on the performance of photocathodes both as simple photoemitters and as sources of polarized electrons. A simple photoemitter is characterized by its effective quantum efficiency,  $QE_{\text{EF}}$ , and by its usable lifetime, herein primarily defined as the  $e$ -fold decay time,  $\tau$ .  $QE_{\text{EF}}$  is defined as the ratio of the number of photoemitted electrons to the number of incident photons. Note that this differs somewhat from the standard definition of the quantum efficiency. A spin-polarized photoemitter is further characterized by the degree of polarization of the photoemitted electrons, where the polarization along a given quantization axis is given by

$$P = \frac{N_{\uparrow} - N_{\downarrow}}{N_{\uparrow} + N_{\downarrow}}$$

and  $N_{\uparrow}$  and  $N_{\downarrow}$  are the number of electrons with spins parallel and antiparallel to the quantization axis respectively. Below we shall describe the test facilities, an experiment on the effects of low temperature activations on  $QE_{\text{EF}}$ , the results of overcesiation on lifetime, preliminary spin-polarization measurements on thin, strained GaAs and the effects of quantum efficiency on the spin-polarization.

## ***Facility Overview***

The test facilities currently consist of two separate ultra-high vacuum (UHV) systems. They will be referred to henceforth as the old cathode test system (CTS) and the new CTS. The primary difference in the two is that the new CTS incorporates an electron spin-polarimeter. The old CTS is shown below in Fig. 1 and the new CTS appears in Fig. 2.

Both systems are comprised of small volume ( $\approx 10^4 \text{cm}^3$ ) ultra-high vacuum systems pumped by a combination of ion and non-evaporable getter pumps<sup>1</sup>. Samples may be transferred into and out of the test chamber via a turbomolecular pumped, metal seal valved load lock volume. Typical turnaround times from sample introduction at atmospheric pressure to insertion into the UHV chambers are 4 hours. Samples are placed in a movable platter immediately after their final chemical preparation. This platter in turn rides atop a fork attached to a linear translator. After the load lock volume has achieved its target pressure, the sample, still in its platter, is moved into the test chamber and deposited onto a heating/cooling station. This tower, in turn, is capable of vertical motion via a bellows coupled linear translator. In the new CTS, the sample assumes two distinct positions. A lower one for activations and an upper one for polarization measurements. Sample temperature above 450°C is monitored via an infrared pyrometer<sup>2</sup>.

Both systems use diode lasers as light sources for activations and absolute  $QE_{EF}(\lambda)$  measurements are accomplished with bandpass filters and a white light source on the old CTS whilst the new CTS utilizes a monochromator with its light source. Relative  $QE_{EF}$  measurements and polarization assays on the new CTS use the monochromized light source ( $\Delta\lambda \approx 5\text{nm}$ ). The light helicity is controlled by a linear polarizer/liquid crystal retarder combination<sup>3</sup>. Each system is equipped with channel cesiators and leak valves for introduction of  $O_2$  or  $NF_3$ . Residual gas pressure is monitored with cold cathode gauges and quadrupole mass spectrometers. Base pressures are typically better than  $1 \times 10^{-11}$  torr with hydrogen comprising the main background gas.

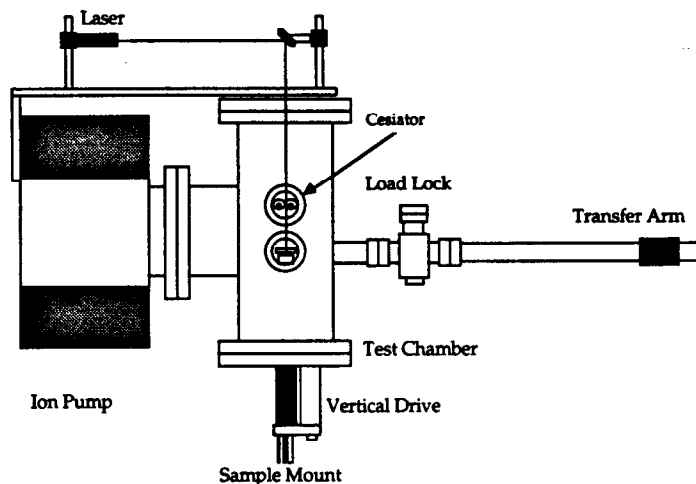


Fig. 1. Old cathode test system. See text for details.

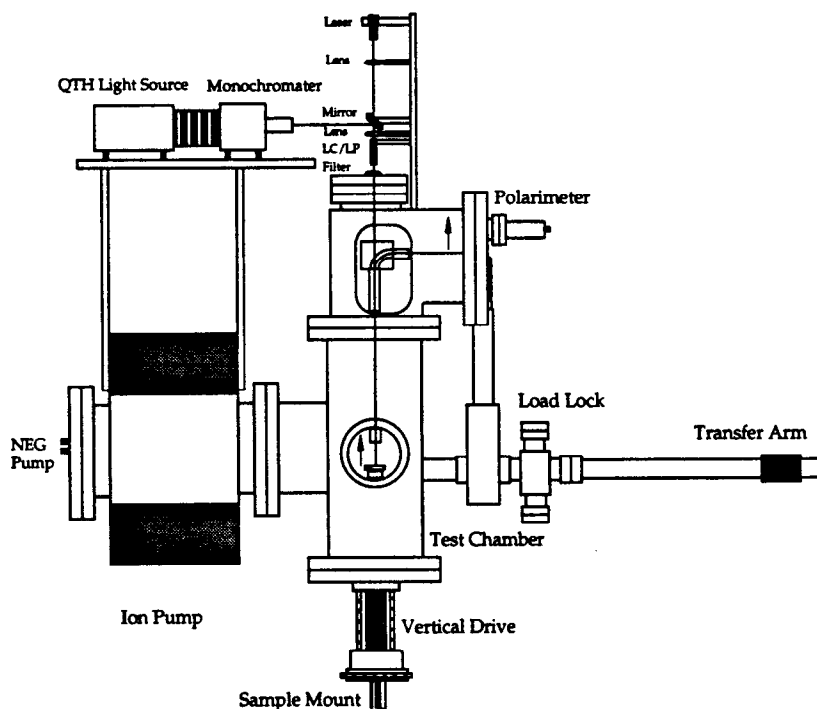


Fig. 2. New cathode test system. See text for details.

Polarization measurements in the new CTS are accomplished by the additional presence of an electron



transport column, a 90° spherical momentum rotator and a Mott type polarimeter. Longitudinally polarized electrons are extracted from the negatively biased photocathode by the entrance aperture of the transport column. The electrons are then focused and transported to the entrance aperture of the 90° spherical deflector. The now transversely polarized electrons are accelerated toward the Mott polarimeter, where the subsequent scattering asymmetry may be converted into a spin polarization using

$$P = \frac{1}{S_{EF}} \frac{X-1}{X+1}$$

where

$$X = \sqrt{\frac{N_L N'_R}{N'_L N_R}}$$

$N_L(N'_L)$  and  $N_R(N'_R)$  are counts into the left and right detectors as acquired with  $\sigma^+(\sigma^-)$  helicity light and  $S_{EF}$  is the effective Sherman function of the Mott detector. The Mott detector is a derivative of the Rice micro-Mott design<sup>4</sup>. Calibration of this version is quoted to be accurate to 5%<sup>5</sup>. The Mott polarimeter on which its calibration is based is accurate to 2%<sup>6</sup>. For scattering at 20 keV with an energy loss window of 1000 eV, this polarimeter has  $S_{EF} = 0.150$ .

### Hi-Lo Activations

The motivation for this series of tests was the possibility of obtaining a higher  $QE_{EF}$  in a two step activation process<sup>7</sup>: First the crystal was activated with Cs and  $NF_3$  according to 'normal' methods after heat cleaning at 600°C. Next, the crystal was reactivated proceeded by a lower temperature heat treatment. Quantum efficiency was monitored for both activations. The results for a range of second temperature heat treatments appear below in table 1.

Trial	T (°C)	$QE_L$ %	$QE_H$ %
1	420	2.91	3.00
2	475	3.03	2.94
3	500	3.00	2.91
4	345	2.82	2.75
5	600	2.83	2.87

Table 1. Quantum efficiency for two activations per trial. The first ( $QE_H$ ) after heating the crystal to 600°C for one hour, the second ( $QE_L$ ) with a heat treatment at the recorded temperature (T) for 45 minutes. The measurements were conducted with a  $\lambda = 750$  nm laser on a 300 nm thick strained GaAs cathode (see below) in the old CTS.

As may be readily seen, the overall effect is to increase the  $QE_{EF}$  by only a negligible amount. All subsequent measurements are for single activations.

### Lifetime Dependence on Overcesiation

These experiments were conducted on a Spire<sup>8</sup> MOCVD grown strained GaAs crystal with a doping concentration,  $\rho = 2 \times 10^{19}/\text{cm}^3$  Zn. The active layer was 300 nm thick. Prior to this set of experiments the crystal had been activated 13 times. Typically, the NEA surfaces exhibited a lifetime greater than 50 hours with peak  $QE_{EF} \approx 3.0\%$  at 750 nm. The tests were conducted in the old CTS. The room temperature  $QE_{EF}$  was measured at discrete points in time so as to minimize cathode pollution due to photoelectron induced gas desorption. All cesiations were done during a single activation cycle. The initial data were

acquired sequentially as the overcesiation value was increased; systematics were addressed by varying the overcesiation values in a pseudorandom sequence for later data. A schematic of the cesiation and decay process appears below in Fig. 3

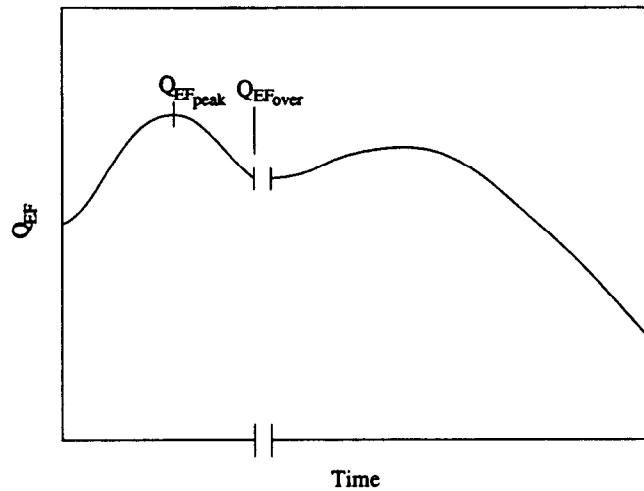


Fig. 3. Schematic of photocurrent during overcesiation and lifetime measurement.  $Q_{EF,peak}$  is the maximal value the photocurrent achieves during the cesiation process.  $Q_{EF,over}$  is the overcesiation photocurrent value. Note the change in time scales after cesiation.

Due to the complex nature of the temporal dependence of the photocurrent, it is not possible to define a simple analytic function with which we may associate a characteristic lifetime. Therefore, an effective lifetime,  $\tau$ , is taken to be the time at which the  $Q_{EF}$  has dropped by  $e^{-1}$  from the peak value,  $Q_{EF,peak}$ . This choice is somewhat arbitrary, but has been chosen as it is closest to the behavior relevant to gun operations. An example of an alternate lifetime definition that could be used is to reference to the value of  $Q_{EF,over}$ , since the act of overcesiation may cause the  $Q_{EF}$  to reapek at a value somewhat lower than its previous maximum.  $\tau$  also has the advantage that it somewhat removes the dependence of the lifetime on the history of cesiation. This is important since a gradual decrease in  $Q_{EF}$  was observed over the span of time during which data was acquired (see Fig. 4). Data will be presented below using exclusively this lifetime definition.

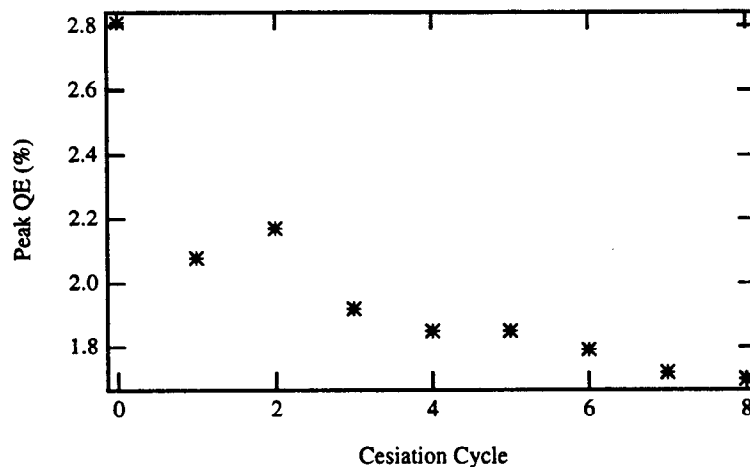


Fig. 4. Peak  $Q_{EF}$  as function of cesiation cycle. Note the gradual decrease in the value over time. The value at cycle 0 is for the freshly activated surface.

Lifetimes, as defined in the above section, are presented in graphical form in fig. 5. The general trend is for  $\tau$  to increase as the overcesiation is increased even though there is some ambiguity as how to arrive at a value for  $\tau$ . As the data were not acquired in a continuous mode, we must estimate the lifetime using a simple exponential function. This is not strictly accurate, since the decay process is best described by the sum of two exponentials as illustrated in fig. 6. From that figure it can be seen that the short time-constant exponential dies off well before the QE drops by  $e^{-1}$ . Therefore, our rather crude estimates for lifetime should not be greatly in error provided that the lifetime size relation is independent of the overcesiation value. Note that there is some scatter, particularly in the initial measurements. This is a result of the short time exponential not being fully damped out for those measurements. The estimates for  $\tau$  that represents the measurement closest to the  $e^{-1}$  value of QE are denoted by an (X) in the figure. Each value of lifetime as calculated from the measurements appears in fig. 5. The grey line represents the sequence of data acquisition.

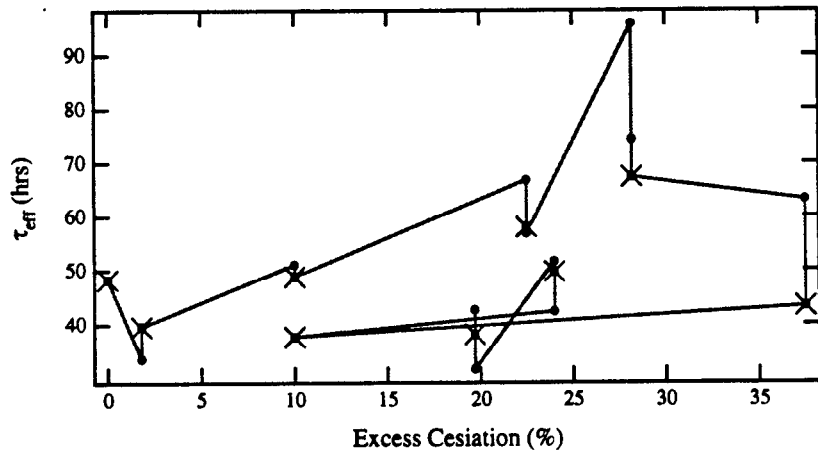


Fig. 5. Lifetime as function of overcesiation. The different lifetimes are defined above. Note that two different lifetime regions exist. This is attributable to an overall drop in cathode performance as a result of a high vacuum background during the greatest (37.5%) overcesiation.

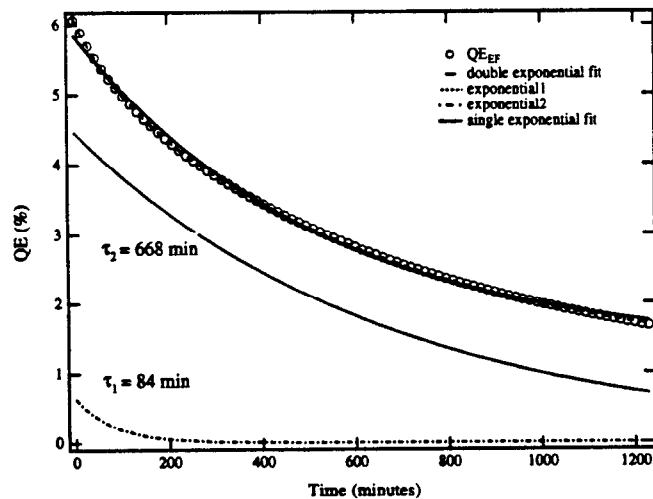


Fig. 6. Fit to lifetime decay curve illustrating that the functional form is best described by  $QE_{\text{EF}}(t) = QE_{\text{EF}}(0) \{e^{-t/\tau_1} + e^{-t/\tau_2}\}$  and not by a simple exponential.

It is apparent that the lifetime,  $\tau$ , only *increases* with the addition of more Cs. A limitation of this study is that no more than a 40% decrease in the peak  $QE_{EF}$  was possible at room temperature. It is plausible (and in fact likely) that at  $LN_2$  temperatures more Cs will adhere to the surface enabling larger values of overcesiation, and hence larger periods between cesiations to be achieved. Whether this is a truly desirable result for gun operations remains unknown. The effects of overcesiation on spin-polarization are likely to be minimal or nonexistent with respect to spin-flipping. The exact degree of influence depends strongly on the joint density of states (occupied and empty) around the Fermi level. However, existing data suggest that no depolarization is likely<sup>9</sup>.

### Candidate Cathodes

As stated above, the primary mission of the cathode test facility is to determine the fitness of a particular cathode material for polarized gun operations. Currently the material of choice is strained GaAs, where the strain is induced in order to lift the degeneracy of the  $p_{3/2}$  band at the  $\Gamma$  point (see Fig. 7).

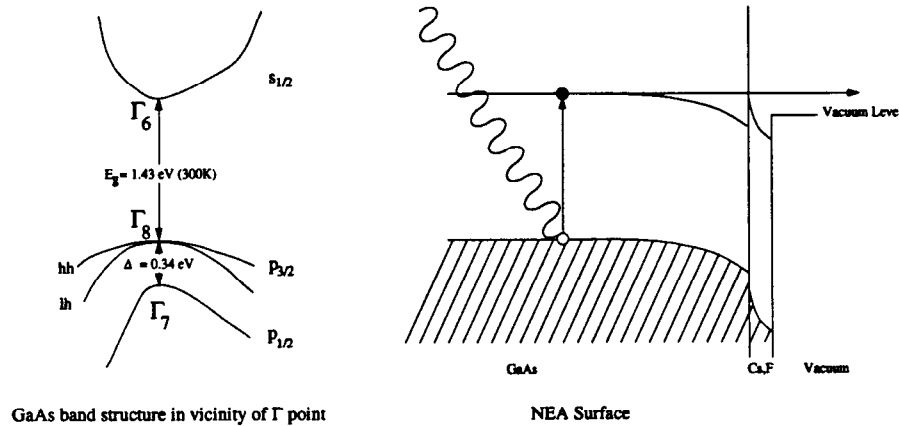


Fig. 7. GaAs band structure in the vicinity of the  $\Gamma$  point. Note that the light and heavy hole bands are degenerate in bulk GaAs. Strain can lift this degeneracy, enabling polarizations in excess of 50% to be achieved.

The strain is introduced by epitaxial growth of an active layer of GaAs on a layer of  $GaAs_{1-x}P_x$ , where  $x$  is adjusted to provide different values of strain<sup>10</sup>. Compressive strain causes both a hydrostatic shift (overall band gap increase) and a separation of the degenerate states. Thus strain may be monitored by measuring the band gap energy. The schematic structure of these samples appears below in Fig. 8. The samples start as a low etch-pit density bulk GaAs wafer. Atop this chemically clean and well oriented substrate is grown a thin buffer layer of GaAs. This insures that a high quality surface is present before the actual strain layer is begun. Graded GaAsP is grown on the buffer layer with increasing phosphorous content as the layer thickness increases. This is done to minimize the possibility of strain relaxation and to insure that crystalline growth is maintained. A layer with the same phosphorous content as the last of the graded layer is grown in continuance on the graded layer. Finally, the active layer of GaAs is grown on the relatively thick GaAsP layer. Since the bandgap of GaAsP is greater than that of GaAs, there is no contribution from the GaAsP layer to the photocurrent at the energy of the band gap of GaAs ( $\approx 1.43$  eV at 300K). Polarizations in excess of 77 % have been measured in the new CTS for crystals in a high  $QE_{EF}$  state. At low  $QE_{EF}$ , polarizations as high as 80% have been measured.

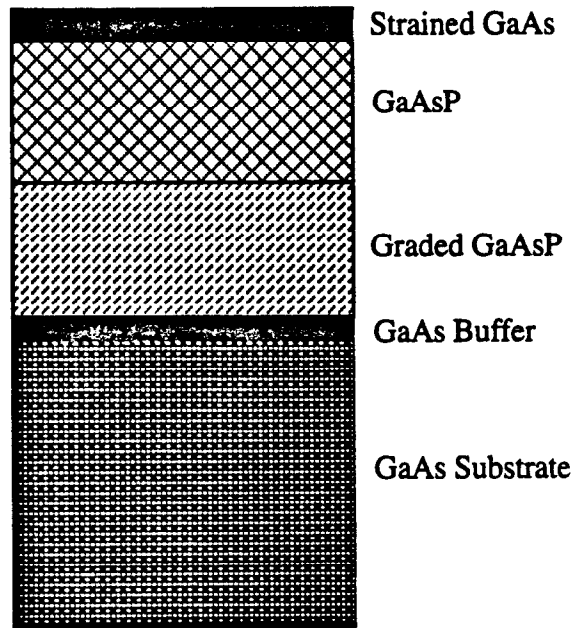


Fig. 8. General structure of strained GaAs cathodes. Thicknesses are exaggerated.

Preliminary results from various thicknesses of strained GaAs appear below in Fig. 9–11. To date, the highest polarization measured at maximal  $QE_{EF}$  (77%) comes from a 100 nm thick  $5 \times 10^{18}/\text{cm}^3$  Zn doped sample with  $x = 0.31$ . All data were acquired at 300K.

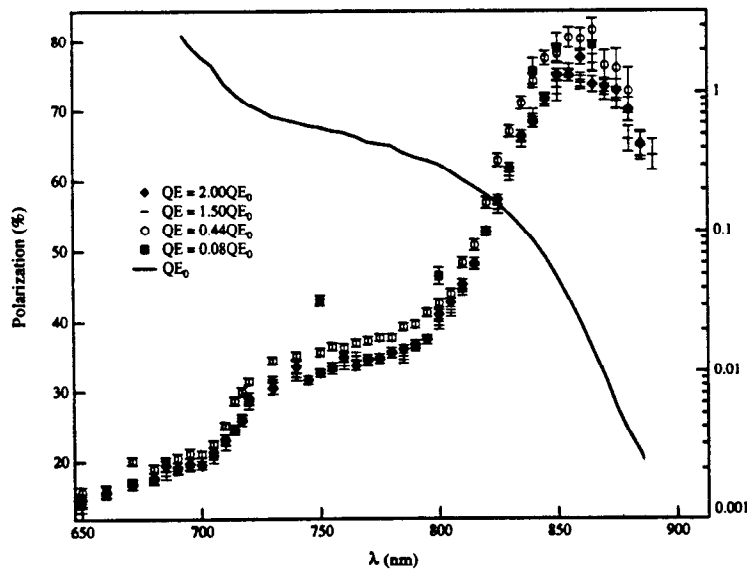


Fig. 9. Polarization as a function of wavelength for various  $QE_{EF}$  states. Sample is 100 nm thick  $5 \times 10^{18}/\text{cm}^3$  Zn doped  $x = 0.31$  strained GaAs, Spire M05-2412.

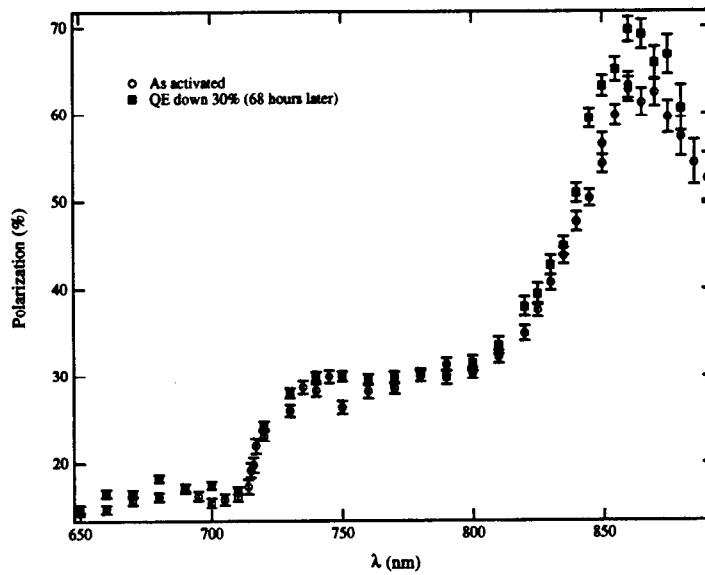


Fig. 10. Polarization as a function of wavelength for two  $QE_{EF}$  states. Sample is 100 nm thick  $2 \times 10^{19}/\text{cm}^3$  Zn doped  $x = 0.30$  strained GaAs, Spire M05-2663.

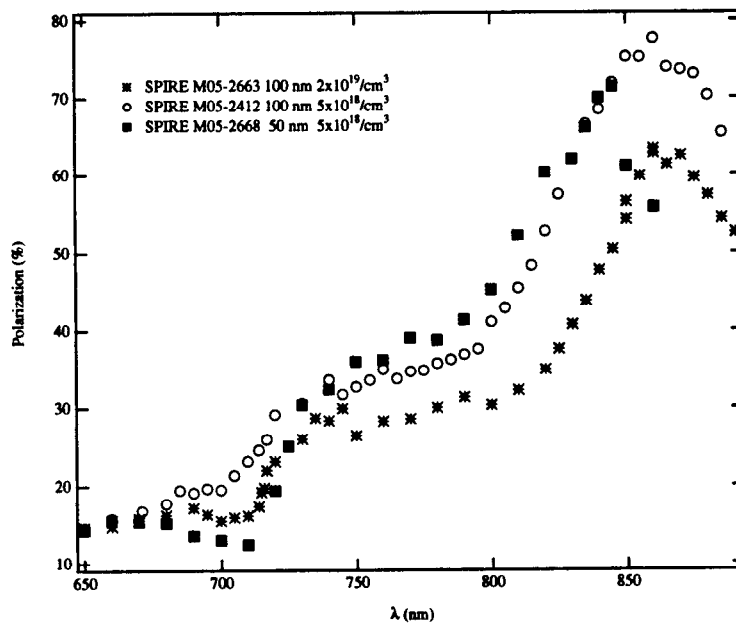


Fig. 11. Comparison of polarization curves for the samples from Figs. 9 and 10 together with data from 50 nm thick strained GaAs ( $\rho = 5 \times 10^{18}/\text{cm}^3$  Zn) for the highest  $QE_{EF}$  obtained from each sample.

The overall trend is for higher polarizations to occur when  $QE_{EF}$  drops below its maximum value. The effect is at first strongest at the gap energy where a relative increase of  $\approx 10\%$  in polarization is seen for small drops in  $QE_{EF}$ . While it requires a greater drop in  $QE_{EF}$ , the effect is eventually larger at the shorter wavelengths, where increases in polarization of near 50% relative have been seen (see e.g., Fig. 9). The increase may be attributable to filtering of highly thermalized electrons in the emission process. As the surface becomes less negative electron affinity (NEA), then the energy of the photoelectrons necessary

for emission increases. Fully thermalized electrons have lost too much kinetic energy to be emitted. For shorter wavelengths the range of energies for emission at high  $QE_{EF}$  is larger than for long wavelengths. Therefore, the relative changes should be larger for the shorter wavelengths. That the highly thermalized photoelectrons are less polarized than the hot electrons suggests that a spin-dependent surface barrier is either missing or is very weak, i.e., depolarization occurs sub-surface and not at the surface-vacuum interface.

### **Conclusions**

This paper has outlined the capabilities of the low energy cathode test facilities at SLAC. We have shown that longer lifetimes may be had by increasing overcesiation, although the effects of high Cs coverage on polarization are as yet unknown. Strained GaAs is clearly a good choice for high polarization photocathodes, albeit with somewhat poor quantum efficiencies at the peak polarization. Clearly, when the highest polarizations are desired, operation at low  $QE_{EF}$  is necessary.

### **References**

---

1. Pump GP500 with ST707 active material from SAES Getters/ USA Inc. Colorado Springs, CO.
2. Iacon Inc., Niles, IL.
3. Model 932 series attenuator, Newport, Irvine, CA.
4. F. B. Dunning, L. G. Gray, J. M. Ratliff, F.-C. Tang, X. Zhang and G. K. Walters, *Rev. Sci. Instrum.* **58**, 1706(1987).
5. H. Tang et al., *Phys. Rev. Lett.* **71**, 444 (1993).
6. H. Hopster and D. L. Abraham, *Rev. Sci. Instrum.* **59**, 49(1988).
7. G. Vergara, L. J. Gómez, J. Capmany and M. T. Montojo, *Surf. Sci.* **278**, 131(1992).
8. Spire Corporation Bedford, MA.
9. S. Hüfner, G. L. Bona, F. Meir and D. Pescia, *Sol. St. Comm.* **51**, 163(1984).
10. T. Maruyama, E. L. Garwin, R. Prepost and G. H. Zapalac, *Phys. Rev. B* **46**, 4261(1992).

**T. Nakanishi**  
**Nagoya U.**

**High Polarization Cathode Research in Japan**



**“ High Polarization  
Cathode Research  
in Japan ”**

**T. Nakanishi (Nagoya University)**

**§ 1 Introduction**

**§ 2 Superlattice**

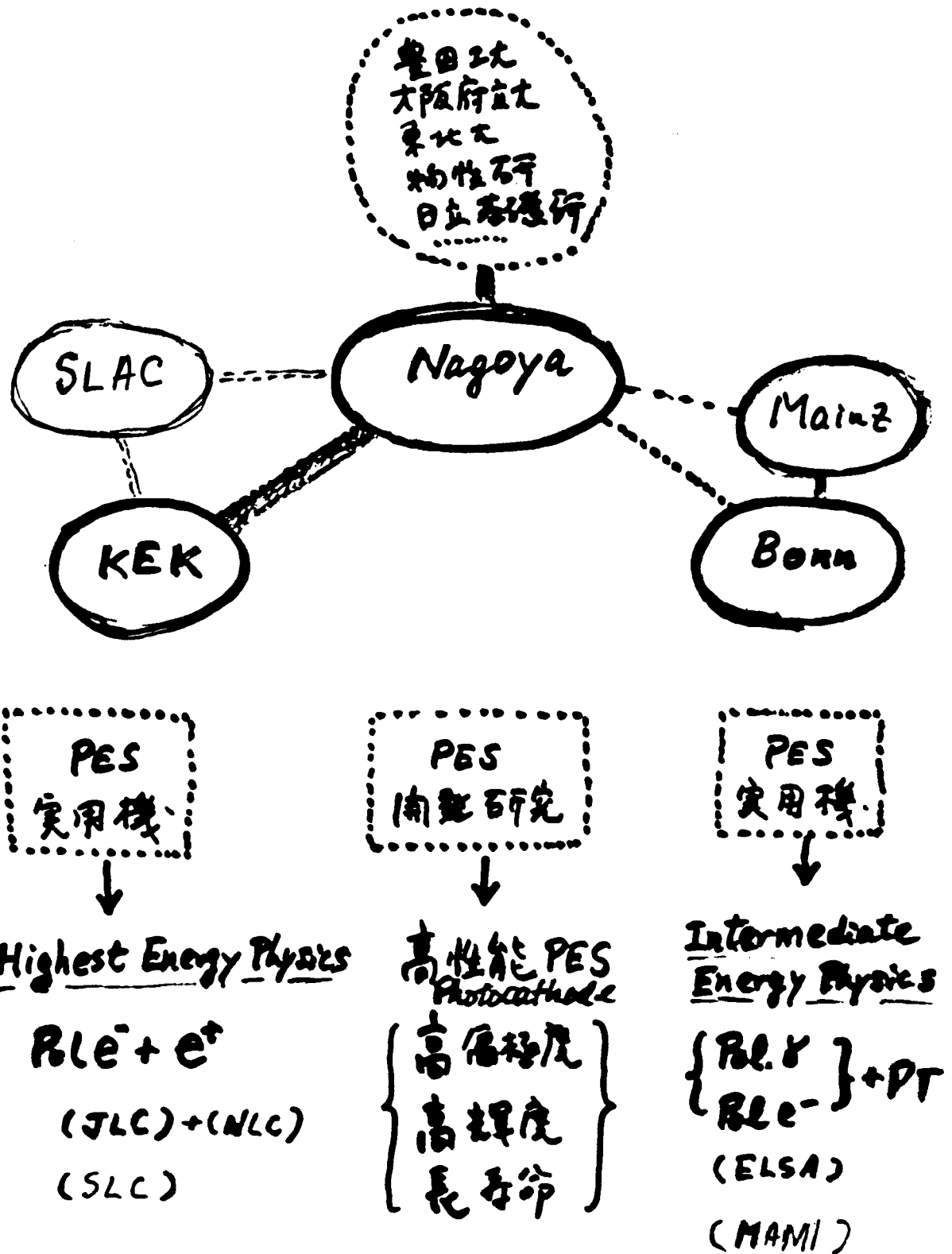
**§ 3 Strained GaAs**

**§ 4 Resonance Absorption Type Photocathode**

**§ 5 Summary**

# Positronium beam 127429 研究計画

当面 3つの場所での Activity を考えている。



# JLC Polarization Group

[KEK] M. Yoshio, Y. Takeuchi,  
T. Omori, Y. Kurihara,  
K. Nishitani<sup>1)</sup> K. Itoga<sup>2)</sup>

[Nagoya Univ.]

T. Nakanishi, S. Okumi,  
S. Nakamura<sup>3)</sup> H. Aoyagi<sup>4)</sup>  
M. Tsubata, M. Tawada,  
K. Togawa, C. Takahashi,  
Y. Tanimoto

## Photocathode development

[Daido Steel Co.] T. Saka, T. Kato  
[Sophia Univ.] K. Kishino  
[NEC] M. Mizuta, T. Baba  
[Osaka Pref. Univ.] H. Horinaka  
[Toyota Tech. Collage] K. Kamiya

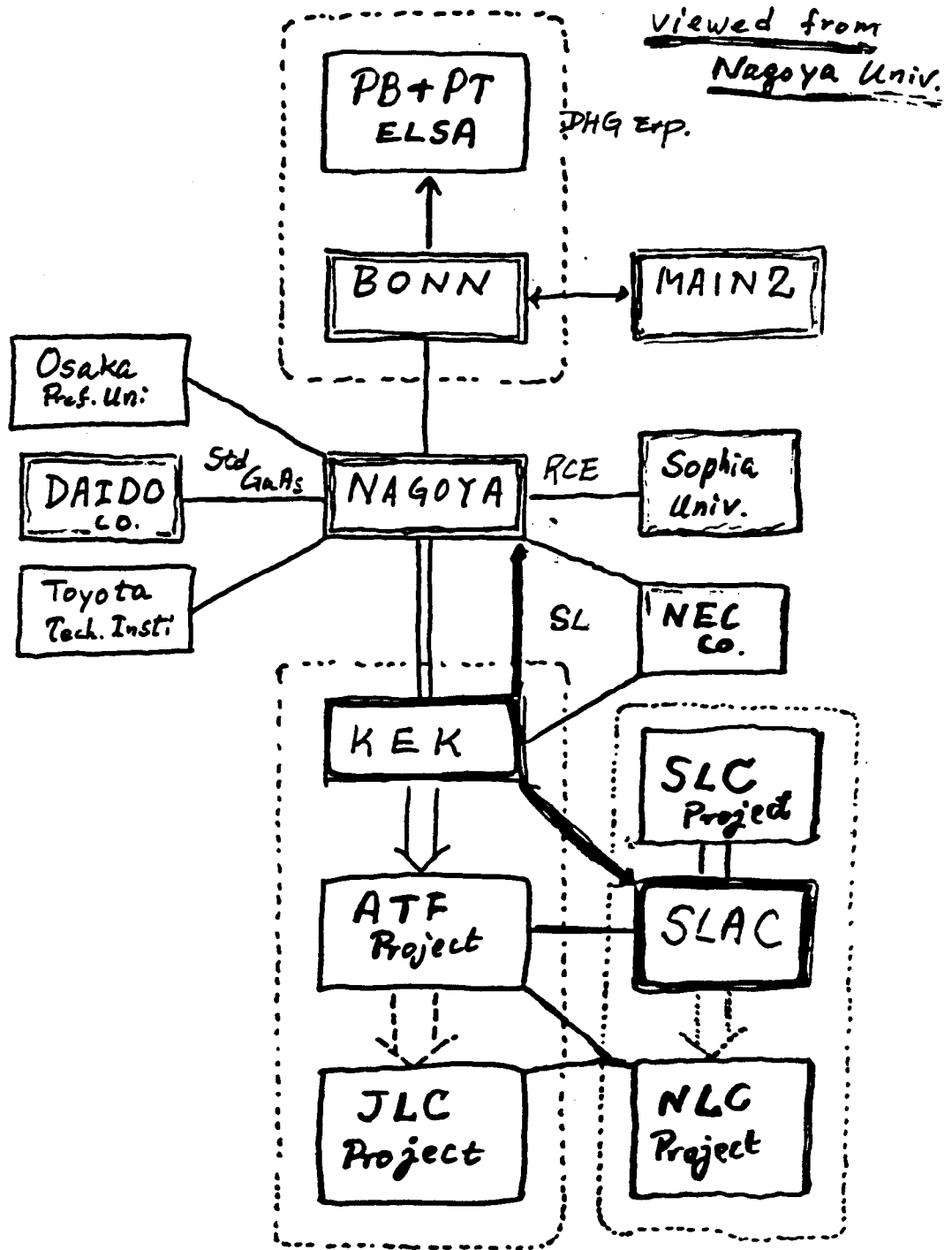
1) ATC Co.

2) Mitsubishi Co.

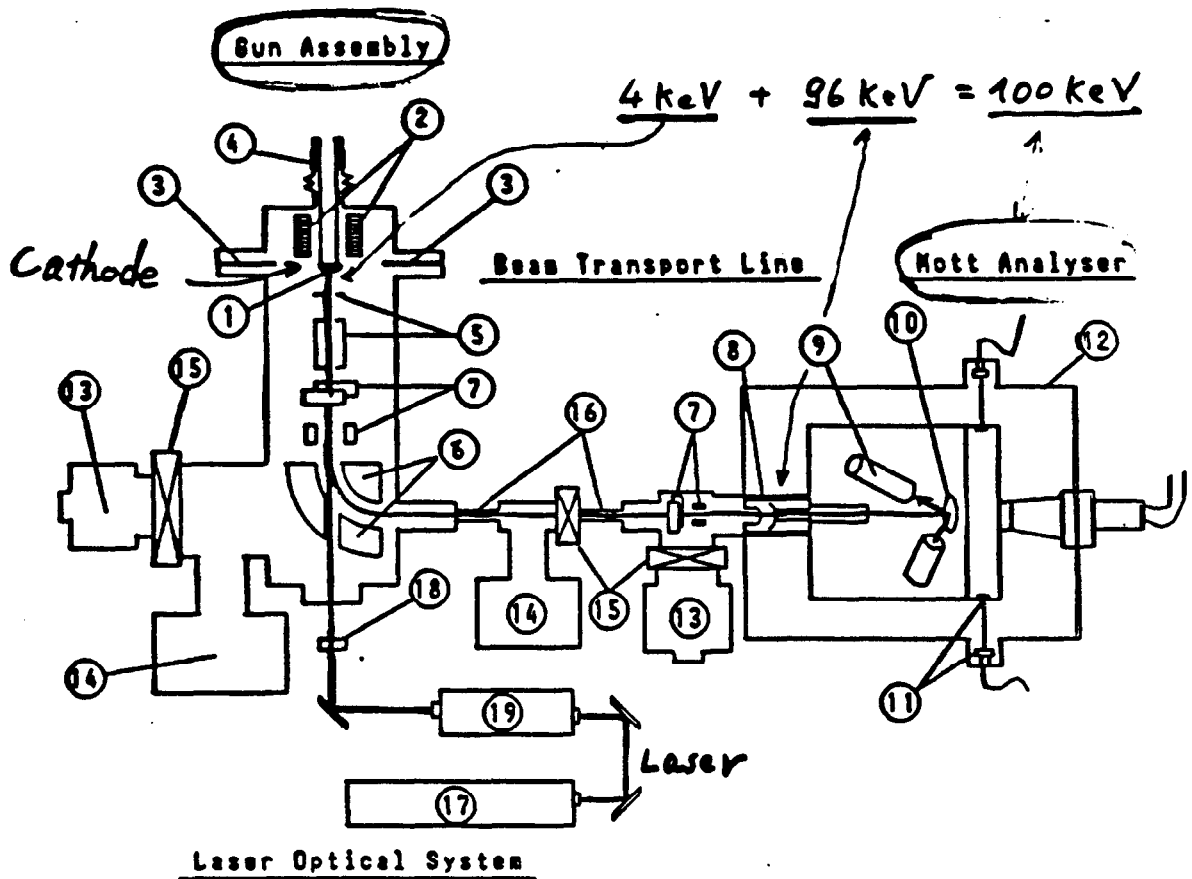
3) Present address : Bonn Univ.

4) " : SLAC

Collaboration Diagram at 1991~1993



# NPES - I (Nagoya Polarized Electron Source #1)



## Sun Assembly

- 1: 6aAs crystal
- 2: Liq. N<sub>2</sub> container
- 3: Activator (Cs<sub>2</sub>O<sub>2</sub>)
- 4: 4[KeV] ceramic bushing
- 5: Extraction electrode
- 6: Spherical condenser
- 7: Electronic Deflector

## Beam Transport Line

- 13: Turbo-molecular pump
- 14: Ion pump
- 15: UHV gate valve
- 16: Conductive adj. tube

## Mott Analyser

- 8: 100[KeV] ceramic bushing
- 9: Surface barrier detector
- 10: Target foil and wheel
- 11: LED and photodiode
- 12: Freon gas tank

## Laser Optical System

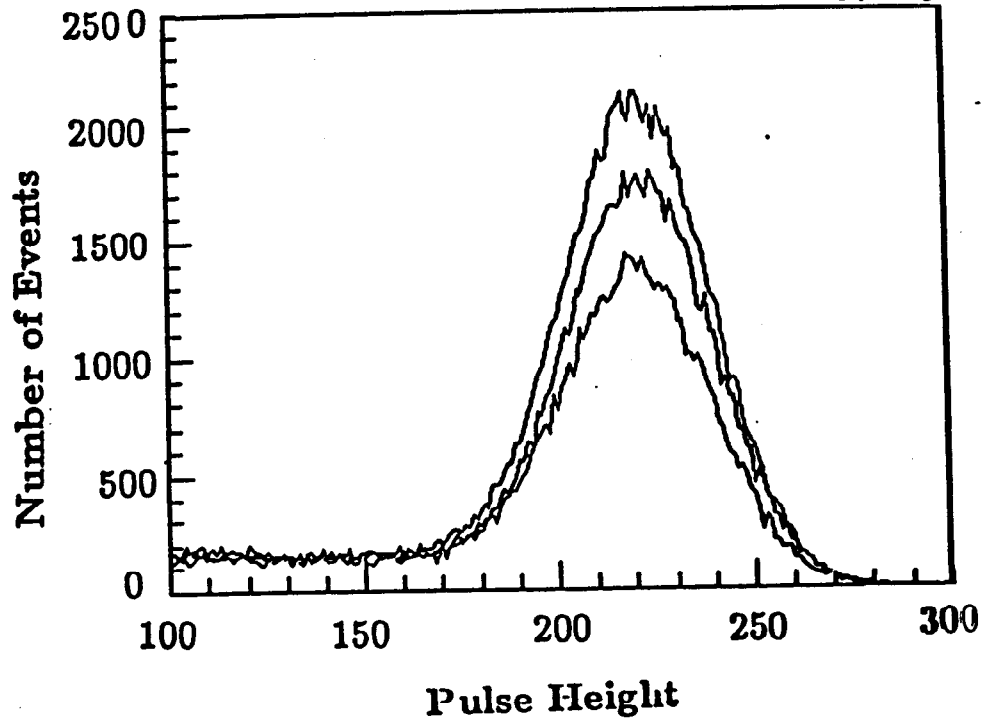
- 17: Ar Laser
- 18: λ/4 filter
- 19: Ti-Sapphire Laser

T. Nakanishi et al; Jpn. J. Appl. Phys. 25 (1986) 766

< Mott Scattered Electrons Energy Spectrum >

Figure 1.

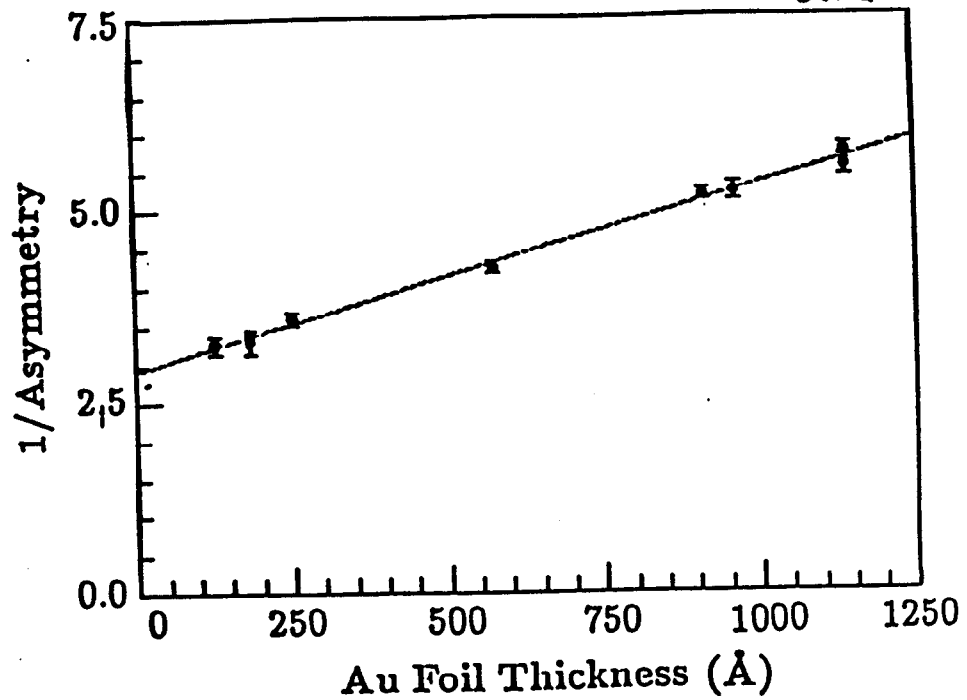
STP#2



< Correction of Multiple Scattering in Au foil >

Figure 2.

STP#2



# Polarized Electron Source for JLC

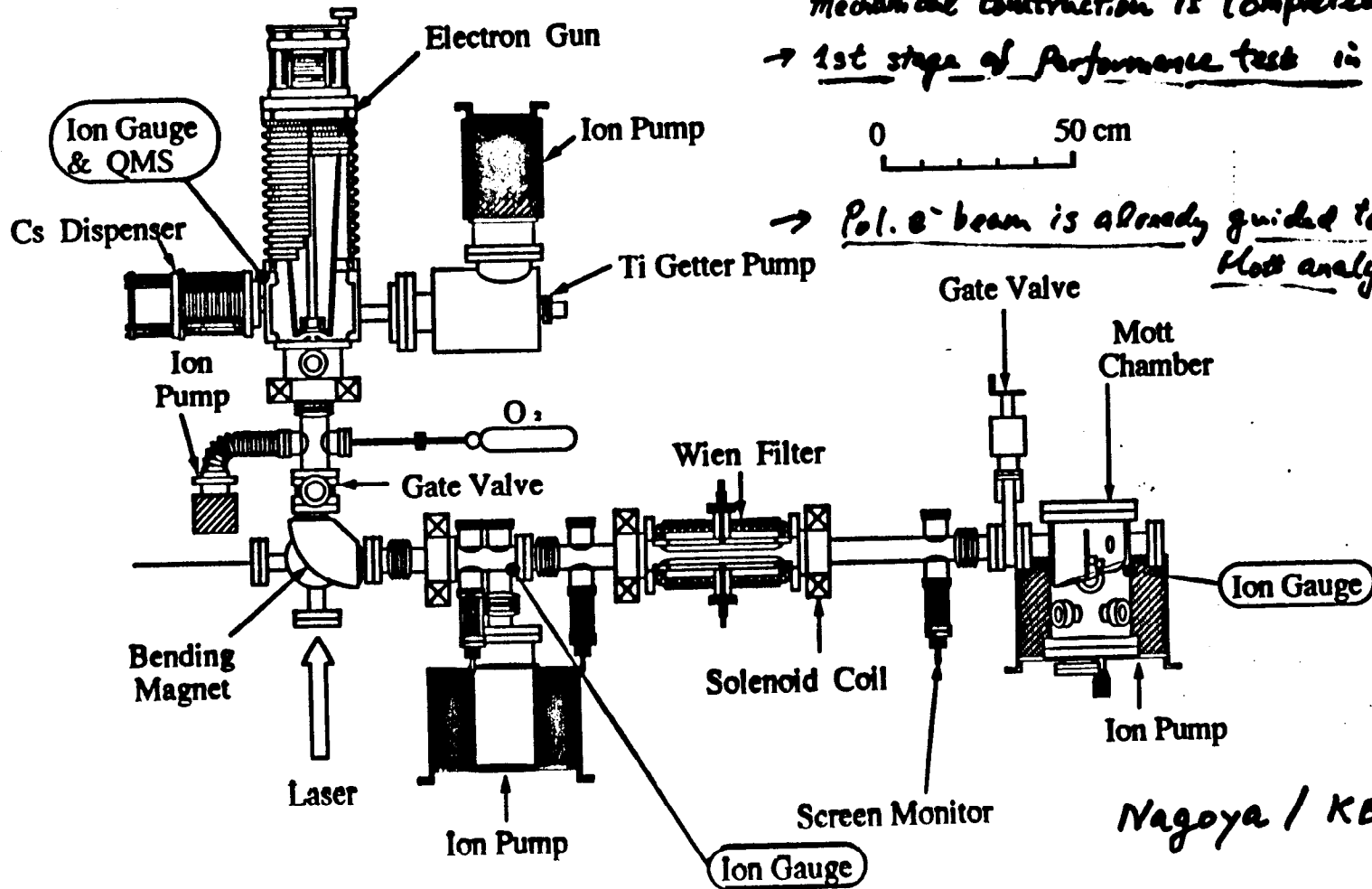
*mechanical construction is completed.*

*→ 1st stage of performance test in progress.*

0 50 cm

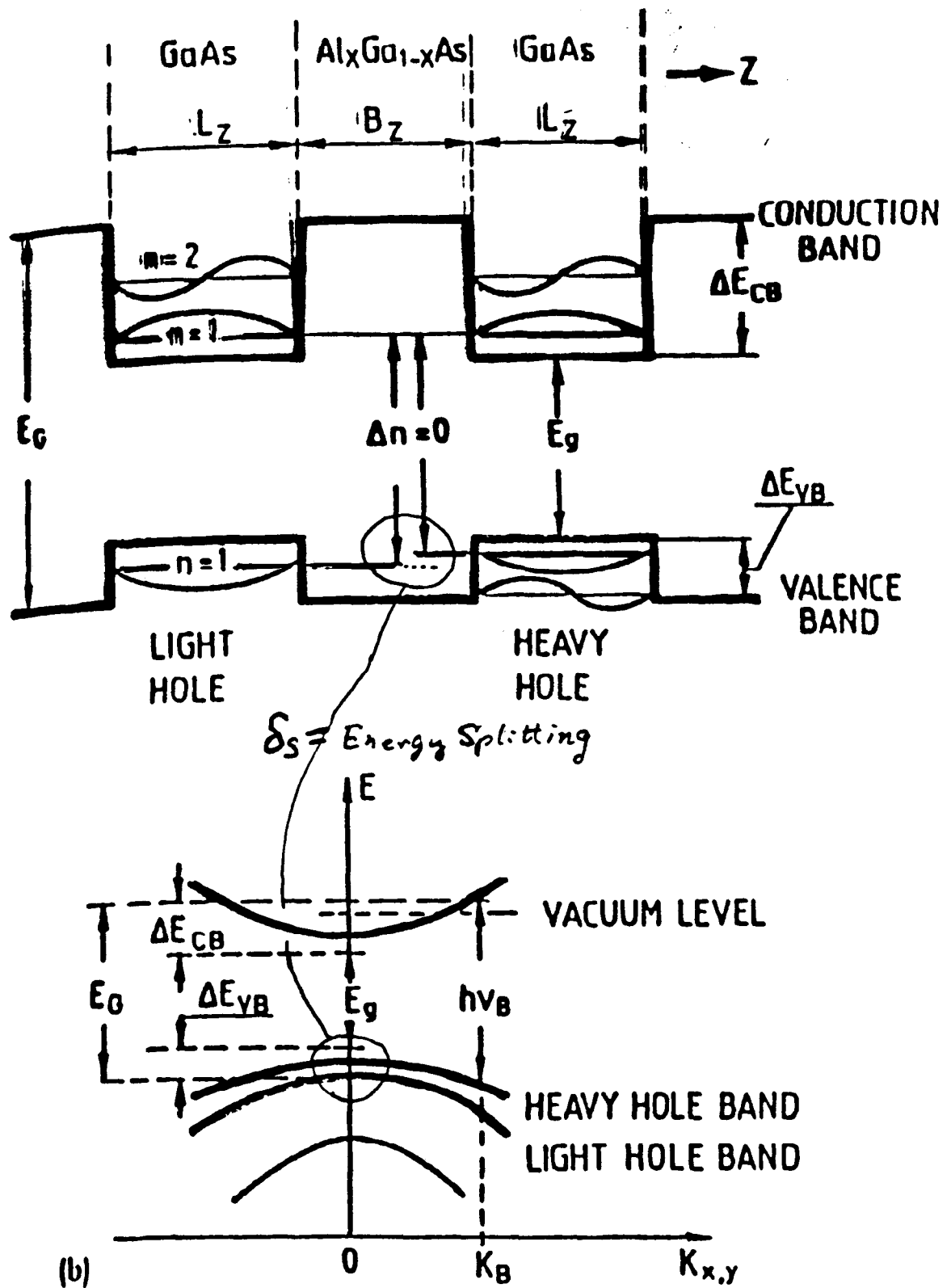


*→ Pol. e<sup>-</sup> beam is already guided to Mott analyzer.*



*Nagoya / KEK*

# Higher Polarization by Superlattice



Past experimental results<sup>\*)</sup> didn't exceed the limit of 50%, due to the depolarizations before electrons can escape to the vacuum.

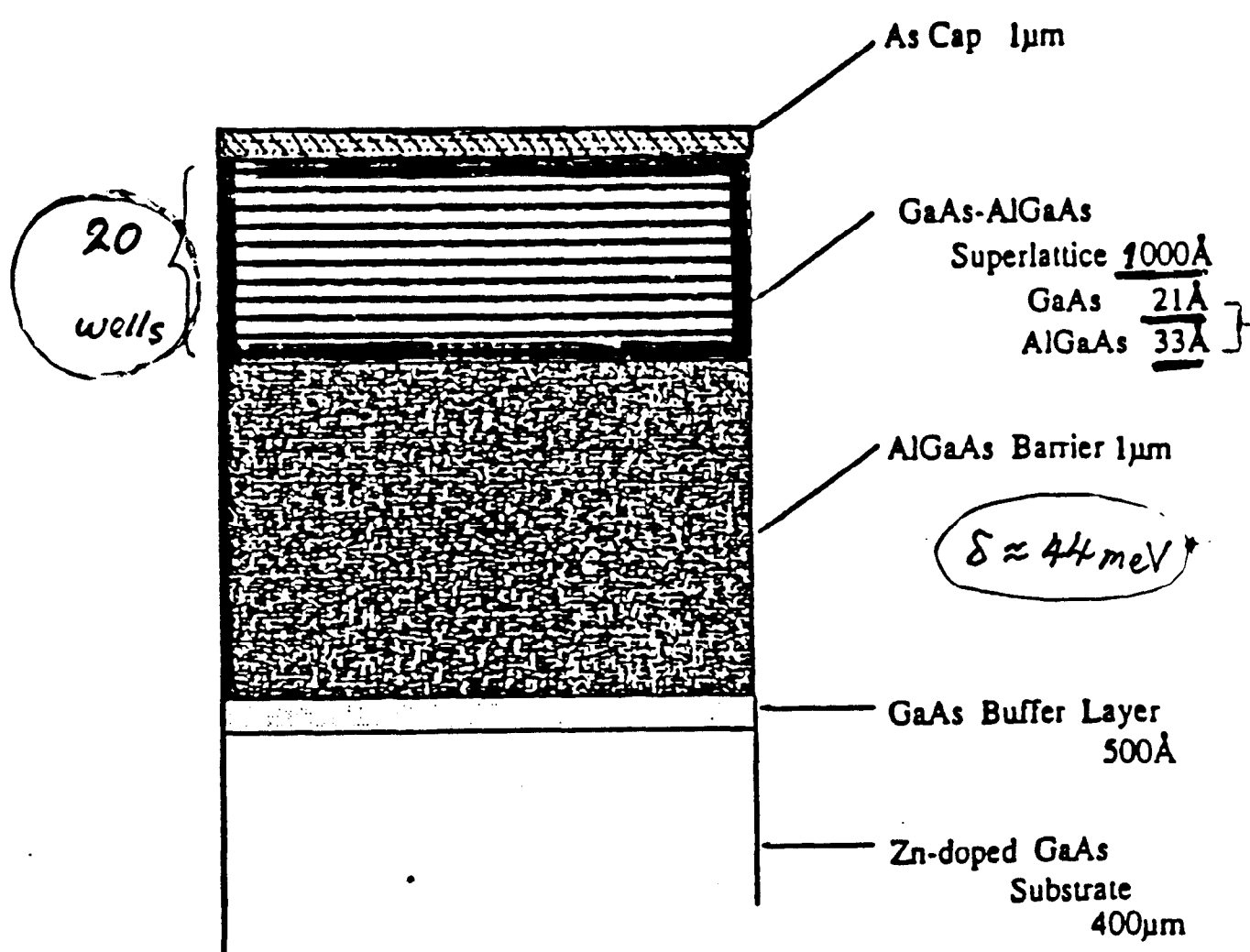
\*) S.F. Alvarado et.al: *Appl. Phys. Lett.* 39 (8) 615-617



As (-2 $\mu$ m, for surface passivation)
Be-doped AlGaAs-GaAs Superlattice (0.1 $\mu$ m) Be-GaAs (19.8 $\text{\AA}$ : 7 monolayers, $p=6.2 \times 10^{18}/\text{cm}^3$ ) Be-Al <sub>0.35</sub> Ga <sub>0.65</sub> As (31.1 $\text{\AA}$ : 11 monolayers, $p=4.0 \times 10^{18}/\text{cm}^3$ )
Be-doped Al <sub>0.35</sub> Ga <sub>0.65</sub> As (1 $\mu$ m, $p=5.0 \times 10^{18}/\text{cm}^3$ , for barrier)
Be-doped GaAs buffer layer (500 $\text{\AA}$ , $p=7.7 \times 10^{18}/\text{cm}^3$ )
Zn-doped GaAs Substrate (400 $\mu$ m, $p=2.0 \times 10^{19}/\text{cm}^3$ , orientation:(100))

As

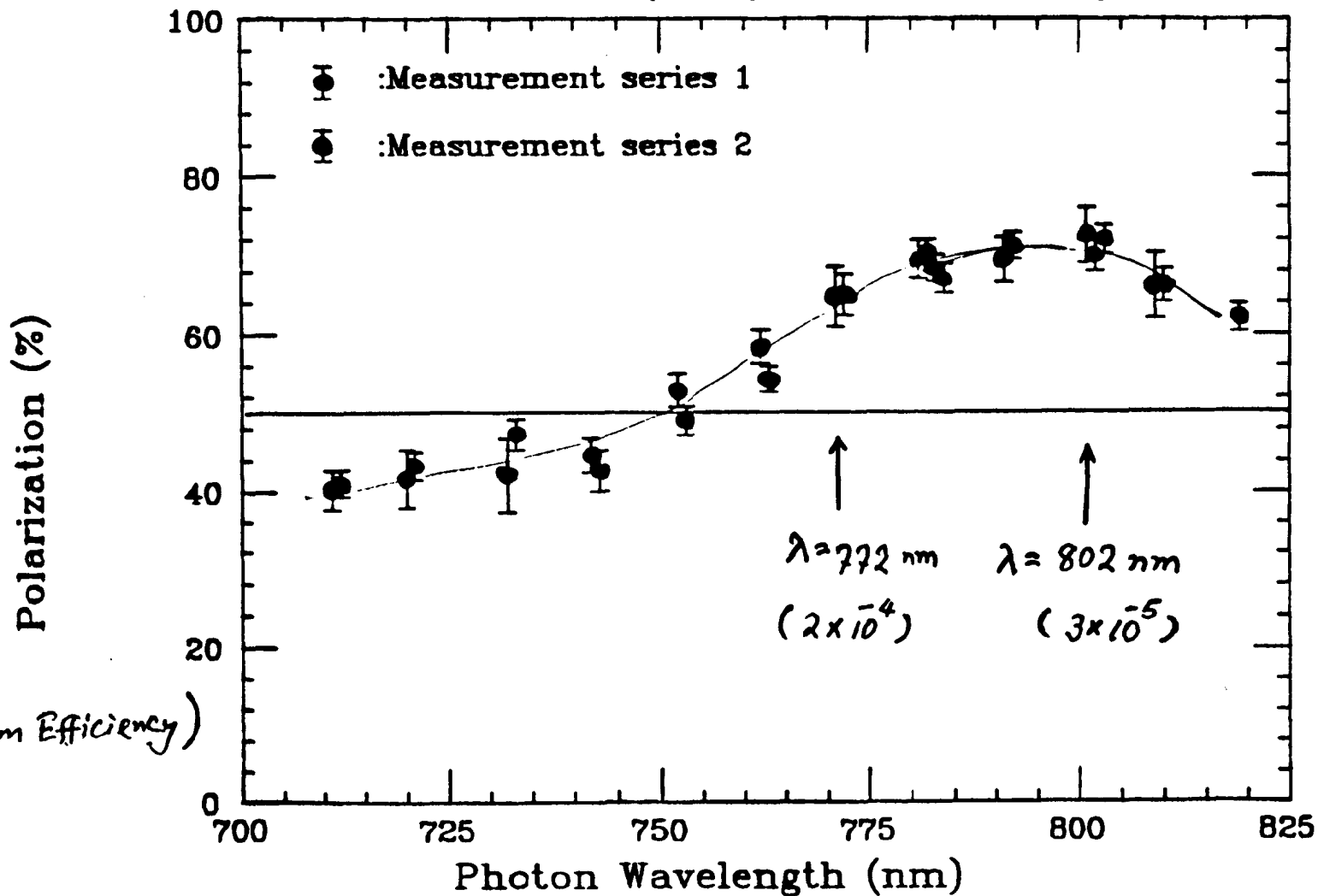
SL



Ref. T. Omori et al., Phys. Rev. Lett. 67(91) 3294

Results from SL #3 Sample

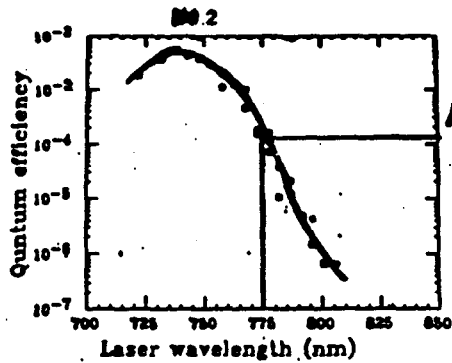
( Those data taken on 19~21. Feb. '91 )



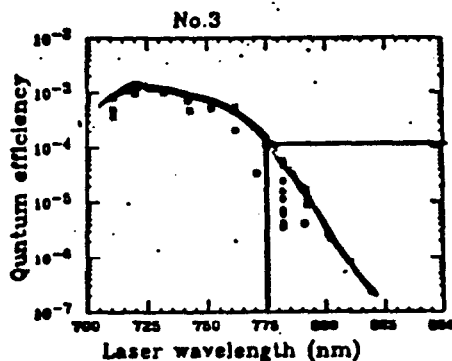
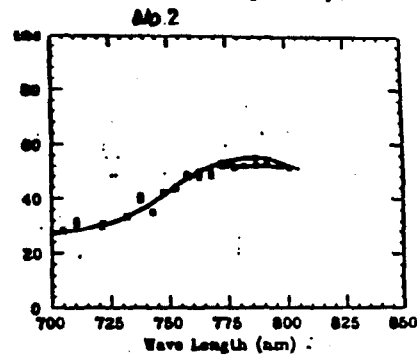
( Typical Quantum Efficiency )

Phys. Rev. Lett 67(1991) 3294-97

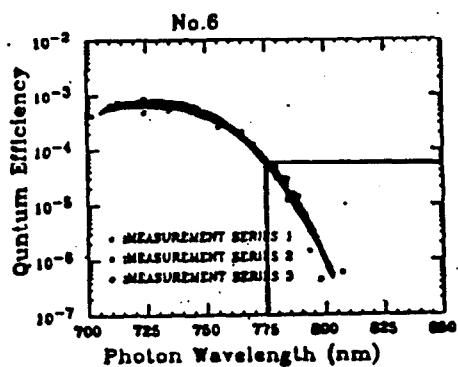
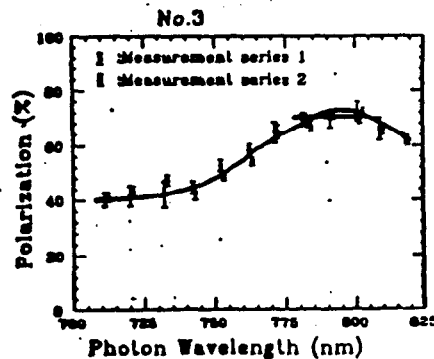
Ref. KEK-Preprint 90-190/DPNU-91-12 (March, '91) ( T. Omori, Y. Kurihara, T. Nakanishi et.al )



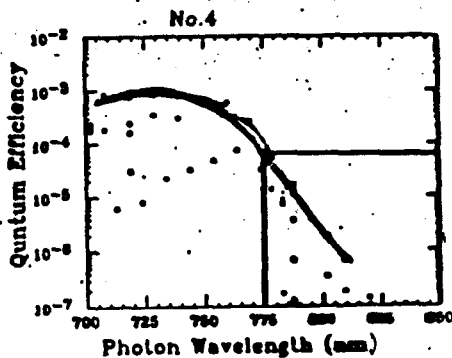
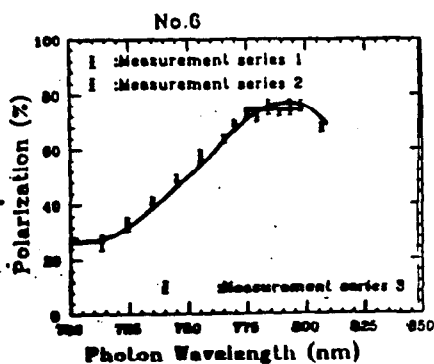
# 4  
 $1.5 \times 10^{-2}$   
 $0.4 \mu\text{m}$   
51.0%



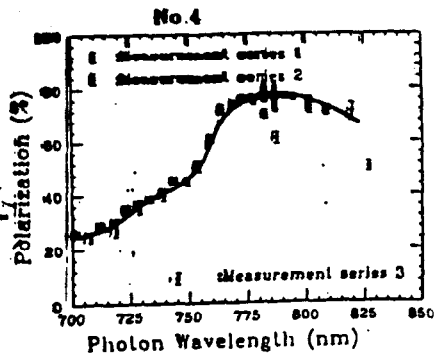
# 2  
 $0.1 \mu\text{m}$   
69.9%  
 $1.2 \times 10^{-2}$

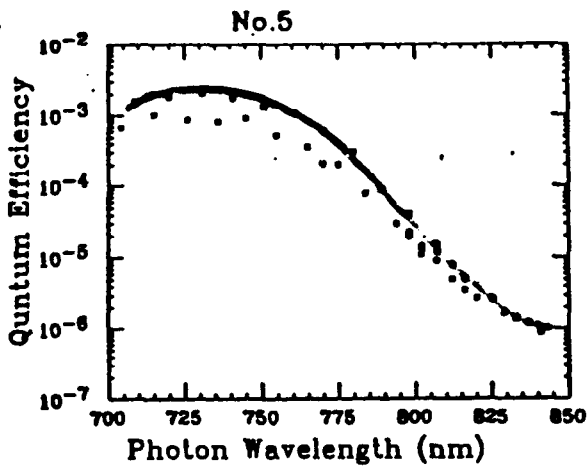


# 3  
 $0.05 \mu\text{m}$   
73.9%  
 $6 \times 10^{-5}$

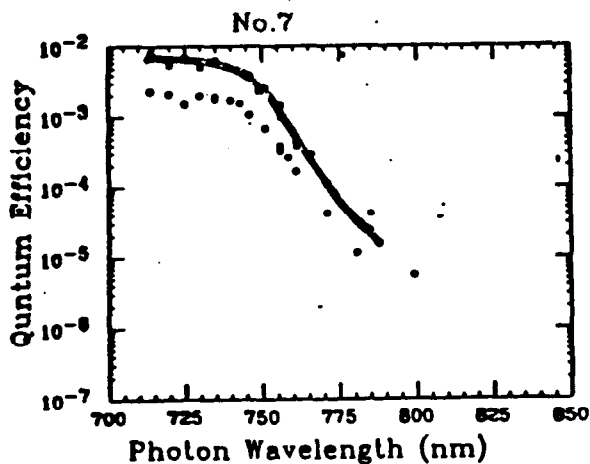
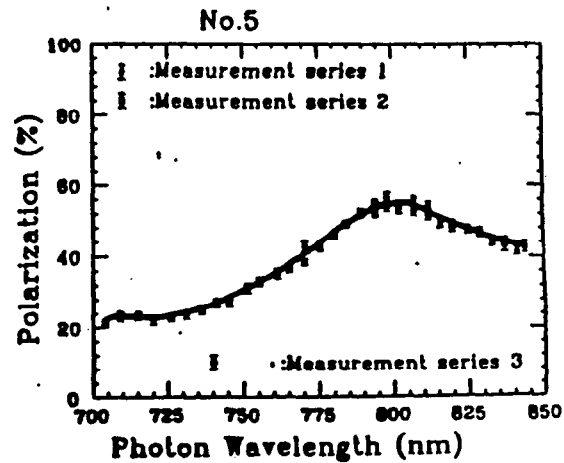


# 4  
 $6 \times 10^{-5}$   
 $0.1 \mu\text{m}$   
74.8%  
 $1.7 \times 10^{-2}$

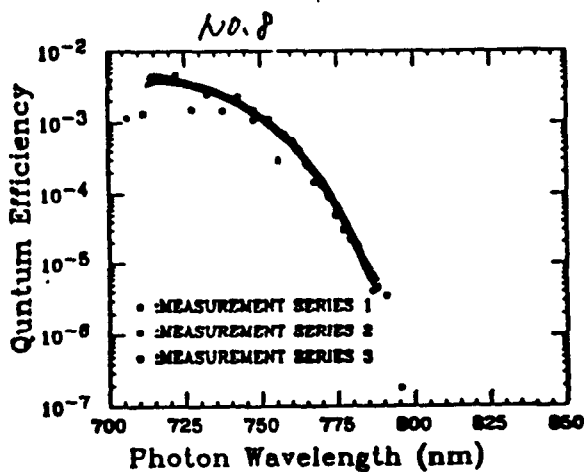
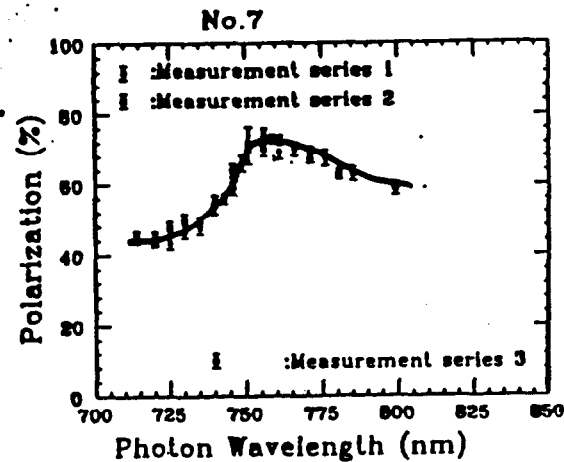




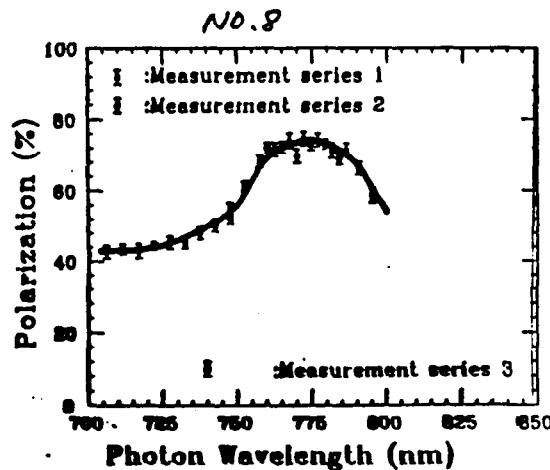
#5  
高純度  
0.1μm  
55%  
 $3 \times 10^{-5}$



#6  
高純度  
0.1μm  
71%  
 $2 \times 10^{-3}$



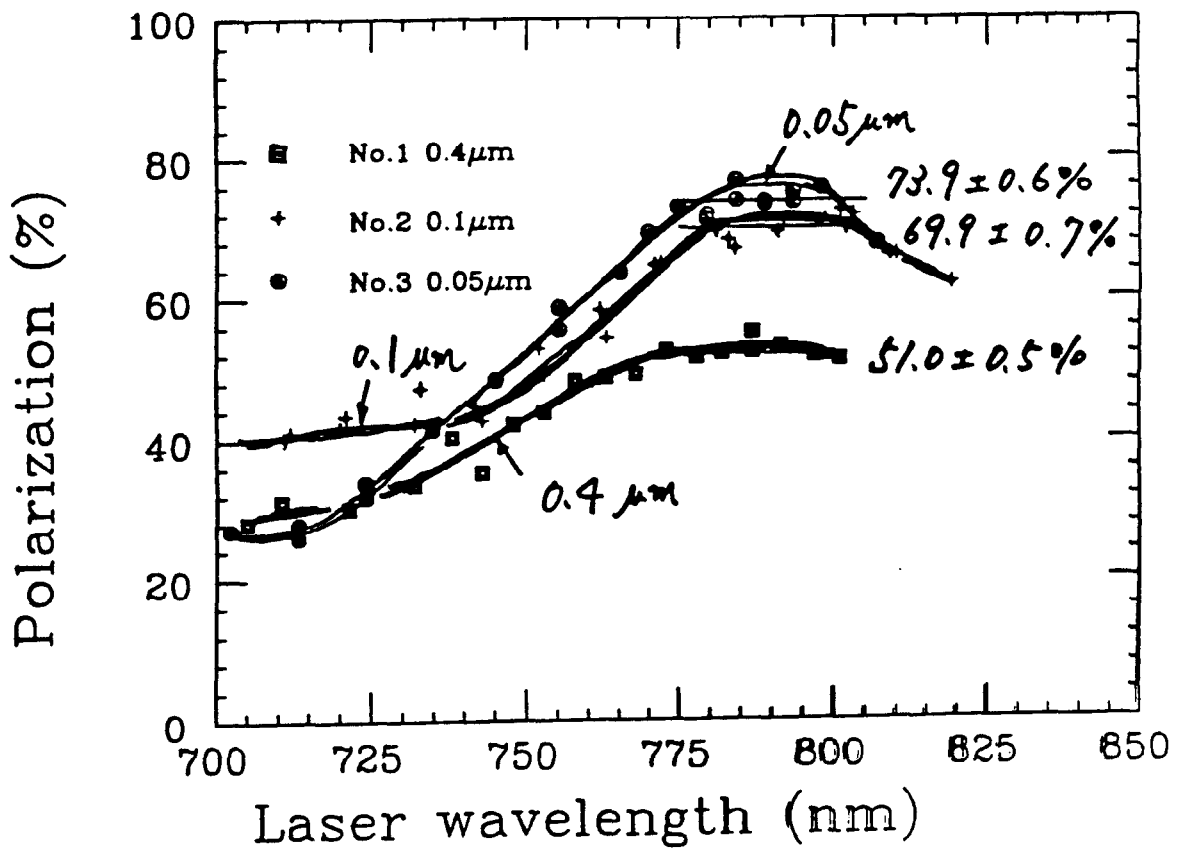
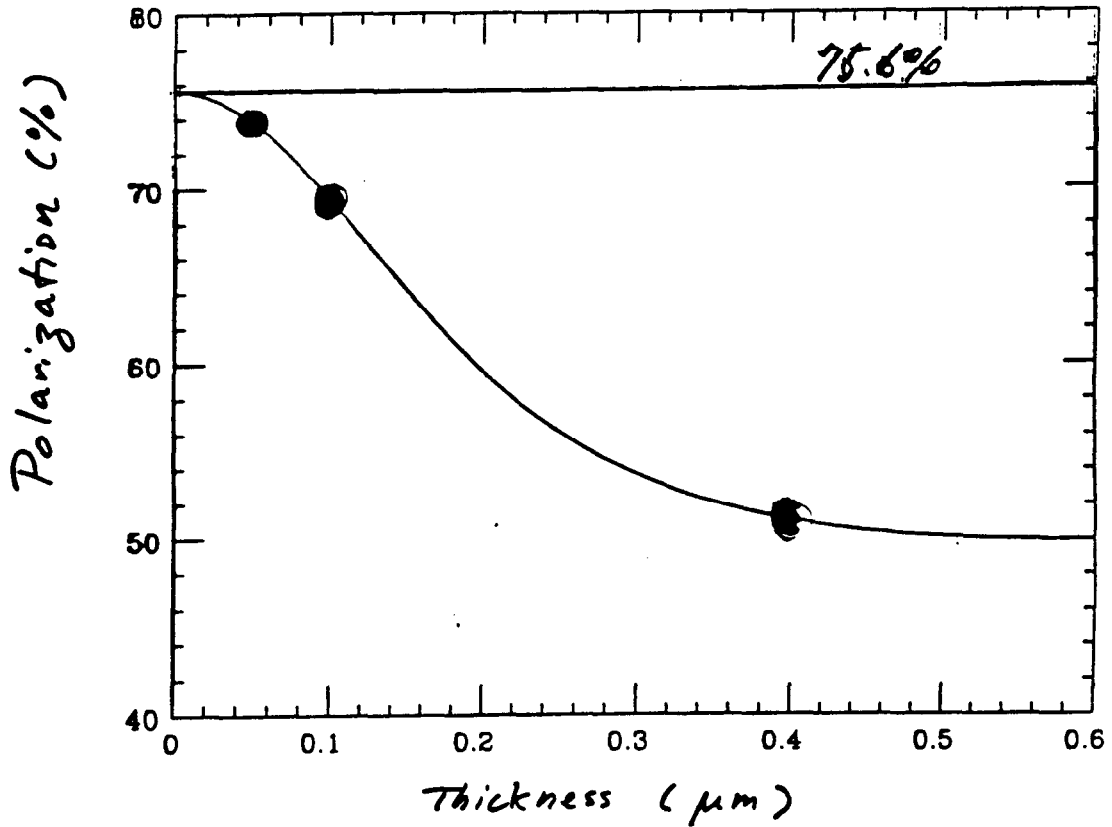
#7  
高純度  
0.1μm  
74%  
 $1.4 \times 10^{-4}$



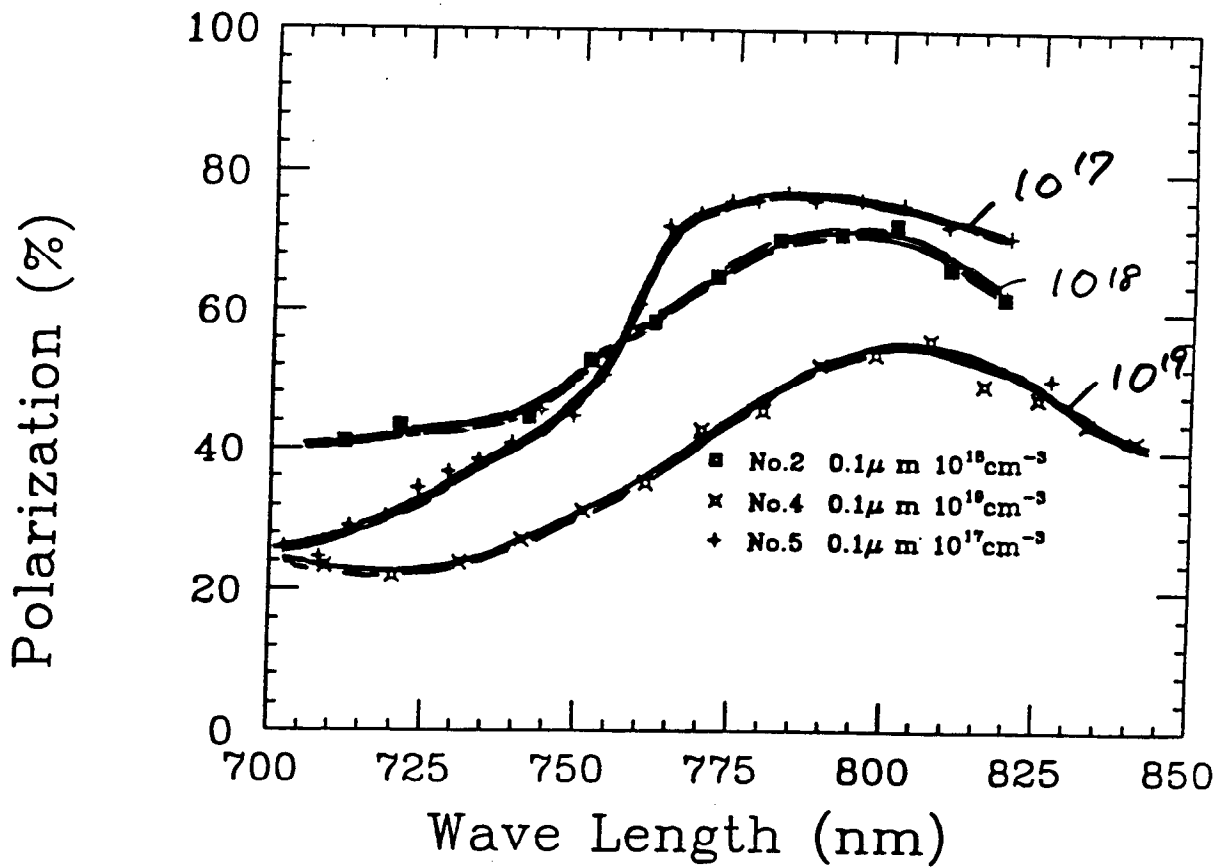
KEK/NGOYA/NE

ref. Y. Kurihara et al., NIMA 313 (92) 393

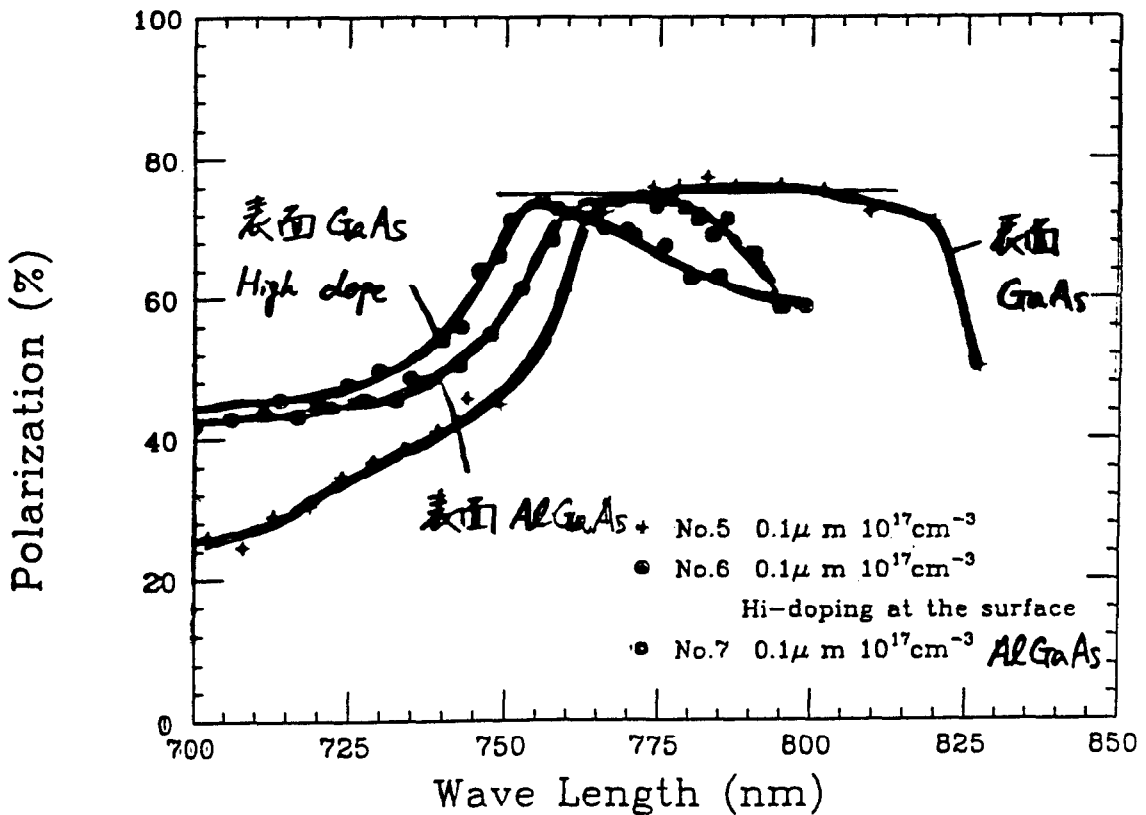
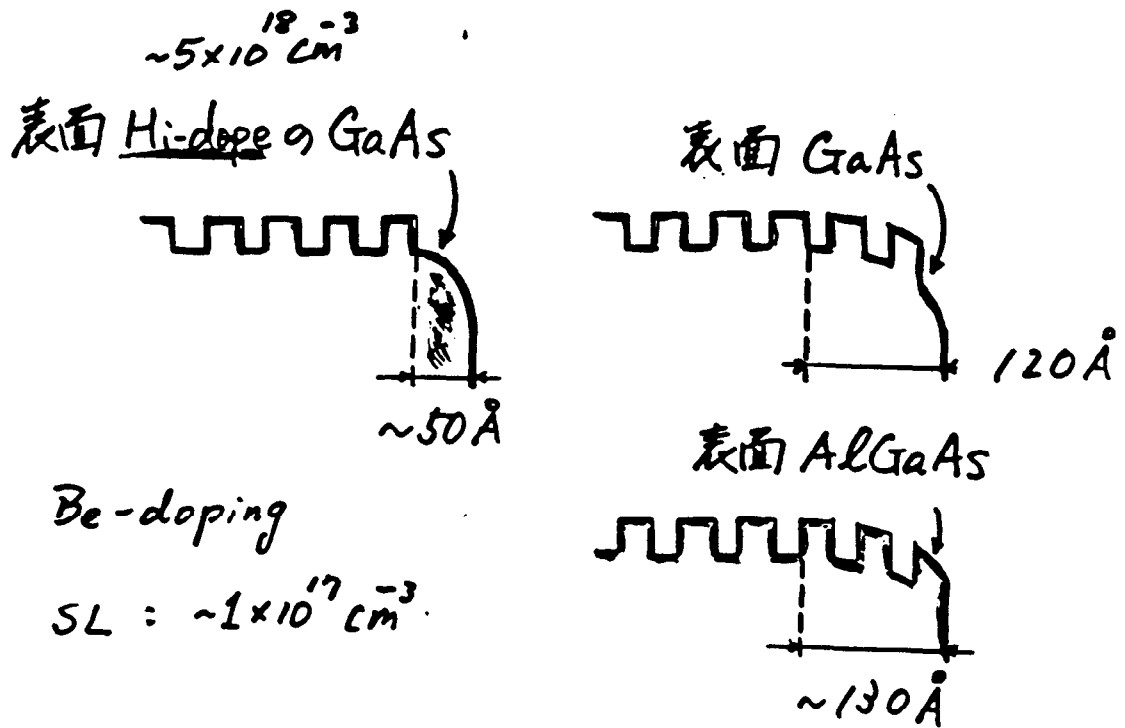
# Polarization dependence on SL thickness



Polarization v.s. P-doping

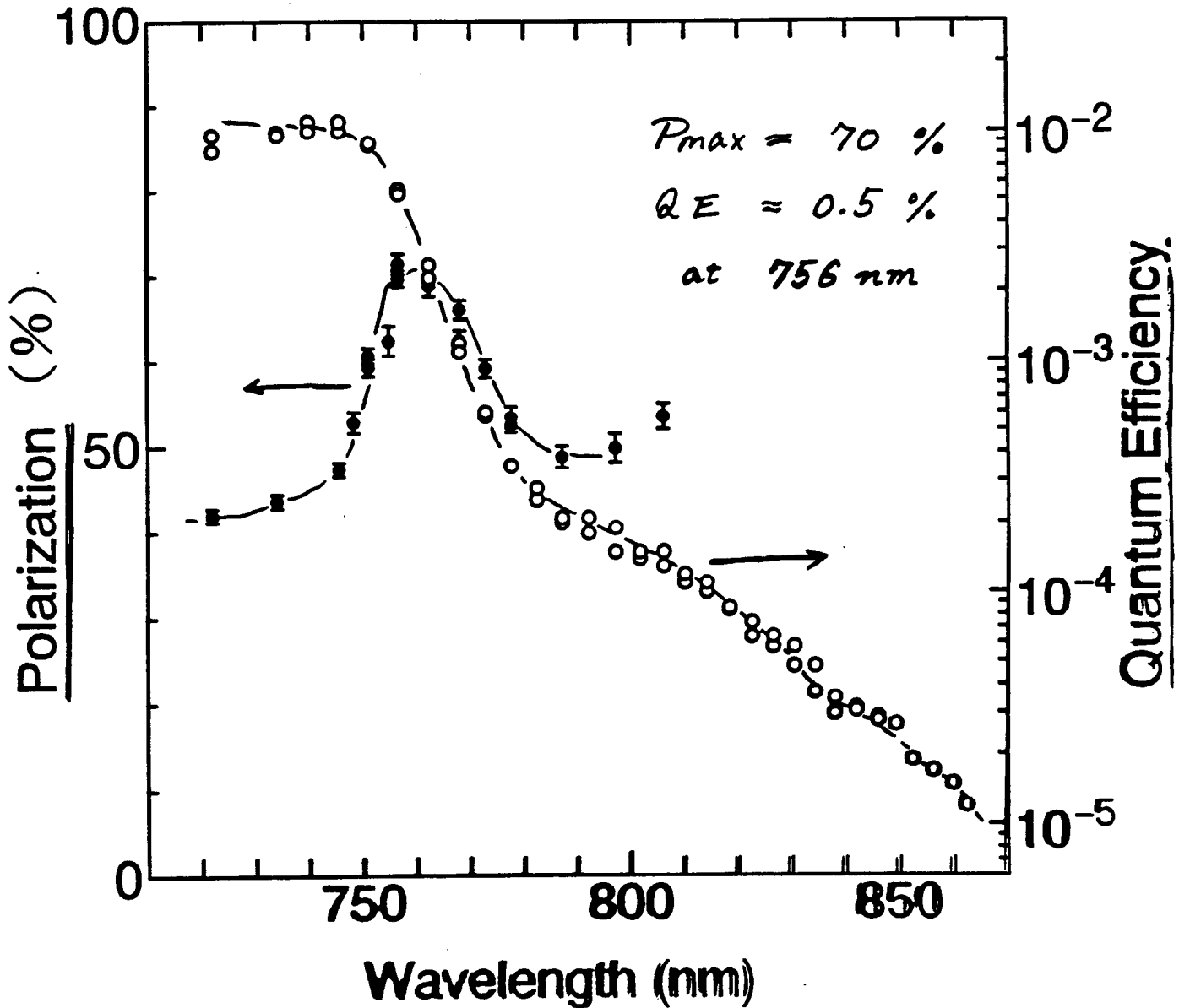
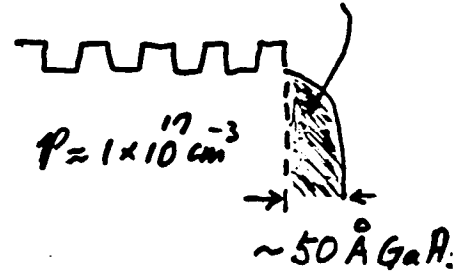


# Polarization v.s. Surface structure



High Q.E. SL

$P = 5 \times 10^{18} \text{ cm}^{-3}$



\* This sample is waiting the test of charge limitation by a SLAC Gun



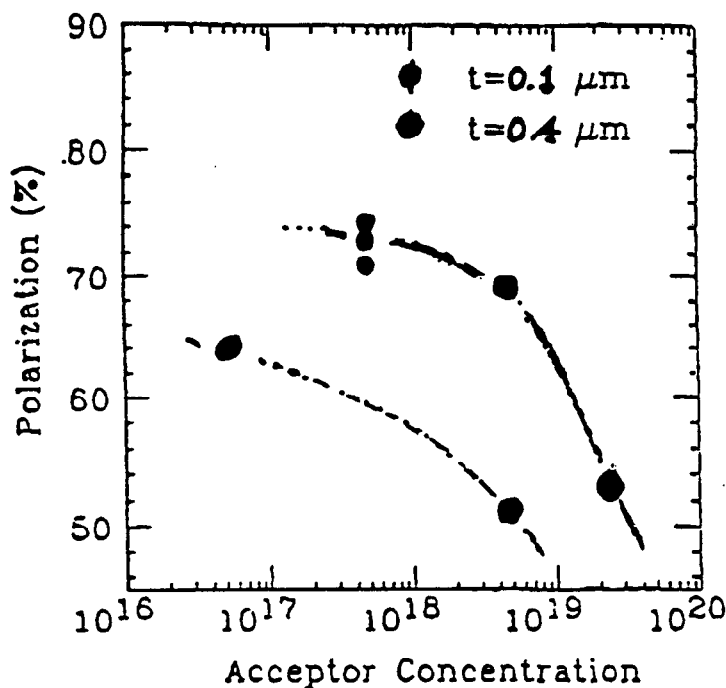
(2) Superlattice Photocathode

- { max. Pol.  $\approx 75\%$  0.5% } attained!  
 { Pol.  $\geq 70\%$  with Q.E.  $\geq 0.2\%$  }

Research toward higher Pol. and Q.E. are continued.

→ "Lower P-dopant concentration is effective to reduce the depolarization inside the superlattice"

The polarization as a function of the dopant concentration.



(3) Construction of Operational Pol. e<sup>-</sup> source

Proto types are being build at KEK and Nagoya.

A new structure gun is also planned.

(4) Feasibility study of Pol. e<sup>-</sup> RF Gun just starts

with a collaboration between KEK and SLAC.

(5) . . . . .

R/D of Strained GaAs at Nagoya

'87.10 Start the study motivated by  
Horinaka's experiments

'88.9 The 8th HE Spin Physics Symposium  
at Minneapolis (Spin-88)

'90.3 LC-90 at KEK  
Design Criteria for Strained GaAs  
(T. Nakanishi et al DPNU-90-16)

'90.9 The 8th HE Spin Physics Symposium at Bonn (Spin-90)

'90.10 STP#1  $P \sim 40\%$

'91.4 STP#2  $P \sim 86\%$   
(T. Nakanishi et al. Phys. Lett A 158 (1991) 345-349)

# Photoluminescence Measurement

by Osaka Pref. Univ. Group

Morinaka et al. *Jap. J. Appl. Phys.* 27 (1972)

765-770

check of the System by GaAs / InP

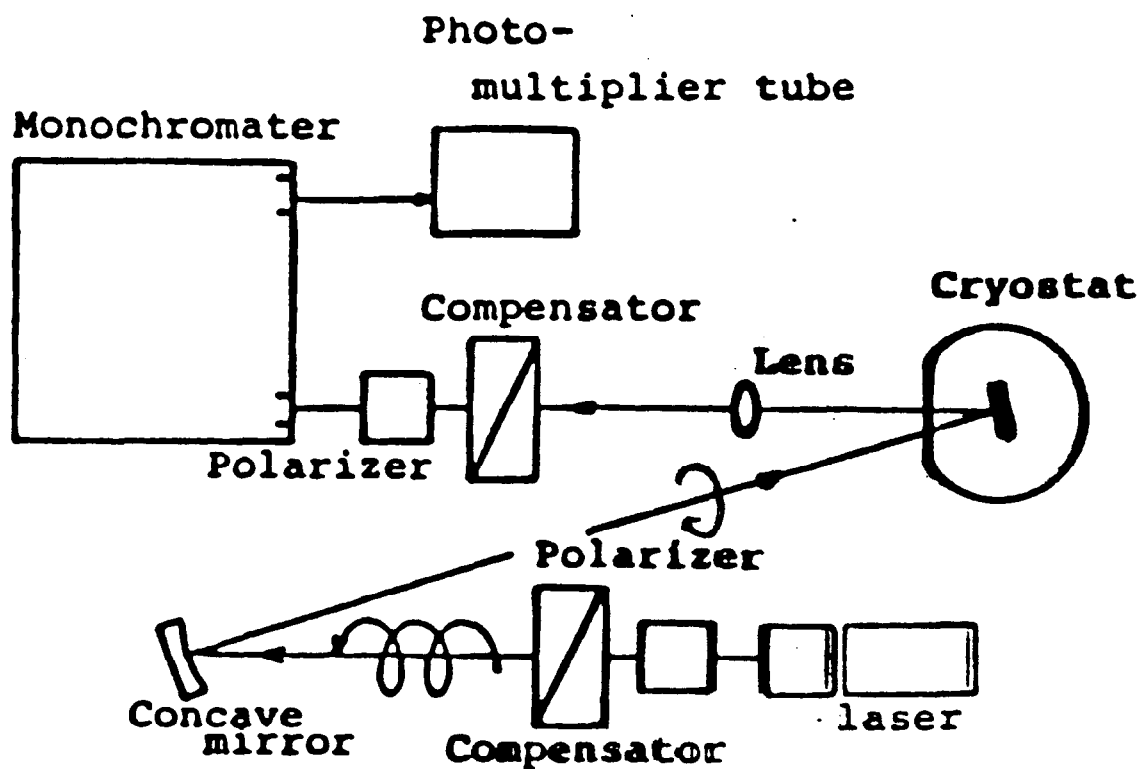
⇒ Pol ≈ 20% at 77K with good reproducibility

ref.  $P_{\text{lumi.}} = 0.25 \frac{T}{\tau + T} P_e$  for Zinc-Blend crystals

$T$ : spin relax. time

$\tau$ : life time

if  $\tau \ll T$   
 $P_{\text{lumi.}} = 0.25 P_e$



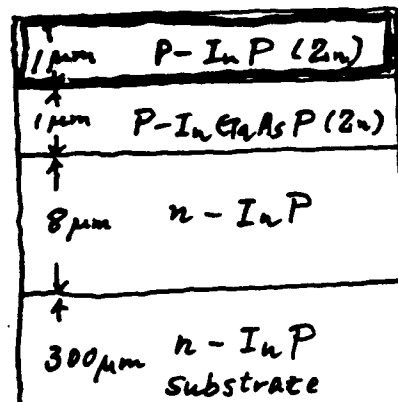
b) Osaka Pref. Univ.

Horinaka's experiment

lattice mismatch  $\approx 0.3\%$



$\delta_s \approx 20 \text{ meV}$

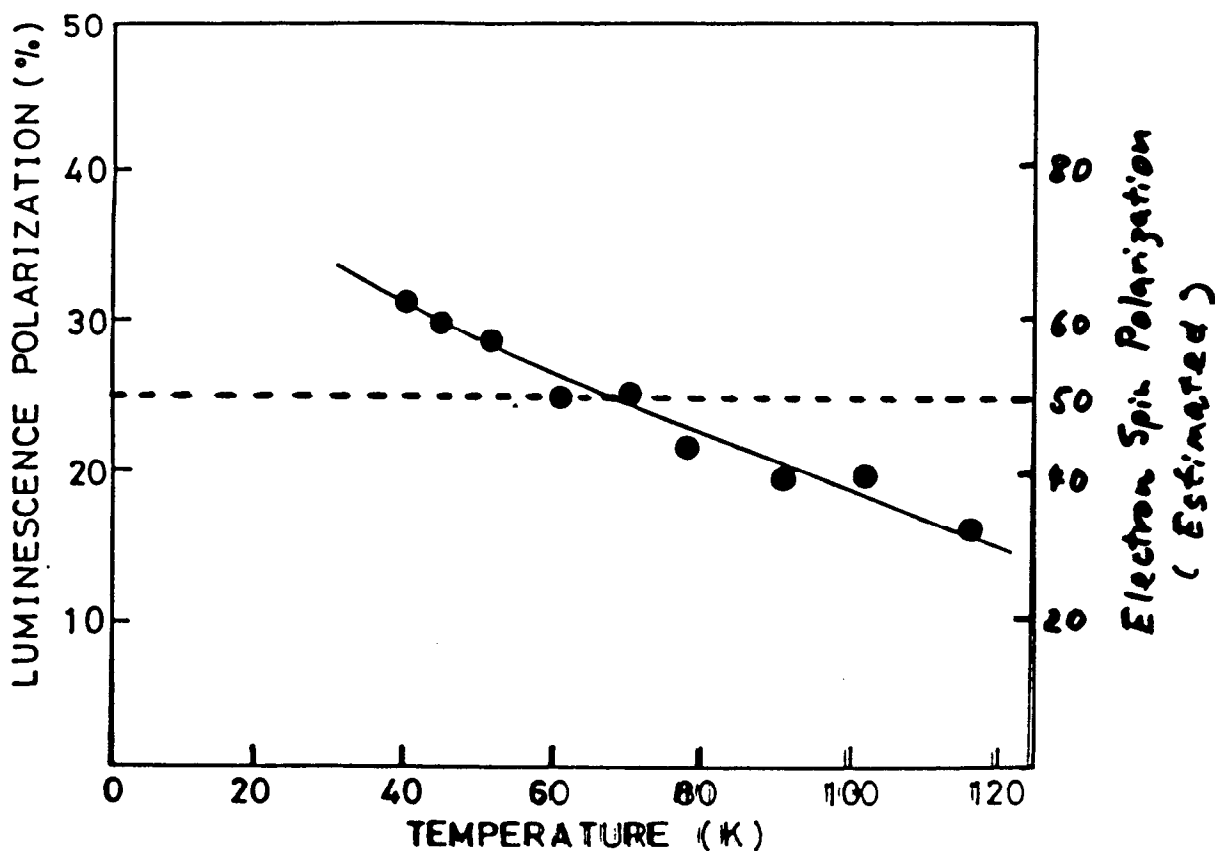


Effect of Stress was observed !!

$P_{\text{lumi}} \geq 25\%$  below 70K



$P_e \geq 50\%$  ( $\sim 60\%$  at  $\sim 40\text{K}$ )



6. Temperature dependence of luminescence polarization due to the interband transition in the strained InP layer.

Horinaka et al., Japan J. Appl. Phys. 27(88) 765

**Strained GaAs layer  
with  
a lattice-mismatch heterojunction**

**: A candidate for a highly spin-polarized electron source**

**Tsutomu NAKANISHI, Shinsuke NAKAMURA, Hideki AOYAGI**

**Shoji OKUMI, Naoaki HORIKAWA**

*Dept. of Physics, Nagoya Univ., Nagoya-464, Japan*

**Hiromichi HORINAKA**

*College of Engineering, Osaka Prefecture Univ., Sakai-591, Japan*

**Yoshihiro KAMIYA**

*Toyota Tech. Inst., Nagoya-468, Japan*

**Toshihiro KATO and Takashi SAKA**

*New Materials Res. Lab., Daido Steel Co. Ltd, Nagoya-457, Japan*

*reported at LC-90 (April 1990 at KEK)*

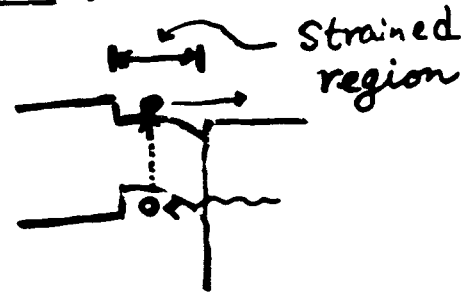
# Design Criteria of Strained Cathodes

[I] NEA must be possible.

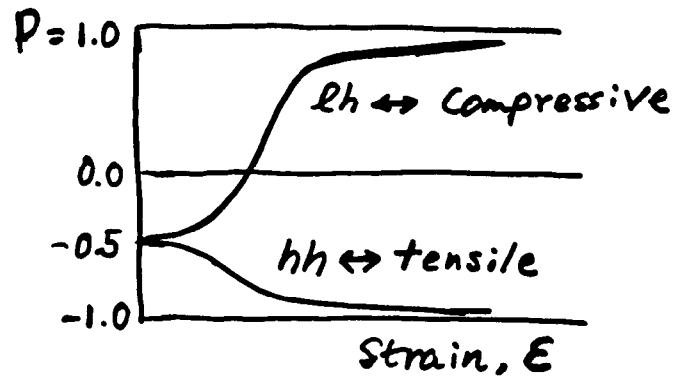
$$a(\text{epi layer}) < a_0(\text{buffer})$$

[II] Tensile strain is favorable, since

1) band gap relation



2) Polarization behavior



[III] Energy Splitting must be enough large.

$$\delta_s \approx 6.5 E \text{ (eV)}$$

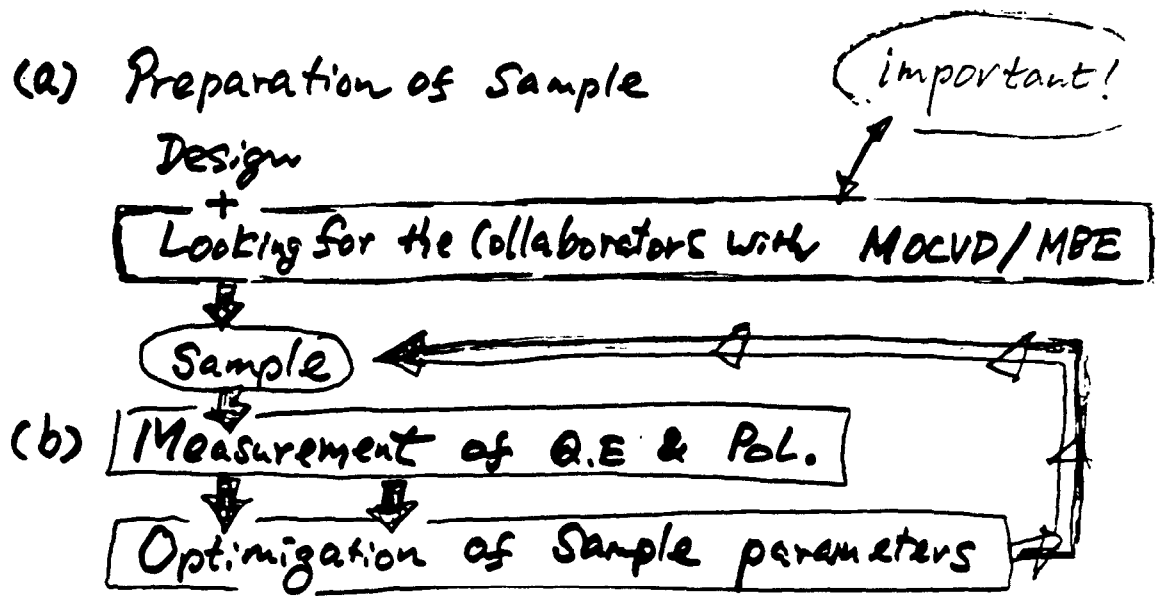
ex.  $\delta_s \approx 40 \text{ meV}$  for  $E \approx 0.6\%$

[IV] Strained layer must be not so thick.

Critical thickness limitation  
for strain relaxation

ex.  $t_c \approx 200 \text{ \AA}$  for  $E \approx 0.6\%$

ref. T. Nakanishi et al DPNU-90-16 (unpublished) (March 1990)



(c) Check of strain by another means

- X-ray diffraction
- Surface inspection
- Photoluminescence

(d) Feasibility as a practical photocathode

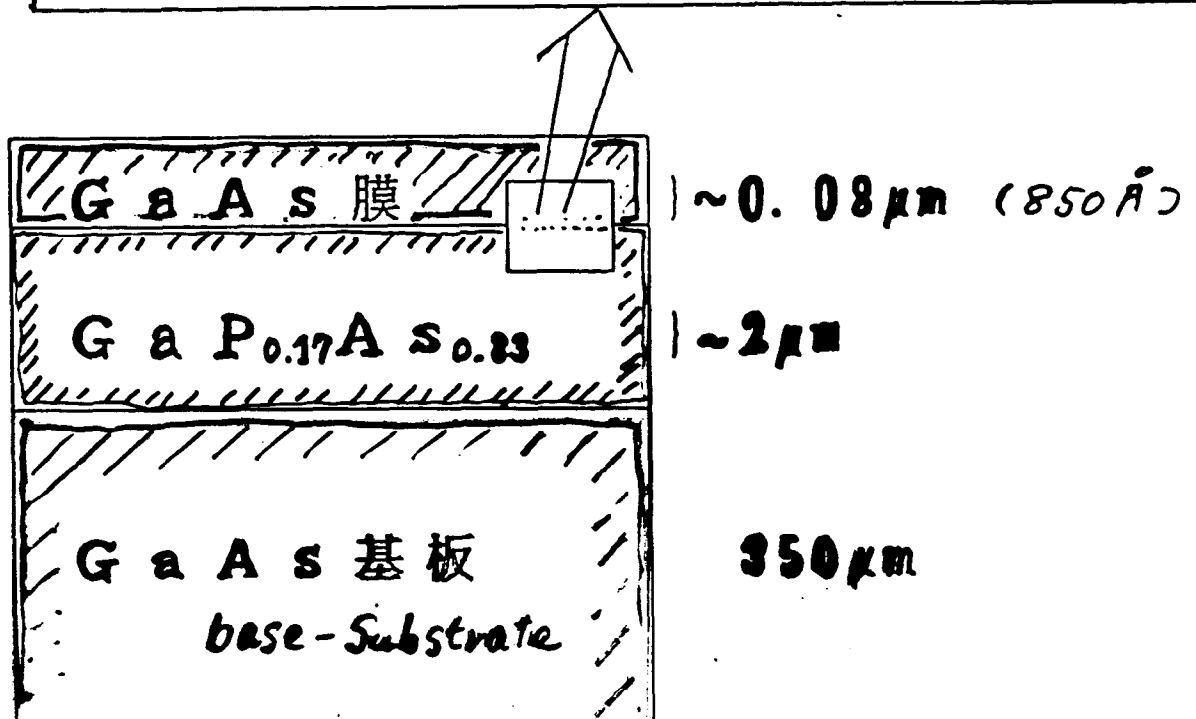
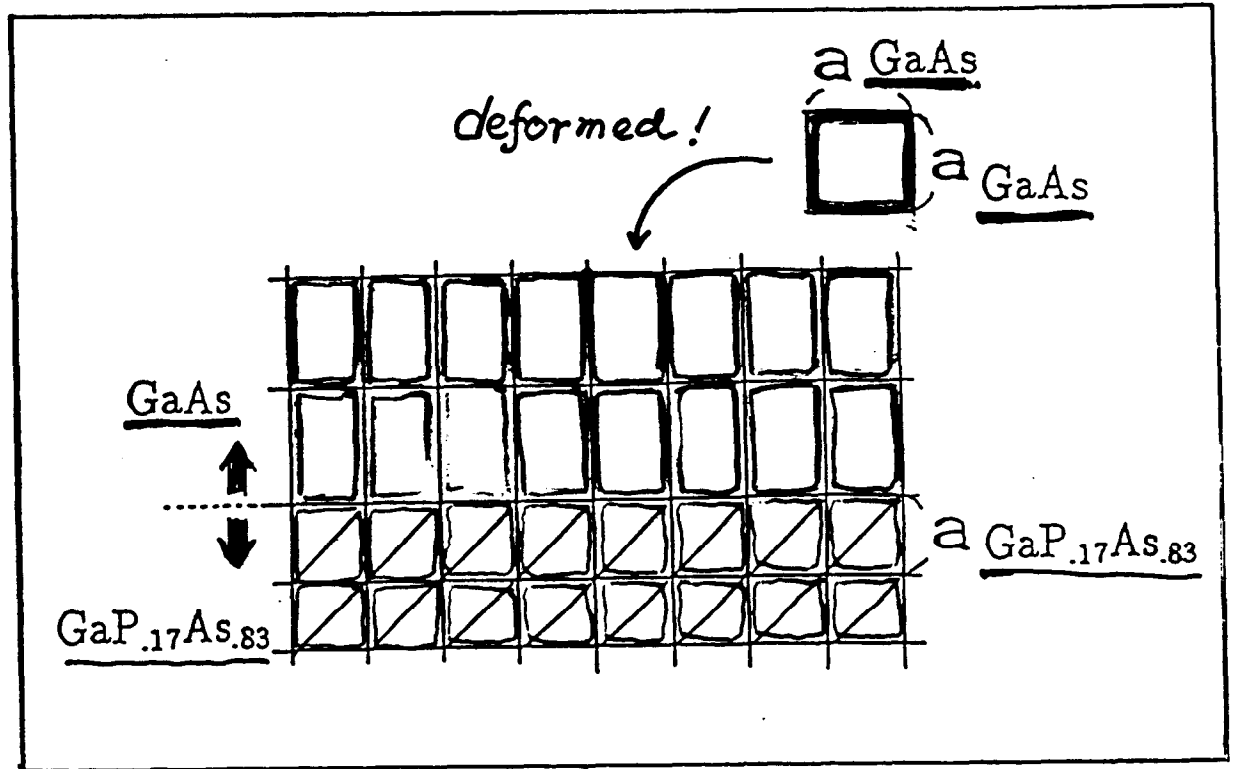
- Toughness of strain
- Surface degradation during storage
- Tuning for the wavelength of LASER



Test by Practical PES

# Sample Structure of Strained GaAs #2

(First Successful sample for strained GaAs)



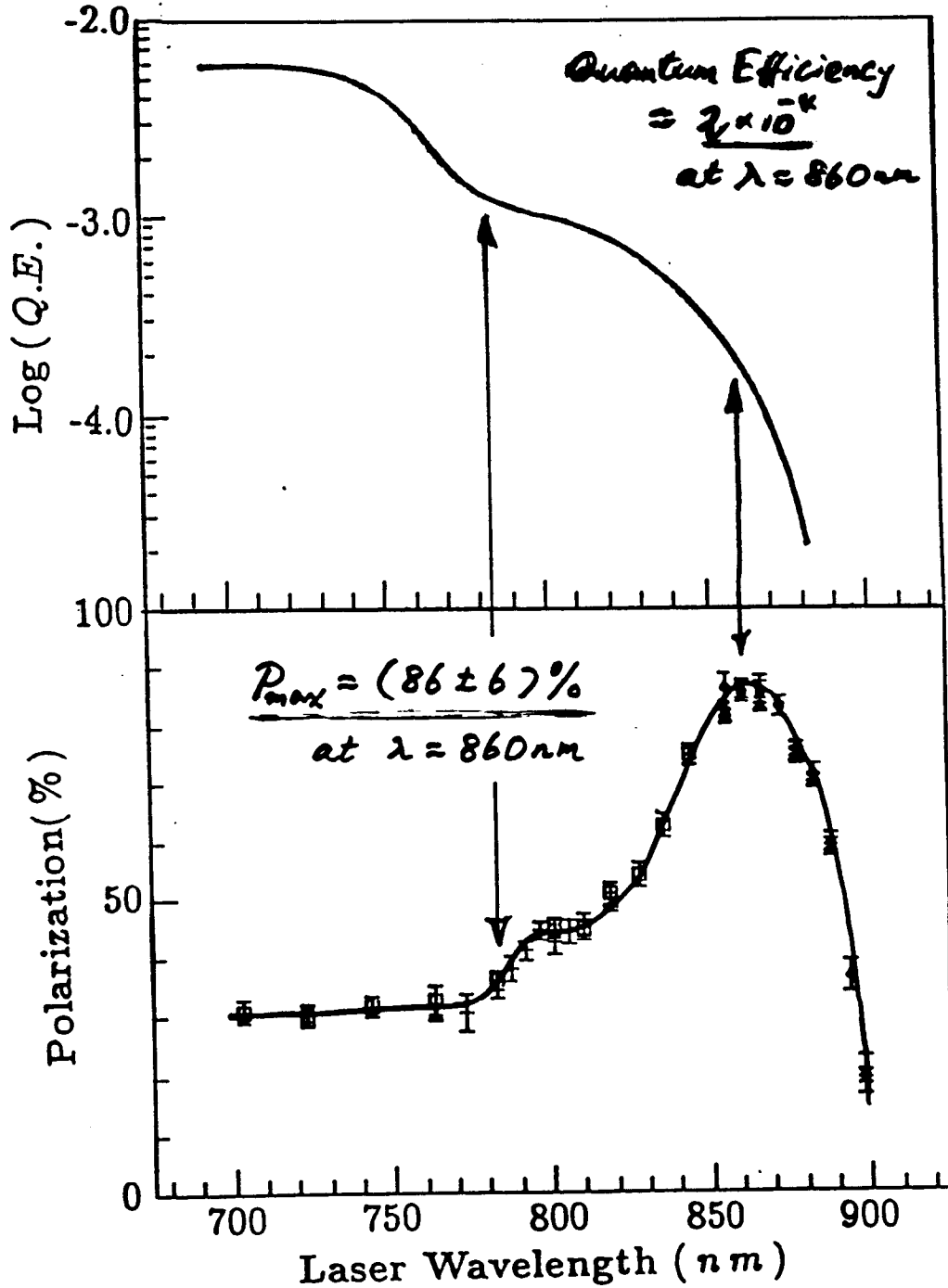
made by  
MOCVD  
apparatus

Ref. T. Nakanishi et al.,  
Phys Lett A 158(01)345



# Strained GaAs/GaP<sub>0.10</sub>As<sub>0.83</sub>

[ thickness of GaAs layer = 800 Å  
a/a = 0.6% →  $\delta_s = 40$  meV ]



Ref: T Nakanishi et al: Phys. Letts A158(1991) 345-349

# Reasons of Poor QE for strained PC Compared with bulk GaAs PC

- ① Single hh (or lh) excitation
- ② Limited thickness of GaAs layer due to strain relaxation



We took two kinds of experimental data :

- 1) Residual Strain/ Lattice mismatch  
vs  
GaAs layer thickness/ Critical thickness
- 2) Strain dependence of  
attained Polarization

with 7 samples having  
different lattice mismatch ( $\epsilon$ )  
and GaAs thickness ( $t$ )

Variable Parameters

( $t$ ,  $x$ )

variable parameter

Zn-doped GaAs	$t = 850 \sim 3100 \text{ \AA}$
Zn-doped Ga <sub>1-x</sub> P <sub>x</sub> As <sub>1-x</sub> ( $t \approx 2 \mu\text{m}$ )	$x = 17 \sim 33 \%$
Zn-doped GaAs <sub>s</sub> (001) ( $t = 350 \mu\text{m}$ )	

t a b l e 1

Sample Structure of  
Strained GaAs

# Table of examined strain GaAs samples (up to

H. Aoyagi et al : DPNU-92-13 (to be published in

	P fraction ↓	Lattice-mismatch ↓	Residual Strain ↓	Energy splitting ↓	Critical thickness ↓	thickness of GaAs ↓
sample	x (%)	$\epsilon$ (%)	$\epsilon_R$ (%)	$\delta_s$ (meV)	$t_c$ (Å)	t (Å)
1	17	0.61	<u>0.53</u> $\pm 0.02$	34	176	<u>850</u>
2	18	0.64	0.47 $\pm 0.02$	31	164	1400
3	26	0.93	0.45 $\pm 0.08$	29	102	2200
4	33	<u>1.18</u>	0.37 $\pm 0.06$	24	74	2000
5	13	0.46	0.34 $\pm 0.03$	22	247	3100
6	27	<u>0.97</u>	<u>0.80</u> $\pm 0.02$	52	97	<u>850</u>
7	20	0.72	0.48 $\pm 0.02$	31	143	2100

Two dimensional plot  $\epsilon_R/\epsilon$  vs  $t/t_c$

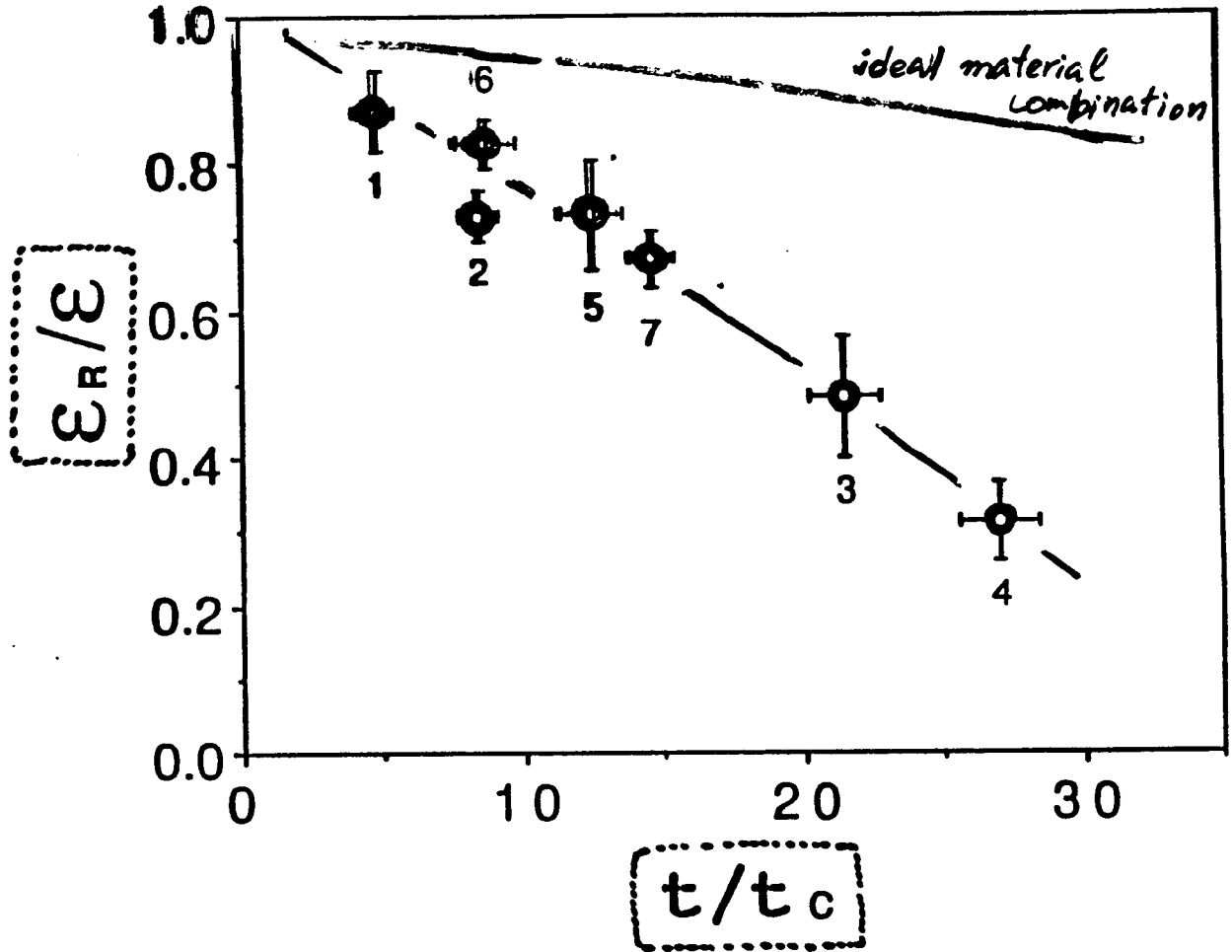


fig. 2

$\underline{t}$  : thickness of GaAs epilayer  
 $\underline{t_c}$  : critical thickness for coherent growth given by Matthews

$\underline{\epsilon_R} = (a_{11} - a) / a$        $\left\{ \begin{array}{l} a: \text{ lattice const. of unstrained GaAs} \\ a_{11}: \text{ " parallel to interface} \end{array} \right.$   
Residual strain  
 $\underline{\epsilon} = (a - a_0) / a_0$        $a_0: \text{ " of GaAs buffer-substrate}$   
lattice mismatch

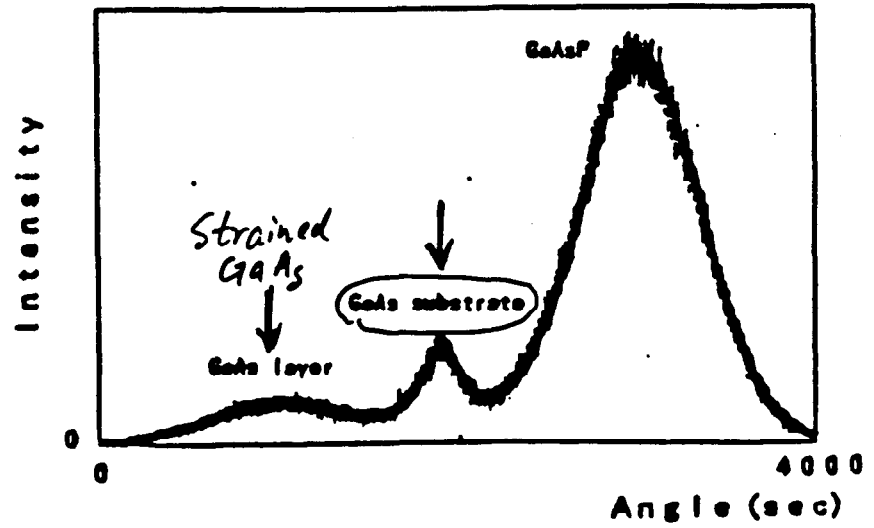
# Strain determination by X-ray diffraction

T. Saka (New material Lab. Daido steel. Co.)

(113)

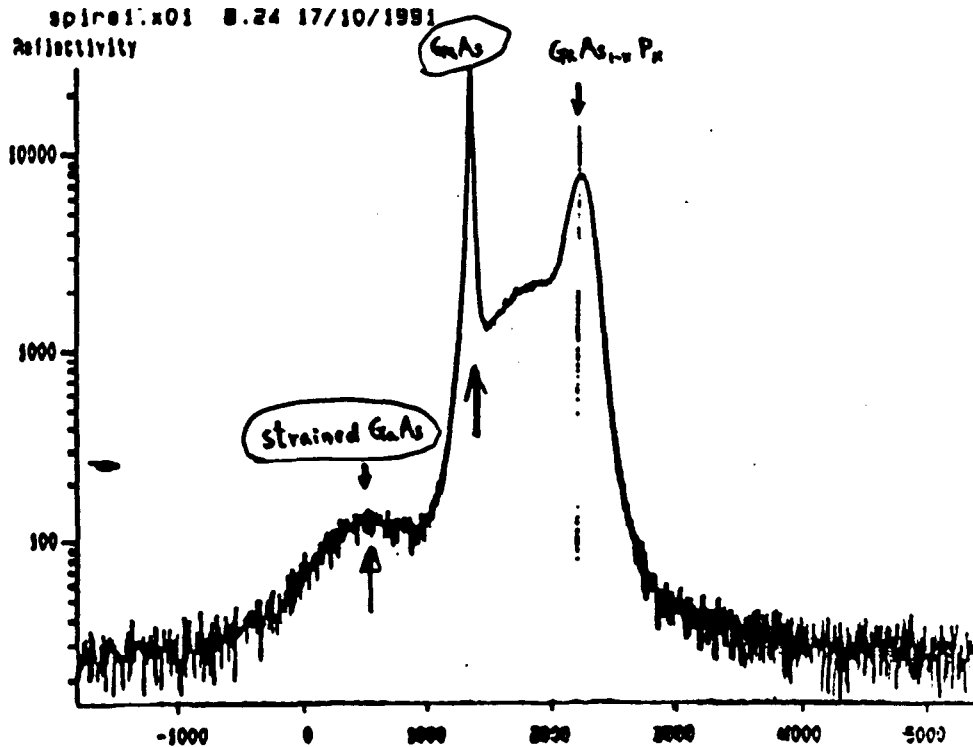
12 kcps

$\alpha = 1.6^\circ$



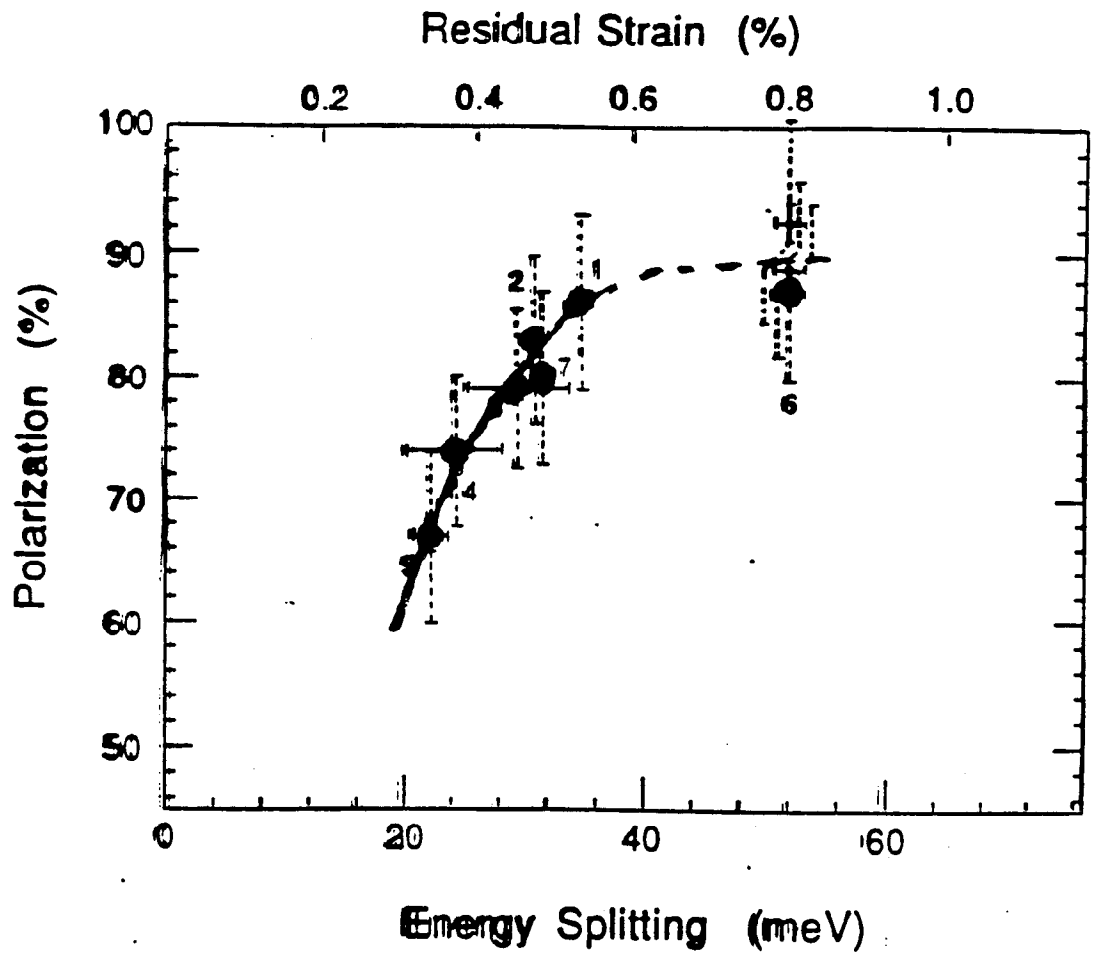
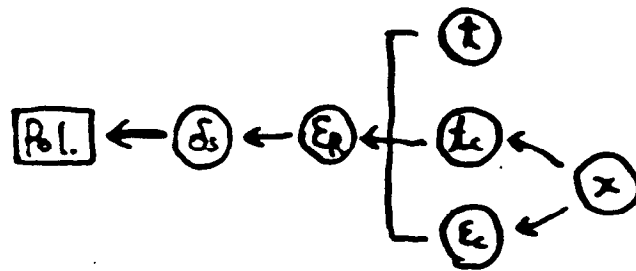
$\alpha$  : Glancing angle

T. Maruyama (SLAC)



# Strain Dependence of Polarization (Conclusion 2)

H. Aoyagi (Nagoya)



ref. H. Aoyagi et al, Phys. Lett. A 167 (1992) 415-420

# R/D of Polarized Electron Source

## (1) Strained GaAs photocathode

- { max. Pol.  $\approx 87\%$   
Pol.  $\geq 80\%$  with Q.E.  $\geq 0.1\%$  } attained!

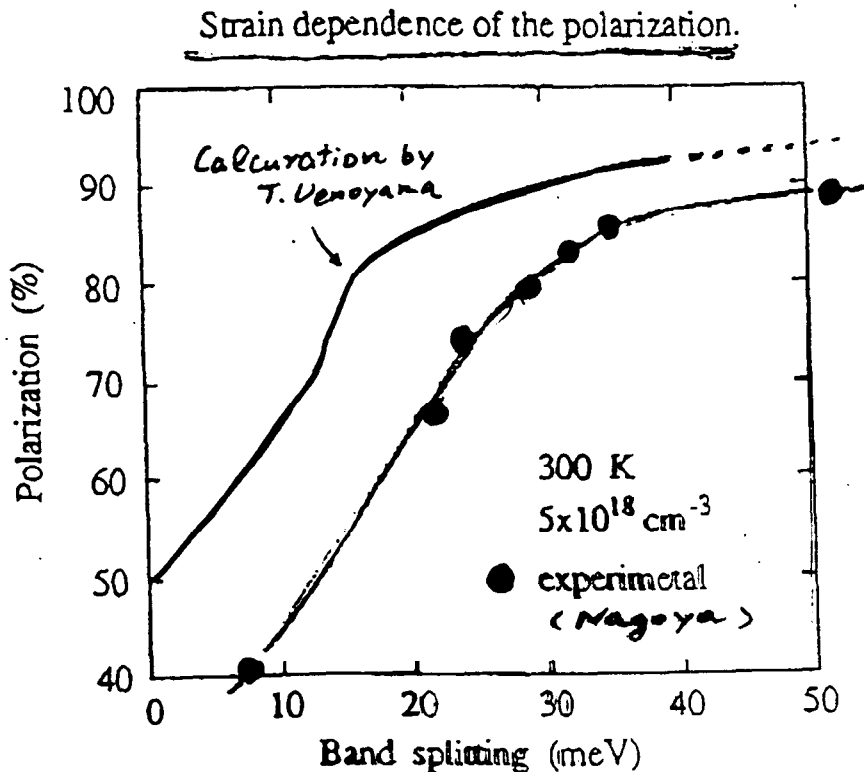
- Further efforts are continued to achieve

Pol.  $\geq 90\%$  with Q.E.  $\geq 0.5\%$

① Q.E. improvement with new device

② Fundamental research toward 100% Polarization

→ Band-mixing effect was estimated by T. Uenoyama.





# A new type photocathode for PES with a $\lambda/4$ DBR

Motivated by a work of K. Kishino et al.

『Resonant Cavity-Enhanced (RCE) Photodetectors』  
IEEE J. of Quantum Electronics 27(1991) 2025~2034

## • QE for Conventional photodetectors

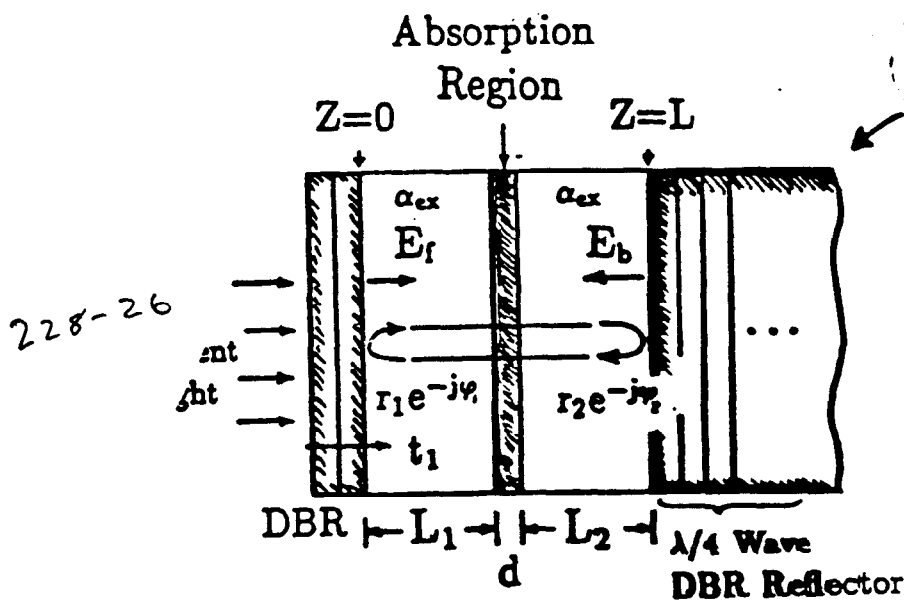
$$QE = (1 - R)(1 - e^{-\alpha d}) \quad (3) \quad // \text{ pp}$$

$$\approx 0.07$$

$$\text{for } \begin{cases} R \sim 0.3 \\ \alpha \sim 1 (\mu\text{m})^{-1} \\ d \sim 0.1 (\mu\text{m}) \end{cases}$$

$R$  reflection  
coefficient  
of active layer

➔ Use of Resonant Absorption of incident light



$$R_1 = r_1^2, R_2 = r_2^2$$

● QE for Resonant Absorption

$$QE = \left\{ \frac{1 + R_2 e^{-\alpha d}}{(1 - \sqrt{R_1 R_2} e^{-\alpha d})^2} \right\} (1 - R_1)(1 - e^{-\alpha d})$$

$$\approx \left\{ \frac{1 + R_2(1 - \alpha d)}{(1 - \sqrt{R_1 R_2}(1 - \alpha d))^2} \right\} (1 - R_1) \alpha d$$

Enhancement factor

under the resonance condition.

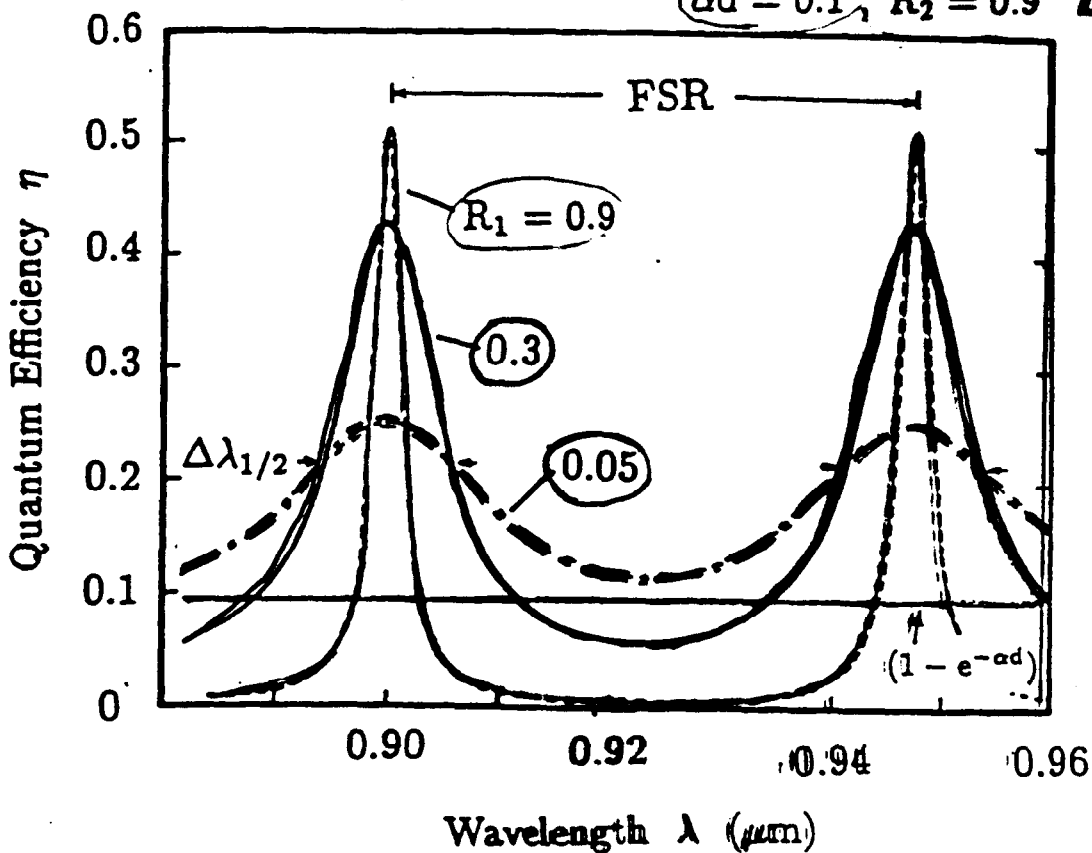
$$\boxed{2nL = m\lambda_R} \quad (m: \text{integer})$$

refractive index                      cavity length

○  $\Delta\lambda_R = \text{FSR (Free Spectral Range)}$

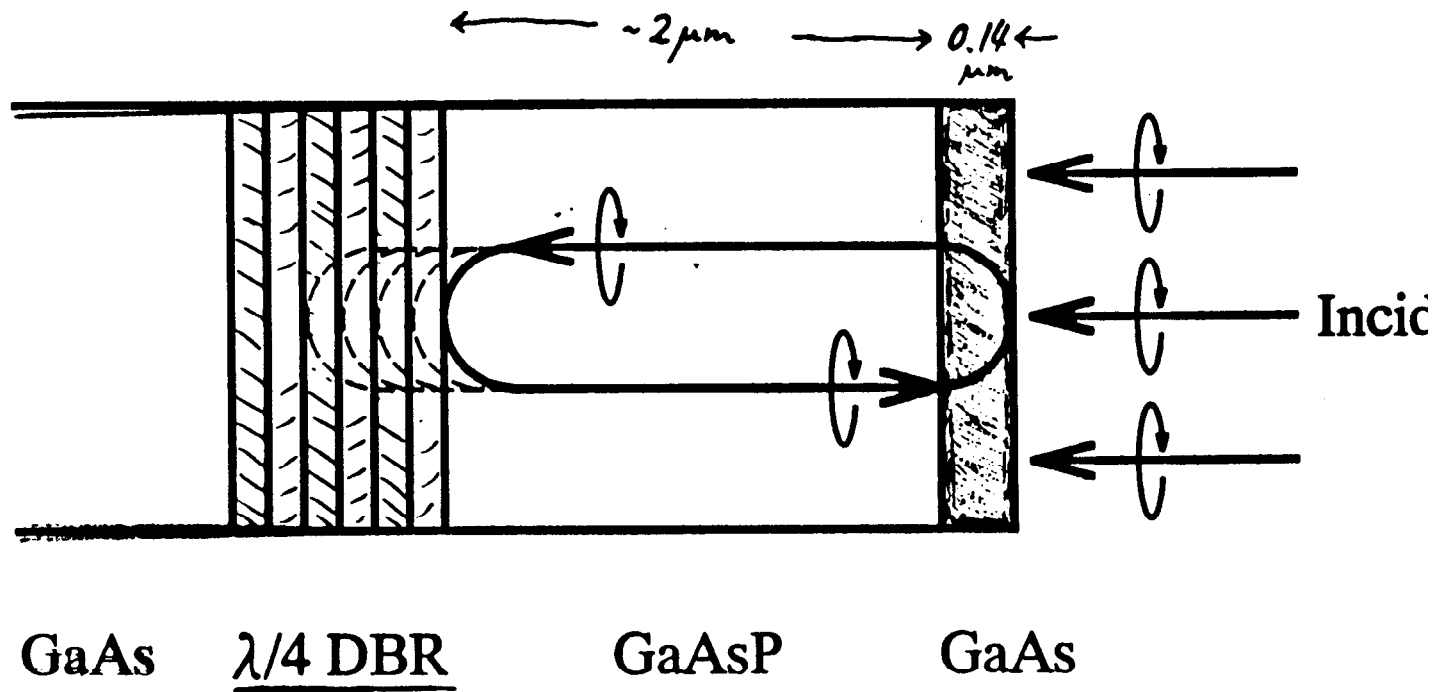
$$= \frac{\lambda_R^2}{2 \cdot n_{\text{eff}} \cdot L}, \quad n_{\text{eff}} = n \left\{ 1 - \frac{\lambda_R}{n} \frac{dn}{d\lambda_R} \right\}$$

$\alpha d = 0.1$ ,  $R_2 = 0.9$   $L = 2\mu\text{m}$



A schematic drawings of resonant absorption type photocath

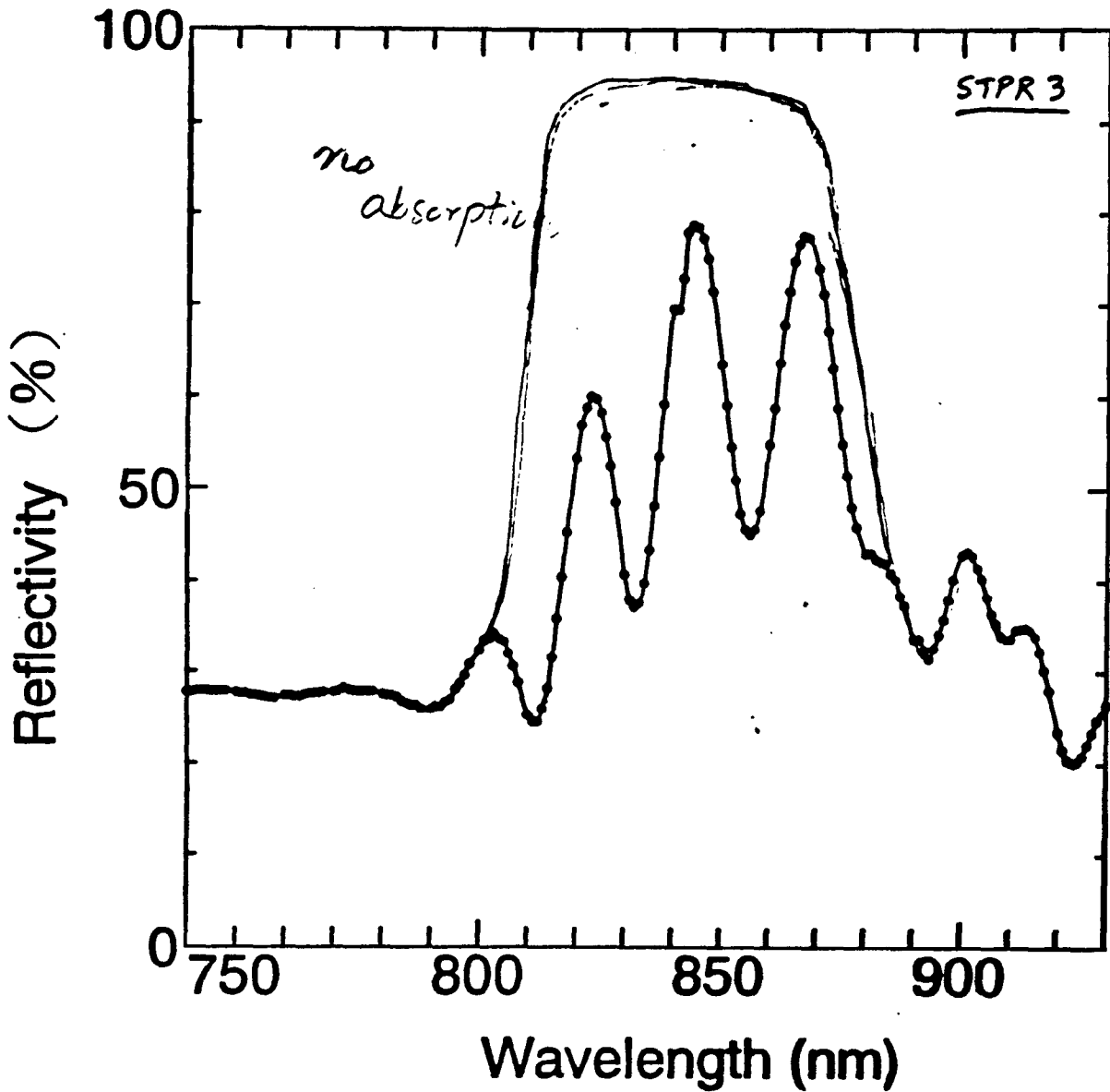
$$\lambda/4 \text{ DBR} : 30 \text{ pairs of } \left( \begin{array}{l} \text{Al}_{0.1}\text{Ga}_{0.9}\text{As} \\ \text{Al}_{0.6}\text{Ga}_{0.4}\text{As} \end{array} \right) \left. \begin{array}{l} n_H = 3.52 \\ n_L = 3.20 \end{array} \right\} n(\text{Al}_x\text{Ga}_{1-x}\text{As})$$





# Reflectivity Spectrum

measured by  
monochromatized light  
with  $3\phi$  diameter

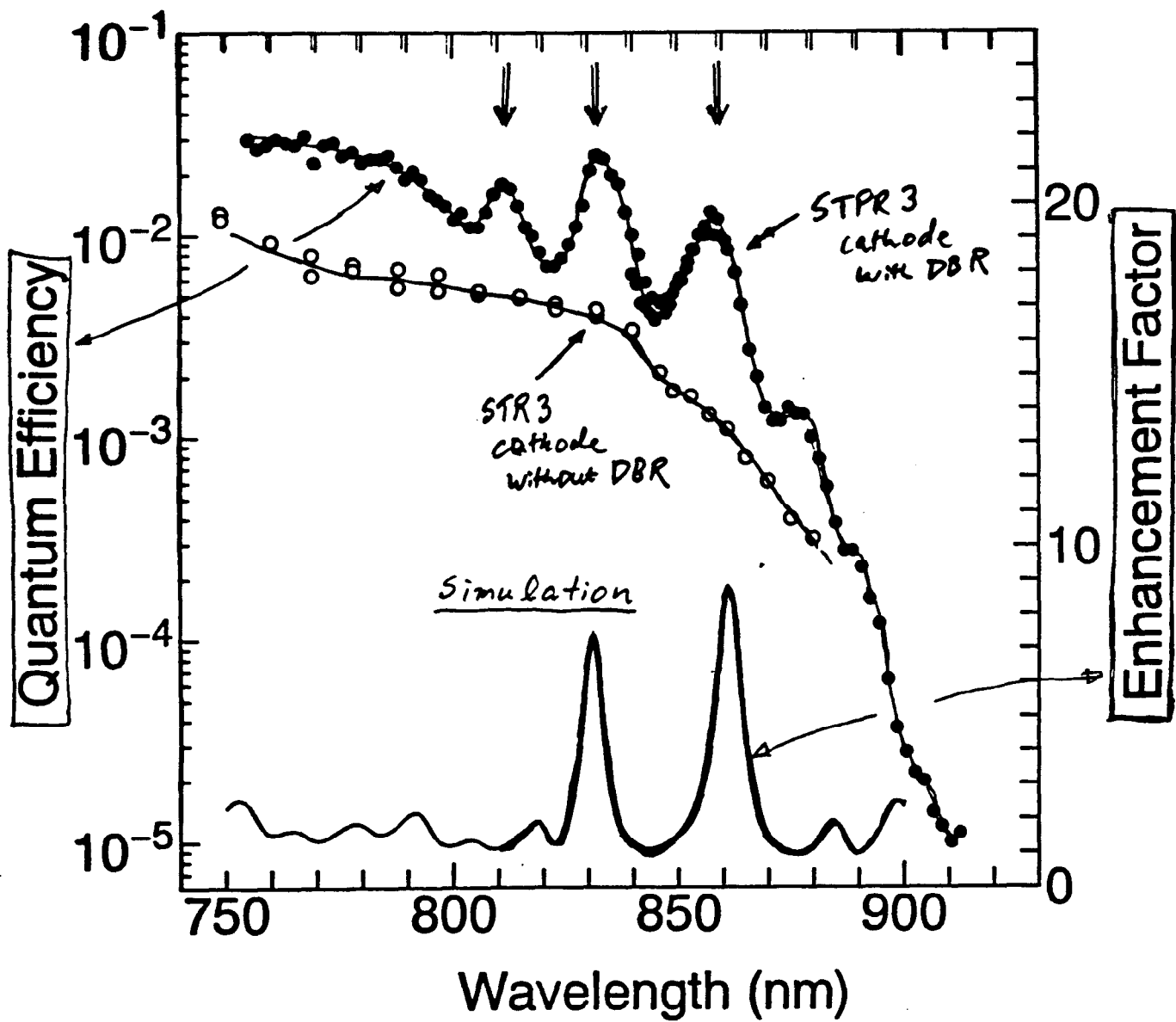


Bandwidth of high reflectivity region

$$\Delta\lambda_B = \frac{4\lambda_B}{\pi} \sin^{-1} \left( \frac{n_H - n_L}{n_H + n_L} \right) \approx 52 \text{ nm}$$

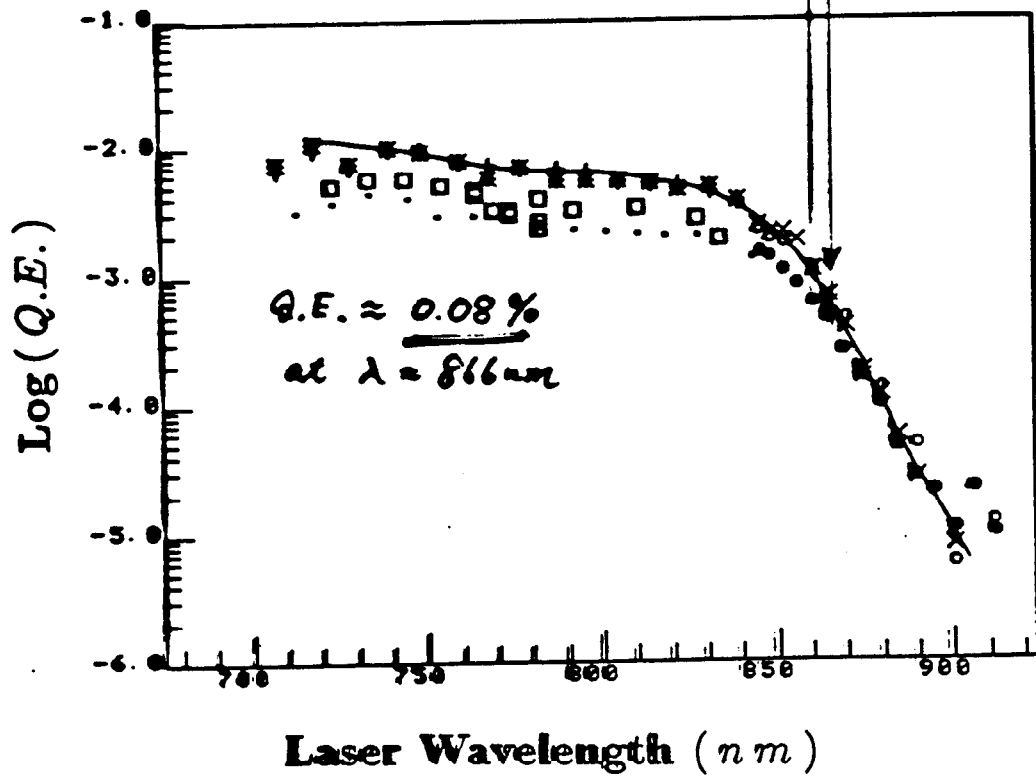
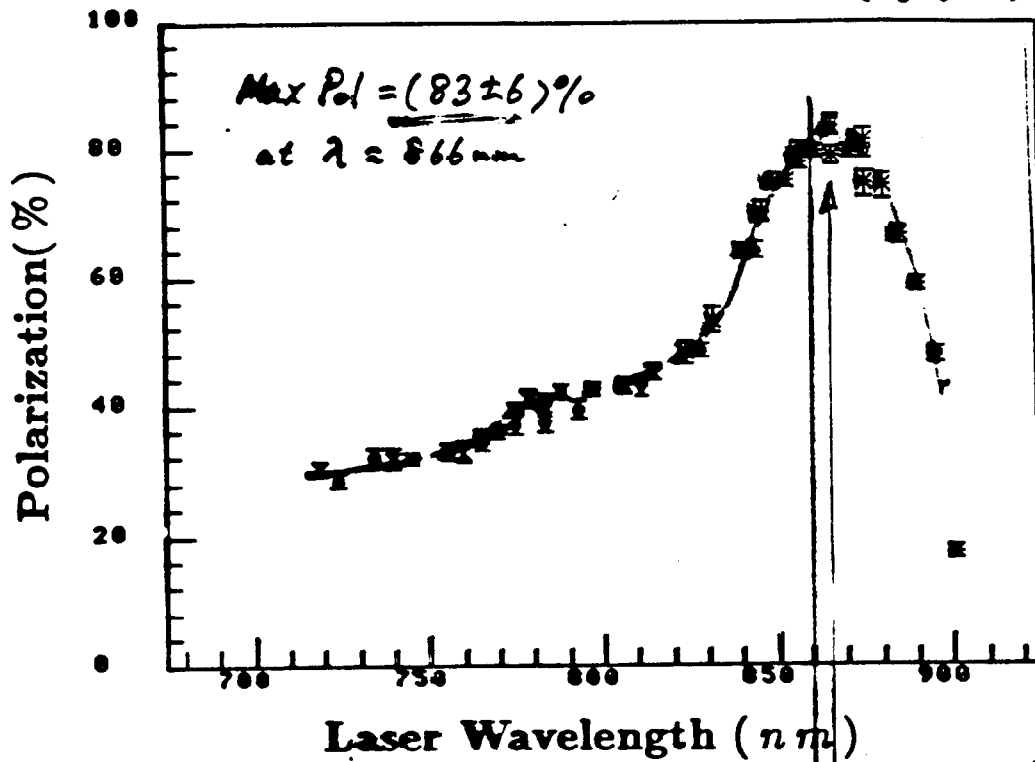
estimated  
↓  
at  $\lambda_B \approx 860 \text{ nm}$

Quantum Efficiency  
and  
a Simulated Enhancement factor



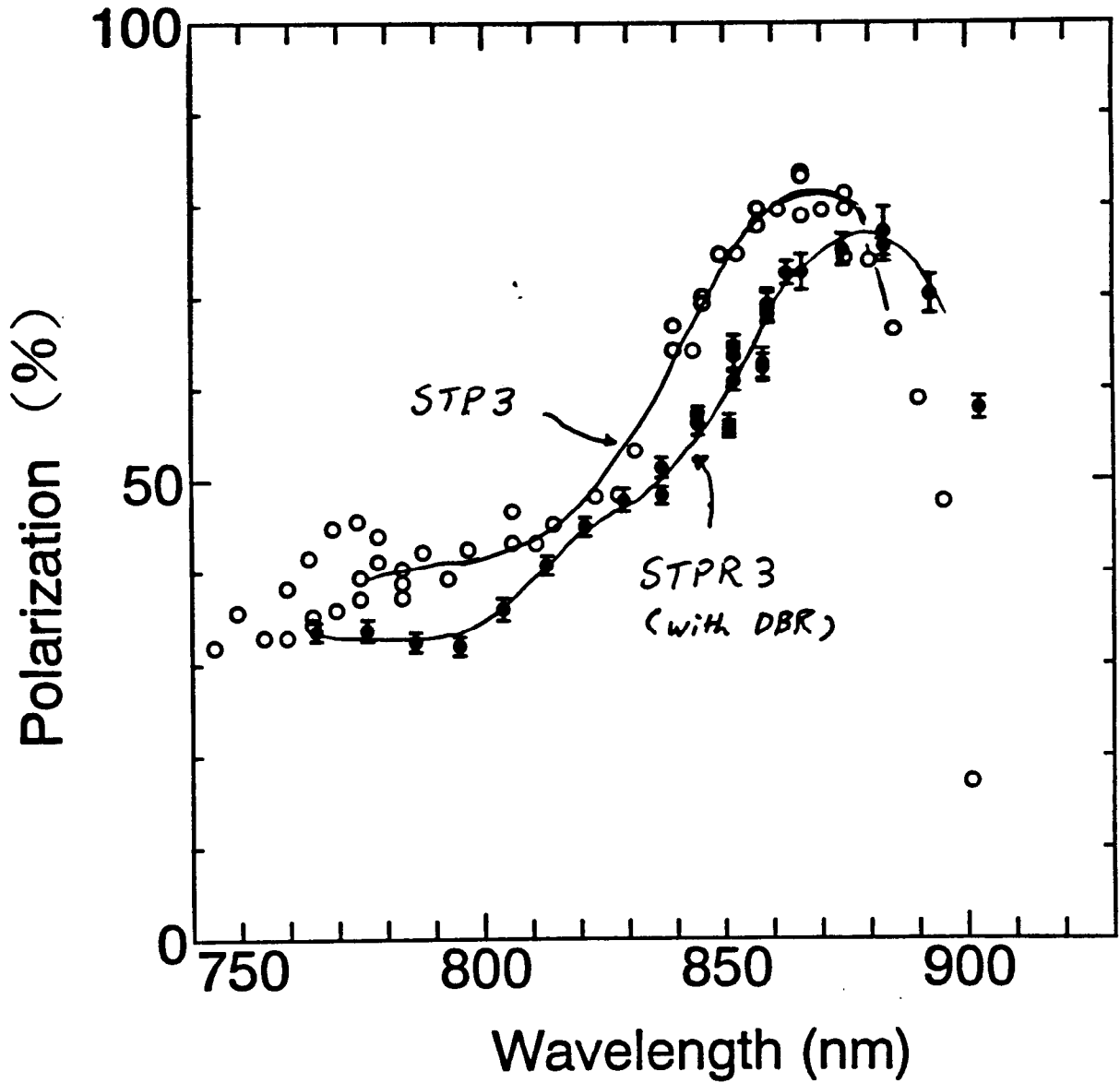
# Strained GaAs #3

( $\Delta a/a \approx 0.6\%$   
thickness  $\approx 1400 \text{ \AA}$ )



(1991. June)

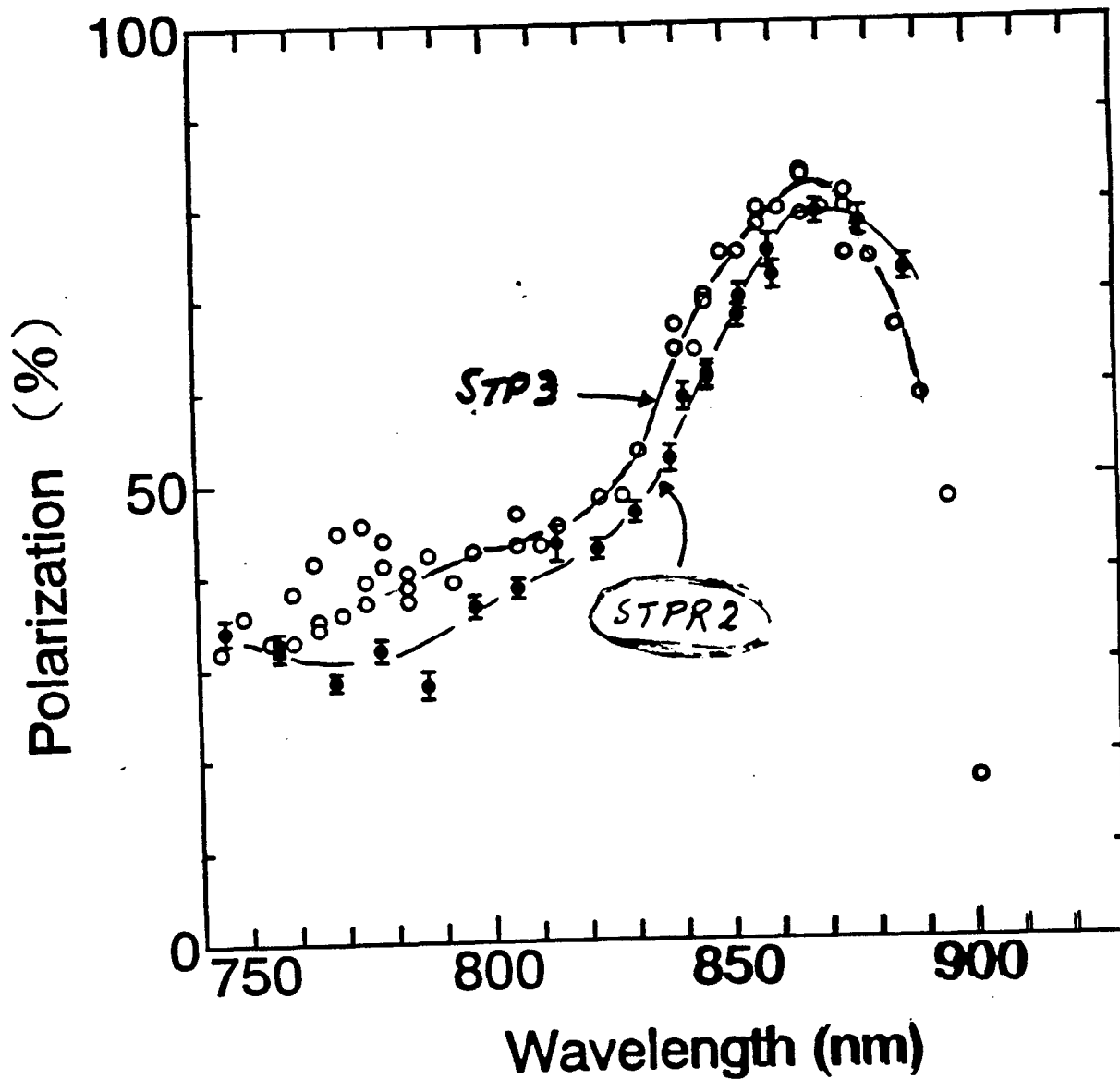
Polarization measurements



- STP3 : GeAs thickness ~140 nm,  $\chi$  ~ 17 %
- STPR3 : " ~140 " ,  $\chi$  ~ 12 %



Polarization measurement



**A new type photocathode for the polarized electron source  
with a distributed Bragg reflector**

**Takashi SAKA<sup>a</sup>, Toshihiro KATO<sup>a</sup>, Tsutomu NAKANISHI<sup>b</sup>,  
Mitsuru TSUBATA<sup>b</sup>, Katsumi KISHINO<sup>c</sup>, Hiromichi HORINAKA<sup>d</sup>  
Yoshihiro KAMIYA<sup>e</sup>, Shoji OKUMI<sup>b</sup>, Chikako TAKAHASHI<sup>b</sup>,  
Yasunori TANIMOTO<sup>b</sup>, Masafumi TAWADA<sup>b</sup>, Kazuaki TOGAWA<sup>b</sup>,  
Hideki AOYAGI<sup>b1</sup> and Shinsuke NAKAMURA<sup>b2</sup>**

- <sup>a</sup> *New Materials Research Laboratory, Daido Steel Co. Ltd., Nagoya 457, Japan*
- <sup>b</sup> *Department of Physics, Nagoya University, Nagoya 464, Japan*
- <sup>c</sup> *Department of Electrical & Electronics Engineering, Sophia University,  
Chiyoda-ku, Tokyo 102, Japan*
- <sup>d</sup> *College of Engineering, University of Osaka Prefecture, Sakai 599, Japan*
- <sup>e</sup> *Toyota Technical Institute, Nagoya 468, Japan*

**Abstract**

In order to increase the quantum efficiency of the strained GaAs photocathode for the highly polarized electron source, we designed a new type photocathode with a distributed Bragg reflector (DBR). A Fabry-Perot cavity is formed by the DBR and the GaAs surface. The large enhancement of quantum efficiency was observed at the laser wavelength which satisfied the condition for the resonant absorption of incident laser light. From this experiment, it becomes promising to make the photocathode which has the quantum efficiency more than ~ 1% together with the electron spin polarization higher than 80%.

Published in *Jpn. J. Appl. Phys.* Vol. 32 (1993) L1837-L1840.  
~~(to be submitted for publication)~~

<sup>1</sup>Present address : Stanford Linear Accelerator Center, Stanford, CA, U.S.A.

<sup>2</sup>Present address : Physikalisches Institute der Universität Bonn, Bonn, Germany

(preliminary)

## Summary of a DBR photocathode (Sept. '93)

- 1) A new type photocathode with a  $\lambda/4$  DBR has been developed to increase the QE of the high polarization cathodes
- 2) QE enhancement by the resonant absorption of incident light was clearly observed.
- 3) QE  $\approx 1.3\%$  with  $\sim 80\%$  polarization was obtained at  $\lambda \approx 860$  nm for a  $0.14 \mu\text{m}$  thick strained layer
- 4) QE  $\approx 1\%$  with Pol  $\approx 80\%$  seems to be promising by further optimization of cathode structure.

**Daniel Pierce**  
**Electron Physics Group, NIST**

**Application of the GaAs Polarized Electron Source to  
Studies of Surface Magnetism**

The GaAs spin polarized electron source grew out of work in the condensed matter physics where its many applications cause workers in this community to be natural allies of high energy physicists in the quest for improved performance of spin polarized electron sources. The exploitation of the features of the GaAs source to investigate magnetic properties of surfaces using the techniques of spin polarized electron scattering, spin polarized inverse photoemission, and spin polarized low energy electron microscopy will be discussed.

**Application of the GaAs Polarized Electron  
Source to Studies of Surface Magnetism**

**D. T. Pierce**

**Electron Physics Group  
National Institute of Standards and Technology  
Gaithersburg, MD 20899**

**Supported by the Technology Administration of the  
Department of Commerce and the Office of Naval Research**

# **Outline**

**This talk will illustrate what we learn about the physics of surface magnetism using polarized electrons from the GaAs source in:**

**Spin Polarized Electron Scattering**

**Elastic**

**Inelastic**

**Spin Polarized Inverse Photoemission**

**Spin Polarized Low Energy Electron Microscopy**

# **Key Features of the GaAs Polarized e<sup>-</sup> Source**

**Polarization**

**Polarization Reversability**

**Intensity**

**Emittance**

**Energy Spread**

**Time Resolution**

**Reliability**

**Features are important in different degrees for experiments**

**which investigate surface magnetism as we shall see**

**Typical energy range — few eV to few hundred eV**

**Implies short electron mean free path and surface sensitivity**

## What Can Polarized Electron Scattering Say About Surface Magnetism

$$H_{\text{int}} = V + V_{\text{so}} + \sum_j J(r-R_j) \mathbf{s} \cdot \mathbf{S}_j$$

$\mathbf{S}_j$  — spin of magnetic ion at  $R_j$   
 $\mathbf{s}$  — incident electron spin  
 $J$  — exchange coupling constant  
 $V_{\text{so}}$  — spin orbit interaction, eliminated by scattering geometry or reversing  $M$   
 $V$  — spin independent Coulomb scattering

Scattering amplitude:

$$A(\mathbf{K}) = (2\pi m/\hbar^2) \sum_j [V(\mathbf{K}) + J(\mathbf{K}) \mathbf{s} \cdot \mathbf{S}_j] \exp(-i\mathbf{K} \cdot \mathbf{r}_j)$$

$$A_{\text{ex}} = \frac{I\uparrow\uparrow - I\uparrow\downarrow}{I\uparrow\uparrow + I\uparrow\downarrow} \xrightarrow{\text{writing simply}} \frac{V J \langle S^z \rangle}{2V^2 + (1/2)J^2 \langle S^z S^z \rangle}$$

$$\approx - J(\mathbf{K}) M^z(T) / g\mu_B V(\mathbf{K})$$

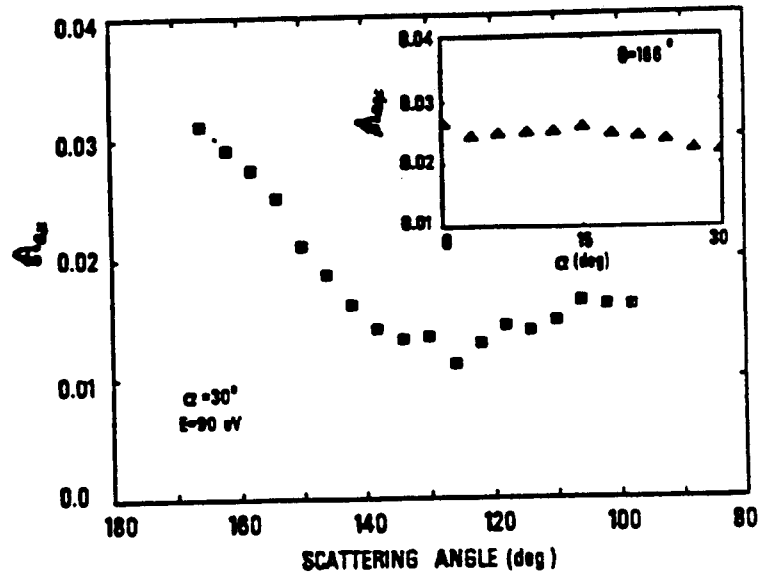
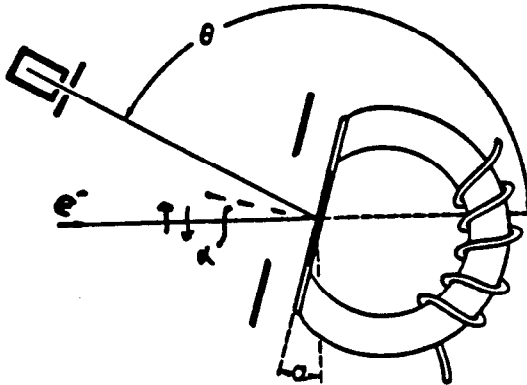
$A_{\text{ex}}$  proportional to  $M^z(T)$  in single scattering approximation

Reference:

D.T. Pierce and R.J. Celotta, *Adv. in Electronics and Electron Physics*, 56, 219 (1981)



# Polarized Electron Scattering From Amorphous Ferromagnets



Measure:

$$A_{ex} = \frac{1}{P_0 \cos \alpha} \frac{I_{\uparrow\uparrow} - I_{\uparrow\downarrow}}{I_{\uparrow\uparrow} + I_{\uparrow\downarrow}}$$

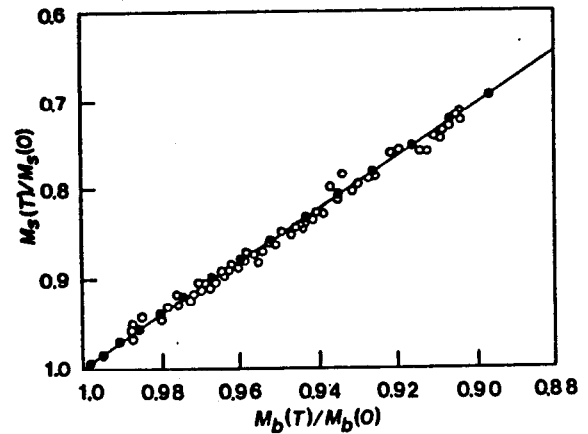
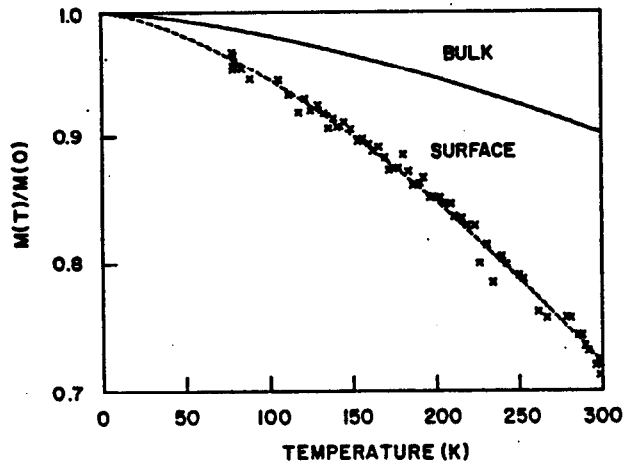
Comments:

- 1) Scattering independent of orientation of surface; depends only on scattering angle.
- 2) No diffraction and multiple scattering weak in back direction
- 3) To a good approximation,  $A_{ex} \propto M$

Reference:

D.T. Pierce, R.J. Celotta, J. Unguris, and H.C. Siegmann, Phys. Rev. B26, 2566 (1982)

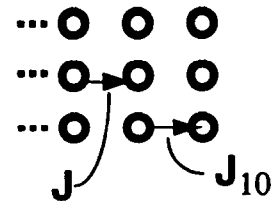
# Temperature Dependence of Magnetization at Low Temperature



## Comments:

1)  $M(T)/M(0) = 1 - BT^{3/2} + \dots$  Theory:  $B_{\text{surface}}/B_{\text{bulk}} = 2$ , Exp:  $B_s/B_b > 2$

2) Results explained by extending theory to include weaker exchange coupling of surface to bulk,  $J_{10} < J$



3)  $B_s/B_b$  is sensitive to chemical state of surface

4) Can't assume surface is a simple termination of the bulk

## References:

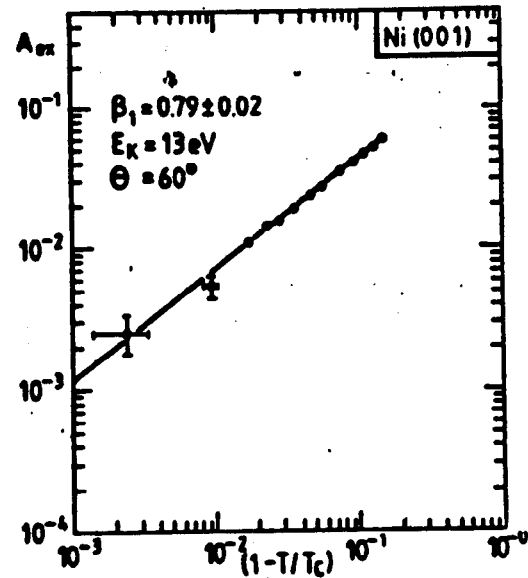
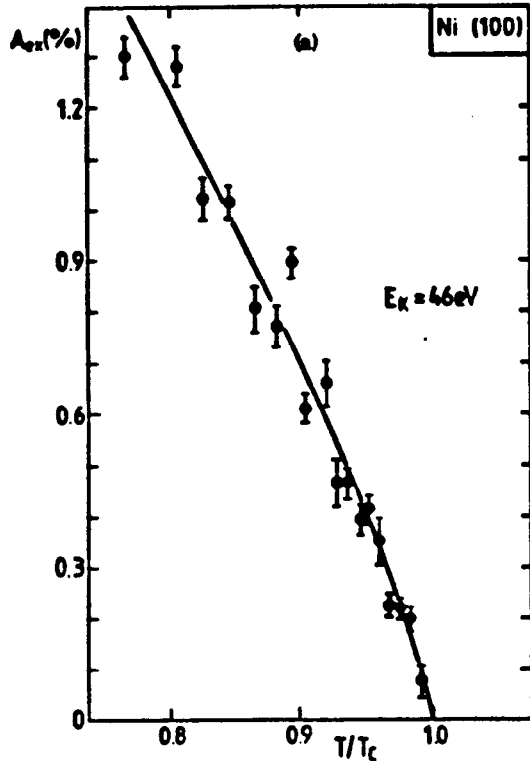
D.T. Pierce, R.J. Celotta, J. Unguris, and H.C. Siegmann,  
Phys. Rev. B26, 2566 (1982)

J. Mathon and S.B. Ahmad, Phys. Rev. B37, 660 (1988)

D. Mauri, D. Scholl, H.C. Siegmann, and E. Kay, Phys. Rev. Lett. 61,  
758 (1988)

# Temperature Dependence of Magnetization

## Critical Behavior at Curie Temperature



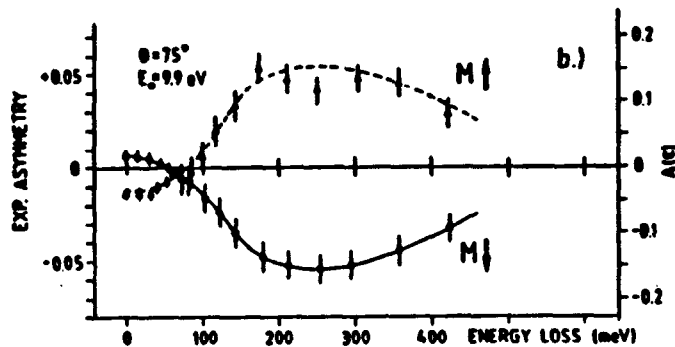
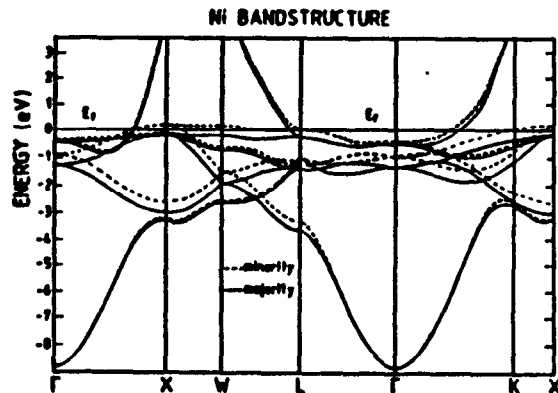
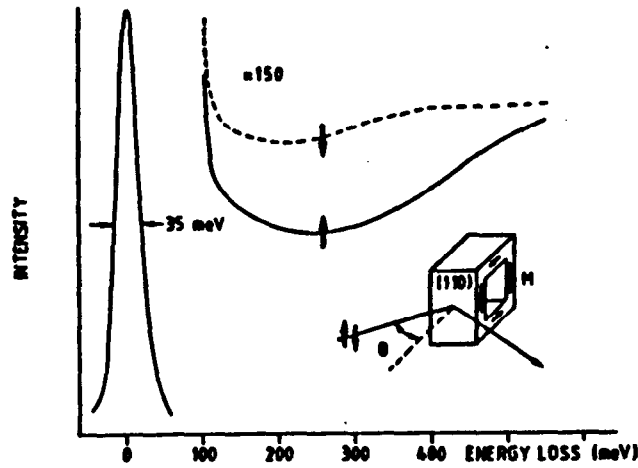
### Comments:

- 1) Much theory, few experiments for critical behavior at surface
- 2)  $A_{ex} \propto M$ , since as  $t = (T_c - T)/T_c \rightarrow 0$   
magnetic coherence length diverges
- 3)  $A_{ex} \propto t^\beta$  with  $\beta = 0.8$  for the surface compared to  $\sim 1/3$  for bulk

### References:

- S. Alvarado, M. Campagna, and H. Hopster, Phys. Rev. Lett. 48, 51 (1982); S. F. Alvarado, M. Campagna, F. Ciccacci, and H. Hopster, J. Appl. Phys. 53, 7920 (1982)

# Inelastic Scattering Asymmetry: Spectrum of Stoner Excitations

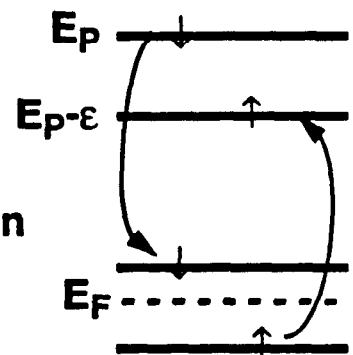


## Comments:

1) Ni(110),  $E_p = 12$  eV,  $\Delta E = 80$  meV

2) Stoner excitation: excitation at given  $q$  between bands of opposite spin.

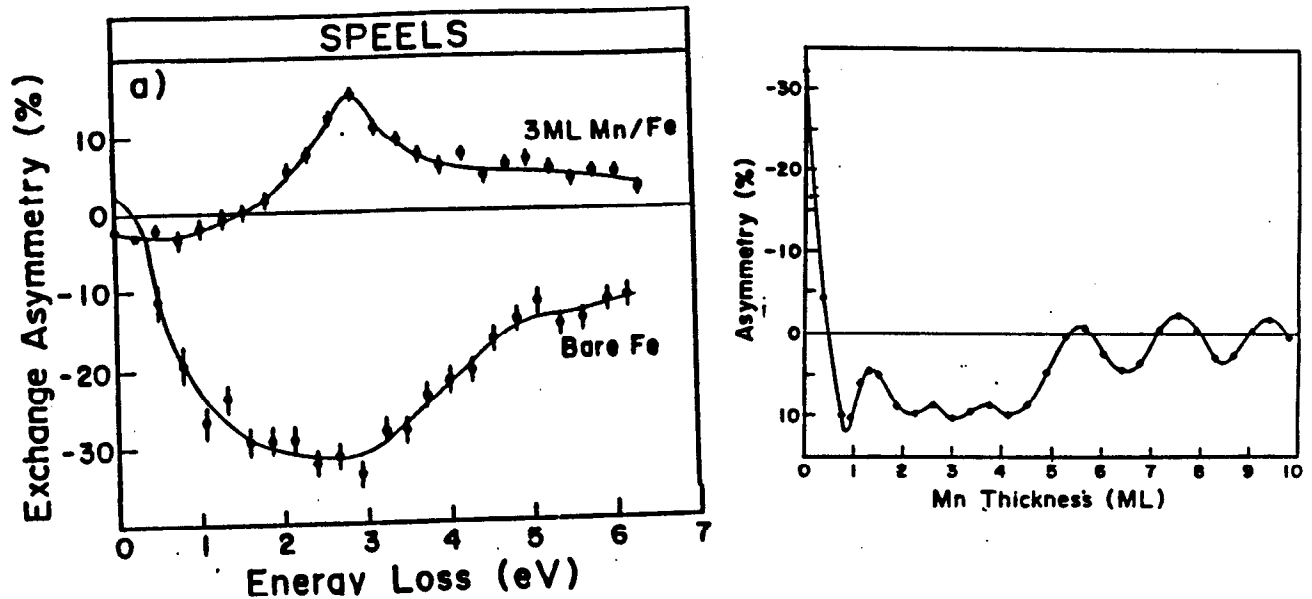
3) Specular scattering,  $q=0$ . Asymmetry spectrum gives most probable value of exchange integrated over Brillouin zone.



## References:

J. Kirschner, in Polarized Electrons in Surfaces Physics (World Sci)

# Magnetic Order in Thin Mn Film on Fe(100)



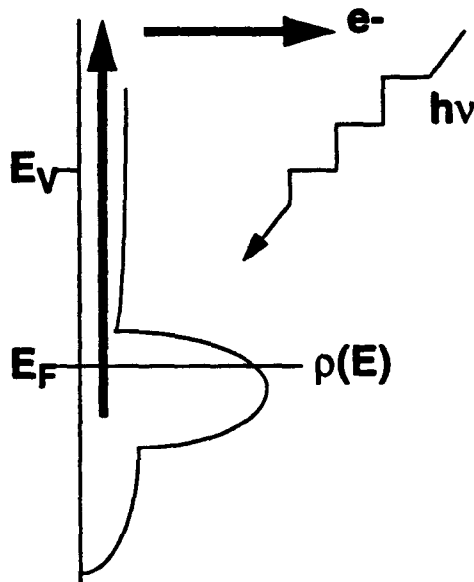
## Comments:

- 1) Peak in inelastic asymmetry indicated Mn exchange splitting of 2.9 eV indicating larger magnetic moment.
- 2) Asymmetry oscillates with period of 2 ML, implies ferromagnetic sheets stacked in antiferromagnetic alignment.

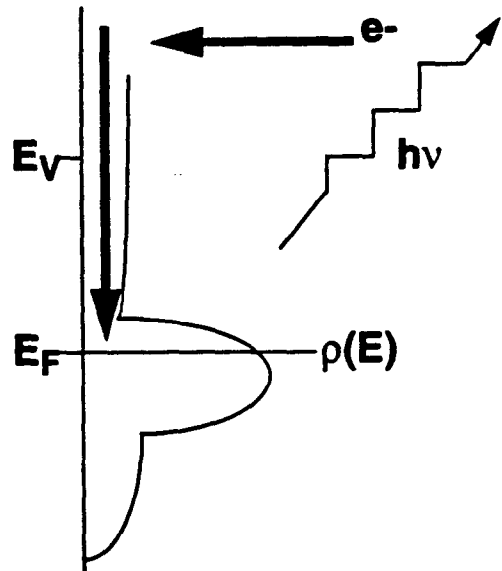
## Reference:

T.G. Walker and H. Hopster, Phys. Rev. B 48, 3563 (1993)

## History : Spectroscopy of Filled and Unfilled States



**Photoemission**



**Inverse Photoemission**

**Photoemission: measure energy of initial and final state**

**C.N. Berglund and W.E. Spicer, Phys. Rev. 136, A1030, A1044 (1964)**

**Spin Polarized Photoemission: measure spin of photoelectrons**

**G. Busch, M. Campagna, P. Cotti, and H.C. Siegmann, Phys. Rev. Lett. 22, 597 (1969)**

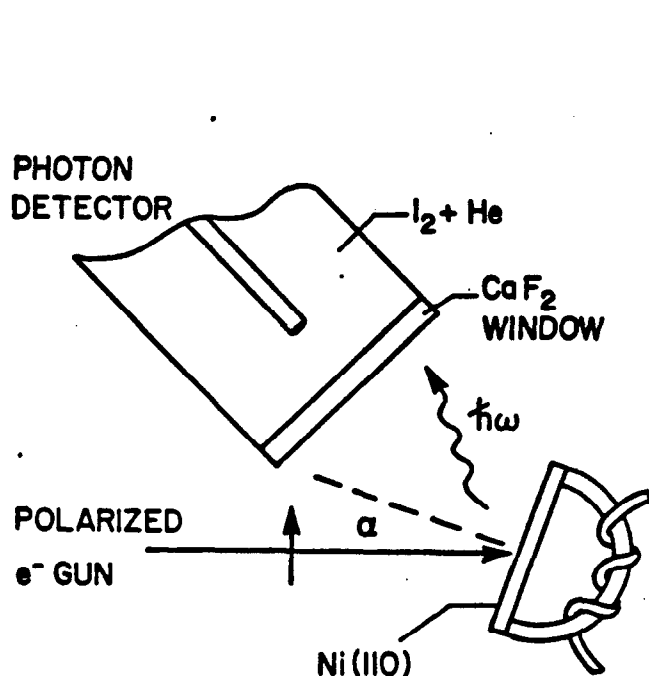
**Inverse Photoemission: measure unoccupied states**

**G. Denninger, V. Dose, and H.P. Bonzel, Phys. Rev. Lett. 48, 279 (1982); D.P. Woodruff and N.V. Smith, Phys. Rev. Lett. 48, 283 (1982)**

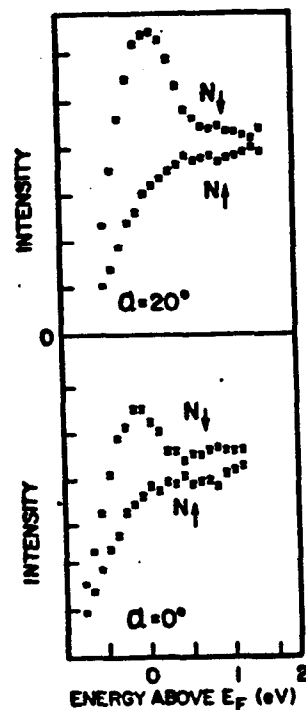
**Spin Polarized Inverse Photoemission: polarized electrons (from GaAs source) incident on sample**

**J. Unguris, A. Seiler, R.J. Celotta, D.T. Pierce, P.D. Johnson, and N.V. Smith, Phys. Rev. Lett. 49, 1047 (1982)**

# Spin Polarized Inverse Photoemission



Apparatus



First Spectra

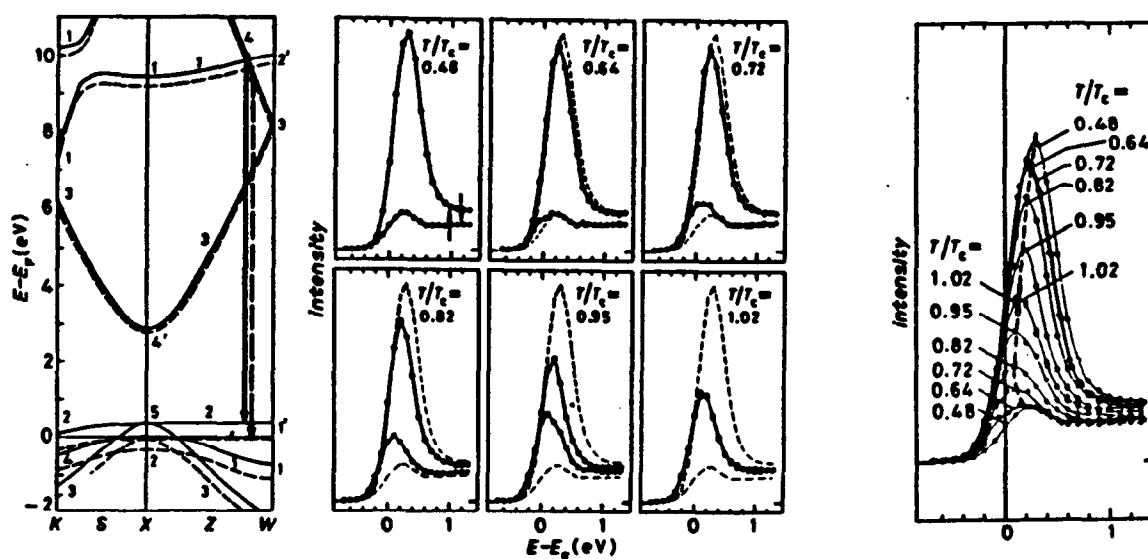
## Comments:

- 1) Energy, Angle ( $k$ ), and Spin-Resolved Inverse Photoemission
- 2) Observe large minority spin peak just above Fermi level from the d-holes responsible for ferromagnetism in Ni

## Reference:

J. Unguris, A. Sella, R.J. Celotta, D.T. Pierce, P.D. Johnson, and N. V. Smith, Phys. Rev. Lett. 49, 1047 (1982)

# Temperature Behavior of Magnetic States in Ni



## Comments:

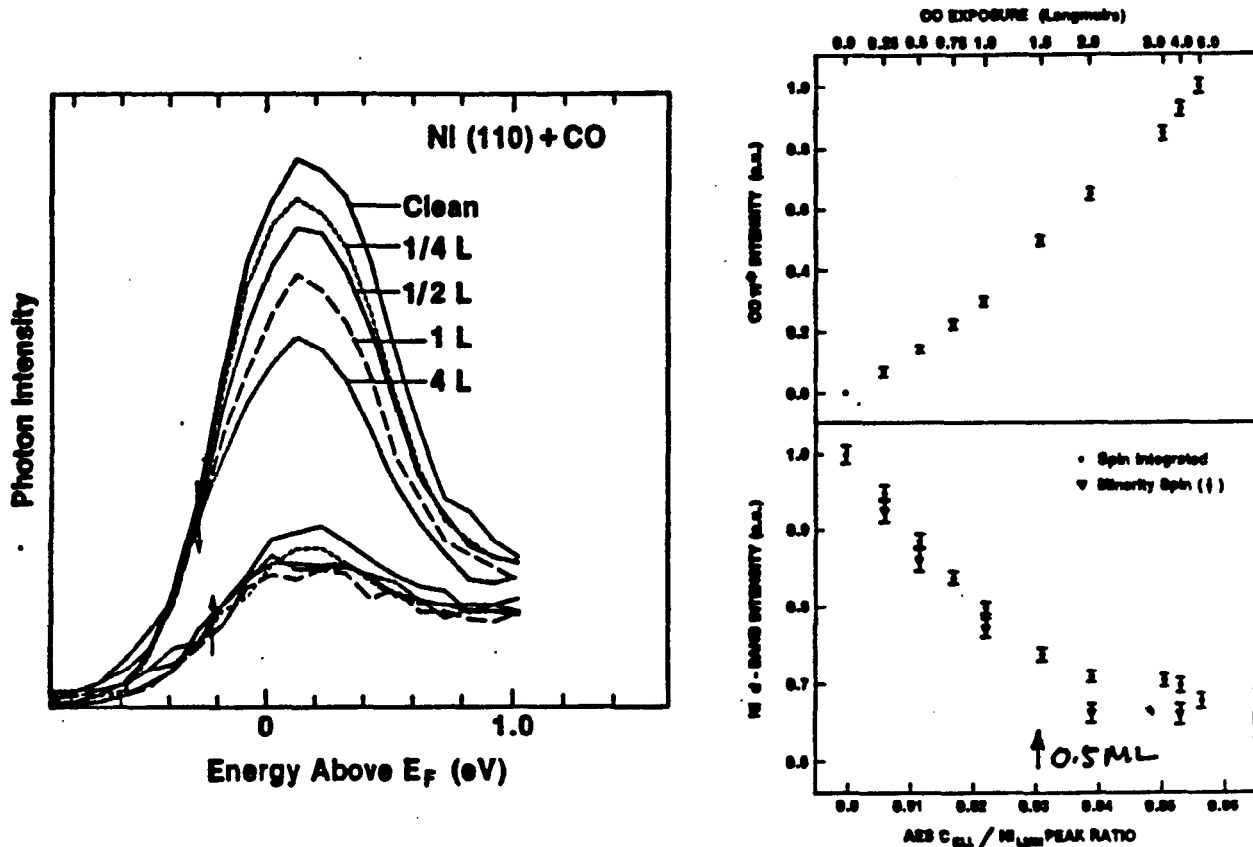
- 1) With increasing temperature, minority peak decreases and majority peak increases
- 2) These changes along with observed energy shifts consistent with temperature dependent exchange splitting vanishing at  $T_c$

## Reference:

M. Donath and V. Dose, *Europhys. Lett.* 9, 821 (1989)



# CO Chemisorption on Ni(110): Effect on Surface Magnetism

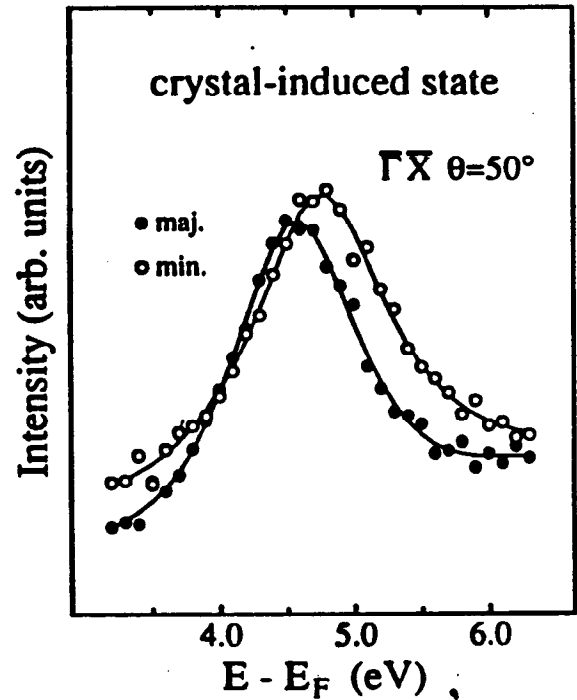
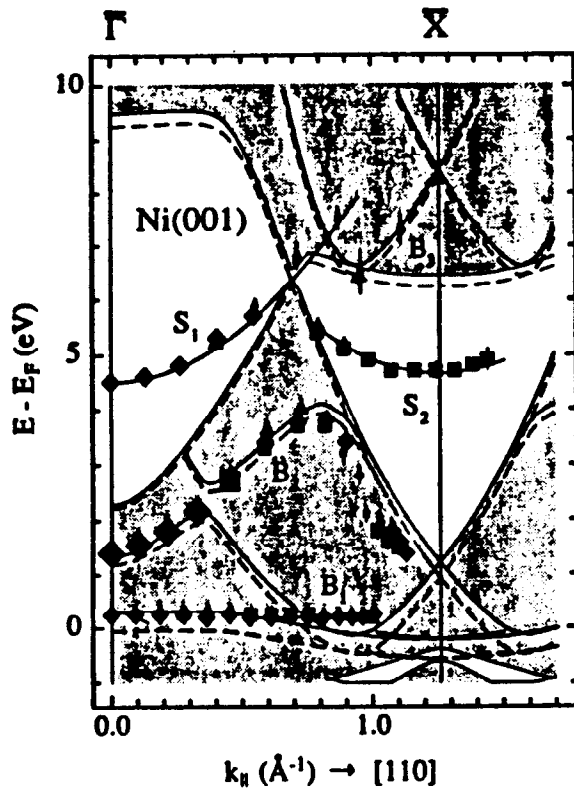


- 1) Minority spin peak does not decrease beyond 0.5 ML CO coverage although CO  $\pi^*$  intensity shows CO adsorption continues.
- 2) Consistent with each CO affecting two surface Ni atoms.
- 3) CO does not randomize Ni moments which would lead to equal up and down spin peaks.
- 4) Rather, CO reduces magnetic moment of surface atoms.

## Reference:

C.S. Feigerle, A. Seller, J.L. Pena, R.J. Celotta, and D.T. Pierce, Phys. Rev. Lett. 56, 2207 (1986).

# Exchange Splitting of Surface States on Ni(100)



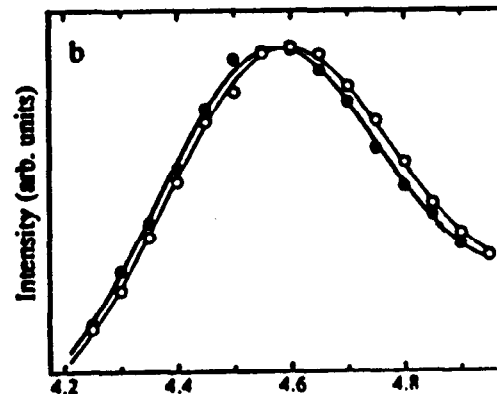
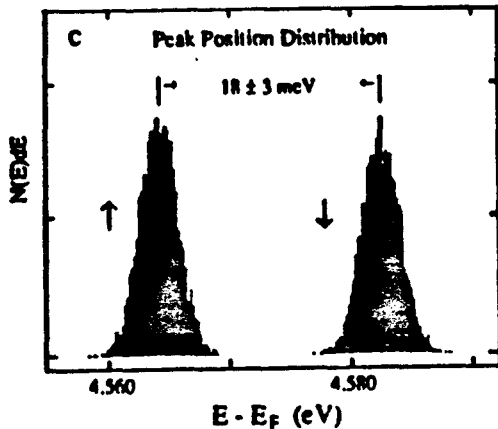
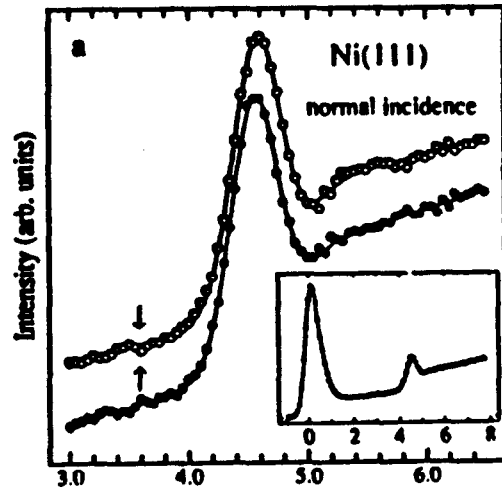
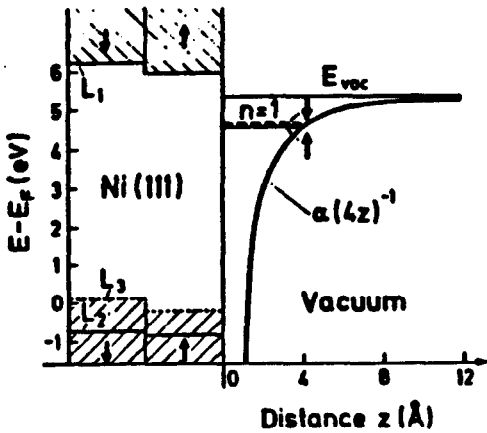
## Comments:

- 1) Measure energy dispersion and spin dependence of bulk and surface states
- 2) Approximately 0.2 eV exchange splitting of crystal induced surface state
- 3) Direct demonstration that top atomic layer of Ni(100) is magnetically active. No "dead layers".

## Reference:

K. Starke, K. Ertl, and V. Dose, Phys. Rev. B 45, 6154 (1992)

# Spin-Split Image Potential Induced Surface State



## Comments:

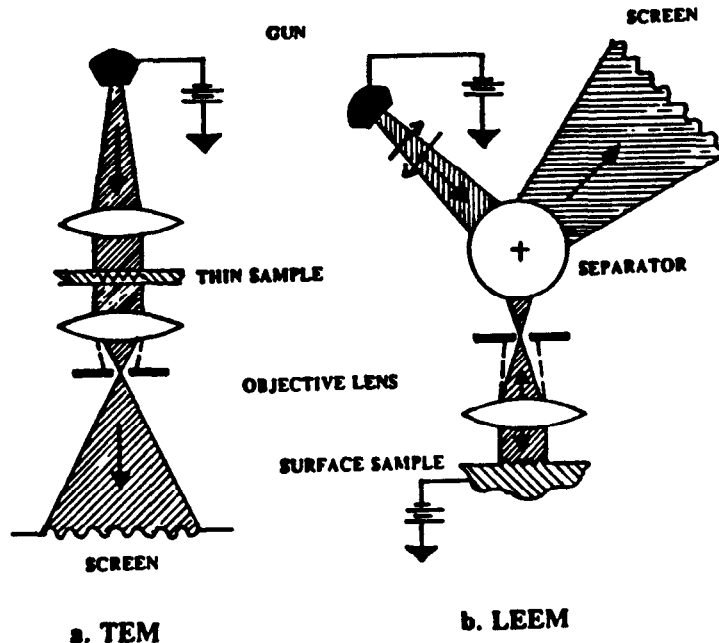
- 1) Rydberg-like series of bound states of electrons trapped between image potential barrier and surface
- 2) Wavefunction maximum well outside surface, splitting small
- 3) Spin resolution allows measurement of splitting much smaller than peak width.

## Reference;

F. Passek and M. Donath, Phys. Rev. Lett. 69, 1101 (1992)

# Low-Energy Electron Microscopy (LEEM)

## Spin Polarized = SPLEEM



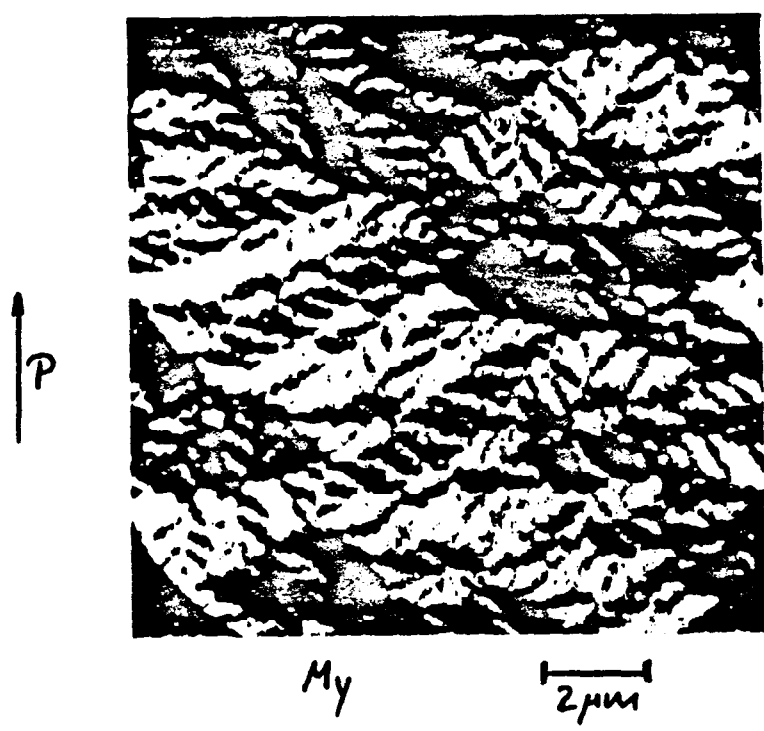
### Comments:

- 1) In both LEEM and TEM, electron gun illuminates sample and lens projects magnified (direct, not scanned) image on screen.
- 2) Many contrast mechanisms in LEEM. Spin polarized incident beam provides magnetic contrast by taking difference of images obtained with each spin direction.
- 3) In LEEM, the sample is the first electrode of the objective, an accelerating immersion lens.

### References:

W. Telieps and E. Bauer, *Ultramicroscopy* 17, 57 (1985)

L.H. Veneklasen, *Rev. Sci. Instrum.* 63, 5513 (1992)



Co (0001)  
E = 3.3 eV

SPLEEM

H. Pinkvos  
unpublished

### SPLEEM Co(0001)

- 1) The image of one component of in-plane magnetization shows that magnetostatic energy due to the surface overcomes the strong uniaxial (out of plane) anisotropy.
- 2) Video image, 512x512 pixels, 8 bit, 10sec/image, resolution=20nm
- 3) Acquire two images with opposite spin polarization and then use subtraction to extract the magnetic contrast.

**Reference:**

H. Pinkvos, TU Clausthal, unpublished

## **Summary**

### **Key Features of the GaAs Polarized e<sup>-</sup> Source**

**Polarization**

**Polarization Reversability**

**Intensity**

**Emittance**

**Energy Spread**

**Time Resolution**

**Reliability**

**Low energy=short mean free path/surface sensitivity**

**Important for investigation of surface magnetism**

**Erwin Reichert,  
U. Mainz**

**Thermal Stability of Cs on NEA III-V-Photocathodes and  
its Effect on Quantum Efficiency**

# Thermal Stability of Cs on NEA III-V-Cathodes and its Effect on Quantum Efficiency.

H. Fischer      P. Drescher

E. Reichert

Johannes Gutenberg University of Mainz

## Abstract

In polarized electron guns using NEA GaAs- or GaAsP-cathodes one observes a decrease of quantum yield with time of operation. This fatigue of efficiency limits the useful lifetime of a cathode. The question is whether Cs-desorption from the NEA layer is responsible for such a loss of yield.

We looked for changes in Cs-content of NEA layers on GaAsP(100)-cathodes with help of X-ray photoelectron spectroscopy (XPS). Cathodes of this type are used in the polarized electron gun of the Mainz race track microtron MAMI. We do not see a decrease of the cesium XPS-signal with time at room temperature, while at the same time the yield may vary over a wide range of values. Cs-desorption rates at elevated temperatures are consistent with activation energies around 1.6 eV for Cs-desorption from layers that are prepared for maximum photoelectron emission. This is in agreement with thermal flash desorption spectra reported by other laboratories for GaAs and indicates a rather strong binding of Cs to a GaAsP(100) surface at coverages typical for NEA preparation.

## 1 Introduction.

A substantial part of the present and near future experimental program at the Mainz race track microtron MAMI needs a beam of polarized electrons. A group of physicists from Mainz university labelled *B2-collaboration* is responsible for setting up and operating a source of polarized electrons attached to MAMI.<sup>1</sup>

---

<sup>1</sup>B2-collaboration at Mainz race track microtron MAMI: H.G. ANDRESEN, K. AULENBACHER, TH. DOMBO, P. DRESCHER, H. EUTENEUER, H. FISCHER, D. V. HARRACH, P. HARTMANN, P. JENNEWAIN, K.-H. KAISER, S. KÖBIS, H.J. KREIDEL, CH. NACHTIGALL, S. PLÜTZER, E. REICHERT (SP), K.-H. STEFFENS, TH. WEIS.



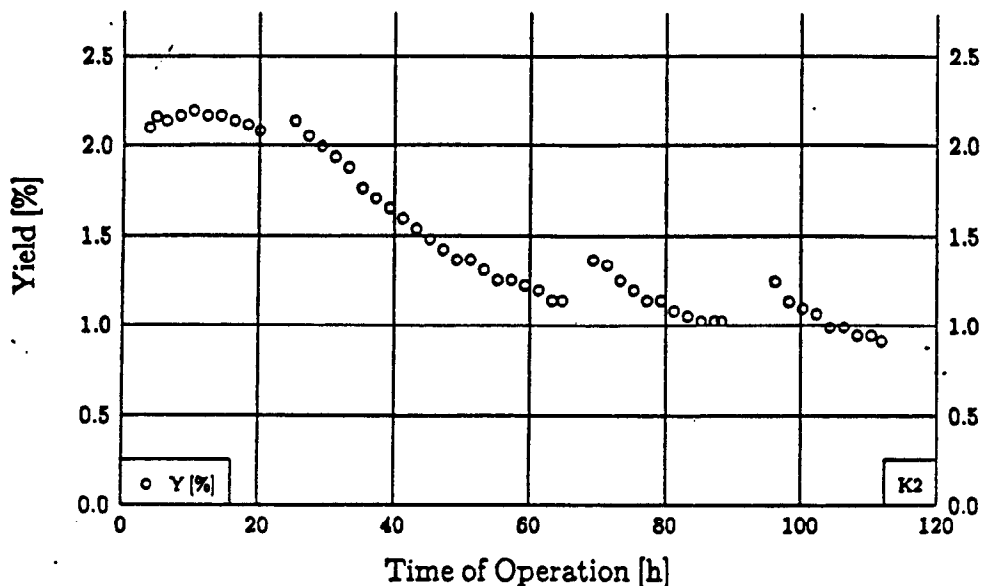


Figure 1: Typical time variation of the quantum yield of a NEA GaAs<sub>0.65</sub>P<sub>0.35</sub>(100)-photoelectron cathode.

The present source of polarized electrons of MAMI is based on photoelectron emission from GaAsP and is applied already in experiments since the beginning of 1992.

A major problem encountered in the operation of III-V-photocathodes in electron guns is the limited life time. The example in figure 1 demonstrates a typical time variation of quantum yield of a GaAs<sub>0.65</sub>P<sub>0.35</sub>(100) photocathode activated to negative electron affinity (NEA) by Cs-coverage. Cathodes of this type are currently in use in the MAMI source of polarized electrons.

The processes that cause the degradation of yield are not known yet. So we set up an X-ray photoelectron spectrometer (XPS) to study the surface of NEA photocathodes. The hope was to see some correlation between decreasing quantum yield and changes in the composition of the NEA-layer eventually.

The first obvious question that we tried to answer was: Is there a change in the amount of cesium at the surface with time, that alter the optimum NEA conditions? Our investigation concerning this point is the topic of this contribution.

## 2 XPS studies of GaAsP-photocathodes.

Figure 2 shows a side view of the XPS apparatus used. In the center of an UHV-chamber (base pressure  $2 \times 10^{-10} mb$ ) there is a target holder that may contain up to four samples. The samples are introduced via a load lock and may be heated from the rear by radiation from a tungsten filament. We use dispenser cathodes of SAES

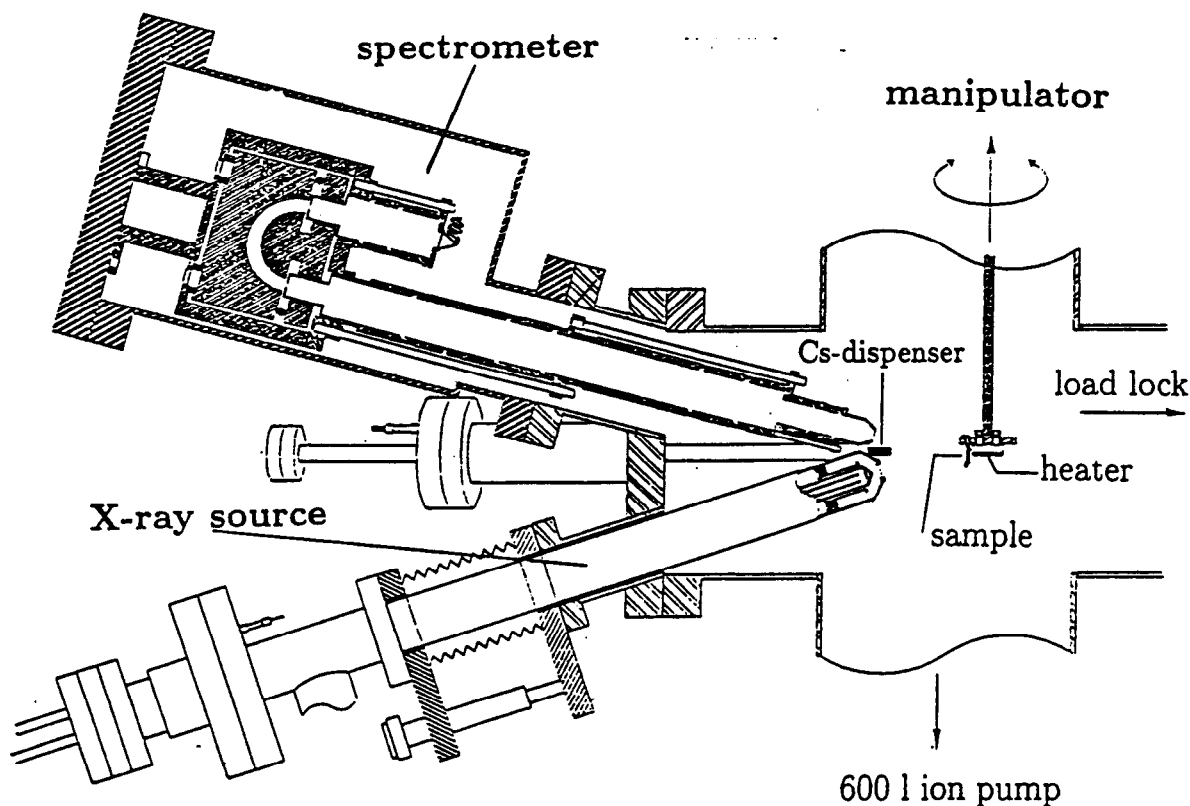


Figure 2: Side view of XPS apparatus.

Getters, Milano in Italy, for cesiation of a sample. Oxygen may be introduced into the chamber via a leak valve. The X-ray source has been purchased from VWS, Great Britain. It possesses two different anodes of aluminum and magnesium respectively. The energy of electrons released at the sample surface by  $K_{\alpha}$ -radiation of Mg or Al respectively is determined with help of a  $\beta$ -spectrometer whose dispersive element consists of an electric spherical condenser.

Figure 3 shows an overall X-ray photoelectron spectrum emitted from an activated  $\text{GaAs}_{.65}\text{P}_{.35}(100)$ -surface irradiated by  $K_{\alpha}$ -light from magnesium. Besides lines stemming from the GaAsP-substrate one sees clear peaks originating from Cs. The most prominent feature is the doublet at an energy around 520 eV that is due to photoionisation of the  $3d_{5/2,3/2}$  inner shell of cesium. In figure 4 the same doublet is shown with expanded energy scale. The cross hatched area under the  $3d_{5/2}$ -peak is taken as a measure of Cs-coverage of a sample in the following. Other lines that are also registered routinely in our investigations are shown in figure 5.

It is known (see e.g. [1]) that only one monolayer of cesium can be adsorbed on a GaAs-surface at room temperature. This fact can be exploited for calibration of the  $3d_{5/2}$ -peak area in our photoelectron spectra in units of Cs-monolayers. Figure 6 shows the result of a cesiation of a clean GaAsP(100) surface. The Cs- $3d_{5/2}$ -signal increases rapidly immediately after the start of cesium flux from a dispenser cathode but saturates after approximately 50 minutes of continuous cesiation in the

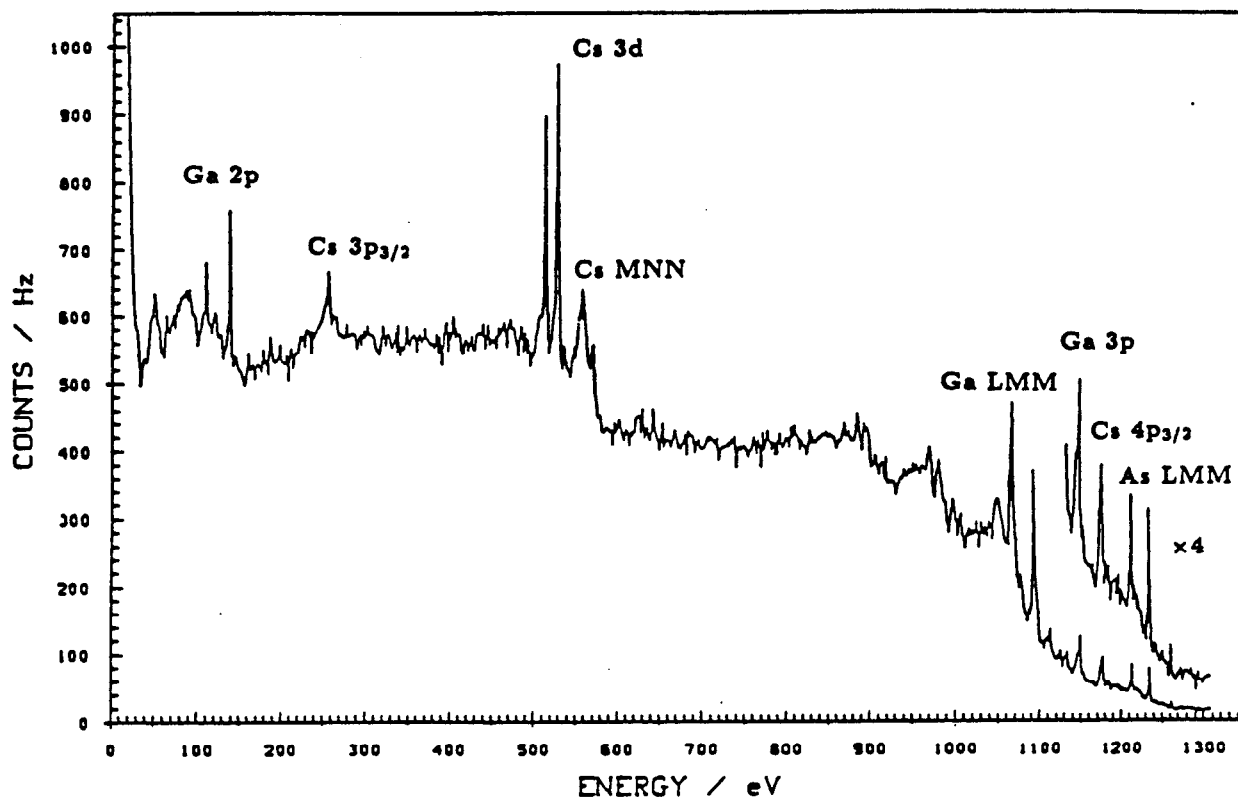


Figure 3: Energy spectrum of electrons released from a cesiated  $\text{GaAs}_{0.65}\text{P}_{0.35}$ -surface by  $\text{MgK}_\alpha$ -radiation.

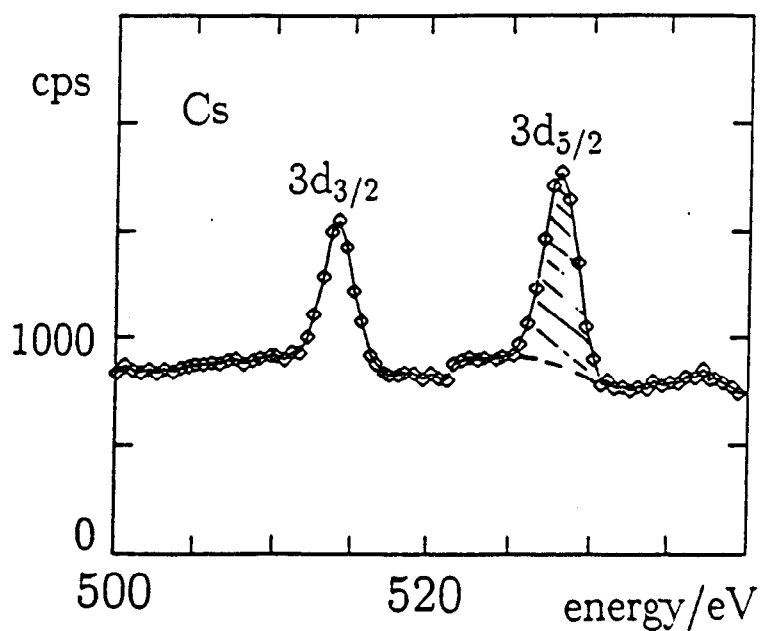


Figure 4: Cs- $3d_{5/2,3/2}$ -doublet.

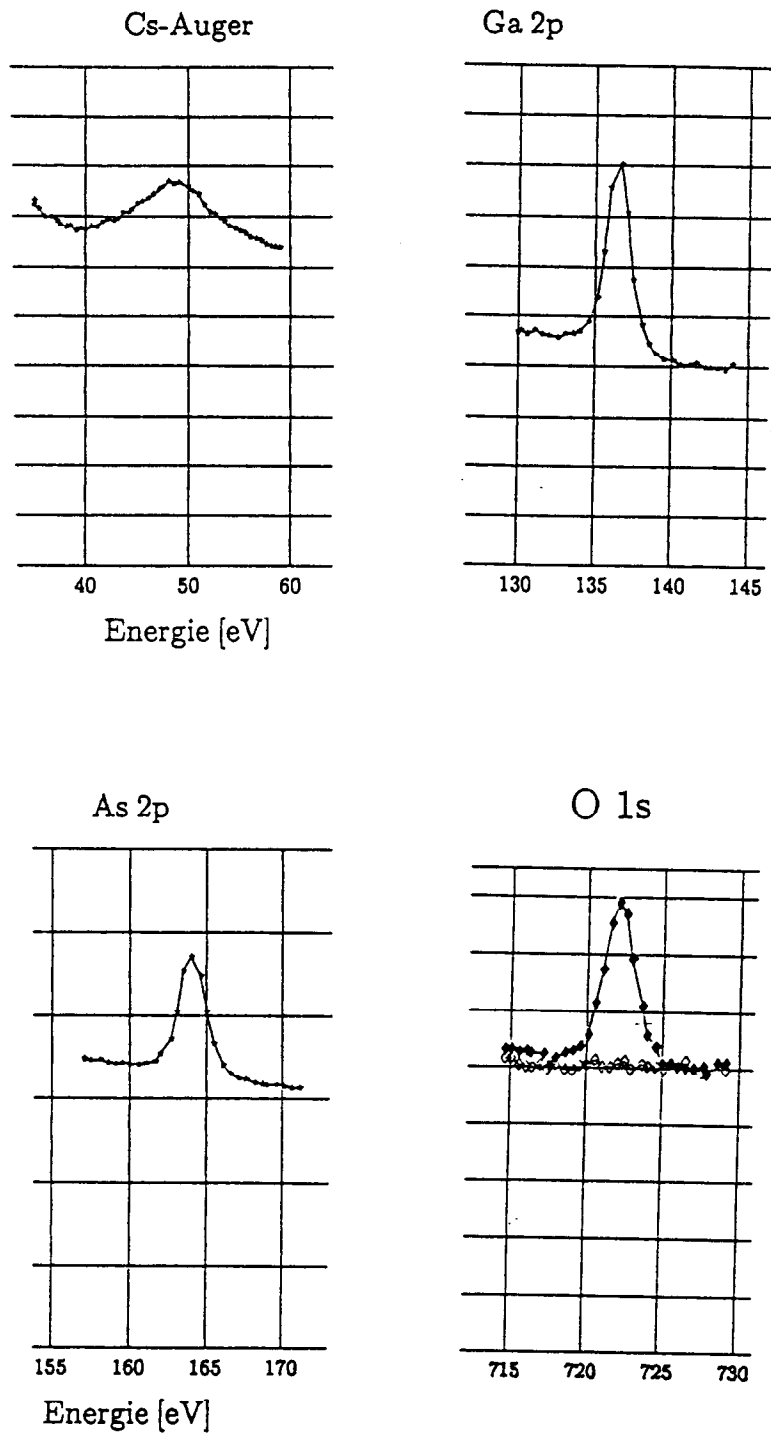


Figure 5: Electron lines due to Auger-process in Cs and photoionisation of Ga-2p-, As-2p-, and O-1s-inner shells.

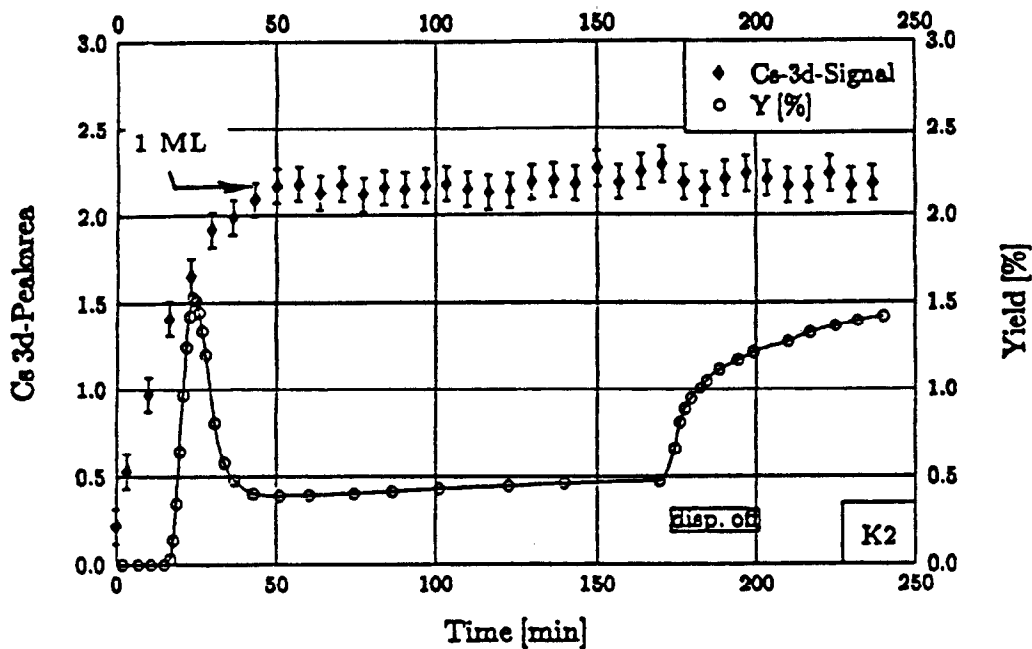


Figure 6: Cs-preparation of a  $\text{GaAs}_{.65}\text{P}_{.35}(100)$ -surface.

- • • Cs- $3d_{5/2}$ -peak area.
- ○ ○ quantum yield

example shown. The saturation signal is that corresponding to a Cs-coverage of one monolayer. During the cesiation procedure the quantum yield is measured at 633 nm (HeNe-laser light). The yield is also plotted in figure 6. It goes through a maximum at coverages below that of one monolayer in agreement with the findings of other experimenters, e.g. of D. Rodway [2] or Kamaratos and Bauer [3]. Switching off the Cs-flux does not affect the Cs-signal in figure 6 within error bars, but the yield increases again. Such a behaviour of the quantum yield has been also reported e.g. by Smith and Huchital [4] and others. We do not understand this second growth of photocurrent, yet, but the point in this context is that we observe a change in yield which obviously is not accompanied by a loss of cesium from the surface.

We believe that the limited life time of a III-V-photocathode activated to negative electron affinity by cesium is not produced by a loss of cesium during its life. Figures 7 and 8 show the Cs- $3d_{5/2}$ -signal and the yield of a  $\text{GaAs}_{.65}\text{P}_{.35}(100)$  cathode as a function of time. Both figures present data of the same measurement, the time scale is different only.

The cathode was activated in the beginning with cesium up to the first yield maximum (figure 6). One sees that the Cs-signal does not change over a period of nearly 100 hours after activation while the yield goes through a flat maximum followed by a decrease by a factor of two roughly. During XPS data taking one sees a recovery of yield in figure 8. We believe this is due to a release of contaminants from the cathode surface because of irradiation with X-rays, but we were not able yet to identify such contaminants.

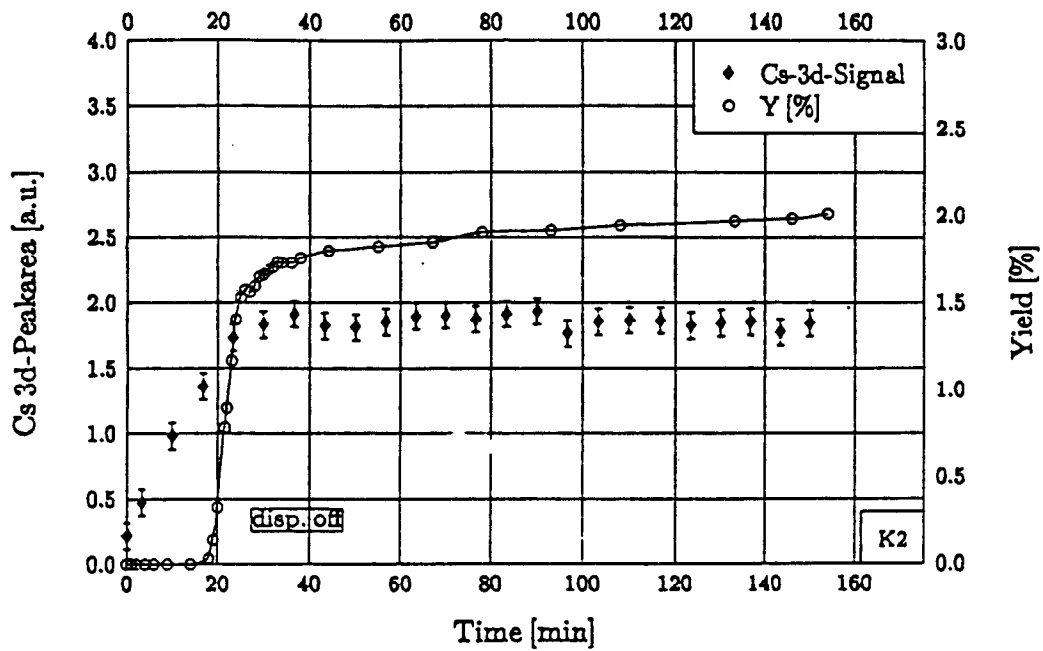


Figure 7: Cs-coverage and quantum yield of a  $\text{GaAs}_{.65}\text{P}_{.35}(100)$ -surface as a function of time.

- • • Cs- $3d_{5/2}$ -peak area.
- ○ ○ quantum yield

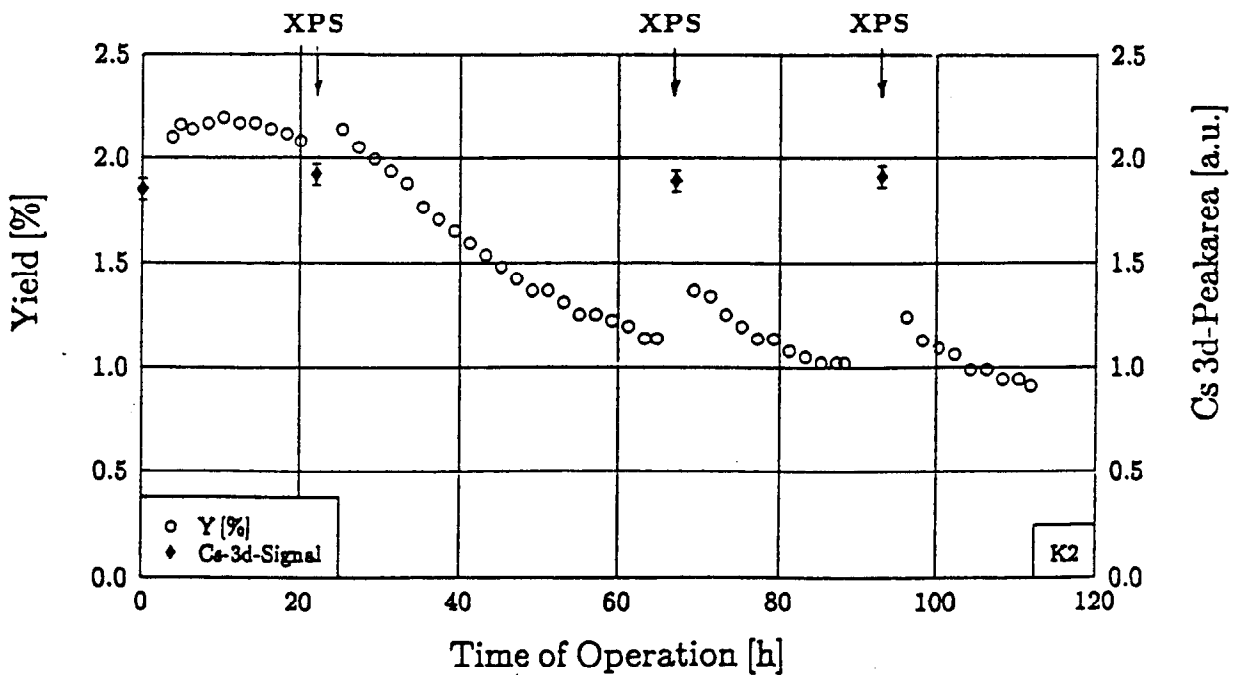


Figure 8: Cs-coverage and quantum yield of a  $\text{GaAs}_{.65}\text{P}_{.35}(100)$ -surface as in figure 7. Different time scale. Quantum yield curve has been reproduced in figure 1.

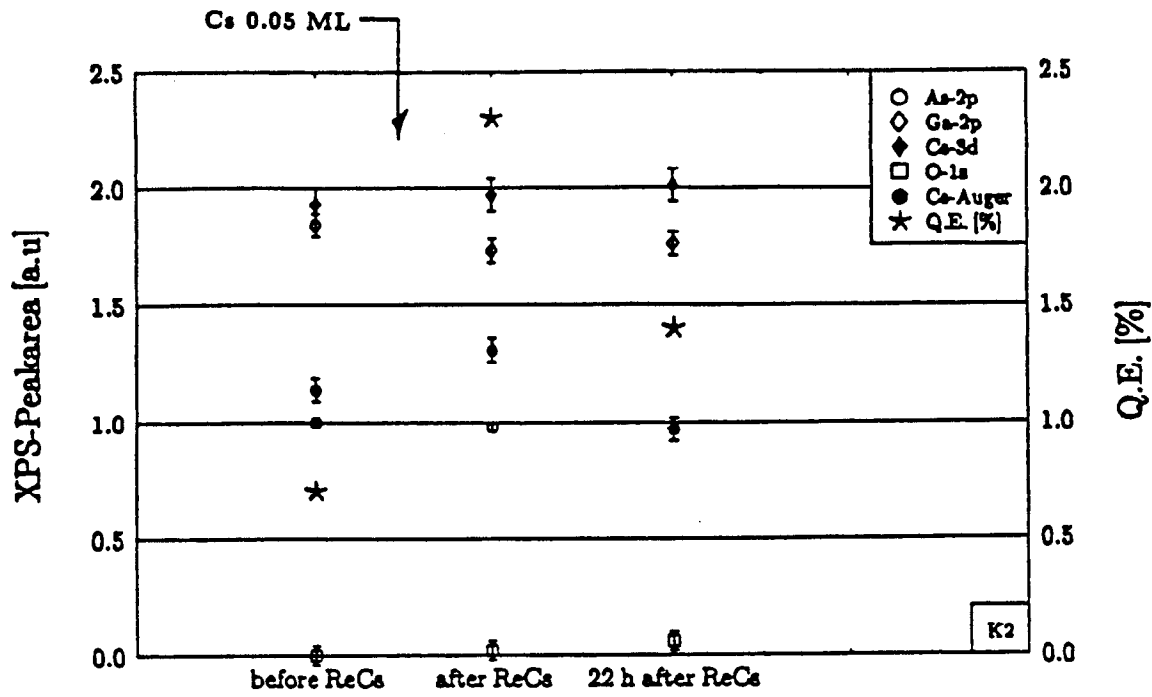


Figure 9: Recesiation of a  $\text{GaAs}_{.65}\text{P}_{.35}(100)$ -surface after 120 h of continuous operation.

Comparison of quantum yield, of photoionisation signals of As-2p, Ga-2p, Cs-3d, O-1s, and of the Cs-Auger line before and after recesiation.

The error bars at the Cs- $3d_{5/2}$ -signal points in figure 8 correspond to an uncertainty of 2% of a monolayer. So our statement of a constant Cs-coverage is true only within 2% also. This is not small enough to rule out a 1% decrease of a monolayer, that might be enough to drop the yield appreciably following Rodway and others [5]. But Rodway argues indirectly only using observations experienced in so-called recesiation. One knows that the yield of an aged III-V-photocathode may be regained by exposing the surface for a short time to another slight cesium flux. A total amount of Cs corresponding to a few percent of a monolayer is enough in most cases to bring the yield up again. It is tempting now to argue, as Rodway does, that recesiation just compensates for cesium losses and restores an optimum coverage with high quantum yield. We do not see that in our spectra. Figure 9 shows several XPS-signals from a  $\text{GaAs}_{.65}\text{P}_{.35}(100)$ -photocathode before and after recesiation. The data are taken with the cathode whose Cs-signal and yield is plotted in figure 8. Recesiation started 120 h after the first Cs-activation (beginning of figure 8). One observes that a total Cs-amount corresponding to 5% of a monolayer brings the yield back to its start value of figure 8. The Cs- $3d_{5/2}$ -signal increases a little bit if at all by recesiation.

An increase of Cs-coverage can also be deduced from the reduction of the Ga-2p-signal. A heatcleaned GaAs(100)-surface has probably a Ga-rich  $c(8 \times 2)$  reconstruction and it is believed that Cs adsorbs preferably at the Ga-sites [3]. If one accepts that heatcleaned GaAsP(100) behaves in a similar way, one should see a

decrease of the Ga-2p-signal on Cs-adsorption, while the As-2p-signal should not change appreciably. Ga- and As- signals just behave like that in figure 9.

The area of the Cs-Auger peak increases also as a result of recession, but decreases again during the following day, while the Cs-d<sub>5/2</sub>-signal stays constant. In our hypothesis recession not only adds cesium to the surface but has also a cleaning effect so that contaminants are taken away from the surface. This should affect most sensitively XPS-signals around 50 eV, at which energies the mean free path of electrons is low. Therefore the Auger-peak at 47 eV should increase more clearly than the d<sub>5/2</sub>-photopeak during recession. The opposite should happen upon subsequent new adsorption of contaminants on top of Cs-atoms.

So in summary in our interpretation the data of figure 9 show that recession of a NEA-III-V-cathode does not compensate for losses in cesium but brings cesium to the surface in addition to that of the primary cesiation.

The sensitivity of XPS for oxygen is an order of magnitude lower than that for cesium [6]. So the O-1s-data in figure 9 only show that the oxygen contribution to the surface layer may be zero, but at present our apparatus is not sensitive enough to exclude a small nonzero oxygen admixture.

### 3 Thermal desorption of Cs from NEA III-V cathodes.

Thermal desorption data from the literature confirm the strong bonding of cesium to a GaAs-surface. This is shown nicely in so-called programmed thermal desorption experiments (PTD). Examples are the works of Wada et al. [7], Kamaratos and Bauer [3], and Goldstein and Szostak [8] who investigated Cs-desorption from GaAs(100), or of Derrien and D'Avitaya [9] who studied GaAs(110).

The PTD-data show at least two binding energies of Cs to GaAs(100), the lower with a value around 1.6 eV for layer thicknesses that correspond to activation to maximum photoelectron yield. If one assumes, that the desorption is governed by a rate equation of Arrhenius form ( see e.g. [10]),

$$\frac{dn}{dt} = -n\nu e^{-\frac{E}{kT}} \quad (1)$$

n = Cs-atoms/m<sup>2</sup>  
E = binding energy  
T = temperature/K  
ν = rate constant



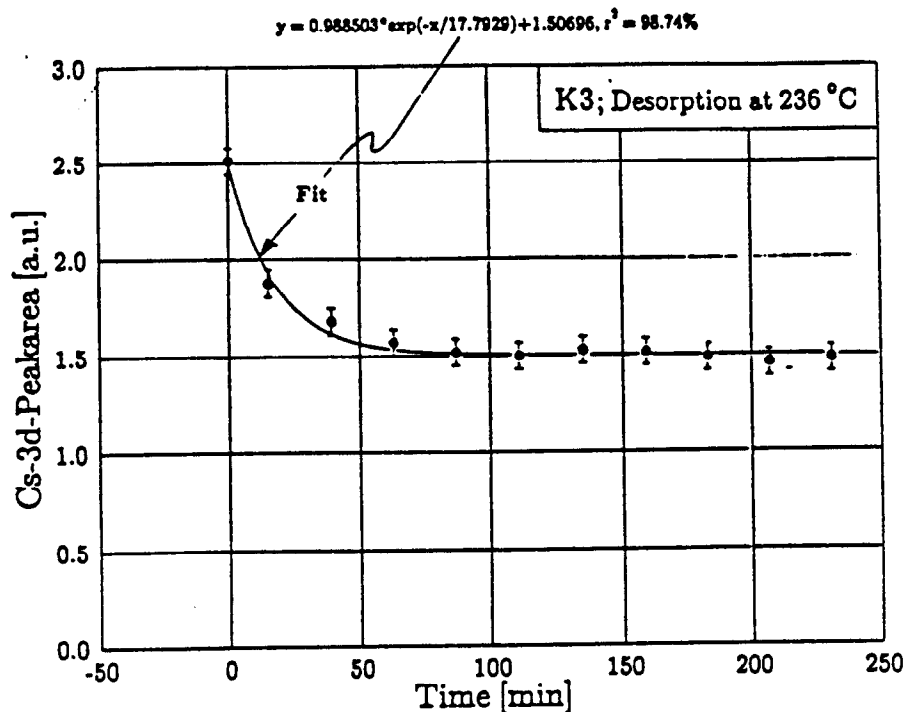


Figure 10: Cs-desorption from a GaAs<sub>0.65</sub>P<sub>0.35</sub>(100)-surface at T = 509 K.

one arrives at a negligible Cs-loss with time at room temperature. Taking for example  $\nu = 10^{13} \text{ s}^{-1}$ , which is a typical value for a vibration frequency of an atom bound to a surface,  $E = 1.6 \text{ eV}$ , and  $kT = 0.026 \text{ eV}$ , the Arrhenius equation gives

$$\frac{1}{n} \frac{dn}{dt} = -2 \times 10^{-14} \text{ s}^{-1} \quad (2)$$

which says that there is practically no desorption of cesium at room temperature.

The data shown in figure 10 confirm the PTD observations. We heated a GaAsP(100) sample prepared by Cs-adsorption up to maximum photoyield by a sudden temperature increase from room temperature to 509 K. The Cs-3d<sub>5/2</sub>-signal decays exponentially in the first hour after the temperature jump, until it levels off at a practically constant value at later times. In our interpretation the exponential decay is due to a binding state at relatively low energy, while the constant Cs-coverage at later times corresponds to Cs-atoms staying in a bond with substantially higher energy. If we assume again a desorption rate given by equation (1) and take again  $\nu = 10^{13} \text{ s}^{-1}$ , we get a binding energy of the low lying Cs-state of 1.6 eV in agreement with the PTD-data.

We admit that the interpretation of the PTD-measurements and of our data sketched in figure 10 by using equation (1) is very crude indeed. So we take the numbers of binding energy and desorption rate as a rough indication only. Nevertheless they confirm our hypothesis that Cs is fairly tightly bound to a GaAs- or GaAsP- surface, so that at room temperature there is practically no loss of cesium from a sample activated to NEA by Cs-coverage.

## 4 Conclusions.

1. Cesium is tightly bound to a GaAs- or GaAsP-surface. Degradation of quantum yield of a cathode activated to negative electron affinity is not due to thermal desorption of Cs at room temperature [11].
2. The question is what else is responsible for III-V-cathode degradation if the first statement is true.

One could think of changes in the surface layer due to disturbance of its crystallographic order. We have indications that in an operational gun the NEA photocathode is damaged by ion bombardement. Ions may be created by electron impact ionisation of the rest gas or by electron stimulated ion desorption from the walls of the gun chamber. K. Aulenbacher will discuss this process in another contribution to this workshop [12].

In addition to that we believe that cathode degradation is produced by contaminating atoms or molecules adsorbed at the cathode surface. Candidates are oxygen and hydrogen which will be found in all UHV systems. One knows that overoxydation of a cesiated cathode will diminish its yield. Oxygen is scarcely seen in the mass spectrum of the rest gas of a well baked UHV apparatus, but it is certainly existing at the walls of a metal vacuum chamber, from where it may be released by electron stimulated desorption. It is true that we do not see oxygen in our XPS-data of a degrading GaAsP-cathode, but this may be due to the low sensitivity of XPS for detection of oxygen.

Hydrogen is the most abundant element in the rest gas of a metal UHV system. We flooded our XPS apparatus with  $H_2$  at a pressure of  $10^{-6}$  mb for several minutes, which did not affect the quantum efficiency of our GaAsP cathode. So we think that  $H_2$ -molecules do not harm. But may be that H-atoms or  $H^+$ -ions produced by electron stimulated desorption, dissociation, or impact ionisation produce a cathode degradation.

3. Recommendations.

We believe that the life time of NEA GaAs- or GaAsP-cathodes is limited because of neutral as well as ionic contaminations coming from the residual gas or from the vacuum chamber walls via electron stimulated desorption. Not knowing the actual degradation process we only may repeat two rules set up in the early days when work with NEA III-V-photocathodes started:

- a) A NEA III-V photocathode should be operated in the best vacuum attainable.
- b) Electron stimulated desorption should be avoided at least in the neighbourhood of the cathode by designing an electron beam line of a transmission as high as possible.

## References

- [1] R. Cao, K. Miyano, T. Kendelewicz, I. Lindau, and W. E. Spicer, "Metallization and fermi-level movement at the Cs/GaAs(110) interfaces," *Phys. Rev. B*, vol. 39, pp. 12655-12663, 1989.
- [2] D. Rodway, "AES, photoemission, and workfunction study of the deposition of Cs on (100) and (111)B GaAs epitaxial layers," *Surface Science*, vol. 147, pp. 103-114, 1984.
- [3] M. Kamaratos and E. Bauer, "Interaction of Cs with the GaAs(100) surface," *J. Appl. Phys.*, vol. 70, pp. 7564-7572, 1991.
- [4] D. L. Smith and D. A. Huchital, "Adsorption kinetics of Cs on GaAs," *J. Appl. Phys.*, vol. 43, pp. 2624-2628, 1972.
- [5] D. C. Rodway and M. B. Allenson, "In situ surface study of the activating layer on GaAs(Cs,O) photocathodes," *J. Phys. D: Appl. Phys.*, vol. 19, pp. 1353-1371, 1986.
- [6] J. Moulder, W. Stickle, P. E. Sobol, and K. D. Bomben, *Handbook of X-ray Photoelectron Spectroscopy*. Perkin-Elmer Corporation, 1992.
- [7] T. Wada, T. Nomura, M. Miyao, and M. Hagino, "A thermal desorption analysis for the adsorption of CO<sub>2</sub> on GaAs photocathodes," *Surface Science*, vol. 285, pp. 188-196, 1993.
- [8] B. Goldstein and D. Szostak, "Different bonding states of Cs and O on highly photoemissive GaAs by flash-desorption experiments," *Applied Physics Letters*, vol. 26, pp. 111-113, 1975.
- [9] J. Derrien and F. A. D'Avitaya, "Kinetics of thermal desorption using Auger electron spectroscopy application to cesium covered (110) gallium arsenide," *Revue de Physique Appliquee*, vol. 11, pp. 377-385, 1976.
- [10] R. J. Madix, *In: Chemistry and physics of solid surfaces, vol.2*, pp. 63-72. CRC Press, 1979.
- [11] V. Guidi, "Private communication," 1993. In investigations using Rutherford Backscattering one also does not see a decrease of Cs-coverage with time of operation of a NEA GaAs-cathode.
- [12] K. Aulenbacher, "Operational experience with the MAMI polarized source," in *Workshop on Photocathodes for polarized electron sources for accelerators, SLAC*, 1993.

**Richard Sheffield**  
**Los Alamos National Laboratory**

**AFEL Accelerator**

This presentation will cover Los Alamos's experiences with cesiated cathodes in rf cavities. This will include multipactoring and breakdown issues. Also, the effects of excess cesium and how to handle cesium contaminated structures will be covered.

# AFEL Accelerator

- Design
- Multipactoring
- Emittance Measurements
- Lifetime Issues
- Other Engineering Issues

Rich Sheffield  
Los Alamos Nat'l Lab.  
505-667-1237

# Gun Parameters

$$E = 10 - 20 \text{ MeV}$$

$$Q \leq 10 \text{ nC}$$

$$\tau_p = 7 - 20 \text{ ps}$$

micropulse sep. 5 to 10 ns

macropulse  $\leq 25 \mu\text{s}$

1300 MHz accel. freq.

< 100 Hz rep rate

# Photoinjectors

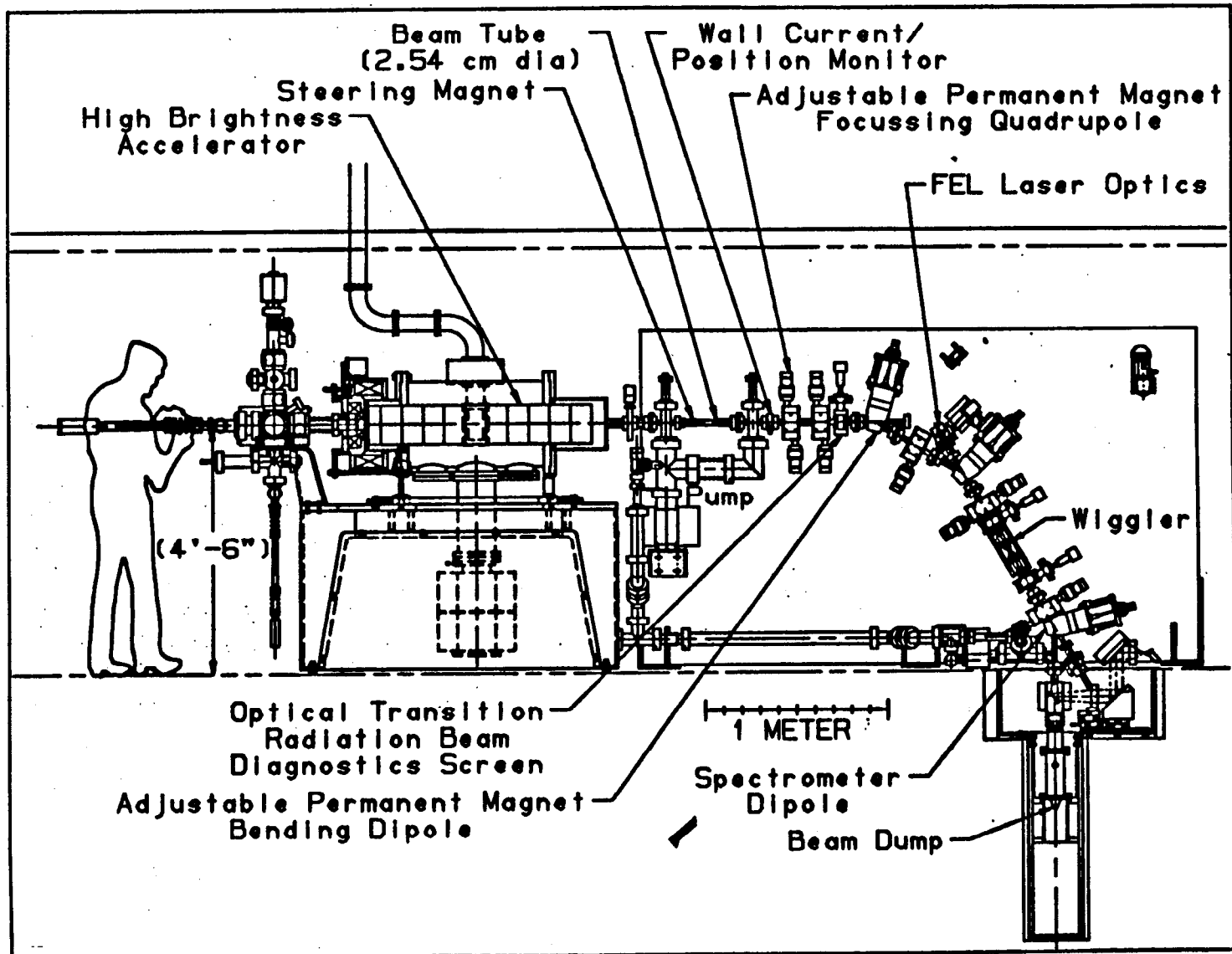
Why?

- Simplicity
- Very High-Brightness for High Q
- High Average Currents

Why not?

- Life time
- ~~Laser~~

$\frac{R}{S}$

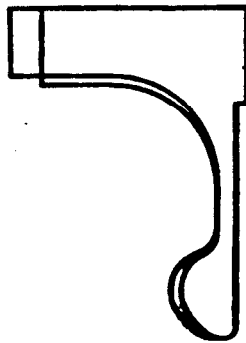




## **OTHER FEATURES**

---

- **FIRST CELL 9 mm LONGER**



30 degrees start phase  
charge independent  
1.5 MeV vs 1.0 MeV

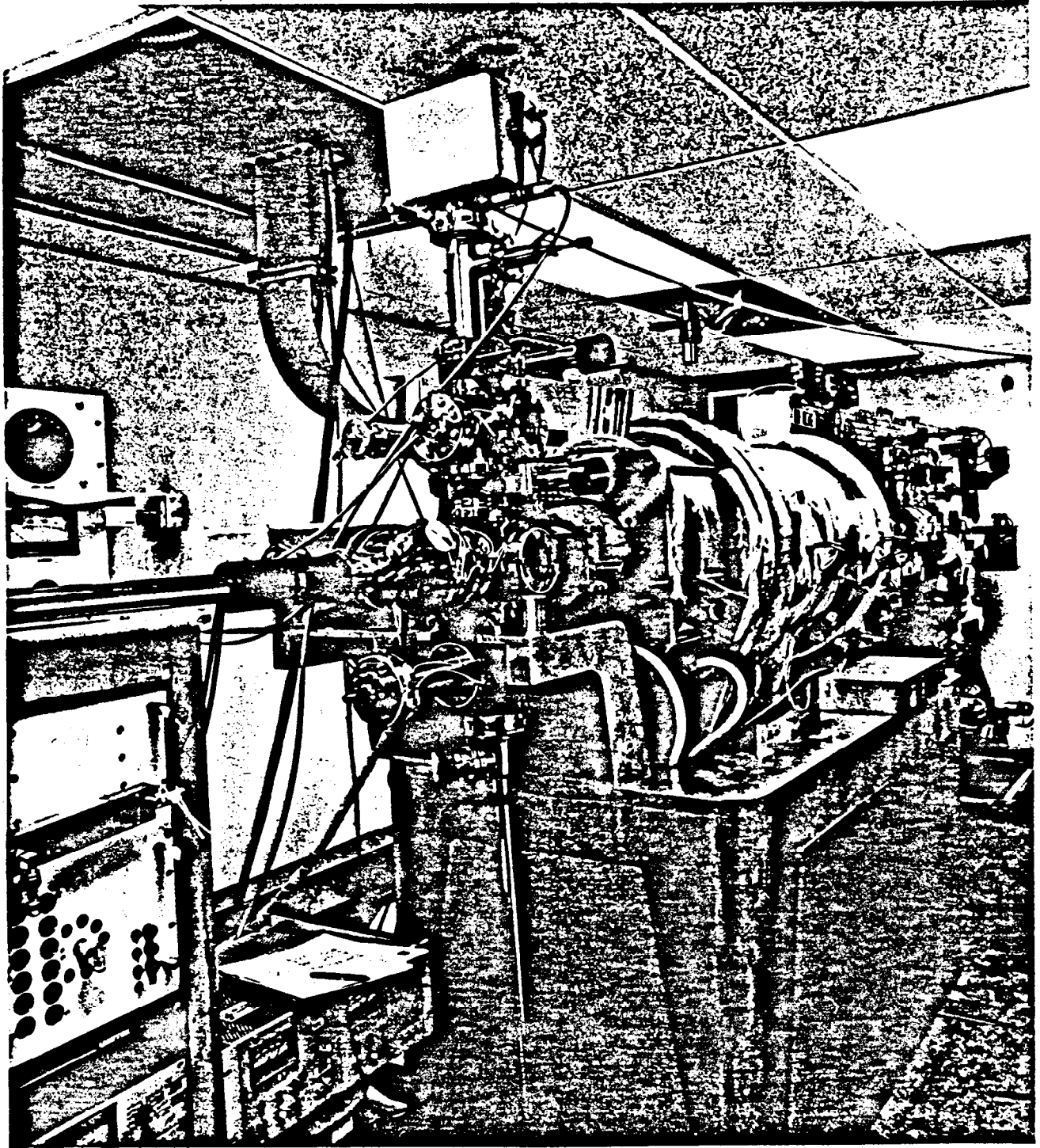
- 
- **HIGH Q, HIGH GRADIENT  
CAVITIES**

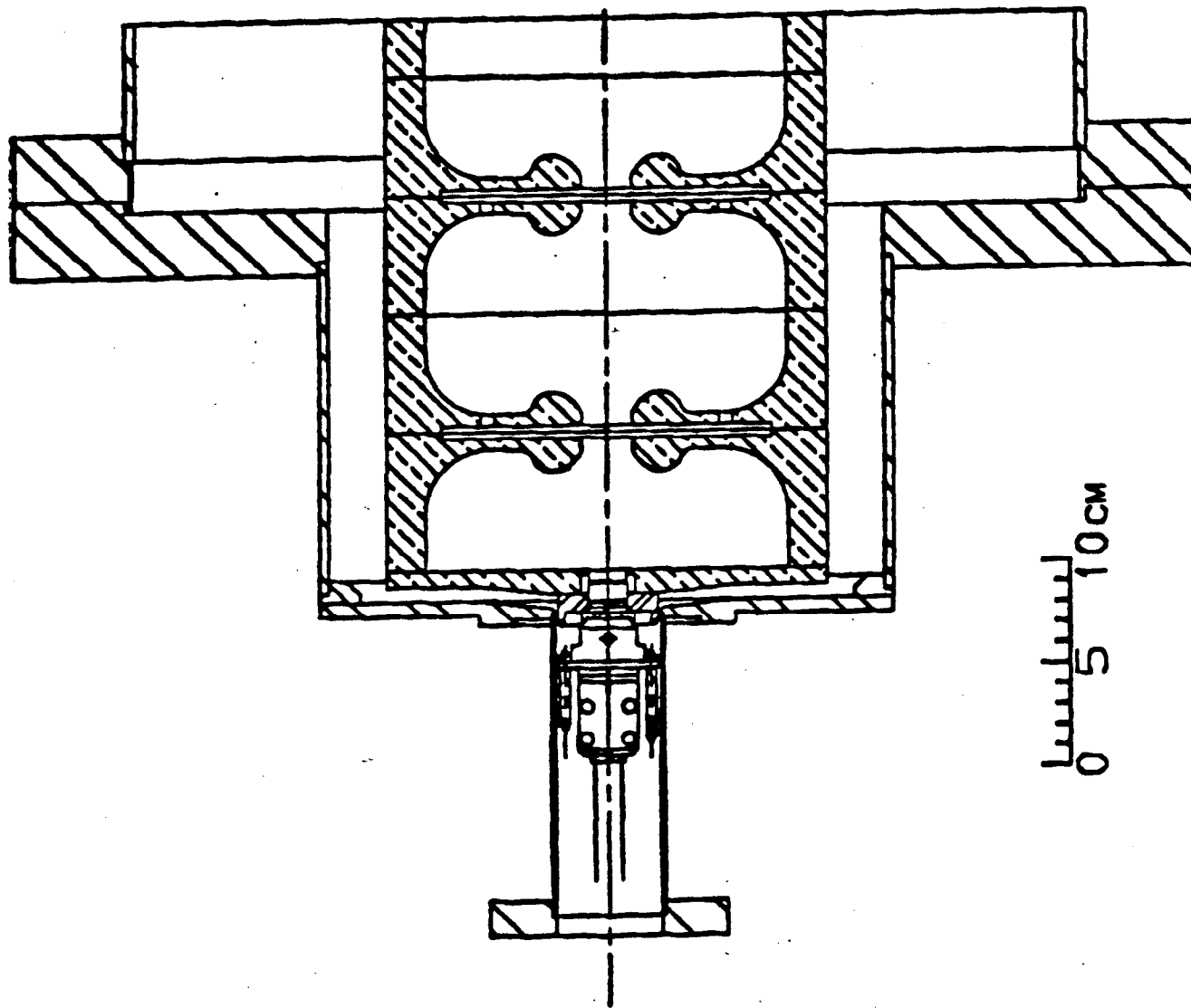
- **SINGLE RF FEED**

(SMALL ENERGY CORRECTING CAVITY DESIGNED IF REQUIRED)

- **CRYOGENIC OPERATION**

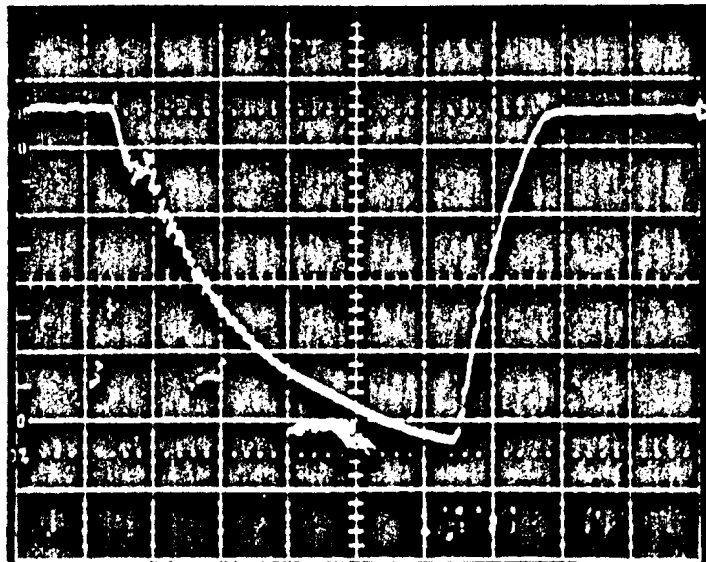
**LOS ALAMOS NATIONAL LABORATORY**



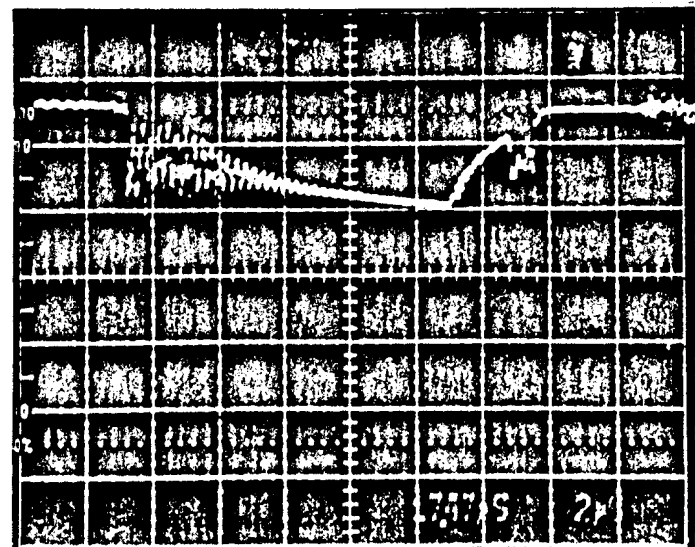


# LOW-LEVEL MULTIFACTORING OCCURS IN THE COUPLING CELLS

---



ACCELERATOR CELL



COUPLING CELL

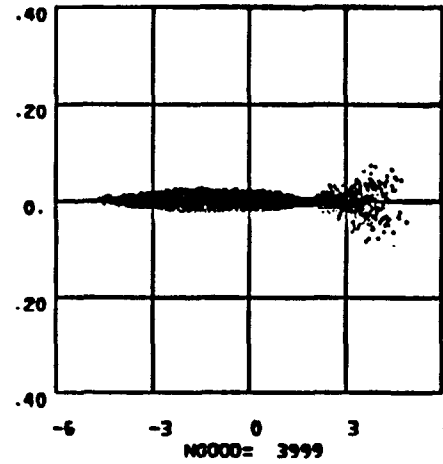
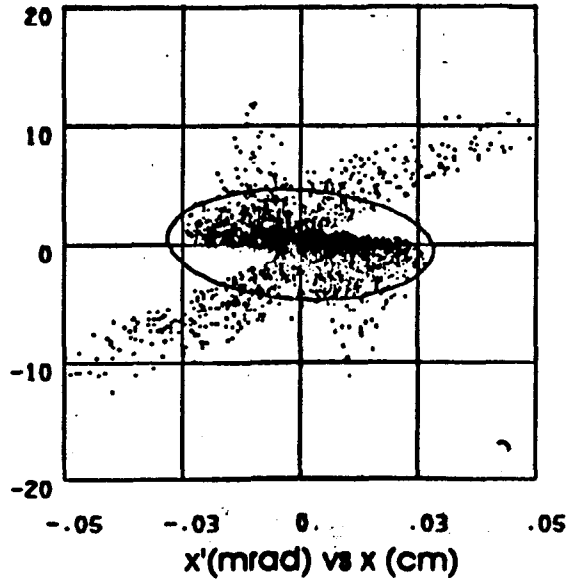
LOS ALAMOS NATIONAL LABORATORY

## MULTIPACTORING RESTRICTED OPERATING PARAMETERS

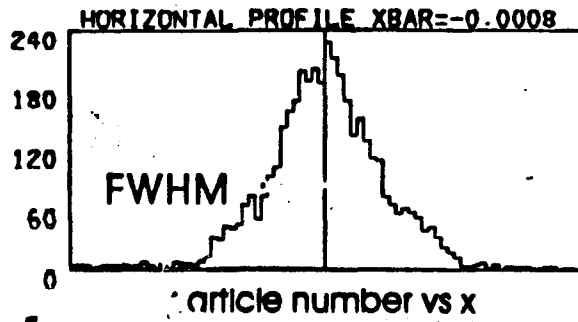
---

- At  $< 2$  MW into accelerator, low-level multipactoring occurs in the coupling cells
- Operated for one year with no multipactoring for  $> 2$  MW
- In March, field collapse occurred at all power levels, dependent on the solenoid fields
- Two possible sources: metal sliver or cesium compounds in cavities
- By cleaning structure, multipactoring was eliminated

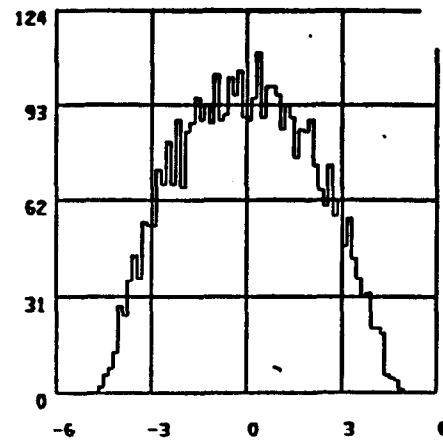
# TEMPORAL END EFFECTS INCREASE RMS EMITTANCE



$x$  (cm) vs time (degrees@1.3 GHz)

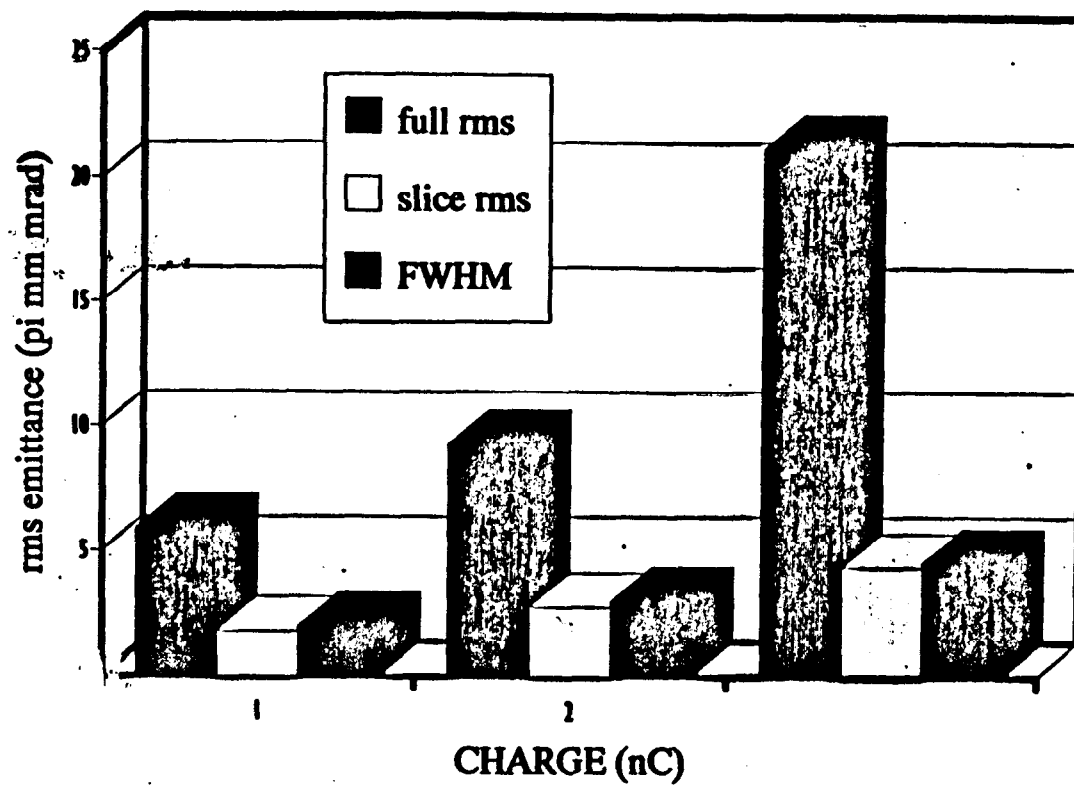


1 nC, 13.5 MeV, 10 ps initial length,  
.3 cm cathode radius

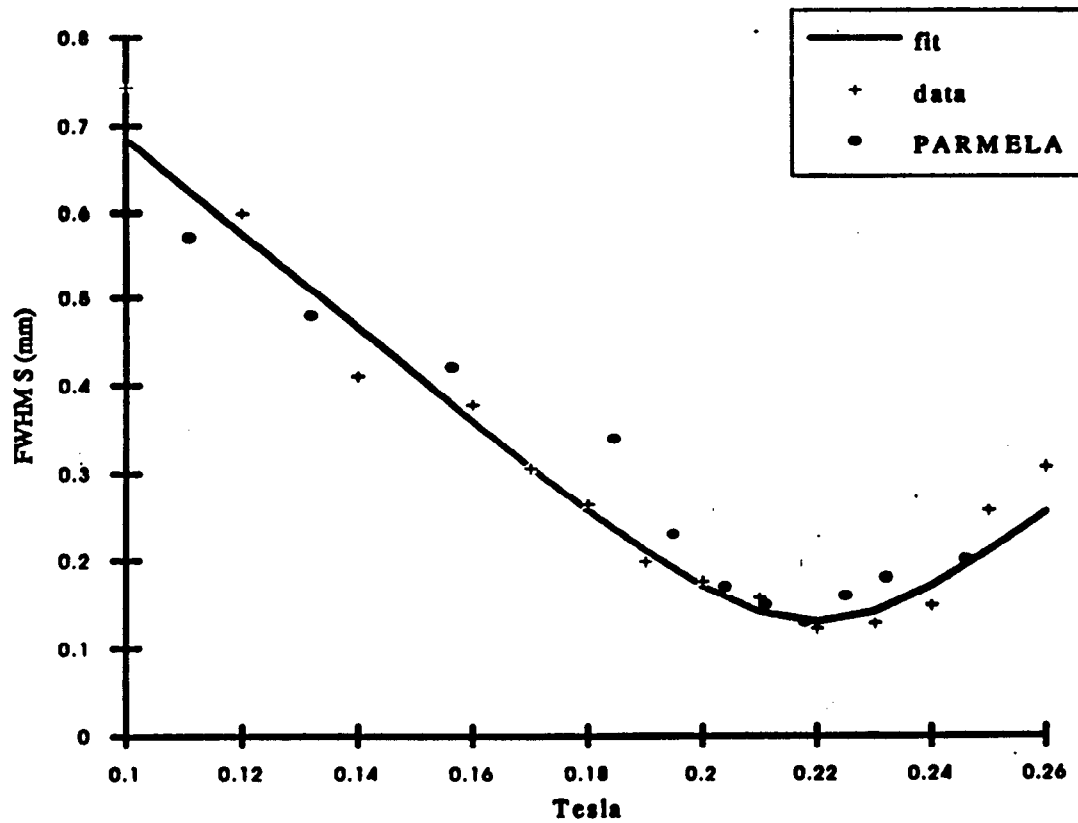


no. of particles vs time (degrees@1.3 GHz)

# THE SLICE RMS EMITTANCE IS CLOSE IN VALUE TO THE FWHM EMITTANCE



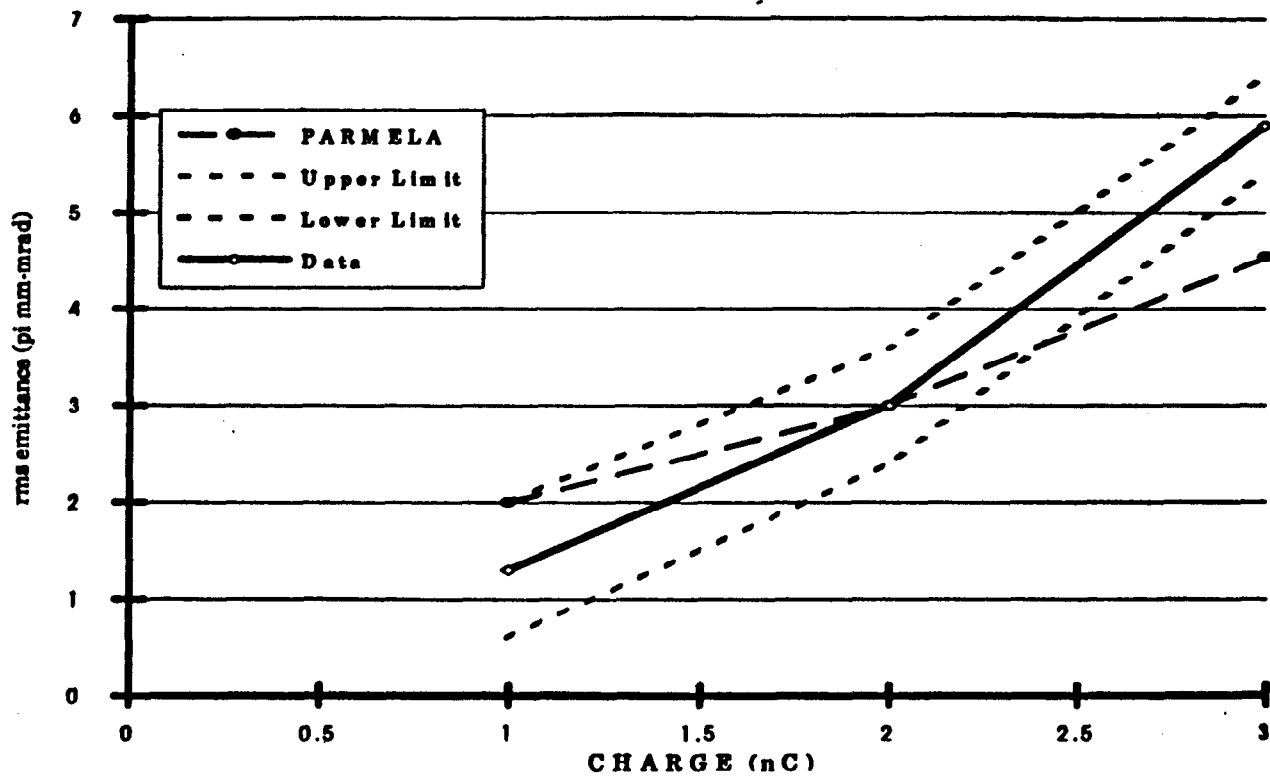
## At 1 nC, experiment and simulation are in good agreement



LOS ALAMOS NATIONAL LABORATORY



# AT 1 nC AND 2 nC, EXPERIMENT AND SIMULATION ARE WITHIN ERROR BARS



# ENGINEERING ISSUES

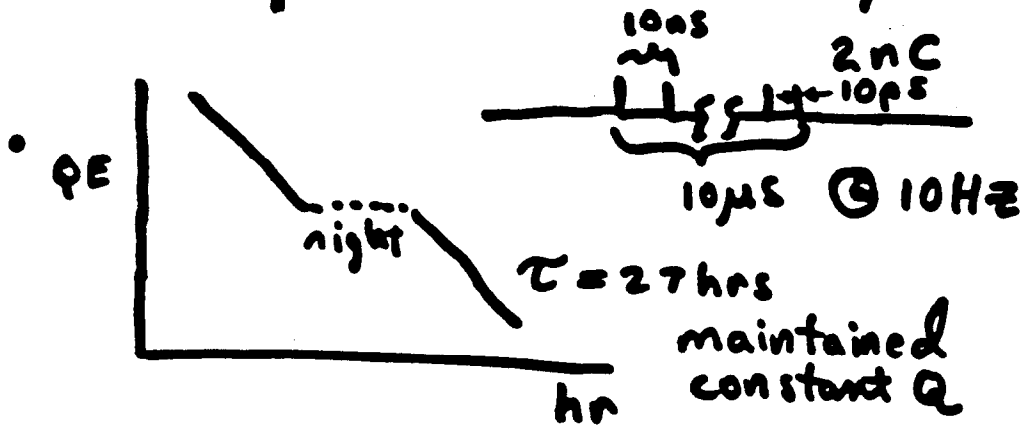
---

- **PHOTOCATHODE MATERIALS:**
  - 1) low QE
  - 2) high QE
- **FIELD EMISSION**
- **UNIFORMITY OF LASER ILLUMINATION AND CATHODE QE**
- **PRESERVATION OF BRIGHTNESS THROUGH REMAINING BEAMLIN**
- **RF AND DRIVE LASER STABILITY**

# Life time Results for Multi-alkali Cathodes

\* Limited by vacuum conditions

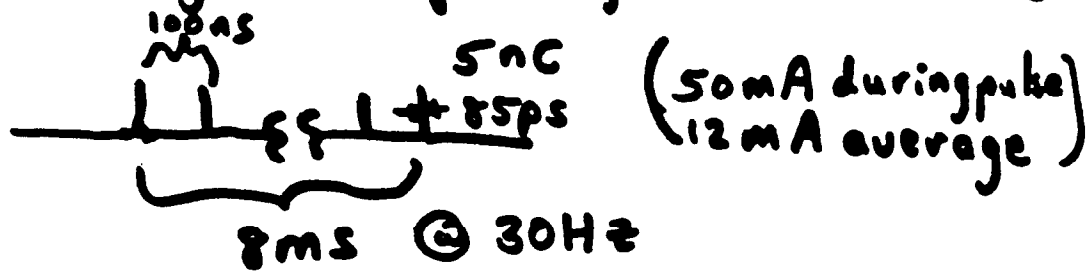
• Over 1yr - minutes to days



• Boeing 26% duty photoinjector

5 MeV, 10 MHz,  $\tau_p = 85 \text{ ps}$ , 5 nC

8ms long macropulse, 433 MHz accel. f



QE 10% ran for 3 hours

# Attempts to Improve Lifetime

- Cs boat for constant Cs background - 2 failed attempts
- Glow discharge - no significant effect
  - Base P is high ( $8 \times 10^{-10}$  to  $4 \times 10^{-10}$ )?
  - Impurities bound tighter than 200eV?
- Run accelerator

For non-pol.  $e^-$  applications

Holy Grail:

$> 0.1\%$  QE

$< 2$  ps response

$p > 10^{-8}$  Torr

$\lambda = 1.05\mu\text{m}, 0.53\mu\text{m}, 0.35\mu\text{m}$

---

## EXPERIMENTAL GOALS

---

- FINISH ELECTRON BEAM PERFORMANCE MEASUREMENTS
  - "USER-FRIENDLY"
- 4 MICRONS AND UP IN FY93, DEMONSTRATE 10% TUNABILITY
- GREATER THAN 200 WATTS IN THE INFRARED IN FY94
  - VISIBLE WAVELENGTH OPERATION

**H. Siegmann**  
**ETH Honggerberg (Zurich)**

**Production and Detection of SPIN Polarized Electrons**

# PRODUCTION AND DETECTION OF SPIN POLARIZED ELECTRONS

by

F. Meier and H.C. Siegmann

Swiss Federal Institute of Technology, 8093 Zürich, Switzerland

## ABSTRACT

The production of pulsed intense and spin modulated electron beams from negative electron affinity surfaces of p-doped GaAs and Ge depends on the space charge generated by the emerging electron pulse outside the sample and on the photovoltage generated by migration of holes and electrons in the band bending zone at the surface. A double pulse experiment is described allowing to experimentally determine the relaxation time of the photocurrent.

Transmission of low energy electrons through ferromagnetic materials depends on the degree of spin polarization of the electrons along the direction given by the magnetization. This phenomenon is due to inelastic electron scattering into the spin polarized holes of the d-band and may be used for highly efficient detection of spin polarization.

## INTRODUCTION

There are many ways in which one can produce and detect spin polarized electrons. The most efficient way to produce polarized electrons is photoemission from a semiconductor surface such as GaAs with negative electron affinity. The first part of this paper will be concerned with one special aspect, namely the phenomena occurring when intense and short pulses of light from a laser are used to induce photoemission from GaAs and Ge. The two main issues are the space charge produced by the large amount of electrons leaving the surface of the semiconductor and the photovoltage induced in the band bending region. Other work in the DC-mode concerned with spin polarized photoemission from noncubic crystals and metastable strained semiconductor layers is published elsewhere [1,2] and will be described in part by Yu. Mamaev in this meeting.

The best way to detect polarized electrons is not so obvious at this time. Most of the schemes used up to now employ differential elastic scattering of the electrons from heavy atoms in which the spin-orbit interaction can induce a partial spatial separation of the two spin states. The figure of merit for such spin detectors is of the order of  $10^{-4}$  with the best possible value of this figure being unity. Hence there is room for significant improvement in the field of detectors of spin polarization. In the 2nd part of this paper a new scheme for detection of spin polarization is proposed yielding figures of merit of several percent. Such a significant improvement would greatly enhance the range of applicability of spin polarized electrons.

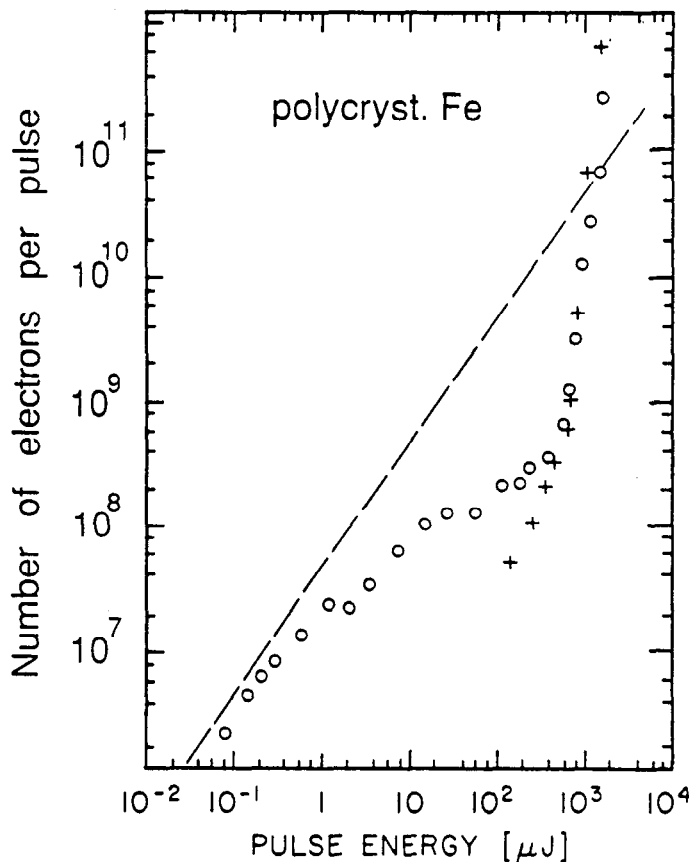


## SPACE CHARGE AND PHOTOEMISSION OF ELECTRONS

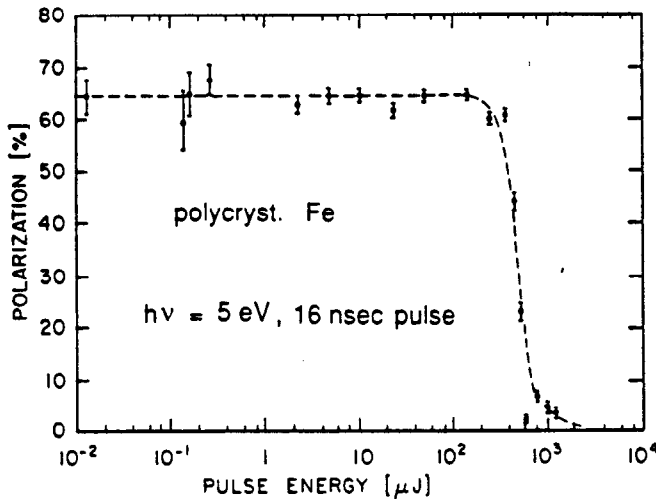
The reason why pulsed lasers only play a minor role in electron spectroscopy is due to the space charge cloud in front of the sample which disturbs the energy distribution and directional characteristics of the photoemitted electrons. This space charge cloud is important as soon as sufficiently large currents of electrons are emitted in a short time. However, it turns out that the space charge has no influence on the total spin polarization of the electrons in the cloud. Although spin exchange collisions may occur between the individual electrons in the cloud, the polarization of all the electrons in the cloud is conserved. This is a consequence of conservation of angular momentum and can be proven in the following experiment.

The photocathode is polycrystalline iron magnetized perpendicular to the surface by the field produced in a superconducting coil. The photoelectrons are excited either by laser pulses of 16 nsec duration or by a monochromatized continuous light beam from a conventional source such as a high pressure arc. The photoelectrons emerging from the sample surface are accelerated and longitudinally extracted from the magnetic field and their intensity and degree of spin polarization  $P$  is measured after further suitable acceleration. The current of positive ions that also might emerge from the sample surface can be measured separately.

Fig. 1 shows that the intensity of the photoelectron pulse increases first linearly with the power of the light pulse but weakens considerably as the light power increases. This is the action of the electronic space charge. The weakening by one or two orders of magnitude of the electron pulse is removed when the space charge in front of the sample is compensated by positive ions. This happens when the surface starts melting in the laser focus. Then the electron pulse shoots up in intensity again even surpassing the strength expected from the initial linear increase.



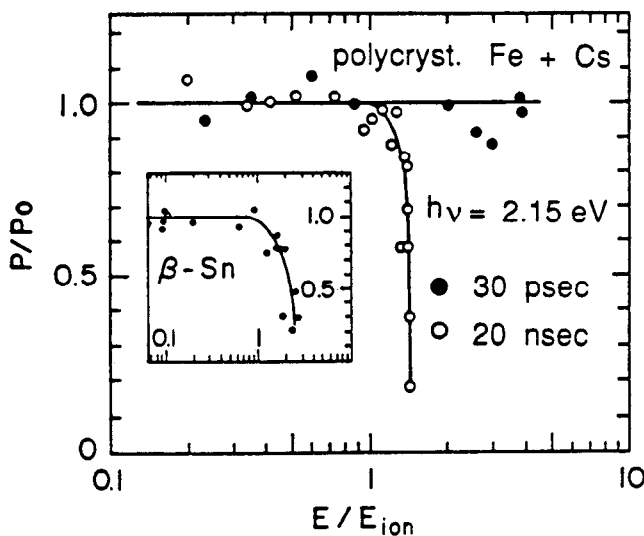
*Fig. 1:* Number of electrons emitted from a sputter cleaned surface of polycrystalline Fe per pulse of light from a KrF-excimer laser with 16 nsec duration and photon energy  $h\nu = 5$  eV (circles). Positive ion emission is indicated by crosses. The straight line is calculated from the yield  $Y \approx 5 \cdot 10^{-5}$  of electrons per incident photon of  $h\nu = 5$  eV as observed with a conventional continuous light source on the same surface. The sample is magnetically saturated perpendicular to the surface in an external field.



**Fig. 2:**  
Spin polarization  $P$  of the electrons vs pulse energy of the laser under the conditions of Fig. 1. The polarization observed with a continuous light source is also 65%. This lamp deposits a photon number on the sample surface which is equivalent to  $10^{-9} \mu\text{J}$  in 16 nsec.

On the same sample where the data of Fig. 1 have been taken a measurement of the spin polarization of the emitted electrons has been made as function of the laser pulse energy, see Fig. 2.

Evidently, the space charge which becomes noticeable above  $1 \mu\text{J}$  according to Fig. 1 has no influence on the spin polarization  $P$ .  $P$  remains at 65% just as observed with the continuous lamp which is  $10^9$  times weaker compared to the  $1 \mu\text{J}$  pulse. This demonstrates impressively that the total spin angular momentum of the photoelectrons is conserved even in the presence of space charge.  $P$  disappears only when the laser pulse heats the ferromagnetic iron sample above the Curie temperature. It should be noted that on the time scale of the 16 nsec pulses used in this experiment the spin system and the lattice are in thermal equilibrium [3].



**Fig. 3:**  
Relative spin polarization  $P/P_0$  of electrons emitted from a cesiated surface of polycrystalline Fe at  $h\nu = 2.15 \text{ eV}$ . The pulse length is 20 nsec (circles) and 30 psec (filled circles). The pulse energy is given in units of the energy  $E_{\text{ion}}$  at which emission of positive ions sets in.  $E_{\text{ion}} = 90 \text{ mJ/cm}^2$  with 30 psec and  $E_{\text{ion}} = 3100 \text{ mJ/cm}^2$  with 20 nsec pulses. The diameter of the pulse focus on the sample is  $110 \mu\text{m}$ . The inset shows the same measurement with circularly polarized light pulses and  $\beta\text{-Sn}$ , in which no difference exists between long and short laser pulses.

The result of an analogous experiment using  $< 100$  psec pulses is *drastically* different, see Fig. 3. With these shorter pulses it is found that the polarization of the Fe sample persists even at pulse energies exceeding the threshold for surface melting as indicated by positive ion emission. The melting process is governed by the electron-lattice relaxation time which is known to be of the order of 1 psec. Accordingly, Fig. 3 shows that on the time scale  $< 100$  psec the thermal equilibrium between the spin system and the lattice is *not* established: the magnetization persists although the Fe is molten. This is another manifestation of conservation of angular momentum. Randomizing the electron spins in the sample means that angular momentum has to be transferred to the lattice. This transfer is slow compared to lattice heating because the electron spin is coupled to the lattice by the weak spin-orbit coupling, acting as a bottleneck for the energy transfer between the two systems.

The fact that melting is fast on a time scale of 30 psec is demonstrated in an experiment where the polarization of optically spin oriented electrons is measured as function of pulse energy. Such a measurement is shown for  $\beta$ -Sn in the inset of Fig. 3. In full contrast to the experiment on Fe the optically induced polarization of the photoelectrons from  $\beta$ -Sn vanishes when the threshold for melting is reached. It is known that from a liquid, i.e., disordered surface optical excitation into spin polarized final states is not possible. In the  $\beta$ -Sn experiment the reaction of the spin polarization to melting is faster than the 30 psec which the laser pulses last. The conclusion is that the electron-lattice relaxation time is shorter than the 30 psec laser pulse - in full agreement with other work - but the spin-lattice relaxation time is not, as proved by the experiment on Fe.

It should be noted that the measurements shown in Fig. 3 have been made on surfaces covered by cesium in order to reduce the work function. Interestingly, the Cs does not disappear from the surface even under exposure to the high energy pulses. The Cs-coverage proved to be stable even after many hundred psec-pulses each heating the sample up to the melting temperature. This is true also for the case of the semiconductor surfaces discussed below.

## EQUILIBRIUM BAND BENDING AND PHOTOEMISSION

Apart from the space charge in front of the surface of the photoemitter, the photovoltage induced in the band bending region is also important to understand high intensity pulsed photoemission from semiconductors. As early as 1968, T.E. Fischer noted that the GaAs surface covered with Cs shows a giant dependence of the work function on temperature [4]. An explanation of this phenomenon was given by Hecht [5].

The band bending in semiconductors is induced by the charge stored in surface or interface states. Such surface states of the Schottky type appear at about the middle of band gap because the periodic potential is abruptly terminated at the surface. If now a metal is evaporated onto the surface, the surface states become occupied with electrons. This defines the position of the Fermi-level at the surface, and band bending must occur depending on where the Fermi-level is located in the undisturbed bulk of the semiconductor. To obtain a negative electron affinity surface, the bands must bend "downwards" for electrons, that is one needs a p-doped semiconductor in which the Fermi-level in the bulk is close to the edge of the valence band. The band bending region in the heavily doped semiconductors used as photocathodes is typically only 10 nm thick. In the electric field of the band bending region, electron hole pairs created by the absorption of the light are separated. The electrons move to the surface and can be trapped there

for a long time, whereas the holes move into the bulk. The charge separation produces an open circuit voltage. In the present application, this photovoltage has a deleterious effect on the performance of the photocathode in that it moves the vacuum level upwards, i.e., it creates a flat band condition removing the band bending and with it the negative electron affinity condition that leads to the high photoelectric yield of the cathode.

The photovoltaic effect has nothing to do with the surface charging effect which occurs due to excitation of electrons from the metal into vacuum, as observed in electron spectroscopy of insulated layers. The photovoltaic effect is far more significant compared to the surface charging in the present case with only about one monolayer of metal at the surface, since most of the photons are absorbed well below the surface.

The surface photovoltage decays in time when the light is switched off. This is due to the fact that - in p-type material - primarily holes are thermoemitted from the bulk into the surface region where they recombine with the electrons. As a consequence the equilibrium band bending is restored. Since the restoring current is thermally activated it depends on temperature exponentially which has been verified in a large number of experiments.

In the following we show that the increase of the vacuum level due to the photovoltage can neatly be observed by measuring the spin polarization of electrons emitted from the semiconductor surface. First, an auxiliary experiment is made with p-doped GaAs in which the work function  $\Phi$  is lowered by successive deposition of very small amounts of cesium at constant temperature  $T = 240$  K. The photon energy of 2.15 eV is chosen such that the spin polarization  $P$  of the total electron current is close to zero at the lowest work function. This means that electrons from both the  $p_{3/2}$ - and the  $p_{1/2}$ -valence states are emitted resulting in  $P \rightarrow 0$ . With higher work functions,  $P$  increases as the emission of electrons from the oppositely polarized and lower lying  $p_{1/2}$ -state is successively cut off. This is indeed what is observed as shown in Fig. 4.

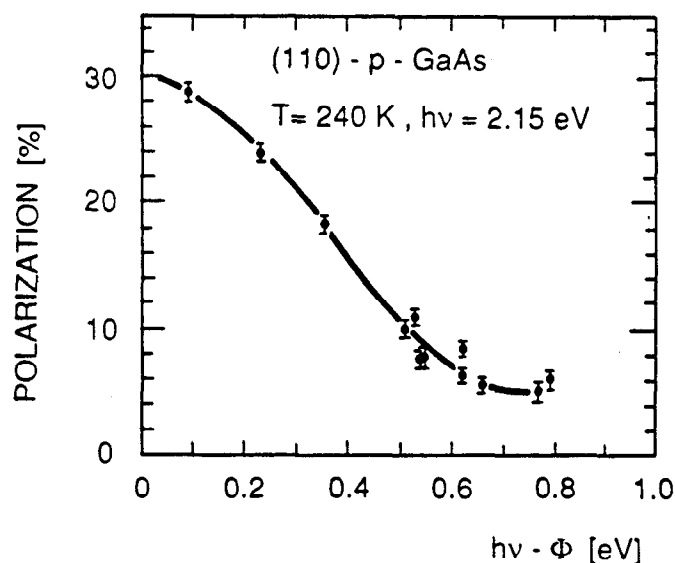
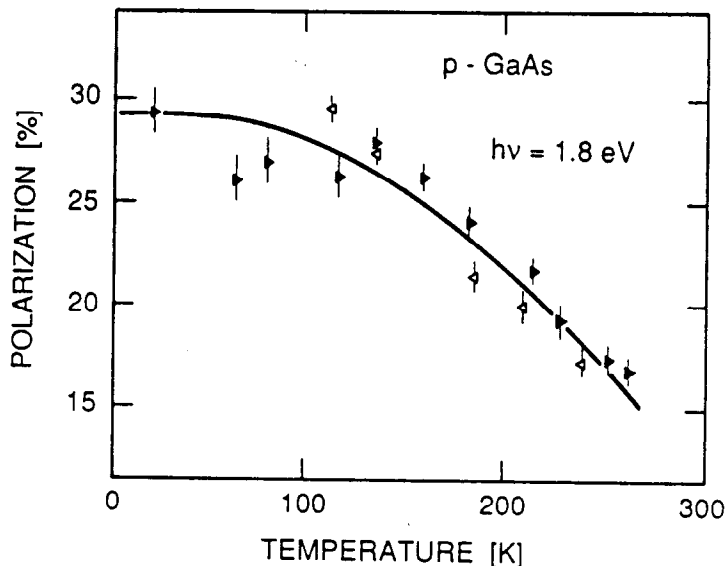


Fig. 4: Spin polarization  $P$  in % of electrons emitted from the cesiated (110)-surface of p-type GaAs (doping with Zn at  $2 \cdot 10^{19}/\text{cm}^3$ ) at  $T = 240$  K and with photons of 2.15 eV from a continuous light source. The work function  $\Phi$  is lowered by successive evaporation of very small amounts of Cs as in the activation process.

Next, we show the effect of the T-dependent surface photovoltage on the polarization. The cesium coverage and the photon energy and intensity are kept constant but the temperature is changed in the range  $10 \text{ K} < T < 300 \text{ K}$ . According to Fischer [4], the work function  $\Phi$  is considerably lowered on heating. This lowering of  $\Phi$  is directly related to the relaxation of the photovoltage; it is clearly larger than the T-dependent shift of the band structure. At very low T, the photovoltage is unable to relax and induces a flat band condition, that is the work function is high even with the little illumination by the continuous light source. As soon as the relaxation of the photovoltage is more effective at higher temperatures, the band bending is restored, that is the work function is lowered. This is why the polarization of the photoemitted electrons decreases in Fig. 5.



*Fig. 5:* Spin polarization P in % of electrons emitted from the surface of Fig. 4, but with photons of 1.8 eV from a continuous light source. P is reduced as the work function decreases due to the restoring of the band bending with increasing temperature T.

In previous work it has been assumed that the increase of the polarization on lowering T is due to the reduction of depolarizing effects while the electrons migrate to the surface. According to the present observations, the photovoltage is the more likely cause of the change in P with T. In fact, no depolarizing effect has so far been clearly identified in photoemission from GaAs negative electron affinity surfaces. This is not to say that depolarization of the electrons in the semiconductor during transport to the surface is totally absent, yet it is certainly not obvious that such a depolarization is needed to explain the increase of P on lowering T.

#### OPTICAL PUMPING AND PHOTOEMISSION OF ELECTRONS WITH PULSED LASER BEAMS

With this knowledge about the effects of space charge and photovoltage one can now proceed to understand the phenomena occurring when pulsed laser beams are used to induce emission of spin polarized electrons from semiconductor surfaces. The most conspicuous observation with strong light pulses is that the result depends very much on whether the light pulse duration is in the nanosecond or picosecond range.

Fig. 6a) and b) display results obtained on surfaces of p-doped GaAs(110) and Ge(111) respectively. The dopant is Ga in Ge and Zn in GaAs, both at a level of  $2 \cdot 10^{19}/\text{cm}^3$ . The energy of the light pulse is given in units of  $E_{\text{ion}}$ , that is in units of the energy at which the surface starts to emit positive ions. With GaAs, the evaporation of As could contribute to positive ion emission, but with Ge,  $E_{\text{ion}}$  definitely indicates the light pulse energy at which the sample melts.

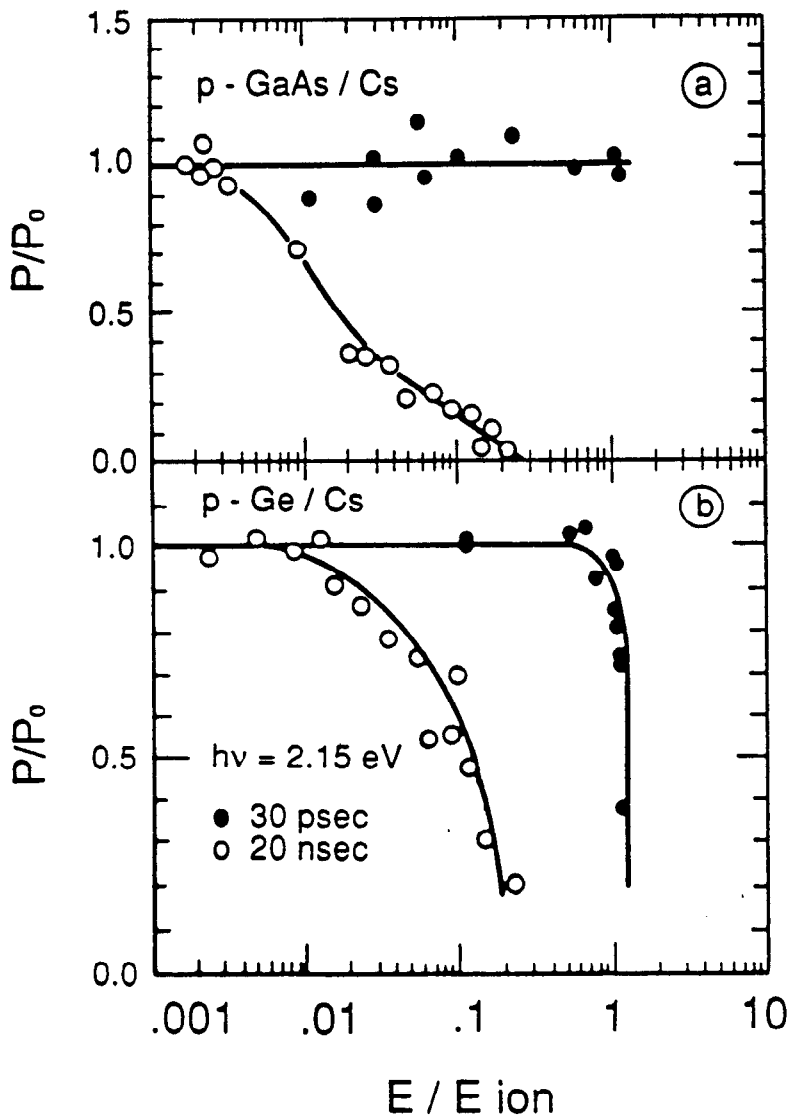


Fig. 6a and b:  
Relative spin polarization  $P/P_0$  of photoelectrons from p-type GaAs(a) and p-type Ge (b) surfaces with Cs vs the energy of the laser pulse in units of  $E_{ion}$  where positive ion emission starts.  $P_0$  is the polarization observed with the continuous lamp at the initial temperature around 230 K before the laser pulses hit the surface. Circles are for 20 nsec and filled circles for 30 psec pulses. Cesiation proved to be stable even with many 100 pulses around  $E_{ion}$ .

Consider now the experiment on Ge: With laser pulses of 30 psec duration  $P$  remains unaffected until the sample emits positive ions. Melting and subsequent cooling can produce a polycrystalline surface but in a cubic crystal the final state polarization obtained by optical pumping near  $\Gamma$  is independent of the crystal orientation with respect to the incident light beam hence also works with polycrystalline samples. Upon melting, i.e., for  $E > E_{ion}$ , the polarization of the photoexcited electrons is destroyed, as observed before in the experiment with  $\beta$ -Sn. For all energies below  $E_{ion}$ ,  $P$  is constant.

The outcome of the analogous experiment using laser pulses of 20 nanoseconds duration is entirely different: As soon as the average temperature of the sample increases by a few degrees K - at pulse energies much below  $E_{ion}$  -  $P$  gradually goes to zero. This applies to GaAs as well as to Ge. Note that for a given intensity profile of the laser pulse the change of temperature in the focus is proportional to the pulse energy. In all cases, the initial temperature of the crystal before the laser pulse hits the surface is around 230 K. As every surface exhibits a somewhat different  $P_0$  at low light intensity depending on the degree of cesiation, the amount of doping, and the nature of the bulk material, the comparison between different surfaces and different

materials is conveniently made by plotting the relative polarization  $P/P_0$ . The results with the laser pulses of 20 nsec appear to reflect the same effect of lattice heating as observed in the stationary experiment where a continuous light source was used and where the temperature of the sample was changed by heating the whole crystal. Obviously, in the laser experiment the measured polarization is an average over all the electrons emitted by the spatially and temporally varying intensity profile of the laser pulse. Nevertheless, the conspicuous change of the polarization at pulse energies which are very modest compared to  $E_{ion}$  is attributed - as in the stationary experiment - to the temperature induced shift of the vacuum level. This shift is due to the strong temperature dependence of the surface photovoltage or, equivalently, the strong T-dependence of the band bending in the surface. The experiment shows that with increasing pulse energy the effect of the temperature-dependent restoring current overwhelms the effect of the additional generation of electron-hole pairs which set up the photovoltage. The reason is that the e-h-pair generation is linear in the pulse energy whereas the restoring current depends on it exponentially.

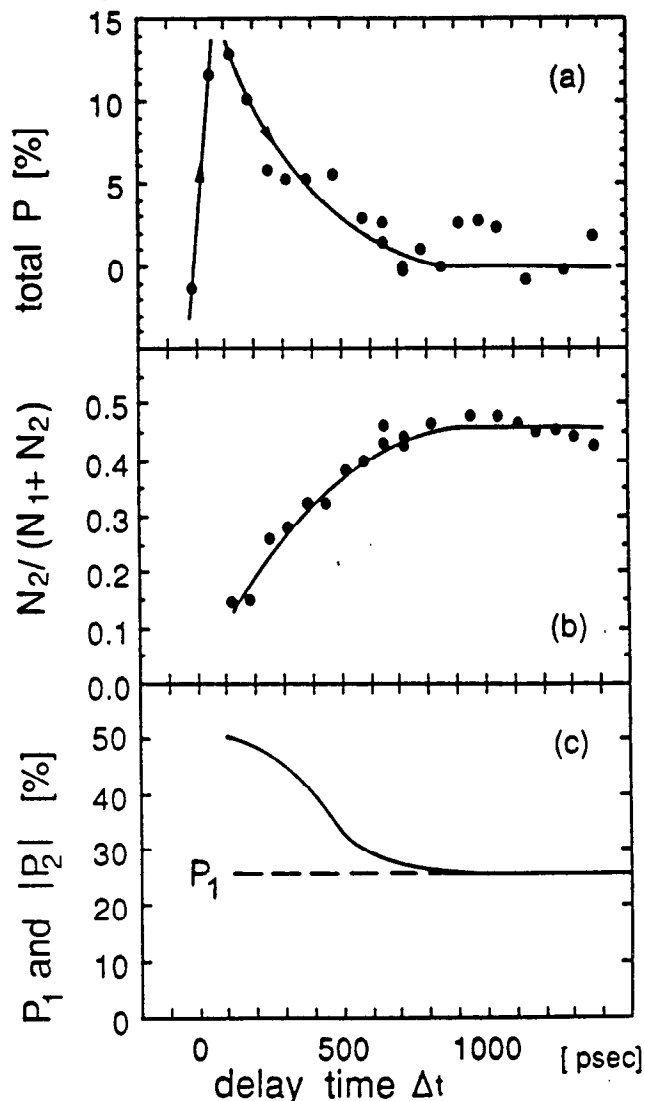
The problem remains why the T-dependent shift of the vacuum level and the accompanying change of P is not observed in the experiments using the 20 psec pulses. The answer is that the effective probing time of the 20 psec pulse must be too short for any appreciable change of the photovoltage to develop. There are experimental indications that the set-up time of the surface photovoltage is of the order of 1 psec or less. Consequently, the *probing time* of the pulse must be considerably less than the *duration* of the pulse. The only mechanism which is able to shorten the probing time of a given pulse with respect to its duration is suppression of electron emission by space charge.

Two factors enter therefore the description of the dynamics of the electron emission - including the polarization of the photoelectrons - from semiconductor surfaces under irradiation by intense laser pulses: the dynamics of the surface photovoltage and the dynamics of the space charge. The first factor is a phenomenon of general physical interest whereas the dynamics of space charge is a problem of more technical nature involving the strength and geometry of the electric and magnetic fields outside of the sample. The program to be pursued is now twofold: First, is it possible to follow the dynamics of the electron emission experimentally on a psec time scale and, secondly, is it possible to attribute the observed time dependence to either of the two mechanisms, photovoltage or space charge ?

Information on the dynamics of the electron emission is obtained from the following differential double pulse experiment. The pulse from the quenched transient dye laser of 30 psec duration is split into 2 pulses, of which one is made up of right circularly polarized light and the other of left circularly polarized light. The two pulses can be delayed by the time  $\Delta t$  with respect to each other using a variable difference in optical path. The left circularly polarized pulse  $\sigma^-$  leads to the emission of down spin electrons, the right circularly polarized pulse  $\sigma^+$  to the emission of up spin electrons. The intensity ratio  $\sigma^+/\sigma^-$  is adjusted such that the total polarization P of the emitted electrons is  $P = 0$  when  $\Delta t = 0$ , i.e., when both pulses hit the sample simultaneously. If now  $P \neq 0$  with  $\Delta t \neq 0$ , the first pulse must have produced either a space charge in front of or a photovoltage within the sample.

The following quantities are directly measured:

1. The total polarization  $P$  of the electrons created by  $\sigma^+$  and  $\sigma^-$  which is given by  $P = (N_1P_1 + N_2P_2)/(N_1 + N_2)$  where  $P_1, N_1$  and  $P_2, N_2$  are the polarizations and intensities of the electrons produced by  $\sigma^+$  and  $\sigma^-$  respectively.
2. The total intensity of electrons  $J = N_1 + N_2$
3. The polarization  $P_1$  and intensity  $N_1$  emitted by the first light pulse alone.



**Fig. 7:** Differential experiment with two circularly polarized light pulses of opposite circular polarization vs the delay time  $\Delta t$  between the 2 pulses. (a) Joint polarization of electrons from both pulses, (b) normalized intensity  $N_2/(N_1 + N_2)$  of the 2nd pulse, and (c) polarization  $P_1$  of the first and  $|P_2|$  of the second pulse.

From these measurements the polarization  $P_2$  and intensity  $N_2$  emitted by the 2nd laser pulse are obtained. Fig. 7 shows the dependence of the various key quantities on the delay time  $\Delta t$  between the  $\sigma^+$  and  $\sigma^-$  pulses. The sample was a Ge(111) crystal, the photon energy 2.15 eV.

Fig. 7a shows that the first pulse sets up the disturbance in a time  $\Delta t < 30$  psec. The polarization of the first pulse is taken to be positive. Over the whole range of  $\Delta t$  the total  $P$  is  $> 0$ , i.e., the dominant contribution to the polarization comes from the first pulse. Why? The reason becomes evident from Fig. 7b: the emission of the second pulse is largely suppressed at short time delays and rises to the value of the first pulse only after 800 psec, the relaxation time



in an exponential fit being 350 psec. This is also the time when  $P$  in Fig. 7a has dropped to zero again, implying that for a time separation  $> 800$  psec the two pulses emit independently from each other. From Fig. 7c it is evident that  $|P_2|$  is as large as 50% at short delays but approaches the single pulse value of 25% also after 800 psec.

The measurements shown in Fig. 7 give full information on the dynamics of the electron emission in this double pulse experiment. The main result is that at short delays the emission  $N_2$  is reduced and the polarization  $P_2$  enhanced indicating that the second pulse sees a larger photothreshold. However, the experiment does not differentiate between photovoltage and space charge. Is the photothreshold seen by the second pulse larger because of band flattening or because the repulsive potential of the space charge has led to a higher apparent vacuum level in front of the surface ?

The distinction between space charge and photovoltage can be done with a metallic sample where no photovoltage is generated, and/or by calculation of the time dependent potential set up by the space charge. Work along both lines is planned and underway in our laboratory. Theoretical estimates for the relaxation time of the photovoltage are given in Ref. [6]. It should be noted that a grounded contact to the metallic ultrathin layer at the surface might be established to reduce the photovoltage.

#### DETECTION OF SPIN POLARIZATION

"Il ne suffit pas de produire des électrons polarisés, il faut savoir reconnaître leur état de polarisation ce qui est sans doute plus difficile" [7]. The spin polarization of an electron beam can be measured by differential scattering of electrons from heavy atoms such as Au or U [8]. We shall show here that the total scattering of electrons in a ferromagnetic solid is also spin dependent and has the potential to lead to a far more efficient scheme for detection of spin polarization. The efficiency of a spin detector is measured by the accuracy with which the degree  $P$  of polarization along the quantization axis can be measured in a given time [8].

In the case of a ferromagnetic material, it is well known that reflection and absorption depend on the spin polarization of the incident electron beam, and that this phenomenon may be used for effective and simple detection of spin polarization [9]. Kisker and coworkers [10] have indeed constructed a detector for electron spin polarization based on the reflectivity of a beam of low energy electrons incident along the surface normal of Fe(100) that is superior by one order of magnitude to previous devices based on spin orbit scattering of electrons. With this spin detector, new applications of electron spectroscopy in, e.g., probing spin polarization of core levels have become more practicable [11]. We show that further improvement in detection of electron spin polarization by one order of magnitude can be achieved if transmission of low energy electrons through ferromagnetic material is observed instead of reflection and/or absorption.

The spin dependence of the transmission of low energy electrons through ferromagnetic materials has been studied previously [12,13]. It is now clear as will be shown below that it is governed by the spin polarization of the holes in the d-bands of transition metals, hence the spin dependence of the transmission directly measures the magnetization. To observe transmission of electrons through ferromagnetic metals, ultrathin ferromagnetic samples have to be prepared. This art has been greatly developed in the recent past, and therefore an extremely efficient detector of spin polarization may now be realized based on the spin dependence of

electron transmission. The detector is applicable to spin polarized electron spectroscopies in general. In conjunction with techniques derived from optical pumping in solids, spin dependent transmission of electrons may also be used for measuring the magnetization in an ultrathin film. S.F. Alvarado has shown that this can be done with nanometer resolution if a tunneling microscope tip is used for injection of electrons [14].

## SPIN DEPENDENT TRANSMISSION OF ELECTRONS IN FERROMAGNETIC MATERIAL

The dominant processes by which electrons at within 15 eV from the Fermilevel  $E_F$  loose energy in a solid are electron-electron scattering and perhaps electron plasmon scattering. The total scattering cross section for inelastic processes is obtained from the measurement of the mean free path  $\lambda$  that an electron of a given energy  $E$  travels in the solid. A large amount of data have been accumulated from the overlayer method in which the attenuation of a prominent substrate feature is measured as a function of the overlayer thickness  $x$  and fitted with an exponential decay  $\exp(-x/\lambda)$ . It turns out that there is a quite simple behavior for low energy electrons in the range  $5 \leq E \leq 15$  eV above  $E_F$  independent of the chemical nature of the transition metal [15]. The total inelastic scattering cross section is given by  $\sigma = 1/\lambda$ . The experimental results obtained in many laboratories are well reproduced by the equation

$$\sigma = \sigma_0 + \sigma_d (5-n) \quad (1)$$

$\sigma_d(5-n)$  is the scattering into the unoccupied d-states; 5 is the total number of d-states available to one spin state and  $n$  the number of occupied d-states.  $\sigma_0$  is a constant accounting for inelastic scattering other than into the holes of the d-states, for example into s-p-states or surface and interface states. The noble metals Cu, Ag and Au have full d-bands ( $n=5$ ) and therefore  $\sigma = \sigma_0$  is small as  $0.6 \text{ nm}^{-1}$ . On the contrary, the early transition metals such as Gd and Ta have low occupancy of the d-states and  $\sigma$  can become as large as  $4 \text{ nm}^{-1}$ .

When a transition metal becomes ferromagnetic, the occupancy of the spin up part of the d-shell increases by  $\Delta n$ , while the occupancy of the spin down subshell decreases by  $\Delta n$ . It follows from eq.(1) that the total inelastic cross section becomes spin dependent according to

$$\sigma(\pm) = \sigma_0 + \sigma_d [5 - (n(\pm)\Delta n)] \quad (2)$$

where  $\sigma(\pm)$  is the cross section for majority (minority) spins. For the bulk of the material,  $\Delta n$  can be calculated from the Bohr magneton number  $n_B$  obtained in conventional magnetometry according to  $n_B = n^+ - n^- = 2 \Delta n$ , because the contribution of s-p-electrons to the magnetization is small.

Eq.(2) postulates that electrons travelling in a magnetic material will change their initial spin polarization  $P_0 = (J^+ - J^-)/(J^+ + J^-)$ . The new spin polarization  $P$  after transport over the distance  $x$  is given by

$$P = \frac{J^+ \exp(-\sigma^+ x) - J^- \exp(-\sigma^- x)}{J^+ \exp(-\sigma^+ x) + J^- \exp(-\sigma^- x)} \quad (3)$$

If  $P_0 \ll 1$ , that is  $J^-/J^+ \cong 1$ , this yields

$$P = P_0 + a \quad (4)$$

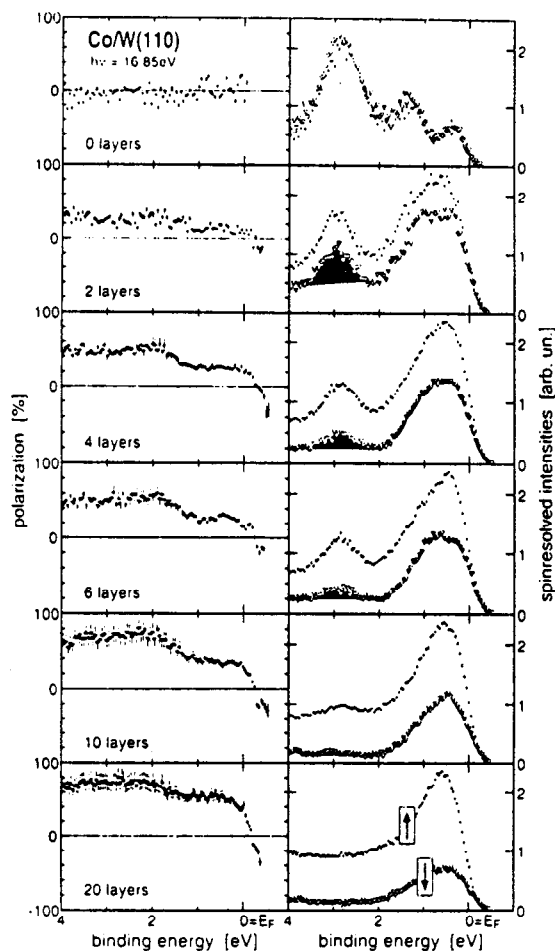
where the spin polarization  $a$  acquired in transport over the distance  $x$  is given by

$$a = \frac{[\exp(\sigma^- - \sigma^+)x] - 1}{[\exp(\sigma^- - \sigma^+)x] + 1} \quad (5)$$

For  $x \rightarrow \infty$ ,  $a \rightarrow 1$  since  $(\sigma^- - \sigma^+) > 0$ , but the transmitted intensity  $\rightarrow 0$ . Hence there is an optimum thickness for the measurement of  $a$ .

### EXPERIMENTS WITH Fe AND Co ON W(100)

The 3d-transition metals Fe and Co grow epitaxially on W(110) surfaces with the easy direction of magnetization in plane [16]. The absence of noticeable island formation is warranted by the fact that the surface energy of the W(110) substrate is higher than the one of Fe and Co, hence an energy gain arises by spreading Fe and Co as much as possible on the W surface.



*Fig. 8:*  
Spin resolved photoelectron energy distribution curves of Co overlayers on W(110) at 300 K and with  $h\nu = 16.85$  eV. The left column shows the spin polarization of the photoelectrons, from Ref. [16].

Furthermore, the energy distribution curves of the photoelectrons excited from the valence bands of W(110) exhibit a sharp feature at a binding energy of  $\sim 2.9$  eV below the Fermi energy  $E_F$ . The attenuation of this sharp feature on depositing overlayers of Fe or Co yields the desired information on the total scattering cross section in the overlayer. Any magnetic domain structure in the ferromagnetic Fe and Co overlayers is removed by applying a magnetic field pulse in the easy direction prior to each measurement. Fig. 8 shows spin resolved energy distribution curves obtained at the photon energy  $h\nu = 16.85$  eV with clean W(110), and with 2, 4, 6, 10 and 20 overlayers of Co. It is seen that the electrons excited from the W(110) orbitals at a binding energy of  $\sim 2.9$  eV can be clearly identified up to 10 layers. It is further clear that the Co films are magnetic at room temperature (300 K) where the measurements were done, even from 2 monolayers on, because the Co 3d-electrons at  $E_F$  are highly polarized. The existence of the transport spin polarization a eq.(5) is directly evident from the difference in amplitude of the 2.9 eV peak in the spin resolved spectra (shaded areas). Since the background intensity under this peak is smooth and flat, it can be readily subtracted. These general phenomena are also observed with Fe on W(110) but the background is somewhat less favorable as evident from Fig. 9 in which the spin resolved energy distribution curves of 3 and 6 overlayers

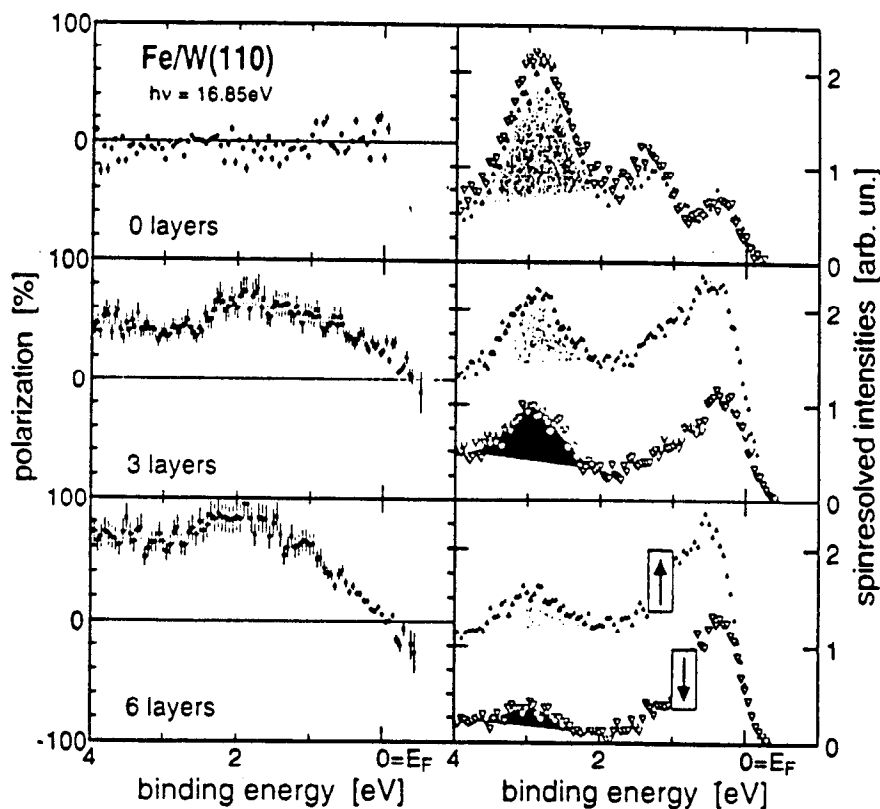
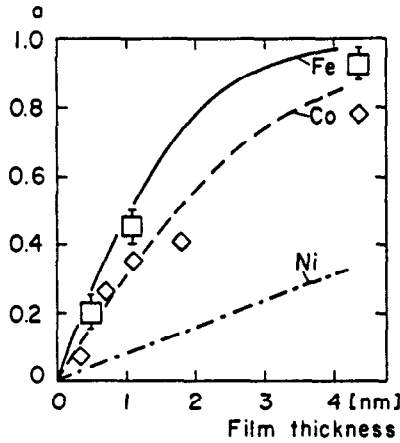


Fig. 9: Spin resolved photoelectron energy distribution curves for Fe overlayers on W(110) at 300 K and  $h\nu = 16.85$  eV. Left column as in Fig. 8, from Ref. 16.

of Fe on W(110) are shown at  $h\nu = 16.85$  eV. Therefore, in the case of Fe the evaluation of a is less reliable.

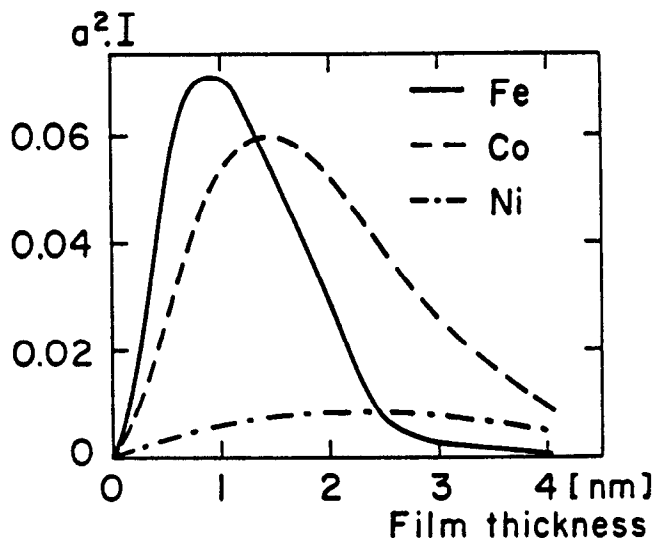


**Fig. 10:**  
Transport spin polarization  $a(x)$  vs thickness  $x$  of the ferromagnetic material for Fe, Co and Ni. The calculated curves are for  $T = 0$  K, whereas the data points were obtained at  $T = 300$  K. Squares denote Fe data, diamonds Co.

In Fig. 10 we show the observed transport polarization  $a$  vs the thickness  $x$  of the magnetic overlayer. The experimental data agree well with the  $a(x)$  calculated from the enhancement of the low energy cascade polarization observed in the ferromagnetic transition metals [15]. In the case of Fe,  $a$  has a tendency to be lower than expected. To discuss this one has to remember that the calculations are for  $T = 0$ , and that for a few monolayers of Fe, the Curie-point  $T_c$  is not very far from room temperature, whereas in the case of Co ultrathin films,  $T_c$  is considerably higher [17]. Yet deviations from the predictions of the simple model larger than the experimental error occur really only with the thickest overlayer of Co where background subtraction is uncertain as can be seen from Fig. 8. The data point obtained by Pappas et al. [12] with Fe on Cu at  $x = 0.7$  nm is  $a = 0.16$ , also taken at  $T = 300$  K and with approximately the same electron energy above  $E_F$ . This is roughly 2 times lower than expected from eq(5). However, Fe on Cu(100) is known to exhibit the fcc structure for which various magnetic properties up to nonmagnetic have been reported [17]. Taking into account the quoted experimental uncertainties one can say that the simple model eq.(5) accounts well for the observations.

## DETECTION OF SPIN POLARIZATION

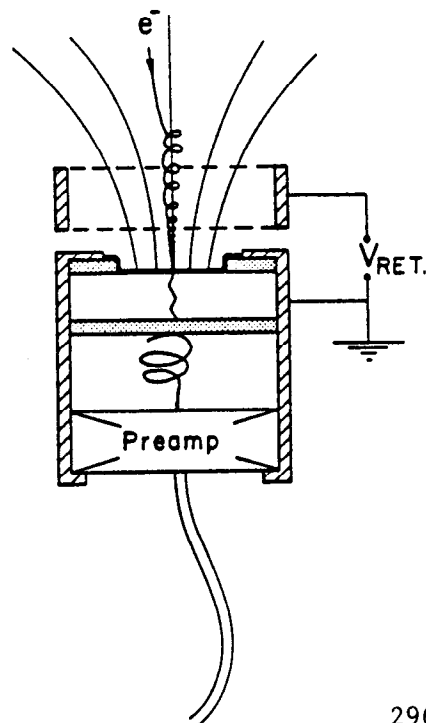
It is now clear that ferromagnetic films are spin filters transmitting preferentially majority spin electrons. This can be used to detect the degree  $P$  of spin polarization of the transmitted electrons along a quantization axis given by the direction of magnetization of the film. The figure of merit of a spin detector is  $S^2 \cdot I$  which is approximately proportional to the inverse time it takes to determine  $P$  with a preset accuracy.  $S$  is the asymmetry in detecting the 2 possible spin states. For the ideal spin detector  $S^2 \cdot I = 1$ , and for the one based on reflection of electrons [10,11] from Fe(001)  $S^2 I = 10^{-3}$ . In transmission,  $S = a(x)$ , and  $I = 2e^{-\sigma \cdot x}$ , where  $\sigma$  is the spin averaged total cross section for electron transport through the ferromagnetic film, hence the figure of merit  $a^2 I$  depends on film thickness  $x$ . Fig. 11 shows  $a^2 I$  for Fe, Co and Ni. We see that the optimal film thickness is 5, 8 and 14 monolayers (ML) of Fe, Co and Ni with figures of merits as high as  $\sim 0.07$ ,  $\sim 0.06$  and  $\sim 0.01$  respectively, hence at least one order of magnitude more than with detectors based on reflection of electrons, and two orders of magnitude more than with detectors based on differential spin orbit



*Fig. 11:*  
Figure of merit  $a^2 I$  for the spin polarization detector based on electron transmission vs thickness of the ferromagnetic material.

scattering. Co is particularly attractive as one can use a film as thick as 8 ML and still achieve almost the same figure of merit as with 5 ML of the more delicate Fe. Alloys of Fe and Co would presumably offer the best choice. The reason why Co is so favorable is the fact that compared to Fe, it has much less majority spin holes, yet still a large number of minority spin holes so that the spin independent scattering cannot assume the leading rôle as in Ni. Furthermore, the Co-films generally have a high  $T_C$  so that the thermal decrease of the surface magnetization is not seizable even at ambient temperature and, quite importantly, the life time of the Co surface is one order of magnitude higher than the one of Fe. The simple model provides helpful guidance in looking for the best spin filter material which might ultimately be found to be an oxide.

Fig. 12 shows how an electron spin polarization detector based on electron transmission could be realized. The principle closely follows the one of the Si surface barrier detectors, the only difference being that the thin gold film at the surface is replaced by an ultrathin



*Fig. 12:*  
Example of a possible spin detector assembly. The thick line is the ferromagnetic spin filter, the dotted materials are gold contacts.  $V_{RET}$  is a potential to retard (or accelerate) the electrons prior to spin filtering. The principle of the measurement of the electron current is taken from Silicon-surface-barrier detectors.

ferromagnetic film consisting, for instance, of 8 monolayers of Co. A magnetic field can, but does not have to be permanently applied perpendicular to the film surface. The longitudinal magnetic field would have the electron optical advantage that the incident electrons could be retarded or accelerated without loss to an energy at which the spin filtering effect of the ferromagnetic film is optimal.

The ferromagnetic film is deposited onto an outer gold ring contacting it to the housing of the detector assembly. In the inner region where the detector accepts the incoming electrons, the ferromagnetic film is deposited either directly onto insulating material, or if needed with an intervening diffusion barrier. The insulator carrying the ferromagnetic spin filter is contacted on the back side to the preamplifier over a thick layer of gold. In this way, an accelerating voltage can be applied across the insulator carrying the spin filter which helps to effectively collect or even amplify by electron-hole-pair production the current reaching the preamplifier input. In this way, the electrons that have been transmitted by the ultrathin ferromagnetic film and thus have been filtered according to their spin state could be counted or measured with great efficiency. The essential part really is the ferromagnetic spin filter after which any of the known electron or current detectors can be used. For instance, a multichannel plate positioned after the semiconductor or insulator carrying the spin filter could provide position sensitive detection of spin polarization which is of great value in spin resolved electron spectroscopy. The life time of the ferromagnetic film could be prolonged by passivating its surface with a material in which electron degradation and absorption is weak.

#### REFERENCES

1. F.P. Baumgartner, M. Lux-Steiner, G. Doell, E. Bucher, F. Meier, and A. Vaterlaus *J. of Crystal Growth* **109** (1991) 318
2. F. Meier, J.C. Gröbli, D. Guarisco, A. Vaterlaus, Y. Yashin, Y. Mamaev, B. Yavich, and I. Kochnev, *Physica Scripta* **T48** (1993) XXX
3. A. Vaterlaus, T. Beutler, and F. Meier, *Phys. Rev. Lett.* **67** (1991) 3314
4. Traugott E. Fischer, *Phys. Rev. Lett.* **21** (1968) 31
5. M.H. Hecht, *Phys. Rev.* **B41** (1990) 7918
6. A. Herrera-Gomez and W.E. Spicer, *SLAC-PUB* **6307**, August 1993
7. A. Kastler, *Proc. Phys. Soc.* **LXVII** (1954) 853
8. T.J. Gay, *Rev. of Sci. Instrum.* **63** (1992) 1635
9. H.C. Siegmann, D.T. Pierce, and R.J. Celotta, *Phys. Rev. Lett.* **46** (1981) 452
10. D. Tillmann, R. Thiel, and E. Kisker, *Z. Phys. B - Condensed Matter* **77** (1989) 1
11. R. Jungbluth, Ch. Roth, F.U. Hillebrecht, and E. Kisker, *Surface Science* **269/270** (1992) 615
12. D.P. Pappas, K.P. Kämper, B.P. Miller, H. Hopster, D.E. Fowler, C.R. Brundle, A.C. Luntz, and Z.-X. Shen, *Phys. Rev. Lett.* **66** (1991) 504
13. R. Feder, *Solid State Commun.* **31** (1979) 821, and references therein
14. S.F. Alvarado, *IBM Techn. Discl. Bull.* **33** (1991) 469
15. G. Schönhense and H.C. Siegmann, *Ann. Physik* **2** (1993) 465
16. Mathias Getzlaff, *Dissertation Universität Bielefeld* 1993, and M. Getzlaff, J. Bansmann, and G. Schönhense, to be publ.
17. H.C. Siegmann, *J. Phys.: Condens. Matter* **4** (1992) 8395

**Charles Sinclair  
CEBAF**

**Emittance Measurements on a 100 keV Beam from a  
GaAs Photocathode Electron Gun**



## EMITTANCE MEASUREMENTS ON A 100 keV BEAM FROM A GaAs PHOTOCATHODE ELECTRON GUN

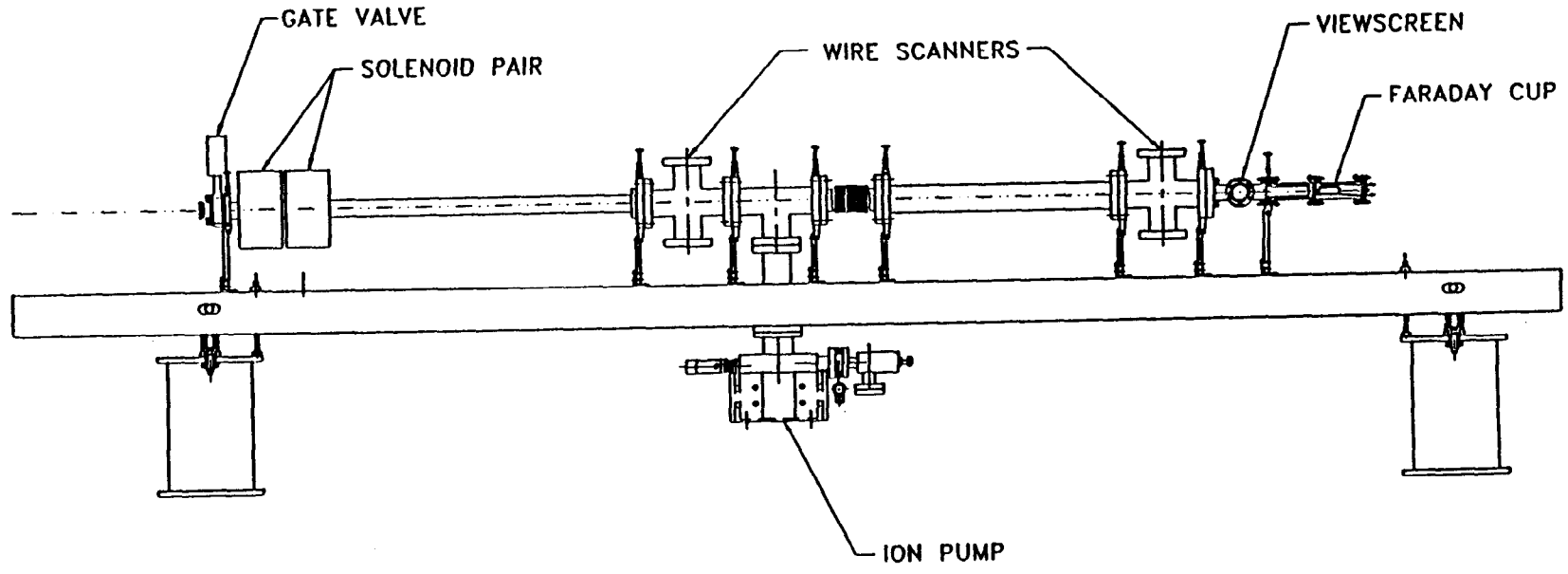
Bruce M. Dunham, Lawrence S. Cardman, and David A. Engwall  
Department of Physics, University of Illinois at Urbana-Campaign

and

Charles K. Sinclair  
CEBAF

We have measured the emittance of a 100 keV DC electron beam emitted from an NEA GaAs photocathode. The measurements were made after the beam had passed through a Mainz style spin manipulation system. Emittances were determined by measuring the electron beam profiles with a wire scanner as the strength of an upstream solenoid pair was varied. Measurements were made for a number of optical wavelengths, beam currents, and optical beam diameters at the photocathode. A "tophat" optical beam profile was used for all measurements. The results demonstrate that, for wavelengths longer than 633 nm, the effective transverse thermal energy of the photoemitted electrons is a factor of three lower than from a thermionic cathode operating at 1160K.

300



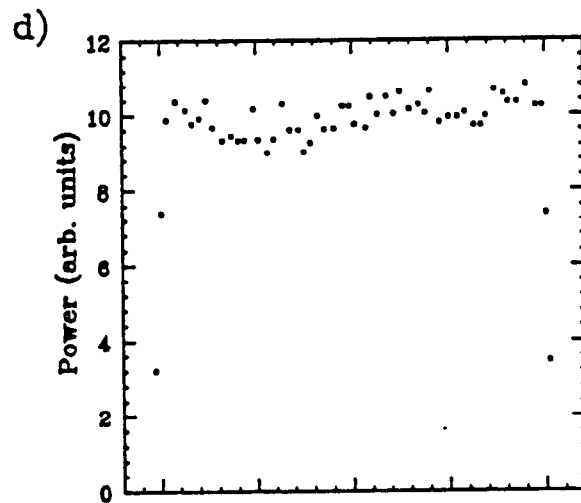
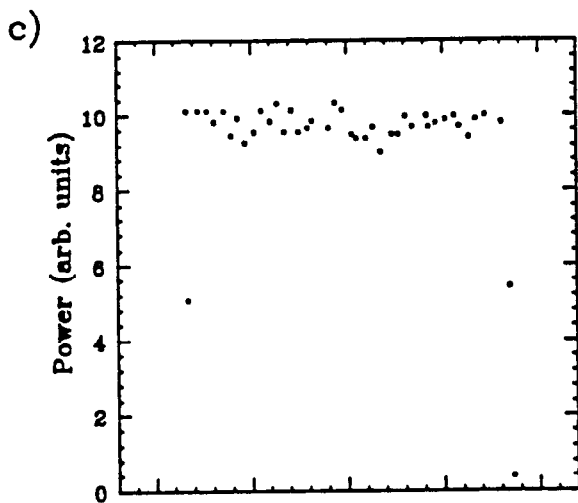
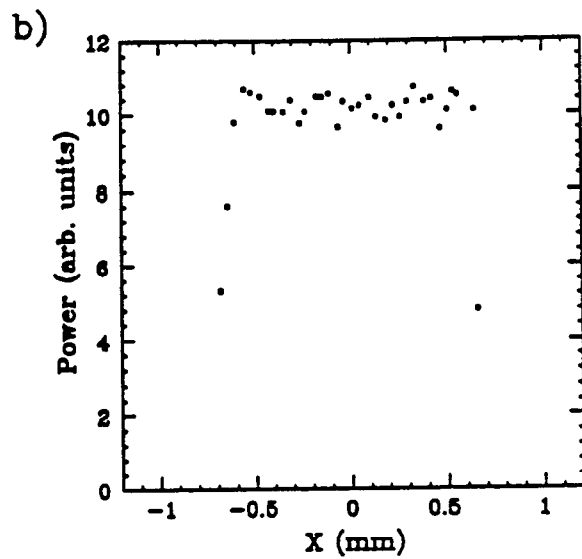
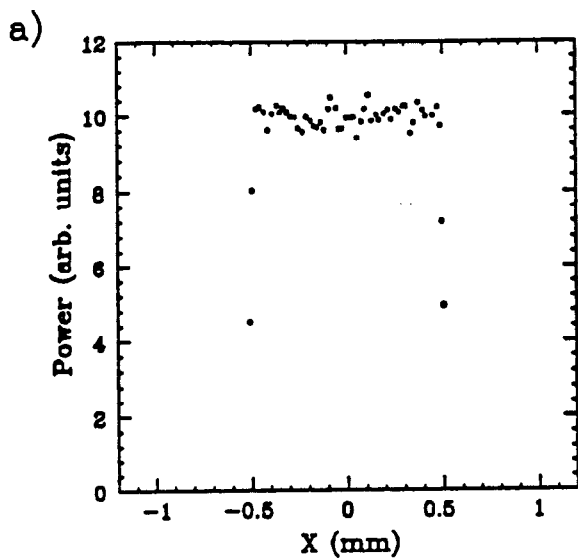
**Emittance Measurement Beamline**

BEAM WAS CHOPPED FOR MEASUREMENTS, TO MAINTAIN LOW AVERAGE POWER AT THE FARADAY CUP.

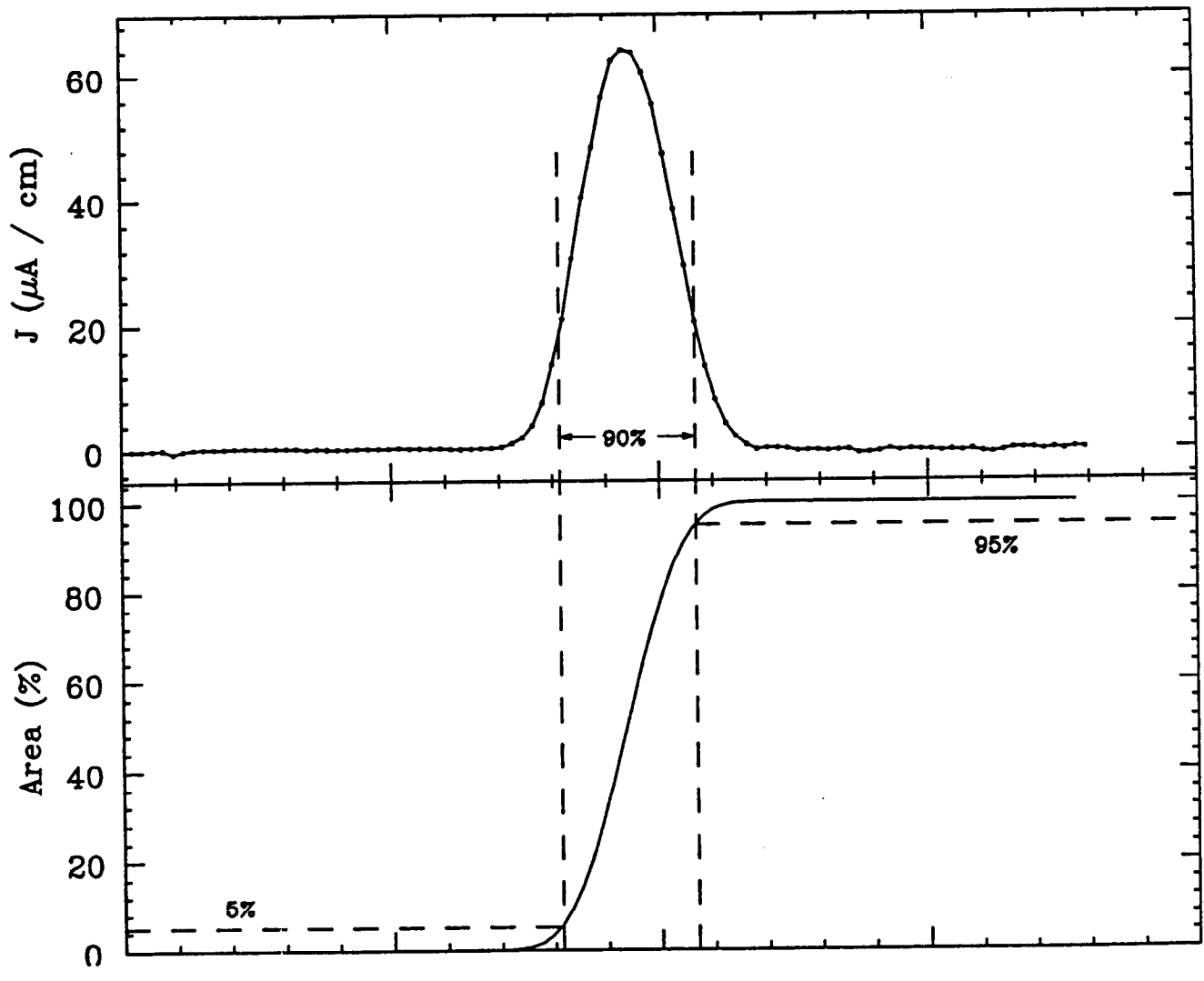
TEN BEAM PROFILES WERE MEASURED FOR EACH OF SIX SOLENOID CURRENTS. BOTH VERTICAL AND HORIZONTAL PROFILES MEASURED.

BEAM PROFILES MEASURED WITH A WIRE SCANNER - 50 MICRON DIAMETER GOLD PLATED TUNGSTEN WIRE - STEPPER MOTOR WITH 15.88 MICRON/STEP MOTION (11.23 MICRON MOTION IN VERTICAL AND HORIZONTAL PLANES)

MEASUREMENTS MADE FOR FOUR OPTICAL SPOT SIZES (1.00, 1.33, 1.70, and 2.00 mm diameter); FOUR OPTICAL WAVELENGTHS ( 514, 633, 710, and 840 nm); AND MANY BEAM CURRENTS UP TO 1.30 mA.



**Horizontal beam profiles measured with a CCD camera for 1.00, 1.33, 1.70, and 2.00 mm apertures**

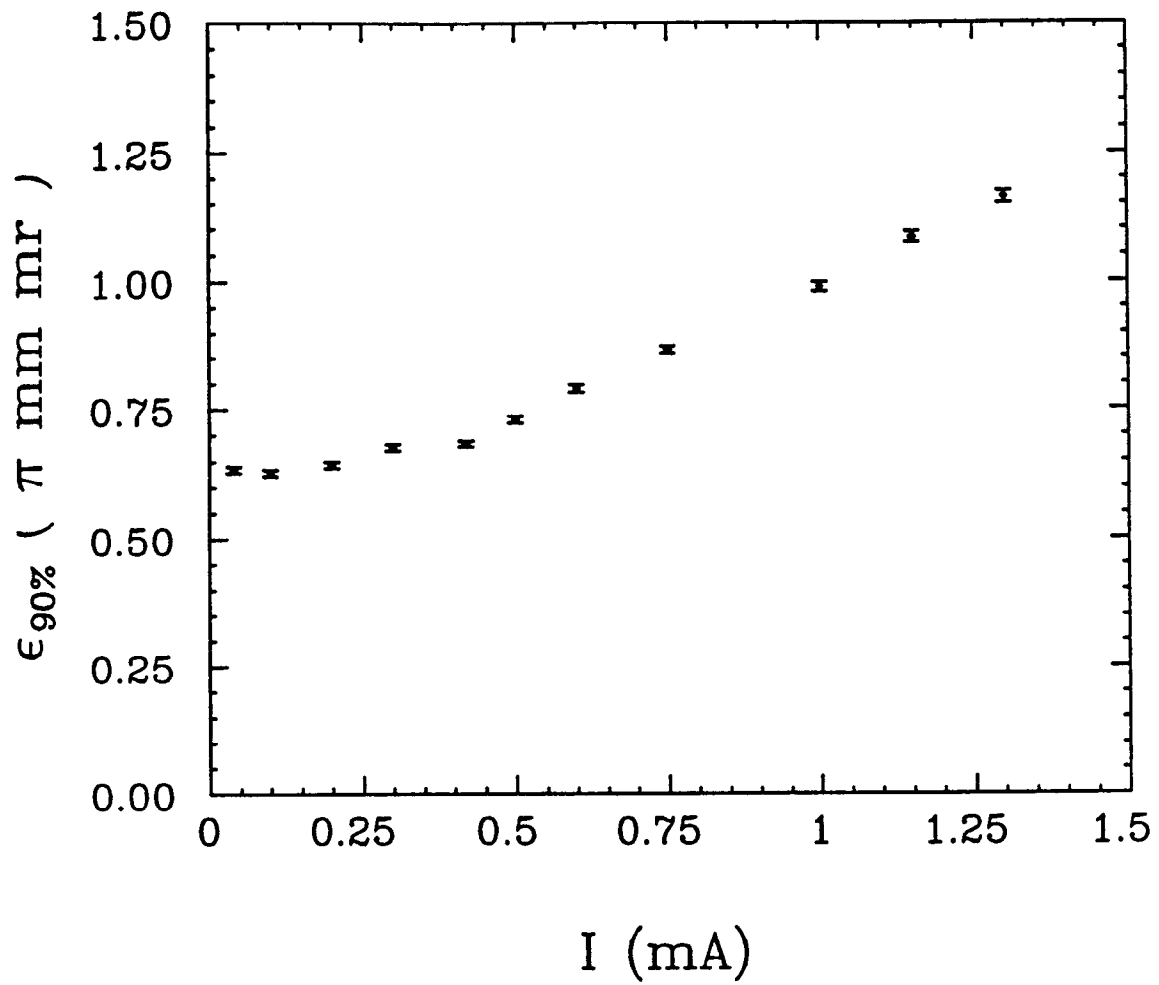


**Typical wire scanner measured beam profile, and integral of beam profile.**

# ESTIMATED ERRORS AND THEIR CONTRIBUTION TO THE UNCERTAINTY IN THE MEASURED EMITTANCE

Error Source	Magnitude	Contribution to Emittance uncertainty
Beam Energy	~ 0.1%	0.0032 $\epsilon$
Solenoid to Wire Scanner Distance	~ 2 mm	0.004 $\epsilon$
Solenoid Magnetic Field	~ 2%	0.030 $\epsilon$
Solenoid Effective Length	~ 2%	0.016 $\epsilon$
Wire Scanner Step Size	0.011 mm	0.010

Summary:  $\Delta\epsilon = 0.053 \epsilon + 0.010$



**Measured 90% emittance versus beam current**

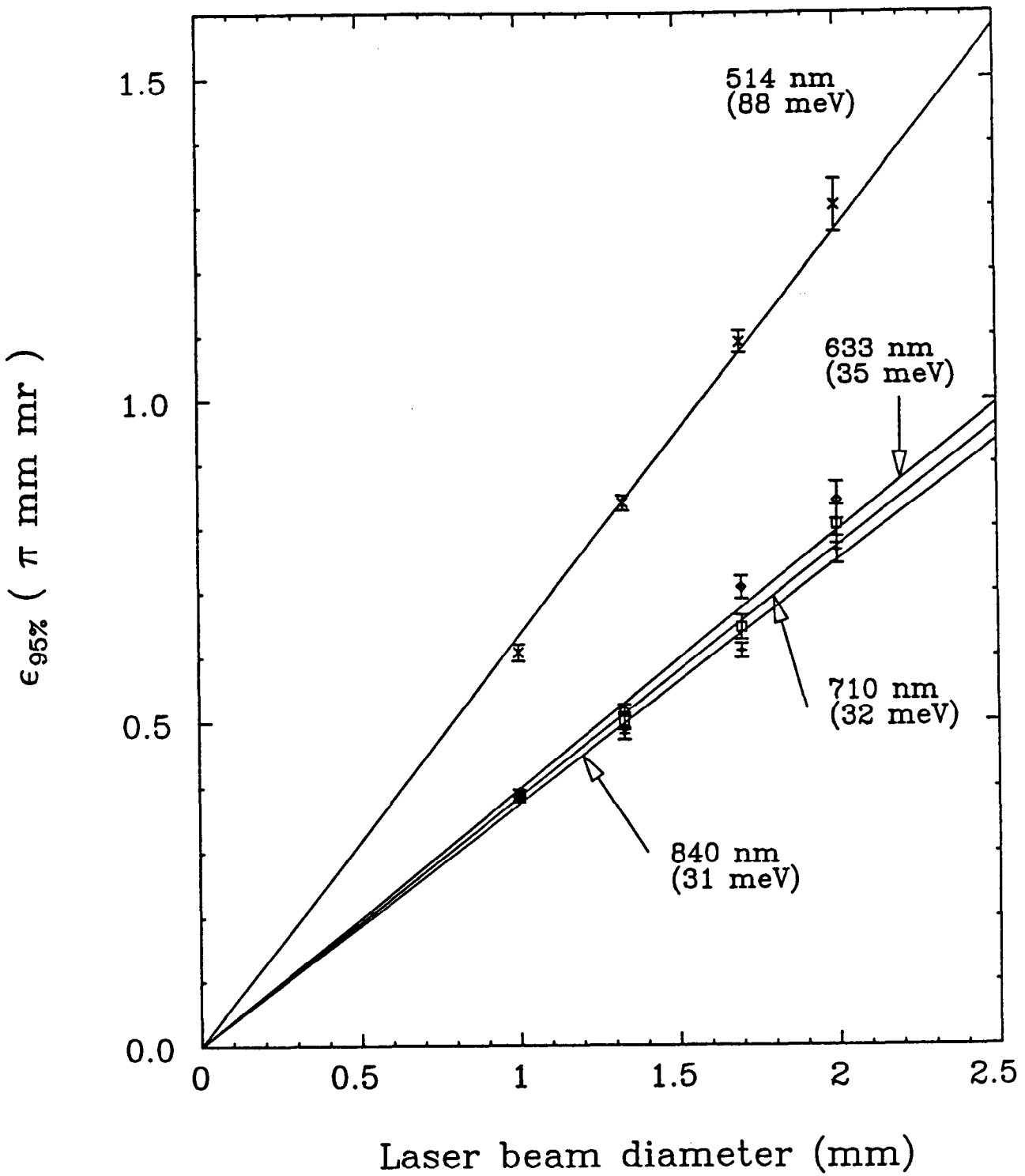
EMITTANCE GROWTH AT LOW CURRENT NOT UNDERSTOOD.

EGUN CALCULATIONS USING THE 5-RAY MODEL AND A CATHODE TEMPERATURE OF 37 meV REPRODUCE OUR LOW CURRENT EMITTANCE VALUES, BUT PREDICT ONLY A 5% EMITTANCE GROWTH AT 5 mA, 10% AT 10 mA.

PROBLEM MAY BE DUE TO THE VERY SMALL BEAM SIZES IN THE ELECTROSTATIC BENDS.

MEASUREMENTS PLANNED AT CEBAF WILL USE A SIMPLE STRAIGHT BEAMLIN, ELIMINATING THE ELECTROSTATIC BENDS.





**Measured 95% emittance versus laser beam spot diameter for various optical wavelengths.**

$$\epsilon_{\text{rms}} = 4(\langle x^2 \rangle \langle x'^2 \rangle - \langle xx' \rangle^2)^{1/2}$$

Compare this to a thermionic cathode operating at a temperature  $T$  (Maxwellian distribution), for which:

$$\langle x^2 \rangle = r_c^2/4$$

$$\langle x'^2 \rangle = kT/(mc^2\beta^2\gamma^2)$$

$$\langle xx' \rangle = 0$$

This gives:

$$\epsilon = (2r_c/\beta\gamma)(kT/mc^2)$$

For example, at  $T = 1160\text{K}$ ,  $kT = 0.1\text{ eV}$ .

With a 1 mm radius cathode, and at 100 kV ( $\beta\gamma = 0.655$ ), we obtain  $\epsilon_{\text{rms}} = 1.35\text{ mm-mrad}$

Using our measured 95% emittance values, we find:

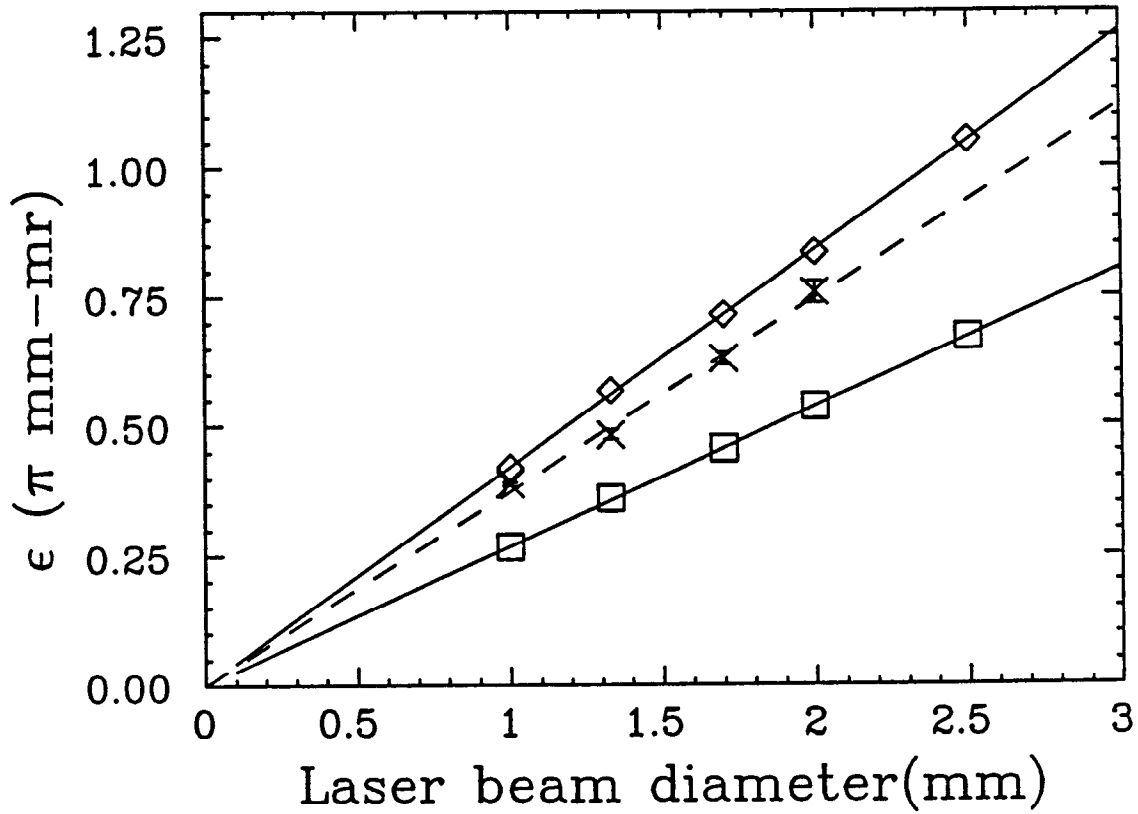
Wavelength (nm)	$\epsilon_{95\%}$ (mm-mrad)	kT (meV)
514	1.30 +/- 0.04	88 +/- 2 (+/- 6)
633	0.84 +/- 0.03	35 +/- .5 (+/- 3)
710	0.80 +/- 0.03	32 +/- .6 (+/- 3)
840	0.76 +/- 0.02	31 +/- .5 (+/-3)

where the smaller errors in the thermal energy are due to statistics in beam radius determination, and the larger error in parentheses include the full instrumental errors

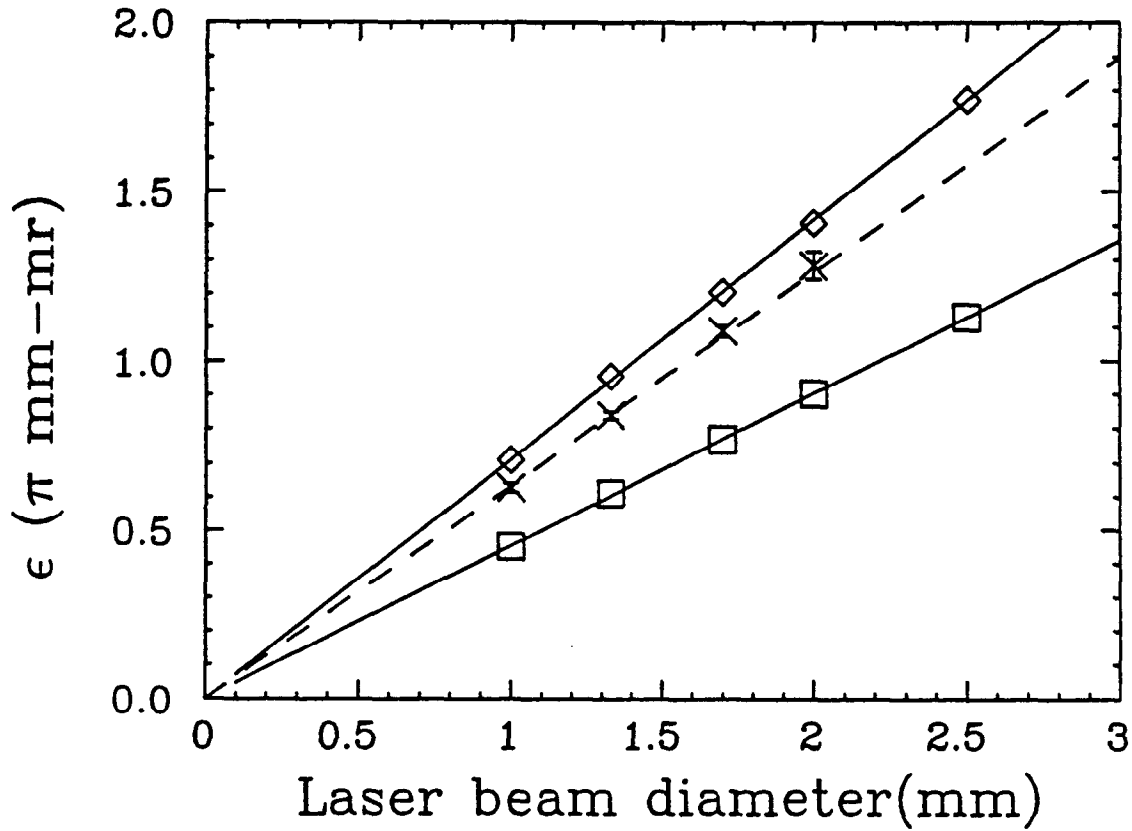
## EGUN MODELS

**3-RAY: DIVIDE EACH RAY LEAVING THE CATHODE INTO THREE RAYS, WITH THE CURRENTS IN THE RATIO OF 1:2:1. THE CENTRAL RAY HAS NO THERMAL ENERGY, WHILE THE OUTER RAYS EACH HAVE  $kT$ . THIS UNDERESTIMATES THE TRUE EMITTANCE.**

**5-RAY: DIVIDE EACH RAY LEAVING THE CATHODE INTO FIVE RAYS, WITH THE CURRENTS IN THE RATIO OF 1:9:0:9:1. THE OUTER RAYS HAVE  $2kT$ , THE INNER HAVE  $kT$ , AND THE CENTRAL RAY IS ABSENT. THIS OVERESTIMATES THE TRUE EMITTANCE.**



**Theoretical emittance for 31 meV thermal energy versus "3-ray" and "5-ray" EGUN model calculation, compared to measurements at 840 nm wavelength.**



**Theoretical emittance for 88 meV thermal energy versus "3-ray" and "5-ray" EGUN model calculation, compared to measurements at 514 nm wavelength.**

## SUMMARY

AT OPTICAL WAVELENGTHS SHORTER THAN 633 nm, THE MEASURED EMITTANCE CONTAINING 95% OF THE BEAM CURRENT IS APPROXIMATELY A FACTOR OF THREE SMALLER THAN THAT FROM A THERMIONIC EMITTER OPERATED AT 1160 K. (RE-ANALYSIS OF THE DATA USING RMS VALUES FROM THE MEASURED BEAM PROFILES GIVES HIGHLY SIMILAR NUMBERS FOR THE EMITTANCE AND EFFECTIVE THERMAL ENERGY.)

THE EMITTANCE WAS OBSERVED TO BEGIN TO GROW AT RELATIVELY LOW BEAM CURRENTS. THIS IS NOT PRESENTLY UNDERSTOOD, BUT IS BELIEVED TO BE A SPACE CHARGE RELATED EFFECT IN THE TOROIDAL CAPACITOR ELECTROSTATIC BENDS OF THE SPIN MANIPULATOR. FURTHER MEASUREMENTS WILL BE MADE AT CEBAF IN A BEAMLINER WITHOUT THESE COMPONENTS.

**William Spicer  
Stanford University**

## **Modern Theory of Photoemission and its Applications to Practical Photocathodes**

Over the last thirty years, the Spicer Three-Step model has provided a very useful description of the process of photoemission for both fundamental and practical applications. By treating photoemission in terms of three successive steps -- optical absorption, electron transport, and escape across the surface -- this theory allows photoemission to be related to parameters of the emitter, such as the optical absorption coefficient, electron scattering mechanisms, and the height of the potential barrier at the surface. Using simple equations and established parameters, the ThreePStep model predicts the performance of cathodes and provides detailed understanding of the unexpected phenomena that appear when photocathodes are pushed into new practical domains. As an example, time responses are estimated for existing cathodes, and are found to cover a range of six orders of magnitude. Further, the time response is found to be directly related to the sensitivity (i.e., quantum efficiency) of the cathode. The quantum yield systematically decreases with the time response. Thus, metals are predicted to have the shortest time response (as little as  $10^{-15}$  Jsec) and the smallest quantum efficiency (as little as  $10^{-4}$  electrons per photon), whereas the negative affinity photocathodes have high yield (as high as 0.6 electrons per photon) but long response times (as long as  $10^{-9}$  Jsec). A second application of this theory which will be presented concerns the charge limit which SLAC has experience with their GaAs sources. Results of Herrera-Gomez and Spicer will be presented which give a detailed explanation of this phenomenon and a suggestion made as to overcoming it.



# Modern Theory of Photoemission and its Applications to Practical Photocathodes

**William E. Spicer**

*Stanford Linear Accelerator Center  
and  
Stanford Synchrotron Radiation Laboratory  
and  
Department of Electrical Engineering  
Stanford, California 94305*

**Alberto Herrera-Gómez**

*Stanford Linear Accelerator Center  
and  
Department of Applied Physics  
Stanford, California 94305*

**Work supported by DOE**

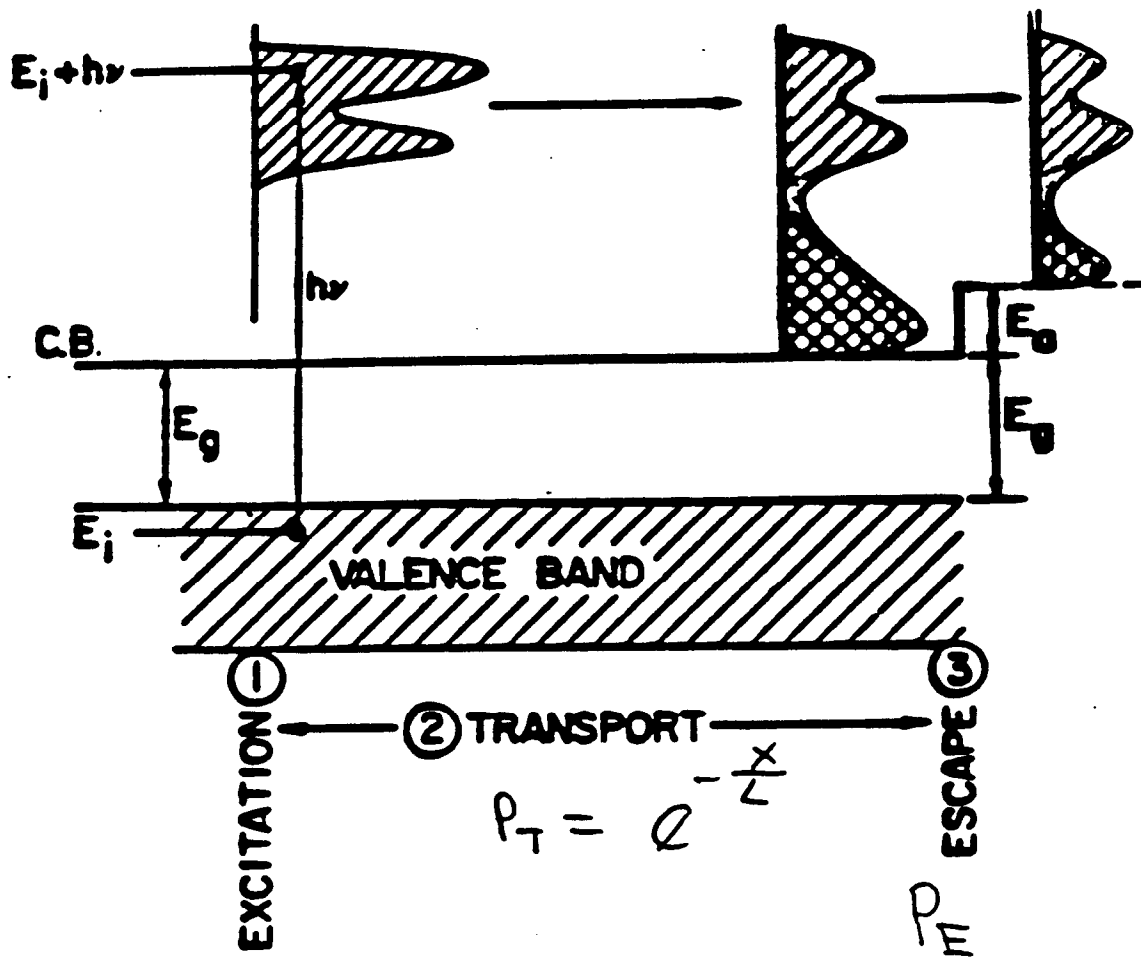
## Why in 1993 are Photocathodes Important?

- **Electron beams in vacuum are useful for many purposes**
- **Of all electron sources, Photoemission is unique in manipulating electrons to give optimum electron characteristics in vacuum. Examples:**
  - **Spin polarization (from scientifically engineered photocathodes)**
  - **Very short electron pulses**
  - **Very sharp energy distribution (~ 50 meV, compared to 500 meV for conventional sources)**

## **Making use of large investments in 3-5 material technology and knowledge of photoemission**

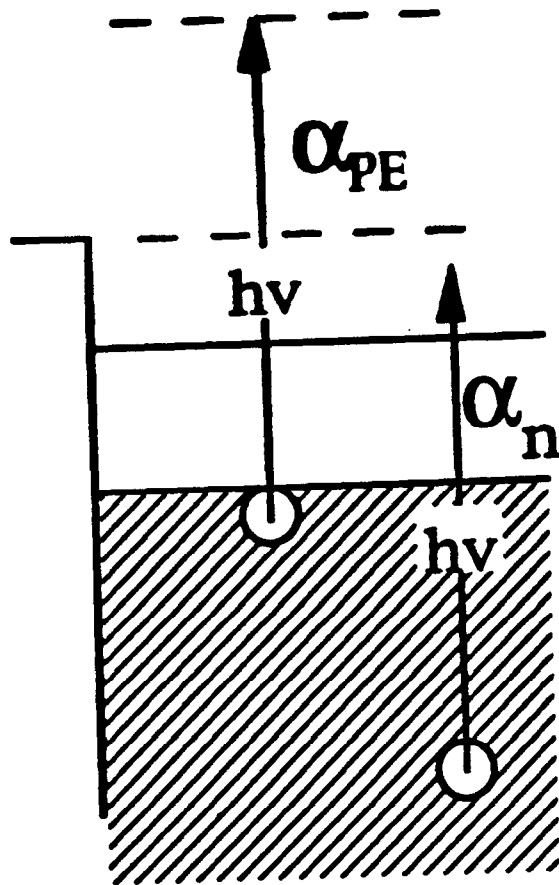
- 3-5 materials can now be engineer to an amazing extent**
- photocathodes can be custom engineer to fit specific needs**

# The Three-Step Model



$$P_{0\alpha} = \alpha_{PE} I_0 (1-R) e^{-\alpha x} dx$$

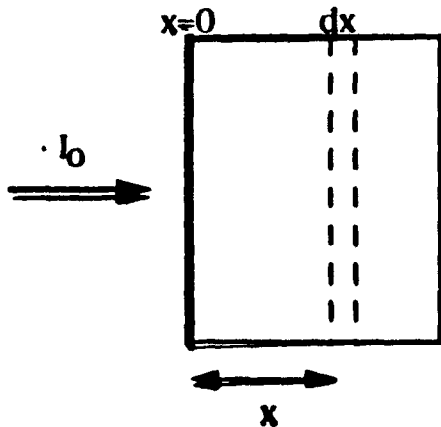
$$d_i = P_{0\alpha} * P_T * P_E$$



$$\alpha = \alpha_{PE} + \alpha_n$$

$$P_0 \alpha(h\nu, x, dx) = \alpha_{PE} I(x) dx$$

$$di(x) = P_0 \alpha(h\nu, x, dx) P_T(h\nu, x) P_E(h\nu)$$



$$\begin{aligned} P_{0\alpha}(h\nu, x, dx) &= \alpha_{PE}(h\nu) I(x) dx \\ &= \alpha_{PE}(h\nu) I_0(1-R) e^{-\alpha x} dx \end{aligned}$$

$$P_T(x, h\nu) = \exp\left\{-\frac{x}{L(h\nu)}\right\}$$

$$di(x) = I_0(1-R) \alpha_{PE} e^{-\alpha x} e^{-\frac{x}{L}} P_E(h\nu) dx .$$

For a semi-infinite slab, the total electron yield is  $i(h\nu) = \int_0^{\infty} di(x)$

$$i(h\nu) = I_0(1-R) \frac{\alpha_{PE}}{\alpha + \frac{1}{L}} P_E(h\nu) .$$

For a semi-infinite slab of thickness  $A$ , the total electron yield is  $i(h\nu) = \int_0^A di(x)$

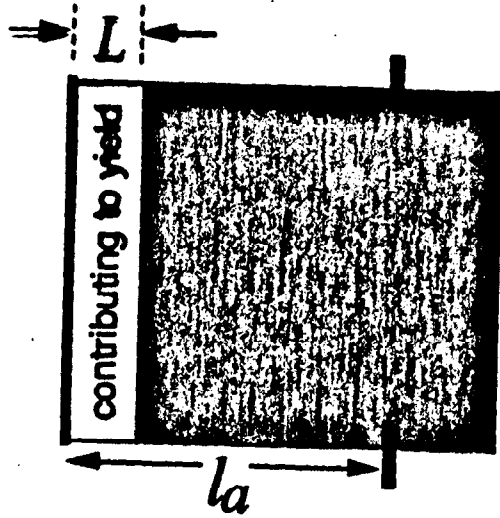
$$Y(h\nu) \equiv \frac{i(h\nu)}{I_0(1-R)} = \frac{\frac{\alpha_{PE} P_E}{\alpha}}{1 + \frac{1}{\alpha L}}$$

$$Y = \frac{\frac{\alpha_{PE} P_E}{\alpha}}{1 + \frac{l_a}{L}}$$

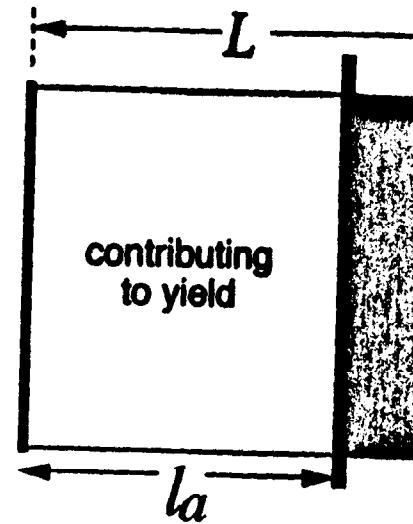
W.E. Spicer, Phys. Rev. 112, 114 (1958)

$$Y = \frac{\alpha_{PE} P_E}{1 + \frac{l_a}{L}}$$

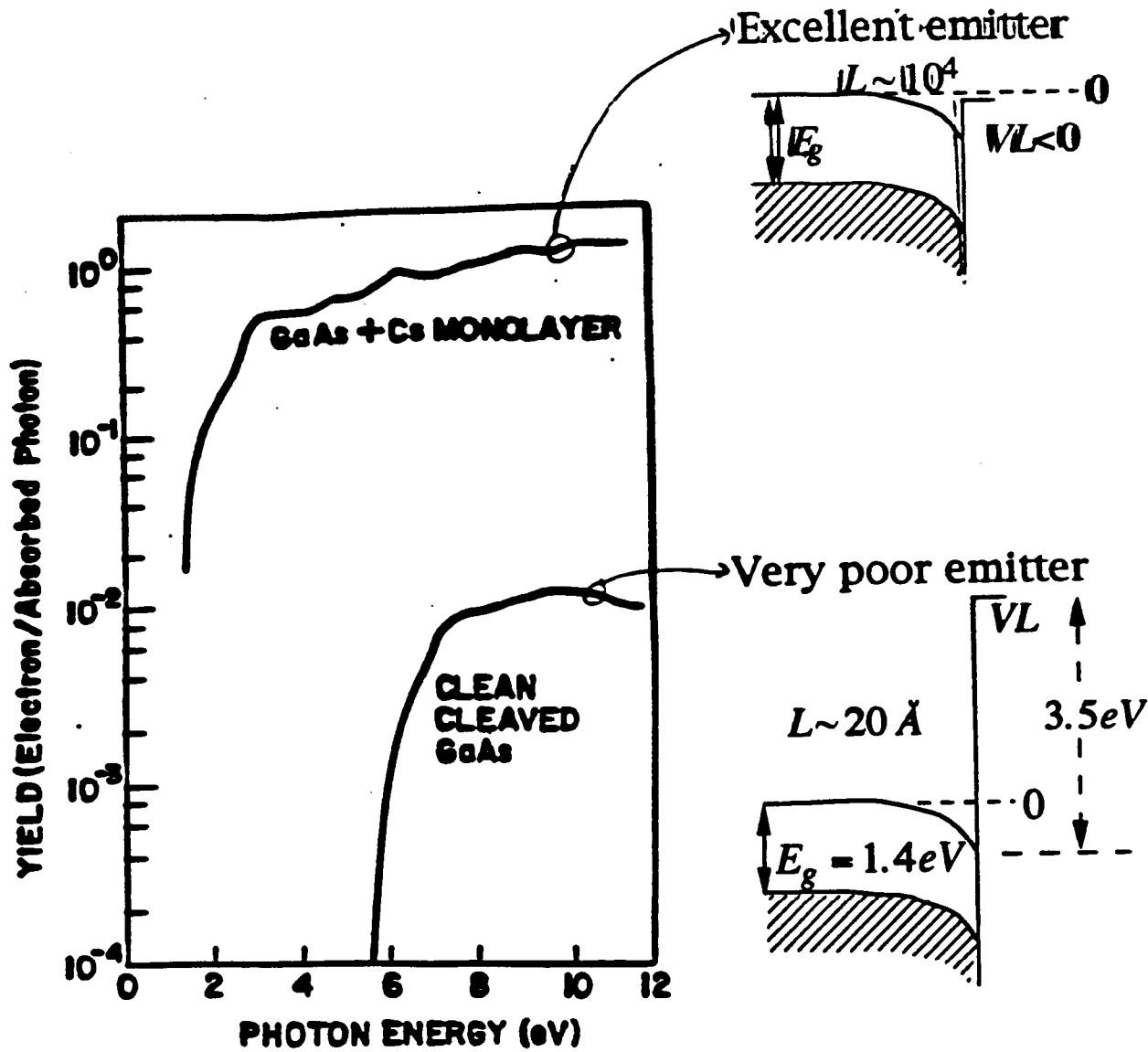
$\frac{l_a}{L}$  large, low yield



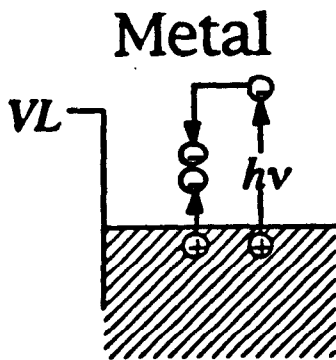
$\frac{l_a}{L}$  small, high yield







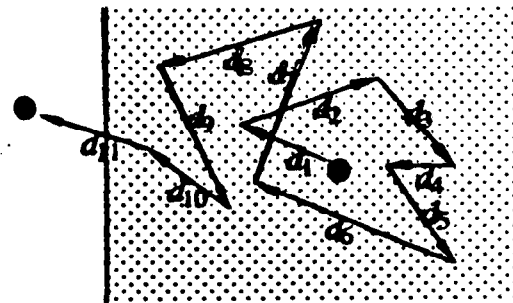
# Electron Scattering Mechanisms



**electron-electron  
scattering**

- $\sim 1/2$  kinetic energy loss in every collision ( $\sim 10^0$  eV)

**Semiconductor**



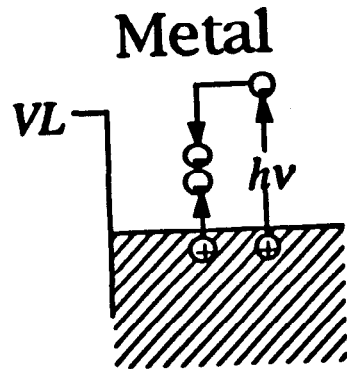
**electron-phonon  
scattering**

- small ( $\sim 0.05$  eV or less) energy loss per collision

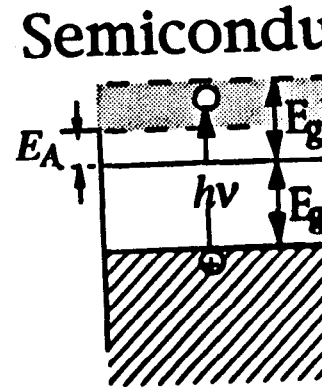
electron-phonon scattering dominates when the presence of the forbidden band gap prevents electron-electron scattering from taking place (semiconductors and insulators)

only semiconductors and insulators have high quantum efficiencies (0.02 to 0.95 elec/photon)

metals have low efficiencies ( $< 0.02$  elec/photon)



Electron-electron scattering can be prevented in semiconductors



325

Poor emitter

$$\frac{l_a}{L} \text{ large}$$

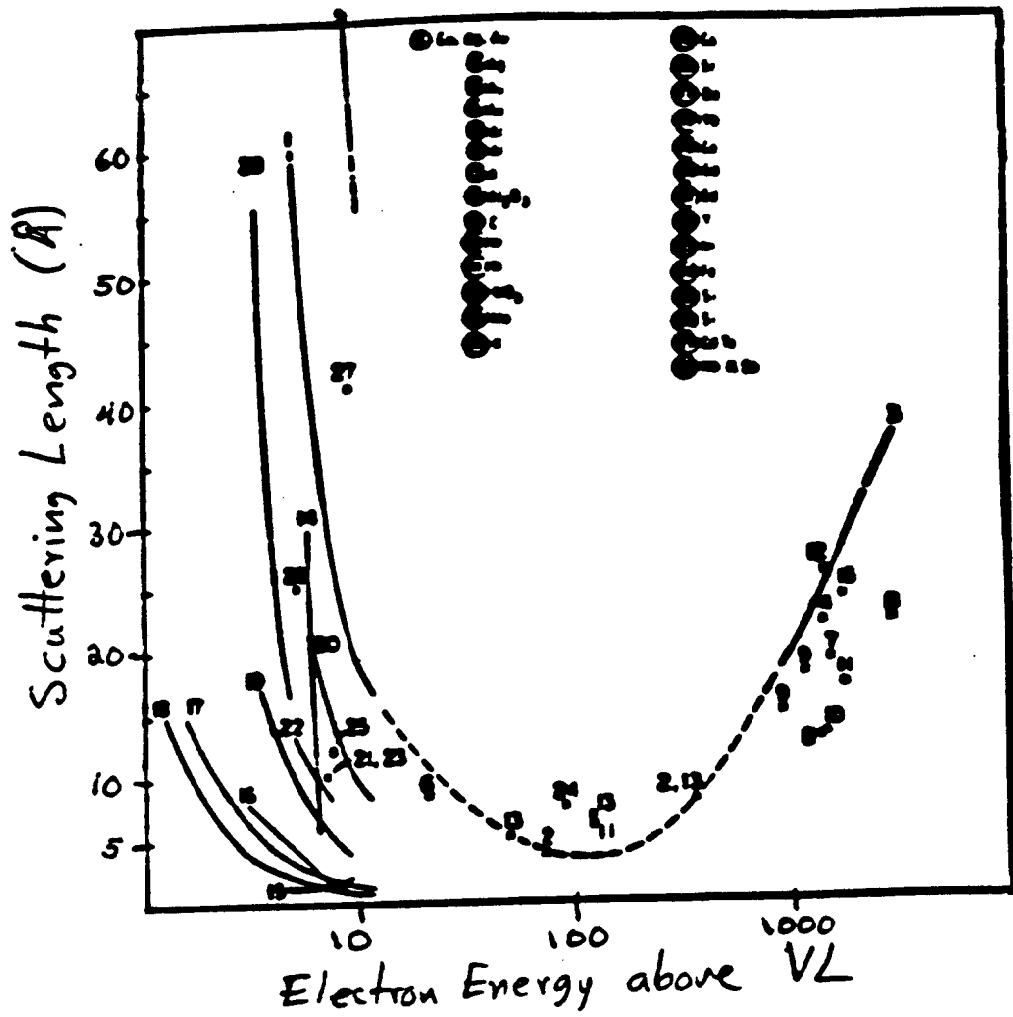
$$\frac{\alpha_{PE}}{\alpha} \text{ small}$$

$$Y = \frac{\alpha_{PE} P_E}{\alpha \left(1 + \frac{l_a}{L}\right)}$$

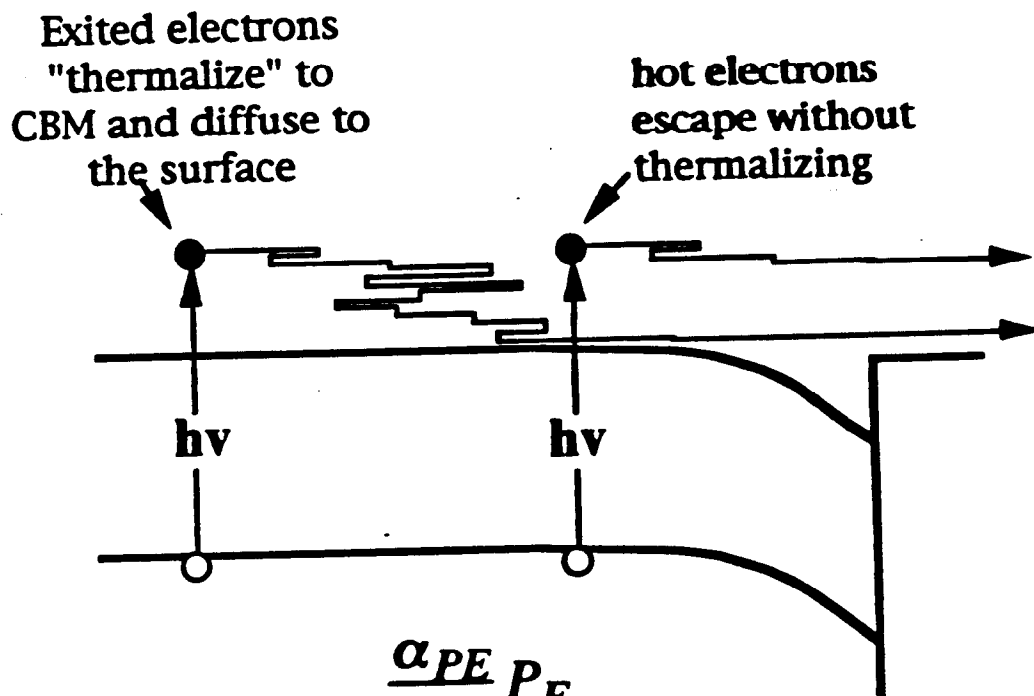
Good emitter

$$\frac{l_a}{L} \text{ small}$$

$$\frac{\alpha_{PE}}{\alpha} \text{ large}$$



# Negative Electron Affinity (NEA) Photoemitters



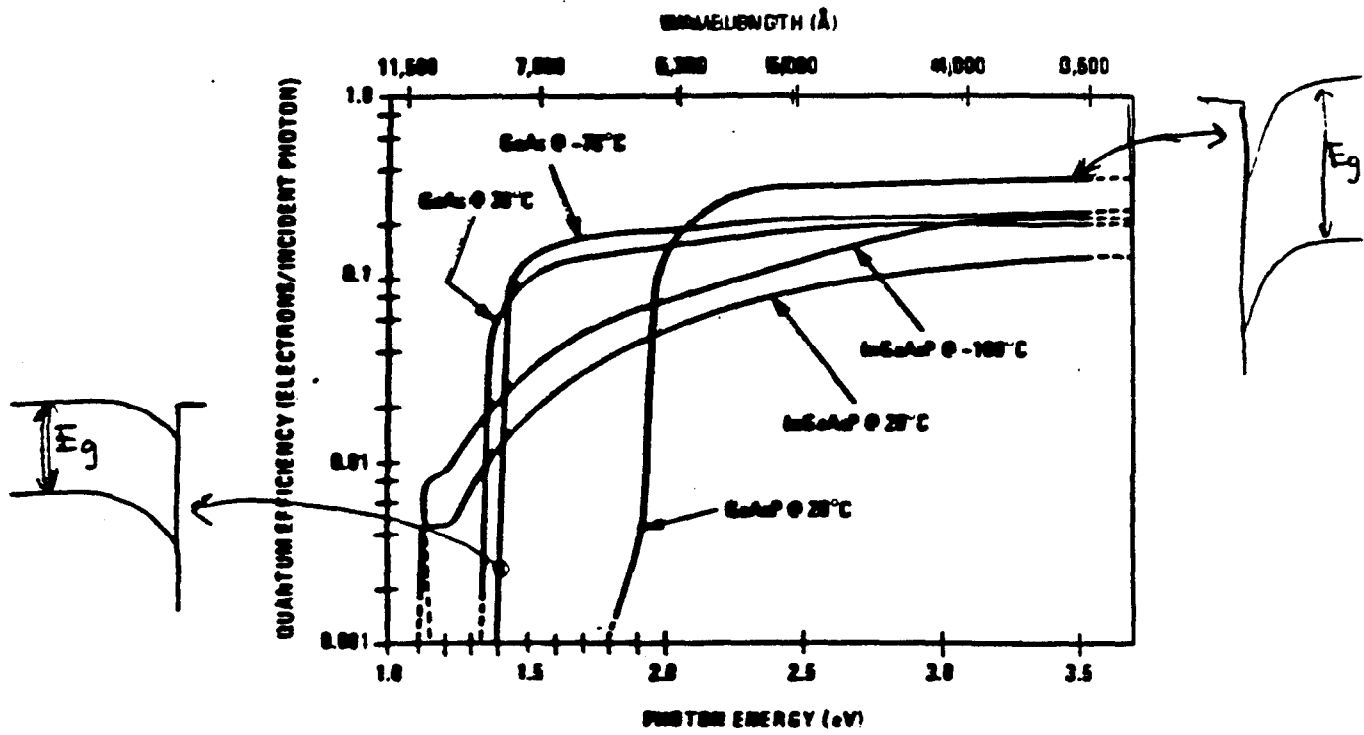
$$Y = \frac{\frac{\alpha_{PE}}{\alpha} P_E}{1 + \frac{l_a}{L}}$$

For GaAs NEA

$$\frac{\alpha_{PE}}{\alpha} \approx 1 \quad P_E \approx \frac{1}{3} \quad \frac{l_a}{L} \approx 0.3$$

$$Y \approx \frac{1 \times \frac{1}{3}}{1 + 0.3} = 0.25 \frac{\text{electrons}}{\text{photons}} \quad (\text{can be larger})$$

# on temperature

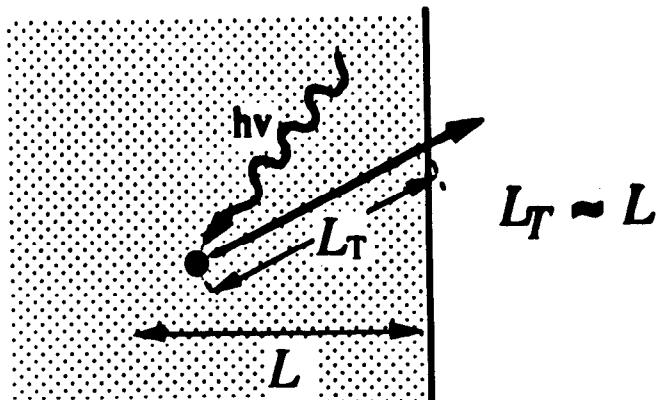


CA 1978

## Calculation of Response Time of Photocathode

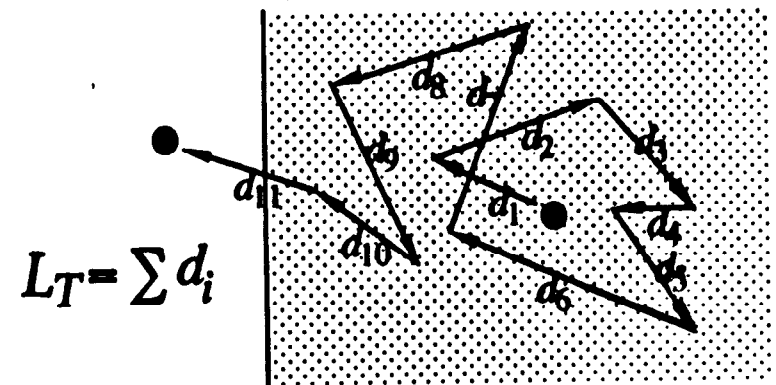
$$\tau = \int_0^{\tau} dt = \int_0^{L_T} \frac{dl}{v(l)} \approx \frac{\int_0^{L_T} dl}{v_a} = \frac{L_T}{v_a},$$

Metal



Electron-electron scattering dominates

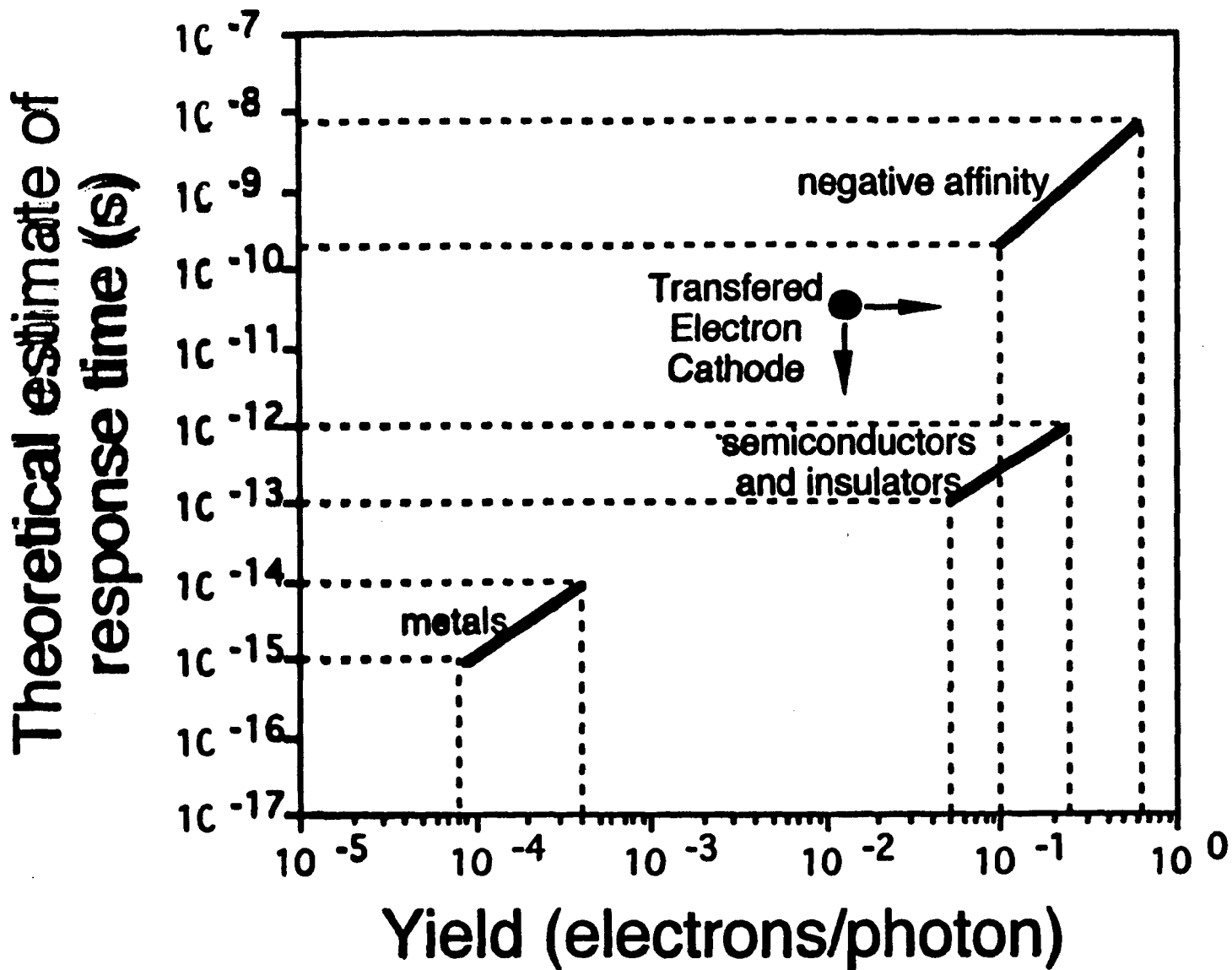
Semiconductor



Electron-phonon scattering dominates

Material	Dominating mode of scattering	Equation for $\tau$	Estimate range of $\tau$ (sec)	Typical yield (e <sup>-</sup> /photon) 1 eV above threshold
Metals	Electron-electron	$\tau = \frac{L}{v_a} \quad (9)$	$10^{-15}$ to $10^{-14}$	$8 \times 10^{-5}$ to $4 \times 10^{-4}$
Semiconductors and Insulators (Cs <sub>3</sub> Sb or multialkali)	Electron-lattice	$\tau = \frac{E_k}{\Delta E_p} \frac{l_p}{v_a} \quad (13)$	$10^{-13}$ to $10^{-12}$	0.05 to 0.25
Negative affinity	Electron-lattice (thermal diffusion of electrons in CBM)	$\tau = \frac{L_D^2}{\mu kT/q} \quad (14)$	$2 \times 10^{-10}$ to $7 \times 10^{-9}$	0.1 to 0.6





(14)

# **The Charge Limit Established at SLAC**

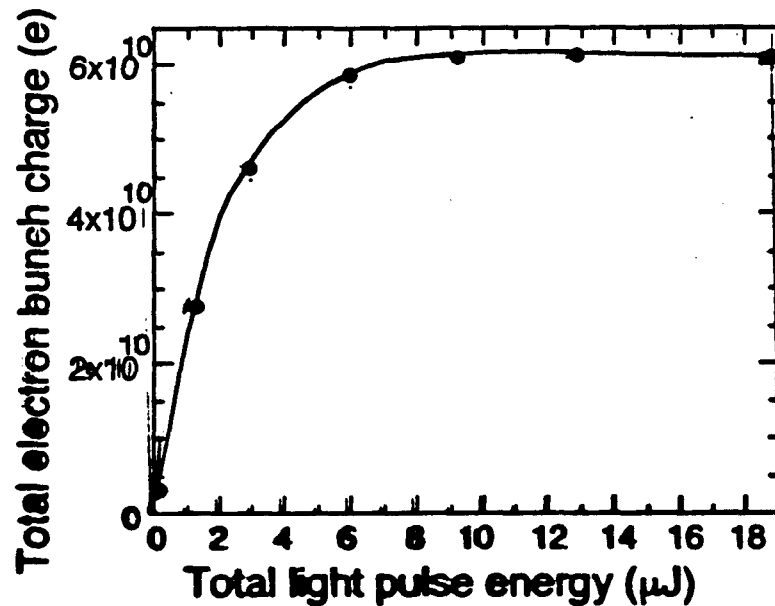
Alberto Herrera

*MODELING*

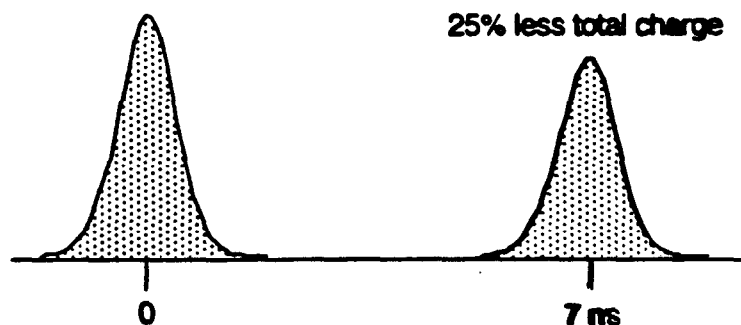
At high light intensity, photoemission yield has a striking time spectra, i.e. QY drops strongly with time

It can be explained by the well established Surface Photovoltaic Effect

# The Charge Limit Effect Discovered at SLAC



There is a limit on the total amount of electrons obtainable from the cathode. This is the Charge Limit (CL) effect.



In some cases it was found that, when two bunches are closely spaced in time, the second bunch has less charge.

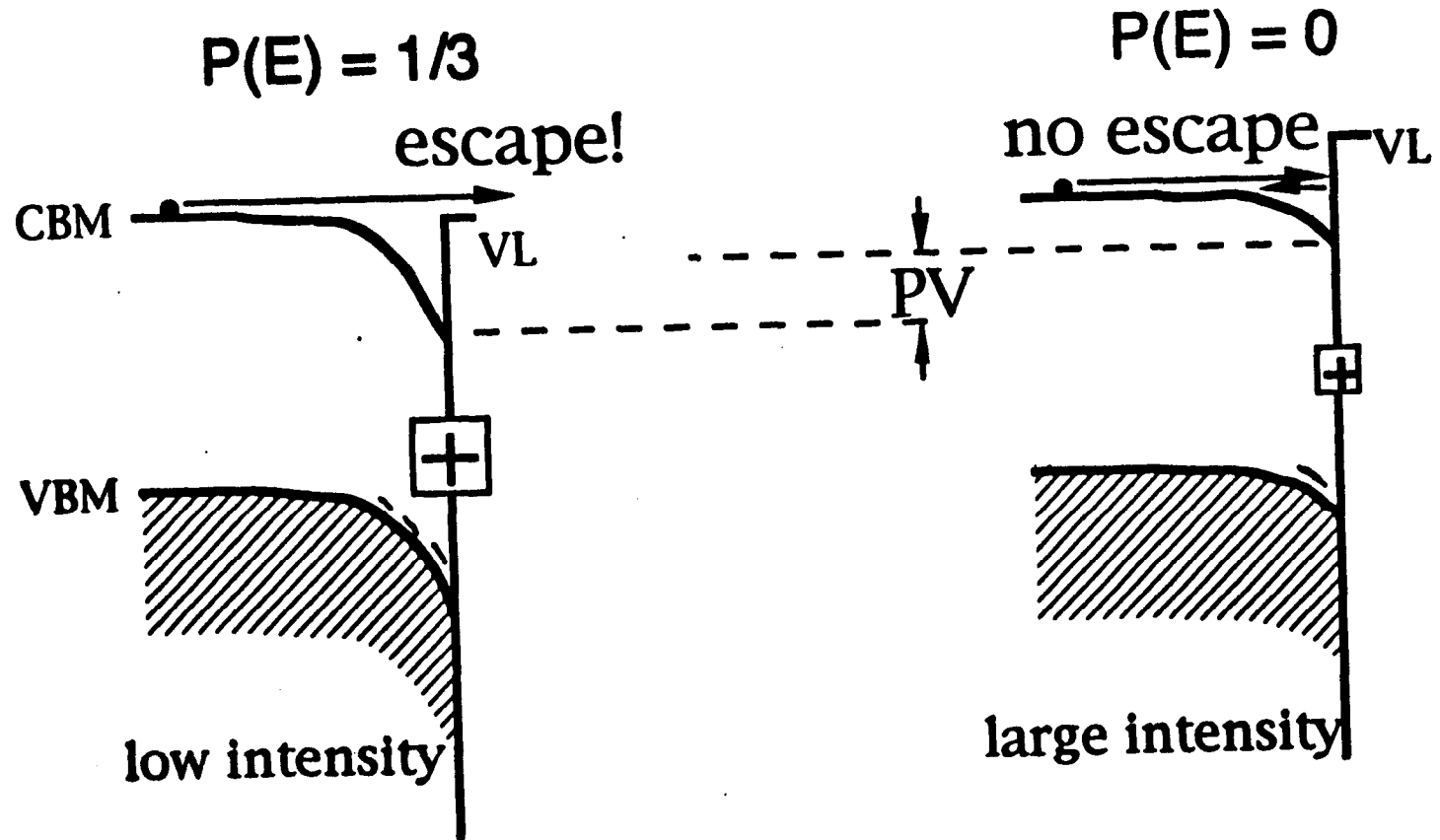
## Main assumptions used to describe the Ca

- The Photoemission process is based on the Three-Step

**Excitation — Escape — Transport to the surface**



- A fraction of the electrons arriving to the surface get trapped producing a Photovoltage



## Summary of Equations

excitation 
$$g(r,t) = \begin{cases} \alpha I_0 e^{-\left(\frac{t-t_0}{\tau_0}\right)^2} e^{-\alpha z} & z < \text{active region} \\ 0 & z \geq \text{active region} \end{cases}$$

transport 
$$\frac{\partial n(r,t)}{\partial t} = g(r,t) - \frac{n(r,t)}{\tau} + D \nabla^2 n(r,t)$$

charging current 
$$J_C(t) = D \left[ \frac{\partial n(z,t)}{\partial z} \right]_{z=0}$$

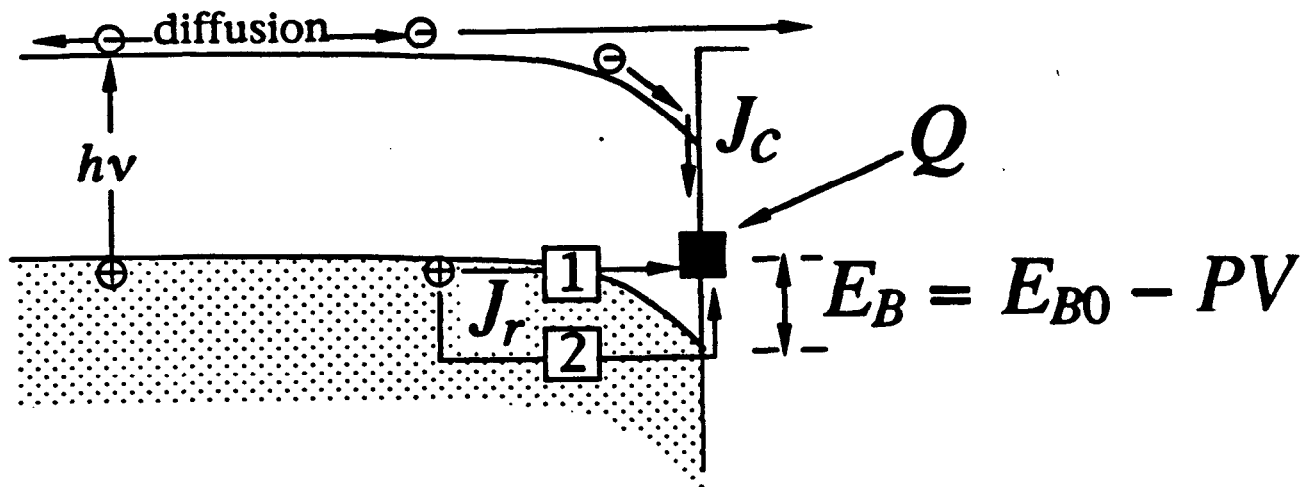
restoring current 
$$J_r = J_{\text{thermionic}} + J_{\text{tunneling}}$$

surface charge 
$$\frac{d}{dt} S_C = J_r - J_c$$

band unbending 
$$VL = VL_0 - \frac{S_{C0}^2 - S_C^2}{2\epsilon N_{\text{dop}}}$$

escape probability 
$$P_e = \begin{cases} \text{constant} & E > VL \\ 0 & E \leq VL \end{cases}$$

# Currents in and out of the Surface



$J_c$  current charging the surface states

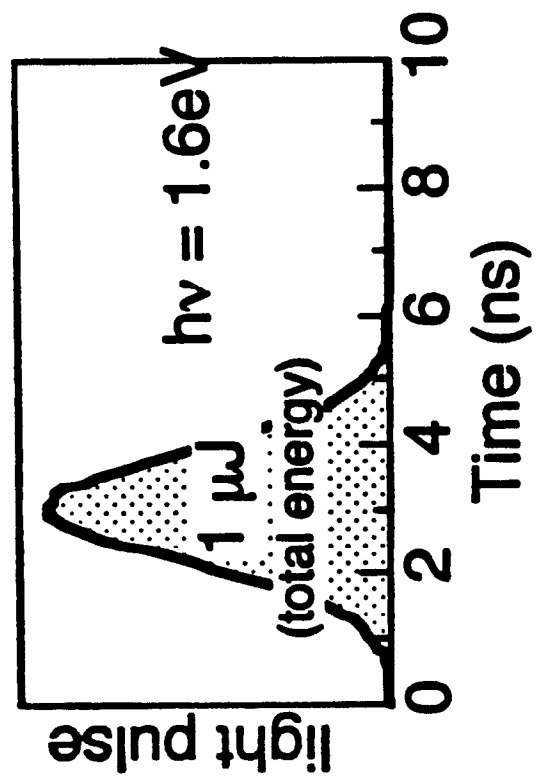
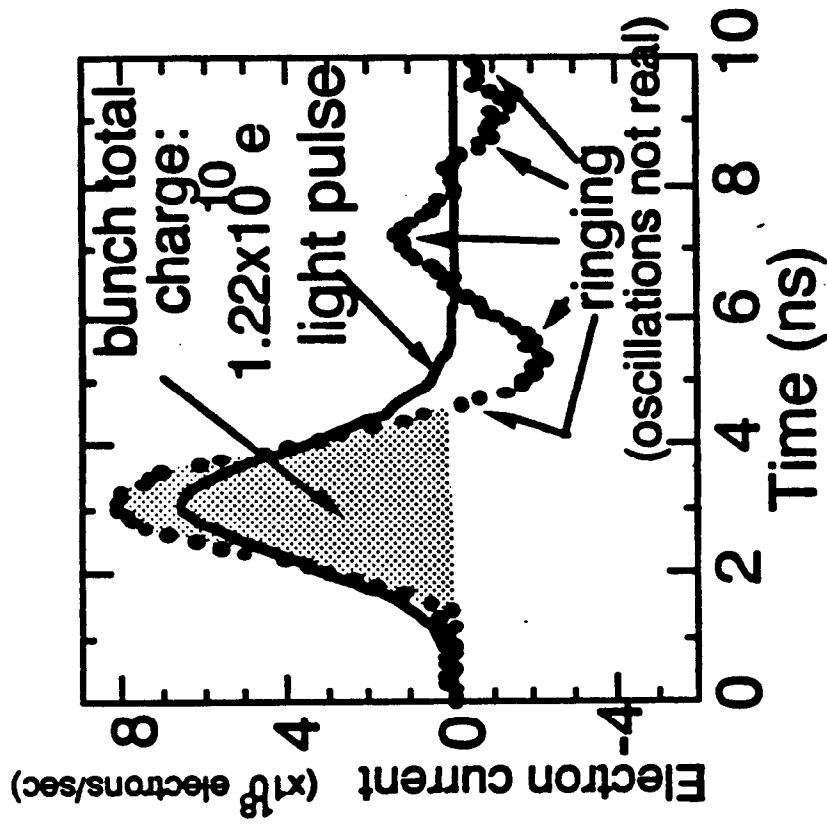
$J_r$  restoring currents:

$J_{FE} \equiv J_{r1}$  field emission

$J_{th} \equiv J_{r2}$  thermionic emission

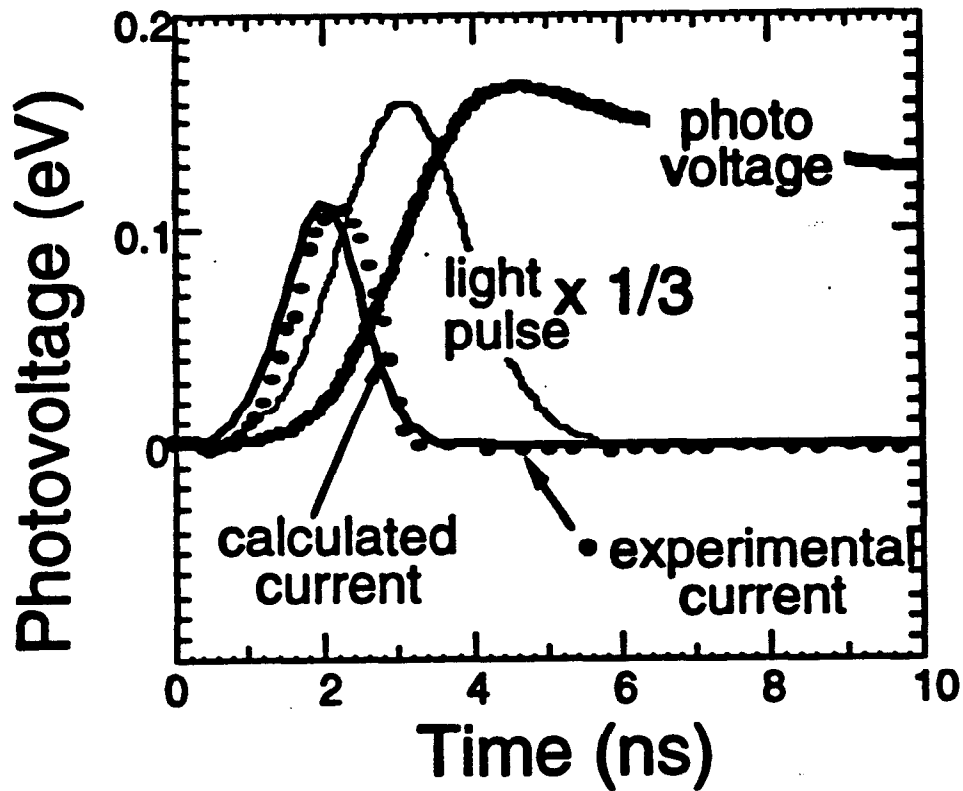
charging = current in - current out

$$\frac{d}{dt}Q = J_r - J_c$$

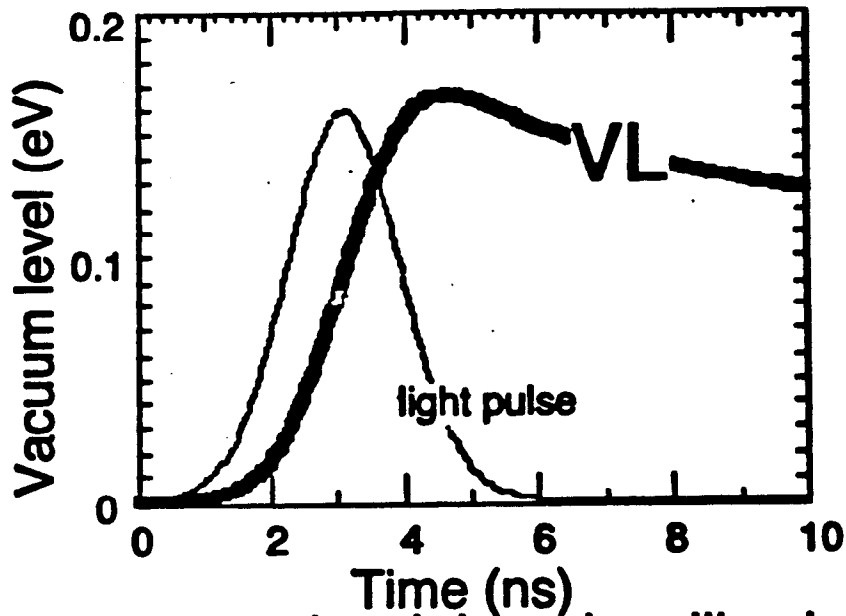


Light pulse and the corresponding electron bunch.  
 In this example the light intensity is low and there is not  
 Charge Saturation.

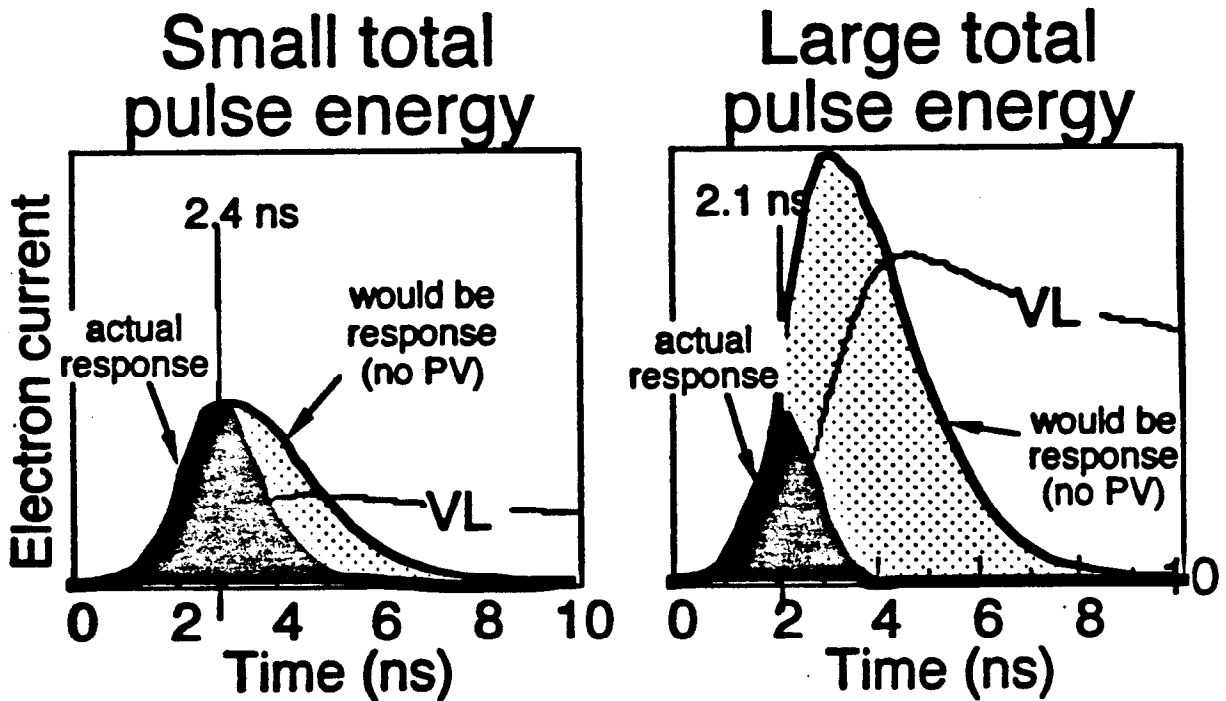




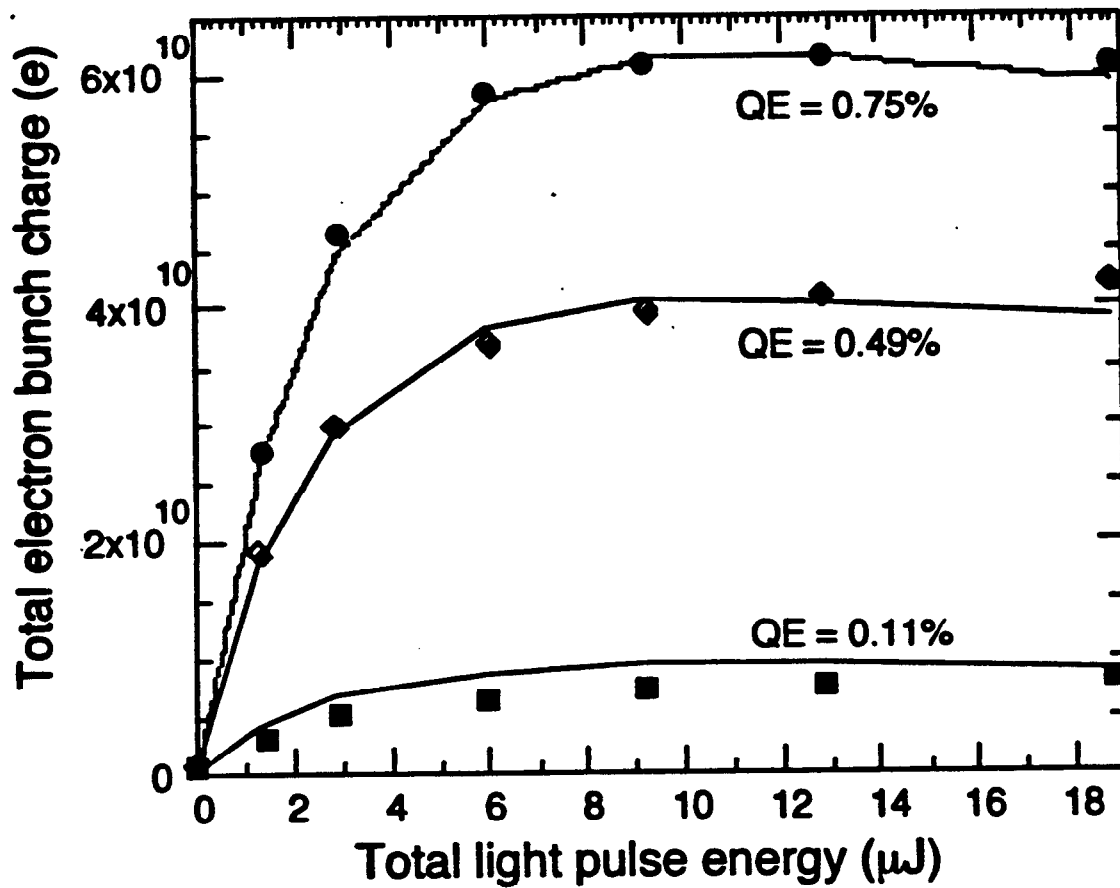
Photovoltage as a function of time. Also shown are the experimental and calculated electron response, as well as the light pulse.



Calculated vacuum level rise when illuminated with a high intensity light pulse of 65 mJ total energy

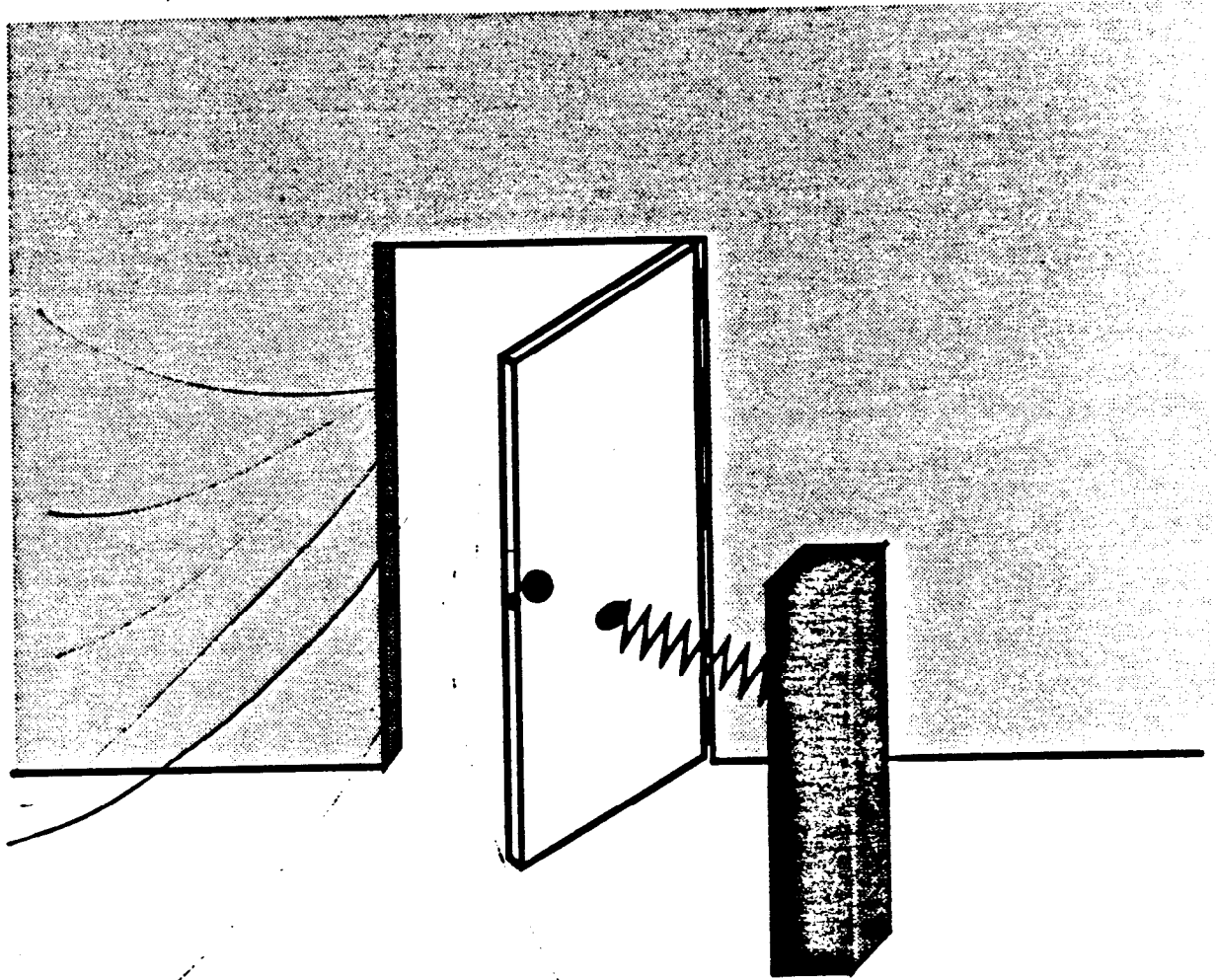


Example of the Charge Limit effect illustrating how a larger pulse may produce a smaller yield



Experimental (dots) versus calculated (lines) total charge versus light intensity

# Alberto's analogy to wind shutting a door



wind	↔	photoelectrons
door	↔	vacuum level
spring	↔	restoring current

# Conclusions

- Spicer's Three-Step theory provides a quantitative description of photoemission
  - can provide Response Times and Yield estimates for all existing cathodes
    - High yields ( $\sim 0.3$  el/ph) come with slow responses ( $10^{-9}$  sec)
    - Low yields ( $\sim 10^{-4}$  el/ph) come with fast responses (10-15 sec)
- Scientifically engineered 3-5 structures, guided by the Three-Step theory of Photoemission, can provide optimum photocathodes
- The photovoltaic model, together with the Three Step theory, explains the Charge Limit Effect found at SLAC and fits the data well
- To remove the Charge Limit create more interface states to assist tunneling
  - metalization is one possibility
  - preliminary experiments give encouraging results (Costello + Tanq)

**Huan Tang**  
**SLAC**

**Experimental Studies of the Charge Limit Phenomenon in  
GaAs Photocathodes**

## Experimental Studies of the Charge Limit Phenomenon in GaAs Photocathodes\*

H. Tang, R. Alley, H. Aoyagi<sup>†</sup>, J. Clendenin, P. Saez, D. Schultz, and J. Turner  
Stanford Linear Accelerator Center, Stanford University, Stanford, CA 94309

### ABSTRACT

GaAs photocathodes have been in use for generating high intensity polarized electron beams (up to a peak current of 6 A in 2 ns pulses) for the SLC high energy physics program. If the quantum efficiency (measured at low light intensities) of a GaAs photocathode is below a certain level, the maximum photoemitted charge is found to be limited by the intrinsic properties of the cathode instead of by the space charge limit. We have studied this charge limit phenomenon in a variety of GaAs photocathodes. The effects of the quantum efficiency, excitation laser wavelength, and extraction electric field on the charge limit have been examined. The temporal behavior of the charge limit as manifested in both intrapulse and interpulse effects has also been studied. These results will be discussed in light of possible mechanisms.

Polarized electrons generated by photoemission from negative electron affinity (NEA) GaAs cathodes with circularly polarized light have been in continuous use for the SLC high energy physics programs at SLAC since the spring of 1992 [1,2]. The demand for the highest possible polarization of the electron beam dictates that the energy of the excitation photons must be very close to the band gap energy of the cathode material. Operating under such a condition revealed a new phenomenon in the physics of photoemission from NEA semiconductor cathodes — if the quantum efficiency (QE) of the cathode is below a certain level the total charge extractable from a cathode within a short pulse (on the order of a few nanoseconds) saturates to a limit that is less than what the space charge limit permits [3,4]. As the beam intensity requirement is very high for the SLC/SLD program, and surely even more so for future linear colliders, this charge limit effect imposes a significant constraint on the usability of NEA photocathodes. We report in this note a systematic study on the charge limit phenomenon.

The experiments were conducted by using the Gun Test Facility at SLAC. The facility consists of a 20 mm cathode aperture diode gun with a loadlock system for easy cathode change, two pulsed Ti:Sapphire lasers pumped by a frequency-doubled Nd:YAG laser, and an electron beamline terminating into a Faraday cup. The two Ti:Sapphire lasers are tuned to 865 nm and 775 nm, respectively, and have a FWHM of about 2 nanoseconds. Their spot sizes are adjusted to >20 mm so that the cathode is fully illuminated in the charge limit studies. Two low power cw diode lasers of 752 nm and 833 nm, respectively, are used for quantum efficiency measurements with a spot size of 14 mm centered on the cathode. An optically isolated nanoammeter, a beam position monitor (BPM), and a gap monitor are used for beam intensity measurements. Unless otherwise stated, the cathode is always biased at -120 kV and maintained at a temperature of  $-5 \pm 2$  °C. The cathode activation method consists of heat cleaning to 600 °C for 1 hour, Cs application until the photoyield peaks, and finally Cs and NF<sub>3</sub> codeposition until the photoyield maximizes. The vacuum in the gun is maintained at about  $1 \times 10^{-11}$  Torr by means of ion and nonevaporative getter pumping. A large number of strained and unstrained GaAs cathodes have been studied. In the following we shall focus our attention on two 300 nm strained GaAs

cathodes doped with Zn to a concentration of  $5 \times 10^{18} \text{ cm}^{-3}$  and  $2 \times 10^{19} \text{ cm}^{-3}$ , respectively, which will hereafter be referred to as cathode 1 and cathode 2.

Before discussing the experimental results, consider an ideal case in which the photocathode is assumed to respond linearly to light illumination. Figure 1 illustrates in a simplistic fashion the charge versus light pulse energy behavior for two temporal forms of light pulses, square pulses and Gaussian-like pulses. For square pulse light illumination, the charge pulse is also square, and its amplitude increases linearly with light pulse amplitude, or energy, and eventually saturates to the space charge limit. The corresponding saturation curve is very simple, consisting of a straight line with a slope corresponding to the quantum efficiency and a zero slope line in the space charge limit region. For Gaussian-like light pulses, the charge pulse initially follows the shape of the light pulse, and changes to a truncated, or flat-topped, Gaussian-like pulse when its maximum amplitude exceeds the space charge limit. The total charge keeps increasing with increasing light pulse energy even in the space charge limit region due to increased contribution from the leading and trailing edges of the light pulse. This case is more relevant to our experimental study because our laser pulses, as shown in Figure 2, is Gaussian like.

Figure 3 shows a typical charge saturation plot and several charge pulses at various laser pulse energies measured with the gap monitor for cathode 1. The saturation plot is characterized by a nearly linear response of the cathode to the laser pulses in the low energy region, and increasingly nonlinear behavior as the laser energy further increases. The maximum charge is much less than the space charge limit, which is in excess of  $16 \times 10^{10}$  electrons/pulse, and the saturation curve is also drastically different from the space charge limit case as illustrated in Figure 1(b). Further increase in laser energy in the charge limit region results in a decrease in the photoemitted charge. The charge pulses shown in the lower panel reveal that as the charge limit sets in, the later portion of the charge pulse becomes suppressed. As a result, the charge pulse becomes narrower and peaks at an earlier time. The peak of the charge pulse, however, hardly shows any increase as the laser energy further increases and remains far below the space charge limit, which is about a factor of 5 larger than the maximum amplitude in the plot. Thus, it is the premature amplitude saturation, i.e., in comparison with the space charge limit, and the suppression of the later portion of the charge pulse that causes the observed charge limit (or charge saturation) behavior. Figure 4 shows a similar set of saturation plot and charge pulses measured at a different laser wavelength.

The suppression of the later portion of the charge pulses in the charge limit region suggests that as a large number of electrons are excited from the valence band into the conduction band under intense light illumination, the escape probability of the excited electrons is decreased. This points to an increase in the work function at the cathode's surface. A plausible scenario to cause a work function increase is the so called photovoltaic effect. As only a fraction of the electrons arriving at the surface successfully escape, there will be a large buildup of electrons at the surface under intense light illumination since the dissipation rate through recombination with holes is limited. The electrons discharge the surface and reduce the band bending in the surface region, thereby effectively raising the work function and causing the charge limit effect. Herrera and Spicer [5] have modeled the charge limit phenomenon based on the photovoltaic effect.

Figures 5 and 6 show the evolution of the charge saturation behavior as the QE of cathode 1 varies. Except for a reduced oversaturation effect in the charge limit region as the QE decays, the overall shape of the saturation curve remains primarily unchanged. In particular, it is noted that the laser pulse energy required to drive the cathode into charge limit remains about the same.



We now turn to the discussion on the results from cathode 2, whose doping concentration is a factor of 4 higher than that of cathode 1. Its QEs measured at 752 nm and 833 nm are comparable to those of cathode 1. Figure 7 shows a saturation plot along with charge pulses recorded at several laser pulse energies. In this case, there is no evidence of oversaturation in the charge limit region, which is in sharp contrast to the results of cathode 1. An examination of the charge pulses indicate that while indeed the charge pulse becomes narrower and peaks at an earlier time in the charge limit region, the later portion of the pulse is suppressed to a much smaller degree in comparison with the case of cathode 1. Apparently, this difference is related to the different doping concentrations in the two cathodes. A similar set of saturation plot and charge pulses measured at a different wavelength is shown in Figure 8, and the evolution of the saturation curve with varying QE is shown in Figures 9 and 10.

Accelerators often require closely spaced (in time) charge pulses for their high energy physics experiments. For example, the SLC/SLD requires two 2-nsec pulses separated by 60 nsec, while the conceptual Next Linear Collider require many more shorter and more closely spaced (about 1 nsec) pulses for every macropulse. It is therefore important to examine the interpulse effect from the standpoints of accelerator sources as well as fully understanding the charge limit phenomenon. Figure 11 shows two saturation plots of cathode 1 for pulse 2 with and without pulse 1 which is 56 nsec earlier [6]. The effect of pulse 1 on pulse 2 is rather significant considering the relatively long time separation. The effect is two-fold: a reduction in the photoemitted charge and an upward shift of the laser energy for maximum charge in pulse 2. The upper panel of Figure 12 shows that the effect of pulse 1 on the amount of charge in pulse 2 monotonically decays with increasing time separation. The lower panel shows that the presence of pulse 1 mainly affects the amplitude of pulse 2 while leaving its pulse shape unchanged.

Figure 13 shows several sets of detailed interpulse effect data for cathode 1. Several conclusions may be drawn upon the data. (1) The harder the first pulse is pumped, the greater its effect on the second pulse. (2) The longer the wavelength (or the smaller the excitation photon energy) for pumping the second pulse, the greater the effect the first pulse has on the second one. (3) The time constant that characterizes the decay of the interpulse effect is on the order of 1  $\mu$ sec, which is rather long. However, the interpulse effect for cathode 2 as shown in Figure 14 is strikingly different in that its decay time constant is orders of magnitude smaller than that of cathode 1. The interpulse effect is almost completely gone for time separations of  $>30$  nsec. This contrasting behavior between the two cathodes, which differ only in doping concentrations, is correlated with their different intrapulse behaviors, i.e., the suppression of the later portion of the charge pulse (and also the degree of oversaturation) is much stronger for cathode 1 than for cathode 2. In the photovoltaic model, basically a single time constant that characterizes the dissipation rate of accumulated electrons at the surface can be used to describe both the interpulse and intrapulse effect. The strong dependence of the time constant on the doping concentration can be understood since the primary electron dissipation mechanism for our highly doped cathodes is holes tunneling to surface to recombine with the electrons [5]. This process is critically dependent on the width of the band bending region which is in turn controlled by the doping concentration. In fact, decay time constant as long as 25 sec has been reported for the surface photovoltaic effect in GaAs materials with a doping concentration of  $1 \times 10^{17}$   $\text{cm}^{-3}$  or less [7].

Figure 15 shows that the charge limit for the 865 nm or 775 nm laser pulses is proportional to the QE measured at 752 nm or 833 nm. It is noted that, while the 865 nm charge limit line has a zero intercept with the ordinate, the 775 nm line does not. To aid theoretical understanding, it would be better to correlate the charge limit with the QE measured at the *same* wavelength, for QEs measured at different wavelengths do not exactly scale with one another as the cathode's

NEA condition deteriorates with time. Although Figure 16 shows that QEs measured at 752 nm and 833 nm scale reasonably well with each other, which imply that thermalized electrons contribute dominantly to the photoyield, care must be taken to generalize to any wavelength since the QE measured at very close to the bandgap threshold is more sensitive to changes in the surface NEA condition.

It is interesting to examine how the charge limit depends on the excitation wavelength. Figure 17 shows that the wavelength dependence of the charge limit is very weak for high QEs, and increases considerably as the QE deteriorates. It suggests that hot electrons (as opposed to thermalized electrons) become increasingly important in contributing to photoemission under the illumination of intense light as the surface work function rises.

Figure 18 shows that the logarithm of the QE depends linearly on the square root of the extraction electric field, which is consistent with the Schottky barrier lowering effect [8]. We may reasonably assume that the excited electrons that arrive at the cathode surface can be described by an effective temperature. Then, from the Schottky effect data the effective temperatures for the electrons excited with the 752 nm and 833 nm lasers may be easily determined to be 205 meV and 198 meV, respectively. The fact that the temperatures for the two cases are about the same implies that the photoexcited hot electrons are rapidly thermalized to the bottom of the conduction band and become hotter after traversing the band bending region to reach the surface. The slight wavelength dependence of the effective temperature may be attributed to incompletely thermalized electrons.

Finally, Figure 19 shows the charge limit as a function of the cathode bias. It is clear that the dependence is almost linear and, unlike in the case of QE, cannot be explained by the Schottky effect. Pulse shape measurements of the charge pulses indicate that the amplitude depends strongly on the cathode bias, which is responsible for the observed bias dependence of the charge limit. The fact that the charge limit does not simply depend on the cathode bias through QE, which is measured at low laser intensity, further illustrates the complicated nature of the charge limit.

In summary, we have studied the various aspects of the charge limit phenomenon. Charge limit is characterized by premature amplitude saturation, i.e., below the space charge limit, and suppressed emission in the later portion of the pulse. These two characteristics may be related and may simply be different manifestations of the same physics behind the charge limit phenomenon. The time constant for the charge limit effect to decay depends very sensitively on the doping concentration of a cathode. The strong dependence of the charge limit on the cathode bias points to the advantage of operating the electron source at the highest possible voltage if high intensity beams are desired.

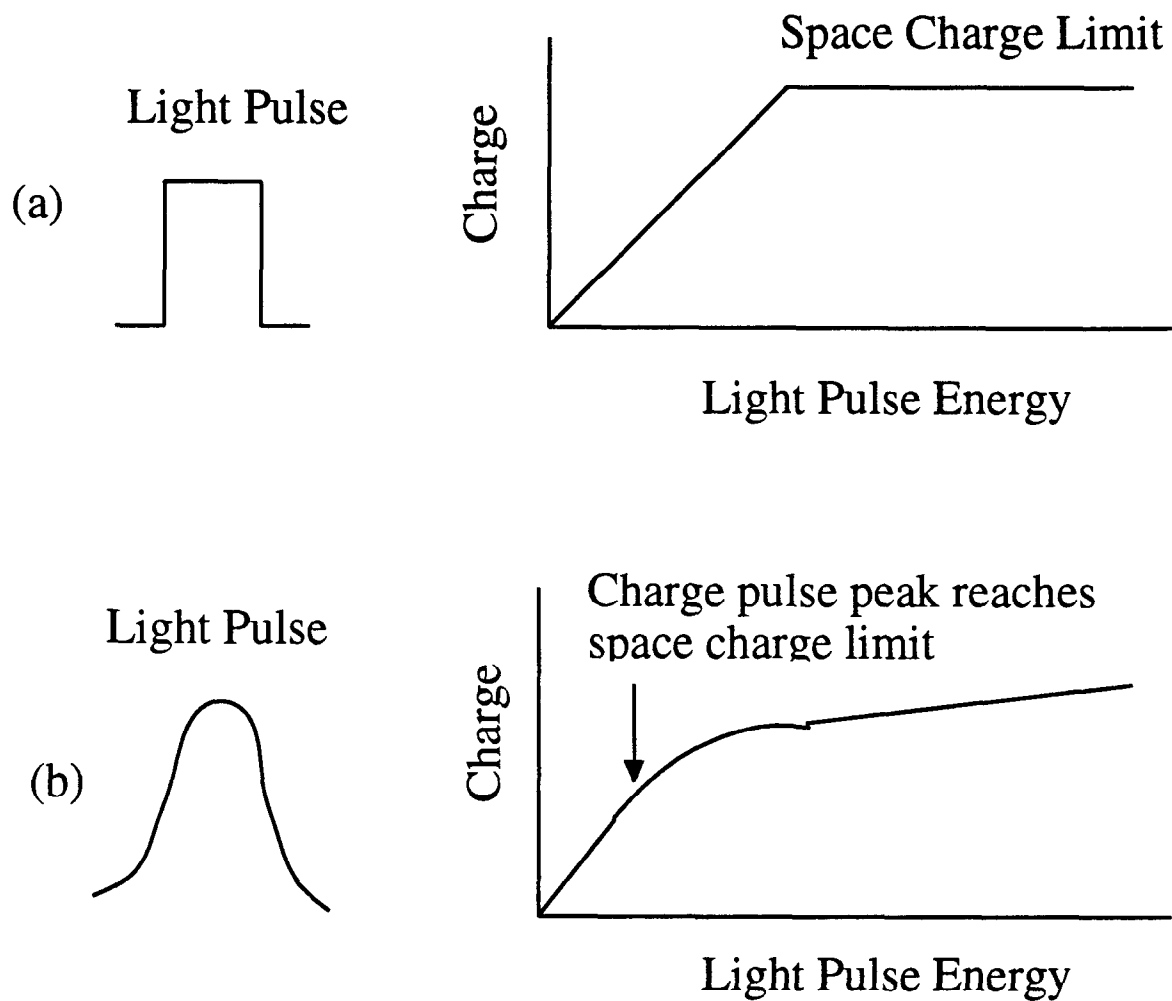
\* Work supported by DOE contract DE-AC03-76SF00515.

† Permanent address: Faculty of Science, Nagoya University, Nagoya 464-01, Japan.

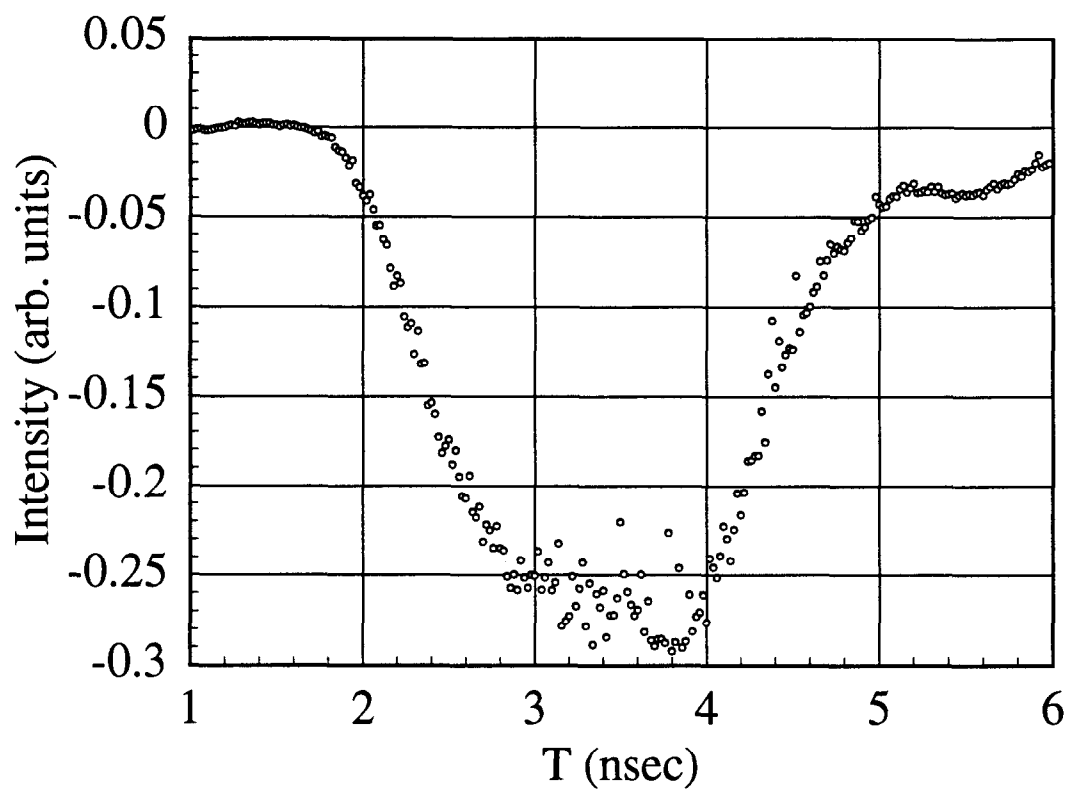
## REFERENCES:

1. D.C. Schultz, *et al.*, "Polarized source performance in 1992 for SLC-SLD", presented at the 10th Int. Sym. on H.E. Spin Physics, Nagoya, Nov. 9-14, 1992.
2. J.E. Clendenin, *et al.*, "Performance of the SLC polarized electron source with high polarization", *Proceedings of the 1993 PAC Conference*, Washington, DC, May 17-20, 1993.
3. M. Woods, *et al.*, "Observation of a charge limit for semiconductor photocathodes", SLAC-PUB-5894, J. Appl. Phys., in press.

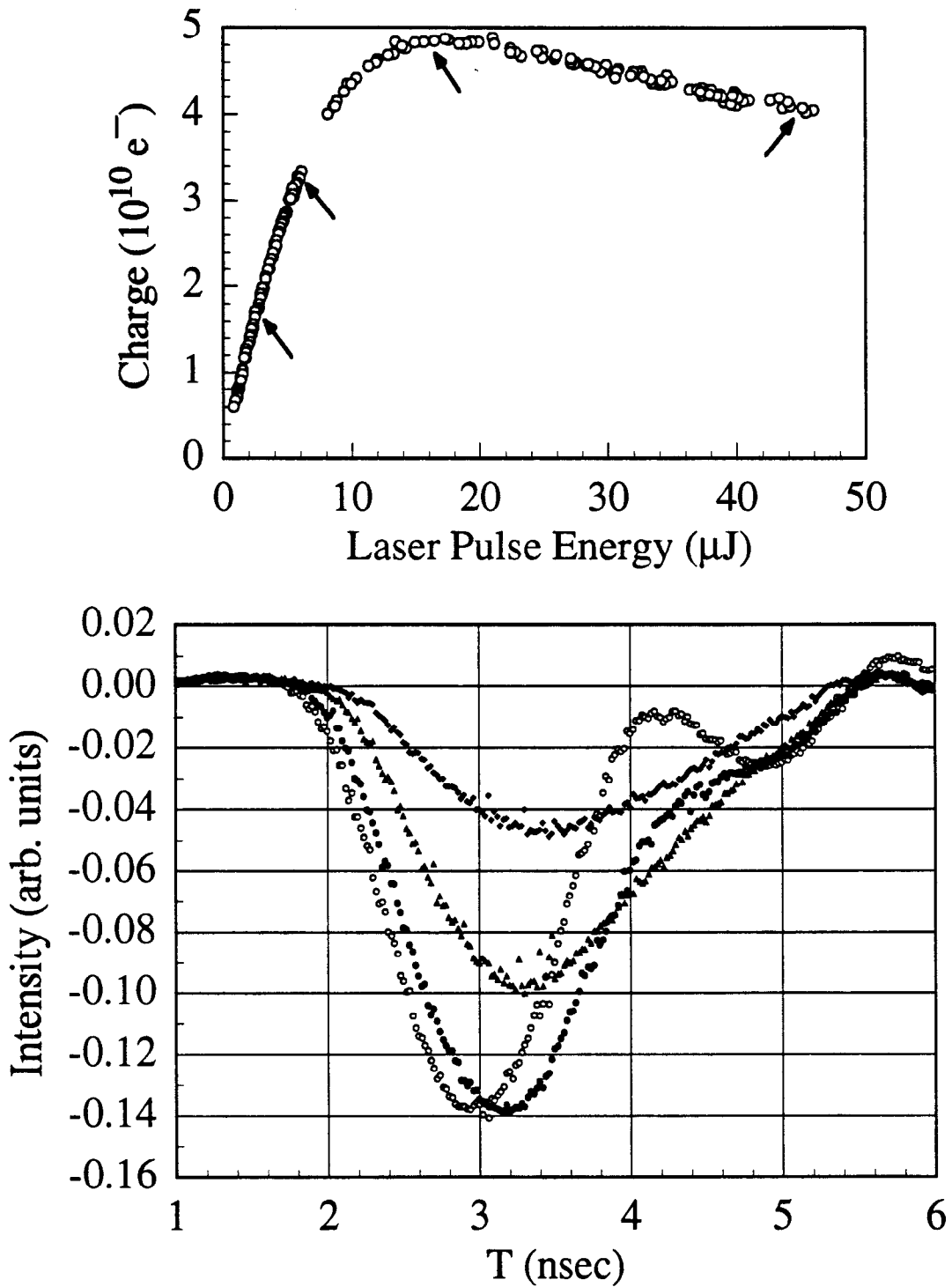
4. H. Tang, *et al.*, "Study of non-linear photoemission effects in III-V semiconductors", *Proceedings of the 1993 PAC Conference*, Washington, DC, May 17-20, 1993.
5. A. Herrera-Gomez and W.E. Spicer, "Physics of high intensity nanosecond electron sources", *Proc. SPIE's 1993 Int. Sym.*, San Diego, CA, July 11-16, 1993. SLAC-PUB-6307.
6. Due to certain instrumental problems, the charge in the second pulse is underestimated by about 5% in all of the double pulse measurements. Therefore, the actual charge in the second pulse should be scaled up by about 5%.
7. J. Qi, *et al.*, "Depletion-electric-field-induced changes in second-harmonic generation from GaAs", *Phys. Rev. Lett.* **71**, 633 (1993).
8. See, for example, S.M. Sze, *Physics of Semiconductor Devices*, p. 250-254, John Wiley & Sons, 1981.



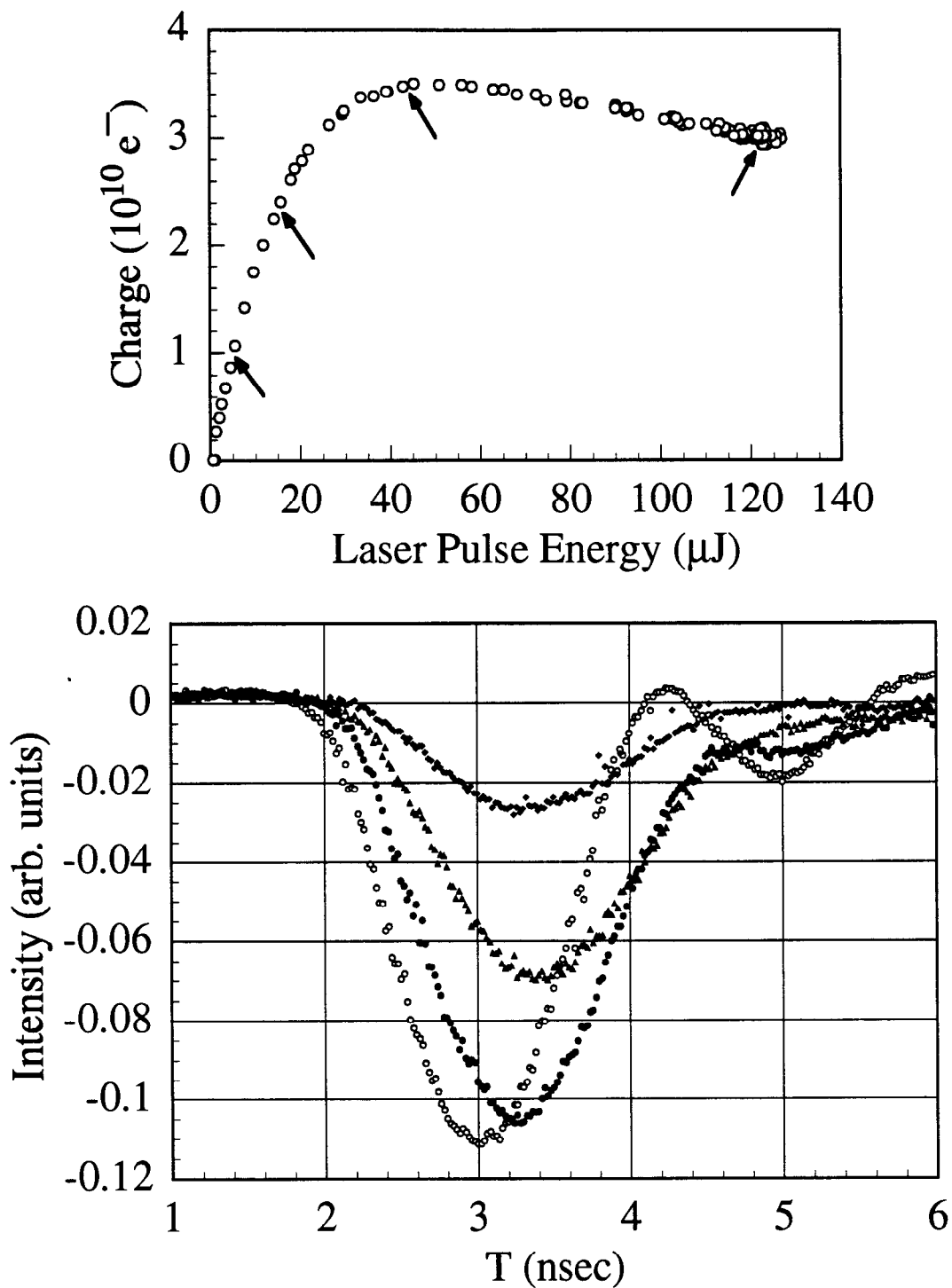
**Fig. 1:** Charge saturation behavior of an idealized linear-response photocathode illuminated with two types of light pulses.



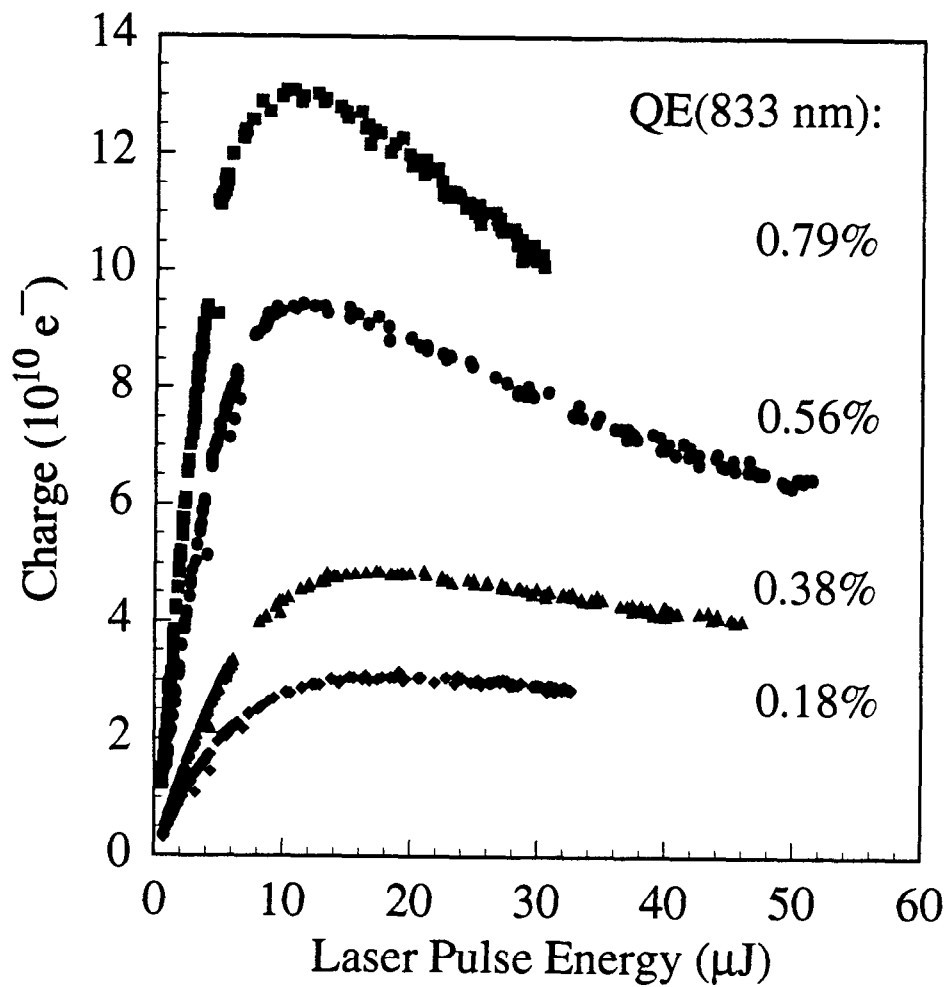
**Fig. 2:** Typical pulse shape of the 775 ns laser pulses used in the charge saturation studies.



**Fig. 3:** Saturation plot and charge pulses for cathode 1 with 775 nm laser. The arrows indicate where the charge pulses are recorded. The QE at 833 nm is 0.38%.

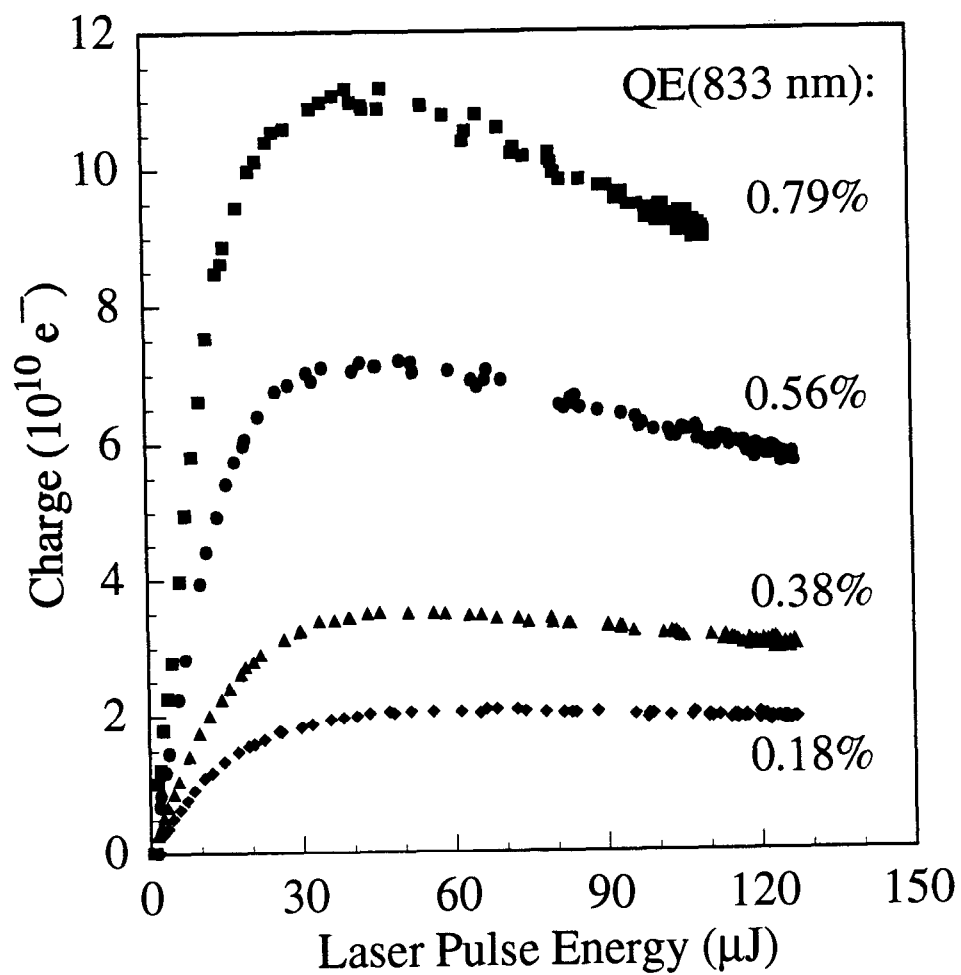


**Fig. 4:** Saturation plot and charge pulses for cathode 1 with 865 nm laser. The arrows indicate where the charge pulses are recorded. The QE at 833 nm is 0.38%.

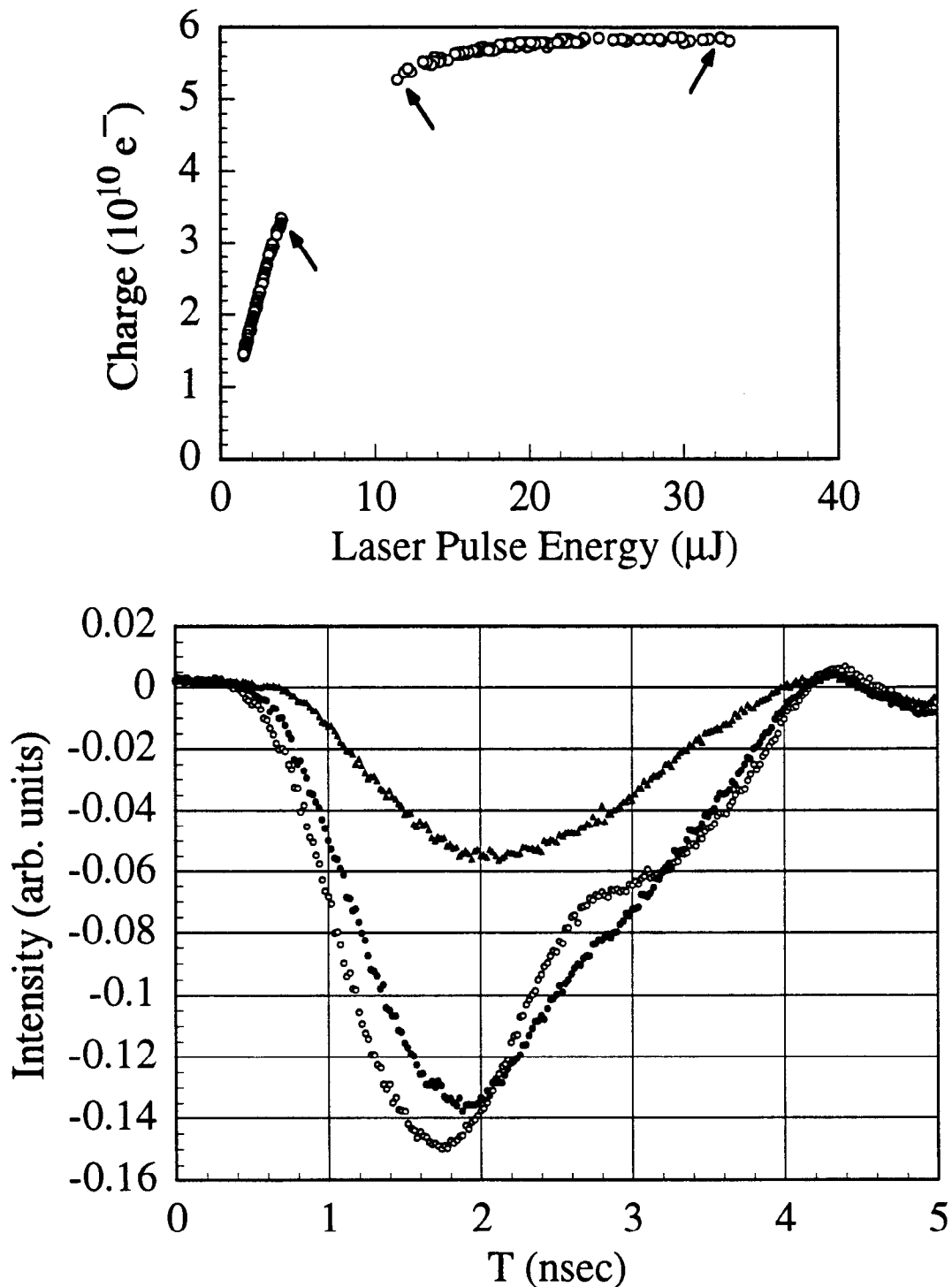


**Fig. 5:** Charge saturation data for cathode 1 with 775 nm laser pulses.

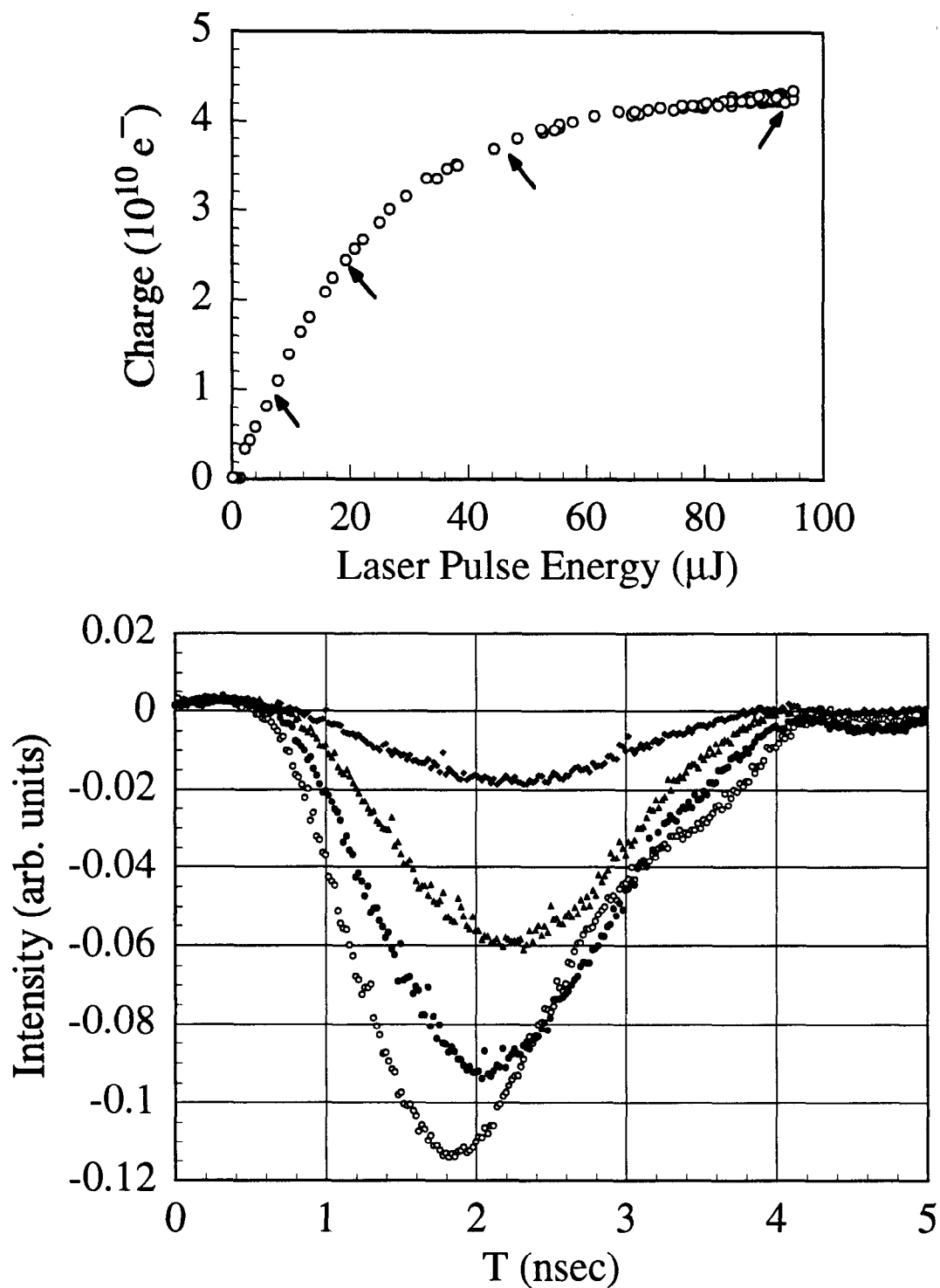




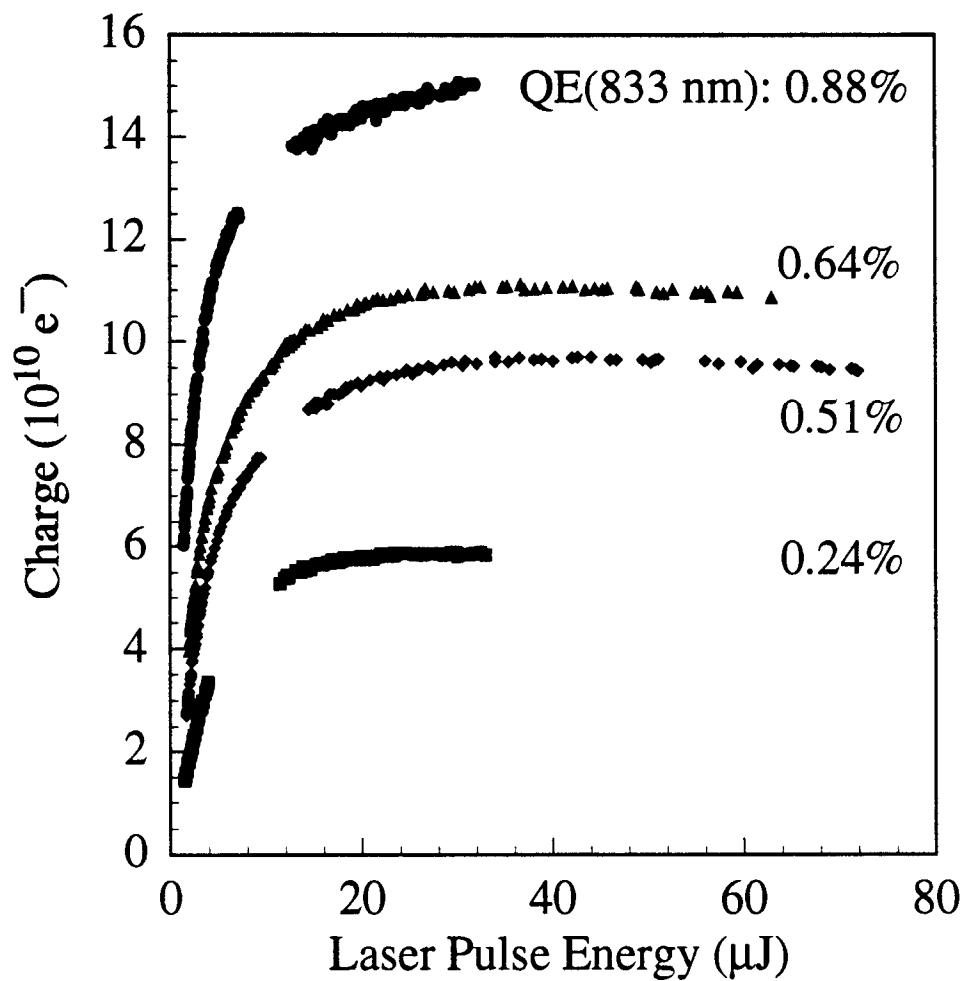
**Fig. 6:** Charge saturation data for cathode 1 excited with 865 nm laser pulses.



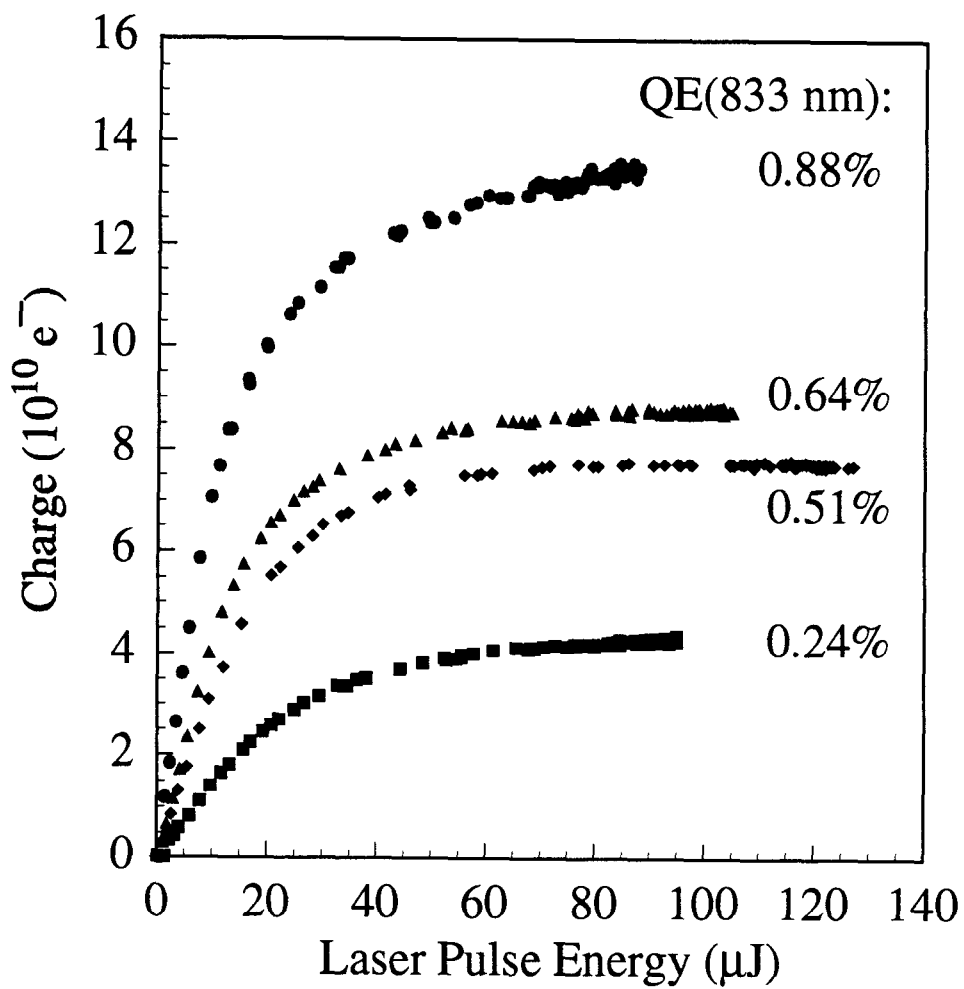
**Fig. 7:** Saturation plot and charge pulses for cathode 2 with 775 nm laser. The arrows indicate where the charge pulses are recorded. The QE at 833 nm is 0.24%.



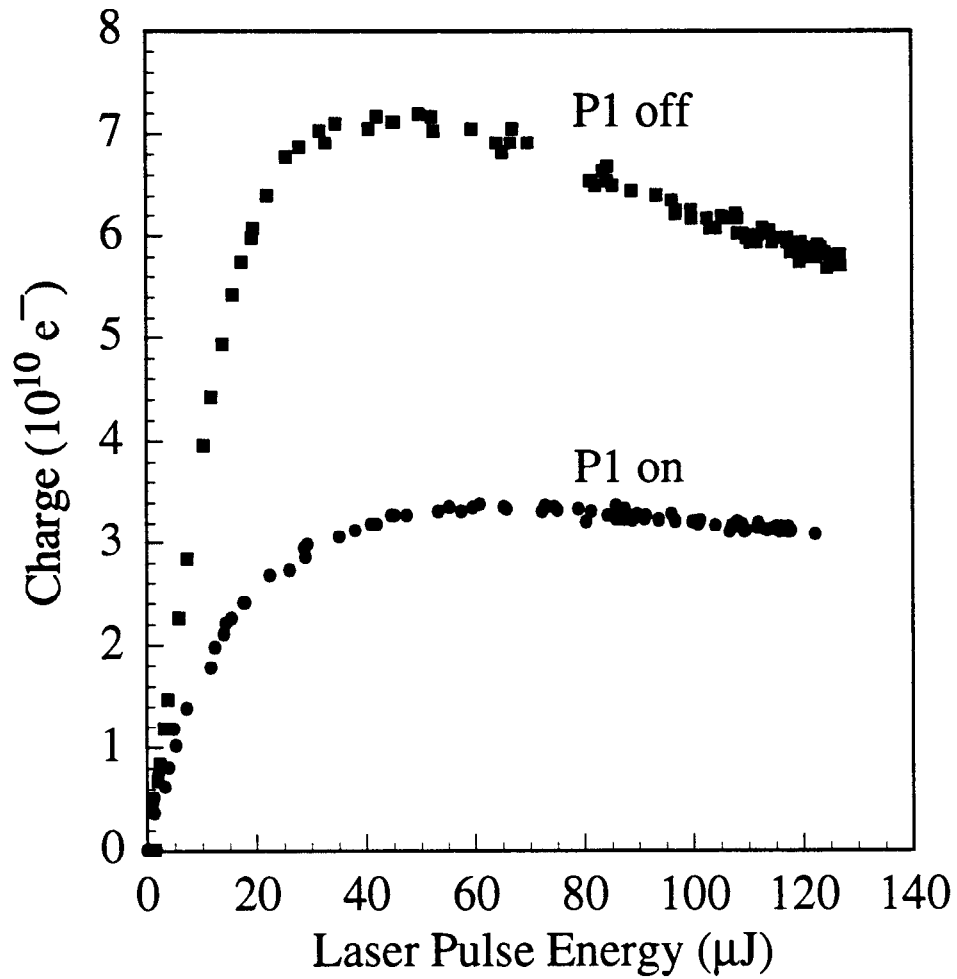
**Fig. 8:** Saturation plot and charge pulses for cathode 2 with 865 nm laser. The arrows indicate where the charge pulses are recorded. The QE at 833 nm is 0.24%.



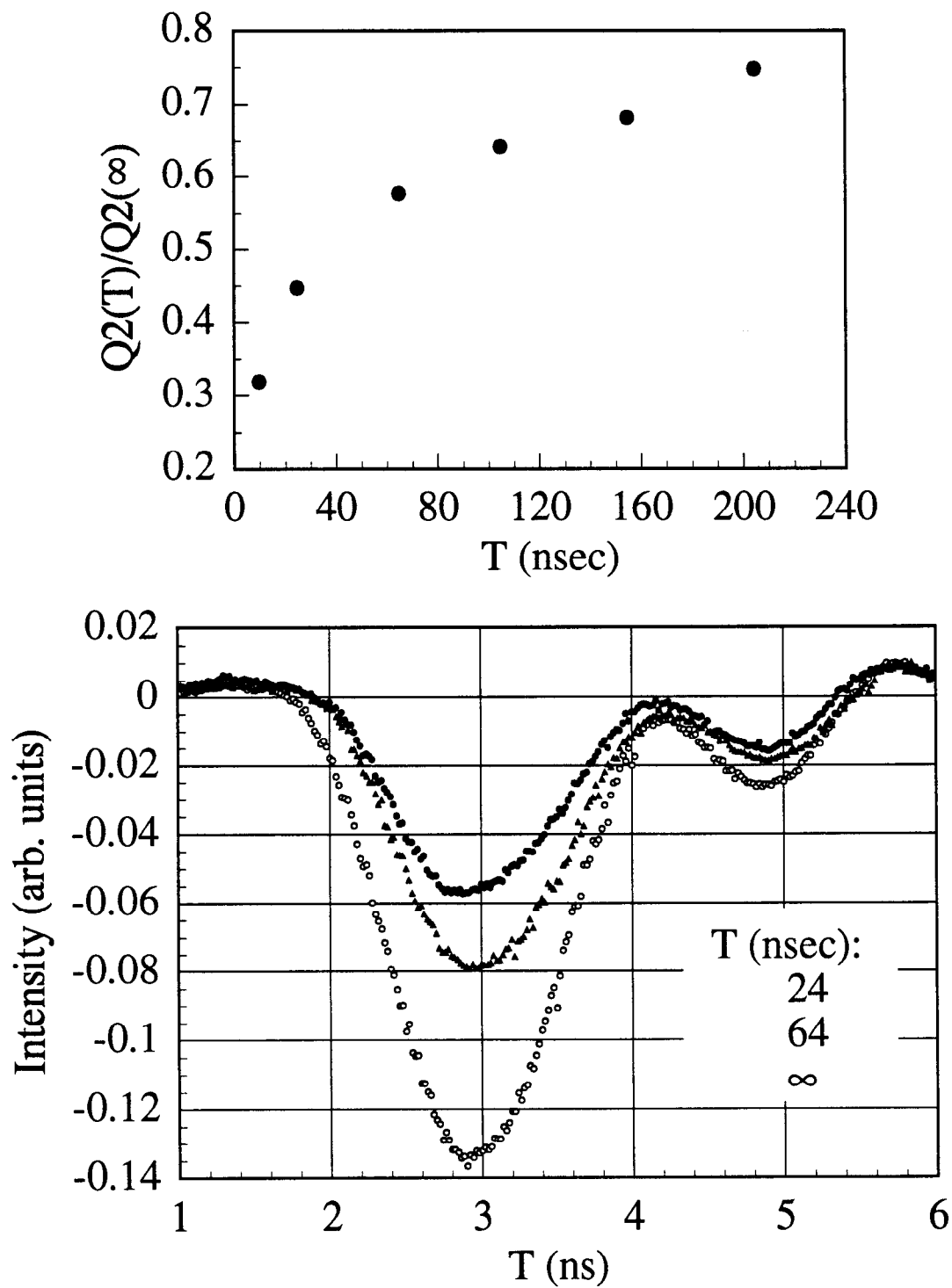
**Fig. 9:** Charge saturation data for cathode 2 excited with 775 nm laser pulses.



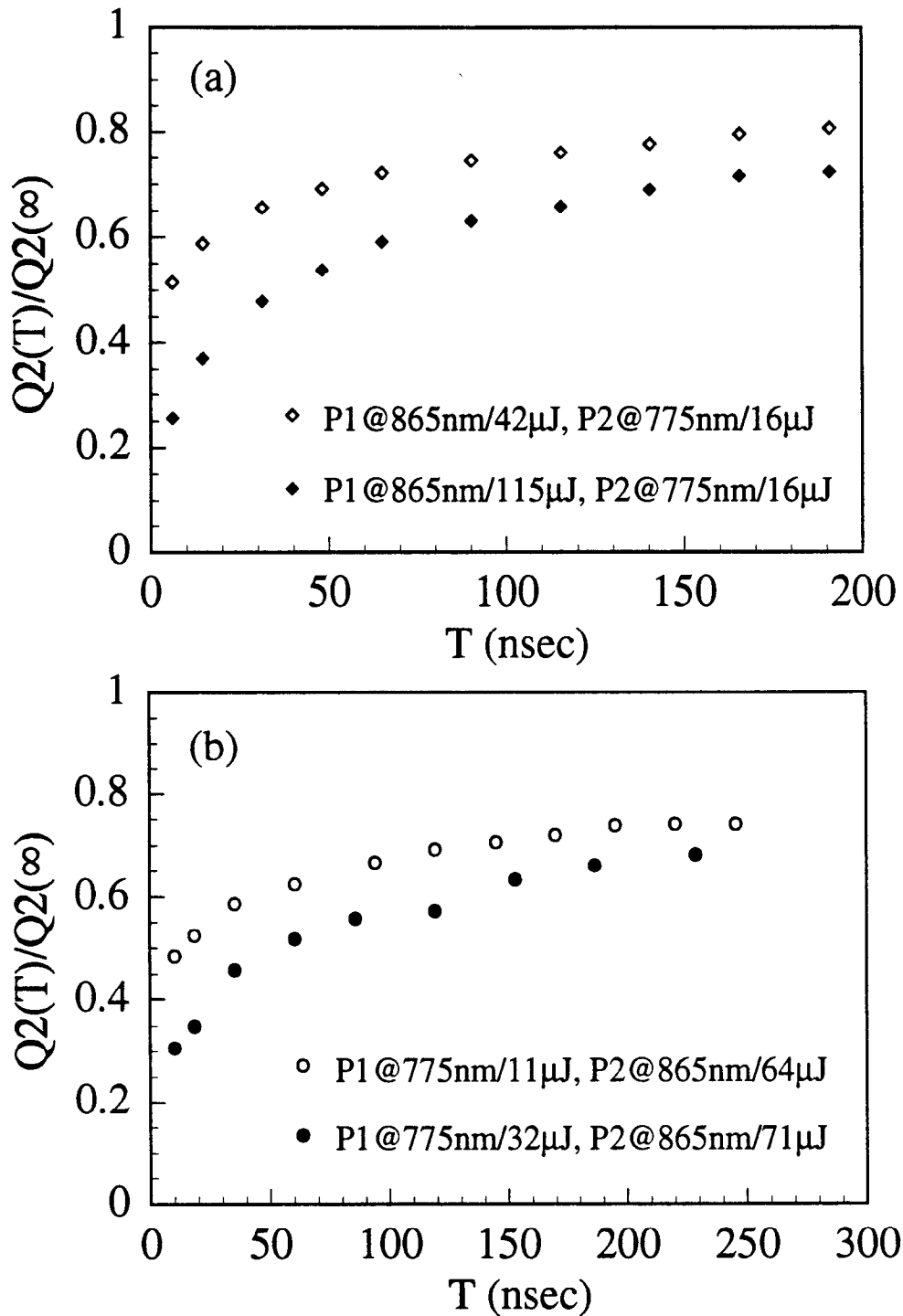
**Fig. 10:** Charge saturation data for cathode 2 excited with 865 nm laser pulses.



**Fig. 11:** Charge saturation data for the second pulse (P2) generated by 865 nm laser pulses with and without the first pulse (P1) generated 56 nsec earlier by 50  $\mu J$  775 nm laser pulses for cathode 1.

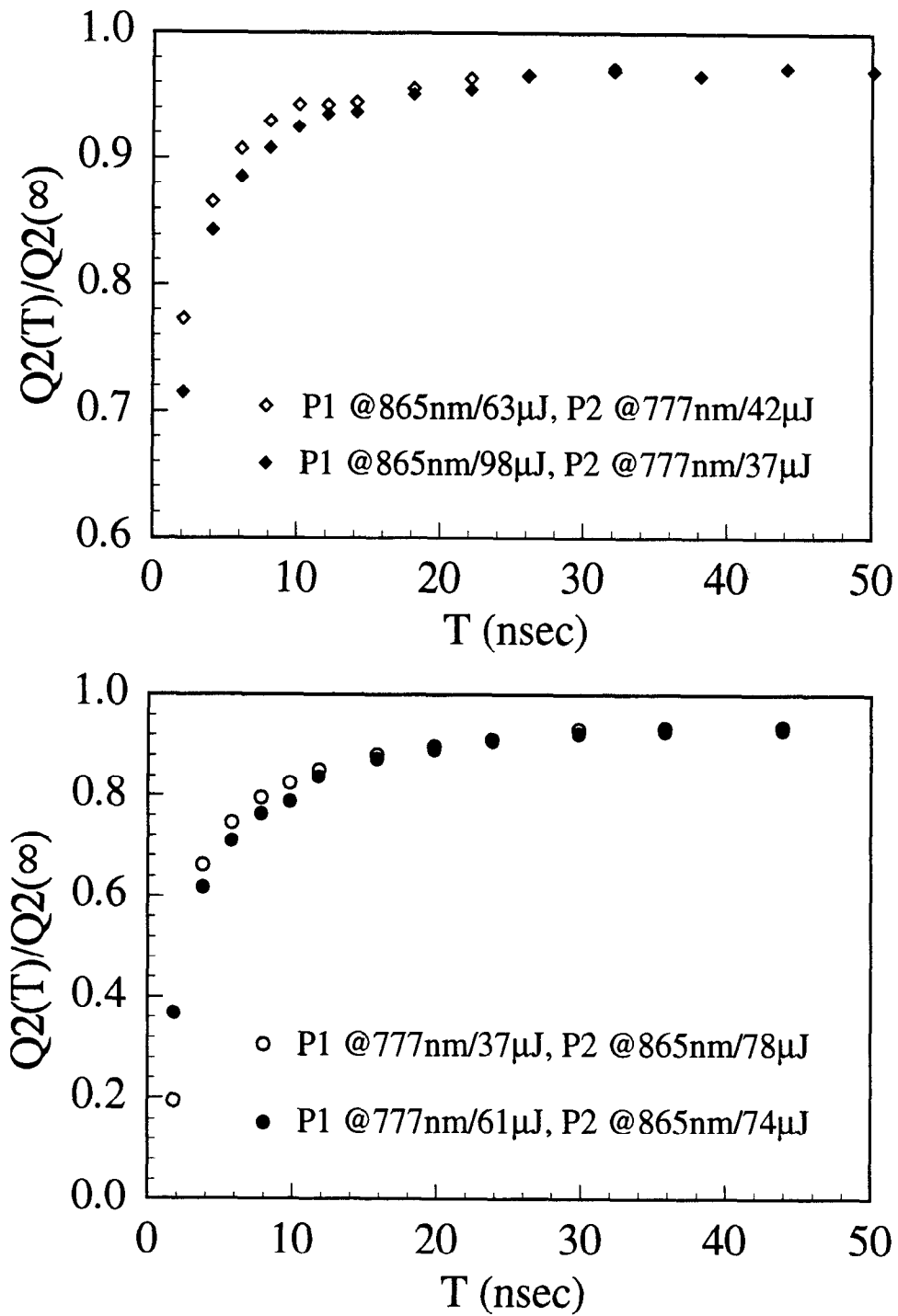


**Fig. 12:** Normalized charge in pulse 2 generated by  $17 \mu\text{J}$   $775 \text{ nm}$  laser as a function of time delay from pulse 1 generated by  $127 \mu\text{J}$   $865 \text{ nm}$  laser (upper panel) and charge pulses for pulse 2 (lower panel) for cathode 1. The QE at  $833 \text{ nm}$  is  $0.34\%$ .

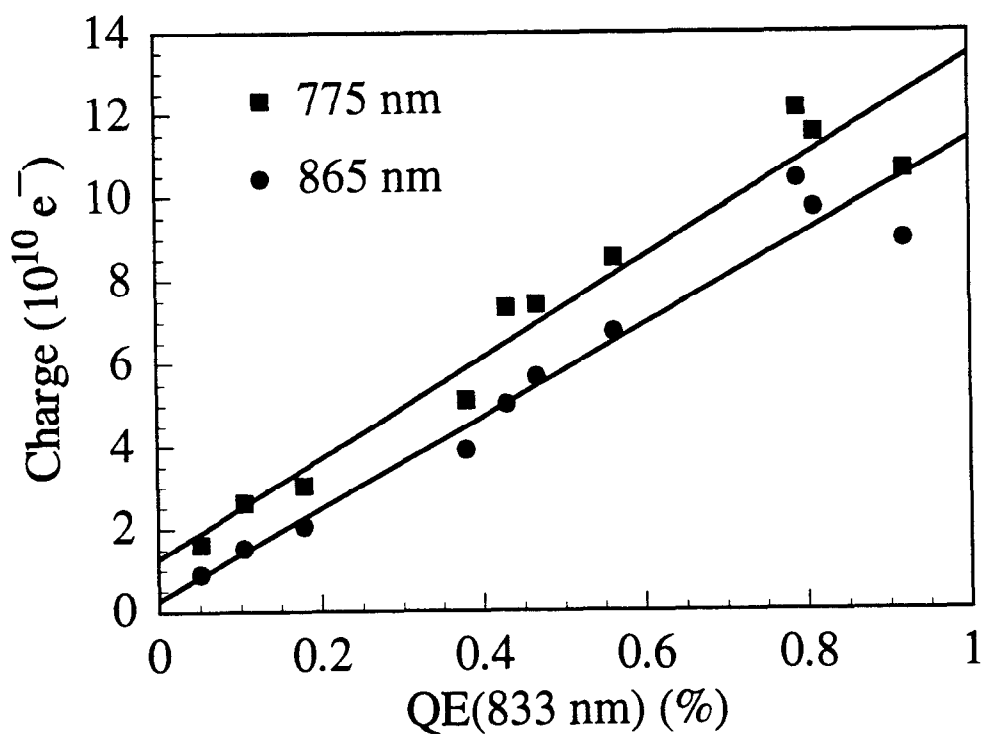
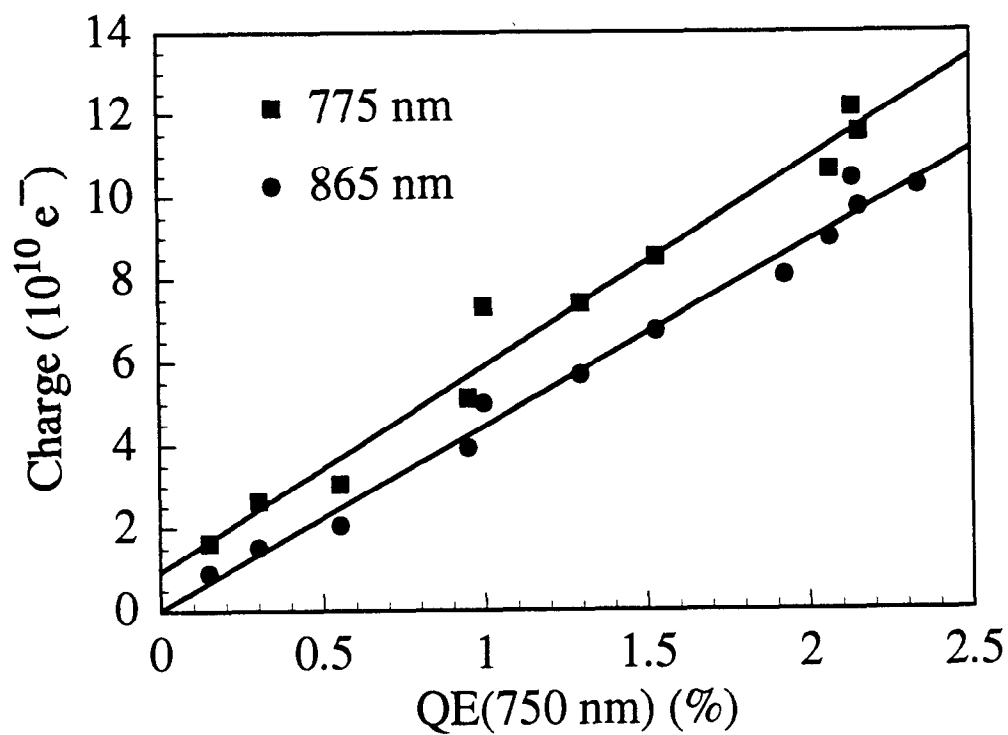


**Fig. 13:** Normalized charge in the second pulse (P2) as a function of time delay from the first pulse (P1) for cathode 1. The QE at 833 nm is 0.79% .

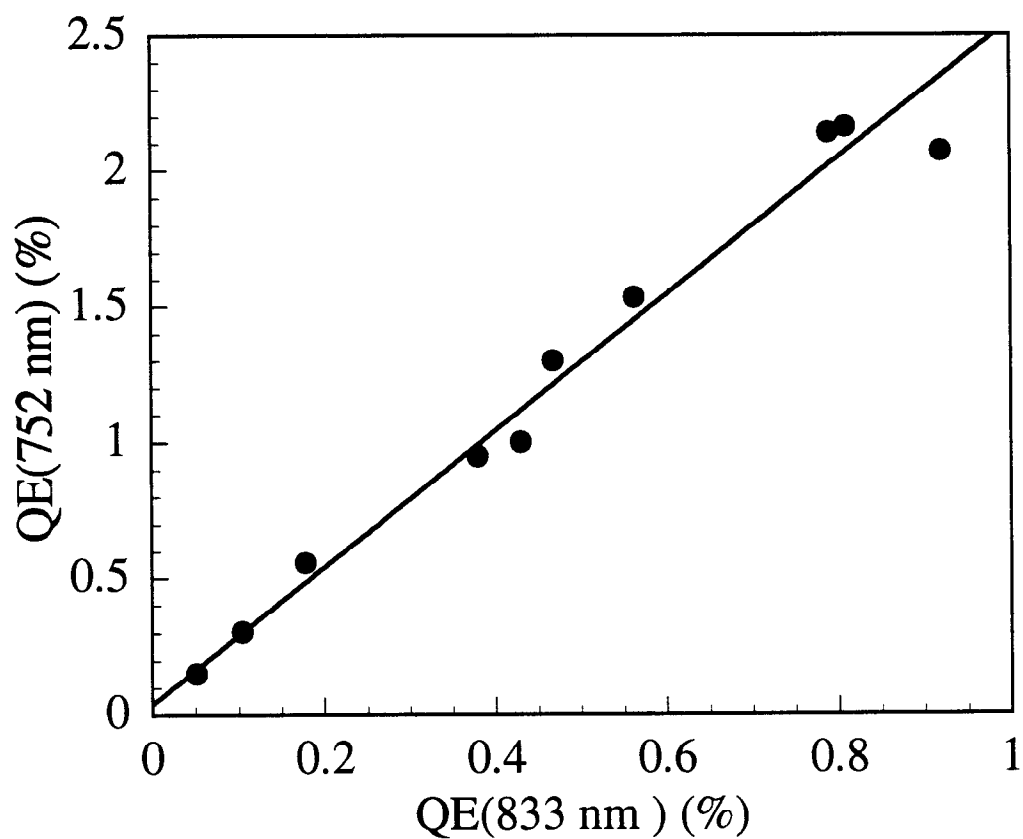




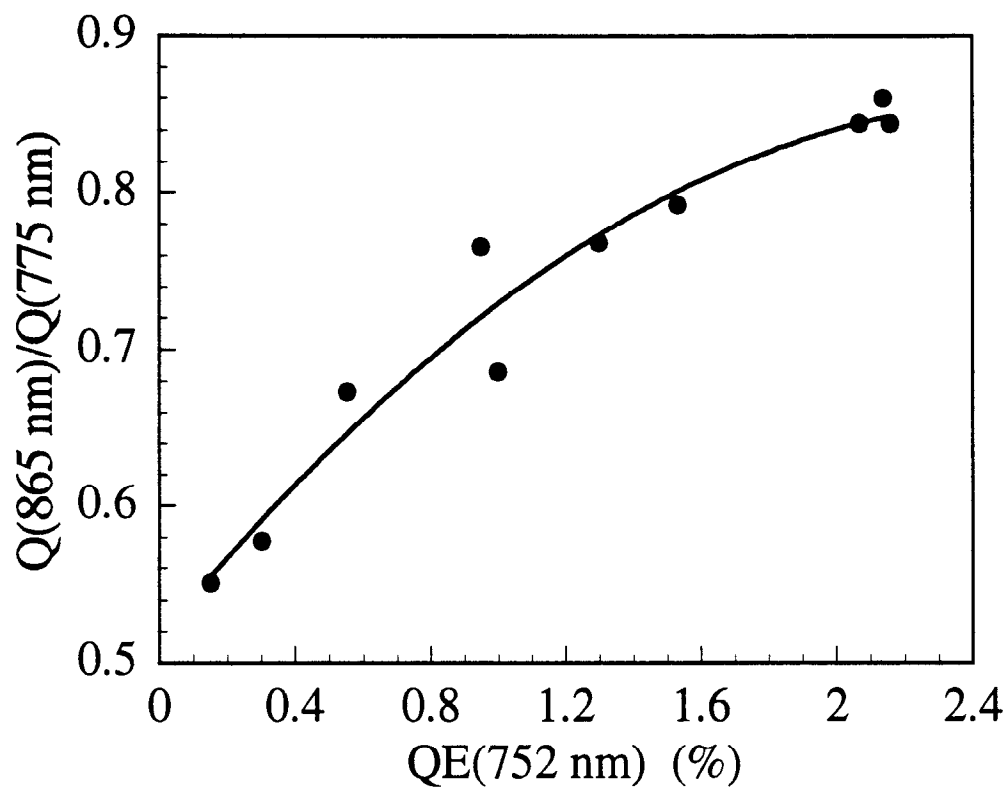
**Figure 14:** Normalized charge in the second pulse (P2) as a function of time delay from the first pulse (P1) for cathode 2. The QE at 833 nm is 0.34%.



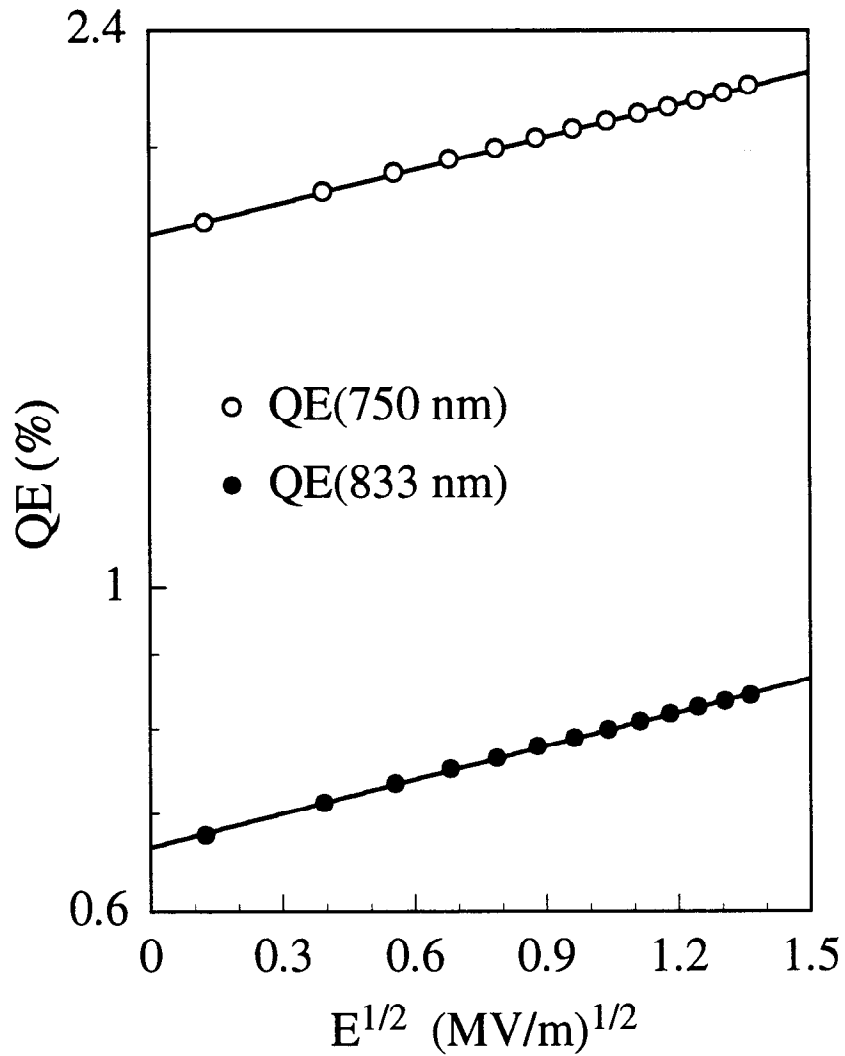
**Fig. 15:** Charge limit for 775 nm and 865 nm laser pulses as a function of QE. The lines are the best fit to the data.



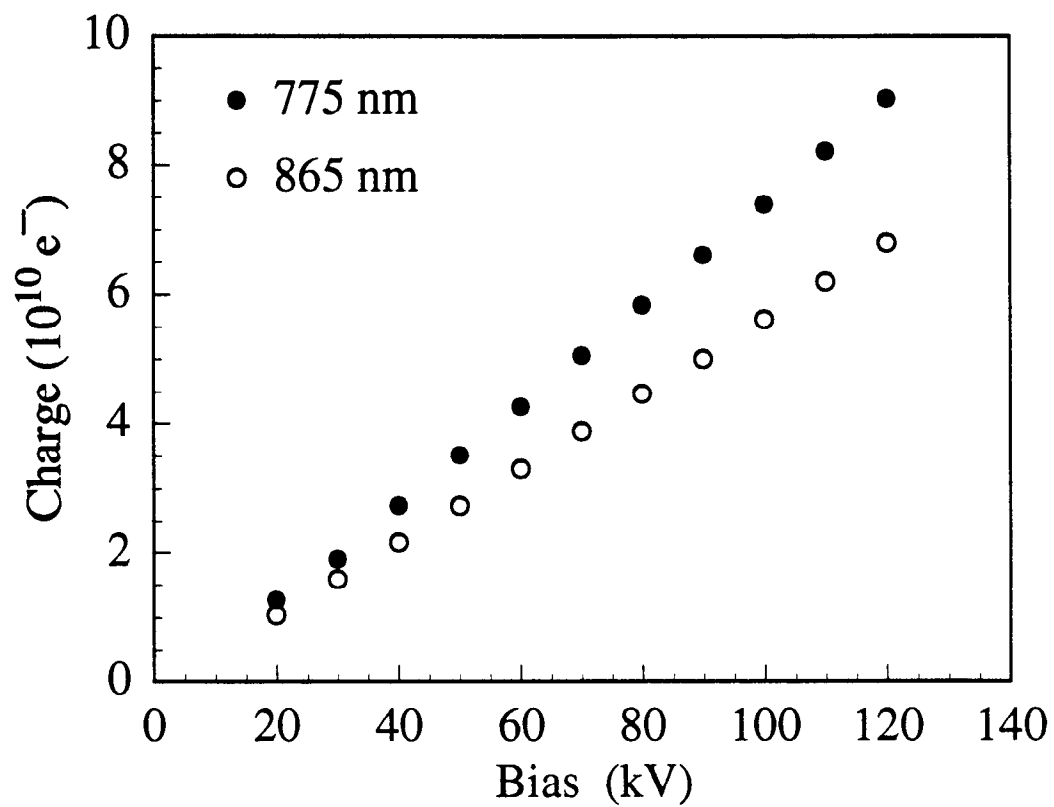
**Fig. 16:** QEs measured at 752 nm and 833 nm scale with each other reasonably well for cathode 1. The line is a best fit to the data.



**Fig. 17:** Ratio of charge limits at 865 nm and 775 nm as a function of QE measured at 752 nm for cathode 1. The solid curve is a guide to the eye.



**Fig. 18:** QEs measured at 752 nm and 833 nm versus the square root of the extraction electric field for cathode 1. The lines are the best fit to the data.



**Fig. 19:** Charge limit at two excitation wavelengths for cathode 2 as a function of cathode bias voltage.

**A.S. Terekhov**  
**Institute of Semiconductors Physics**

**New Material for Photoemission Electron Source:  
Semiconductor Alloy InGaAsP Grown on GaAs Substrate**

Epitaxial  $\text{In}_x\text{Ga}_{1-x}\text{As}_y\text{P}_{1-y}$  layers were shown to be promising for use in polarized electron sources (PES). By variation of  $x$  and  $y$ , both thick (of about one micron) lattice-matched unstrained and thin (of about 0.2 micron) lattice-mismatched strained layers with direct energy gap from 1.78 eV to 1.92 eV were grown on GaAs substrates. The layers were chemically treated in a glove-box, loaded into UHV via a loading chamber without exposure to air, heat cleaned, and activated to the state of negative electron affinity (NEA). The estimated e-folding lifetime of InGaAsP was much higher than that of GaAs at the same conditions. Lifetime limitation factors (residual atmosphere and electron stimulated desorption) are discussed. Strain-induced splitting of the valence band up to 32 meV was observed in the lattice-mismatched films; this observation gives prospects for the increase of electron spin polarization beyond the 50% limit. The possibility of using spontaneous ordering of InGaP alloys grown on GaAs substrates for the increase of spin polarization is discussed.

**New Material for Photoemission  
Electron Source:  
Semiconductor Alloy InGaAsP  
Grown on GaAs Substrate**

**Alexander S. Terekhov**

**co-workers: V.L. Alperovich  
Yu.B. Bolkhovityanov  
A.G. Paulish  
A.S. Jaroshevich**

***Institute of Semiconductor Physics  
pr. Lavrent'eva 13, Novosibirsk 630090, Russia***

**Outline:**

**InGaAsP/GaAs Photocathode:  
Advantages and Disadvantages**

**NEA Surface Preparation Technique  
and Setup**

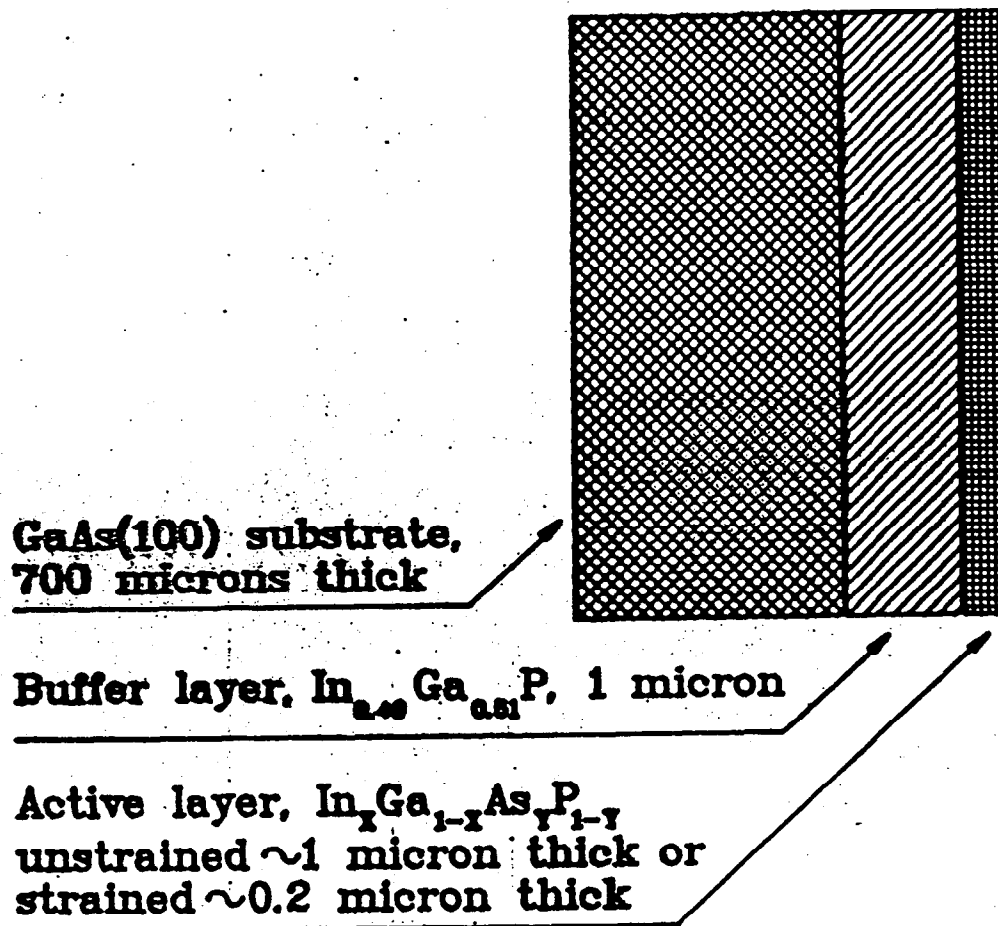
**Lifetime**

**Non-linear Effect**

**Measurements of Straines**



## Strained InGaAsP Photocathode on GaAs Substrate



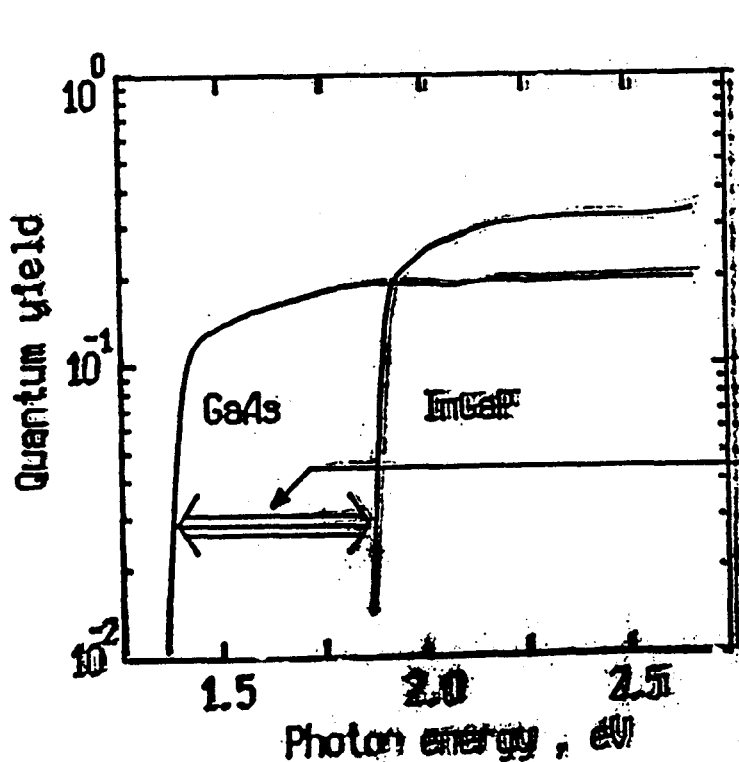
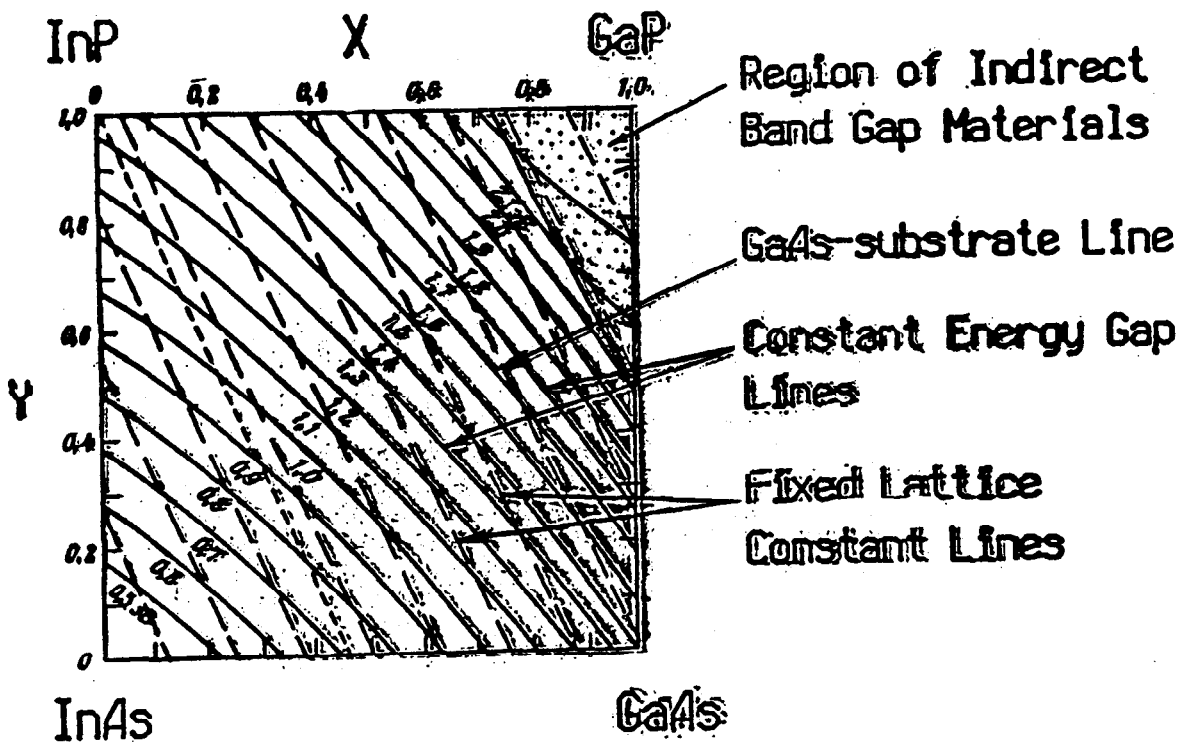
### Advantages:

1. Tunable band gap.
2. Low dislocation substrate promise higher thickness of strained active layer.
3. Wider band gap -
  - higher NEA and stability,
  - higher QE,
  - higher maximum current.

### Disadvantage:

High NEA-value may lead to polarization loss due to scattering inside BBR.

# Choosing of the Optimal Composition of $\text{In}_{1-x}\text{Ga}_x\text{As}_{1-y}\text{P}_y$ Layer for GaAs Substrate

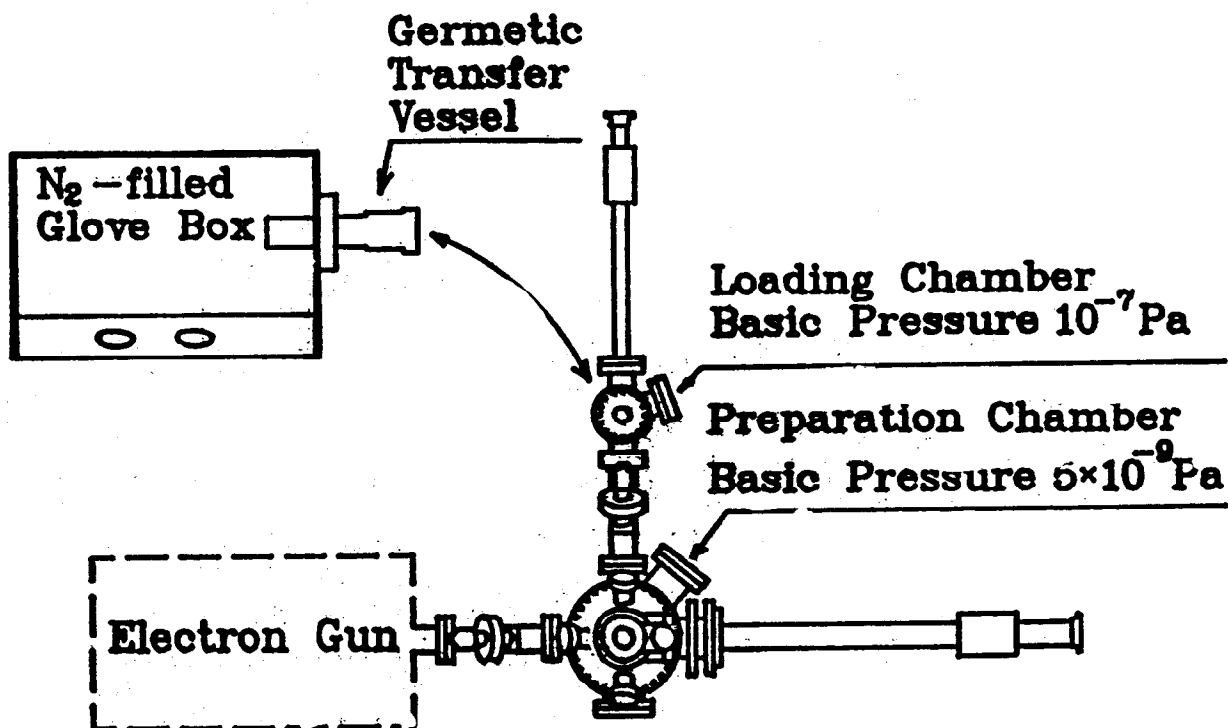


Photoemission spectra of GaAs and InGaP. The spectral thresholds correspond to band gap values  $E_g = 1.43$  eV and 1.92 eV for GaAs and InGaP respectively.

Possible variations of band gap of  $\text{In}_{1-x}\text{Ga}_x\text{As}_{1-y}\text{P}_y$  layers on GaAs substrates without misfit dislocations.

# Photocathode Surface Preparation

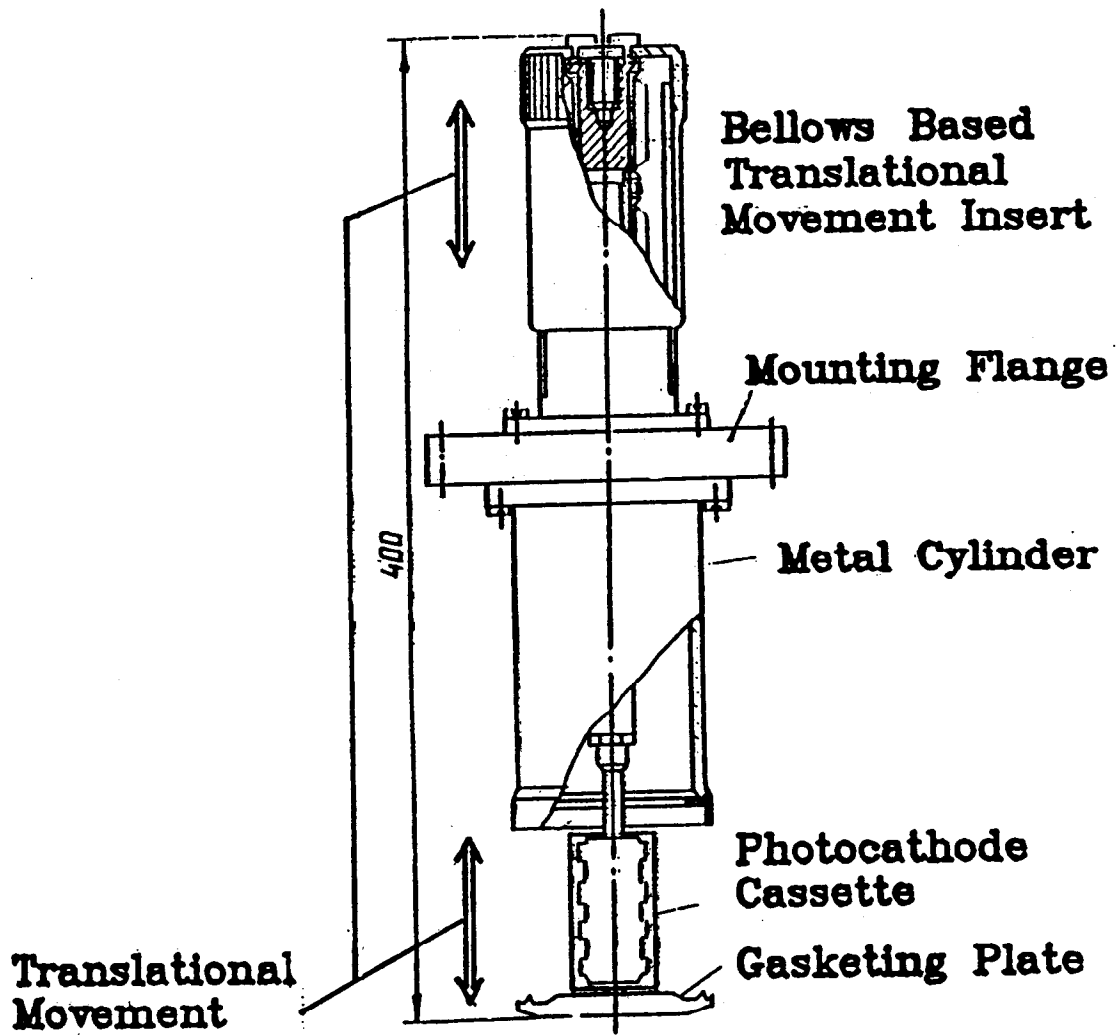
## UHV Setup



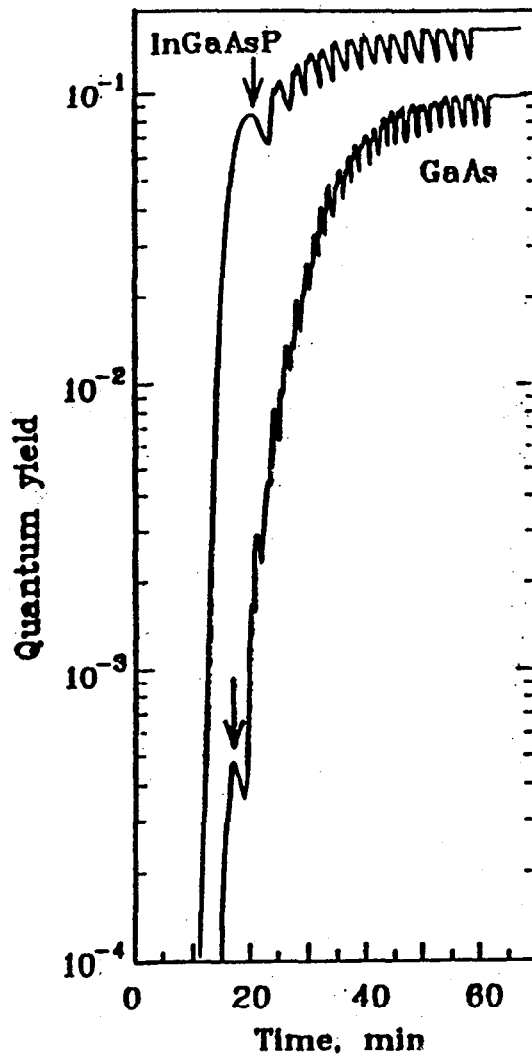
## Surface Preparation Technique:

1. Oxide removal by HCl-treatment in glove-box.
2. Photocathode transfer to loading chamber without oxidation and pollution in residual atmosphere.
3. Thermal precleaning in the loading chamber.
4. Final thermal cleaning in the preparation chamber (computer controlled).
5. Activation by Cs and O<sub>2</sub> (computer controlled "yo-yo" procedure).

# Germetic Transfer Vessel



## Activation Curves

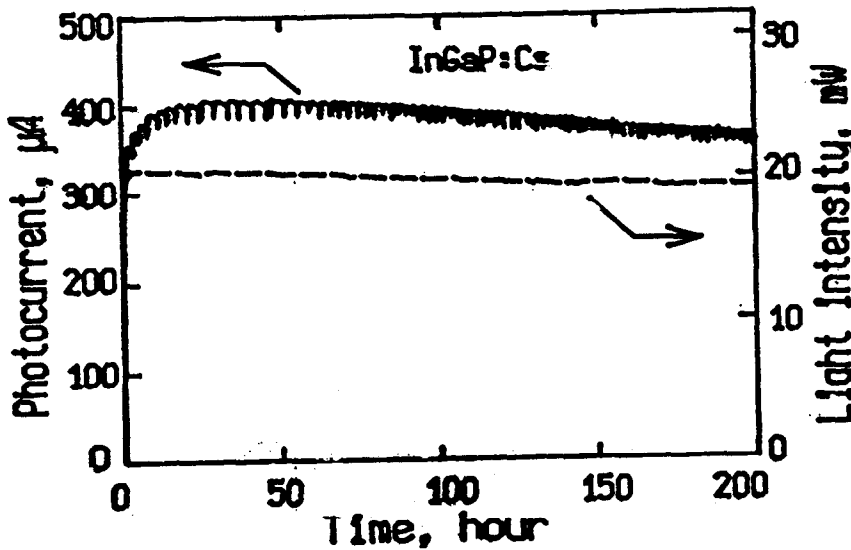


The activation "yo-yo" curves for (100) GaAs and (111)A  $\text{In}_{0.48}\text{Ga}_{0.54}\text{As}_{0.08}\text{P}_{0.94}$ . The quantum yield peaks corresponding to the first cesiation of the clean surfaces are marked by arrows. Note that the first Cs peak InGaAsP is two orders of magnitude higher than the peak for GaAs.

Typical quantum yields at  $\lambda=832.8$  nm:

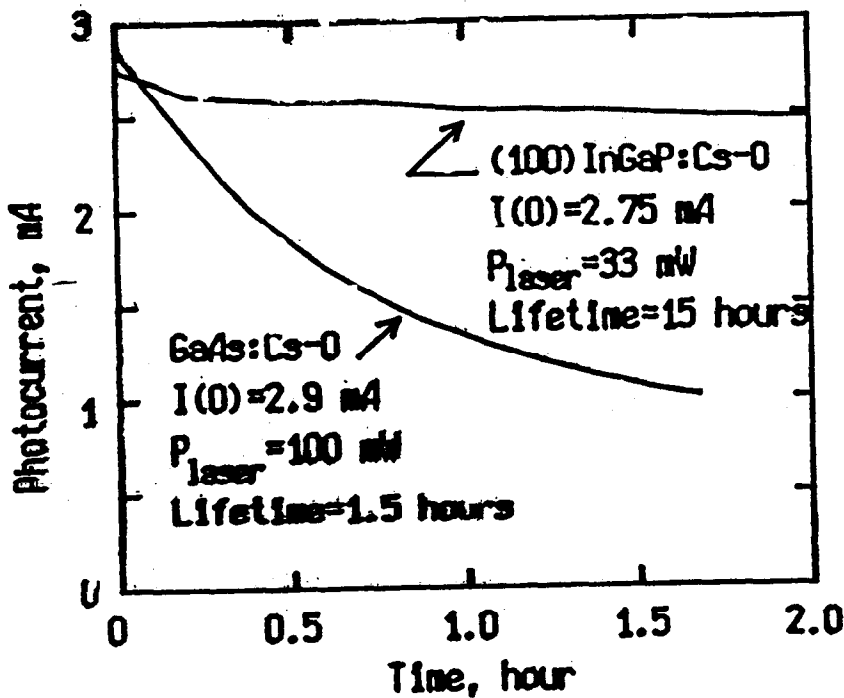
(100)GaAs	10-15%	(first activation)
(100)GaAs	20-25%	(second activation)
(111)InGaAsP	10-15%	
(100)InGaAsP	20-25%	

# Lifetime Test



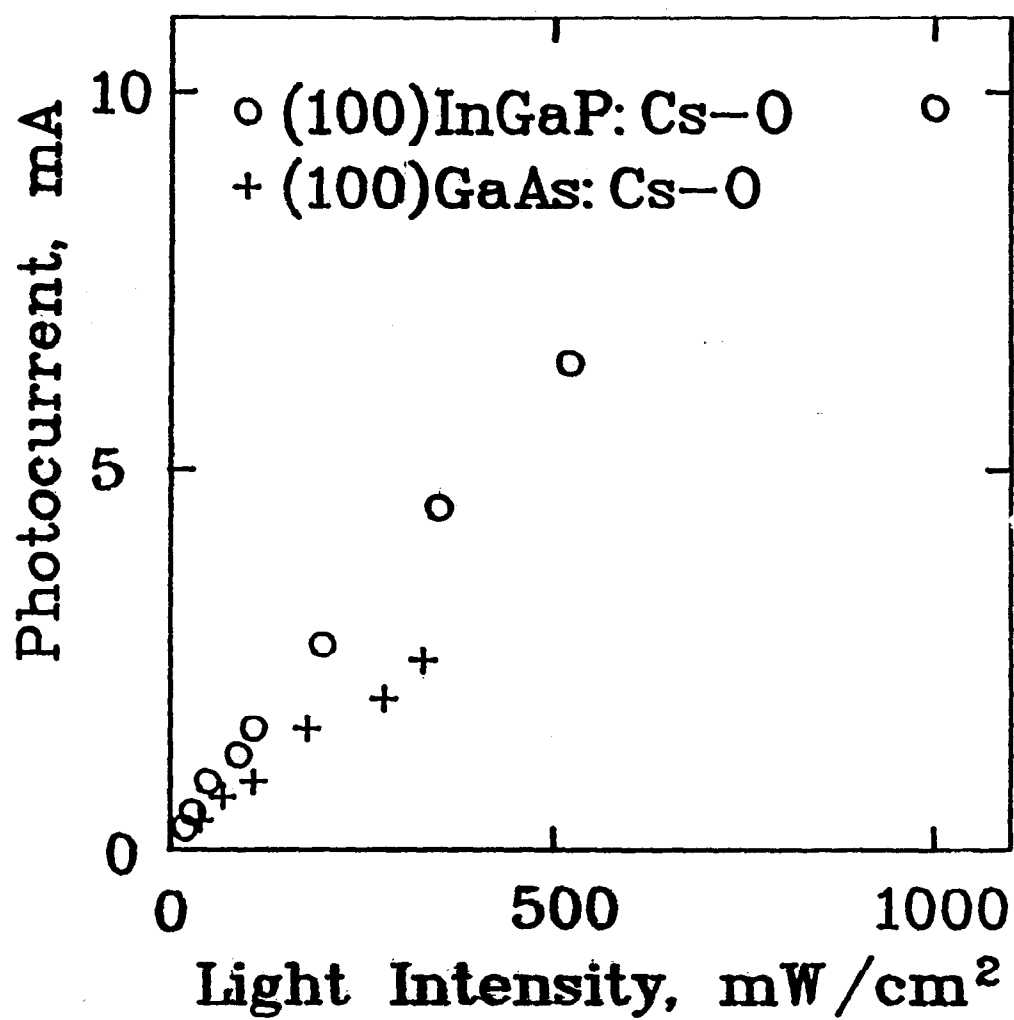
Time-dependence of the photocurrent for InGaP at multiple renewal of photocathode sensitivity by periodical depositions of Cs.

The sharp vertical segments of the plot correspond to switching on the cesium source for about two minutes. Estimated e-folding lifetime >1500 hours.

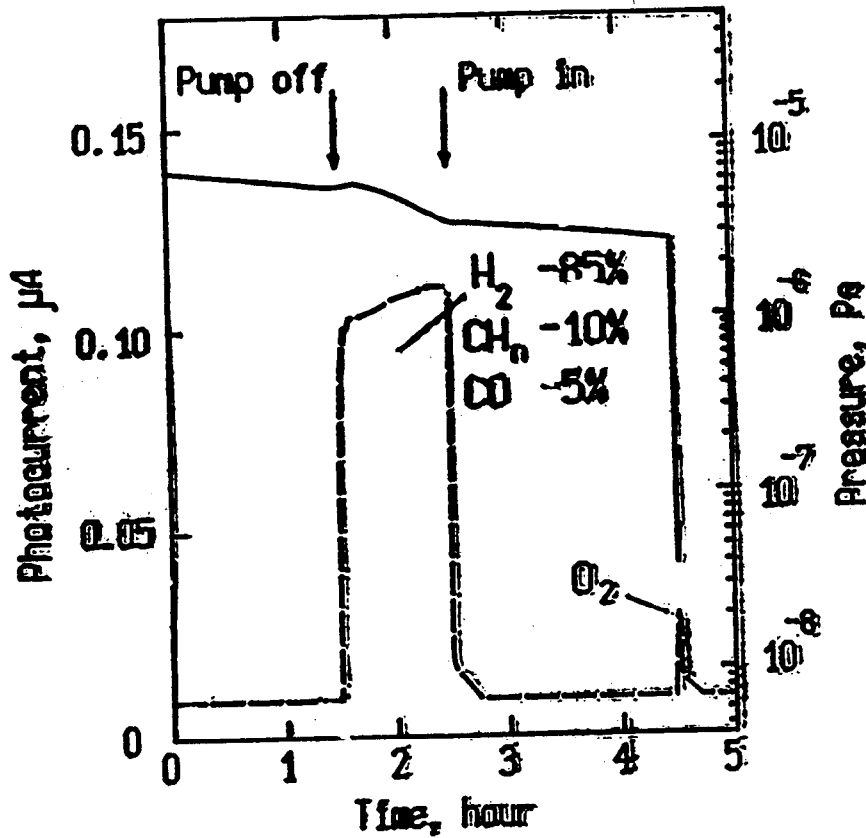


Time-dependences of photocurrent for GaAs and InGaP under argon laser illumination.

## DC-photocurrent Test



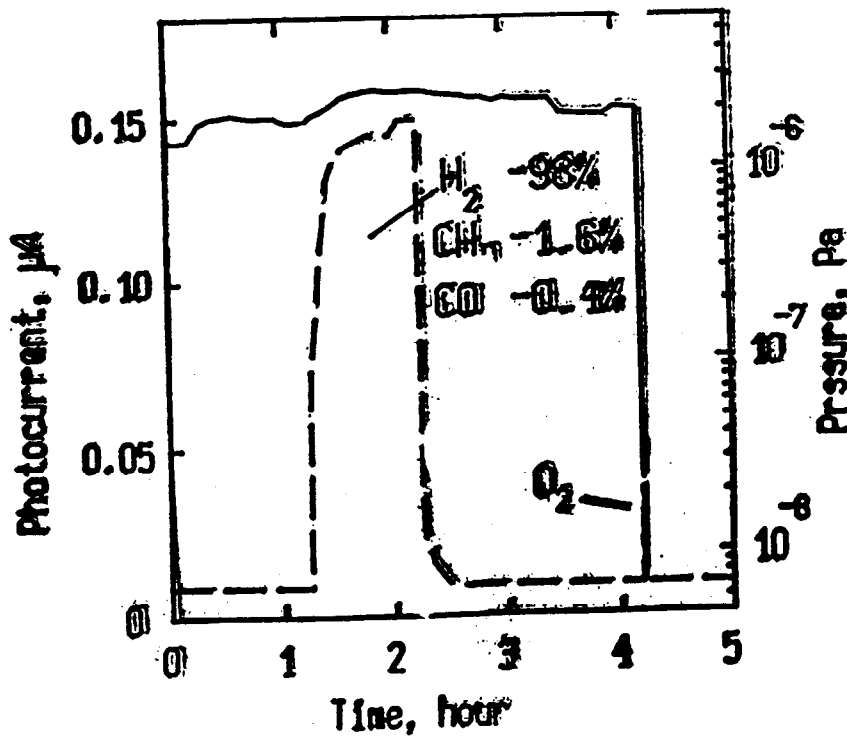
# Influence of Residual Atmosphere on Dark Lifetime



$\text{H}_2$  - is not dangerous.

$\text{CH}_4$  and  $\text{CO}_2$  -  
estimated fatal  
exposure - 1.5 L

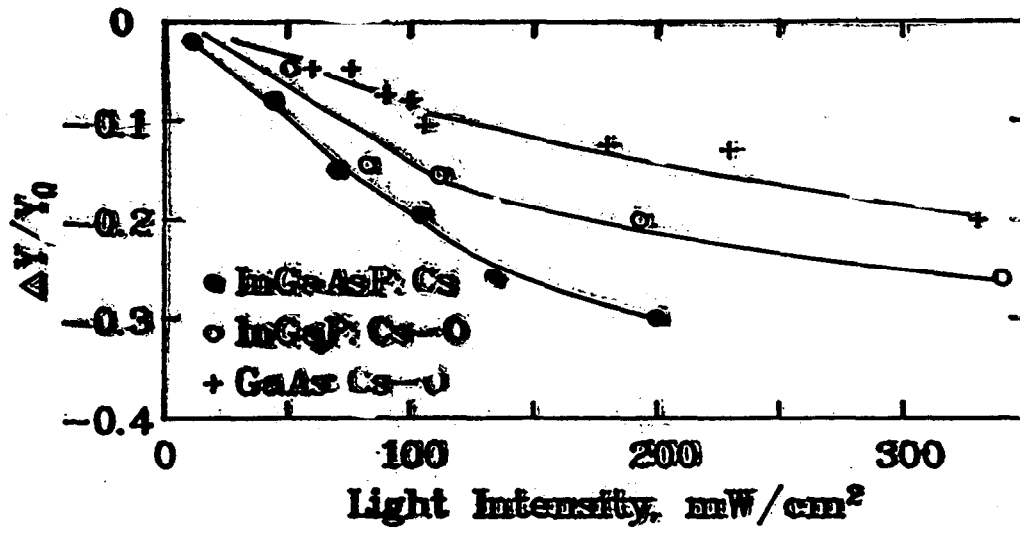
$\text{O}_2$  - fatal  
exposure - 0.01 L



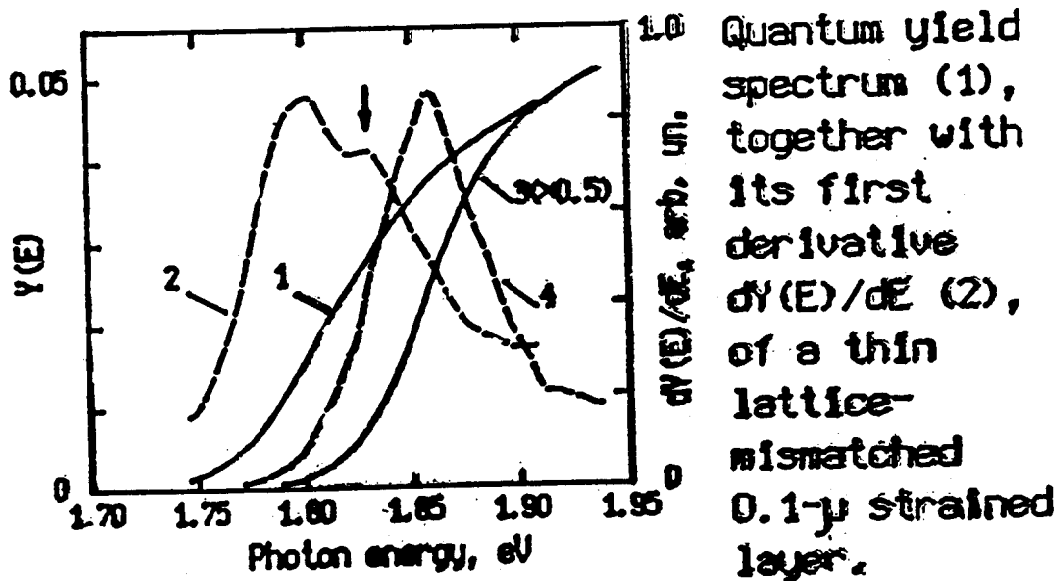
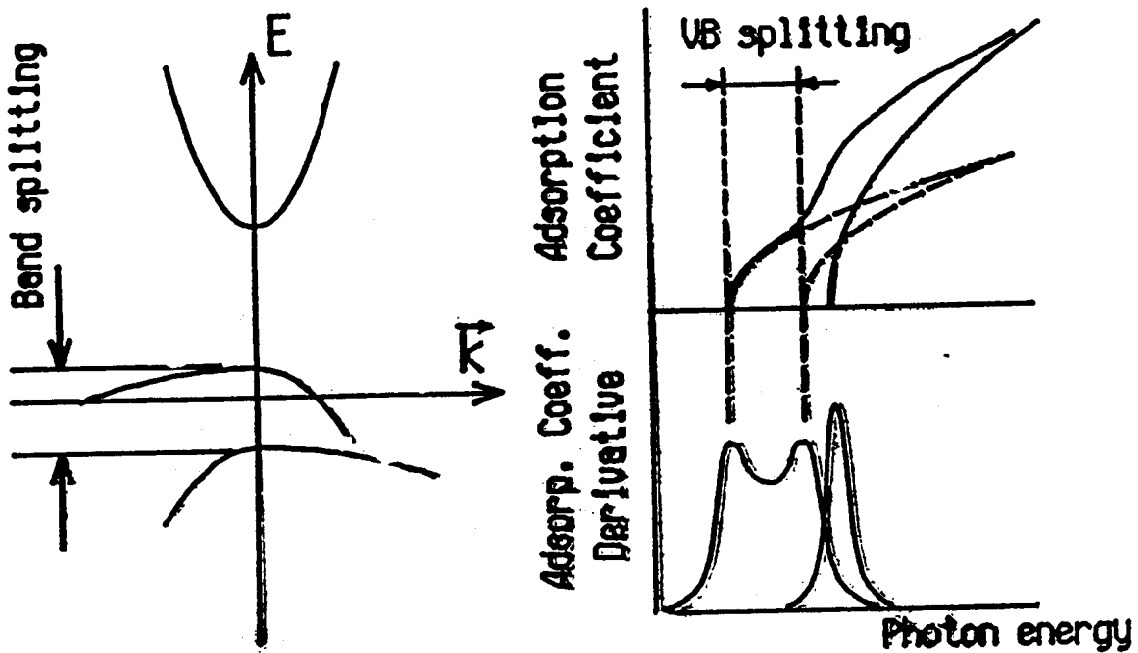
The sample holder  
and collector are  
more extensively  
cleaned. This  
cleaning reduces  
 $\text{CH}_4$ ,  $\text{CO}$  components.



# Non-linear Effect in Photoemission

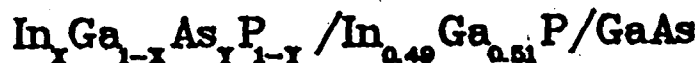


# Measurements of Elastic Strains from Quantum Yield Derivative Spectrum



The spectra  $Y(E)$  (3) and  $dY(E)/dE$  (4) of a thick 1- $\mu$  unstrained layer are shown for comparison. Strain-induced 30-meV splitting is clearly seen in the derivative of the thin layer.

**Final Remarks about**



1. Dislocation-free substrate promises more thick strained active layer.
2. Choosing the appropriate values of  $x$  and  $y$  it is possible to tune the band gap to the wavelength of untunable lasers.
3. NEA photocathodes  $\text{InGaAsP}$  with  $E_g = 1.8-1.9$  eV are much more stable in comparison with GaAs and may be recommended for RF-guns.
4. High NEA-value (0.8 eV for  $\text{In}_{0.49}\text{Ga}_{0.51}\text{P}$ ) promises higher ~~maximum~~ photocurrent.
5. Self-layering effect in  $\text{In}_{0.5}\text{Ga}_{0.5}\text{P}$  material may lead to valence-band splitting without elastic strain.
6. High NEA-value (0.8 eV for  $\text{In}_{0.49}\text{Ga}_{0.51}\text{P}$ ) may lead to polarization loss due to scattering inside BBR.

**A.S. Terekhov**  
**Institute of Semiconductors Physics**

**NEA-photocathode Surface Preparation: Technology and  
Physics**

# NEA-photocathode Surface Preparation: Technology and Physics

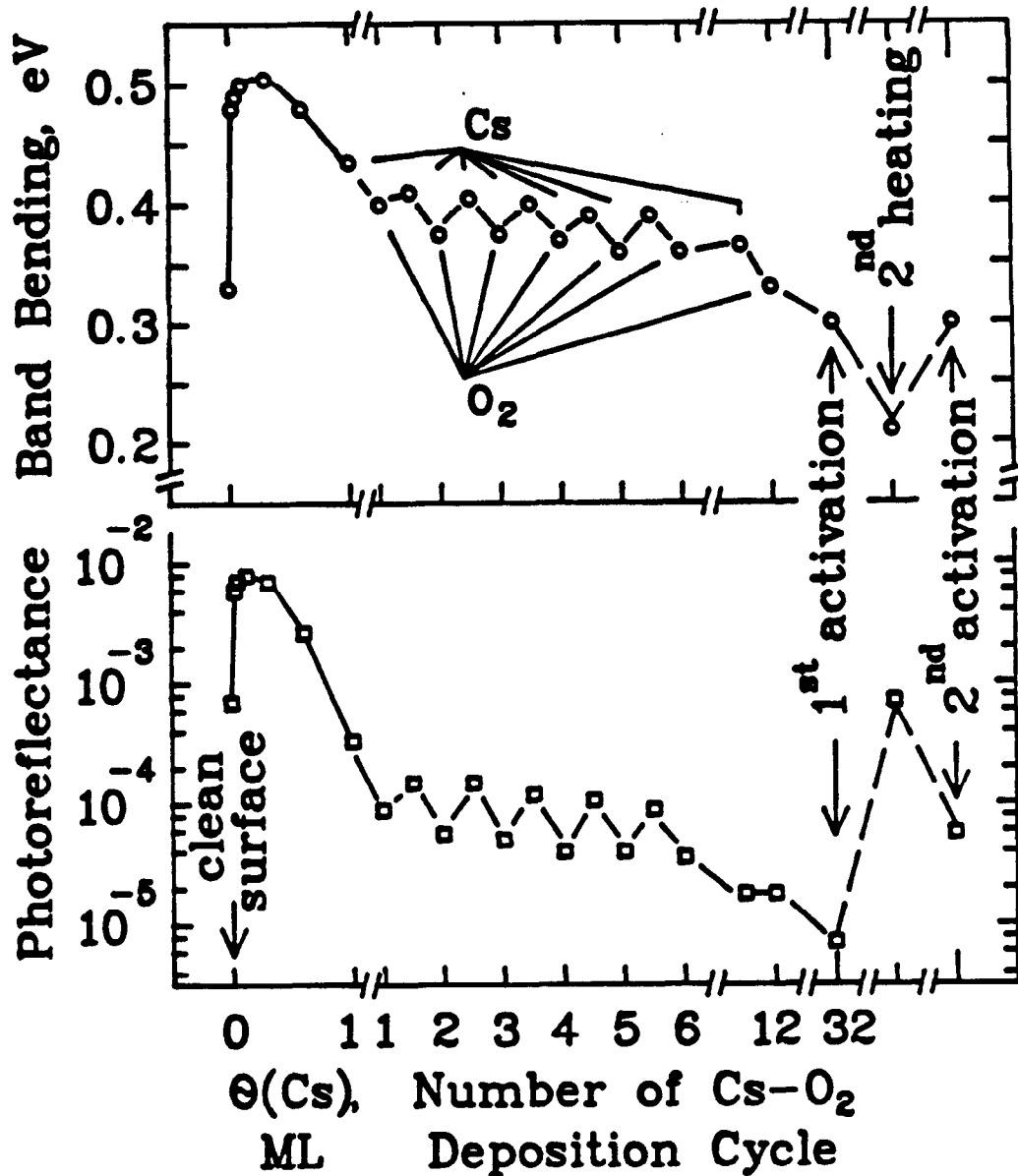
Alexander S. Terekhov

co-workers: V.L. Alperovich  
V.N. Kuzaev  
A.G. Paulish  
S.V. Shevelov  
G.E. Scheibler

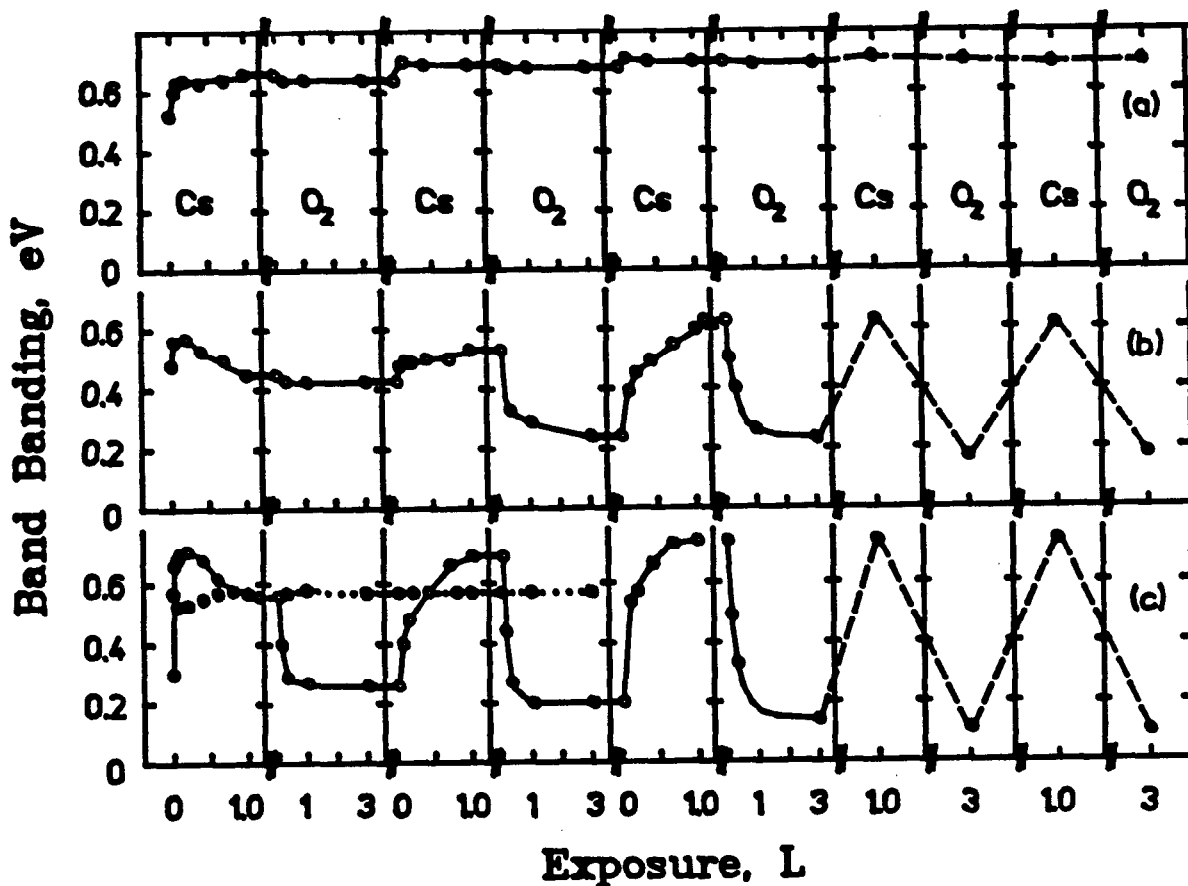
*Institute of Semiconductor Physics*  
*630090 Novosibirsk, Russia*  
*pr. Lavrent'eva 13, Novosibirsk 630090, Russia*

## Outline:

1. Photorefectance and photoluminescence are useful methods to check electroproperties of surface during cleaning activation and degradation.
2. Fermi-level is not pinned on p-GaAs surface during Cs, O<sub>2</sub> adsorption.
3. Surface recombination and trapping are varied along "yo-yo" activation curve together with electron affinity and band bending.
4. Activation procedure varies in order to satisfy specific requirements to photocathode.



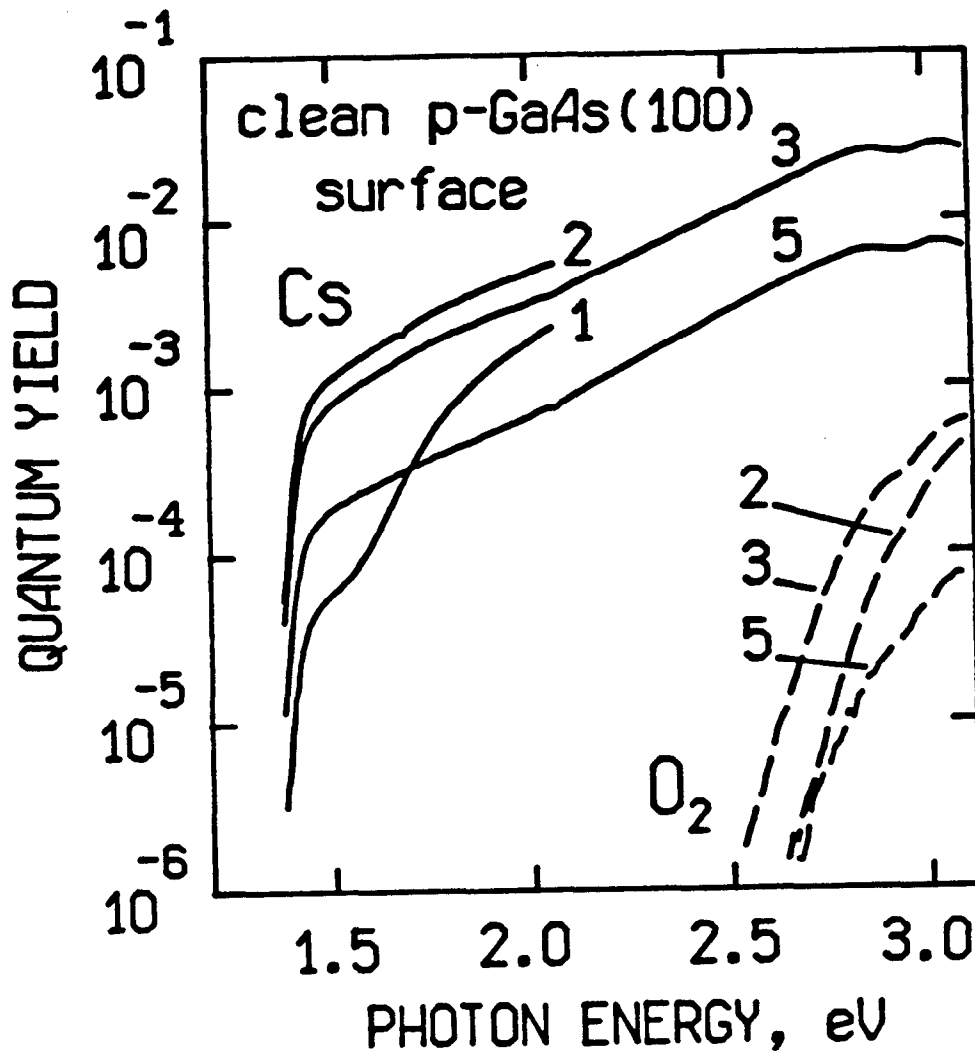
Evolution of band bending and photorefectance amplitude along the "yo-yo" activation curve. The deposition of the first monolayer of Cs shown in detail. The other points corresponds to photoemission peaks along the "yo-yo" activation curve.



The evolution of the band bending under successive deposition of Cs and  $O_2$  are shown for the differently prepared surfaces:

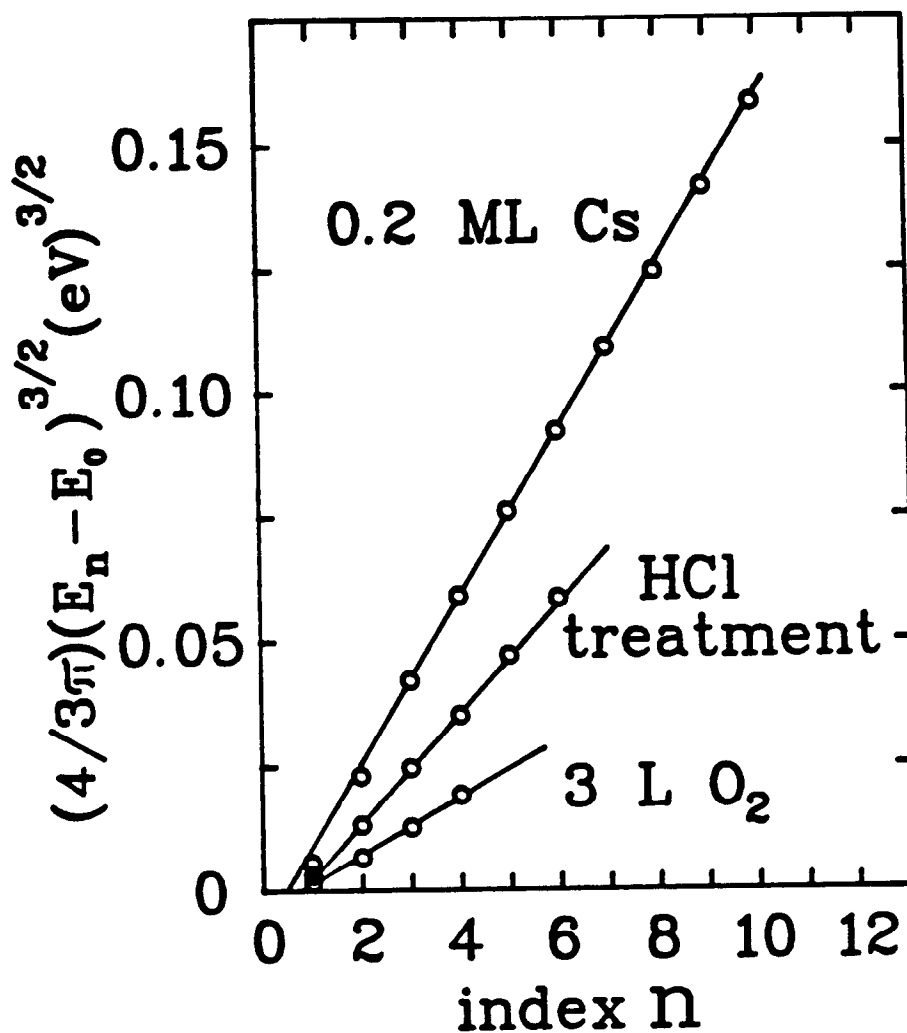
- (a) untreated surface with a native oxide;
- (b) treated in HCl without annealing;
- (c) atomically clean surface after HCl treatment and annealing in UHV at 650 K.

Open and closed circles corresponds to  $SIP^+$  and  $SIN^+$  structures, respectively.

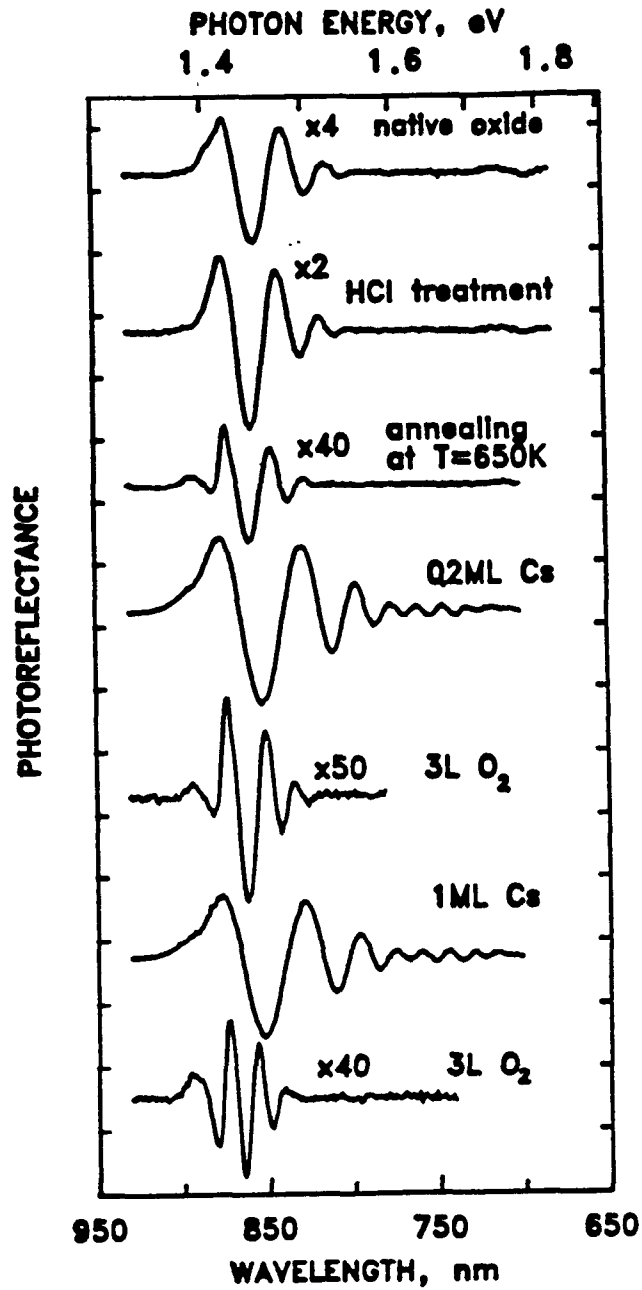


Quantum yield spectra of MBE-grown SIP<sup>+</sup>-structure (i-GaAs/p-GaAs(100)) under successive deposition of cesium (solid line) and oxygen (dashed line) on clean surface. The surface was treated in HCl and annealed at 400°C. The number of the curve corresponds to the number of Cs-O<sub>2</sub> cycle. Spectrum for the first oxygen deposition (not shown) lies in the ultraviolet range with photoemission threshold >3.5 eV.

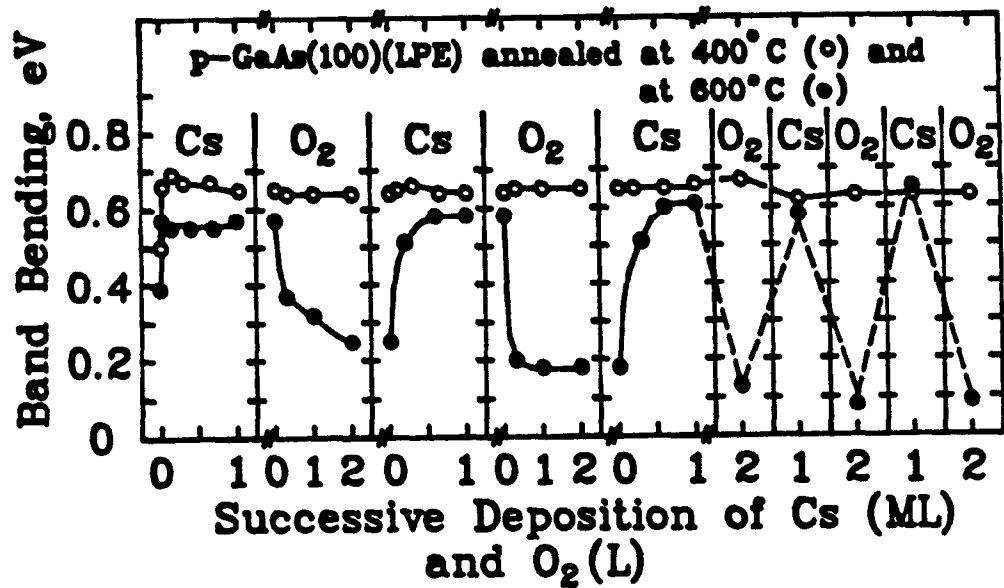




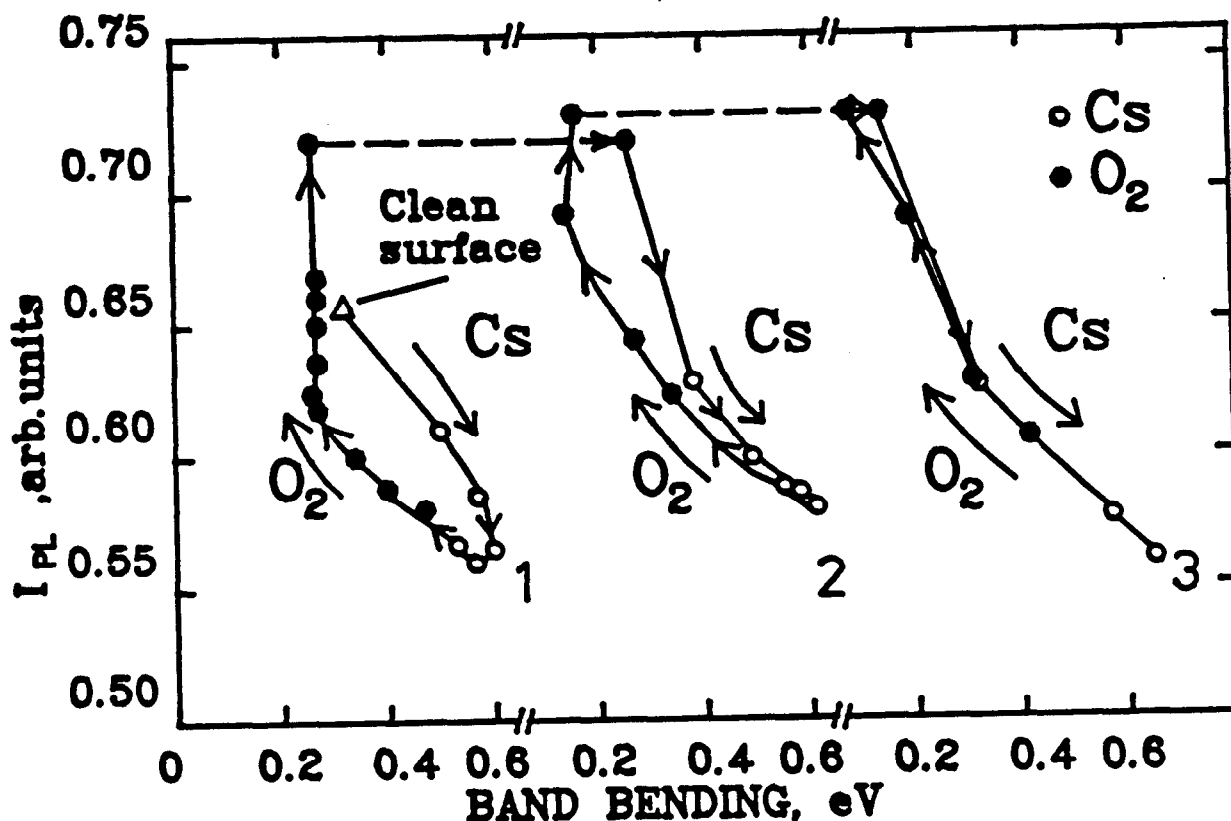
Dependence of  $(4/3\pi)(E_n - E_0)^{3/2}$  on index  $n$ , where  $E_n$  is position of the extrema of Franz-Keldysh oscillations,  $E_0$  is the bandgap. Theoretical straight lines are the best fit of the experimental dependencies shown by circles. The slope of the lines gives the values of surface electric field.



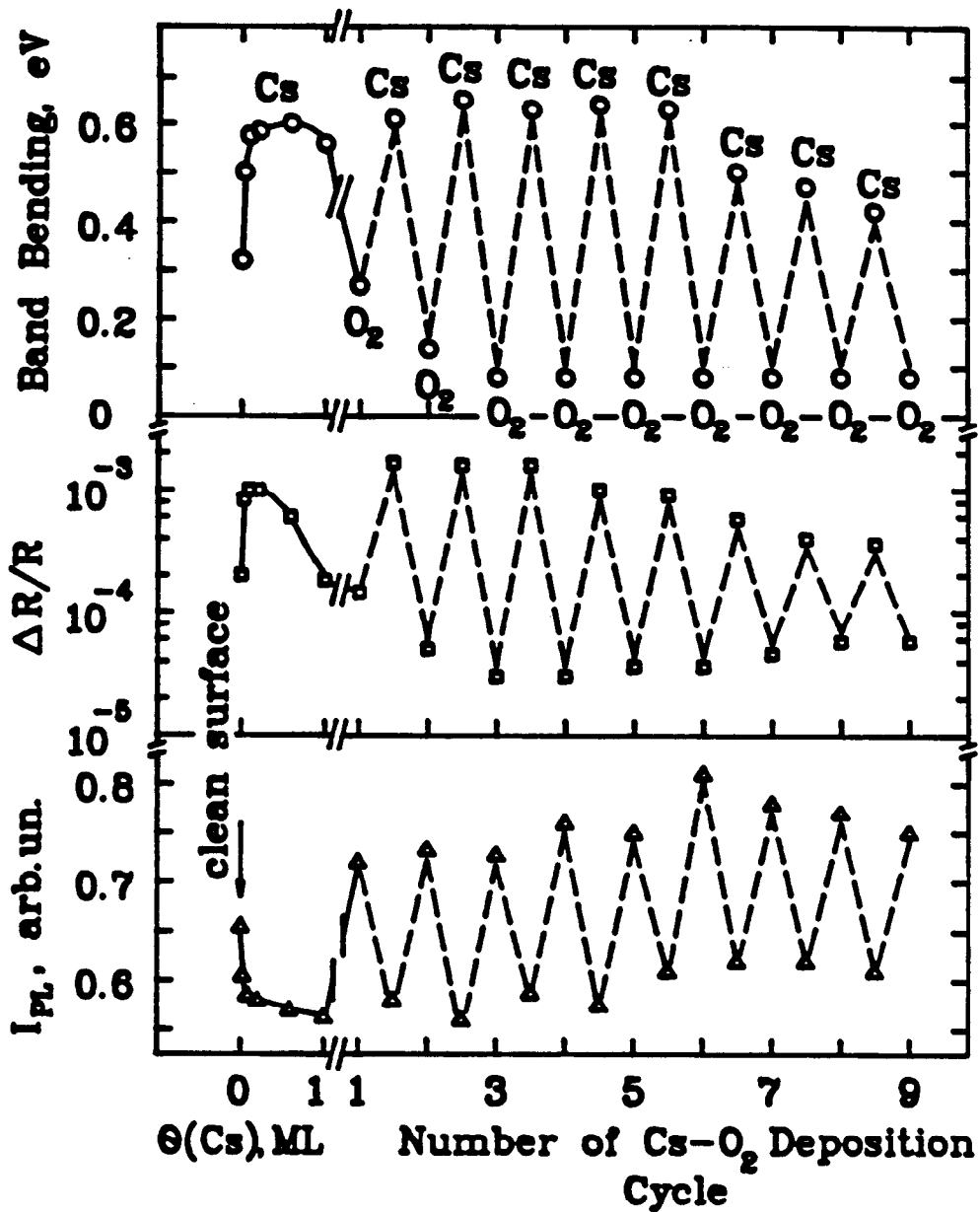
Photoreflectance spectra of  $\text{SIP}^+$  structure. A reversible switching of the amplitude, period and shape the FKO oscillations at successive depositions of Cs and  $\text{O}_2$  are clearly seen.



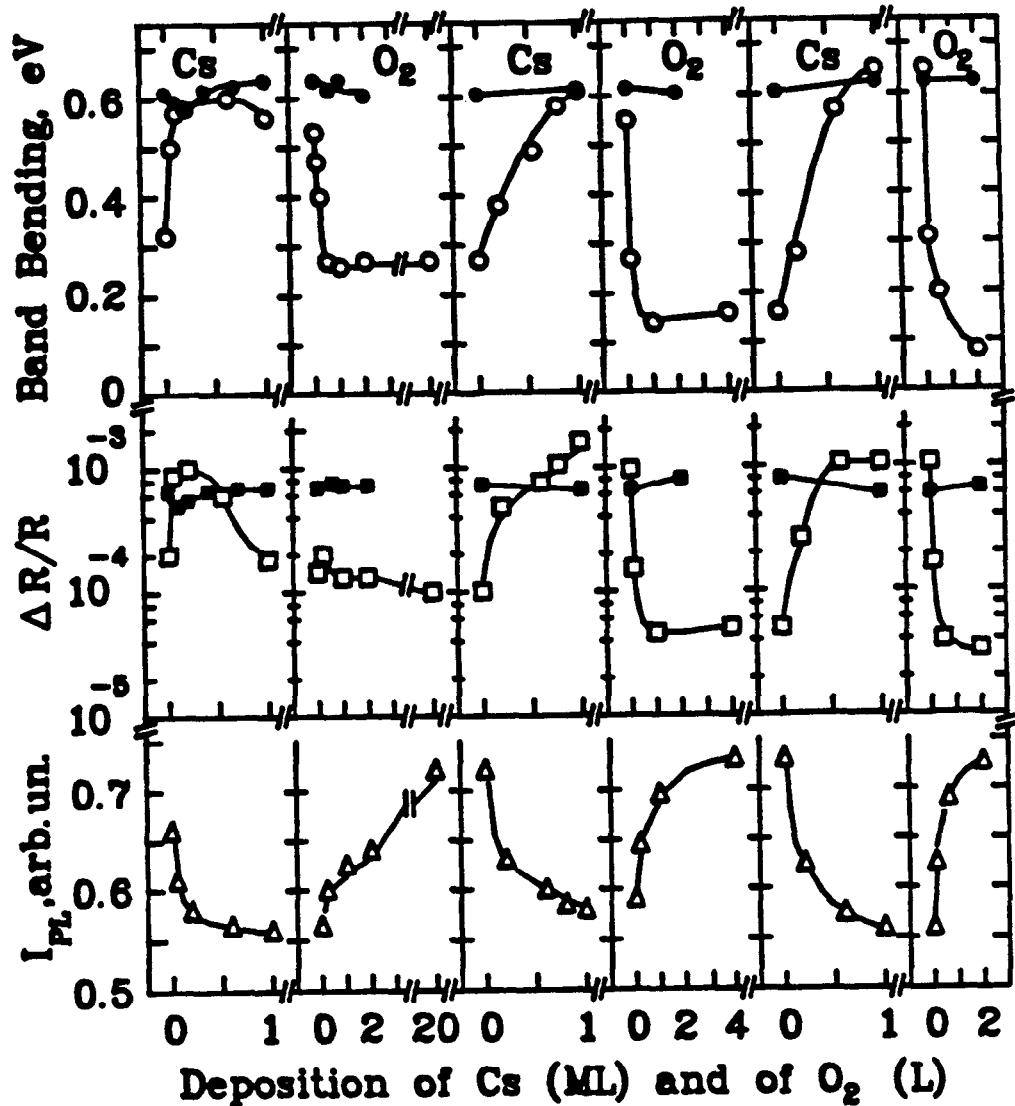
Evolution of band bending at the p-GaAs(100) surface under successive deposition of cesium and oxygen. The surface was treated in 20:1:1 H<sub>2</sub>SO<sub>4</sub>:H<sub>2</sub>O<sub>2</sub>:H<sub>2</sub>O and annealed at 400°C (opened circles) and at 600°C (closed circles).



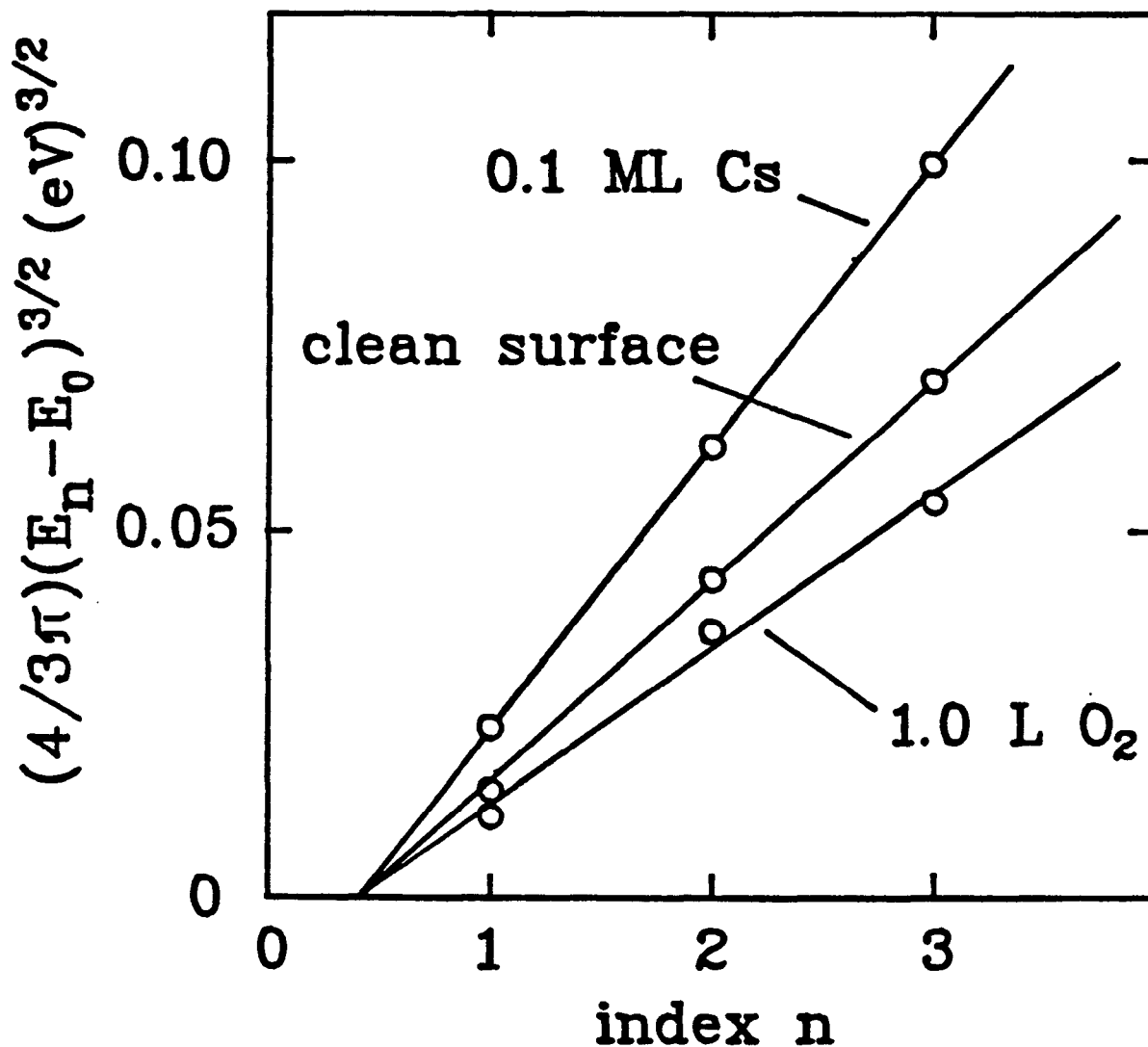
The plot of PL intensity versus band bending  $\phi_s$  for the first three cycles of Cs and  $O_2$  deposition. The atomically clean surface is shown by a triangle. Empty and closed circles correspond to the deposition of Cs and  $O_2$ , respectively. The evolution of  $I_{PL}$  and  $\phi_s$  under successive deposition of Cs and  $O_2$  are shown by arrows. The horizontal dashed arrows show the transition from previous to the next cycle, the last point of the previous cycle being the same as the first point of the next cycle. The highest  $O_2$  exposures used in the present experiment are equal to 20 L, 4 L, 2 L for the first, second and third cycles, respectively.



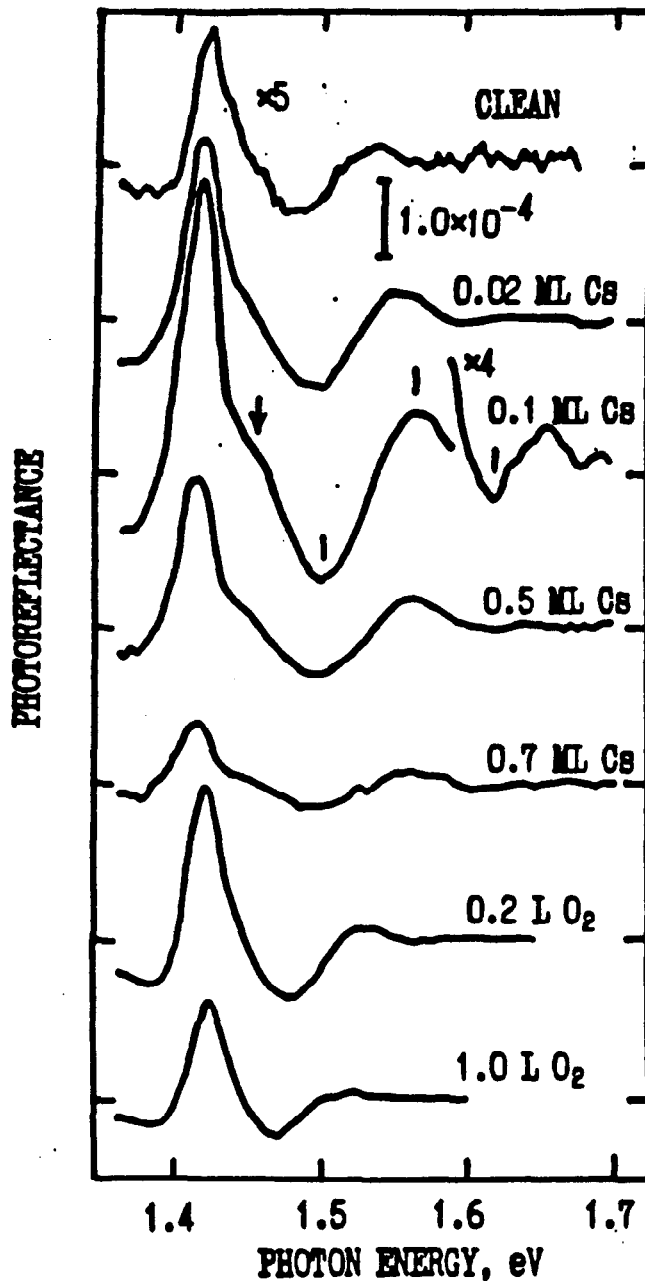
Switching of band bending (circles), photoreflectance amplitude (squares), and PL intensity (triangles) during the alternate deposition of cesium and oxygen. Deposition of the first monolayer of Cs is shown in detail. The exposure of oxygen corresponds to 20 L for first cycle, to 4 L for second cycle and to 2 L for the other cycles.



Evolution of band bending (circles), photoreflectance amplitude (squares), and PL intensity (triangles) during the first three deposition cycles of Cs and O<sub>2</sub> on clean GaAs(100) surface of p-type (open symbols) and n-type (closed symbols).

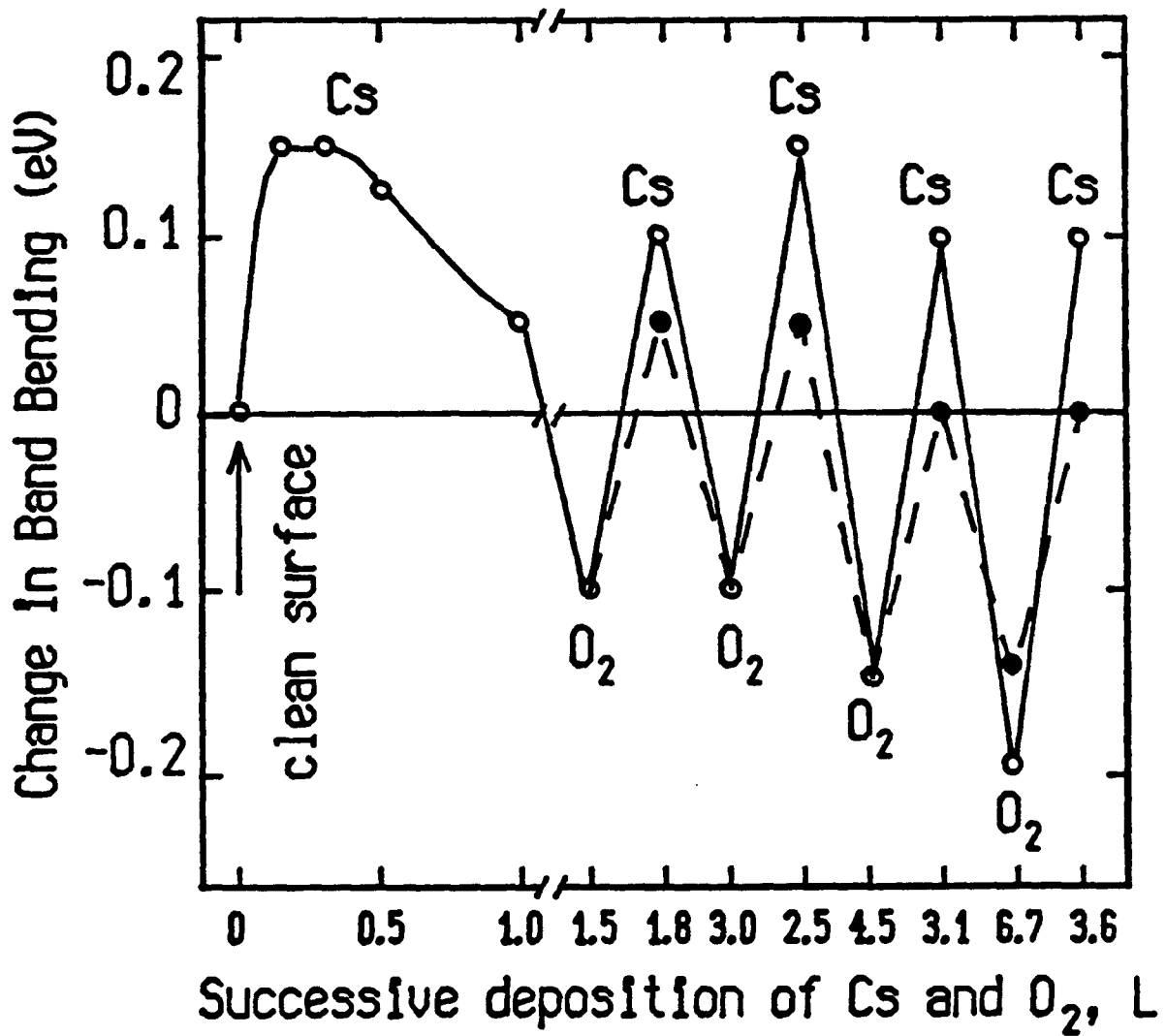


Dependence of  $(4/3\pi)(E_n - E_0)^{3/2}$  on index  $n$ , where  $E_n$  is position of the extrema of Franz-Keldysh oscillations,  $E_0$  is the bandgap. Theoretical straight lines are the best fit of the experimental dependences shown by circles. The slope of the lines gives the values of surface electric field.



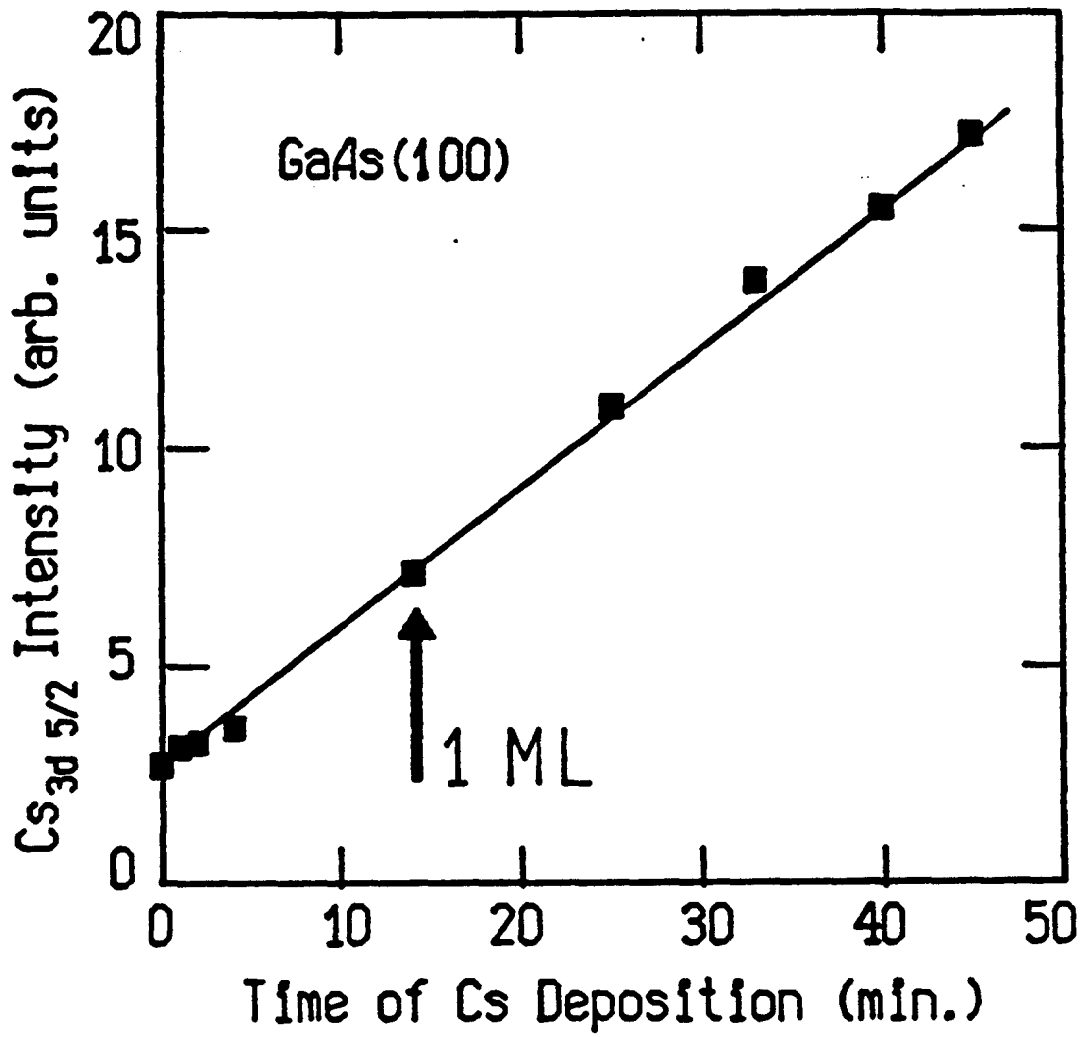
Photoreflectance spectra of a p-GaAs(100) surface after thermal cleaning and under successive deposition of cesium and oxygen. Spectra for oxygen deposition were measured at a pump-laser intensity an order of magnitude higher than for cesium deposition. The position of the oscillation extrema are marked by the vertical bars on one of the spectra.





- 'Fresh' surface (10 min after deposition)
- 'Relaxed' surface (30 min after deposition)

Change in band bending on p-GaAs(100) surface under successive deposition of Cs and O<sub>2</sub>, measured by x-ray photoelectron spectroscopy. Deposition of the first monolayer of Cs is shown in detail.



**S.M. Vernon  
Spire Corporation**

**Metalorganic Chemical Vapor Deposition of GaAs -  
GaAsP Spin-polarized Photocathodes**

**METALORGANIC CHEMICAL VAPOR DEPOSITION  
OF GaAs - GaAsP SPIN-POLARIZED PHOTOCATHODES  
S.M. VERNON, K.J. LINDEN, AND E.D. GAGNON**

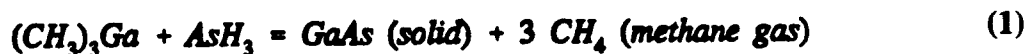
Spire Corporation  
One Patriots Park  
Bedford, MA 01730-2396

**ABSTRACT**

High-quality spin-polarized-electron sources for the Stanford Linear Accelerator have been produced from strained-layer photocathodes. The semiconductor layers have been grown by metalorganic chemical vapor deposition (MOCVD) at Spire Corporation, with negative-electron-affinity device fabrication being performed at SLAC. Excellent photoemission yields and electron polarizations over 90% have been measured, attesting to the quality of the MOCVD-grown layers, the design of the photocathode structure, and the excellent device processing. This manuscript gives a basic description of MOCVD as it relates to production of polarized-electron, strained-layer photocathodes.

**INTRODUCTION**

Metalorganic chemical vapor deposition (MOCVD) is a technique used to deposit layers of a material, often a compound semiconductor, by a chemical vapor deposition process in which at least one of the source chemicals is a metalorganic. The most common example of this method is growth of epitaxial gallium arsenide (GaAs) from trimethylgallium (TMG) and AsH<sub>3</sub>. Basic chemistry of this reaction is shown in equation 1



The process is carried out at high temperature, in the neighborhood of  $\approx 700^\circ\text{C}$ , often in a flowing hydrogen ambient. Pressure in the reaction chamber is typically between 0.05 and 1.0 atmosphere. A simplified schematic of an MOCVD system is shown in Figure 1.

**BASICS OF MOCVD GROWTH**

Reactant gases and metalorganic vapors, diluted in a large flow of high-purity hydrogen, are admitted to a reaction chamber containing substrates held at elevated temperature. For growth of III-V materials, this is often in the range of 600 - 800°C. Pressure in the reaction vessel, typically made of fused silica or stainless steel, is usually controlled at a value between 0.05 and 1.0 atmospheres. The gases are heated by the hot wafers and wafer carrier and pyrolyze to release their elements. Organic radicals and hydrogen molecules leave the chamber as gaseous effluents. The process is shown schematically in Figure 2.

For typical deposition of most III-V semiconductors, growth rate is linearly proportional to flowrate of group III, so long as a large excess of group V is supplied. Growth is most often carried out in a mass-transport-limited regime, where growth rate is quite insensitive to growth temperature. At lower temperatures, growth is limited by pyrolysis of incoming species, while at high temperatures, desorption of surface species limits deposition. These three regions are shown in Figure 3.

### MOCVD STRONG POINTS

MOCVD has demonstrated high-quality, high-purity layer growth of numerous semiconductors. Excellent uniformity of thickness, composition, and doping are routinely achieved in many laboratories. Other advantages of this method include

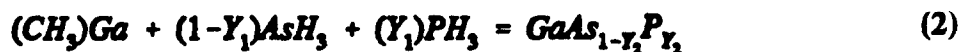
- excellent reproducibility
- excellent control of thin layers, interfaces, composition, and doping
- flexibility to grow strained-layer and/or superlattice structures
- economic, large-area production
- the ability to handle phosphorus compounds
- growth of high-quality layers of all semiconductor materials relevant to strained-layer photocathodes, such as
  - GaAs
  - $\text{Al}_{(x)}\text{Ga}_{(1-x)}\text{As}$
  - $\text{Ga}_{(1-x)}\text{In}_{(x)}\text{As}$
  - $\text{Al}_{(y)}\text{Ga}_{(1-x-y)}\text{In}_{(x)}\text{As}$
  - $\text{GaAs}_{1-y}\text{P}_y$
  - $\text{Ga}_{(1-x)}\text{In}_{(x)}\text{P}$
  - $\text{Ga}_{(1-x)}\text{In}_x\text{As}_{(1-y)}\text{P}_y$

### EXPERIMENTAL PROCEDURES

The basic structure grown and studied for this work is shown in Figure 4. In this structure, all layers are doped with zinc to  $p = 5 \times 10^{18} \text{ cm}^{-3}$ . Epitaxial layers are grown in the SPI-MOCVD™ 100-S reactor, which has a batch capacity of one two-inch- or three-inch-diameter wafer per run. Growth of the strained-layer photocathode epitaxial structure typically requires a total time of approximately three hours. Process temperature is  $\approx 700^\circ\text{C}$ , with the reactor pressure being 0.1 atm (76 torr). Typical growth rate is 4  $\mu\text{m}/\text{hour}$ . Source chemicals include trimethylgallium (TMG),  $\text{AsH}_3$ ,  $\text{PH}_3$ , and dimethylzinc (DMZ) diluted in  $\text{H}_2$  as the p-type dopant.

## MOCVD GROWTH OF GaAs<sub>1-y</sub>P<sub>y</sub>

Control of the composition of GaAs<sub>1-y</sub>P<sub>y</sub> is given by the following equation



In general, Y<sub>1</sub> (gas) ≠ Y<sub>2</sub> (solid). The ratio, Y<sub>1</sub> / Y<sub>2</sub> depends on several parameters, such as growth temperature, system pressure, reactor geometry, and flow velocity. The following example is for MOCVD growth of GaAs<sub>1-y</sub>P<sub>y</sub>, as performed in our laboratory:

Example:      Growth temperature = 650°C  
                 Reactor pressure = 76 torr  
                 System = "100-S"  
                 Main H<sub>2</sub> = 5 slpm

Ratio of input flows: PH<sub>3</sub>/AsH<sub>3</sub> = Y<sub>1</sub>/(1-Y<sub>1</sub>) = 3.3

Measured GaAs<sub>1-y</sub>P<sub>y</sub> composition: P/As = Y<sub>2</sub>/(1-Y<sub>2</sub>) = 0.3/0.7 = 0.43

Strain in the GaAs active layer is controlled by film thickness, and by lattice constant mismatch with the underlying GaAs<sub>1-y</sub>P<sub>y</sub> region. If the stress in the layer exceeds a critical value, because of excessive thickness and/or mismatch, the layer "relaxes," forming defects to relieve lattice strain. Figure 5 shows a theoretical curve of critical thickness versus lattice mismatch; several compositions of GaAs<sub>1-y</sub>P<sub>y</sub> on GaAs are indicated here.

For a given thickness, as lattice mismatched is increased (in our case, by increasing Y in a GaAs-GaAs<sub>1-y</sub>P<sub>y</sub> structure), the layer first deforms elastically to the lattice of the underlying material, in a so-called pseudomorphic region. With increasing strain, the layer is plastically deformed, until a critical stress level is reached, and the film begins to fail and crack. This behavior is illustrated schematically in Figure 6.

## CHARACTERIZATION

Surface quality is studied by use of Nomarski interference-contrast microscopy; the surface of a photocathode epitaxial structure is displayed in Figure 7. The "cross-hatch" pattern reveals the network of misfit dislocations parallel to the interface plane, and is indicative of partial strain relaxation in the layers.

Carrier concentration is measured by two methods: Hall-effect measurements, and capacitance-voltage (C-V) profiling. For single calibration layers on a semi-insulating substrate, Hall-effect data gives good accuracy for highly p-type layers. For complex, multilayer epitaxial structures, the "Polaron" instrument, using a liquid electrolyte to form a Schottky barrier, can measure carrier concentration versus depth throughout the material.

Composition of GaAs<sub>1-y</sub>P<sub>y</sub> is measured by double-crystal X-ray rocking curve analysis (XRRC). For quick calibration of layer composition, room-temperature photoluminescence (PL)

gives useful information. The composition indicated by PL is usually about 2 -3 phosphorus percentage points less than the true value.

Strain level in the GaAs top layer is measured by double-crystal X-ray rocking curve analysis. This time-consuming measurement, due to the small thickness of the layer, has been performed on our samples, at the University of Wisconsin, courtesy of Dr. R. Prepost.

## CONCLUSIONS

Metalorganic chemical vapor deposition (MOCVD) is a simple, production-amenable process, which has demonstrated the ability to deposit high-quality strained-layer photocathode structures. Spin-polarization values over 90% and excellent photoemission yields have been measured on negative-electron-affinity devices processed at SLAC. MOCVD offers flexibility, uniformity, reproducibility, layer purity, and good control over complex structures of most any III-V material.

## ACKNOWLEDGEMENTS

The authors gratefully acknowledge the many valuable contributions of Dr. Earl Hoyt, Dr. James Clendenin, and Dr. Richard Prepost, and financial support from the Department of Energy.

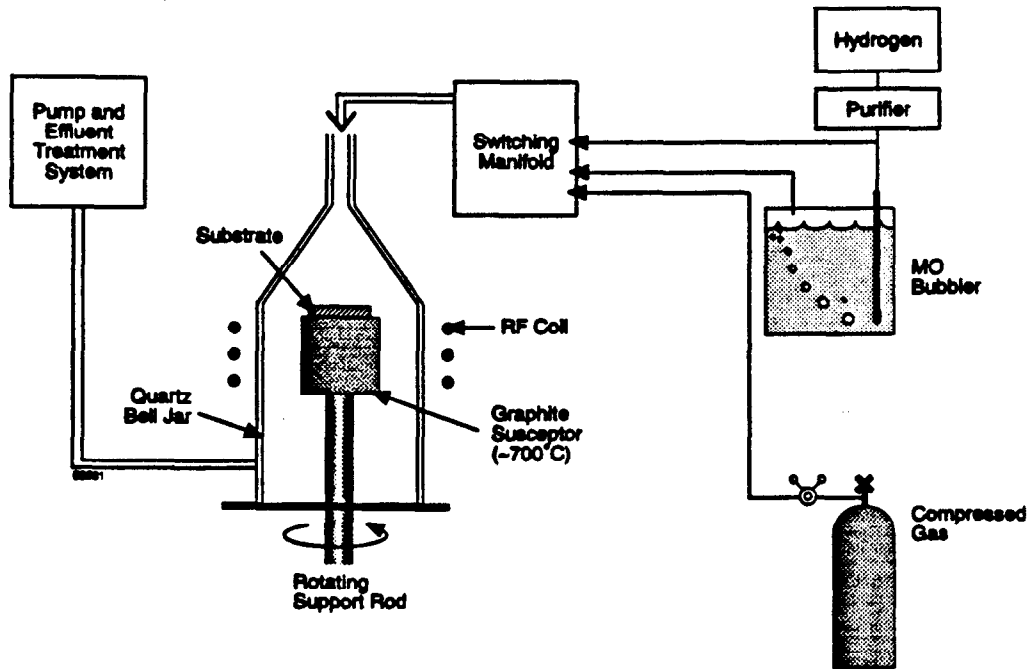


Figure 1 *Simplified schematic of the Spire metalorganic chemical vapor deposition (MOCVD) system.*

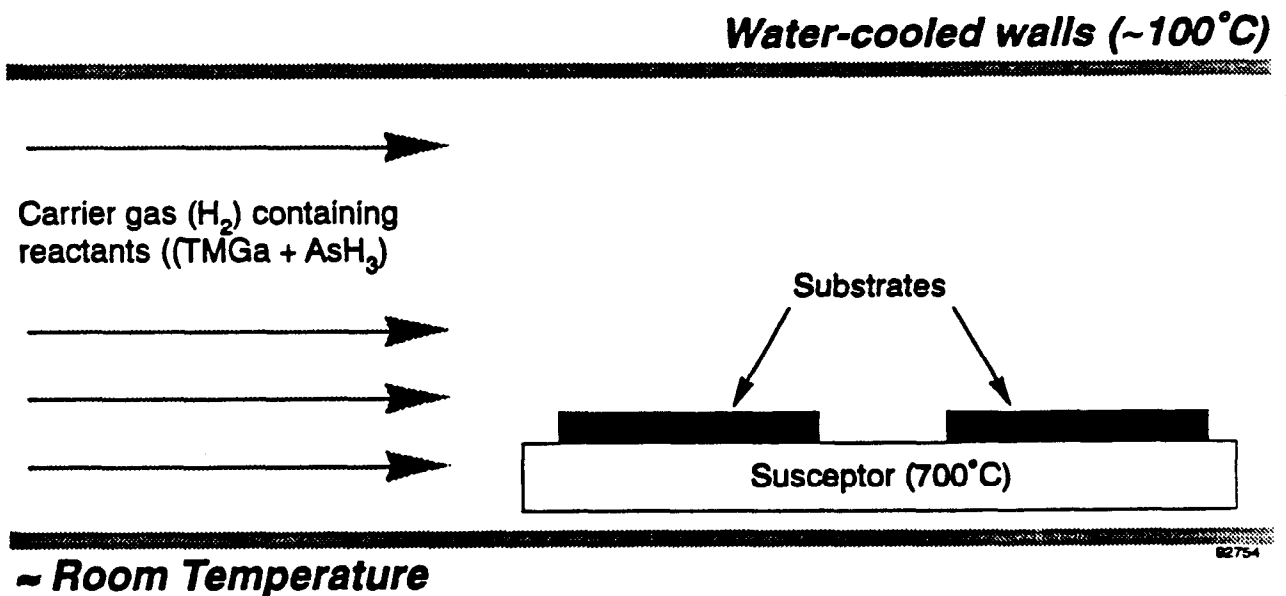
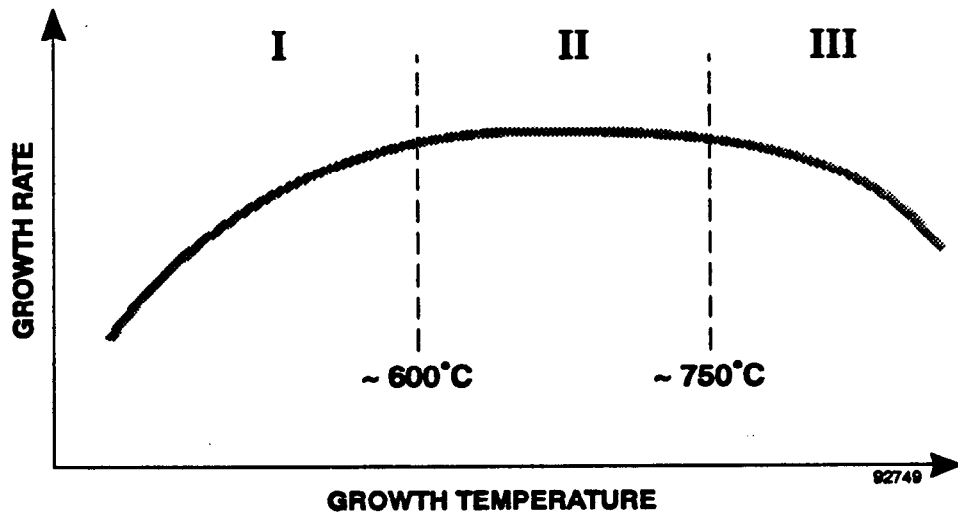


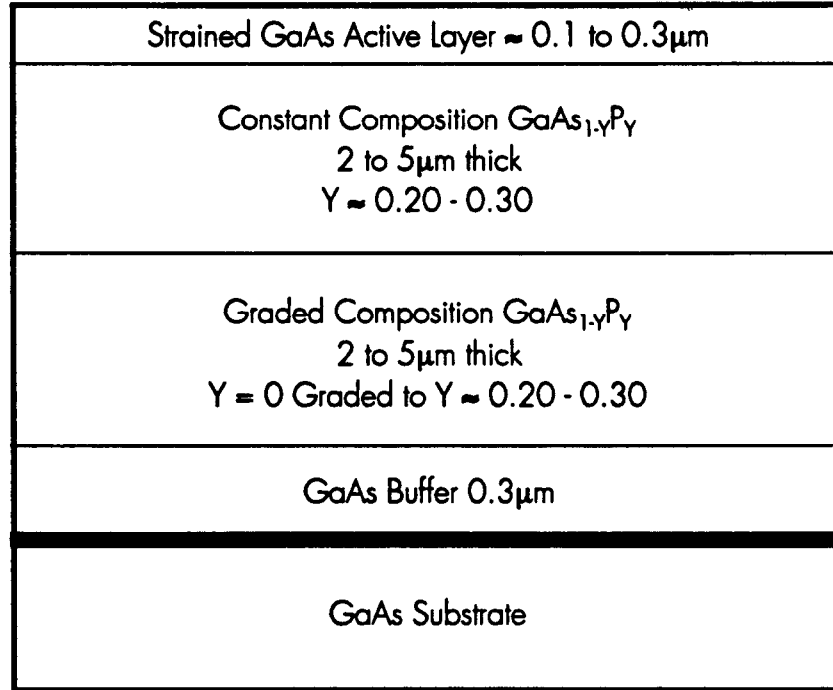
Figure 2 *Representation of the basic MOCVD process; example shown is for growth of GaAs.*





- ▶ **Region I:** Limited by pyrolysis and reactions
- ▶ **Region II:** Limited by diffusion across boundary layer
- ▶ **Region III:** Limited by desorption of species from surfaces

**Figure 3** Growth rate versus temperature in a typical MOCVD process.



932243

**Figure 4** Design of the strained-layer photocathode epitaxial layers used in this work.

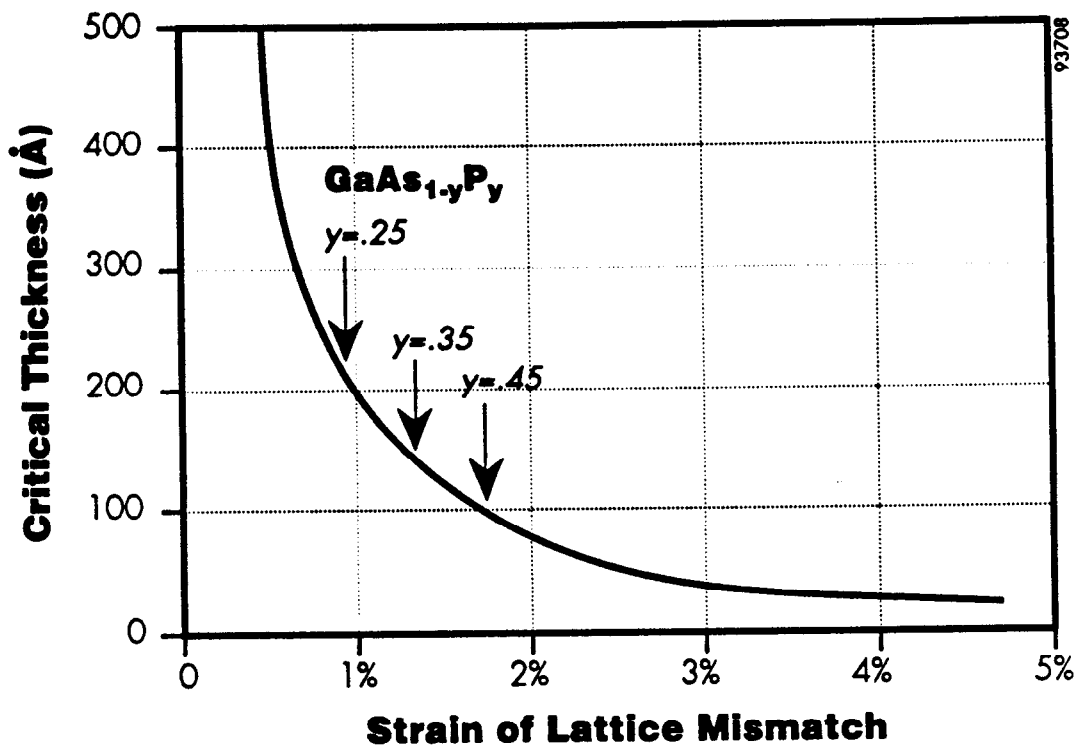
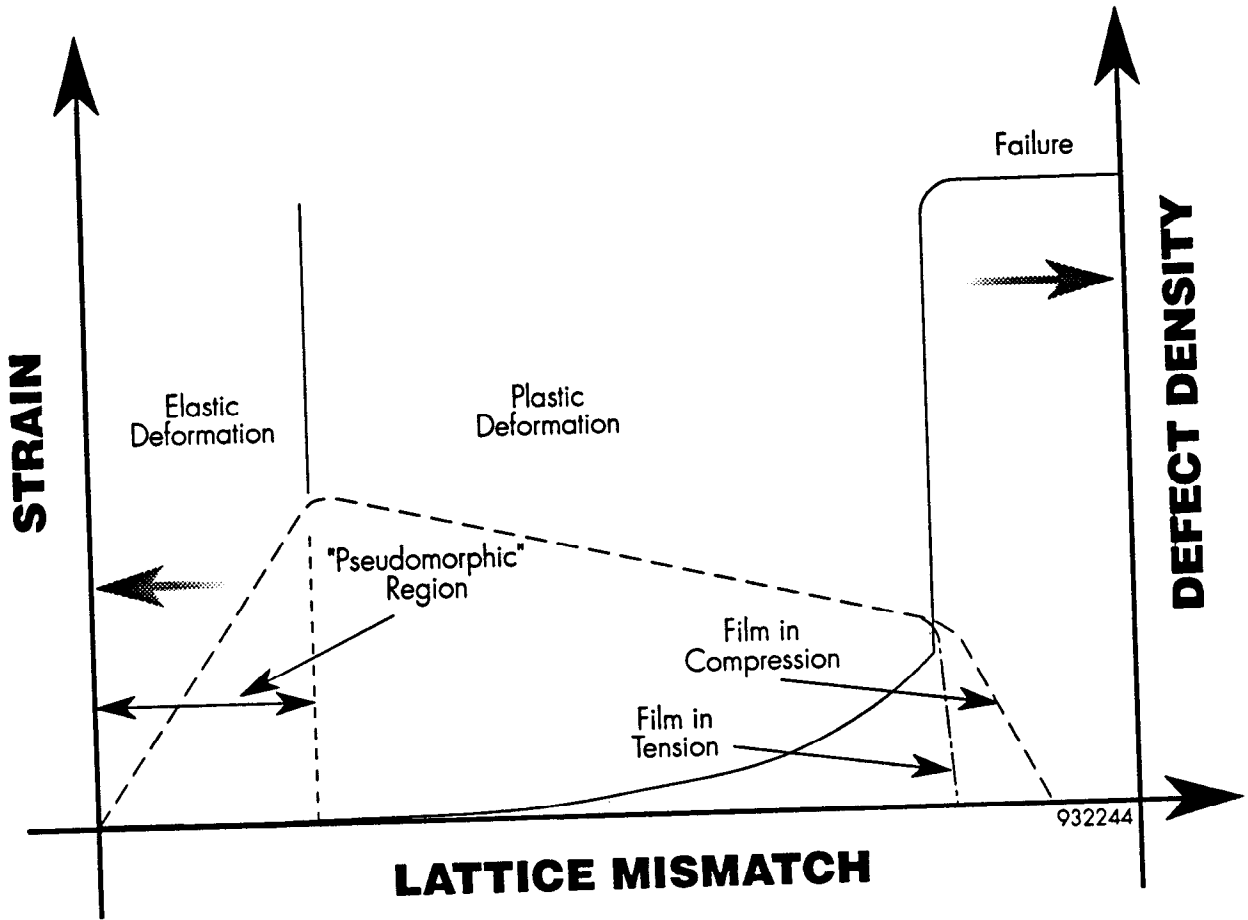
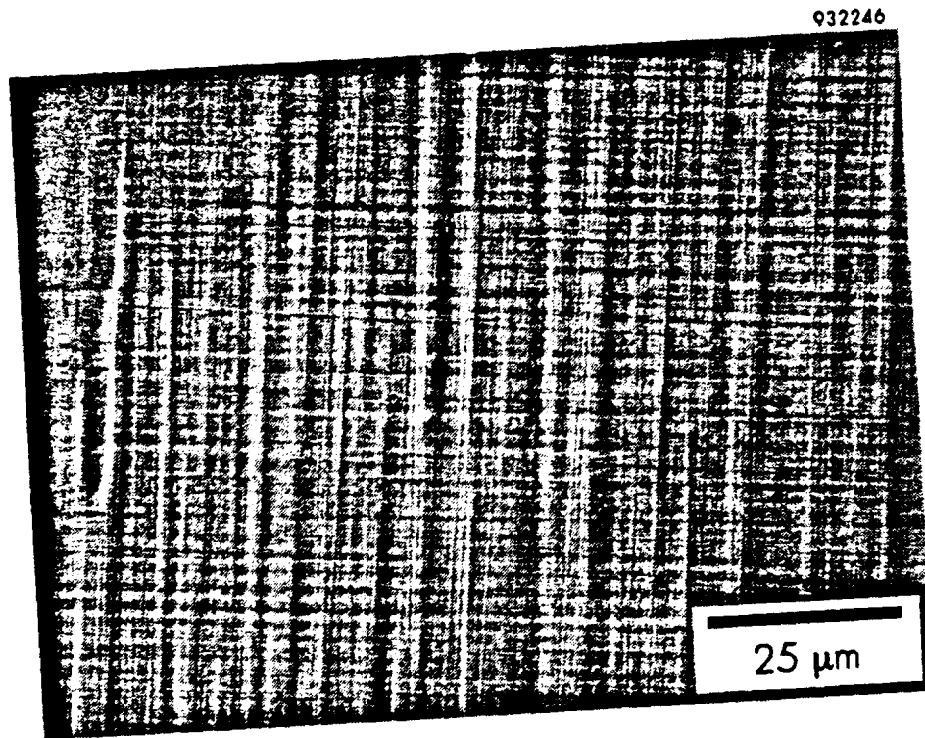


Figure 5 Theoretical curve of critical thickness versus lattice mismatch.



**Figure 6** *Qualitative behavior of strain and defect density versus lattice mismatch at constant film thickness.*



**Figure 7** *Nomarski interference contrast micrograph of surface morphology of a strained-layer GaAs-GaAs<sub>1-y</sub>P<sub>y</sub> photocathode.*

**M. Yoshioka**  
**KEK**

**Development of Photocathode Injectors for JLC-ATF**

Japan Linear Collider (JLC): The JLC is a e+e- linear collider to cover the c.m. energy range of up to 500 GeV with a peak luminosity of  $5E33/cm^2/s$ . The electron source of JLC-I must be able to produce 55-90 intense electron bunches separated by a spacing of 1.4, 2.8 or 5.6 ns with a rep. frequency of 150 Hz. Each bunch consists of  $0.7 - 1.5 E10$  electrons. Accelerator Test Facility (ATF): an accelerator test facility is constructed to study the accelerator physics and technical problems of linear colliders at KEK. It is mainly consisted of an 1.5 GeV S-band injector linac and a damping ring to produce multi-bunch, extremely low emittance and flat beams. Photoinjectors: In order to produce multi-bunch beam, a thermionic gun with a fast grid pulser is under developed. An alternate way to produce multi-bunch beam using laser triggered photocathodes has been also studied, which is an RF-gun. A preliminary experiment was performed by using a single cell S-band cavity with 40 MV/m and the bunched beam was extracted successfully. After that, we concentrate our efforts to study how to reduce the dark current of the high gradient cavities and how to develop the long life photocathode. Also a polarized gun using GaAs-AlGaAs superlattice has been developed under the collaboration with Nagoya University and NEC Inc. A test bench to evaluate the performance of the cathode has been constructed, which is composed with a gun (100 KV DC) and Mott analyzer. Present status of these studies will be reported.

# Development of Photocathode Injectors for JLC-ATF

Masakazu Yoshioka

KEK, National Lab. for High Energy Physics,  
Oho 1-1, Tsukuba, Ibaraki, 305 Japan

"Workshop on Photocathodes for Polarized  
Electron Sources for Accelerators"

Sep. 10, 1993

---

Collaborators: JLC- Study Group

\* Polarized Source Group

T. Omori, Y. Kurihara, Y. Takeuchi (KEK)  
T. Nakanishi, M. Tsubata, S. Okumi, C. Takahashi  
Y. Tanimoto, M. Tawada, K. Togawa (Nagoya)  
H. Baba, M. Mizuta (NEC) -----

\* Injector for ATF Damping Ring.

S. Takeda, H. Matsumoto, M. Akemoto,  
H. Hayano, T. Naito, K. Oide, J. Urakawa,  
K. Yokoya, T. Shintake, ----- (KEK)

- 
1. JLC-1 (Requirements for Source)
  2. Accelerator Test Facility (ATF)
  3. Photo injectors

RF-gun

Polarized  $e^-$

(Thermionic Gun  
with Grid Pulser)

# 1. Japan Linear Collider "JLC-I"

Joint LC, Joyful LC

↑

International Collaboration

(MoU prepared by SLAC/KEK/DESY)

Detailed Descriptions on JLC-I appear

→ "JLC-I" KEK Report 92-16, December 1992

By JLC Group

Beam Energy : 150 → 250 GeV  
Luminosity :  $\sim 5 \cdot 10^{33}$  /cm<sup>2</sup>/s  
Total Wall Plug Power : < 200 MW  
Total Length : < 25 km

---

↑↑↑↑

rms Beam Size at IP  $\sigma_y^* / \sigma_z^* \sim 4 \text{ nm} / 300 \text{ nm}$   
Multi Bunch Scheme 50 ~ 90 Bunch/Pulse

---

Future Improvements → JLC-II

150 ~ 250 GeV ⇒ 750 GeV/Beam

$5 \cdot 10^{33}$  /cm<sup>2</sup>/s ⇒  $> 10^{34}$

---

\* Main Linac of JLC-I

2.856 GHz, 5.712 GHz or 11.424 GHz

\* Main Linac of JLC-II

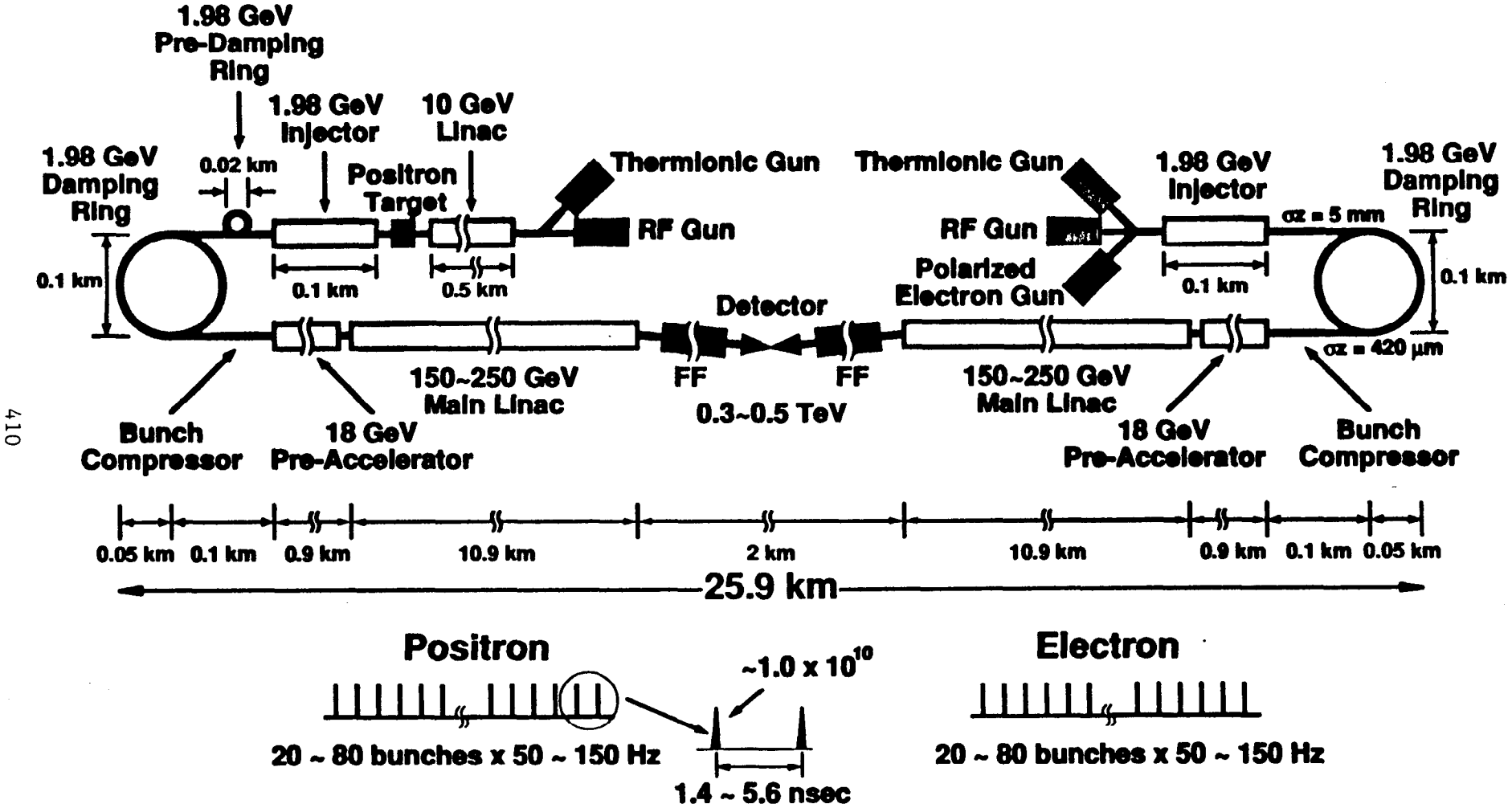
5.712 GHz or 11.424 GHz

But the Injector Part is common!!

Time Schedule : "Design Report"

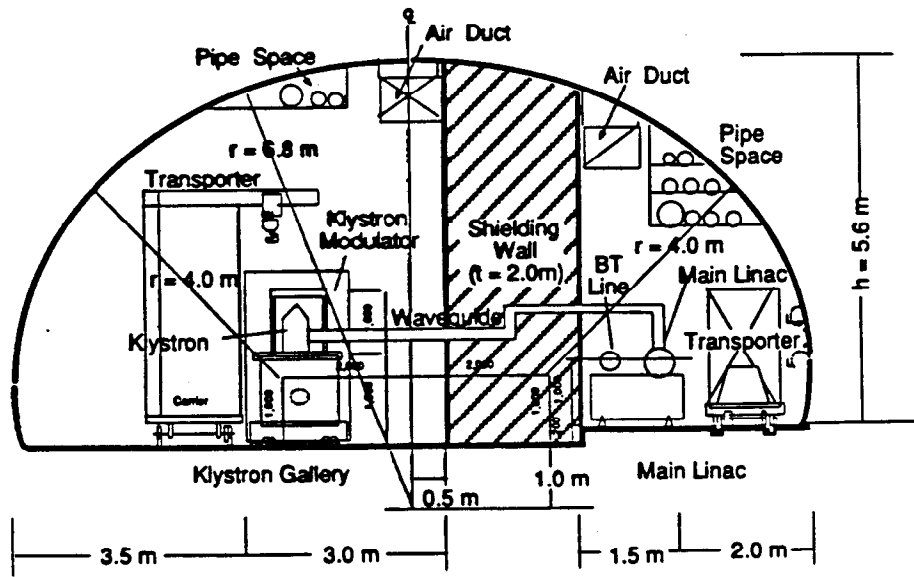
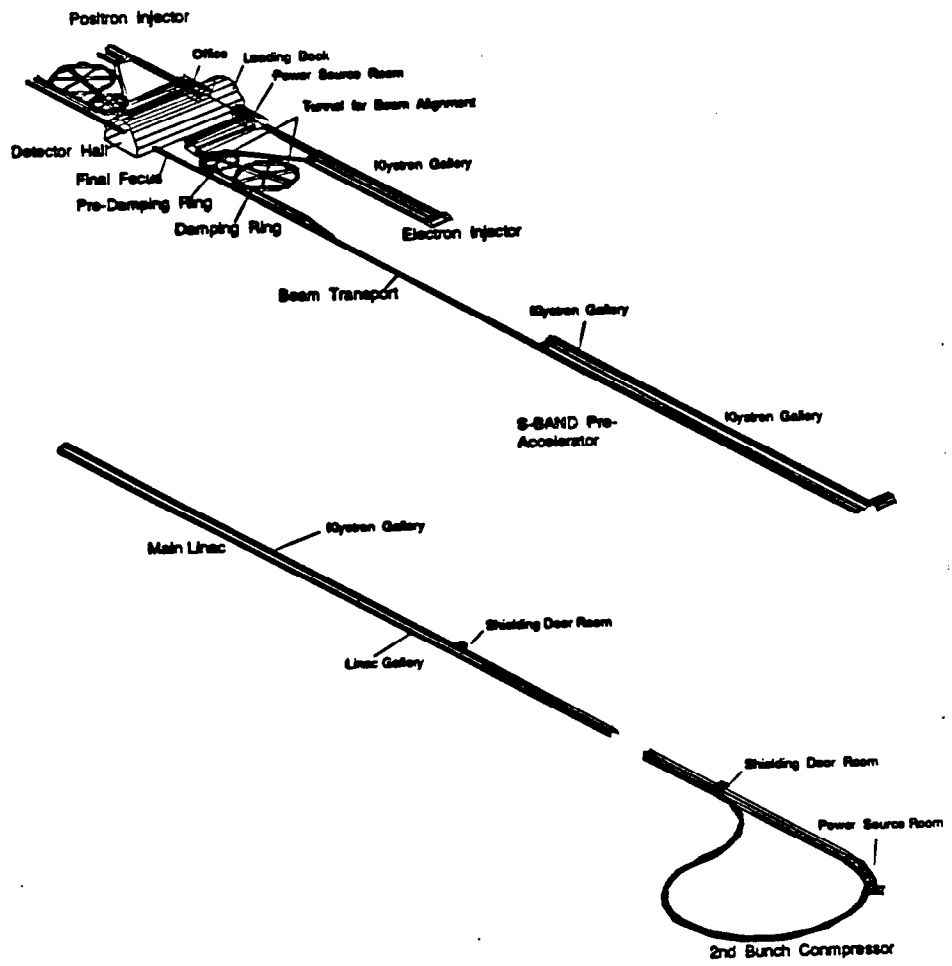
⇒ 1996 or 1997!!

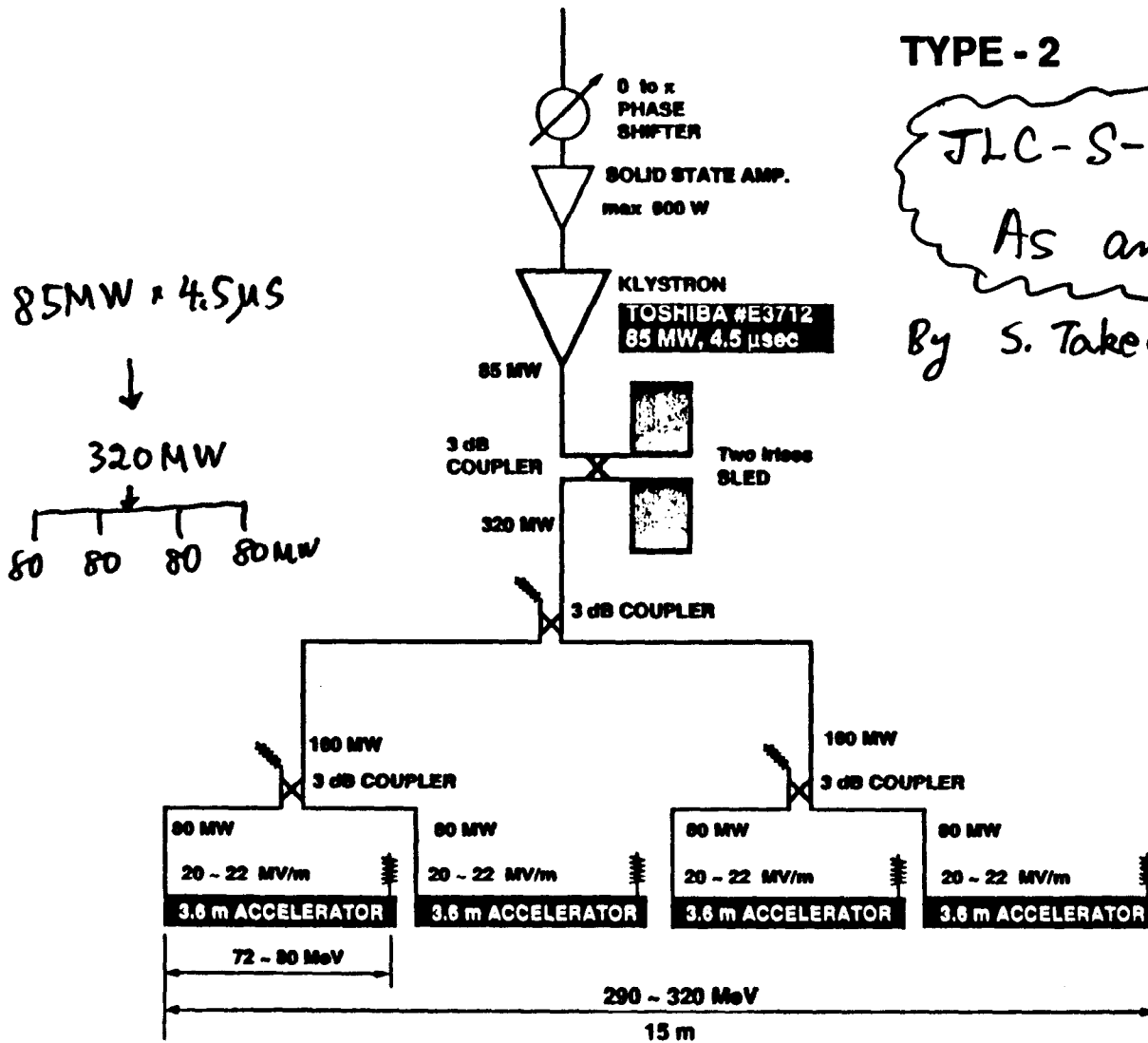
# Schematic Diagram of JLC-1



410







85 MW  $\times$  4.5  $\mu$ s  
 $\downarrow$   
 320 MW  
 $\downarrow$   
 80 80 80 80 MW

### TYPE - 2

JLC-S-Band Linac  
 As an Example

By S. Takeda, H. Matsumoto, ...

300 MeV/15m

300 GeV/1000 Units

# Accelerator Test Facility (ATF) (K. Takata)

- 1st stage [
- 1.54 GeV S-band Injector Linac
  - Damping Ring
- ↑ S. Takeda  
 H. Matsumoto  
 ⋮  
 ↑ J. Uehara, ----
- 2nd stage ( + Bunch Compressor + Final Focus )  
 \* e<sup>+</sup> Generation Test )

## • Purpose of ATF

• Multi Bunch + Flat Beam

Extremely Low Emittance

20 - Bunches, 2.8 n Spacing

$$\gamma E_{xy} \rightarrow \underline{\underline{5 \cdot 10^{-6} / 5 \cdot 10^{-8} \text{ rad m}}}$$

- August 1993 Commissioning of Injector Part of S-Band Linac (80 MeV)
- End of JFY 1995 Construction Completed

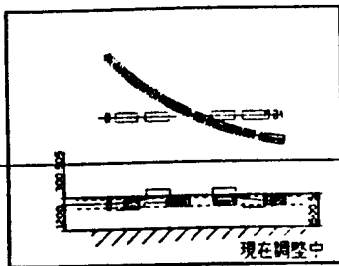
- Solid
- Air pipe
- Water pipe

JLC-ATF [ Multi-Bunch  
Flat-Beam

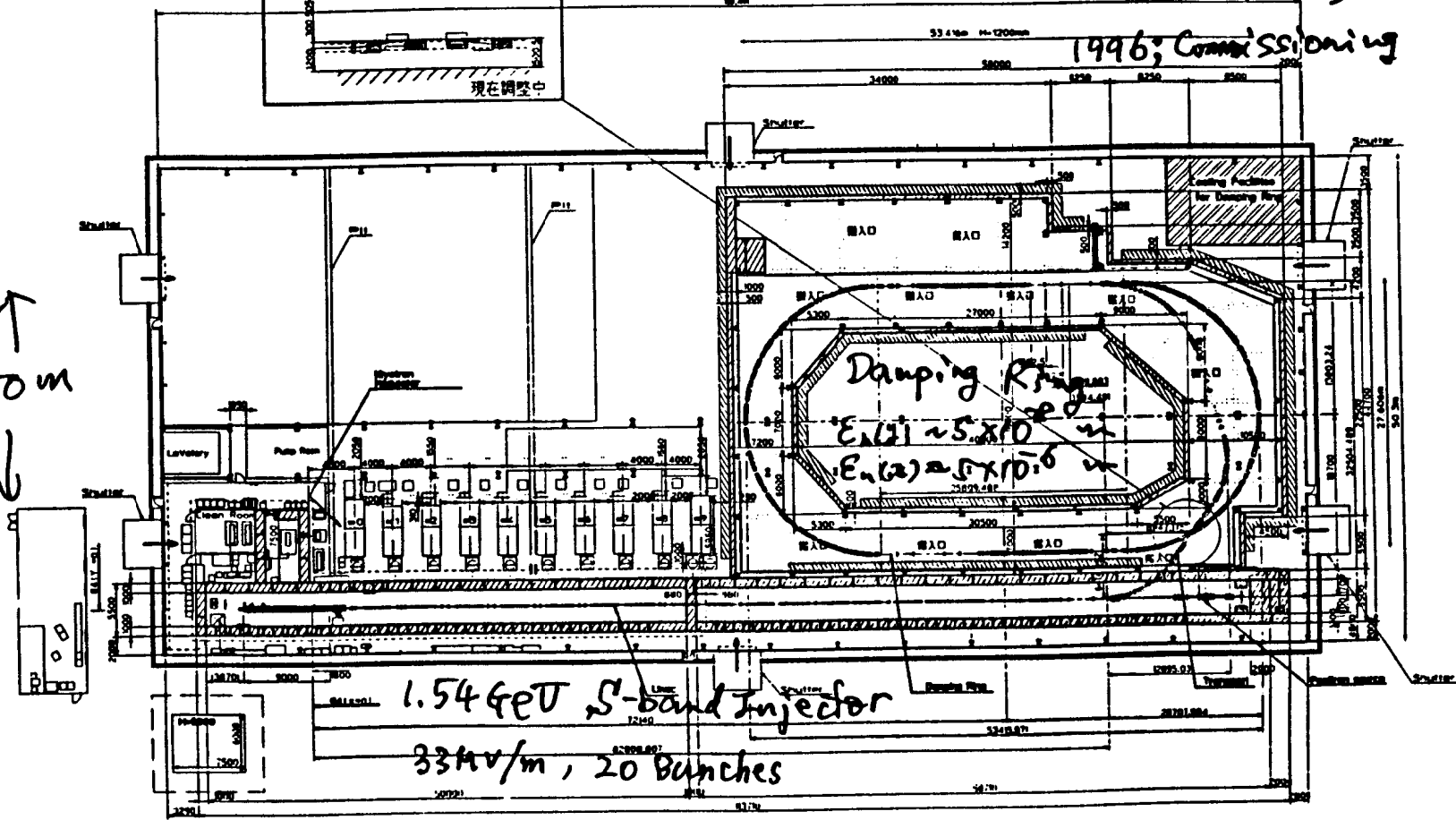
$\delta \sim 1\%$

$\Delta y < 30 \mu\text{m}$

1996; Commissioning



↑ 0 m  
↓

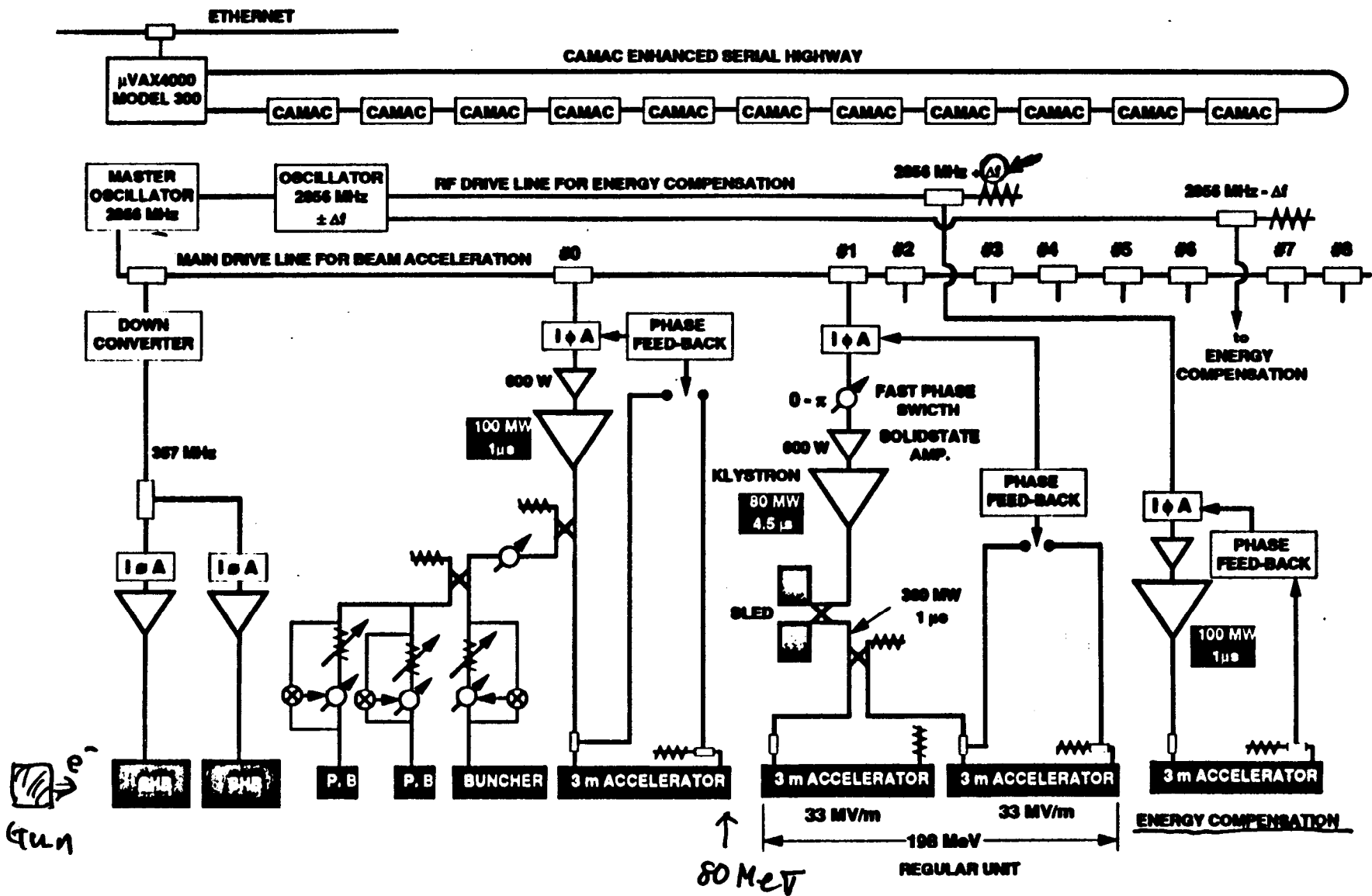


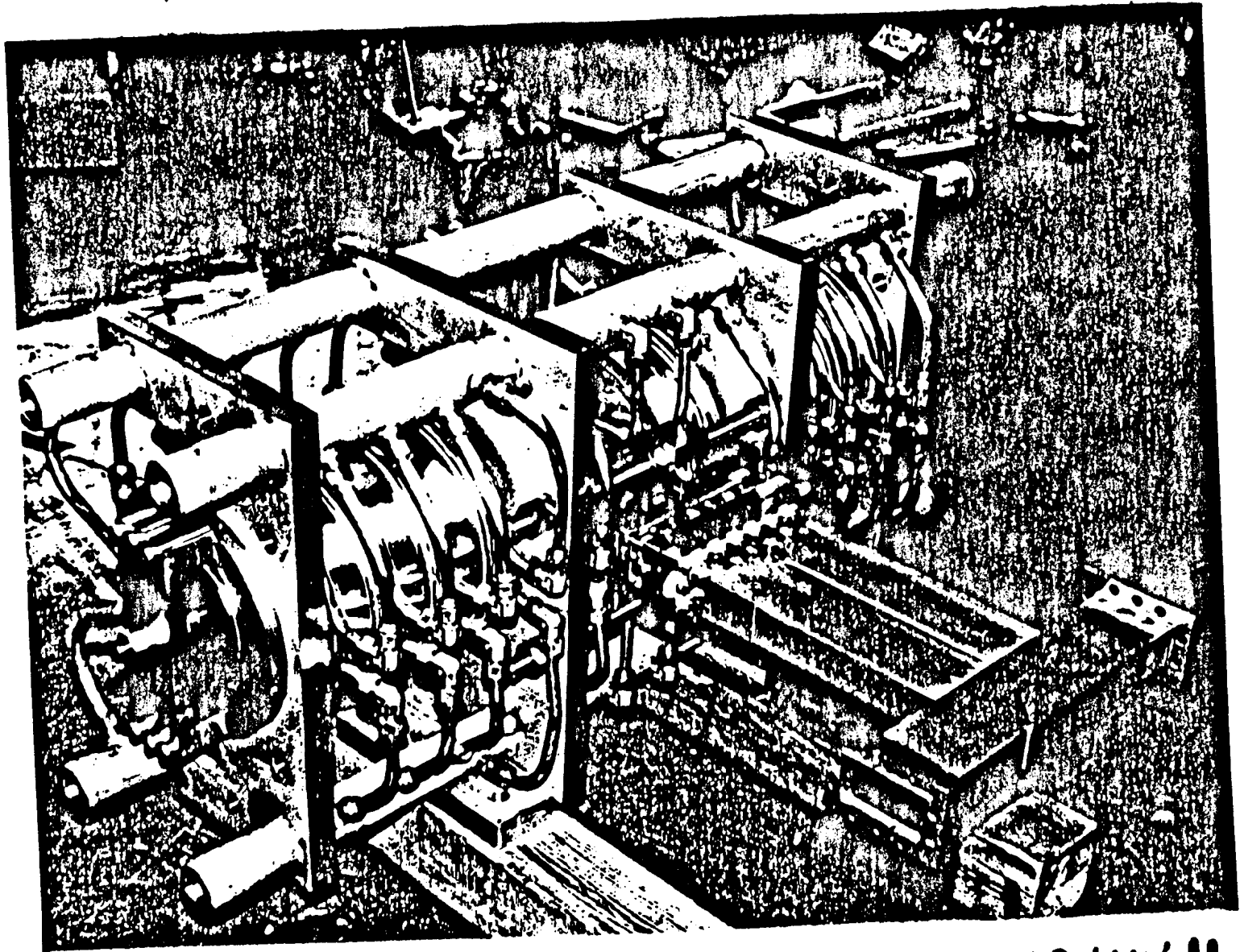
1.54 GeV S-band Injector  
33 kV/m, 20 Bunches

← 120 m →

# RF DRIVE SYSTEM FOR S-BAND INJECTOR LINIAC

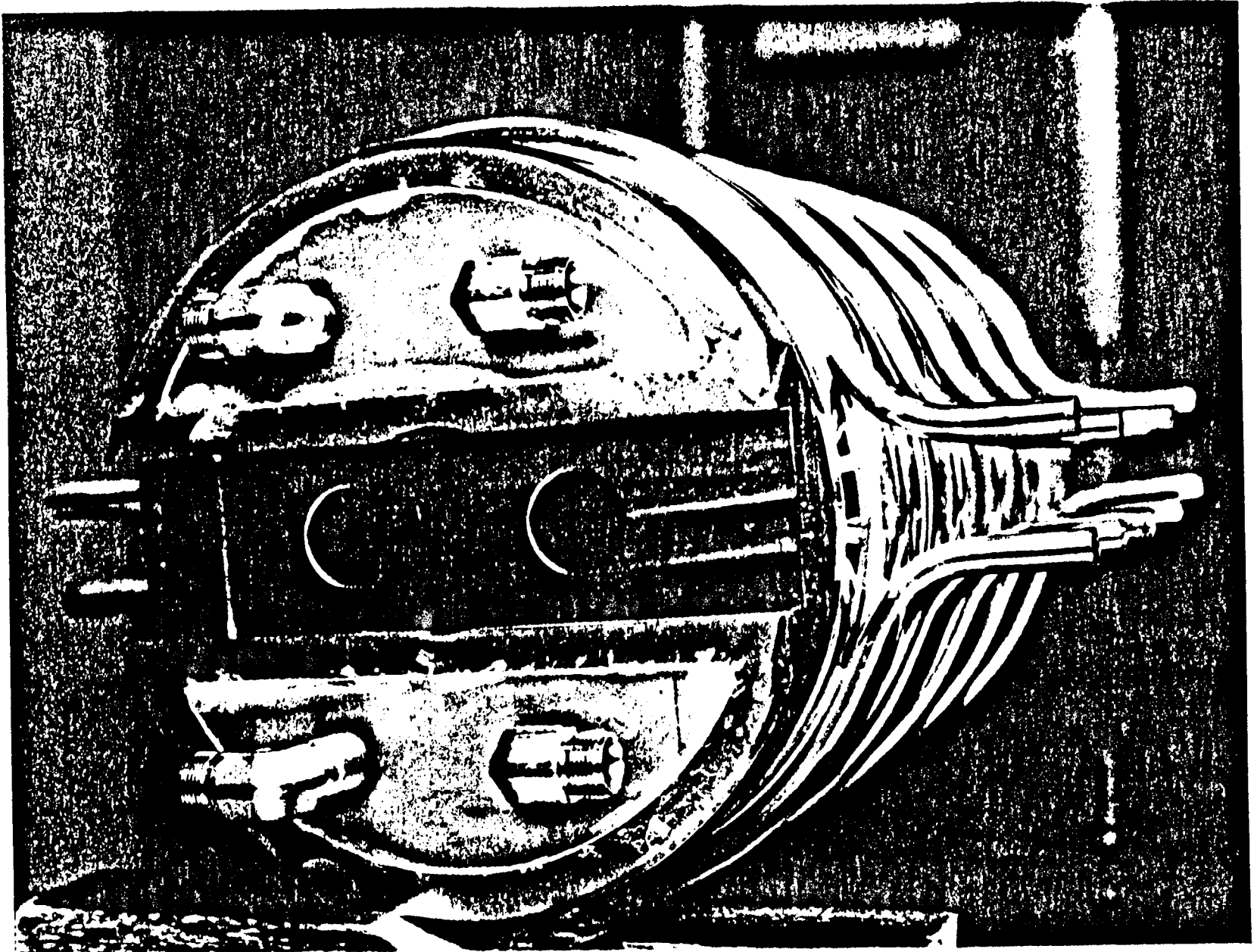
415





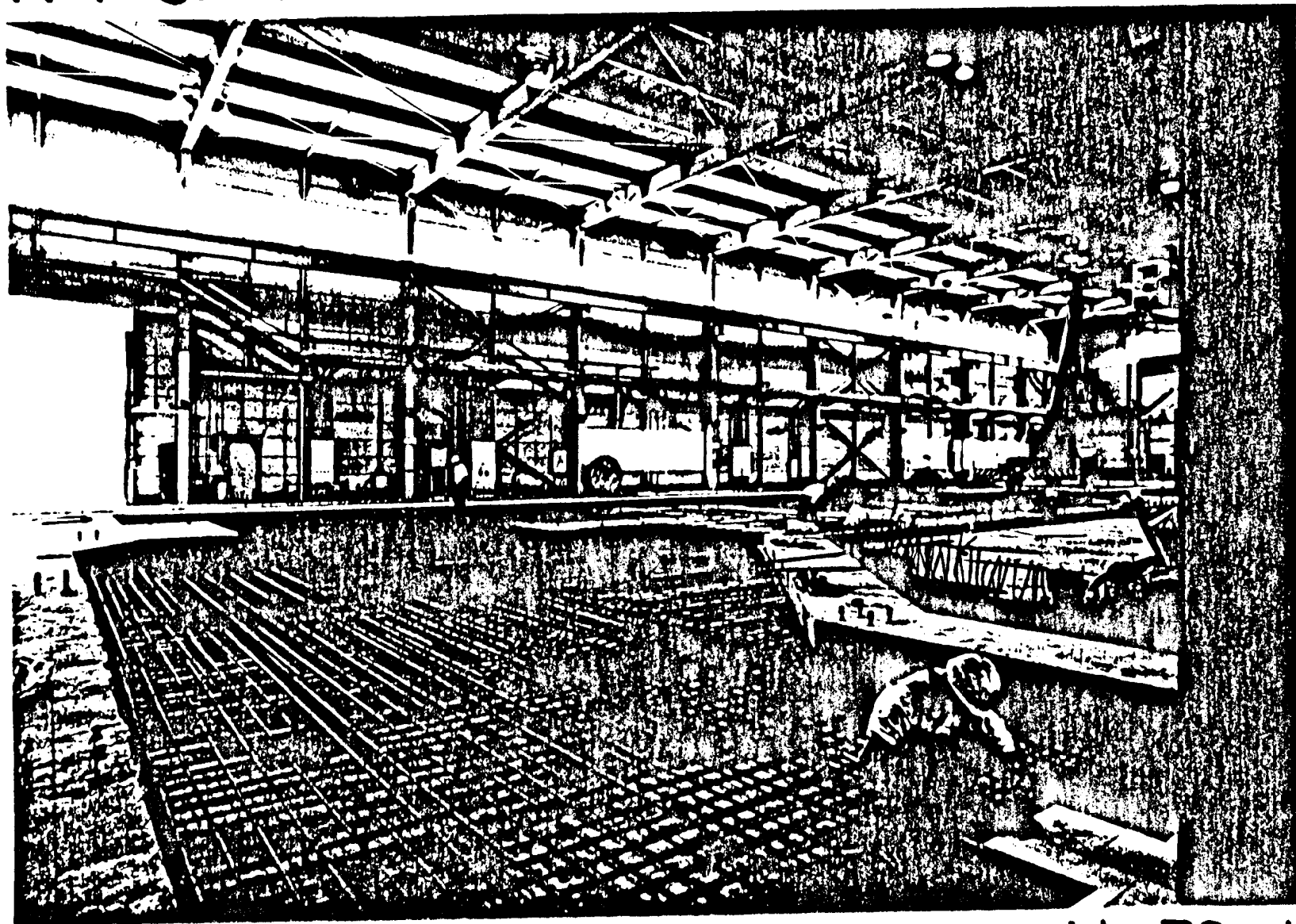
New SLED (Matsumoto, KEK)

85MW → 400 MW !!



# ATF Construction

MAY/1993



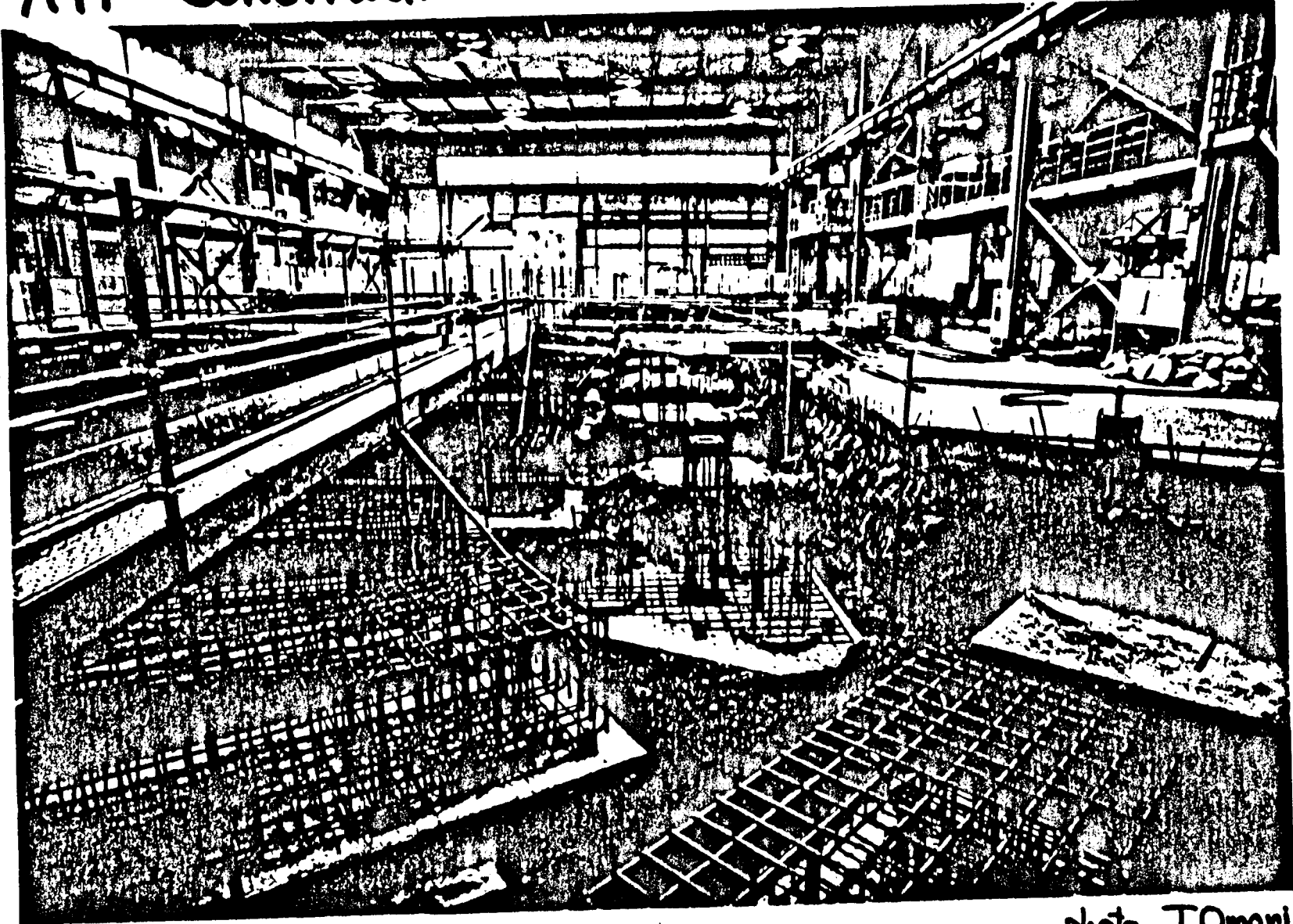
818

photo T. Omori



ATF Construction

APR./1993



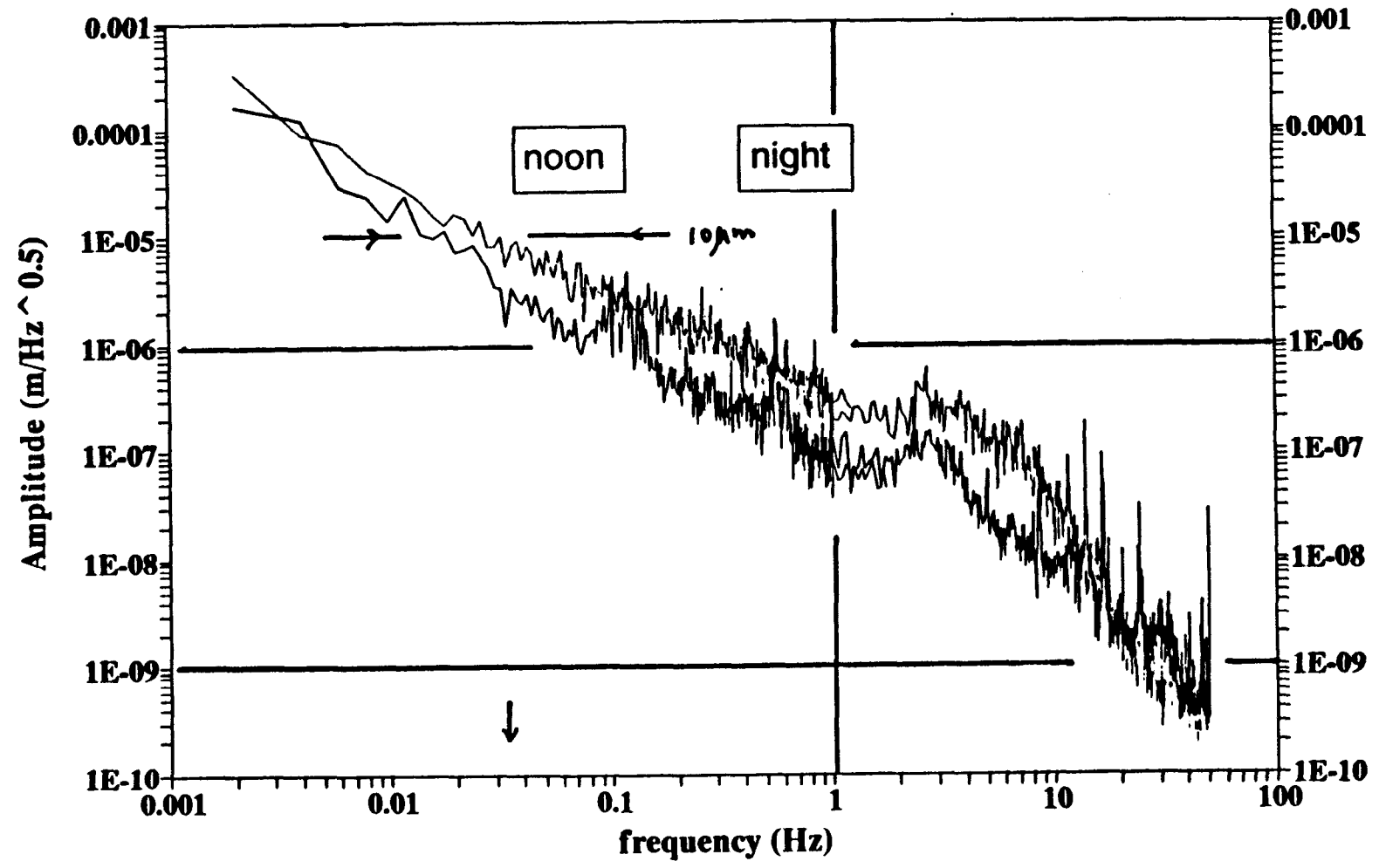
419

Floor for Damping Ring

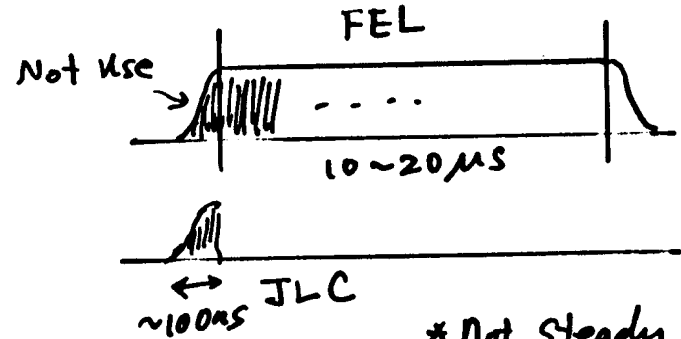
photo T.Omori

Spectrum of Ground Motion  
at the KEK ATF floor

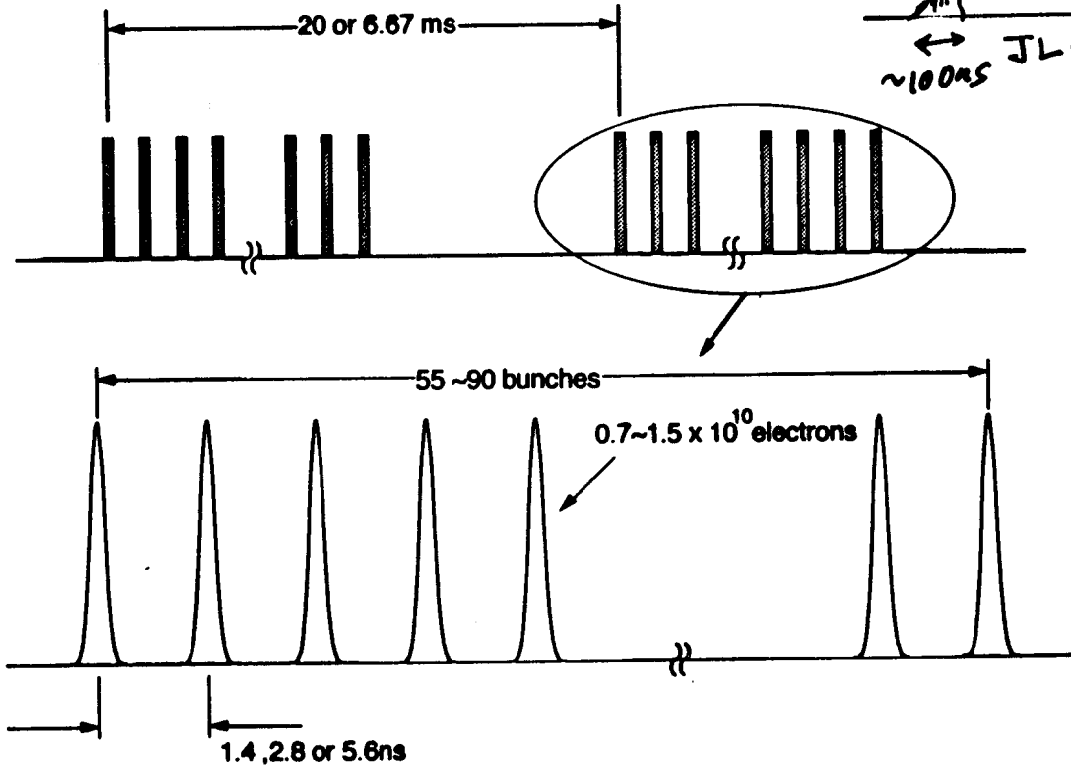
竹田 繁 (KEK 加速器)  
Shigern Takeda et al.



# Beam Parameters of JLC



- \* Not Steady State!!
- \* Heavy Beam Loading
- \* Stability



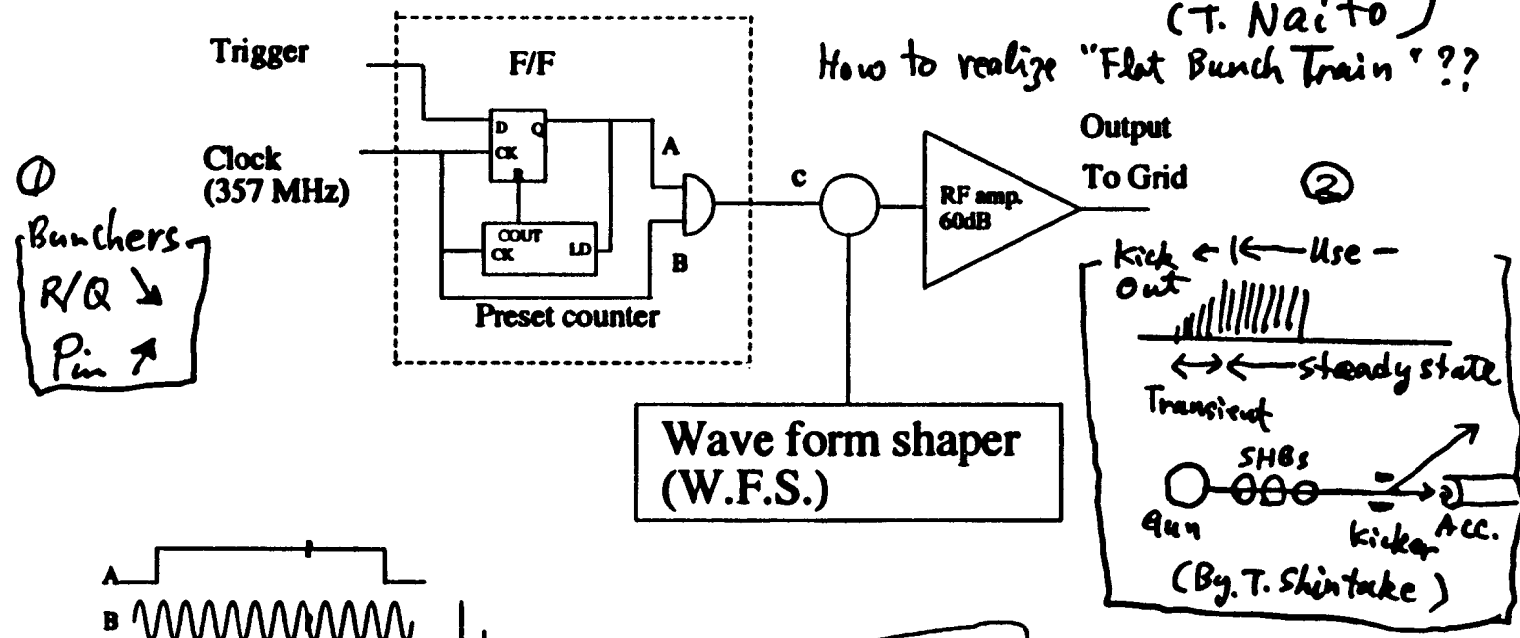
$\Delta N$  : 1% stability

# ① Thermionic Gun + Grid Pulser

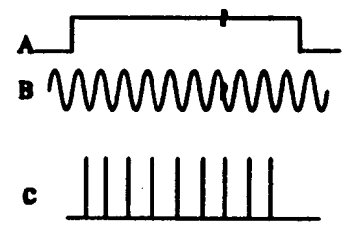
(T. Naito)

How to realize "Flat Bunch Train"??

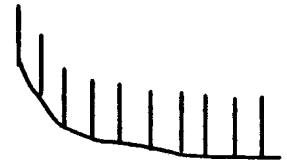
Fast ECL Circuit + RF Power Amplifier



① Bunchers  
R/Q ↓  
Pin ↑



ECL output



input of RF amp.



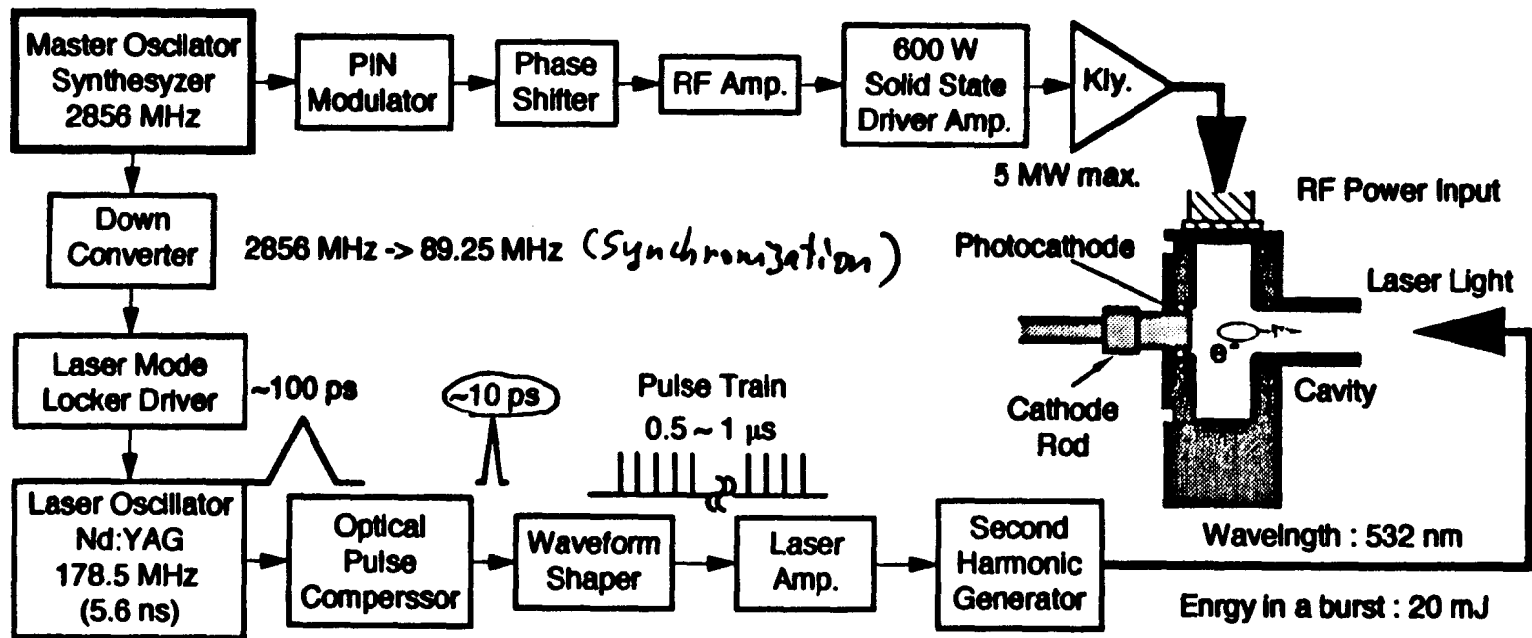
Pulse response of RF amp.

Band width ↑



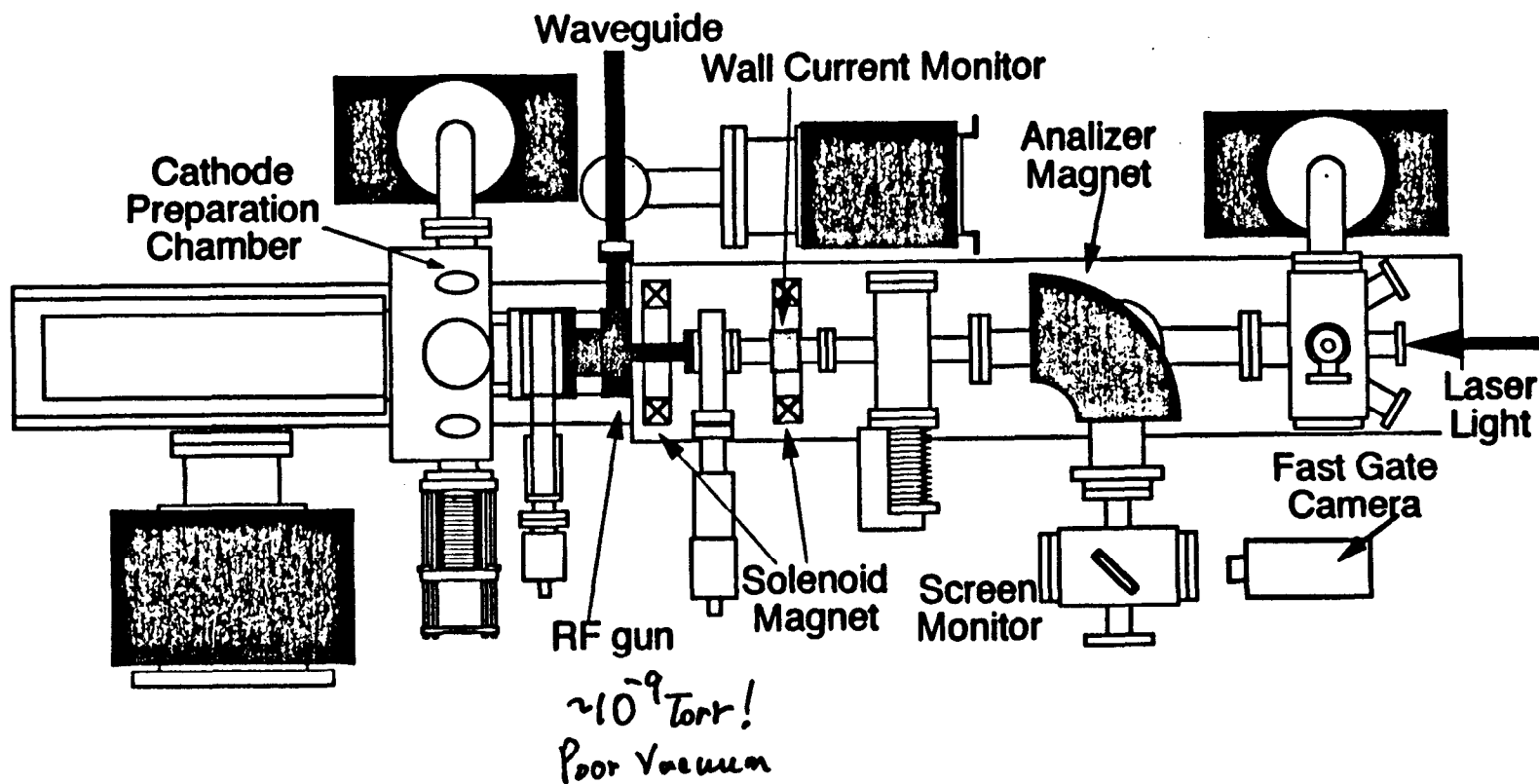
output (with W.F.S.)

## ② RF Gun



# RF Gun (H. Akiyama)

424



- March 1991 ,
- $2 \times 10^{10}$  / Bunch
  - 5.6 ns Spacing
  - 170 Bunch / Pulse ( $\approx 1 \mu\text{s}$  Macro Pulse width)
  - 10PS Bunch width (Emittance not measured)

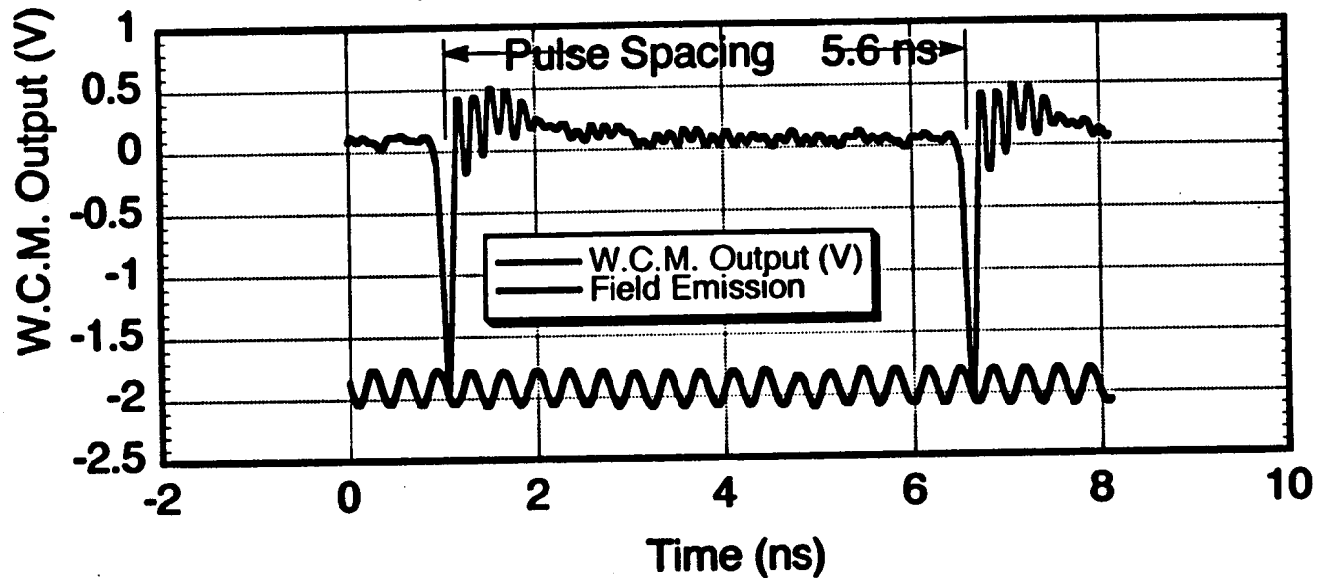


Figure Wall Current Monitor Output

- S-Band Single Cell  $40 \text{ MV/m} \rightarrow 900 \text{ keV}$
- Sb Cs Cathode + 530 nm Laser  $2 \text{ W}$  of Nd:YAG (10PS, 109uJ)

Cathod Test Chamber (K.Nishitani)

JUL / 1993

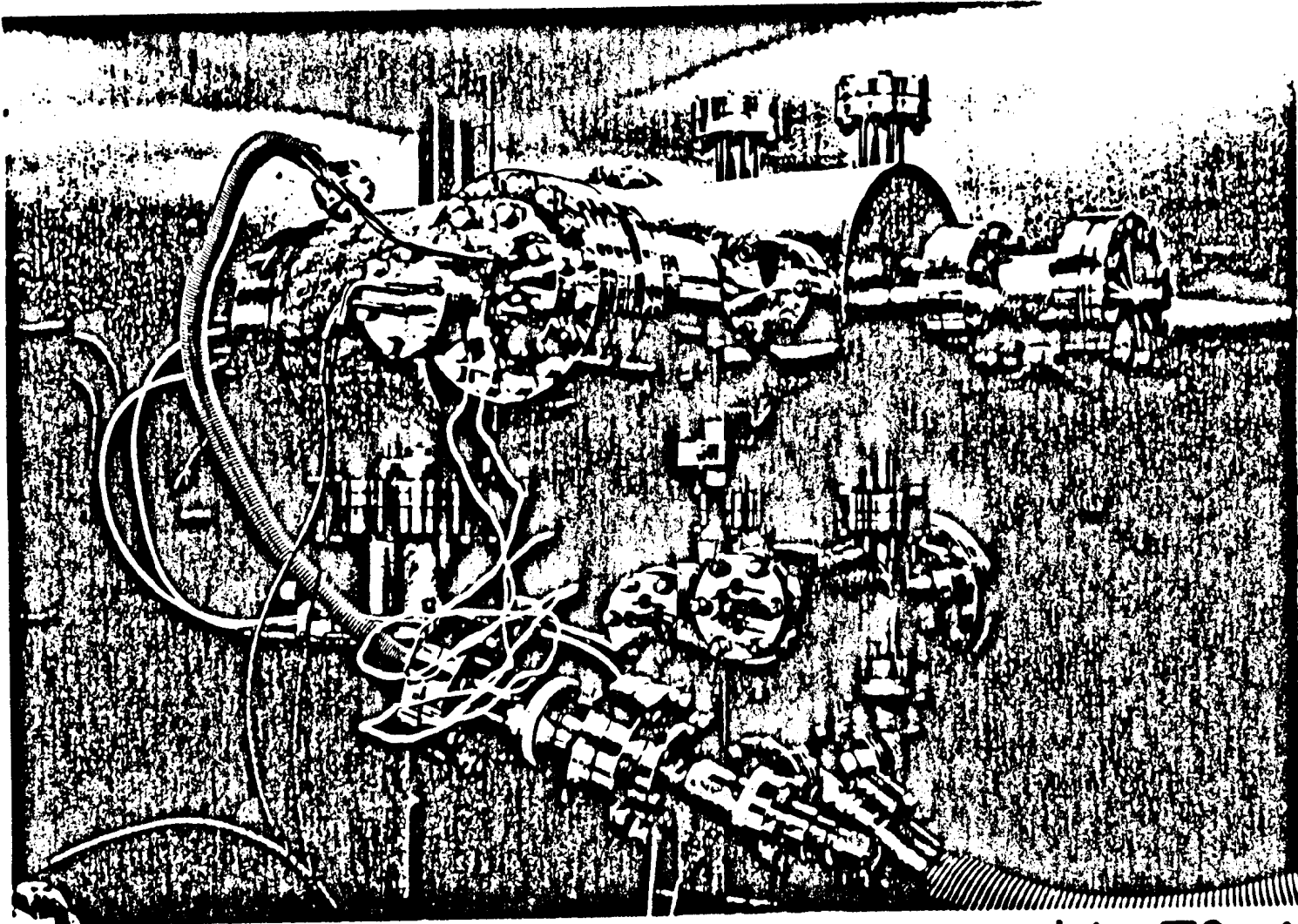
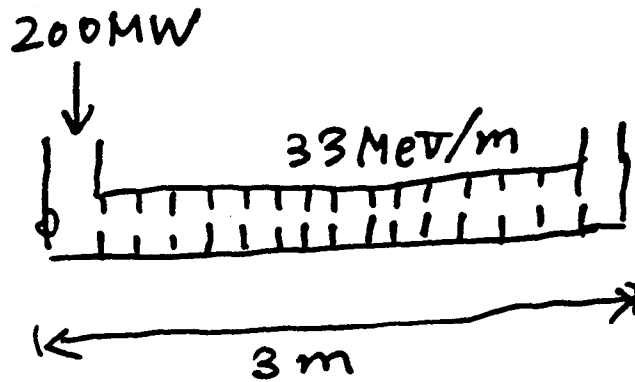


photo T.Omori



# Accelerator Structure of ATF Injector

By H. Matsumoto, S. Takeda, ---



① Material

Cu (Class-1, Hitachi)

② HIP (Hot Isostatic Pressing)

Ar-Gas

800°C

1200 kg/cm<sup>2</sup>

} reject "Oil"

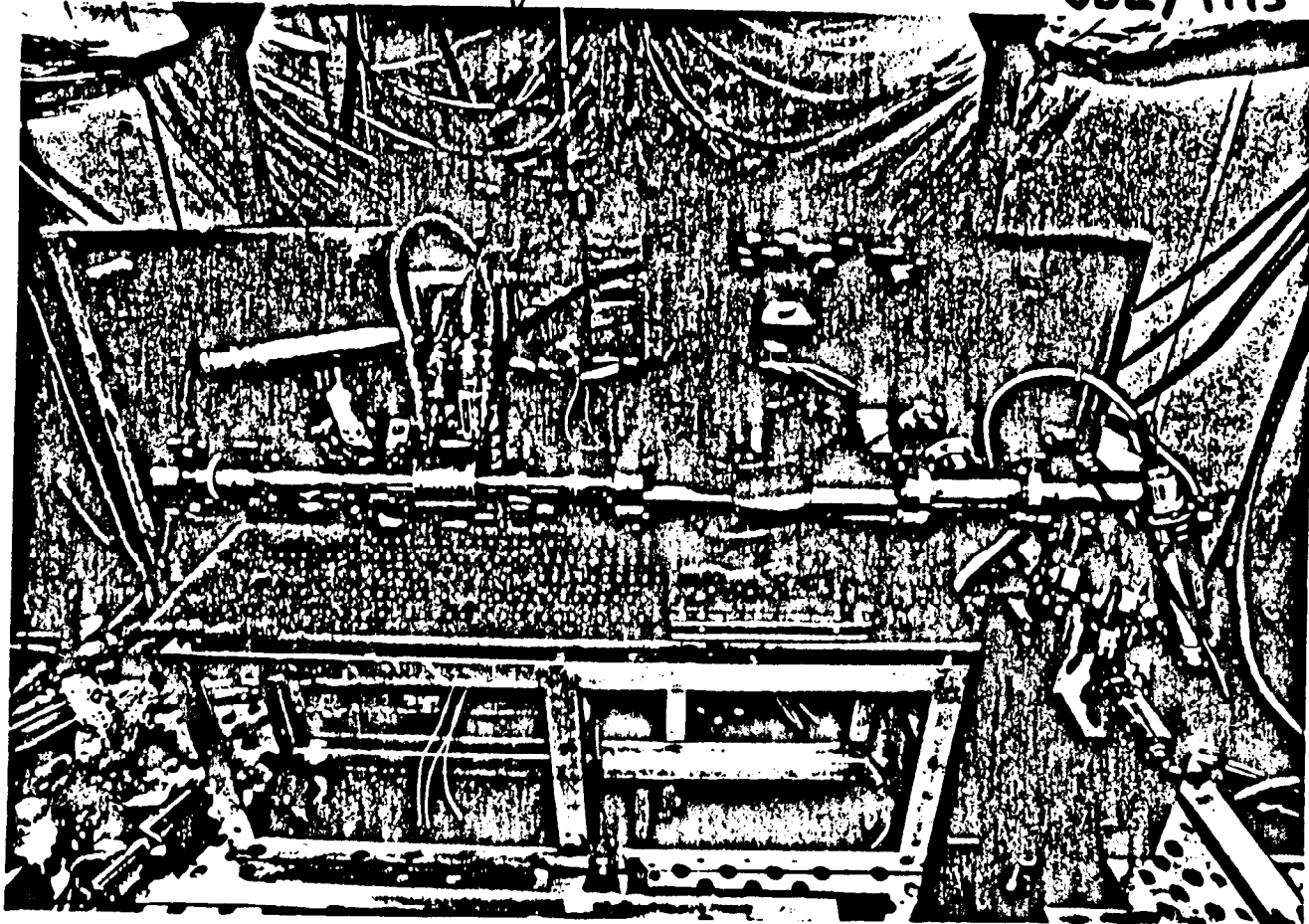
③ Clean

(Detail → LC93)

# Study of High Gradient Cavity (Dark Current)

↓ 5MW KLYSTRON

JUL / 1993

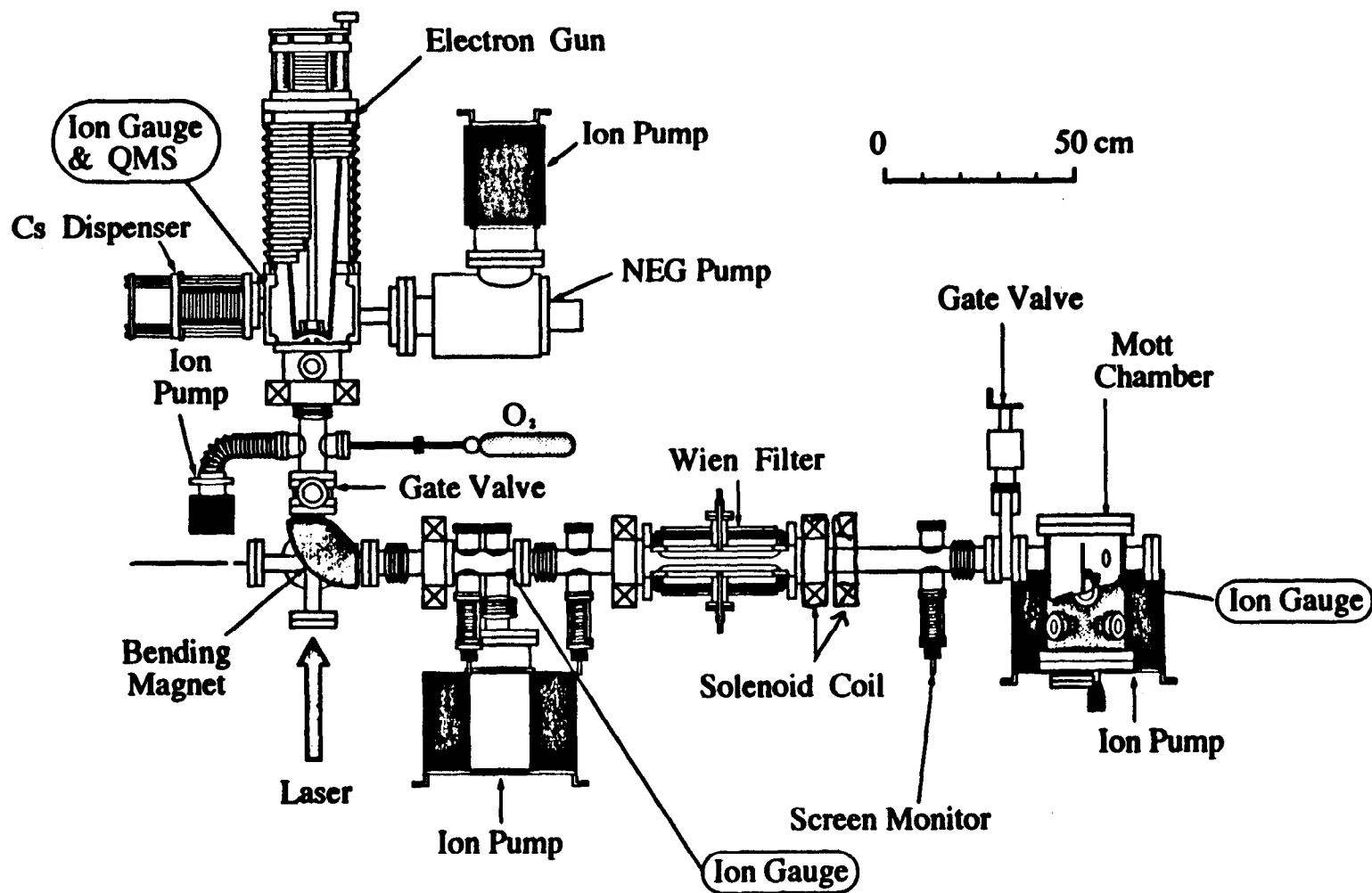


- + Material of Cu cavity
- \* Machining of Surface
- + Treatment, Assembling

↓ Reduce  
Field Emission

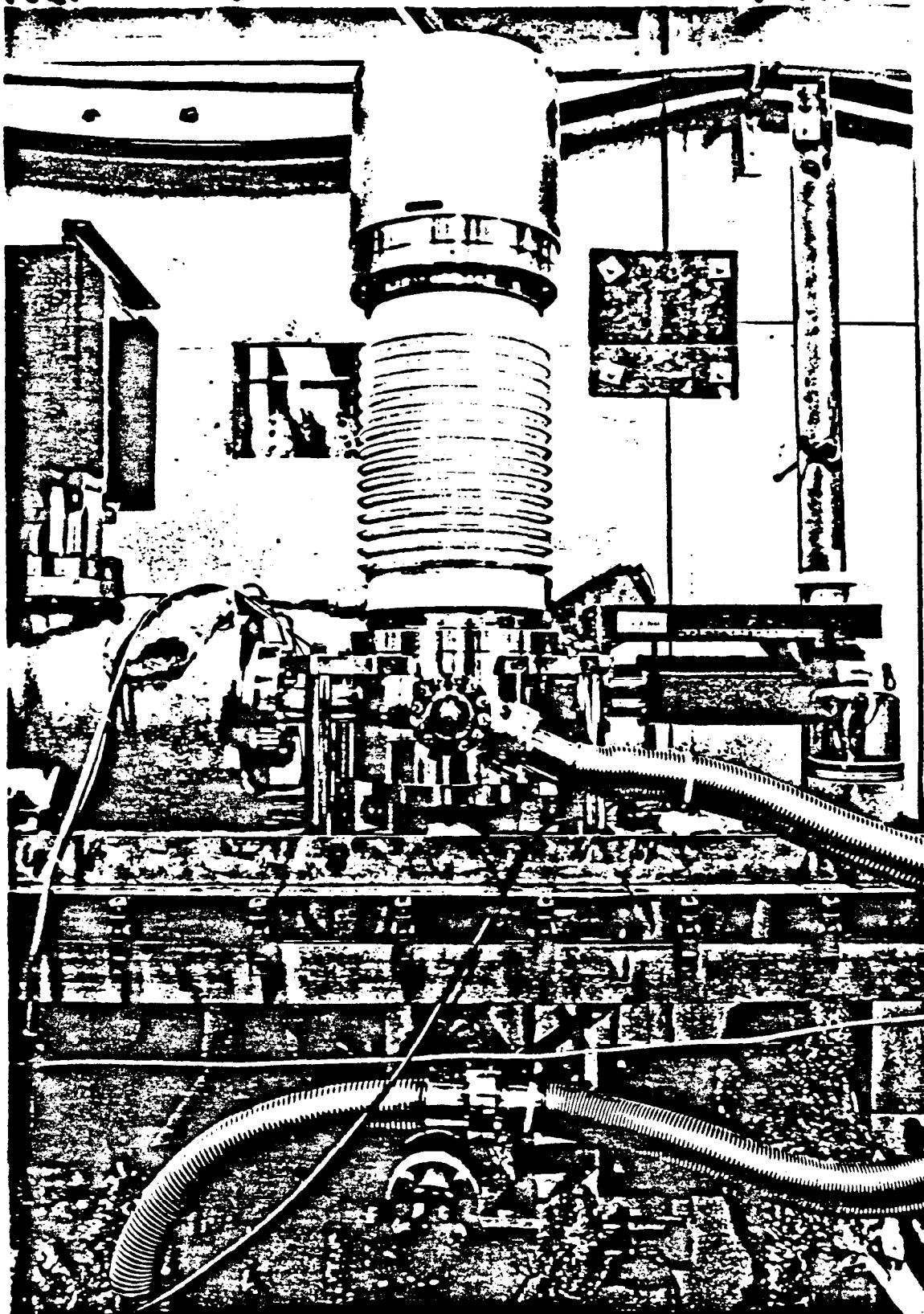
photo T. Omori

# Polarized Electron Source for JLC (k. Itoga)



Pol. e<sup>-</sup> Gun

JUL/1993

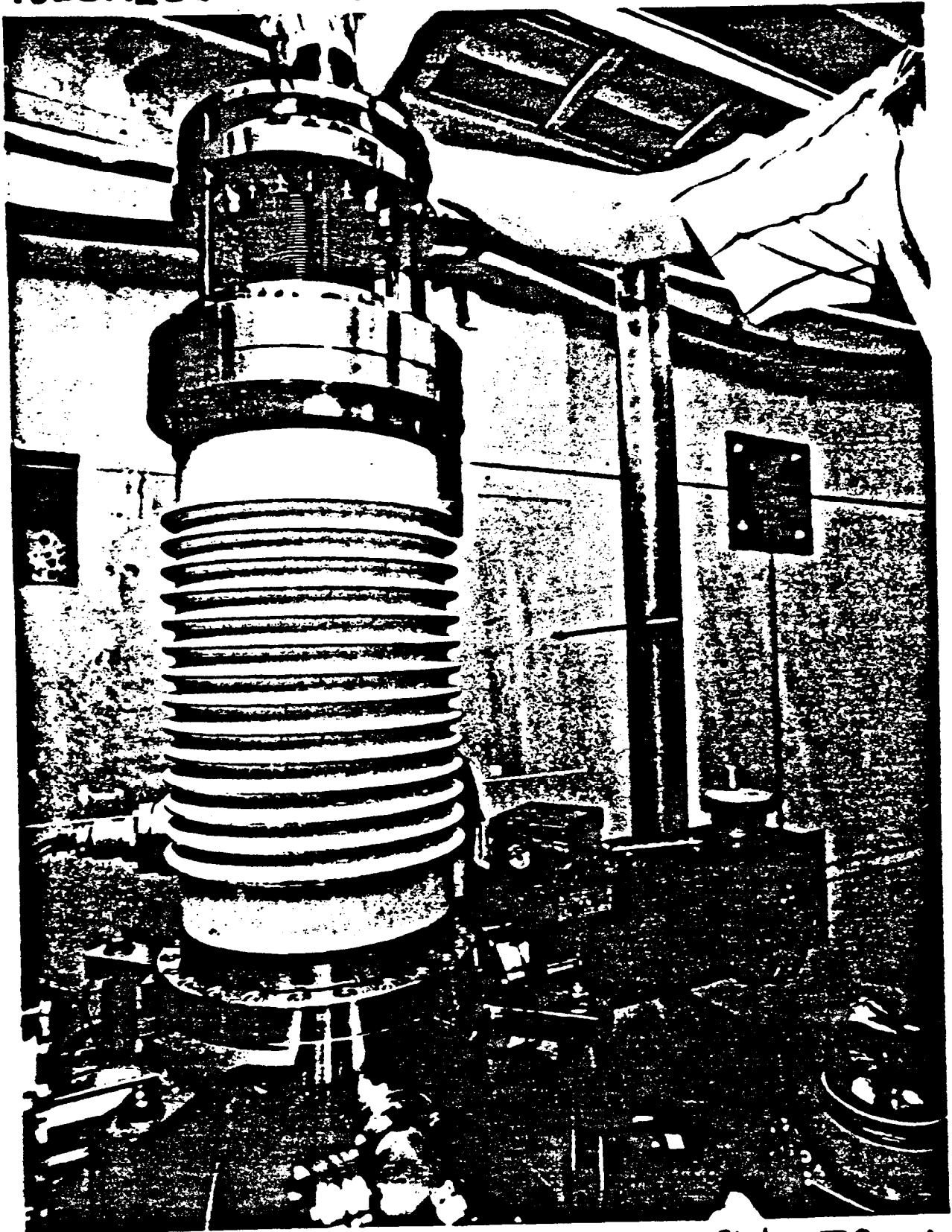


( 8x10<sup>-11</sup> Torr  
100 kV DC )

photo T.Omori

# Polarized Electron Gun

JUN./1993



# Polarized Electron Gun

APR. / 1993

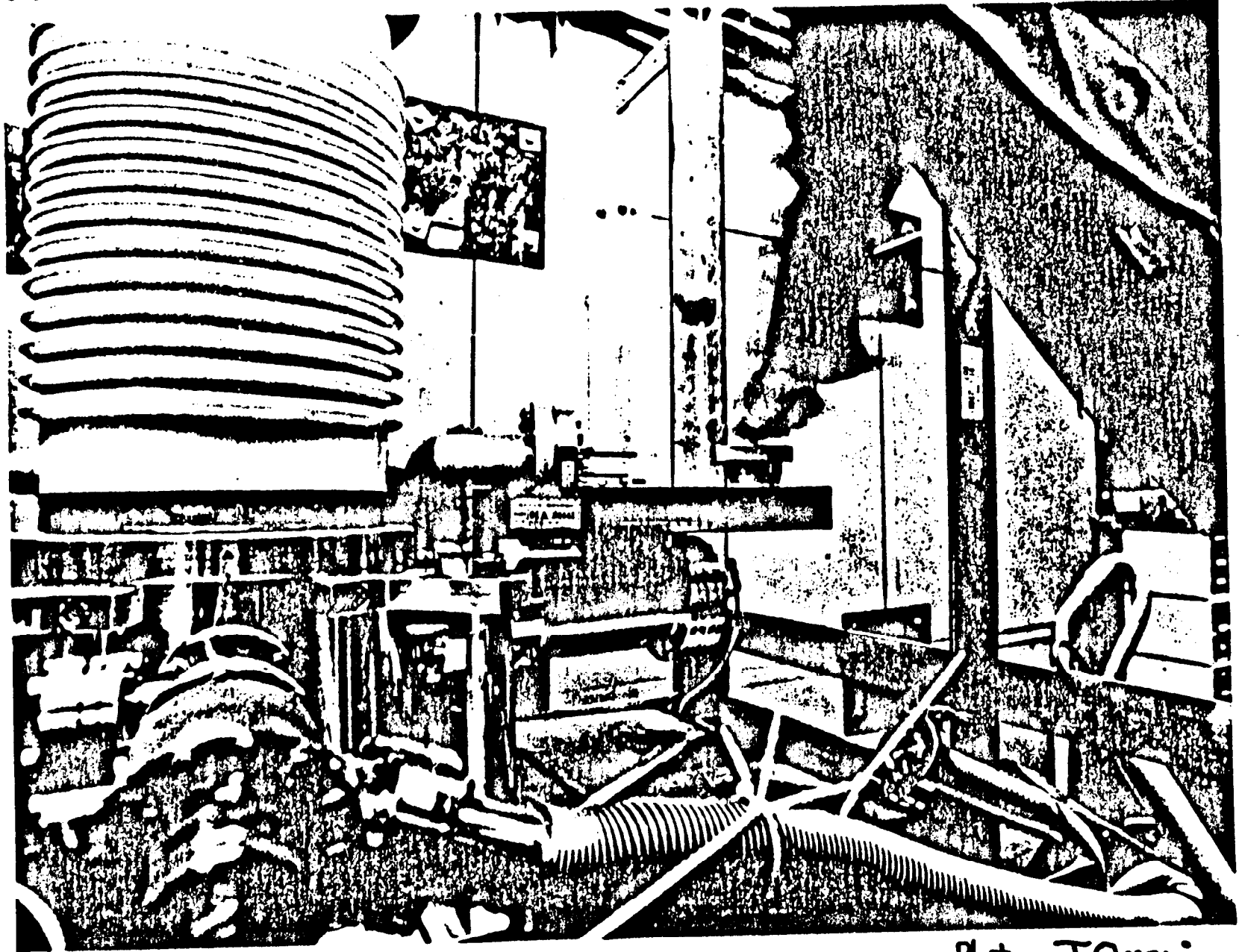
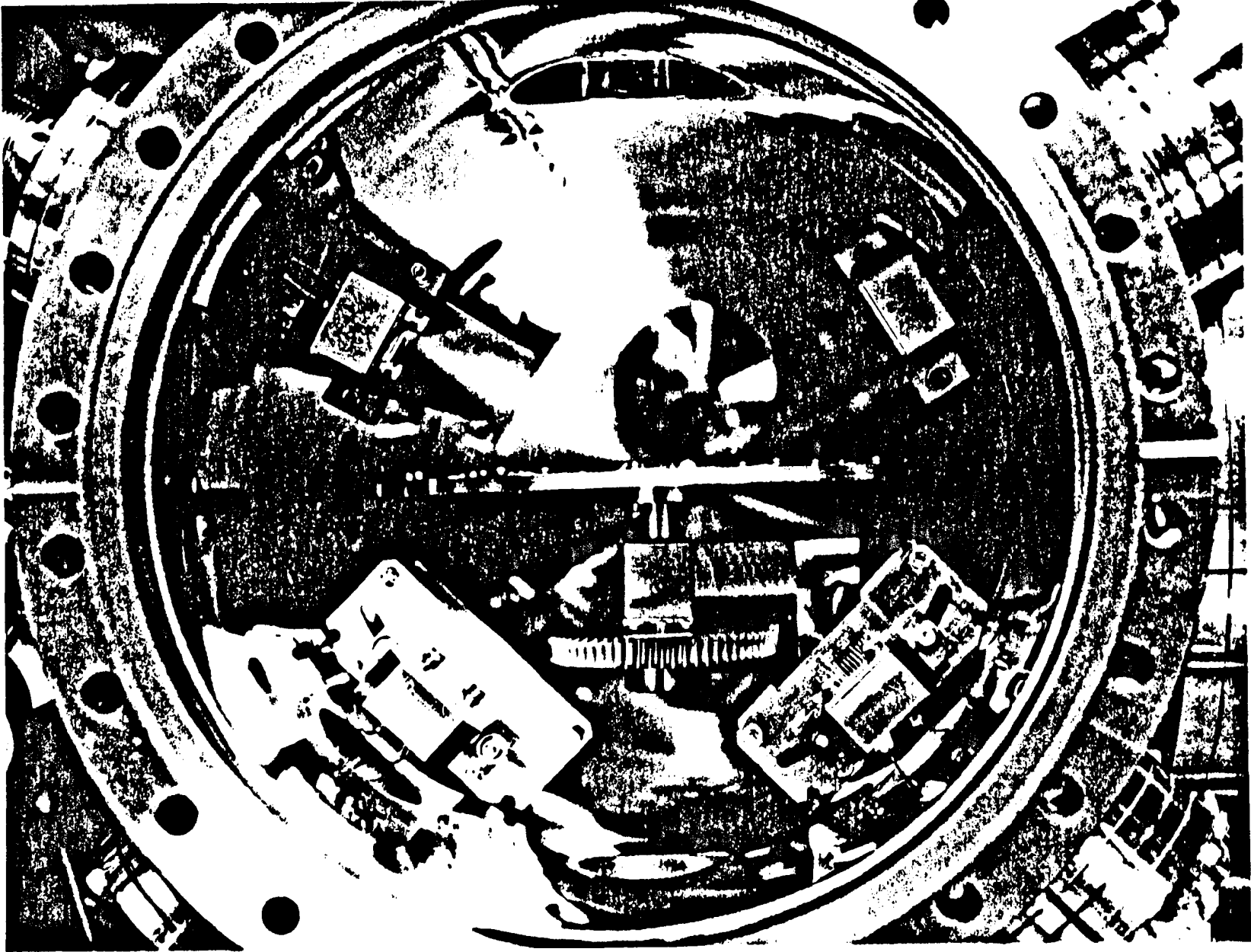


Photo T.Omori

Mott Analyser

JUN/1993



433

T. Omori

## Conclusions

- \* Single Bunch Polarized Source for Linear Collider

$$\text{(SLC)} \rightarrow \mathcal{L} \sim 10^{30} / \text{cm}^2 / \text{s}$$

- \* Next Linear Collider

$$\text{Luminosity} > 10^{33} / \text{cm}^2 / \text{s}$$

Multi Bunch

$$N_e \sim 10^{10}, 50 \sim 100 \text{ Bunches}$$

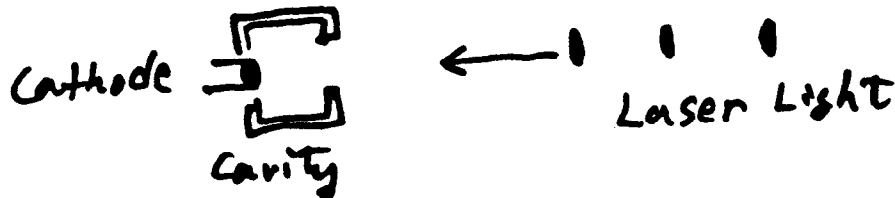
$$\rightarrow \text{Pulse Train} \sim 100 \text{ ns}$$

---

Heavy Loading, Short Pulse Train, High Stability

---

- ① Polarized RF Gun Proposed By Jim Glendenin



- ② "DC" Gun + Long Pulse Laser + SHBs

- ③ "DC" Gun + Pulse Laser



**Max Zolotarev  
SLAC**

**Effect of Radiation Trapping on Polarization of  
Photoelectrons from Semiconductors**

# Effect of Radiation Trapping on Polarization of Photoelectrons from Semiconductors

M. Zolotarev, A. Kulikov, and J.E. Clendenin

*Stanford Linear Accelerator Center  
Stanford University, Stanford, California 93409*

## Abstract

Radiation trapping is a well known effect in semiconductors as well as in atoms. Polarization of atoms by optical pumping is recognized to be limited by radiation trapping. The possibility that the polarization of photoemitted electrons from III-V semiconductors will be limited by radiation trapping is discussed.

## Introduction

Polarized electron sources based on photoemission from p-doped III-V semiconductors are now widely used in accelerators and other applications [1]. An extensive literature is available showing that the maximum polarization for unstrained materials under optimum conditions should be 50% [2]. This result is easily seen from an examination of Fig. 1 which shows relative transition probabilities (derived from Clebsch-Gordon coefficients) between the top of the valence band ( $P_{3/2}$  symmetry) and the bottom of the conduction band ( $S_{1/2}$  symmetry). For example, if the crystal is illuminated with right circularly polarized light ( $\sigma +$ ) with wavelength near the band gap [3], the electron polarization,  $P_e$ , will be

$$P_e = \frac{n_{\uparrow} - n_{\downarrow}}{n_{\uparrow} + n_{\downarrow}} = \frac{1/6 - 1/2}{1/6 + 1/2} = -1/2. \quad (1)$$

However, as was noted some time ago [4], the experimental data from all sources showed that the achieved polarization was distributed in two main groups, one centered at  $\sim 45\%$  and the other at  $\sim 30\%$ . The source of this depolarization was not completely understood.

Several models have been proposed to explain this depolarization, including interaction with the lattice, surface effects, interaction with surface Cs deposits, and doping effects. No single model proposed to date explains all the data.

Radiation trapping, which is discussed below, is a well known effect in semiconductors as well as in atoms. Since polarization of atoms by optical pumping is recognized to be limited by radiation trapping [5], it is surprising that the equivalent phenomena in semiconductors has not been discussed as a depolarization factor.

### **Radiation trapping**

Radiation trapping is reabsorption of photons emitted in the transition of electrons from the conduction to the valence band. The polarization of the emitted light will be a function of the emitted angle. As a result of the reabsorption of this emitted light, electrons will be excited into the conduction band spin states with the probabilities given in Fig. 1. If the size of the material is large enough, this process will result in a drop in the polarization of the conduction band electrons.

It is well known, that for particles with spin 1/2, the polarization is very stable and is difficult to change in processes like scattering. From this point of view, radiation trapping should be the main cause of the depolarization in photoemitters for which the thickness is at least comparable to the diffusion length, while thin photoemitters should have polarization close to 50%.

### **Simple self-absorption model**

A complete self-absorption model of the electron polarization in the crystal, which must include electron, hole, and polarized light diffusion, non-homogeneity of absorption light, and non-radiation decay, trapping, etc., is first of all mathematically difficult and secondly we don't yet know many of the necessary parameters. Thus we find it more useful to develop a semi-quantitative model that will describe this depolarization process in simple terms.

The inverse lifetime of an electron in the conduction band,  $1/\tau$  is given by

$$1/\tau = 1/\tau_r + 1/\tau_{nr}, \quad (2)$$

where  $1/\tau_r$  is the probability for electron transition from the conduction to the valence band with accompanying radiation of a photon. Since the refractive index of the crystal is rather high, we neglect losses of photons through the surface of the crystal. The second term on the right of Eq. (2),  $1/\tau_{nr}$ , represents all other possibilities for an electron to leave the conduction band. We divide these possibilities into two general processes, neither of which result in emission of photons energetic enough to excite electrons into the conduction band. Thus we let

$$1/\tau_{nr} = 1/\tau_D + 1/\tau_L, \quad (3)$$

where  $\tau_D$ , the average time for conduction-band electrons to diffuse to a surface, may be approximated by

$$\tau_D = \frac{d^2}{2D}. \quad (4)$$

Here  $D$  is the diffusion coefficient for electrons in the conduction band and  $d$  is the thickness of the crystal. It is assumed that  $d \ll (\text{surface area})^{1/2}$ . Electrons at the surface not escaping to vacuum are assumed to be trapped in surface states without accompanying radiation.

Electrons diffusing into the bulk of the crystal can be trapped in intermediate energy states created by impurities and other processes. The probability for these processes,  $1/\tau_L$ , can be expressed in terms of  $D$  and the electron diffusion length,  $l_D$ :

$$1/\tau_L = \frac{D}{l_D^2}. \quad (5)$$

We make the simplifying assumption that in steady-state conditions, the density of electrons in the conduction band is uniform.

With this assumption, a set of 2 rate equations describing the electron population of the polarization states in the conduction band can be written:

$$\begin{aligned}\frac{dn_{\downarrow}}{dt} + \frac{n_{\downarrow}}{\tau} - \frac{7}{12} \frac{n_{\downarrow}}{\tau_r} - \frac{5}{12} \frac{n_{\uparrow}}{\tau_r} &= \frac{3}{4} \dot{n}_{ph} \\ \frac{dn_{\uparrow}}{dt} + \frac{n_{\uparrow}}{\tau} - \frac{7}{12} \frac{n_{\uparrow}}{\tau_r} - \frac{5}{12} \frac{n_{\downarrow}}{\tau_r} &= \frac{1}{4} \dot{n}_{ph}\end{aligned}\quad (6)$$

The first term of the equations describes population change of the states with electron spin up and down orientations. The second term represents decay of the states. The next two terms characterize radiation trapping: 7/12 and 5/12 are the probabilities that the light emitted in radiation decay of particular spin state will excite an electron into the same state or into the opposite state respectively. The right side of the equations represents the absorption of the right circularly polarized light ( $\sigma+$ ) generated by an external source. All numerical coefficients are derived from the transition probabilities shown in Fig. 1.

The steady-state solution to these equations gives the electron polarization,  $P_e$ , as a function of  $\tau_r/\tau_{nr}$  :

$$P_e = -\frac{1}{2} \left( \frac{1}{1 + \frac{5}{6} \left( \frac{\tau_r}{\tau_{nr}} \right)^{-1}} \right) \quad (7)$$

Using Eqs. 3, 4 and 5 one can obtain:

$$\frac{\tau_r}{\tau_{nr}} = \tau_r \left( \frac{1}{\tau_D} + \frac{1}{\tau_L} \right) = \tau_r D \left( \frac{2}{d^2} + \frac{1}{l_D^2} \right) \quad (8)$$

For a very thin crystal,  $d$  goes toward zero, thus the parameter  $\tau_r/\tau_{nr}$  goes toward infinity, and consequently  $P_e$  goes toward -1/2. On the other hand, for a thick crystal,  $2/d^2$  can be neglected in Eq. (8), and thus the polarization reaches a value <50%. For the case of thick GaAs at room temperature,  $\tau_r/\tau_L \sim 1$  for doping concentrations  $>10^{18} \text{ cm}^{-3}$  [6]. Thus for thick GaAs,  $|P_e|$  approaches a saturated value of ~0.3.

For thick crystals, we can examine the dependence of the polarization on doping concentration and temperature. For high doping, both  $1/\tau_r$  and  $1/\tau_L$  are proportional to

doping concentration [6]. Thus for highly doped crystals,  $P_e$  to first order should be independent of doping concentration. The temperature dependence is discussed next.

### Temperature dependence

Experimentally it has been observed that the depolarization in thick semiconductor cathodes has a strong dependence on temperature. From Eq. (8), it is clear that for thick crystals, the temperature dependence of  $P_e$  is given by the temperature dependence of  $\tau_r/\tau_L$ . The probability for radiation decay,  $1/\tau_r$ , is proportional to the hole density,  $n_h$ :

$$1/\tau_r = An_h. \quad (9)$$

The hole density is given by the Boltzman distribution for ionized acceptors,

$$n_h = N_A e^{-\frac{\epsilon_A}{kT}}, \quad (10)$$

where  $N_A$  is the acceptor concentration,  $\epsilon_A$  the acceptor ionization energy, and  $T$  the temperature of the crystal. Thus, as the temperature is lowered, the radiation lifetime increases.

For high-doped material, to first order  $\tau_L$  has no strong dependence on temperature. It is assumed that  $1/\tau_L$  depends on the density of empty impurity states near the top of the band gap. The probability that at a given temperature an impurity state will be occupied is governed by the Boltzman distribution for that temperature. For band gap energies on the scale of 1 eV, i.e., for all III-V crystals, the states near the top of the band gap remain unfilled for all practical temperatures, and thus  $\tau_L$  as stated is essentially independent of temperature. Thus as the temperature is lowered, the radiation lifetime increases resulting in less radiation light and consequently less depolarization of thick photocathodes.

Thus for thick crystals, the temperature dependence of  $P_e$  is given solely by  $\tau_r$ .

## Comparison with experiment

Polarization measurements would be expected to conform to the model developed above only in the case of an NEA surface. An approximate guide to the affinity of the surface is given by the quantum efficiency, QE, defined as the ratio of emitted electrons to incident photons in vacuum. For highly doped GaAs, the electron scattering length as well as the depletion region width at the surface are  $\sim 10$  nm, while the photon absorption length and diffusion lengths for GaAs are about 1000 nm. Thus for an NEA surface,  $\sim 1\%$  of the conduction band electrons originate in the depletion region. Only these "hot" electrons can escape to vacuum when the surface barrier is high. Thus if  $QE \ll 1\%$ , the surface is PEA. In this case, the measured electron polarization should be high regardless of crystal thickness or temperature. On the other hand, if  $QE \gg 1\%$ , then the surface is NEA, and the measured polarization should follow our model rather closely. For QE on the order of 1%, one would expect some variation in the measured polarization that will depend on the details of the actual surface barrier.

A survey of representative polarization data for III-V crystals is given in Table 1. This data includes most if not all the published measurements of  $P_e$  for semiconductor photocathode polarized electron sources presently being used with high energy accelerators. The average of the 4 polarization measurements that can be associated with thick crystals is  $0.31 \pm 0.04$ , while the average of the 11 measurements using thin crystals or crystals operated at or near cryogenic temperatures is  $0.45 \pm 0.03$ , consistent with the conclusions of reference 4 mentioned earlier.

For NEA unstrained GaAs, the electron polarization given by Eq. (7) is plotted in Fig. 2 as a function of crystal thickness for several temperatures. For this curve, the temperature dependence for thick crystals is assumed for thin crystals as well. Also plotted is the experimental data of reference 11. It can be seen that the agreement between the measured values and the model is quite good. The distribution of measured polarization values in two main groups as mentioned earlier appears to be primarily the result of a distribution of crystal thicknesses and temperatures governed by practicality. Although this model simplifies a number of physical details, nevertheless it is sufficient to explain semi-quantitatively the polarization data available to us.

## References

1. J. Kessler, *Polarized Electrons*, 2nd ed., Springer-Verlag (1985); also L.S. Cardman, Nucl. Phys. **A546** (1992) 317.
2. Recently, III-V photocathode materials have been developed that remove the degeneracy between the  $m_j = 3/2$  and the  $m_j = 1/2$  states in the valence band at the  $\Gamma_8$  symmetry point, making  $P_e \gg 50\%$  possible if the correct wavelength of the excitation light is chosen. These materials use thin active layers and thus are relatively insensitive to the depolarization mechanism discussed here.
3. The wavelength must be long enough so as to not excite electrons from the split-off valence band.
4. C.K. Sinclair, in K. J. Heller, ed., *High-Energy Spin Physics*, AIP Conf. Proc. No. 187, (1988) 1412.
5. D. Peterson and L.W. Anderson, Phys. Rev. A **43** (1991) 4883.
6. H.C. Casey, Jr. and F. Stern, J. Appl. Phys. **47** (1976) 631.
7. C.K. Sinclair, *et al.*, in *H.E. Physics with Polarized Beams and Targets*, AIP Conf. Proc. 35 (1976) 424.
8. C.K. Sinclair, in *1980 Symp. on H.E. Phys. with Polarized Beams and Polarized Target*, Lausanne, Switzerland (1980).
9. C.K. Sinclair, *et al.*, IEEE Trans. Nucl. Sci. **NS-28** (1981) 2649.
10. S.F. Alvarado, *et al.*, Z. Phys. B **44** (1981) 259.
11. T. Maruyama, *et al.*, Appl. Phys. Lett. **55** (1989) 1686.
12. G.D. Gates, *et al.*, NIM **A278** (1989) 293.
13. G.D. Gates, *Polarized Electrons from GaAs for Parity Nonconservation Studies and Moller Scattering at 250 MeV*, Ph.D Dissertation, Yale University (1987), unpublished.
14. W. Hartmann, *et al.*, NIM **A286** (1990) 1.
15. T. Maruyama, *et al.*, J. Appl. Phys. **73** (1993) 5189.
16. Y. Takeda and T. Nakanishi in T. Hasegawa, *et al.*, eds., Proceedings of the Workshop on the Experiments by Polarized Proton and Electron Beams, KEK, Tsukuba, October 27-29, 1988, KEK Report 89-12 (1989), p. 134.
17. D.T. Pierce, *et al.*, Appl. Phys. Lett. **26** (1975) 670.
18. D.T. Pierce, *et al.*, Phys. Lett. **51A** (1975) 465.
19. F.C. Tang, *et al.*, RSI **57** (1986) 3004.
20. X.Q. Guo, *et al.*, RSI **61** (1990) 1858.
21. D.M. Crowe, *et al.*, J. Phys. B: At. Mol. Opt. Phys. **23** (1990) L325.



Table 1. Survey of Polarization Measurements<sup>a</sup>

Cathode Material	Thick-ness (μm)	Growth Tech-nique <sup>b</sup>	Face	Dopant	Concen-tration (cm <sup>-3</sup> )	Temp-erature (K)	Max. Polar-ization	Tech-nique	Ref.
GaAs		Bulk				77	0.43	Mott	7,8,9
		Bulk				300	~0.3	Mott	7,8,9
GaAs	0.2	MBE	111	Be	6 x 10 <sup>18</sup>	300	49		10
	to	MBE	100	Be	to	300	45		10
	0.5	MBE	110	Be	4 x 10 <sup>19</sup>	300	41		10
GaAs	0.9	MBE	100	Be	5x10 <sup>18</sup>	300	0.41	Mott	11
	0.7	MBE	100	Be	5x10 <sup>18</sup>	300	0.43	Mott	11
	0.425	MBE	100	Be	5x10 <sup>18</sup>	300	0.48	Mott	11
	0.2	MBE	100	Be	5x10 <sup>18</sup>	300	0.49	Mott	11
GaAs	>380		100	Zn	5x10 <sup>18</sup>	300	0.36	Moller	12,13
	>380		100	Zn	to 2x10 <sup>19</sup>		to 0.4	Moller	12,13
GaAsP	"thin"		100	Zn	4x10 <sup>19</sup>	300	0.44	Compton	14
AlGaAs	0.3	MBE	100	Be	5x10 <sup>18</sup>	300	0.43	Mott	15
GaAs		Bulk		Zn	~1x10 <sup>19</sup>		0.312	Mott	16
GaAs				Zn	1.3x10 <sup>19</sup>	10	0.45	Mott	17,18
GaAs	325	Bulk	100	Zn		300	0.27	Indirect	19,20,21

a A blank is used in the table below when the information isn't given in the indicated reference.

b "Bulk" is the process for growing thick crystals. Individual monolayers can be added to an appropriate substrate by molecular beam epitaxy (MBE). MBE active layers are almost always "thin" in the context of this paper.

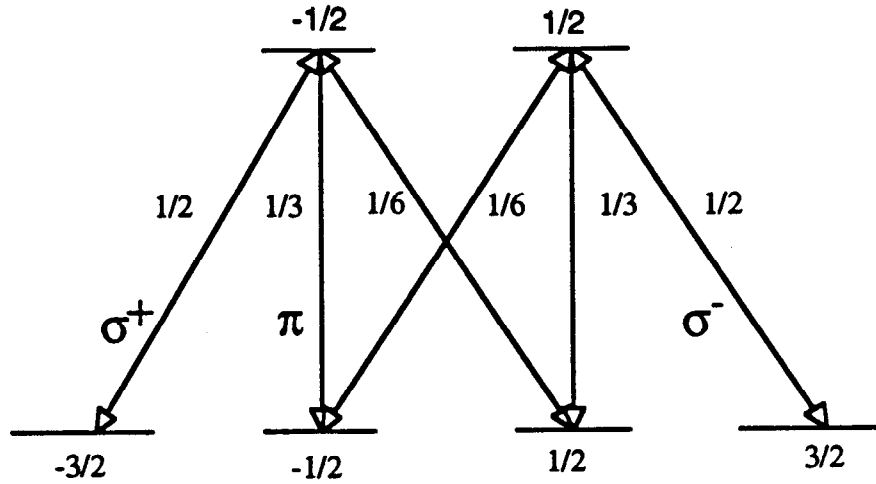


Fig. 1. Relative transition probabilities between  $J=3/2$  and  $J=1/2$  symmetry states.

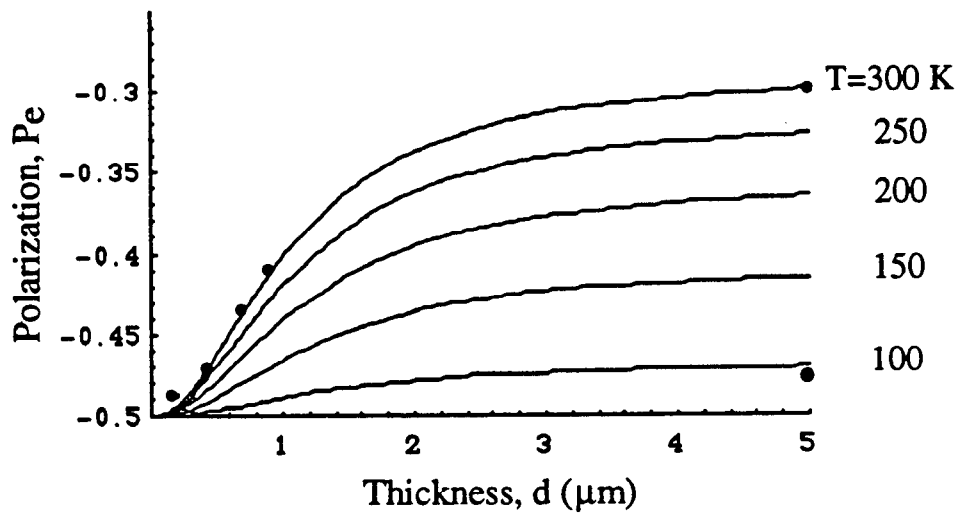


Fig. 2. Polarization vs. thickness. The solid line is a plot of Eq. (7) for several temperatures. The data points are all from reference 11.

**S. Zwickler  
U. Heidelberg**

**Energy Analysis of Electrons Emitted by a Semiconductor  
Photocathode**

# ENERGY ANALYSIS OF ELECTRONS EMITTED BY A SEMICONDUCTOR PHOTOCATHODE

*S.Zwickler, D.Habs, P.Krause, S.Pastuszka, D.Schwalm and A.Wolf*

Max-Planck-Institut für Kernphysik, Postfach 103980

and Physikalisches Institut der Universität,

D-69029 Heidelberg, Germany

*A.S.Terekhov*

Institute for Semiconductor Physics,

630090 Novosibirsk, Russia

## Abstract

In this paper we present measurements of the initial longitudinal energy spread  $\Delta E_{\parallel 0}$  of electrons emitted by a  $\text{In}_{0.46}\text{Ga}_{0.54}\text{As}_{0.06}\text{P}_{0.94}$ -photocathode with current densities up to  $20 \text{ mA/cm}^2$ . Furthermore we present a method of measuring the mean transverse energy  $\langle E_{\perp 0} \rangle$  making use of adiabatic invariants for the electron motion in a decreasing longitudinal magnetic field. It was successfully tested with an electron beam emitted by a thermocathode and will soon be used to measure  $\langle E_{\perp 0} \rangle$  for the photoelectrons, expected to be considerably smaller than for thermal electrons.

## 1. INTRODUCTION

High quality electron beams needed for electron cooling devices are characterized by small temperatures  $T_{\parallel} = m_e(\langle v_{\parallel}^2 \rangle - \langle v_{\parallel} \rangle^2)$  and  $T_{\perp} = \frac{m_e}{2}(\langle v_{\perp}^2 \rangle - \langle v_{\perp} \rangle^2)$ . These can be reduced significantly by using a cold semiconductor photocathode with negative electron affinity (NEA) instead of a thermocathode employed in present devices and by accelerating these electrons adiabatically [1]. In the last few years it was demonstrated by different groups [2,3] that continuous currents of about 1mA, needed for an electron cooling device with a photocathode, where the beam diameter is 2mm [4], can be produced with a lifetime of several weeks. If the semiconductor photocathode is precleaned in a separate chamber and brought into the ultrahigh vacuum gun chamber using a fast entry lock system [2],

reproducible quantum efficiencies (QE) of about 25% are reached without problems.

However, no systematic measurements concerning the initial longitudinal energy spread  $\Delta E_{\parallel 0} = \sqrt{\langle E_{\parallel 0}^2 \rangle - \langle E_{\parallel 0} \rangle^2}$  (that influences  $T_{\parallel}$ ) and the initial mean transverse energy  $\langle E_{\perp 0} \rangle$  (that influences  $T_{\perp}$ ) of the electrons emitted by a semiconductor photocathode were published until now. In contrast to a heated thermocathode, where  $\Delta E_{\parallel 0} = \langle E_{\perp 0} \rangle = k_B T_{cath}$ , it will be shown in this paper for current densities relevant for an electron cooling device that the energy spread of electrons emitted by a NEA-photocathode is not only determined by the temperature of the cathode  $T_{cath}$  but also strongly dependent on the NEA condition.

## 2. LONGITUDINAL ENERGY DISTRIBUTIONS AND $\Delta E_{\parallel 0}$

The experimental setup is presented in fig.1. The photocathode (1) is a lattice-matched InGaAsP epitaxial (111)A-layer, grown on (100) GaAs by liquid phase epitaxy and p-doped with Zn to  $5 \cdot 10^{18}/\text{cm}^3$ . It is activated to NEA by covering it with small amounts of Cs and  $\text{NF}_3$  in ultra high vacuum. The NEA-InGaAsP-photocathode has a better stability than a NEA-GaAs-photocathode; according to [2] this is caused by the higher band gap of  $E_g = 1.89\text{eV}$  (measured by photoluminescence).

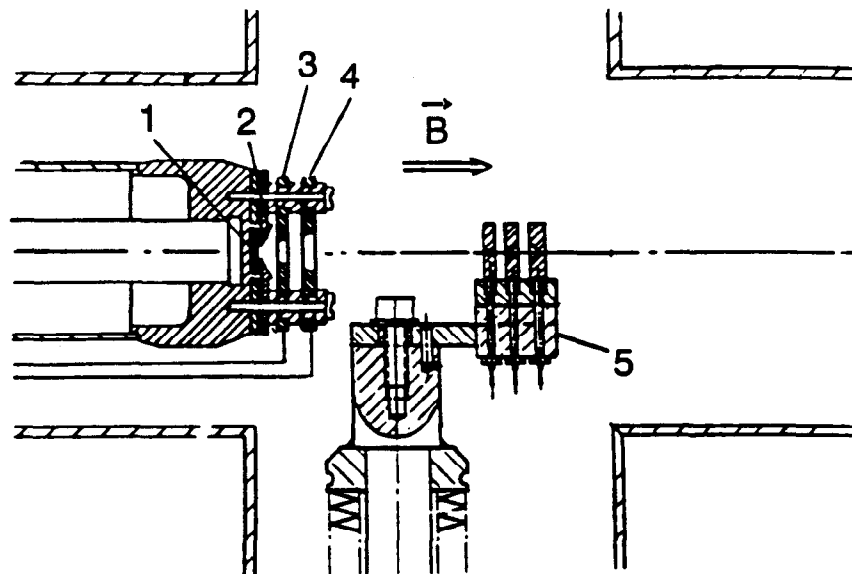


fig.1: Experimental setup with electron gun and retarding field energy analyzer (for further explanations see text).

The Pierce-electrode (2) with a hole diameter of 2 mm determines the diameter of the electron beam. The first anode (3) is situated 2mm in front of the cathode, the second anode (4) is kept on ground potential - therefore the electron energy is always given by the negative cathode voltage  $U_{cath}$ .

After leaving the cathode, the electron beam is guided in a longitudinal magnetic field of  $B=1400$  Gauss, produced by a pair of Helmholtz coils. This high field strength ensures that the relaxation of transverse energy into longitudinal energy is suppressed [1]. A 3-plate retarding-field energy analyzer (5), moveable in transverse direction, is located at a distance of 4 cm in front of the cathode to measure the longitudinal energy distribution  $f(E_{||})$  of the electron beam. Using a  $25 \mu\text{m}$  pinhole in the entrance diaphragm, only a  $10^{-4}$  fraction of the beam is analyzed. The collector current  $I_{coll}$ , detected on the third plate as a function of the retarding voltage  $U_{ret}$  on the second plate, gives the integrated electron distribution curve (EDC). The differential signal is obtained online via lockin-technique. Both voltages  $U_{cath}$  and  $U_{ret}$  were produced by batteries to avoid voltage ripple and are monitored continuously with differential voltmeters (accuracy 0.5meV).

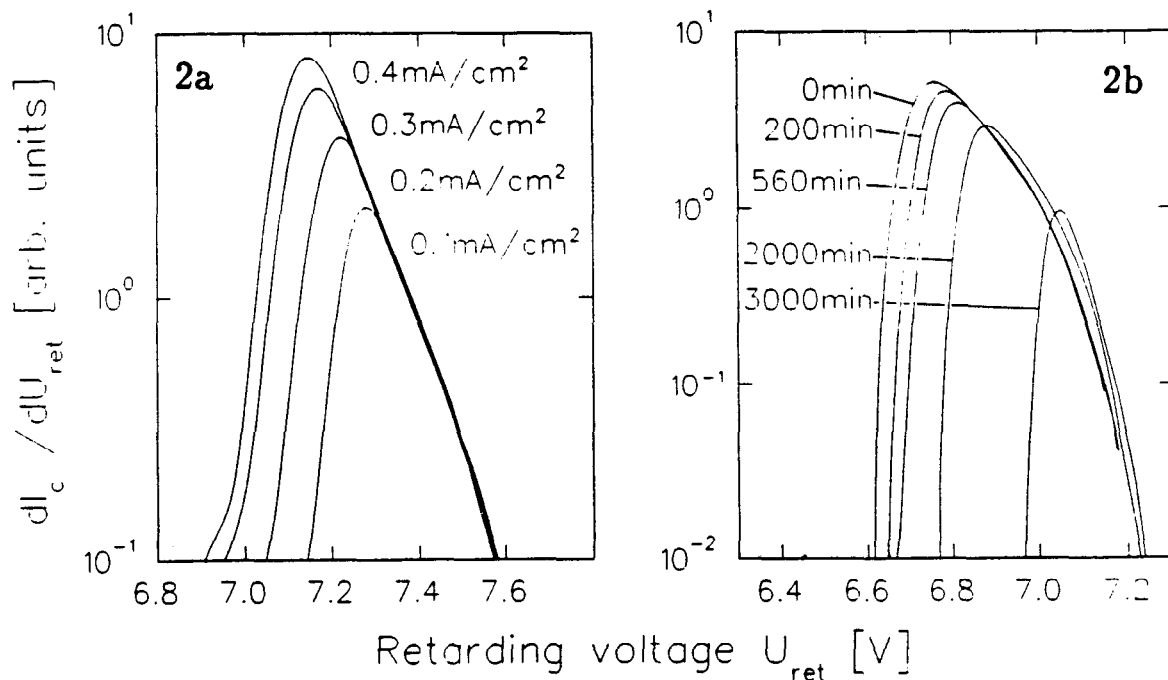


fig.2: Longitudinal EDCs measured for electrons produced a) by a thermocathode at different current densities and b) by the  $\text{In}_{0.46}\text{Ga}_{0.54}\text{As}_{0.06}\text{P}_{0.94}$ -photocathode at different aging times.

Prior to the experiments with the NEA-photocathode, the system was tested with an electron beam produced by a conventional thermocathode. EDCs for four different currents of the thermocathode are presented in fig.2a in a semilogarithmic plot. As the gun is operated in space charge limitation, the mean energy of the electron beam decreases with increasing current: the potential produced by the space charge plasma directly in front of the cathode acts as a low energy cut-off [5]. Due to the strong magnetic field, the small current density (maximum  $0.4\text{mA}/\text{cm}^2$ ) and the low kinetic energy ( $\approx 7\text{eV}$ ) of the extracted electron beam, the energy distributions  $f(E_{\parallel 0})$  of the emitted electrons are not substantially affected by relaxation processes [1]. Thus we have for the distribution measured by the retarding field analyzer  $f(E_{\parallel}) \approx f(E_{\parallel 0})$  and  $\Delta E_{\parallel} \approx \Delta E_{\parallel 0}$ . Therefore all EDCs have the same asymmetric exponential shape.

As the main part of the longitudinal energy  $E_{\parallel}$  is distributed proportional to  $\exp(-E_{\parallel}/k_B T_{cath})$ , it is possible to determine  $k_B T_{cath}$ ; the deduced value of  $98 \pm 2\text{meV}$  is in very good agreement with pyrometer measurements. The energy spread  $\Delta E_{\parallel} = \sqrt{\langle E_{\parallel}^2 \rangle - \langle E_{\parallel} \rangle^2}$  for each curve is  $\Delta E_{\parallel} \approx 102\text{meV}$  which also agrees with  $k_B T_{cath}$ .

The EDCs of photoelectrons produced by illuminating the photocathode, held at room temperature, with  $30\mu\text{W}$  emitted by a single-mode HeNe-Laser ( $h\nu = 1.96\text{eV} \approx E_G$ ) are shown in fig.2b. Again the current densities are very small (between 3 and  $30\mu\text{A}/\text{cm}^2$ ) so that the EDCs reflect the longitudinal energy distributions of the electrons leaving the cathode  $f(E_{\parallel}) \approx f(E_{\parallel 0})$ ,  $\Delta E_{\parallel} \approx \Delta E_{\parallel 0}$ . For the measurement shown in fig.2b the electron gun was operated in the current limited regime (both anodes are grounded) and the different current densities are obtained after different aging times (indicated in fig.2b) of the activated photocathode. Aging is caused by pollution of the activated surface by components of the residual atmosphere which leads to an increase of the vacuum level (decrease of NEA and QE) that acts as a low energy cut-off. Due to this aging the photocathode has a so called 'dark' lifetime of about two days. Subsequent reactivations to the initial maximum NEA are possible by recesiation. The left curve in fig.2b (0min), measured after activating the cathode to highest NEA and QE, is rather broad ( $\Delta E_{\parallel} \approx 110\text{meV}$ ). When NEA and QE get smaller, the EDCs become narrower (down to  $\Delta E_{\parallel} \approx 48\text{meV}$ ).

Comparison of the EDCs shown in fig.2a and fig.2b reveals a basic difference between thermo- and photocathode: the longitudinal energy spectra

of the emitted photoelectrons do not have an exponential high energy slope. Hence the widths  $\Delta E_{\parallel}$  of these EDCs are not constant but they mainly depend on the potential (height of vacuum level) that the electrons have to overcome before they leave the cathode. Only in the case of very small NEA the slope of the EDC is exponential and  $T_{cath}$  as well as the photonenergy has a substantial influence on  $\Delta E_{\parallel 0}$ , for example  $\Delta E_{\parallel 0} \approx 25\text{meV}$  at  $T_{cath} = 150\text{K}$  and  $h\nu = 2\text{eV}$ .

The explanation for the non-exponential shape of the EDCs is energy-loss of the photoelectrons during their transport through the band bending region. The only problem is to explain this energy loss by inelastic scattering: neither phonon-emission, nor electron-hole scattering, nor excitation of surface plasmons in the hole-plasma near the internal boundary of the band bending region, nor their combination are fast enough to explain the measured large low energy intensities of the EDCs. To overcome these difficulties, a strong reflection of the photoelectrons at the surface of the semiconductor was proposed [6]. This reflection is caused by some very narrow barrier which lies near the semiconductor surface and may include the activation layer. By introducing this reflection layer, the energy loss of electrons in the band bending region can be explained by accumulating very high path lengths due to multiple reflection at this barrier. With this model it is possible to explain every measured lineshape of EDCs: it is only necessary to design a surface barrier with appropriate reflection and transmission coefficient depending on the electrons energy.

Although this concept is well accepted and has been used by many workers to calculate the emission properties of NEA photocathodes, it is faced with different problems. If the reflection coefficient is high enough, surface quantized states appear in the band bending region above and below the vacuum level [7]. The energy positions of these states depend on the width of the bandbending region and, hence, on the doping level. The presence of these states must strongly influence the energy loss in this region and therefore the EDC. However, up to now no one observed some features from different semiconductor photocathodes that show the presence of these surface states. Unfortunately direct measurements of the proposed semitransparent barrier are not developed until now and there is no experimental evidence for the presence of such a layer.

On the other hand, the measured transformations of the EDCs due to natural degradation presented in fig.2b and in other publications [8,9] strongly support the negligible influence of surface reflections on the most



part of the energy distribution. It is not possible to find any physical reason which permits to explain the absence of any changes in the most part of the EDCs when the vacuum level is increased due to surface contamination. We agree that the lineshape of the EDCs in the vicinity of the low energy cutoff may be governed by the energy dependence of surface reflection (or transmission), but this small part of the energy spectrum does not reflect the energy loss process in the bandbending region.

The EDCs in fig.2 measured after 2000min and 3000min demonstrate, that for long aging time, when the vacuum level cuts off most part of the EDC, the residual part of the energy distribution begins to change: the negative slope of the high energy tail and the probability of the electrons from this energy region to escape into vacuum increases. The same behavior was observed for GaAs [9]. This transformation of the EDC shows, that the energy loss inside the band bending region decreases. It is impossible to explain this decrease by a variation of a 'surface reflection coefficient', because the reflection coefficient should increase when the thickness of the surface contamination increases and the NEA reaches a value of zero. Therefore we conclude that there is no reflecting barrier near the surface so that the photoelectrons loose their energy during a single-pass through the band bending region. To explain the large energy loss during this pass we propose a new mechanism of transport and fast energy loss inside the band bending region. It is based on enhancement of phonon emission probabilities due to violation of the momentum conservation law. This violation is caused by strong continuous momentum scattering of photoelectrons by the unscreened potential fluctuations of randomly distributed impurities and defects. The amplitude of these spatial fluctuations is high because the mean distance between impurities and defects is of the same order of magnitude as the width of the band bending region (for doping concentrations of  $10^{18} - 10^{19} \text{cm}^{-3}$ ).

We measured the same non-exponential EDCs if the gun with photocathode was operated in space charge limitation. This important result shows that the electrons do not thermalize in the space charge region before they leave it. Thus it is very probable that also no thermalization between the relatively high longitudinal temperature and the expected small transverse temperature of the electrons occurs in the spacecharge region.

One of the aims of these experiments was to determine  $\Delta E_{||0}$  for current densities used in an electron cooling device. Therefore the photocathode ( $T_{cath}=150K$ ) was illuminated with 30mW emitted by a single mode dye-laser ( $h\nu=2.2eV$ ),  $U_{cath}$  was set to -100V and the current was extracted in space charge limitation. Currents of about 1mA were produced with a lifetime of 10h. This lifetime is sufficient to ensure stable conditions during the measurement of the EDCs. Their  $\Delta E_{||}$  are plotted as a function of the current density in fig.3 (dots).

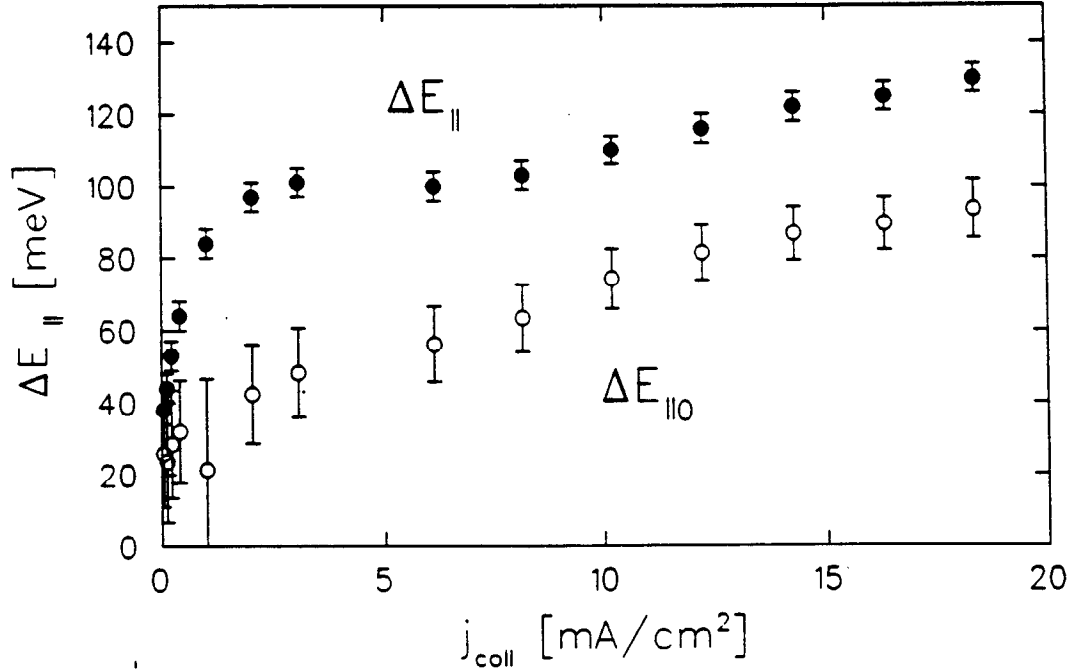


fig.3: Measured energy widths  $\Delta E_{||}$ (●) and deduced original widths  $\Delta E_{||0}$ (○) for different electron current densities emitted by the InGaAsP-photocathode.

Due to the high kinetic energy  $E_{kin}$ , relaxation of potential energy [1] in the accelerated beam already leads to a substantial energy broadening at current densities as low as 0.2mA/cm<sup>2</sup>. Thus the originally asymmetric EDCs displays a Gaussian shape and the measured width  $\Delta E_{||}$  is larger than  $\Delta E_{||0}$  according to [1]:

$$k_B T_{||} = \frac{(\Delta E_{||})^2}{2E_{kin}} = \frac{(\Delta E_{||0})^2}{2E_{kin}} + 2\langle E^{Relax} \rangle, \quad 2\langle E^{Relax} \rangle = C e^2 n^{\frac{1}{3}}$$

$\langle E^{Relax} \rangle$  is the mean relaxed potential energy in the rest frame,  $n$  the electron density and  $C$  a value between 0 and 1.3, depending on the number of plasmaoscillations  $n_{osc}$ , the electrons experienced on their flight to the retardation analyzer;  $C$  is a constant of about 0.7 for a nonadiabatically

accelerated beam if  $n_{osc}$  is larger than one [1]. In our setup the flight time is very short and  $n_{osc}$  is smaller than one for current densities below  $10\text{mA}/\text{cm}^2$ . To determine  $C$ , we measured  $\Delta E_{\parallel}$  as a function of  $n$  for an electron beam emitted by the thermocathode using the upper formula and  $\Delta E_{\parallel 0} = 97\text{meV}$ .

The deduced widths  $\Delta E_{\parallel 0}$  for electron beams emitted by the photocathode is shown in fig.3 (circles). The situation is very similar to that shown in fig.2b; if the majority of the electrons lifted to the conduction band are not emitted because they are prevented from leaving the cathode by the vacuum level or by the space charge potential,  $\Delta E_{\parallel 0}$  is rather small. By reducing this potential, the emitted current and  $\Delta E_{\parallel 0}$  increases. Note that even at current densities of  $20\text{mA}/\text{cm}^2$   $\Delta E_{\parallel 0}$  is smaller than  $100\text{meV}$ , i.e.  $\Delta E_{\parallel 0}$  does not exceed the initial energy spread of electrons from a thermocathode. The longitudinal temperature  $T_{\parallel}$  of an electron beam with energies higher than  $E_{kin} \approx 1\text{keV}$ , generated by a semiconductor photocathode as well as a thermocathode, is therefore determined by the mean relaxed energy in the beam. This can be strongly reduced by adiabatic acceleration [1], if the electron beam is guided in a strong longitudinal magnetic field.

### 3. MEAN TRANSVERSE ENERGY $\langle E_{\perp 0} \rangle$

In a proper accelerated electron beam, guided in a constant longitudinal magnetic field, the transverse temperature  $k_B T_{\perp}$  is equal to the initial mean transverse energy  $\langle E_{\perp 0} \rangle$  of the electrons. The great advantage of a cooled semiconductor photocathode in contrast to a heated thermocathode is a small  $\langle E_{\perp 0} \rangle$ ; if the tangential component of the electrons momentum is conserved when they cross the interface between crystal and vacuum (like in UPS and XPS experiments),  $\langle E_{\perp 0} \rangle$  is expected to be as small as  $1\text{meV}$  due to the small effective mass of the electrons inside the semiconductor [7].

All experiments concerning  $\langle E_{\perp 0} \rangle$  [7,10,11,12] measured the angular distribution of the emitted electrons but could not take into account space charge effects in the electron beam. Their results differ extremely ( $1\text{meV} < \langle E_{\perp 0} \rangle < 120\text{meV}$ ) and were never compared with measurements of the well known  $\langle E_{\perp 0} \rangle$  of a thermocathode. We have developed a technique for measuring  $\langle E_{\perp 0} \rangle$  with an accuracy of  $3\text{meV}$  independently of any spacecharge and relaxation effects.

For these measurements the distance between cathode and analyser (see

fig.1) is increased to 26cm. Moreover, the longitudinal magnetic field  $\vec{B}$ , produced by three pairs of magnetic coils, decreases in a defined way (see fig.4) from  $\vec{B}_0$  (at the cathode position) to  $\vec{B}_a$  (at the analyzer position).

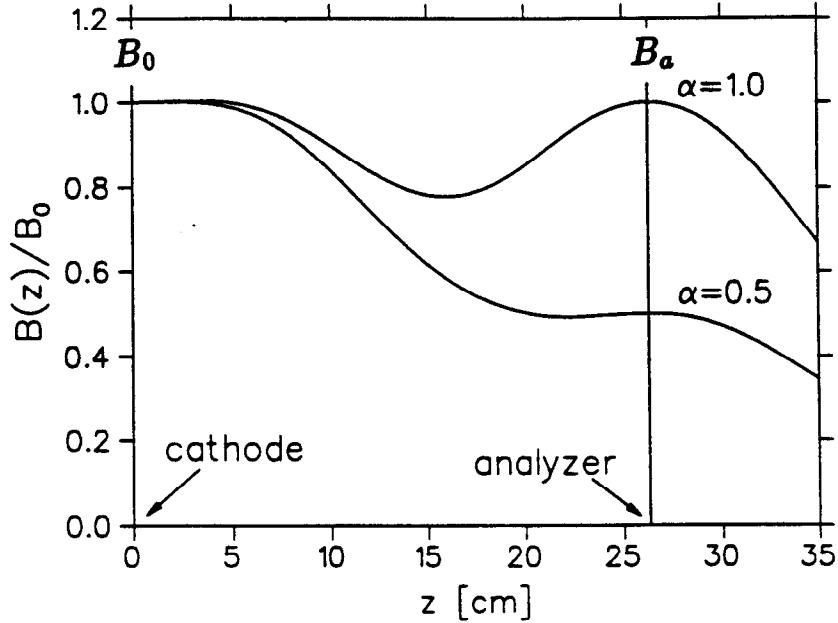


fig.4: Different field structures used for an adiabatic expansion of the electron beam.

The ration  $\alpha = B_a/B_0$  can be varied between 1 and 0.5 with  $B_0 = 1400\text{G}$ . As the electron beam expands adiabatically [13], the mean transverse energy  $\langle E_{\perp} \rangle$  divided by  $B$  is a constant of motion. Adiabatic expansion means, that the change in the magnetic field acting on the electron during one gyration orbit is very small compared to the total field so that the spiral length  $\lambda_c = \frac{eB}{2\pi m v_{\parallel}}$  of the electron divided by the magnetic field  $B_z$  is much smaller than  $dB/dz$ :

$$\left(\frac{dB}{dz}\right) \cdot \frac{\lambda_c}{B} \ll 1$$

From the energy conservation law  $\langle E_{\perp 0} \rangle + \langle E_{\parallel 0} \rangle = \langle E_{\perp} \rangle + \langle E_{\parallel} \rangle$  it follows that the mean longitudinal energy of the electron beam at the analyzer position  $\langle E_{\parallel a} \rangle$  increases proportional to  $(1-\alpha)$ :  $\langle E_{\parallel a} \rangle - \langle E_{\parallel 0} \rangle = (1 - \alpha)\langle E_{\perp 0} \rangle$ . The change of the mean longitudinal energy  $\langle E_{\parallel a} \rangle - \langle E_{\parallel 0} \rangle$  can be measured with an error smaller than 1.5meV and thus  $\langle E_{\perp 0} \rangle$  can be deduced.

In fig.5  $\langle E_{\parallel a} \rangle$  is plotted as a function of  $B_a/B_0$  for two different temperatures of the heated thermocathode,  $T_{cath}=1070\text{K}$  (●) and  $T_{cath}=1150\text{K}$  (○).

From the slope of the fitted curves it is possible to deduce  $\langle E_{\perp 0} \rangle$  with an error of 3meV, which is in very good agreement with  $k_B T_{cath}$  for both curves. Corresponding measurements of  $\langle E_{\perp 0} \rangle$  for InGaAsP- and also for GaAs-photocathodes are in progress.

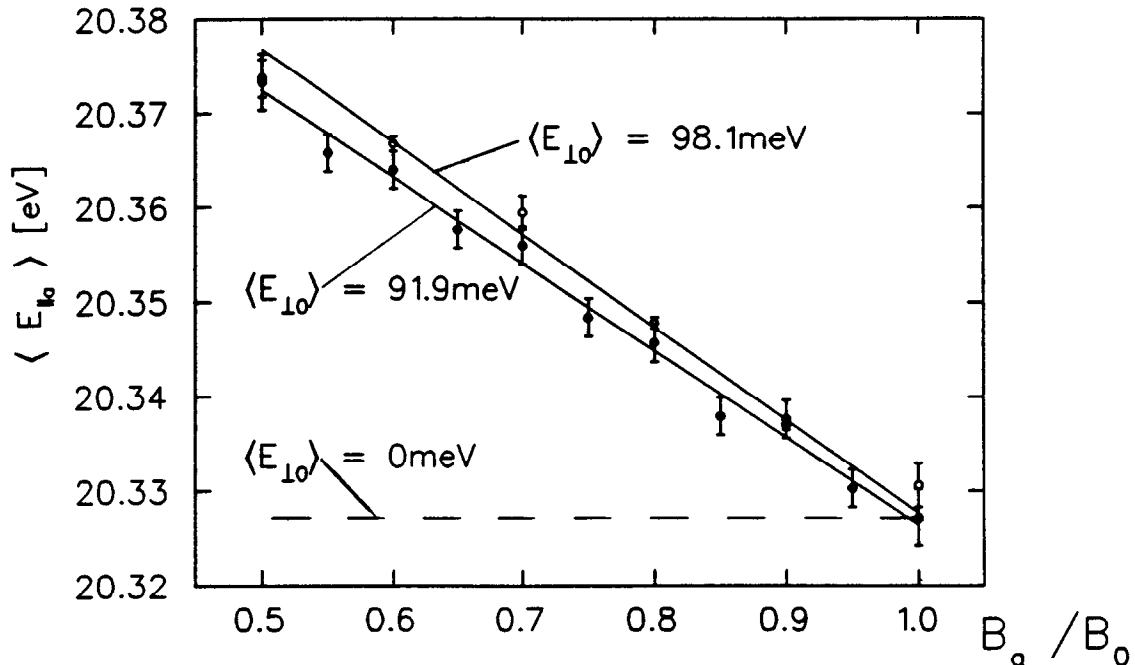


fig.5: The measured mean energy of the electron beam  $\langle E_{\parallel a} \rangle$  is plotted as a function of  $B_a / B_0$  for two different  $T_{cath}$  of the thermocathode. The broken curve would be obtained for  $\langle E_{\perp 0} \rangle = 0 \text{ meV}$ .

#### REFERENCES

- [1] P. Krause, D. Habs, D.Schwalm, S. Pastuszka, A. Wolf and S. Zwickler, to be submitted to Phys. Rev. E
- [2] V. L. Alperovich, Yu. B. Bolkhovityanov, A. G. Paulish and A. S. Terekhov, subm. to NIM
- [3] R. Calabrese, V. Guidi, G. Lamanna and L. Tecchio, J. Phys.3 France 2, 473 (1992).
- [4] D. Habs, J. Kramp, P. Krause, K. Matl, R. Neumann, and D. Schwalm, Physica Scripta T22, 269 (1988).
- [5] P.T.Kirstein, G.S.Kino, W.E.Waters, Space charge flow, (Mc Graw Hill), New York, 269, (1967)
- [6] M.G.Burt and J.C.Inkson J.Phys.D9 43 (1976)
- [7] R.L. Bell, Negative Electron Affinity Devices, Clarendon, Oxford (1973)
- [8] J.Kirschner, H.P.Oepen, H.Ibach, Appl.Phys.A 30 177 (1983)
- [9] H.-J.Drouhin, C.Hermann, G.Lampel, Phys.Rev.B, 31/6 3859 (1985)
- [10] C.A.Sanford and N.C. Mac Donald J. Vac.Sci.Technol. B8(6) 1853 (1990)
- [11] D.C.Rodway and M.B.Allenson, J. Phys. D: Appl. Phys. 19 1353 (1986)
- [12] D.J. Bradley et al., Jou. App. Phys. 10 (1977)
- [13] T.M. O'Neil and P.G. Hjorth, Phys. Fluids 28 (1985) 3241

## List of Workshop Participants

Verle Aebi  
Intevac  
6011 California Avenue  
Palo Alto, CA 94304

Ray Alley  
Mail Stop 66  
Stanford Linear Accelerator Center  
P.O. Box 4349  
Stanford, CVA 94309  
Office: (415) 926-3668  
FAX: (415) 926-2407  
EMAIL: RAZAR@SLACVM

Hideki Aoyagi  
Nagoya University  
Department of Physics  
Furo-cho, Chikusa-ku  
Nagoya-shi 464, Japan  
EMAIL: AOYAGI@JPNKEKVX

K. Aulenbacher  
Universität Mainz  
Institut für Physik  
Staudinger Weg 7  
Postfach 3988, D-6500 Mainz 1  
Germany  
Office: 0049-6131-394384  
FAX: 0049-6131-392991  
EMAIL: AULENBACHER@VIPMZA.PHYSIK.UNI-MAINZ.DE

Günter Baum  
Universität Beilfeld  
Fakulät für Physik, P.O. Box 100131  
D-33501 Beilfeld 1, Germany  
Office: (0)521 106-5383  
FAX: (0)521 1-5-2959  
EMAIL: BAUM@PHYSF.UNI-BIELFELD.DE

F. Ciccacci  
Politecnico di Milano  
Istituto de Fisica  
Piazza Leonardo da Vinci 32  
1-20133 Milano, Italy  
Office: 39-2-23996179  
FAX: 39-2-23996126  
EMAIL: 39075::2FISIC5

Jym Clendenin  
Stanford Linear Accelerator Center  
Mail Stop 66  
P.O. Box 4349  
Stanford, CA 94309  
Office: (415) 926-2962  
FAX: (415) 926-2407  
EMAIL: CLEN@SLAC.STANFORD.EDU

Kenneth Costello  
Intevac  
601 California Avenue  
Palo Alto, CA 94304

Franz-Josef Decker  
Stanford Linear Accelerator Center  
Mail Stop 66  
P.O. Box 4349  
Stanford, CA 94039  
Office: (415) 926-3606  
FAX: (415) 926-2407  
EMAIL: DECKER@SLAC.STANFORD.EDU

Stan Ecklund  
Stanford Linear Accelerator Center  
Mail Stop 66  
P.O. Box 4349  
Stanford, CA 94309  
Office: (415) 926-3182  
FAX: (415) 926-2407  
EMAIL: ECKLUND@SLAC.STANFORD.EDU

Manouchehr Farkhondeh  
MIT-Bates Linear Accelerator Center  
P.O. Box 846  
Middleton, MA 01949  
Office: (617) 245-6600  
FAX: (617) 245-0901  
EMAIL: MANOUCH@MITBATES

Josef Frisch  
Stanford Liner Accelerator Center  
Mail Stop 66  
P.O. Box 4349  
Stanford, CA 94309  
Office: (415) 926-4005  
FAX: (415) 926-2407  
EMAIL: FRISCH@SLACVM

Edward Garwin  
Stanford Linear Accelerator Center  
Mail Stop 72  
P.O. Box 4349  
Stanford, CA 94309  
Office: (415) 926-2415  
FAX: 926-2395  
EMAIL: GARWIN@SLAC.STANFORD.EDU

Timothy Gay  
University of Nebraska  
Behlen Laboratory  
Lincoln, NE 68588  
Office: (402) 472-2770  
FAX: (402) 472-2879

V. Guidi  
Univ. of Ferrara  
Via Paradiso, 12  
44100 Ferrara  
Italy  
Office: 39-532-781865  
FAX: 39-49-641925  
EMAIL: GUIDI@FERRARA.INFN.IT

William Hermannsfelt  
Stanford Linear Accelerator Center  
Mail Stop 66  
P.O. Box 4349  
Stanford, CA 94309  
Office: (415) 926-3342  
FAX: (415) 926-4999  
EMAIL: WBHAP@SLAC.STANFORD.EDU

Alberto Herrera-Gómez  
McCullough 228, MC 4055  
Stanford University  
Stanford, CA 94305



Robert Kirby  
Stanford Linear Accelerator Center  
Mail Stop 66  
P.O. Box 4349  
Stanford, CA 94309  
Office: (415) 926-2795  
EMAIL: REK@SLAC.STANFORD.EDU

Lowell Klaisner  
Stanford Linear Accelerator Center  
Mail Stop 17  
P.O. Box 4349  
Stanford, CA 94309  
Office: (415) 926-2726  
FAX: (415) 926-4999  
EMAIL: KLAISNER@SLACVM

Artem Kulikov  
Stanford Linear Accelerator Center  
Mail Stop 66  
P.O. Box 4349  
Stanford, CA 94309  
Office: (415) 926-2071  
FAX: (415) 926-2407  
EMAIL: KART@SLACVM

Georges Lampel  
Ecole Polytechnique  
Laboratoire de Physique de la Matiere Condensee  
91128 Palaiseau, France  
Office: 33-1-69334659  
FAX: 33-1-69333004

Robin Mair  
Stanford Linear Accelerator Center  
Mail Stop 94  
P.O. Box 4349  
Stanford, CA 94309  
Office: (415) 926-3373  
EMAIL: MAIR@SLACVM

Yuri A. Mamaev  
Division of Experimental Physics  
St. Petersburg Technical University  
Polytechnicheskaya, str. 29  
195251 St. Petersburg, Russia  
Office: (812) 552 77 93  
FAX: (812) 5526086  
EMAIL: YAVICH@MOCVD.PTI.SPB.SU

Takashi Maruyama  
Stanford Linear Accelerator Center  
Mail Stop 78  
P.O. Box 4349  
Stanford, CA 94309  
Office: (415) 926-3398  
EMAIL: TVM@SLAC.STANFORD.EDU

Roger Miller  
Stanford Linear Accelerator Center  
Mail Stop 26  
P.O. Box 4349  
Stanford, CA 94309  
Office: (415) 926-4457  
FAX: (415) 926-4999  
EMAIL: RHM@SLACVM

Greg Mulhollan  
Stanford Linear Accelerator Center  
Mail Stop 66  
Stanford, CA 94309  
Office: (415) 926-4889  
FAX: (415) 926-2407  
EMAIL: MULHOLLA@SLAC.STANFORD.EDU

Tsutomu Nakanishi  
Nagoya University  
Faculty of Science, Chikusa-ku  
Nagoya 464-01, Japan  
OFFICE: 81 52 782 1967  
FAX: 81 52 783 8365  
EMAIL: NAKANISI@JPNKEK VX

Alan Odian  
Stanford Linear Accelerator Center  
Mail Stop 65  
P.O. Box 4349  
Stanford, CA 94309  
Office: (415) 926-3459  
EMAIL: ODIAN@SLAC.STANFORD.EDU

N. Papadakis  
NIKHEF-K  
Postbus 41882  
1009 DB Amsterdam  
The Netherlands  
Office: 31-20-592-2089  
FAX: 31-20-592-2165  
EMAIL: PAPAD@NIKHEF.NL

Daniel Pierce  
NIST  
Metrology B-206  
Gaithersburg, MD 20899  
Office: (301) 975-3711  
FAX: (301) 926-2746  
EMAIL: PIERCE@EPG.NIST.GOV

Helmut Poppa  
IBM Research Division  
Almaden Research Center  
650 Harry Road  
San Jose, CA 95120-6099  
Office: (408) 927-2446  
FAX: (418) 927-3311  
EMAIL: POPPA@ALMADEN

Richard Prepost  
Department of Physics, UW  
1150 University Avenue  
Madison, WI 53706

Charles Prescott  
Stanford Linear Accelerator Center  
Mail Stop 78  
P.O. Box 4349  
Stanford, CA 94309  
Office: (415) 926-2856  
EMAIL: PRESCOTT@SLAC.STANFORD.EDU

E. Reichert  
Universität Mainz  
Institut für Physik  
Staudinger Weg 7  
Postfach 3988, D-6500 Mainz 1  
Germany  
Office: (49) 6131-392729  
FAX: (49) 6131-392991  
EMAIL: REICHERT@VIPMZW.PHYSIK.UNI-MAINZ.DE

Marc Ross  
Stanford Linear Accelerator Center  
Mail Stop 66  
P.O. Box 4349  
Stanford, CA 94309  
Office: (415) 926-3526  
FAX: (415) 926-2407  
EMAIL: MCREC@SLACVM

Pablo Sáez  
Stanford Linear Accelerator Center  
Mail Stop 66  
P.O. Box 4349  
Stanford, CA 94309  
Office: (415) 926-3935  
FAX: (415) 926-2407  
EMAIL: PABLO@SLACVM

Rafe Schindler  
Stanford Linear Accelerator Center  
Mail Stop 96  
P.O. Box 4349  
Stanford, CA 94309  
Office: (415) 926-3450  
FAX: (415) 926-2923  
EMAIL: RAFE@SLACVM

David Schultz  
Stanford Linear Accelerator Center  
Mail Stop 66  
P.O. Box 4349  
Stanford, CA 94309  
Office: (415) 926-2459  
FAX: (415) 926-2407  
EMAIL: DCS@SLACVM

Richard Sheffield  
Los Alamos National Laboratory  
MS\_H825  
Los Alamos, NM 87545  
Office: (505) 667-1237  
FAX: (505) 667-0919  
EMAIL: SHEFF@ATDIV.LANL.GOV

Zhixun Shen  
McCullough 232, MC 4005  
Stanford University  
Stanford, CA 94305  
Office: (415) 723-8254  
FAX: (415) 723-4659  
EMAIL: SHEN@SIERRA

John Sheppard  
Stanford Linear Accelerator Center  
Mail Stop 66  
Stanford, CA 94309  
Office: (415) 926-3498  
FAX: (415) 926-2407  
EMAIL: MAURA@SLACVM

H. Siegmann  
ETH Hönggerberg  
Laboratorium für Festkörperphysik  
CH-8093 Zurich, Switzerland

Charles Sinclair  
CEBAF  
12000 Jefferson Avenue  
Newport News, VA 23606  
Office: (804) 249-7679  
FAX: (804) 249-7363  
EMAIL: SINCLAIR@CEBAFVAX

Joe Sodja  
Stanford Linear Accelerator  
Mail Stop 55  
P.O. Box 4349  
Stanford, CA 94309  
Office: (415) 926-2390  
EMAIL: JOESOD@SLACVM.SLAC.STANFORD.EDU

William Spicer  
McCullough 228, MC 4055  
Stanford University  
Stanford, CA 94305  
Office: (415) 723-4643  
FAX: (415) 723-4659  
EMAIL: SPICER@SIERRA.STANFORD.EDU

Huan Tang  
Stanford Linear Accelerator Center  
Mail Stop 66  
P.O. Box 4349  
Stanford, CA 94309  
Office: (415) 926-2487  
FAX: (415) 926-2407  
EMAIL: TANG@SLACVM

Alexander Terekhov  
Institute of Semiconductor Physics  
13 Lavtenjva Pr.  
630090 Novosibirsk  
Russia  
Office: 3832 356874  
FAX: 3832-357-502

Eugeni Tsentalovich  
MIT-Bates Linear Accelerator Center  
Middleton, MA 01949-2846  
Office: (617) 245-6600  
FAX: (617) 245-0901  
EMAIL: TSENTALOVICH@MAX.MIT.EDU

Jim Turner  
Stanford Linear Accelerator Center  
Mail Stop 39  
P.O. Box 4349  
Stanford, CA 94039  
Office: 926-3619  
EMAIL: JTURNER@SLAC.STANFORD.EDU

Stan Vernon  
SPIRE Corp.  
1 Patriots Park  
Bedford, MA 01730  
Office: (617) 275-6000  
FAX: (617) 275-7470

Dian Yeremain  
Stanford Linear Accelerator Center  
Mail Stop 26  
P.O. Box 4349  
Stanford, CA 94309  
Office: (415) 926-4444  
EMAIL: ANAHID@SLACVM

M. Yoshioka  
KEK  
Accelerator Division, Oho 1-1, Tsukuba  
Ibaraki 305  
Japan  
EMAIL: YOSHIOKA@JPNKEKVX

G. Zapalac  
Stanford Linear Accelerator Center  
Mail Stop 94  
P.O. Box 4349  
Stanford, CA 94309  
Office: (415) 926-3368

Max Zolotarev  
Stanford Linear Accelerator Center  
Mail Stop 55  
P.O. Box 4349  
Stanford, CA 94309  
Office: (415) 926-4670  
EMAIL: MAXZ@SLAC.STANFORD.EDU

Sebastian Zwickler  
Max-Planck Institut für Kernphysik  
Universität Heidelberg  
Postfach 103980, D-69029 Heidelberg  
Germany  
Office: 06221/516504  
FAX: 06221/516540  
EMAIL: ZWICK@DXNHD1.MPI-HD.MPG.DE